Rôle de l'interaction entre PIEZO1 et KCNN4 dans la pathophysiologie érythrocytaire

Benoit Allegrini

UNIVERSITÉ CÔTE D'AZUR | ÉCOLE DOCTORALE SCIENCES DE LA VIE ET DE LA SANTÉ

THÈSE DE DOCTORAT

Rôle de l'interaction entre PIEZO1 et KCNN4 dans la physiopathologie érythrocytaire

Benoit ALLEGRINI

Institut de Biologie de Valrose – Equipe Canaux Ioniques et Cancers

Présentée en vue de l'obtention du grade de docteur en Sciences de la vie et de la santé
d'Université Côte d'Azur
Dirigée par : Hélène Guizouarn
Soutenue le : 27 septembre 2023

Devant le jury, composé de :
Wassim El Nemer, DR, Etablissement Français du sang : Rapporteur
Stéphane Egée, PR, Sorbonne Université : Rapporteur
Sébastien Roger, PR, Université de Tours : Examinateur
Véronique Picard, MD-PU, Hôpital Bicêtre : Examinatrice
Isabelle Mouro-Chanteloup, CR, Université Paris Cité : Examinatrice
Hélène Guizouarn, DR, Université côte d'azur, Directrice de thèse

anr

sfh Société Française d'Hématologie

Rôle de l'interaction entre PIEZO1 et KCNN4 dans la physiopathologie érythrocytaire

Jury :

Wassim El Nemer, DR, Etablissement Français du sang : Rapporteur.

Stéphane Egée, PR, Sorbonne Université : Rapporteur.

Sébastien Roger, PR, Université de Tours : Examinateur.

Véronique Picard, MD-PU, Hôpital Bicêtre : Examinatrice.

Isabelle Mouro-Chanteloup, CR-Inserm, Université Paris Cité : Examinatrice.

Hélène Guizouarn, DR, Université côte d'azur : Directrice de thèse.

Rôle de l'interaction entre PIEZO1 et KCNN4 dans la physiopathologie érythrocytaire

Résumé (Français)

Le globule rouge (GR) est la cellule la plus abondante du corps humain et assure le transport d'O_2 et de CO_2 tout en étant dépourvue de noyau et d'organelles. Durant ses 120 jours de vie le GR effectue plus de 200 000 passages dans la circulation, lors desquels il est soumis à d'intenses stress physiques, osmotiques et oxydatifs. La moindre défaillance face à ces stress peut le fragiliser et raccourcir son espérance de vie comme c'est le cas dans la Xérocytose Héréditaire (XH). La XH est une anémie hémolytique autosomique dominante qui touche 1/50 000 personnes. Elle est due à une altération de la perméabilité ionique et hydrique du GR, entraînant une hémolyse précoce par déshydratation. Cette maladie est causée génétiquement par des mutations gain de fonction sur deux canaux ioniques : PIEZO1 ou KCNN4, qui sont couplés fonctionnellement. PIEZO1 est un canal mécanosensible cationique non sélectif dont la découverte en 2010 est à l'origine du prix Nobel de médecine et physiologie en 2021. KCNN4 est un canal potassique sensible au calcium, responsable de l'effet « Gardos » découvert dans les années 1950. Fonctionnellement, l'activation de PIEZO1 induit une entrée de calcium dans le GR qui stimule KCNN4 dont l'ouverture permet au K^+ de sortir. Cette sortie de K^+ est accompagnée de Cl^- et d'eau osmotiquement liée. Il est donc proposé que la XH résulte d'une suractivation de PIEZO1 ou KCNN4 due aux mutations gain de fonction qui provoque une perte de KCl et d'eau ne pouvant pas être compensées car le GR humain est dépourvu de mécanisme de régulation de volume. Néanmoins, nous avons observé que la plupart des mutations gain de fonction sur KCNN4, qui est l'effecteur final de la déshydratation, ne sont pas associées à une déshydratation des GR contrairement aux mutations sur PIEZO1. C'est un paradoxe qui traduit la forte hétérogénéité phénotypique de la XH rendant le diagnostic long et difficile. Ce dernier repose bien souvent sur la nécessité de caractériser les mutations en laboratoire permettant de confirmer ou d'infirmer la pathogénicité d'une mutation. Mes travaux de thèse s'inscrivent dans ce contexte et visent à corréler le changement de fonctionnement des canaux PIEZO1 et KCNN4 induit par les mutations et le phénotype érythrocytaire des patients atteints d'anémie hémolytique héréditaire. En collaboration avec des cliniciens nous avons caractérisé de nombreuses nouvelles mutations portées par PIEZO1 ou KCNN4 dans des suspicions de XH. Nos résultats confirment la grande disparité de phénotype observée entre les mutations sur PIEZO1 ou KCNN4. Les méthodes d'analyse mises au point se sont avérées indispensables pour caractériser le phénotype des mutations à des fins diagnostic. Dans un contexte plus fondamental mes travaux ont permis de mieux comprendre les

mécanismes qui sous-tendent le couplage fonctionnel entre PIEZO1 et KCNN4. Nous avons mis en évidence un nouveau mécanisme de régulation du canal KCNN4 par la pompe calcium ATP dépendante, PMCA. Ce mécanisme permet un découplage entre l'influx de Ca^{2+} dans le GR et l'activation du canal KCNN4 et donc la déshydratation. C'est une découverte majeure dans le contrôle de l'homéostasie hydrique des GR et une piste pour le traitement de la XH.

Mots clés : PIEZO1, KCNN4, Erythrocyte, Anémie, Electrophysiologie.

Role of PIEZO1-KCNN4 interaction in erythrocyte pathophysiology

Abstract (English)

The red blood cell (RBC) is the most abundant cell in the human body and is responsible for oxygen et carbon dioxide transport while it is lacking nucleus and organelles. During its 120-day lifespan, the RBC undergoes over 200,000 passages through the circulation, subjecting it to intense physical, osmotic, and oxidative stresses. Any dysfunction in front of these stresses can weaken the RBC and shorten its lifespan, as seen in Hereditary Xerocytosis (HX), a rare autosomal dominant hemolytic anemia affecting 1 in 50,000 individuals. HX is caused by genetic gain-of-function mutations in two ion channels: PIEZO1 or KCNN4, which are functionally coupled. PIEZO1 is a non-selective cationic mechanosensitive channel discovered in 2010 leading to the Nobel Prize in Physiology and Medicine in 2021. KCNN4 is a calcium-sensitive potassium channel, responsible for the "Gardos" effect described in the 1950s. Functionally, activation of PIEZO1 allows calcium entry into the RBC, subsequently activating KCNN4, which opens and allows K^+ efflux. This K^+ efflux is accompanied by Cl^- and osmotically linked water. It is proposed that HX is caused by the overactivation of either PIEZO1 or KCNN4, due to gain-of-function mutations, leading to an uncompensated loss of KCl and water because RBC are lacking volume regulation mechanism. Surprisingly concerning KCNN4, which is the final effector of dehydration, we do not observe any water loss of patient's RBC for most of the gain of function mutations. However, we measured dehydration with most of PIEZO1 mutations. This paradox reflects the high phenotypic heterogeneity of HX, making diagnosis lengthy and challenging. Often, the diagnosis relies on the need to characterize mutations in the laboratory to confirm or refute their pathogenicity. My thesis work contributes to this context by correlating changes in PIEZO1/KCNN4 functioning and Erythrocyte phenotype from patients with hemolytic anemias. In collaboration with clinicians, we characterized numerous novel mutations on PIEZO1 or KCNN4 in suspected HX cases. Our results confirmed the significant disparity in phenotype observed between PIEZO1 and KCNN4 mutations. The combined analysis tools we used were essential for the rapid description of mutations' phenotype for diagnostic purposes. In a more fundamental context, our results helped to understand more precisely the functional coupling between PIEZO1 and KCNN4. We discovered a new mechanism of KCNN4 regulation by the ATP-dependent calcium pump, PMCA. This mechanism allows an uncoupling between Ca^{2+} influx in the RBC and the

activation of the KCNN4 and therefore dehydration. This is a major discovery in the control of RBC water homeostasis and a lead for the treatment of XH.

Key word: PIEZO1, KCNN4, Erythrocyte, Anemia, Electrophysiology.

Publications et communications associées à ces recherches :

Publications:

Rapetti-Mauss, R., Berenguier, C., Allegrini, B., & Soriani, O. (2020). Interplay between ion channels and the Wnt/β-catenin signaling pathway in cancers. *Frontiers in Pharmacology*, *11*, 525020.

Guizouarn, H., & Allegrini, B. (2020). Erythroid glucose transport in health and disease. *Pflügers Archiv-European Journal of Physiology*, *472*(9), 1371-1383.

Jakob, D., Klesen, A., Allegrini, B., Darkow, E., Aria, D., Emig, R., ... & Peyronnet, R. (2021). PIEZO1 and BKCa channels in human atrial fibroblasts: Interplay and remodelling in atrial fibrillation. *Journal of Molecular and Cellular Cardiology*, *158*, 49-62.

Yamaguchi, Y., Allegrini, B., Rapetti-Mauss, R., Picard, V., Garçon, L., Kohl, P., ... & Guizouarn, H. (2021). Hereditary Xerocytosis: Differential Behavior of PIEZO1 Mutations in the N-Terminal Extracellular Domain Between Red Blood Cells and HEK Cells. *Frontiers in Physiology*, *12*, 736585.

Allegrini, B., Jedele, S., David Nguyen, L., Mignotet, M., Rapetti-Mauss, R., Etchebest, C., ... & Guizouarn, H. (2022). New KCNN4 variants associated with anemia: stomatocytosis without erythrocyte dehydration. *Frontiers in Physiology*, *13*, 918620.

Rapetti-Mauss, R., Nigri, J., Berenguier, C., Finetti, P., Tubiana, S. S., Labrum, B., ... & Soriani, O. (2023). SK2 channels set a signalling hub bolstering CAF-triggered tumourigenic processes in pancreatic cancer. *Gut*, *72*(4), 722-735.

Lohia, R., Allegrini, B., Berry, L., Guizouarn, H., Cerdan, R., Abkarian, M., ... & Wengelnik, K. (2023). Pharmacological activation of PIEZO1 in human red blood cells prevents Plasmodium falciparum invasion. *Cellular and Molecular Life Sciences*, *80*(5), 124.

Allegrini, B., NGuyen, L. D., Mignotet, M., Etchebest, C., Fenneteau, O., Platon, J., ... & Da Costa, L. (2023). Next generation sequencing (NGS) interest in deciphering erythrocyte molecular defects' association in red cell disorders: Clinical and erythrocyte phenotypes of patients with mutations inheritance in PIEZO1, Spectrin ß1, RhAG and SLC4A1. *Blood Cells, Molecules, and Diseases*, 102780.

Communications:

Juin 2023, Gordon Research Conference: Red Cells, Salve Regina University Newport, Rhode Island, United States
Presentation d'un poster: « **Control of KCNN4 activity by the calcium pump PMCA4b: a regulatory mechanism to uncouple PIEZO1 stimulation and red blood cell dehydration.** »

Mars 2023, Congres SFH 2021 : Société Française d'Hématologie, Paris
Présentation orale de 15 minutes : « **La pompe Calcium ATPase : nouveau partenaire régulateur de l'activité du canal Gardos dans les globules rouges** »

Mai 2022, Journée Ecole Doctorale de Nice, Institut de Biologie Valrose, Nice
Présentation de 15 minutes : « **Role of PIEZO1 – KCNN4 interactions in erythrocyte pathophysiology** »

Avril 2022, Congres European Red Cell Society, Gazzado Schiano, Italie
Présentation orale de 15 minutes : « **New KCNN4 mutations in herediditary anemias : Stomatocytosis without dehydration** ».

Septembre 2021, Congres SFH 2021 : Société Française d'hématologie, Paris
Présentation orale de 15 minutes : « **Caractérisation fonctionnelle de mutations N-terminales du canal PIEZO1 dans les globules rouges et dans les cellules HEK293T** »

Tables des matières

Table des matières

Abréviations

2,3DPG	2,3 diphosphoglycérate
AC	Adénylate cyclase
ATP	Adénosine triphosphate
BAPTA	1,2-bis(2-aminophénoxy) éthane-N,N,N',N'-tétraacétique
BE	Erythroblaste basophile
BFD	Blackfan Diamonds
BFU	Bursting forming unit
BME	β-mercaptoéthanol
BMP	Bone morphogenetic proteins
CAF	Cancer associated fibroblast (Fibroblastes associés au cancer)
CCMH	Concentration corpusculaire moyenne en hémoglobine
CFTR	Cystic Fibrosis Transmembrane Conductance Regulator
CFU	Colony forming unit
CLC	Chloride Channel 2
CME	Cryo Microscopie Electronique
DAPI	4',6-diamidino-2-phénylindole
DEL	Délétion
DHA	Dehydroascorbic Acid (acide déhydroascorbique)
DHS	Dehydrated Stomatocytosis (Stomatocytose Déshydratée)
DMEM	Dulbecco's Modified Eagle's Medium
DO	Densité Optique
EGTA	Éthylène glycol-bis(β-aminoéthyléther) -N,N,N',N'-tétraacétique

EPO	Erythropoïétine
E_R	Potentiel de membrane
E_X	Potentiel d'équilibre d'un ion (X)
FEM	Force Electro-Motrice
FSC	Forward Scatter
GHK	Goldmann Hodgkin Katz
GPC	Glycophorine C
Hb	Hémoglobine
HBA	Hémoglobine A
HBB	Hémoglobine B
HEK	Human Embryonic Kidney 293 (cellules de rein embryonnaire humain)
HEPES	4-(2-hydroxyéthyl) pipérazine-1-éthane-sulfonique
HRP	Horseradish peroxydase
HSC	Hematopoietic stem cell (Cellule souche hématopoïétique)
HSPC	High Speed Pressure Clamp
JH	Jonction Horizontale
JV	Jonction verticale
KO	Knock-out (invalidation génétique)
LIS	Low Ionic Strength (Faible force ionique)
LPA	Lysophosphatydic acid (acide lysophosphatidique)
MAGUK	Membrane-Associated Guanylate Kinase
MB	Milieu de blocage
MCH	Mean Corpuscular Hemoglobin (Hémoglobine corpusculaire moyenne)
MCV	Mean Corpuscular volume (Volume corpusculaire moyen)

ML Milieu de lavage

NADH Nicotinamide Adénine Dinucléotide

NGS Next Generation sequencing

NMDAR N-Méthyl-D-Aspartate Receptor

NO Nitric Oxyd

NSCC Non selective cation channel (Canal cationique non sélectif)

NSVDC Non-selective voltage dependant Channel (Canal voltage dépendant non sélectif)

OE Overexpressed (surexpression)

PBS Phosphate-buffered saline

PCE Erythroblaste polychromatique

PDZ PSD-95, Dlg, ZO-1 (domaine d'interaction protéique initialement découvert entre ces 3 protéines)

PE Proérythroblaste

PFA Paraformaldéhyde

P_K Perméabilité potassique

PLA Proximity Ligation Assay

PMCA Plasma Membrane Calcium ATPase (Pompe calcique membrane ATP dépendante

PPP Pentose Phosphate Pathway (voie des pentoses phosphates)

PS Phosphatidylsérine

PVDF Polyvinylidene Fluoride (polyvinylidène difluoride)

PX Perméabilité ionique

RBC Red Blood cell

RO Résistance Osmotique

RT Room temperature (température ambiante)

RVD Regulatory Volume Decrease

RVI Regulatory Volume Increase

SDS Sodium Dodecyl Sulfate

SERCA Sarco-Endoplasmique Réticulum ATPase (pompe calcique ATP dépendante du réticulum endoplasmique)

SK Small Conductance Calcium activated potassium channel (Canaux potassique de faible conductance, activés par le calcium)

SM Sphingomyéline

TBS Tris-Buffered Saline

TM Transmembranaire

TRP Transcient Receptor Potential

VCM Volume Corpusculaire Moyen

VDAC Voltage dependant anion channel (Canal anionique voltage dépendant

WB Western Blot

WT Wild type (sauvage)

XH or HX Hereditary Xerocytosis (Xérocytose Héréditaire)

Liste des figures

Liste des tables

Liste des équations

Introduction

1. Érythropoïèse et vieillissement du Globule rouge humain.

1.1. Erythropoïèse

L'Erythropoïèse est le processus de production du Globule Rouge (GR). Il débute dès l'embryogenèse (vague primitive) dans des îlots sanguins du sac vitellin, afin de permettre la croissance rapide des tissus puis plus tardivement dans le foie et la rate. L'Erythropoïèse à l'âge adulte (vague définitive) se déroule dans la moelle osseuse pour 95% du processus (et thymus (Albert et al., 1966)) à partir de cellules souches hématopoïétiques (HSCs). Ces HSCs donnent naissance à toutes les cellules de la lignée Myéloïde/Érythroïde (GR, plaquettes, monocytes) et Lymphoïde (lymphocytes), c'est ce qu'on appelle l'Hématopoïèse. C'est un processus complexe, englobant l'Erythropoïèse, dont l'orientation vers un type cellulaire est finement contrôlé génétiquement (Jagannathan-Bogdan and Zon, 2013). L'Érythropoïèse, propre à la lignée Erythroïde, se déroule dans des îlots Érythroblastiques, unités fonctionnelles de la moelle osseuse (Bessis, 1958). Ce processus passe par de nombreux stades très bien caractérisés au niveau cellulaire (Figure 1) que l'on distingue en 2 phases principales : la phase initiatrice et la phase terminale. La phase initiatrice concerne la différenciation des HSC en BFU-E (Burst forming unit Erythroblast) puis en CFU-E (colony-forming unit Erythroblast) (Elliott et al., 2008) et enfin en P_E (Proérythroblaste) (Hattangadi et al., 2011) marquant le début de la phase terminale. Lors de cette phase, le P_E va se différencier en B_E (Erythroblaste Basophile), PC_E (Erythroblaste Polychromatique) et O_E (Erythroblaste Orthochromatique). Du P_E jusqu'au stade O_E, la taille de la cellule diminue et la chromatine se condense. Le stade B_E constitue un tournant décisif dans la différenciation érythrocytaire avec notamment un remodelage protéique important (Gautier et al., 2016). C'est d'ailleurs à partir de ce stade que l'on voit apparaître l'Hémoglobine (Hb). Dès le stade O_E le futur GR va subir une énucléation, en parallèle de son passage dans la circulation, qui se déroule en 3 étapes (Mei et al., 2021): (1) polarisation du noyau à une extrémité de la cellule, (2) expulsion du noyau sous forme de pyrénocyte, (3) détachement de la cellule résultante, le Réticulocyte. Cette énucléation est dépendante de la présence de Ca^{2+} extracellulaire (Wölwer et al., 2016) et se déroule à l'aide de la formation d'un anneau contractile d'actine (Ji et al., 2011). Le Réticulocyte nouvellement formé, dans la circulation périphérique, va subir un remodelage important de ses protéines (Gautier et al., 2018) et lipides membranaires ainsi qu'une expulsion de ses organelles pour aboutir à un GR mature. Dans les îlots Érythroblastiques, les précurseurs érythroïdes interagissent et communiquent avec les macrophages et la matrice extracellulaire environnante (Chasis and Mohandas, 2008). Les macrophages présents sont extrêmement importants dans le processus d'Érythropoïèse puisqu'ils permettent la phagocytose du pyrénocyte en reconnaissant

l'exposition de la phosphatidylsérine (PS) (Yoshida et al., 2005) et fourniraient le fer et l'hème dans la synthèse d'Hb (Soares and Hamza, 2016).

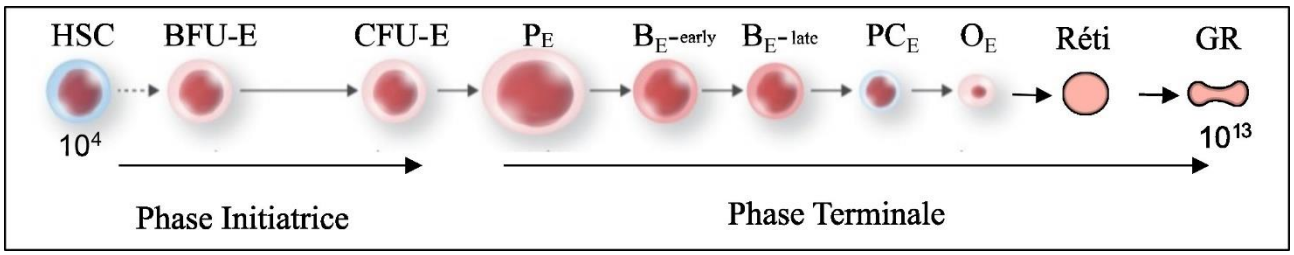

Figure 1 : Schéma représentatif de l'Erythropoïèse.

Adaptée de (Narla and Mohandas, 2020): Schéma de l'Érythropoïèse avec les différents stades cellulaires pendant la phase initiatrice et la phase terminale. Le nombre de HSC et GR est la quantité totale estimée d'un individu mâle de 70 kg mesurant 1m70 (Cosgrove et al., 2021).

Environ 5 jours s'écoulent entre la phase initiatrice et le stade de GR mature. La grande quantité de HSCs permet une production d'environ 2 millions de GR chaque seconde, renouvelant 1% de nos GRs chaque jour. Tout ce processus d'Erythropoïèse vise à maintenir une grande quantité de GR dans la circulation ce qui fait de cette cellule la plus abondante du corps ($2{,}63 \times 10^{13}$ GR) (Bianconi et al., 2013; Cosgrove et al., 2021). Il existe un équilibre permanent entre la production et la destruction de GR, avec un intervalle d'environ 120 jours entre ces deux processus. Durant sa vie, le GR va subir de nombreux stress physiques, chimiques et oxydatifs mettant à l'épreuve sa résistance. Tous ces stress agissent en quelque sorte comme une alarme de fin de vie permettant le retrait des GR vieillissants.

1.2. Vieillissement

L'absence de synthèse protéique du GR le rend vulnérable aux dommages accumulés sur le long terme affectant les protéines de la membrane, du cytosquelette ou encore de la machinerie enzymatique. Bien qu'il compense cela par sa résistance aux stress physiques, oxydatifs et chimiques, le vieillissement est inévitable. Les défauts de résistance surviennent naturellement au cours de la vie du GR. Le déclin de l'activité des transporteurs importants pour l'homéostasie du volume couplé à la baisse de production d'ATP rendent le GR plus fragile et moins apte à assurer sa fonction (Lew and Tiffert, 2017). En effet, il a été observé que la quantité d'ATP mesurée dans les GR âgés pouvait être diminuée de 40%. La conséquence la plus importante concerne le déclin d'activité des pompes ioniques ATP dépendantes, la Na^+/K^+ ATPase et la pompe calcique (PMCA). Cela va altérer l'homéostasie volumique du GR et modifier ses propriétés rhéologiques, c'est-à-dire sa capacité à circuler dans le sang. La PMCA étant responsable de la régulation du Ca^{2+} intracellulaire, une diminution de son activité provoque une augmentation de la concentration intracellulaire de ce cation

divalent ce qui enclenche progressivement une multitude de mécanismes de sénescence aboutissant au retrait de la circulation du GR vieillissant. Il existe dans la circulation une forte hétérogénéité de population de GR. Les GR les plus vieux étant retrouvés dans la fraction la plus dense. Ceci s'explique par le fait que le vieillissement induit une augmentation de la $[Ca^{2+}]_i$ qui entraîne la déshydratation du GR. De plus, l'augmentation de la $[Ca^{2+}]_i$ induit l'activation de caspases calcium sensibles, l'activation de TMEM16F, une scramblase présente dans le GR humain qui permet l'exposition de la PS au feuillet externe de la membrane plasmique. Cette exposition serait importante pour la reconnaissance des GR par les cellules immunitaires et leur destruction. Cependant, l'exposition de la PS suite à une augmentation de $[Ca^{2+}]_i$ reste sujette à débat car les deux ne semblent pas être directement corrélés (Wesseling 2016).

2. Propriétés du Globule rouge humain

2.1. Transport de gaz

La fonction principale du GR est de transporter l'O_2 et une partie du CO_2 grâce à l'hémoglobine qui constitue 97.5% de sa masse protéique. L'Hb est une protéine tétramérique composée de deux chaînes alpha et deux chaînes bêta. Chaque monomère comporte un Hème dont l'atome de fer logé en son centre sert de fixateur pour l'O_2. La fixation de l'O_2 et CO_2 est régulée par deux effets opposés : (1) l'effet Bohr qui induit la libération de l'O_2 fixé sur l'Hb et (2) l'effet Haldane qui induit la libération du CO_2 de l'Hb (Figure 2). Les effets Bohr et Haldane sont favorisés par une augmentation de la pCO_2 et pO_2 respectivement. L'augmentation de la pCO_2, dans les tissus périphériques, induit indirectement la formation de $HCO3^- + H^+$ via l'Anhydrase Carbonique (AC) ce qui provoque une diminution du pH, diminuant l'affinité de l'Hb pour l'O_2.

2.2. Echange $Cl^-/HCO3^-$ et régulation du pH.

La bande 3 (SLC4A1, AE1: Echangeur anionique) est la protéine membranaire la plus abondante du GR avec ~1,2 million de copies (Bryk and Wiśniewski, 2017; Fairbanks et al., 1971). C'est une protéine codée par le gène SLC4A1 de 911 aa (chez l'humain) répartis en 2 domaines principaux: (1) domaine N-terminal (0-360) dont les interactions avec d'autres protéines maintiennent l'intégrité structurale du GR (Low, 1986). (2) Un domaine C-terminal, composé de répétitions transmembranaires, qui est dédié au transport (361-911) (Lux et al., 1989). Des défauts de fonctionnement ou de structure de la bande 3 sont à l'origine d'anémies hémolytiques et d'acidose tubulaire distale du rein, son KO chez la souris n'est pas létal (Peters et al., 1996). La bande 3 est responsable du "chloride-shift" ou phénomène Hamburger. Le CO_2, produit de la respiration, est dissous dans le sang et diffuse passivement dans le GR où l'AC l'hydrate en H_2CO_3 et inversement en fonction de la pCO_2. Le H_2CO_3 se dissocie spontanément en $HCO_3^- + H^+$ qui est transporté en dehors du GR par la bande 3 en échange de Cl^-. Ce transport permet de mettre en place un tampon bicarbonate important pour la régulation du pH sanguin (cycle de Jacob-Stewart). Le pH intracellulaire (7.2) varie en fonction du pH extracellulaire (7.3) (Hilpert et al., 1963) dû à l'échange $Cl^-/HCO3^-(+H^+)$ constant assuré par l'AE1.

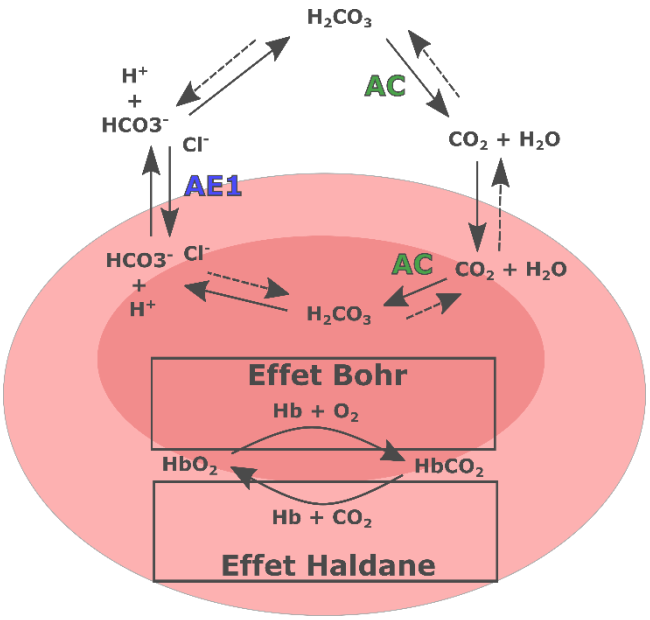

Figure 2 : Transport de gaz et régulation du pH dans le GR.

La bande 3 (AE1) transporte du $HCO3^-$ contre du Cl^- en fonction de la pO_2 et pCO_2. Dans les tissus périphériques ou la pCO_2 est forte, l'AC catalyse la réaction de $CO_2 + H_2O$ en H_2CO_3 qui se dissocie spontanément en $HCO3^- + H^+$, transportés à l'extérieur du GR. Le $HCO3^-$ est la forme de stockage d'environ 70% du CO_2, 20% est fixé à l'Hb et le reste est directement dissous dans le sang. Dans les poumons où la pO_2 est forte (et donc la pCO_2 faible), l'AC catalyse la réaction inverse en produisant du CO_2. L'Hb fixe l'O_2 (effet Haldane) ou le CO_2 (effet Bohr) en fonction des pO_2 et pCO_2.

2.3. Métabolisme

Le fonctionnement normal du globule rouge est directement lié à son métabolisme glycolytique. Il est important pour: (1) le fonctionnement des transporteurs ATP dépendants qui maintiennent le gradient électrochimique des ions, (2) faire face au stress oxydatif important que le GR subit dans la circulation pulmonaire notamment, (3) maintenir le Fer de l'Hb dans son état réduit, ferreux et (4) garder l'asymétrie phospholipidique de la membrane plasmique (van Wijk and van Solinge, 2005). Le Glucose (Glc) utilisé pour la Glycolyse entre dans le GR suivant son gradient de concentration par le transporteur GLUT1 (SLC2A1) (Kasahara and Hinkle, 1977) qui transporte également l'acide déhydroascorbique (DHA) (Montel-Hagen et al., 2007). Le DHA est le précurseur de la Vitamine C qui joue un rôle d'anti-oxydant (Rumsey et al., 1997; Vera et al., 1993). Le Glc entrant, est immédiatement pris en charge par la glucose-6-phosphatase en consommant un ATP pour produire un Glucose-6-Phosphate (G6P). 7% du G6P ainsi produit alimente la voie pentose phosphate (voie PPP) (Delgado et al., 2004) par le biais de la G6P déshydrogénase (G6PD). La voie PPP est régulée par l'oxygénation, avec une activité plus faible en conditions désoxygénées et plus forte en conditions oxygénées (Messana et al., 1996). Un mécanisme expliquant cette régulation provient de la bande 3,

protéine membranaire, qui est la base d'un complexe métabolique. En fixant des enzymes de la glycolyse: phosphofructokinase, aldolase et G3PD la bande 3 diminue leur activité en présence d'O_2 (Lewis et al., 2009; Low et al., 1993) favorisant ainsi l'utilisation du G6P dans la voie PPP. L'inverse est observé en condition pauvre en O_2. Une illustration de la glycolyse et de la voie PPP est disponible dans une publication incluse dans cette thèse (Guizouarn and Allegrini, 2020), p218.

Le G6P non utilisé par la voie PPP continue dans la glycolyse et permet la formation de NADH, important pour la réduction de la méthémoglobine, la production d'ATP et de 2,3 diphosphoglycérate (2,3DPG). Une des caractéristiques uniques du globule rouge concerne la prise en charge du 2,3DPG. Celui-ci entre dans le cycle Rapoport-Luebering qui représente 19% de l'utilisation totale de glucose (Puckeridge et al., 2013). La présence de la 2,3 diphosphoglycérate mutase dans le GR permet de produire continuellement du 2,3DPG à partir de 1,3 diphosphoglycérate, constituant un stock important. Le GR fait ainsi une réserve d'énergie utilisable à tout moment pour réintégrer la glycolyse avec la 2,3 diphosphoglycérate phosphatase qui transforme le 2,3 DPG en 3 phosphoglycérate. Le 2,3 DPG stocké est aussi un régulateur allostérique de l'Hb favorisant le relargage d'O_2 dans les tissus périphériques (Benesch and Benesch, 1967).

3. Structure du Globule rouge humain :

3.1. Un cytosquelette ancré à la membrane plasmique.

Le cytosquelette du GR est basé sur une architecture de spectrine et d'actine organisée en structure hexagonale (Liu et al., 1987). Les sous unités alpha et beta spectrine forment des dimères qui s'oligomérisent en tétramères de façon dynamique permettant l'adaptation au stress physique que subit le GR (Nans et al., 2011; Ursitti and Wade, 1993). Ces contraintes physiques importantes provoquent une dissociation des tétramères de spectrine en dimères, "fluidifiant" le cytosquelette (An et al., 2002). Les tétramères de spectrine sont interconnectés par des nœuds de protofilament d'actine formant des complexes jonctionnels, aussi appelées jonctions horizontales, localisées sous la membrane (Gokhin and Fowler, 2016). Les protofilaments d'actines sont constitués de monomères de beta actine qui s'organisent sous forme de double hélice (Picart and Discher, 1999). De manière similaire à ce qui est observé dans les sarcomères du muscle strié, les protofilaments sont renforcés par la tropomyosine qui se lie à son extrémité moins (-), stabilisant sa longueur (Fowler, 1996; Mohandas and Gallagher, 2008). La liaison de la spectrine et de l'actine au niveau des jonction horizontales est grandement renforcée par la protéine 4.1 (Ohanian et al., 1984) qui interagit également avec la bande 3 et la GPC (Han et al., 2000). Ceci confère une localisation tangente à la membrane de l'actine favorisée par la tropomoduline, la dématine (ou bande 4.9 (Rana et al., 1993)) et l 'adducine en permettant l'ancrage à GLUT1 (Khan et al., 2008). Le Ca^{2+} joue un rôle important dans la dynamique du cytosquelette. Par exemple, les interactions de la protéine 4.1 avec l'actine sont régulées par le Ca^{2+} via sa liaison avec la calmoduline (Takakuwa and Mohandas, 1988). L'adducine, une protéine hétérodimérique (alpha et beta) (Joshi et al., 1991) favorise d'une part la polymérisation de l'actine en se fixant à son extrémité plus (+), régulée par le Ca^{2+} (Kuhlman et al., 1996); et d'autre part, aide au recrutement de la spectrine sur l'actine (Li et al., 1998). L'augmentation de la concentration calcique intracellulaire peut ainsi avoir des répercussions importantes sur la déformabilité du GR en modulant les interactions entre ces différentes protéines.

Comme mentionné, le cytosquelette est largement ancré à la membrane plasmique (Figure 3). Ce, à l'aide de deux types de jonctions principales : les jonctions verticales (JV) (ou complexe ankyrine) et les jonctions horizontales (JH) (ou complexes jonctionnels d'actine). Ces complexes se structurent autour de l'AE1 sous forme dimérique pour les JH et tétramérique pour les JV. L'AE1 a ainsi un rôle structurant via sa partie cytosolique N-terminale (Jarolim et al., 1996). Les JV sont basées sur l'ankyrine qui interagit avec la spectrine tandis que les JH sont indépendantes de l'ankyrine.

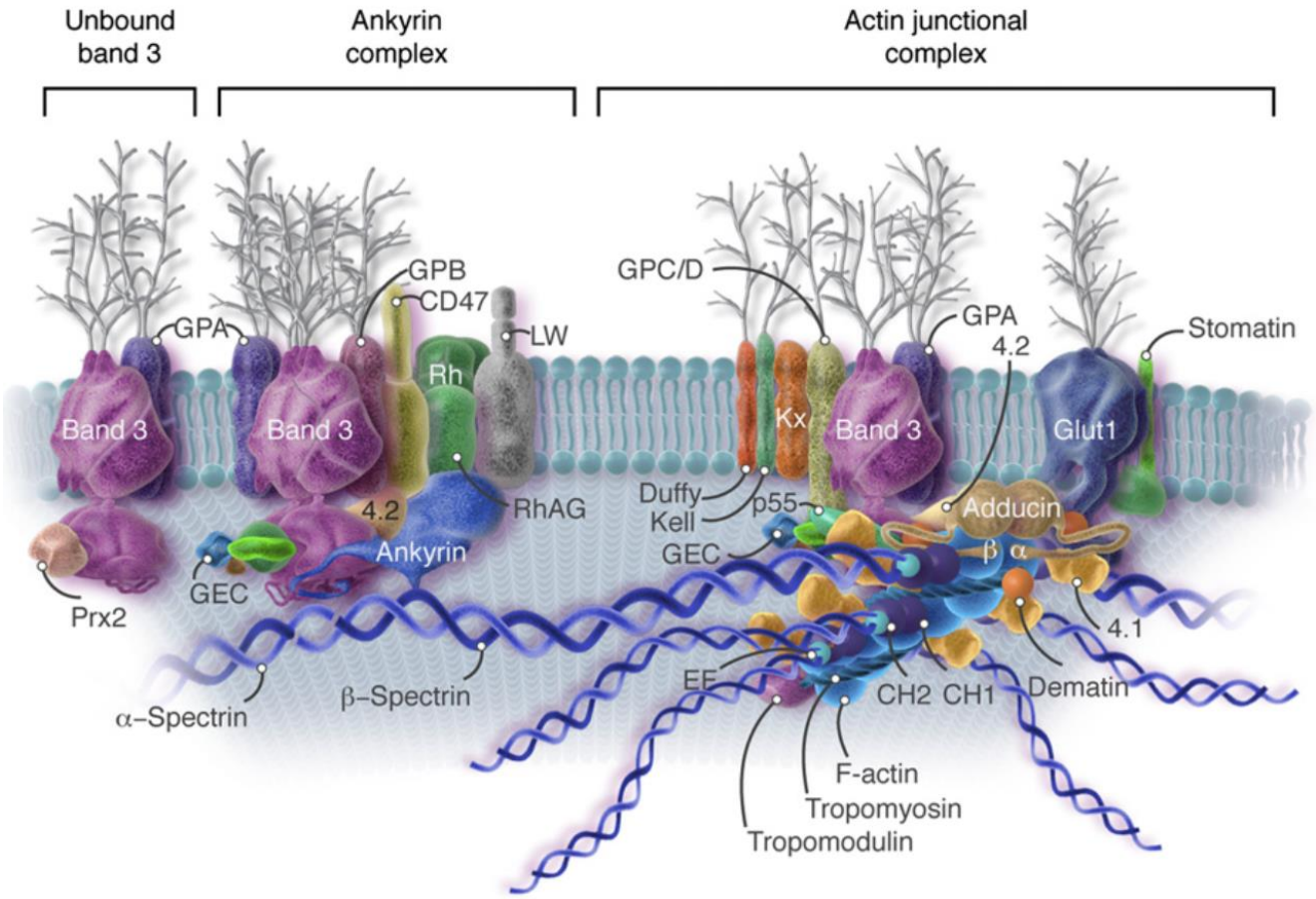

Figure 3 : Modèle de la membrane plasmique du GR.

Les deux complexes principaux sont schématisés avec le complexe Ankyrine (Ankyrin complex) qui correspond aux jonctions verticales et le complexe de jonction d'actine (Actin junctional complex) qui correspond aux jonctions horizontales (Lux, 2016).

3.2. Composition lipidique

La composition lipidique de la membrane plasmique du GR est fondamentale pour sa résistance et son élasticité. Les lipides sont des molécules amphipathiques qui structurent la membrane et s'organisent sous forme de bicouche, avec une couche externe et une couche interne. Les queues hydrophobes des lipides de la face interne et externe de la membrane interagissent par interactions hydrophobes et les têtes polaires sont tournées vers le milieu cytosolique et extracellulaire. L'étude de la composition lipidique du GR humain dans les années 1970 a été réalisée en utilisant une succession de lipase spécifiques dont les activités de dégradation permettaient de déterminer les lipides majoritaires (Verkleij et al., 1973) (Figure 4A). Néanmoins, les analyses plus récentes de spectrométrie de masse apportent une analyse bien plus exhaustive de la composition lipidique du GR (Leidl et al., 2008) (Figure 4B).

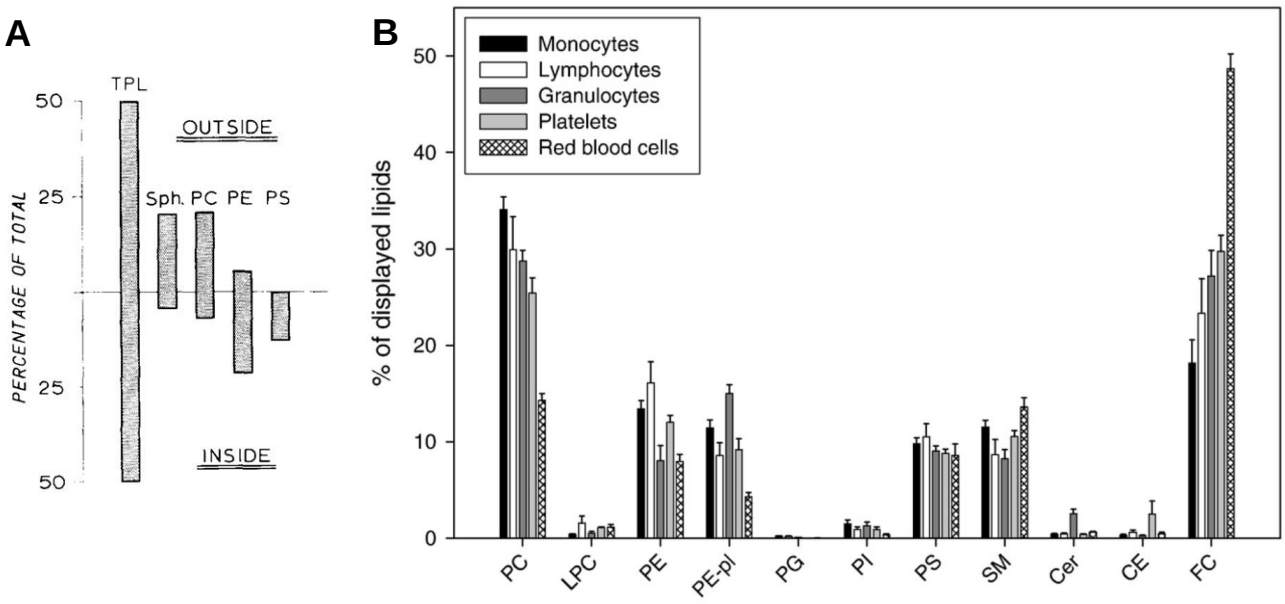

Figure 4 : Composition lipidique de la membrane plasmique du GR humain.

(A) Caractérisation des lipides présents dans la membrane du GR humain par utilisation de lipases (Verkleij et al., 1973) et (B) par spectrométrie de masse (Leidl et al., 2008). TPL : Lipides totaux, Sph-SM : sphingomyéline, PC : phosphatidylcholine, PE : phosphatidyléthanolamine, PS : phosphatidylsérine, LPC : lysophosphatidylcholine, PG : phosphatidylglycérol, PI : phosphatidylinositol, Cer : céramide, FC : cholestérol libre.

D'après ces études, la membrane du GR est principalement composée de PC (15%), PE (10-15%), PS (10%), SM (10%) et cholestérol (50%). Sa composition est différente des autres types cellulaires présents dans le sang. Notamment concernant la quantité de cholestérol qui est presque 2 fois plus importante dans les GR. Dans la majorité des cellules de l'organisme le ratio Cholestérol/Phospholipide (C/PL) est compris entre 0.1 et 0.5 (van Meer et al., 2008) alors qu'il est

de 0.9-1 dans le GR. Pour des ratios C/PL supérieurs, le cholestérol commence à saturer la membrane et forme des domaines de cholestérol purs.

Pourquoi une telle différence existe-t-elle dans le GR ? Une des hypothèses avancée est que le GR s'est spécialisé au cours de l'évolution et l'accumulation de cholestérol dans sa membrane lui confère un avantage en terme de résistance et d'élasticité (Subczynski et al., 2017). Il est connu que les proportions d'acides gras saturés/insaturés et le ratio C/PL modifient la tension de la membrane, la rigidifiant ou la fluidifiant. Par exemple, une augmentation du ratio C/PL au-delà de 1 va induire une diminution de la fluidité membranaire (Cooper, 1978). Le cholestérol, du fait de sa structure, s'insère dans la bicouche lipidique et réduit fortement les mouvements d'autres lipides, ce qui la rend rigide. Cette rigidité n'empêche pas une certaine souplesse de la membrane qui permet au GR de subir d'intenses déformations lorsqu'il traverse les fentes spléniques ou circule dans les microcapillaires. L'abondance de cholestérol participe à l'étanchéité de la membrane ralentissant la diffusion d'eau (Finkelstein and Cass, 1967).

La bicouche lipidique du GR est asymétrique. Les lipides composant la face interne et externe de la bicouche sont différents. Cette asymétrie est maintenue par des transporteurs lipidiques ATP dépendants : Flippase (P4-ATPase qui transporte la PS et PE vers la face interne) et Floppase (transporteurs ABC qui transportent la PC vers la face externe). Il existe également des transporteurs de type Scramblase (ex : TMEM16F) qui transportent les lipides dans le sens de leur gradient. Leur fonctionnement n'est pas dépendant de l'ATP mais du gradient de concentration lipidique. Dans le cas de TMEM16F, c'est l'augmentation du Ca^{2+} intracellulaire qui active ce transporteur permettant le transport de PS vers la face externe de la membrane plasmique (Yan et al., 2022).

Durant la vie du GR, la composition lipidique de la membrane reste stable et ne varie que légèrement avec l'alimentation. L'utilisation de différents régimes d'acide gras chez la souris montre que la composition lipidique du plasma varie largement au contraire de celle du GR (Farquhar and Ahrens, 1963) qui n'effectue pas ou peu de lipogenèse. Initialement, il était suggéré que le GR puisse synthétiser quelques espèces lipidiques bien que ces observations aient pu être faussées par la présence de réticulocytes (Rowe et al., 1960). En effet, il apparait que les GR matures sont complètement dépourvus de synthèse lipidique (Percy et al., 1973).

4. Homéostasie hydrique et ionique du globule rouge humain

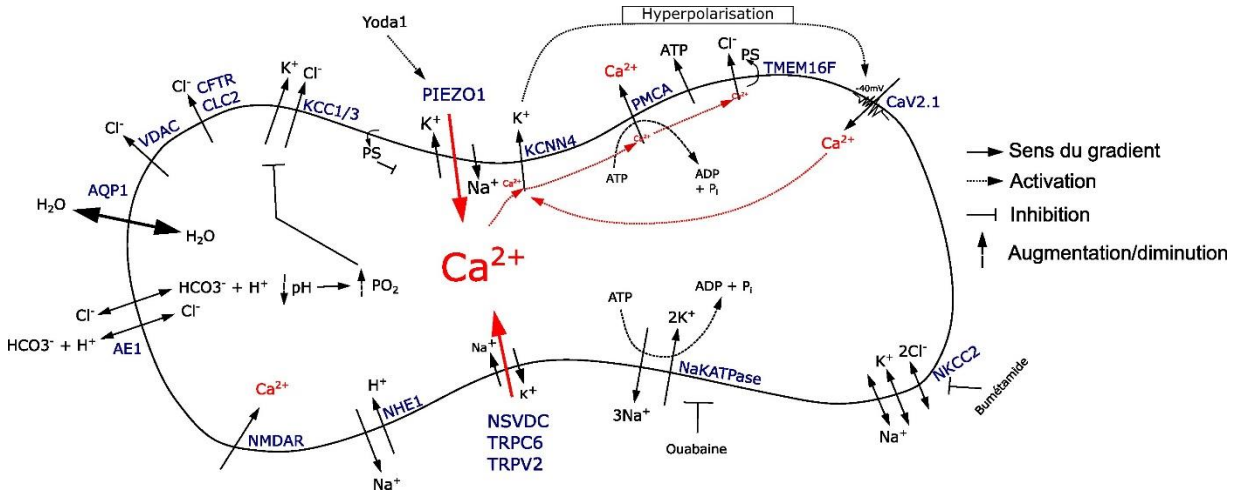

Figure 5 : Schéma représentant les principales perméabilités ioniques du GR humain.

4.1. Composition ionique et potentiel de membrane du GR.

Les GR humain possède une distribution inégale des ions inorganiques de part et d'autre de la membrane plasmique. Le maintien de ce déséquilibre se fait grâce à un compromis entre perméabilités passives et transports actifs avec : (1) des transporteurs actifs ATP dépendants qui créent le gradient électrochimique : ATP1A1 (pompe Na^+/K^+ ATPase, NaK, NaKATPase) et ATP2B4 (pompe calcium ATPase membranaire, PMCA4 et (2) des canaux ioniques qui dissipent le gradient passivement (canaux de fuite) ou lors de leur ouverture (canaux activables).

Les différences de concentrations créent un gradient chimique et les différences de charge créent un gradient électrique. Ce gradient électrochimique va dicter le fonctionnement des canaux ioniques qui, lors de leur ouverture vont faire passer une ou plusieurs espèces ioniques dans le sens de ce gradient. En fonction des canaux ioniques présents, la membrane plasmique aura un potentiel de repos (E_R exprimé en Volt, V) différent, dicté par le potentiel d'équilibre de l'ion X (E_X, "X" étant l'ion en question, également en V) ayant la plus forte Perméabilité (P_X). Chaque E_X (E_K, E_{Na}, E_{Cl}, etc.) dépend des concentrations externe/interne de l'espèce ionique.

E_X est donné par l'équation de Nernst :

$$E_X = \frac{RT}{zF} ln(\frac{[X]_o}{[X]_i})$$

Équation 1 : Equation de Nernst.

E_x : potentiel d'équilibre de l'ion (Volt, V : $kg.m^2. A^{-1}. S^{-3}$) ; R : Constante des gaz parfaits (8,314 $J.mol^{-1}. K^{-1}$) ; T : Température en Kelvin (K) ; z : la valence de l'ion ; F : Constante de Faraday (96500 $A.s.mol^{-1}$) ; [X] : concentration de l'ion externe $[X]_e$ et interne $[X]_i$ (mol. L^{-1}).

Ion (mEq/L H_2O)	$[X]_e$ (mmol. L^{-1})	$[X]_i$ (mmol. L^{-1})	P_X	E_X (mV)
Chlore, Cl^-	110.7	71.0	1	-11.86
Potassium, K^+	4.7	143.7	~0.01	-91.36
Sodium, Na^+	152	23	~0.01	+50.44
Calcium, Ca^{2+}	1-2	10^{-6}	~0.01	+154.88

Tableau 1 : Composition ionique et potentiel de membrane adapté au GR.

La concentration externe $[X]_e$, interne $[X]_i$, perméabilité membranaire de l'ion P_X et potentiel d'équilibre de l'ion E_X sont donnés pour les quatre principales espèces ioniques (Aribi et al., 2010; Barbosa et al., 2015; Funder and Wieth, 1966).

Dans une cellule chaque espèce ionique possède une perméabilité (P_X) qui représente la facilité avec laquelle elle traverse la membrane plasmique. P_X est directement dépendante du nombre de canaux ioniques présents et ouverts à la membrane plasmique. L'équation de Goldman-Hodgkin-Katz (GHK) (Hodgkin and Katz, 1949) est la généralisation de l'équation de Nernst si il existe plus d'une espèce ionique avec une P_X non nulle. Lorsqu'on ne prend en compte que les ions principaux Na^+, K^+ et Cl^-, l'équation de GHK donne :

$$E_R = \frac{RT}{F} ln(\frac{P_{Na}[Na]_e \ + \ P_K[K]_e \ + \ P_{Cl}[Cl]_i}{P_{Na}[Na]_i \ + \ P_K[K]_i \ + \ P_{Cl}[Cl]_e})$$

Équation 2 : Equation de GHK.

E_R : potentiel de repos de la membrane (Volt, V : $kg.m^2. A^{-1}. S^{-3}$) ; P_{Na}, P_K, P_{Cl} : perméabilités propres aux ions Na^+, K^+ et Cl^- ; R : Constante des gaz parfaits (8,314 $J.mol^{-1}. K^{-1}$) ; T : Température en Kelvin (K) ; F : Constante de Faraday (96500 $A.s.mol^{-1}$) ; [X] : concentration de l'ion externe $[X]_e$ et interne $[X]_i$ (mol. L^{-1}). Dans cette équation la valence du Cl^- est prise en compte en inversant le numérateur et dénominateur ($P_{Cl}[Cl]_i$ et $P_{Cl}[Cl]_e$).

Dans le cas du GR, P_{Cl} est environ 100 fois plus grande que P_K et P_{Na}. Cela est dû au fait que la bande 3 effectue un échange $Cl^-/HCO3^-$ électroneutre mais est aussi capable de découpler le transport de chlore. Ce découplage résulte en une fuite de chlore qui fixe le potentiel de repos de la membrane du GR au potentiel d'équilibre du Cl^-. En condition de repos la conductance pour le Cl^- atteint 25 $\mu S.cm^{-2}$ largement plus importante que celle du K^+ et Na^+ ce qui permet de simplifier l'équation de GHK en :

$$E_R = \ E_{Cl} \ = \frac{RT}{F} ln\left(\frac{P_{Cl}[Cl]_i}{P_{Cl}[Cl]_e}\right) = \ E_H \ = \frac{RT}{F} ln\left(\frac{P_H[H]_e}{P_H[H]_i}\right) \sim \ -12 \text{ mV}$$

Équation 3 : Equation de GHK adaptée au GR.

La perméabilité chlore est largement supérieure aux autres perméabilités ce qui simplifie l'équation. E_R : potentiel de repos de la membrane (Volt, V : $kg.m^2. A^{-1}. S^{-3}$) ; P_{Na}, P_K, P_{Cl} : perméabilités propres aux ions Na^+, K^+ et Cl^- ; R : Constante des gaz parfaits (8,314 $J.mol^{-1}. K^{-1}$) ; T : Température en Kelvin (K) ; F : Constante de Faraday (96500 $A.s.mol^{-1}$) ; [X] : concentration de l'ion externe $[X]_e$ et interne $[X]_i$ (mol. L^{-1}).

Expérimentalement, l'estimation de E_R pour le GR a été réalisée à l'aide de microélectrodes (Lassen and Sten-Knudsen, 1968), sondes fluorescentes (Hoffman and Laris, 1974) et en mesurant la distribution de Cl^- (Funder and Wieth, 1966) et elle est proche de -10 mV.

4.2. Maintien de l'homéostasie hydrique et ionique

Le volume du GR est réglé par un équilibre de Donnan. Ce dernier est maintenu par (1) une quantité importante d'anions non perméants (Hb, ATP, 2.3DPG) intracellulaires exerçant une forte pression oncotique et (2) l'effet « pump-leak » (Ellory et al., 1998). La forte pression oncotique interne crée un gradient important pour l'entrée de cations. Comme tout mouvement ionique est accompagné d'eau osmotiquement liée, une entrée de soluté due à cette pression devrait lyser le GR par gonflement. Or, la membrane du GR est quasiment imperméable aux cations et de fait, il n'y pas de mouvement net entrant : à l'état d'équilibre les fuites cationiques sont compensées par la pompe NaK et la pompe calcique PMCA, c'est l'effet « pump-leak ».

4.2.1. Bande 3, AE1, SLC4A1.

Le rôle de l'AE1 dans le maintien du potentiel de membrane est fondamental. Sa capacité à découpler son transport de Cl^- et sa cinétique très rapide règlent le potentiel de membrane au potentiel d'équilibre du Cl^- (-12mV). Ce découplage, aussi appelé "slippage", a été décrit pour la première fois dans les années 1980. L'AE1 transporte plus de 10^4 ions par seconde ce qui fait d'elle un transporteur très rapide. Cette cinétique rapide couplée au gradient électrochimique du Cl^-, permet le passage d'un ion Cl^- découplé tous les 10 000 échanges. De plus l'AE1 est la protéine la plus abondante de la membrane du GR avec plus d'1 millions de copies.

Des mutations de l'AE1 sont associées à des défauts de structure mais aussi à des défauts de perméabilité. Dans ce dernier cas les mutations de l'AE1 entrainent une anémie hémolytique : la Cryohydrocytose. La bande 3 mutée devient alors perméable aux cations entrainant une augmentation du contenu en Na^+ des GR associée à une hyperhydratation, phénomène qui se manifeste aux températures inférieures à la température corporelle (Bruce et al., 2005; Caulier et al., 2018; Haines et al., 2001).

4.2.2. NaK, ATP1A

L'étude de la pompe Na^+/K^+ est intimement liée au GR, où les premières descriptions de son fonctionnement ont été faites. En 1949 Flynn et Maizels ont observé que les GR stockés à basse température inversaient progressivement leur contenus en K^+ et Na^+, suggérant l'existence de petites fuites cationiques (Flynn and Maizels, 1949). De manière intéressante, les concentrations de K^+ et Na^+ sont revenues à un niveau basal lorsque les GR ont été incubés à 37°C en présence de glucose. Cette observation posa les jalons d'un possible transporteur actif ATP dépendant permettant de maintenir un déséquilibre en K^+ et Na^+ de part et d'autre de la membrane plasmique. Ce transport est assuré par la pompe Na^+/K^+ ATPase (NaK, ATP1A1) qui permet l'échange de 3 Na^+ et 2 K^+ contre

leur gradient électrochimique en consommant de l'ATP. C'est une pompe de type P, c'est-à-dire qu'elle forme un intermédiaire phosphorylé (aspartyl-phosphate) dans son site catalytique à la suite de l'hydrolyse de l'ATP. Cette phosphorylation change la conformation de la pompe qui devient capable de transporter des ions (Kherd et al., 2017). La NaK fonctionnelle du GR est composée d'une sous-unité catalytique α de 110 kDa (ATP1A1) et d'une sous-unité auxiliaire β de 50 kDa (ATP1B1). L'activité de la NaK est très bien adaptée pour compenser les petites fuites cationiques à moindre coût énergétique. En revanche, tout changement drastique de contenu cationique (sortie de K^+, entrée de Na^+) sera difficilement compensé.

4.2.3. PMCA, ATP2B et la régulation du Ca^{2+}

Le Ca^{2+} est important pour de nombreux aspects de la vie cellulaire et est probablement un des seconds messagers les plus importants. Dans le GR, il est finement régulé et son augmentation participe au remodelage du cytosquelette, à la déshydratation et à la sénescence(Bogdanova et al., 2013; Kaestner et al., 2020; Tiffert et al., 2003). Le GR humain tamponne peu efficacement le Ca^{2+} en comparaison d'autres cellules. En effet, il ne possède pas de stock intracellulaire pouvant réguler sa concentration cytosolique et l'ouverture de conductances calciques a des effets immédiats sur sa physiologie. Cette ouverture de conductances calciques a lieu dans certaines conditions :

- Un stress mécanique subit par le GR (Larsen et al., 1981)
- La senescence du GR
- Infection du GR par Plasmodium *falciparum.*
- Drépanocytose (Psickle)
- Xérocytose Héréditaire

Le GR maintient donc une [Ca^{2+}] interne faible, de l'ordre du nanomolaire (30-60 nM) (Tiffert et al., 2003), afin de ne pas altérer son fonctionnement. Pourtant, le plasma sanguin possède une [Ca^{2+}] ~10^4 fois plus importante (1,8 mM). Ce gigantesque gradient de concentration alimente des fuites calciques, dont la ou les protéines responsables sont encore mal connues (se référer à 4.4.4.2). Deux protéines permettent d'effluer le Ca^{2+} : deux pompes calciques ATP dépendantes, PMCA1b et PMCA4b.

La mise en évidence de pompes calciques dans le GR remonte aux années 1960. Durant cette période la grande question était de comprendre comment le GR maintenait une faible [Ca^{2+}] (Dunham and Glynn, 1961). C'est Schatzmann qui apporte les premiers éclaircissements en 1966. Il a utilisé des ghosts de GR afin de mesurer un efflux de Ca^{2+} allant à l'encontre de son gradient électrochimique et ayant une dépendance à l'ATP (Schatzmann, 1966). Ce n'est qu'à la fin des années 1980 que la PMCA fut clonée (Verma et al., 1988). Il existe 4 PMCA différentes (PMCA1-4) codées par les gènes

ATP2B1-4. Elles sont soumises à un épissage alternatif, débouchant sur plus de 20 isoformes de PMCA connues à ce jour. Il existe 2 sites d'épissage A (isoformes x, w et z) et C (isoformes a, b, c, d et e). Le site C est de loin le plus complexe et module la sensibilité calcique de la pompe. Ici, il sera question plus précisément de la PMCA1b et PMCA4b et du site d'épissage C. En effet, les isoformes PMCA1b et PMCA4b sont exprimées dans le GR dont 70-80% est représenté par la PMCA4b (Bryk and Wiśniewski, 2017; Strehler et al., 1990). Les isoformes "b" ont des cinétiques lentes comparées aux isoformes "a" qui sont adaptées aux signalisations calciques rapides du tissu nerveux (Caride et al., 2007). Cela est cohérent avec la faible perméabilité calcique dans le GR. Etant donné la grande similarité entre PMCA1b et PMCA4b et le fait que la PMCA4b est majoritaire, il sera question de cette dernière dans les sections suivantes.

A ce jour la structure complète de la PMCA4b n'a pas été résolue. On peut néanmoins déduire sa taille de sa séquence : 134 kDa. L'utilisation d'anticorps monoclonaux et de marqueurs chimiques ont permis d'identifier 10 domaines transmembranaires (TM) avec les deux parties N et C terminales baignant dans le cytoplasme (Madácsy et al., 2022). Entre ces TM on retrouve principalement 3 longs domaines intracellulaires (Figure 6) :

- Le premier situé entre les TM2 et TM3 qui serait important pour le couplage entre l'hydrolyse de l'ATP et l'efflux de Ca^{2+}.
- Site catalytique : situé entre TM4 et TM5.
- Domaine C-terminal (C-ter) qui comprend notamment le site de fixation de la Calmoduline (CaM).

Tout comme la NaK, la PMCA est une pompe de type P. Cependant, une différence importante qui dicte son fonctionnement provient de son interaction avec la Calmoduline (CaM) (James et al., 1988). Cette interaction se fait par l'intermédiaire de 25 résidus du domaine C-ter, lui conférant une sensibilité au Ca^{2+}. Cette propriété l'éloigne également de la pompe SERCA (sarco/endoplasmic reticulum Ca^{2+}-ATPase), dépourvue de régulation par la CaM. En absence de CaM, la PMCA est auto-inhibée par son domaine C-ter qui se fixe au niveau du site catalytique (Falchetto et al., 1991) empêchant presque totalement son fonctionnement. C'est un mode de fonctionnement basal avec un Vmax faible. Les états de transition de la PMCA durant la fixation du Ca^{2+}/CaM et hydrolyse de l'ATP ont été très bien étudiés (Mangialavori et al., 2013) et sont potentiellement à l'origine de changements conformationnels importants. La fixation de la CaM au domaine C-ter à la suite d'une

élévation du Ca^{2+} interne induit le décrochage du domaine C-ter du site catalytique levant ainsi l'inhibition et augmentant l'activité d'efflux de Ca^{2+}.

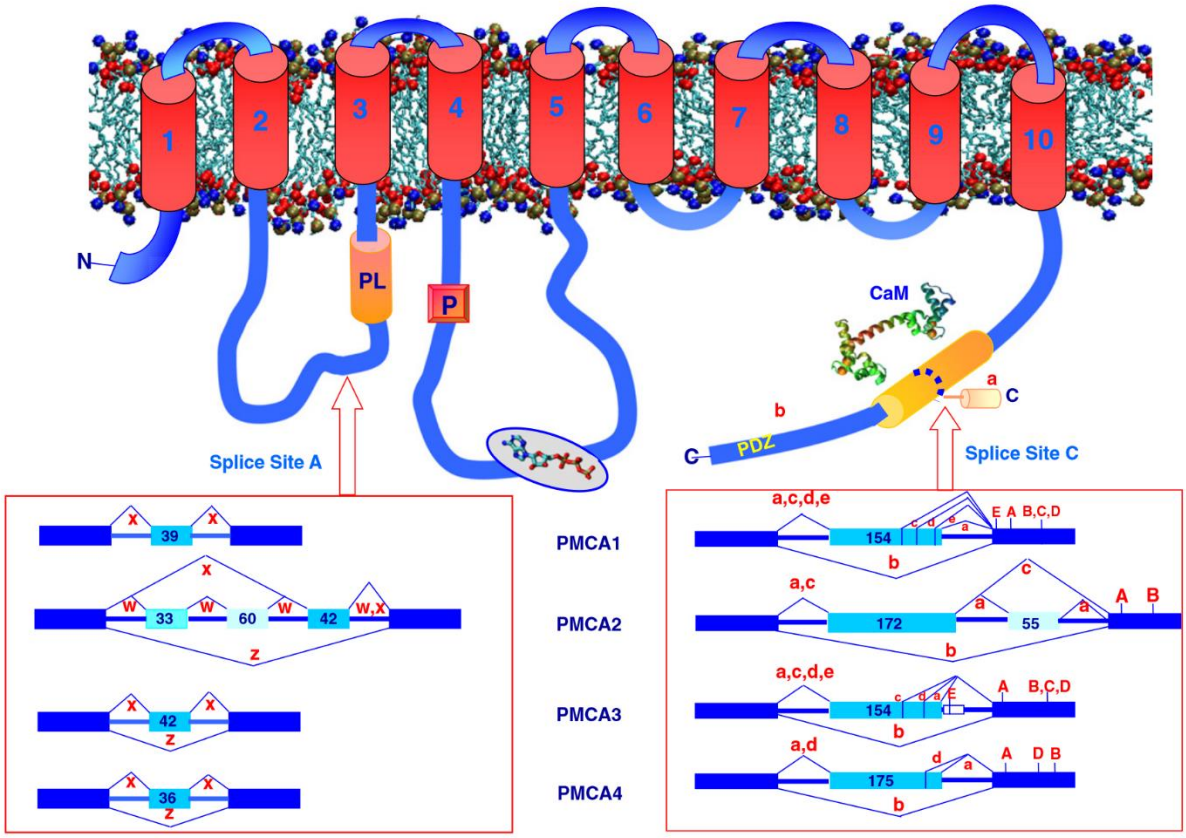

Figure 6 : Topologie et site d'épissage de la PMCA (Krebs, 2015).

Les carrés bleu foncé représentent les exons constitutifs et les carrés bleu clair les exons introduit par épissage alternatif. Les lettres en capital (A, B, C, D, E) donnent la position du codon stop pour l'isoforme correspondant. Par exemple, l'épissage "a" de la PMCA4 introduit un exon de 175 aa et l'apparition d'un codon stop précoce. En revanche, cet exon de 175 aa est absent de la PMCA4b.

Ce domaine C-ter de la PMCA est également un site de clivage par la Calpaïne. La Calpaïne-1 (CAPN1), qui est exprimée dans le GR, est une endopeptidase à cystéine sensible au Ca^{2+}. CAPN1 s'active à la suite d'une augmentation du Ca^{2+} intracellulaire et clive la PMCA avant le domaine de liaison à la CaM. Il en résulte alors une pompe active même en absence de CaM (Enyedi et al., 1993). L'invalidation de CAPN1 chez la souris provoque une diminution de l'activité de la PMCA en absence de CaM et une augmentation de son activité en présence de CaM (Wieschhaus et al., 2012). La PMCA peut également dimériser ce qui augmente son activité (Kosk-Kosicka and Bzdega, 1988; Kosk-Kosicka and Inesi, 1985). Son domaine C-ter contient un motif PDZ important pour l'interaction avec d'autre protéines et est un lieu de phosphorylation par des kinases (Smallwood et al., 1988). La pompe est également régulée par des phospholipides comme PiP2.

Il n'existe pas d'inhibiteur spécifique de la PMCA. En revanche, plusieurs méthodes ont été décrites pour bloquer plus ou moins efficacement la pompe :

- Utiliser un chélateur de Ca^{2+} comme le BAPTA (pour maintenir la $[Ca^{2+}]$ en dessous du seuil d'activation de la PMCA.

- Utiliser du Vanadate (VO^{3-}) pour bloquer non spécifiquement la pompe. Le VO^{3-} est un compétiteur de l'ATP pour le site catalytique. 1 mM de VO^{3-} induit une inhibition de 99.7% (Tiffert and Lew, 1997). Le vanadate est de fait également un inhibiteur de la pompe NaK et de tous les processus faisant intervenir de l'ATP, comme les phosphorylations.

- Vider les stocks d'ATP de la cellule. Cette méthode peut être réalisée en incubant les GR à 37°C en absence de glucose ou de substrat énergétique. Néanmoins comme mentionné dans la section 2.3 relative au cycle de Rapoport-Luebering, le GR possède un stock important de 2,3 DPG qui peut fournir de l'ATP via la fin de la glycolyse. Ainsi, la concentration en ATP descend difficilement en dessous du µM.

Les PMCA1 et 4 sont exprimées de façon ubiquitaire. L'invalidation de PMCA1 est létale à l'état embryonnaire alors que l'invalidation de PMCA4 induit une infertilité chez les souris mâles (Lessard et al., 2017; Okunade et al., 2004; Schuh et al., 2004). Cela suggère que malgré un rôle commun à toutes les PMCA (efflux de Ca^{2+}), l'isoforme d'épissage revêt une importance primordiale en fonction du tissu où elle est exprimée (Hegedűs et al., 2015). En effet, la PMCA1 est indispensable pour la survie, probablement très tôt dans l'embryogenèse, ce qui n'est pas le cas de la PMCA4.

De manière générale, l'activité d'efflux de Ca^{2+} de la PMCA est plus faible que celle de la SERCA ou que l'échangeur Na^{+}/Ca^{2+} qui sont bien plus efficaces pour diminuer la $[Ca^{2+}]$. Néanmoins, le rôle de la PMCA semble être plus fin, permettant de réguler le Ca^{2+} dans des microdomaines membranaires en interagissant avec d'autres protéines régulées par le Ca^{2+} (Krebs, 2017). Ces interactions sont notamment permises par le domaine PDZ qui interagit avec la guanylate cyclase MAGUK (Kim et al., 1998), avec la NO synthase (nNOS) (Oceandy et al., 2007) ou encore avec TMEM20 (POST) qui inhibe la pompe (Krapivinsky et al., 2011). Ce domaine PDZ est retrouvé dans les isoformes "b" mais absent des isoformes "a" (Kim et al., 1998; Krebs, 2022)

Le gène codant pour la PMCA4, ATP2B4 est régulé par un élément intronique (amplificateur) qui se trouve être spécifique de la lignée Érythroïde (Lessard et al., 2017). La délétion de 927 paires de base de cette partie intronique induit une diminution de l'expression de ATP2B4. Cette délétion serait impliquée dans la résistance à la malaria (Zámbó et al., 2017). C'est une information importante car elle pourrait constituer un lien entre la PMCA4b et la pathophysiologie érythrocytaire.

4.3. Le GR humain ne régule pas son volume

L'état d'équilibre maintenu par l'AE1, PMCA, NaK et les fuites est rompu lorsqu'une perméabilité ionique est stimulée. Cela provoque un mouvement de cations ou anions important dans le sens du gradient électrochimique, accompagné d'eau. Dans le GR humain, cette perte ou ce gain d'eau ne seront jamais compensés. Cela implique que si le GR se déshydrate à la suite à une sortie de K^+, ou s'hydrate via une entrée de Na^+, il ne récupérera jamais son volume d'origine. Pourtant, le GR humain possède tous les transporteurs et canaux nécessaires pour établir une régulation de son volume par les phénomènes de RVI (Regulatory Volume Increase) et RVD (Regulatory Volume Decrease). Le RVI est une augmentation du volume par entrée de solutés en réponse à une perte d'eau. Il est le plus souvent médié par le cotransporteur $Na^+/K^+/2Cl^-$ (NKCC1, NaK2Cl) et le cotransporteur Na^+/H^+ (NHE1). Une perte d'eau va induire une entrée de Na^+, via ces transporteurs, qui est suivie par une entrée d'eau pour rétablir le volume d'origine. En revanche, le RVD est une diminution du volume par sortie de solutés en réponse à un gain d'eau et est médié par le cotransport KCl (KCC1). Les mécanismes de régulation de volume ont pu être étudiés sur les GR nucléés qui, au contraire des GR anucléés des mammifères, sont capables de compenser un gain ou une perte d'eau et maintenir un volume d'équilibre dans un environnement osmotique perturbé.

4.3.1. NHE1

NHE1 est un échangeur Na^+/H^+ exprimé dans le GR (Canessa et al., 1990). Comme mentionné précédemment (cf. 2.2), le pH intracellulaire du GR varie en fonction du pH extracellulaire, du fait de la bande 3. Cela empêche le fonctionnement de NHE1 qui est considéré comme inactif dans le GR humain (Ellory et al., 1998; Richter et al., 1997). En revanche cet échangeur Na^+/H^+ est activable dans les GR de poissons où il répond à une stimulation par les catécholamines (Borgese et al., 1987) et est à l'origine d'un gonflement des GR par entrée de NaCl qui déclenche une RVD.

4.3.2. NKCC1

Wiley and Cooper, sont les premiers à avoir mentionné la présence d'un co-transporteur Na^+/K^+ sensible au furosémide mais insensible à l'ouabaïne : NKCC1, codé par le gène SLC21A1, dans le GR humain (Wiley and Cooper, 1974). C'est un co-transporteur $Na^+/K^+/2Cl^-$ électroneutre dont le fonctionnement dépend de la FEM du Cl^-. Il est important pour la régulation du volume des GR nucléés. L'activité du NaK2Cl est pratiquement à l'équilibre dans les GR au vu des gradients de K^+, Na^+ et Cl^-, donc le flux entrant est égal au flux sortant. Néanmoins, dans le GR humain, des changements de ces gradients ne déclenchent pas l'activation de NKCC1 (Duhm and Otto Göbel, 1984). D'autre part, chez la souris, nkcc1 peut être activé en conditions désoxygénées par des phosphorylations et permettrait de moduler le volume du GR murin (Zheng 2019). En effet il a été

montré que la déoxy Hb pouvait se fixer au domaine N-terminal de l'ae1 et induire un détachement de wnk1 (with no lysine kinase 1). wnk1 phosphoryle alors osr1 (oxydative stress-responsive kinase 1) qui phosphoryle à son tour nkcc1 et induit son activation. Cette activation, en conditions physiologiques, serait à l'origine d'une augmentation du volume des GR de souris. Ces mécanismes de phosphorylations pourraient néanmoins être absents du GR humain.

4.3.3. KCC1

KCC1 est un cotransporteur K^+-Cl^- régulé par la pression en O_2 et les changements de volume dans les GR nucléés (Drew et al., 2004). KCC1 est activé à la suite d'un gonflement de la cellule, provoquant une sortie de K^+ et Cl^- et une perte d'H_2O associée pour rétablir le volume d'origine (Guizouarn et al., 2000). Dans le GR humain, KCC1 a perdu cette capacité n'autorisant pas de RVD. La raison pour laquelle KCC1 a perdu ce rôle n'est pas bien comprise mais pourrait provenir d'une différence d'environnement protéique et/ou lipidique. Dans le GR nucléé de poisson et d'amphibien, le RVD est médié à 50% par le cotransport KCl et à 50% par la perte d'osmolytes organiques (taurine, méthylamine, etc.) (Motais et al., 2003). De manière intéressante, le cotransporteur K^+-Cl^- des GR de souris placés dans un milieu hypotonique seraient capable d'effectuer du RVD (Armsby et al., 1995). Cela rend compte de toute la complexité des mécanismes à l'œuvre dans un GR qui dépendent de l'espèce étudiée.

.

4.4. Altération de l'homéostasie ionique et hydrique du Globule rouge humain.

La membrane du GR humain est composée d'une multitude de canaux cationiques et anioniques. Leur conductance unitaire est suffisamment forte pour qu'une activation altère l'homéostasie ionique et hydrique du GR. Que ce soit des conductances K^+, Na^+, Ca^{2+} ou Cl^-, elles sont quiescentes à l'état physiologique et sont pour la plupart décrites en conditions expérimentales de déséquilibres ou pathologiques (Thomas et al., 2011).

Protéine	Conductance	Référence
PIEZO1	Na^+, K^+ et Ca^{2+}	(Coste et al., 2010)
NSVDC	Na^+, K^+ et Ca^{2+}	(Christophersen and Bennekou, 1991; Halperin et al., 1989)
CaV2.1	Ca^{2+}	(Andrews et al., 2002)
TRPC6	Ca^{2+}, Na^+, K^+	(Föller et al., 2008)
NMDAR	Ca^{2+}	(Makhro et al., 2013)
KCNN4	K^+	(Hoffman et al., 2003)
VDAC	Cl^-	(Bouyer et al., 2011)
TMEM16F/TMEM16A	Cl^-	(Skals et al., 2010; Yang et al., 2012)
CFTR	Cl^-	(Lange et al., 2006; Sprague et al., 1998)
TRPV2	Ca^{2+}, Na^+, K^+	(Belkacemi et al., 2021)

Tableau 2 : Liste des principales conductances décrites dans le GR humain.

4.4.1. PIEZO1

4.4.1.1. Découverte

En 1981 a été décrite une augmentation de la perméabilité Ca^{2+} des GR soumis au stress physique de la circulation, imité par un viscosimètre rotatif (Larsen et al., 1981). Ce n'est que 30 ans plus tard qu'un canal impliqué dans ce phénomène est découvert : PIEZO1. PIEZO1 est un canal mécanosensible cationique non sélectif dont la famille a été mise en évidence pour la première fois en 2010 dans des cellules Neuro2A. Il a été montré que le siRNA dirigé contre la protéine codée par le gène *FAM38A* induisait la plus forte diminution du courant mécanosensible (Coste et al., 2010). La protéine codée par Fam38a sera nommée PIEZO1, en référence au mot grecque, "πίεση" (píesi) signifiant "pression". Cette découverte fût marquée en 2021 par le prix Nobel de physiologie et de médecine pour Ardem Patapoutian et son équipe.

Il existe 2 protéines PIEZO, PIEZO1 et PIEZO2, conservées au cours de l'évolution et qui font la médiation entre les stimuli mécaniques et les processus biologiques associés. Elles sont impliquées dans la nociception chez Drosophila melanogaster où l'invalidation de Dmpiezo conduit à une insensibilité à la douleur (Kim et al., 2012). Chez le poisson zèbre ou encore chez Caenorhabditis elegans (Kamajaya et al., 2014) et quelques parasites protozoaires (Prole and Taylor, 2013), piezo2b est médiateur de la sensation de toucher dès l'embryogenèse (Faucherre et al., 2013). Également dans le règne végétal un homologue, Arabidopsis PIEZO1, est important pour la morphologie des vacuoles (Radin et al., 2021) et la croissance racinaire (Mousavi et al., 2021).

En 10 ans l'effervescence autour de PIEZO1 a permis de mettre en évidence de multiples rôles chez l'homme, majoritairement dans les cellules non-excitables (Qin et al., 2021). PIEZO1 est certainement important dans le développement précoce car son invalidation chez la souris est létal au stade embryonnaire (Cahalan et al., 2015; Li et al., 2014). On peut citer ses rôles dans le développement vasculaire (Li et al., 2014; Ranade et al., 2014), la formation des os (Sun et al., 2019), l'inflammation (Solis et al., 2019), la survenue de pancréatite suite à un stress physique important de la glande(Romac et al., 2018), le métabolisme (Zhao et al., 2019), la différenciation des adipocytes (Wang et al., 2020), le fonctionnement cardiaque (Jiang et al., 2021), la formation des valves lymphatiques (Nonomura et al., 2018) et des microcapillaires pulmonaires (Friedrich et al., 2019) et enfin l'homéostasie volumique du GR (Cahalan et al., 2015; Faucherre et al., 2014) qui sera le sujet de la prochaine section.

4.4.1.2. Rôle dans le GR

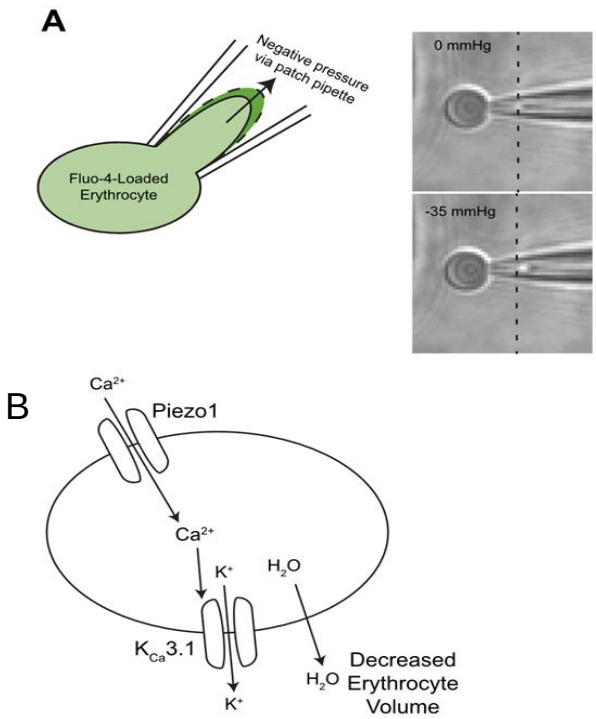

Figure 7 : Rôle de PIEZO1 dans l'homéostasie volumique du GR.
(A) Technique de stimulation mécanique associée à de l'imagerie calcique (Fluo4-AM). (B) Modèle de régulation de l'homéostasie volumique du GR par PIEZO1. Adaptée de (Cahalan et al., 2015)

Chez la souris, l'invalidation conditionnelle de PIEZO1 dans la lignée hématopoïétique (souris Vav1-P1cKO) n'induit pas d'anémie notable mais une augmentation de la taille (FSC), du VCM (Volume corpusculaire moyen), de la MCH (Teneur corpusculaire moyenne d'hémoglobine), une réduction de la CCMH (Concentration corpusculaire moyenne d'hémoglobine) et RO (Résistance Osmotique) des GR. Cela suggère que l'absence de PIEZO1 induit une hyperhydratation des GR, sans pour autant causer d'anémie significative. Il a été démontré que la stimulation mécanique du GR murin induisait une entrée de Ca^{2+} (Fig. 7A). Cette entrée de Ca^{2+} provoque l'activation du canal KCNN4 entraînant une perte de K^+ et d'H_2O (Fig. 7B). C'est à partir de cette étude que naît l'hypothèse d'activation répétée de PIEZO1 dans la circulation induisant des pertes d'eau non compensées et endommageant peu à peu le GR.

PIEZO1 est également impliqué dans l'Érythropoïèse (Caulier et al., 2020; Narla and Mohandas, 2020). Dans cet article de Caulier *et al.*, l'activation chimique de PIEZO1 par la molécule Yoda1 retarde la différenciation érythrocytaire dans un modèle cellulaire mais aussi dans des cellules souches érythroïdes (HSC). Le mécanisme est dépendant des voies de signalisation NFAT, STAT5 et ERK1/2. La différenciation des HSC est également retardée chez les patients porteurs de mutation PIEZO1 associée à la Xérocytose Héréditaire. Ce rôle de PIEZO1 est encore mal connu et pourrait être fondamental dans la pathophysiologie du GR, ce qui sera discuté par la suite.

4.4.1.3. Structure

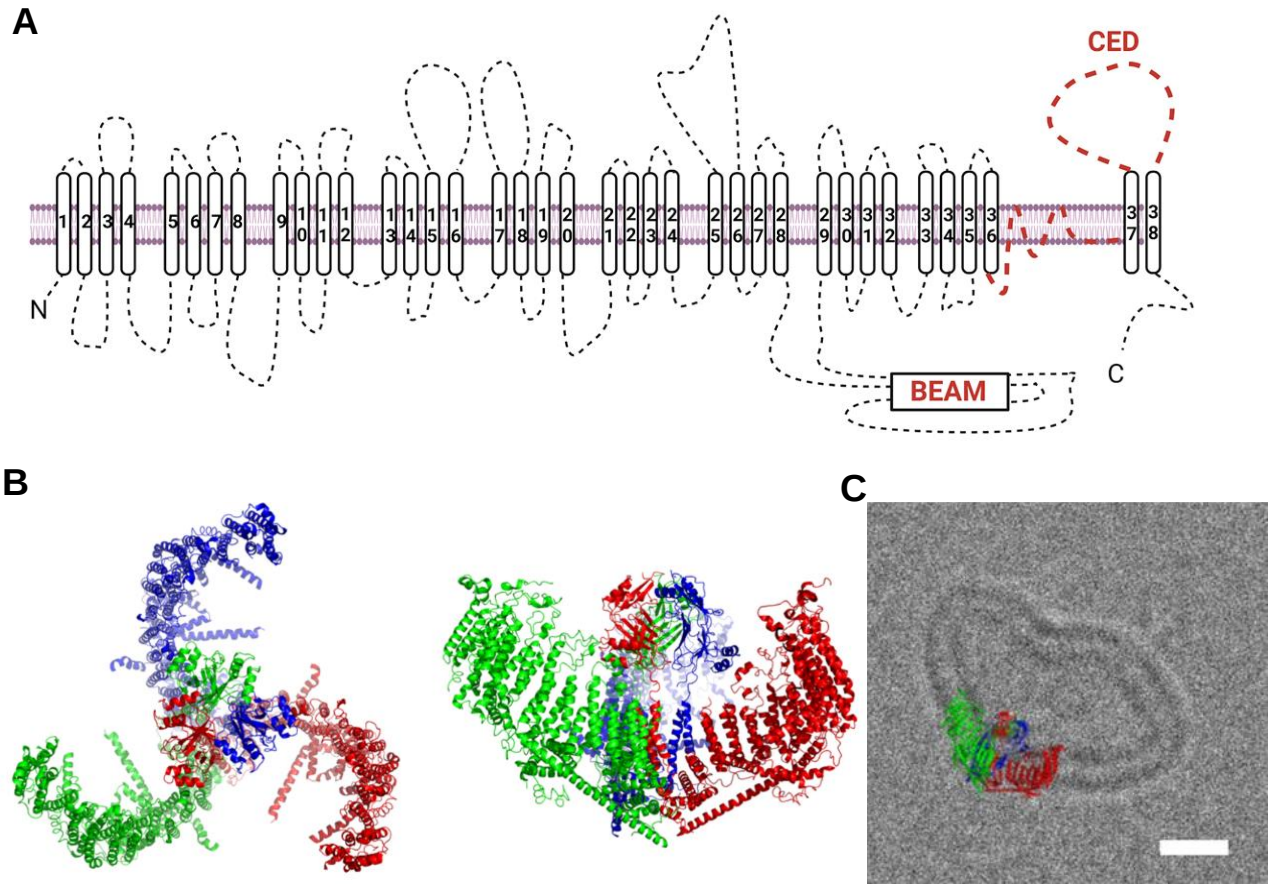

Figure 8 : Structure de PIEZO1.

(A) Structure 2D de PIEZO1 composée de 38 domaines transmembranaire (TM), d'un long domaine intracellulaire (BEAM) entre TM28 et TM29 et d'un domaine CED extracellulaire entre TM37 et TM38, formant le pore du canal. (B) Structure tridimensionnelle de la forme trimérique fonctionnelle de PIEZO1 vu de haut (gauche) et de face (droite). Chaque monomère possède une couleur différente. (C) Image de microscopie électronique de PIEZO1 dans une bicouche lipidique artificielle, formant un dôme. Adaptée de (Guo and MacKinnon, 2017).

Sa structure est d'abord décrite en Cryo microscopie électronique à partir du canal PIEZO1 murin (mPIEZO1), faisant 2547 aa avec une résolution de 4.8 Angström (Ge et al., 2015; Zhao et al., 2018). Très vite décrit comme étant fonctionnel sous forme multimérique (Coste et al., 2012). C'est un trimère de de 900 kDa en forme d'hélice à 3 pales (triskèle). Chaque monomère forme une pale périphérique avec sa partie N-terminale et une partie du pore central avec la partie C-terminale (CED). Les parties N-terminale et C-terminale sont reliées par une longue boucle intracellulaire formant une armature (BEAM) liant les hélices périphériques et centre du canal (Fig. 8). Sa masse est telle qu'il courbe localement la membrane formant un dôme (Guo and MacKinnon, 2017). Chaque monomère

est composé de 9 répétitions de 4 domaines transmembranaires (TM) et 2 TM centraux, comprenant au total 38 domaines TM.

4.4.1.4. Propriétés :

PIEZO1 est un canal mécanosensible cationique non sélectif. Perméable au K^+, Na^+ et Ca^{2+} avec une conductance unitaire comprise entre 20 et 70 pS. La conductance de PIEZO1 dépend du modèle cellulaire, des solutions de patch, du protocole de stimulation (poke ou pressure clamp), de la force mécanique et du potentiel appliqué. Par exemple: il a été montré que la présence de $MgCl_2$ dans la pipette, en configuration cellule attachée, réduisait de 50% la conductance de PIEZO1 comparée à une solution riche en K^+ (Coste et al., 2012; Gottlieb et al., 2012). En revanche, en configuration cellule entière, l'absence de $MgCl_2$ réduit la réponse de PIEZO1 au stimulus mécanique. Lors d'une stimulation mécanique, PIEZO1 s'active et s'inactive rapidement malgré la persistance du stimulus. (Gottlieb et al., 2012; Wu et al., 2017). En effet, à la différence d'un mécanisme d'adaptation où le canal peut être réactivé avec une stimulation plus forte (Figure 9), l'inactivation ferme le canal jusqu'à suppression du stimulus mécanique.

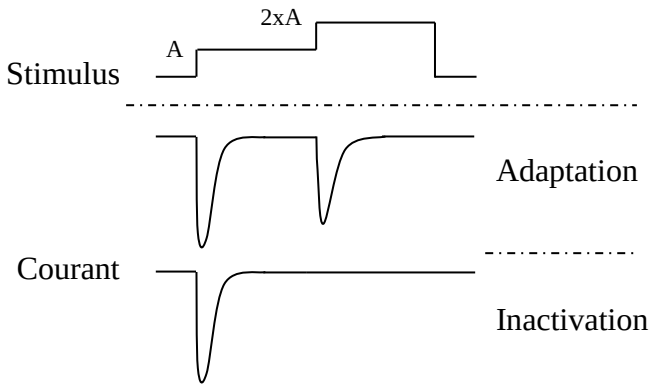

Figure 9 : Schéma du phénomène d'activation et d'adaptation.

Un stimulus appliqué de force A induit une augmentation rapide du courant qui diminue rapidement jusqu'à un état basal. Si une force d'intensité 2xA est appliquée et que le canal s'active une seconde fois avec une amplitude comparable, on parle d'adaptation. Si le canal reste fermé on parle d'inactivation.

Le premier agoniste chimique de PIEZO1 a été décrit en 2015 en testant plus de 3.25 millions molécules pour leur capacité à induire un influx calcique dans les cellules HEK293T transfectées avec PIEZO1. Ils validèrent ainsi l'efficacité d'un des composés et le nommèrent Yoda1 (Syeda et al., 2015). Référence cinématographique amusante au célèbre personnage de la saga Star Wars (Yoda). Les molécules Jedi1 et Jedi2 sont aussi des activateurs chimiques de de PIEZO1 (Wang et

al., 2018). La molécule Dooku1 est un analogue de Yoda1 modifié chimiquement qui antagonise ses effets sur PIEZO1 (Evans et al., 2018) (le comte Dooku est un personnage antagoniste de Yoda dans Star Wars). Le mode d'action de Yoda1 est encore peu connu mais les résultats récents sont en faveur d'une interaction physique avec PIEZO1, comme démontré en Résonance Plasmonique de Surface (Wang et al., 2018). Un domaine d'interaction entre les résidus 1961 et 2063 est décrit comme indispensable (Lacroix et al., 2018). Des simulations prédisent l'interaction d'une molécule Yoda1 par monomère de PIEZO1, entre deux domaines hydrophobes (répétition A et B) (Botello-Smith et al., 2019). Le cross-link de ces deux domaines inhibe l'effet du Yoda1 (Jiang et al., 2023). Cela semble également être le site où Dooku1 se fixe pour empêcher l'effet de Yoda1, allant en faveur d'une interaction récepteur/ligand. Néanmoins on ne peut pas exclure un autre effet, indirect, de Yoda1 sur PIEZO1 par le biais de la membrane plasmique. Yoda1 altère fortement la structure membranaire en formant des GR échinocytaires (Lohia et al., 2023). Les changements de tension membranaire pourraient alors être à l'origine de l'activation de PIEZO1. Un résultat récent, décrit paradoxalement un effet agoniste de Dooku1 sur PIEZO1 dans les GR (Hatem et al., 2023) contrairement à ce qui est décrit dans d'autres types cellulaire. Comme décrit dans la partie 3.2, le GR est atypique quant aux espèces lipidiques qui le compose, ce qui pourrait expliquer un tel effet contradictoire.

L'activité de PIEZO1 est largement dépendant de la composition lipidique de la membrane plasmique. Cette dernière est composé par différents type d'acide gras (AG) que l'on classe par la longueur de leur chaine carbonée et leur degré d'insaturation (ex : C18:2, 18 carbones et 2 insaturations). Il a été montré que l'acide margarique (C17:0) augmente le seuil d'activation de PIEZO1 alors que l'acide eicosapentaénoïque (C20:5) raccourci le temps d'inactivation (Romero et al., 2019) rendant globalement PIEZO1 moins actif. De façon intéressante, l'acide margarique et l'acide eicosapentaénoïque ont un effet synergique inhibiteur de PIEZO1 alors que le premier augmente la rigidité de la membrane et le second la diminue. Le cholestérol est également important puisqu'il interagit directement avec PIEZO1. Contrairement aux lipides, le cytosquelette ne semble pas indispensable à l'activité du canal car PIEZO1 demeure actif dans des vésicules lipidiques dénuées de cytosquelette (Coste et al., 2012; Syeda et al., 2016). Néanmoins, exprimé dans des modèles cellulaires, l'altération du cytosquelette d'actine peut modifier son activité (Cox et al., 2016; Wang et al., 2022).

4.4.1.5. Enregistrements :

Les mesures de courant sur PIEZO1 se font principalement avec deux techniques de stimulation mécanique: “stretch” et “poke” (Lewis and Grandl, 2021). La technique de “poke” consiste à appliquer une pression sur la cellule avec une pipette de verre en borosilicate à l’aide d’un système piézoélectrique. La mesure du courant à la suite de cette stimulation est réalisée en patch-clamp sur cellule entière. Le courant ainsi mesuré est la résultante macroscopique de l’activité de tous les canaux mécanosensibles présents dans la cellule (Hao et al., 2013; Hao and Delmas, 2011). La technique de “stretch” nécessite un High Speed Pressure Clamp (HSPC) communiquant avec la pipette de patch. En “stretch” la mesure du courant se fait en cellule attachée : en utilisant le HSPC on applique une pression négative ou positive sur la portion de membrane sous la pipette. Ainsi, la technique de stretch permet la mesure de quelques canaux avec une grande précision sur la valeur de pression appliquée par le HSPC (Lewis and Grandl, 2015).

4.4.2. KCNN4

4.4.2.1. Découverte

L’effet « Gardos » est décrit pour la première fois en 1956 par György Gardos qui observa une perméabilité K^+ activée suite à une incubation des GR avec iodoacétate et adénosine en présence de Ca^{2+}(Gardos, 1958, 1956). Ce n’est que 40 ans plus tard que l’identité du canal à l’origine de cet effet fut découverte dans le GR: hSK4 ou KCNN4 (Hoffman et al., 2003). Des caractéristiques similaires furent d’abord observées avec hIK1 cloné à partir de tissus pancréatiques humain (Ishii et al., 1997) et mIK1 cloné à partir de tissus murin (cellules erythroleucémique, estomac et thymus) (Vandorpe et al., 1998). IK1 fait référence à un canal K^+ de conductance intermédiaire activé par le Ca^{2+} ressemblant aux canaux SK découverts quelques années auparavant (Marty, 1981). La caractérisation fonctionnelle de ce canal fut réalisée en 1997 (Joiner et al., 1997). Ce sont ces différents travaux qui ont mené à la découverte publiée en 2003: le canal Gardos est le canal KCNN4 (Hoffman et al., 2003).

KCNN4 est très sélectif au K^+ (K^+>Na^+ 15 :1). Pour son fonctionnement, la [Ca^{2+}] doit dépasser 150nM (Tiffert et al., 1988) avec une amplitude maximale atteinte pour 2µM de Ca^{2+}. De plus, du potassium doit être présent dans le milieu externe, sans quoi KCNN4 reste inactif (Grygorczyk and Schwarz, 1983). En effet, l’incubation de ghosts de GR humains dans un milieu dépourvu de potassium pendant plus d’une heure, induit une inhibition irréversible de KCNN4. Une dépendance au Ca^{2+} extracellulaire a été suggérée sans que le mécanisme soit élucidé (Dyrda et al., 2010). Dans cet article, le courant unitaire de KCNN4 a été mesuré dans des GR humains en présence de 1mM Ca^{2+} externe et 100 nM interne à la suite d’une déformation de la membrane. De façon surprenante,

KCNN4 reste inactif avec 100 nM Ca^{2+} externe et 1mM interne, ce qui est bien au-delà de la $[Ca^{2+}]_i$ suffisante pour activer le canal. Cela suggère que la $[Ca^{2+}]_e$ ne doit pas être inférieure à une certaine concentration.

KCNN4 est indépendant du voltage contrairement au canal KCNMA1, un autre canal K^+ activé par le Ca^{2+}. KCNN4 est caractérisé par une rectification entrante pour des potentiels dépolarisés dont l'origine reste assez mal comprise. Sa conductance unitaire γ est comprise entre 20 pS et 60 pS et varie en fonction des conditions expérimentales. Il se distingue des canaux SK1,2,3 du fait qu'il est insensible à l'apamine.

Les premières estimations de la quantité de KCNN4 dans le GR donnaient entre 100 et 200 canaux par GR (Alvarez and García-Sancho, 1987; Lew et al., 1982). Cette estimation est assez différente d'une autre réalisée en mesurant des flux de $^{86}Rb^+$: 75% des GR ayant entre 1-5 canaux activables et 25% entre 11-55 (Grygorczyk et al., 1984), et ce malgré des conditions ioniques similaires. Les récentes études de spectrométrie de masse quantitative faites à partir de GR humain dressent un tout autre tableau: le GR contient plus de 3000 copies du canal KCNN4 (Bryk and Wiśniewski, 2017). Ces différences de quantification s'expliquent vraisemblablement par les techniques utilisées. En patch clamp, c'est le nombre de canaux activables qui est quantifié malgré la présence d'autres canaux fermés à la membrane. Une explication possible à ces différences de mesures viendrait du fait qu'uniquement 3% (100/3000) des canaux KCNN4 dans le GR sont activables. Les 97% restant étant dans un état non-activable.

4.4.2.2. Structure :

Le canal fonctionnel est formé par 4 monomères KCNN4 qui s'arrangent en tétramère. Chaque monomère est composé de 6 segments transmembranaires (S1-6) avec S5 et S6 qui forment le pore du canal. Les parties N et C terminales sont cytosoliques. Le domaine C terminal est structuré en 3 domaines HA, HB et HC (Fig. 10A). HA et HB sont des domaines de liaison à la CaM conférant la sensibilité au Ca^{2+} et également importants pour l'assemblage du tétramère (Joiner et al., 2001). Le domaine C-terminal est important pour l'assemblage et l'adressage de KCNN4 à la membrane (Syme et al., 2003). En 2018, Lee et Mackinnon publient la structure de KCNN4 couplée à la Calmoduline en Cryo Microscopie Electronique (CME) (Lee and MacKinnon, 2018). Bien que l'interaction et la régulation de KCNN4 avec la CaM soit connue depuis longtemps, Lee et MacKinnon démontrent que KCNN4 est constitutivement lié à la CaM avec ou sans Ca^{2+} et cette liaison gouverne l'activation de KCNN4 dépendante du Ca^{2+}. Plus précisément, la CaM est une protéine formée par deux lobes N et C. Le lobe C est constitutivement attaché à KCNN4 au niveau des domaines HA et HB, alors que le lobe N est plus dynamique. En absence de Ca^{2+} KCNN4 est fermé, le pore est maintenu dans un état

non perméant grâce au résidu V282 dont l'encombrement stérique empêche tout passage d'ion K^+. L'augmentation du Ca^{2+} intracellulaire permet la fixation du N lobe de la CaM au niveau de la boucle intracellulaire reliant S4 et S5 ($S_{45}A$) de KCNN4. Ceci induit un changement de conformation qui élargit le pore du canal. A ce stade le canal est activé mais reste non conducteur car le diamètre du pore ne permet toujours pas le passage d'ion K^+ : c'est l'état activé fermé. Éventuellement, un mouvement supplémentaire du N-lobe permet l'ouverture complète du canal (Fig 10B). Cette publication de Lee et Mackinnon suggère que la forme majoritaire de KCNN4 est la forme activée fermée.

Une propriété unique de KCNN4 concerne son Histidine 358 dont la phosphorylation est nécessaire pour l'activation du canal. Dans son état phosphorylé, l'interaction d'un ion cuivre avec H358 maintiendrait KCNN4 dans un état inactif (Ji et al., 2018).

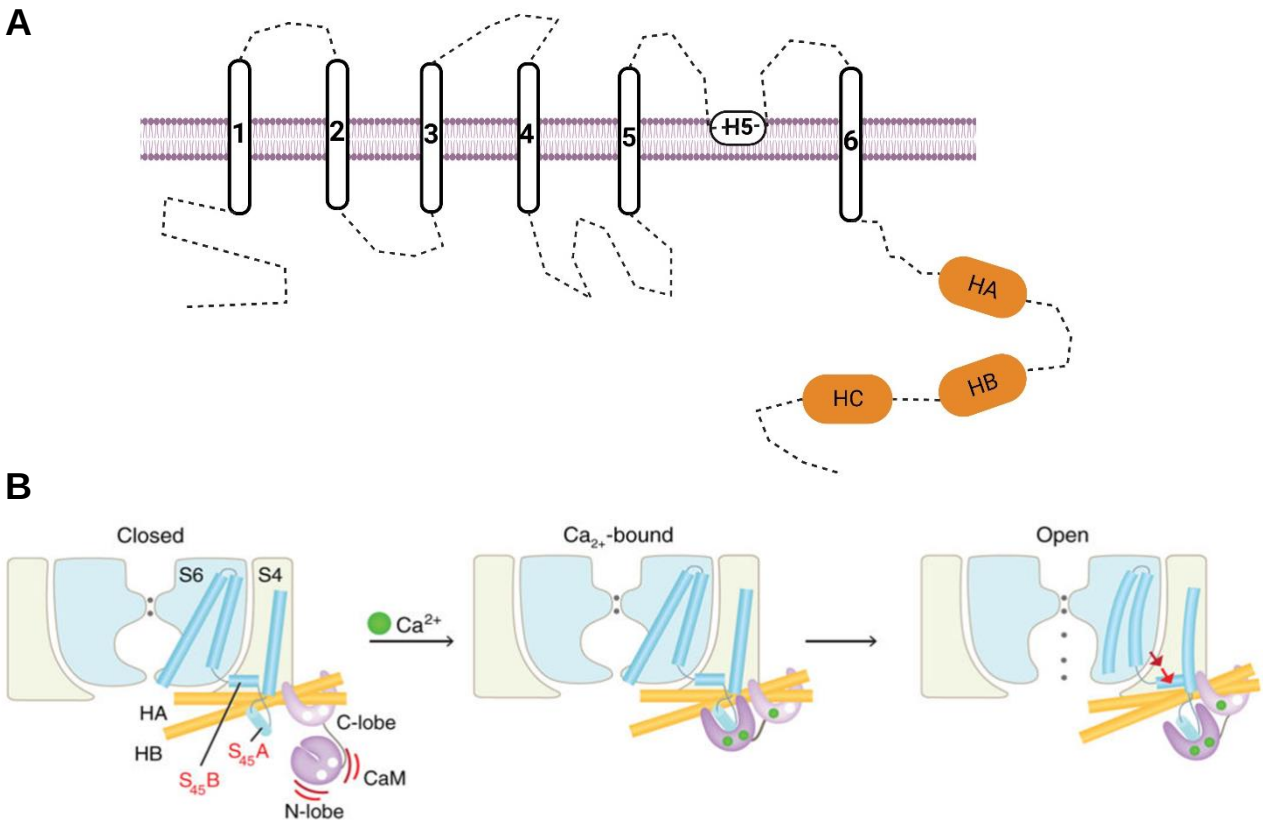

Figure 10 : Structure de KCNN4 et mécanisme d'activation par la CaM.

(A) Structure 2D de KCNN4 (B) De gauche à droite : forme non activée fermée, forme activée fermée, forme activée ouverte. En absence de Ca^{2+}, KCNN4 est fermé, le C-lobe de CaM est attaché au canal mais le N-lobe est détaché. En présence de Ca^{2+}, le N-lobe interagit avec le domaine $S_{45}A$ du canal ce qui induit un élargissement du pôre. Dans cet état, le résidu V282 empêche toujours le passage d'ion K^+. C'est le déplacement supplémentaire du domaine $S_{45}A$ qui pourra entraîner indirectement l'ouverture complète de KCNN4.

4.4.2.3. Rôles de KCNN4

Physiologiquement, KCNN4 est important pour la fonction des épithélium (Maruyama et al., 1986) et l'activation des lymphocytes T (Fanger et al., 2001; Ghanshani et al., 2000). L'invalidation de KCNN4 chez la souris est viable mais conduit à une altération de la régulation du volume des lymphocyte T (Begenisich et al., 2004). Au niveau pathologique son rôle est largement décrit: Adénocarcinome pulmonaire (Xu et al., 2021), pro-environnement tumoral (Ohya et al., 2022), métabolisme et croissance du carcinome hépatocellulaire (Fan et al., 2022) ou encore cancer colorectal (Ibrahim et al., 2021).

Dans le GR, KCNN4 n'est probablement jamais actif en conditions physiologiques. Premièrement, son activation est secondaire à une augmentation de la concentration Ca^{2+} qui est extrêmement bien régulée par la PMCA. Deuxièmement, la faible quantité de canaux activables à la membrane du GR en contradiction avec les données de spectrométrie de masse, suggère l'existence d'un mécanisme régulateur de l'activité de KCNN4. Nous verrons plus loin qu'il joue un rôle dans la pathologie érythrocytaire.

4.4.3. Cas de $Ca_v2.1$

Le canal calcique $Ca_v2.1$ étant impliqué dans la signalisation calcique, j'estime important d'y consacrer quelques lignes d'autant plus que de nombreux travaux démontrent son existence dans le GR. C'est un canal calcique voltage dépendant, impliqué majoritairement dans la libération de neurotransmetteur synaptique, actif à des potentiels négatifs (-45 à -35 mV) (Llinás et al., 1989). Ce canal a été décrit dans les GR en utilisant du LPA (Lysophosphatydic Acid, Acide Lysophosphatidique), qui, dans 25% des cas, a induit un influx calcique (Yang et al., 2000). Deux années plus tard, l'influx calcique provoqué par le LPA est bloqué par la ω-agatoxin-TK (inhibiteur spécifique de $Ca_v2.1$) a permis de confirmer l'existence de ce canal calcique dans le GR (Andrews et al., 2002). Les auteurs de cet article ont validé sa présence, par immunodétection, dans la membrane du GR. On peut se demander pourquoi un canal calcique voltage dépendant est présent dans le GR, notamment au vu de son rôle dans le système nerveux. Le potentiel de repos du GR étant de -12 mV (maintenu par le Cl^-), il est improbable que $Ca_v2.1$ puisse s'activer. Néanmoins, l'activation du canal Gardos induit une hyperpolarisation importante due la sortie d'ions K^+. Cette transition vers des potentiels très négatifs peut activer $Ca_v2.1$ (Baunbæk and Bennekou, 2008). Récemment, l'hypothèse de fluctuation du potentiel a été avancée (Jansen et al., 2021), notamment dans le cas de mutations gain de fonction de KCNN4 (Glogowska et al., 2015; Rapetti-Mauss et al., 2015), qui rendent le canal plus sensible au Ca^{2+} ou augmentent l'amplitude du courant. Cette étude montre que l'activation du canal KCNN4 par le NS309 provoque une augmentation de la population de GR avec une quantité

de Ca^{2+} importante. Cette augmentation est moindre en inhibant KCNN4 ou $Ca_v2.1$. Néanmoins le pourcentage de GR portant la mutation R352H sur KCNN4, qui répondent par une augmentation de Ca^{2+} est identique avec ou sans NS309 (~15%). La mutation R352H de KCNN4 est décrite comme gain de fonction car elle augmente la sensibilité calcique de KCNN4. On devrait alors s'attendre à un effet synergique avec le NS309, augmentant davantage la quantité de GR positifs au Ca^{2+}.

Il est suggéré que $Ca_v2.1$ est en interaction avec KCNN4. Selon moi, c'est une assomption tout à fait plausible, puisque KCNN4 et $Ca_v2.1$ sont tous deux en interaction avec la CaM (Lee et al., 2003). Un argument en faveur de cette hypothèse est l'interaction entre CFTR et la PMCA4, deux protéines interagissant avec la CaM, dans les cellules canalaires pancréatiques (Madácsy et al., 2022). Dans cet exemple, un défaut de liaison de CFTR à la CaM provoque une diminution du pourcentage d'interaction avec la PMCA4. Ainsi, il est possible que $Ca_v2.1$ et KCNN4 interagissent par l'intermédiaire de la CaM. Pour l'heure, des mutations gain de fonction de $Ca_v2.1$ sont associées à une forme de migraine hémiplégique familial (Sutherland et al., 2019). A ma connaissance, $Ca_v2.1$ n'a pas été associé à quelconque maladie relative au GR. Il serait alors intéressant d'étudier ce gène dans les analyses génomiques chez les patients adressés pour des anémies hémolytiques héréditaires.

4.4.4. Autres

4.4.4.1. Canaux anioniques

CFTR

CFTR (Cystic fibrosis transmembrane conductance regulator) est un canal chlore exprimé à la membrane apicale des cellules épithéliale. Il est largement connu dans la mucoviscidose où sa mutation perte de fonction entraîne un défaut de fluidité du mucus pulmonaire. Dans le GR, CFTR serait impliqué dans la libération d'ATP induite par un stress mécanique (Sprague et al., 1998). Cependant, il n'est pas retrouvé au niveau transcriptomique dans les précurseurs érythroïdes, ni au niveau protéique dans les GR (Bryk and Wiśniewski, 2017).

TMEM16A/TMEM16F

L'alpha hémolysine, produite par *Escherichia coli*, est une substance capable d'induire une lyse osmotique des GR par gonflement. Cette substance induit une entrée de Ca^{2+} et il a été montré que cette entrée de Ca^{2+} pouvait activer KCNN4 et un canal de type TMEM16 dans les GR humains (Skals et al., 2010). C'était TMEM16A (ou ANO1) qui avait été proposé dans ce mécanisme. Néanmoins, dans cette étude ils observent également une augmentation de l'exposition de PS à la couche externe de la membrane du GR, de façon Ca^{2+} dépendante. Or, il a été récemment montré qu'un autre membre de la famille TMEM16, à savoir TMEM16F (ou ANO6) était exprimé dans les GR. TMEM16F est

un canal Cl^- Ca^{2+}-dépendant qui exerce en plus une activité de scramblase dans le GR humain (Yan et al., 2022). Les études de protéomiques montrent que TMEM16F est exprimé dans le GR au niveau protéique ce qui n'est pas le cas de TMEM16A (Bryk and Wiśniewski, 2017). Ainsi, dans l'étude de Skals *et al*. de 2010, mentionnée ci-dessus, le canal responsable du courant Cl^-, Ca^{2+}-dépendant, associé à l'exposition de la PS dans les GR était très probablement TMEM16F et non pas TMEM16A.

CLC2

CLC-2 est un canal chlore rectifiant entrant (ayant un courant plus faible pour les potentiels positif que pour les potentiels négatifs) qui est inhibé par le Zn^{2+} et sensible à des changements de volume. Son existence a été démontré dans le GR par WB et mesuré suite à l'infection par *Plasmodium* (Huber et al., 2004).

VDAC

VDAC (Voltage dependant anion channel, canal anionique voltage dépendant), contrairement à ce que son nom indique, est perméable au Cl^-, K^+, Na^+ mais aussi à des anions plus gros comme le glutamate, l'ATP et d'autre cation de grande taille (Shoshan-Barmatz et al., 2010). VDAC est connu pour son rôle de régulation du potentiel mitochondrial (Shimizu et al., 1999) dans les mécanismes d'apoptose. La présence de VDAC a été démontré dans le GR humain (Bouyer et al., 2011) ce qui est confirmé par des analyses de protéomiques quantitatives (Bryk and Wiśniewski, 2017). Fermé dans des conditions physiologiques, il a été proposé qu'il puisse s'activer à la suite de changement du potentiel de membrane comme après l'activation de PIEZO1 ou KCNN4 dans le GR humain (Bouyer et al., 2011). Il pourrait alors être responsable, en partie, de la sortie Cl^- accompagnant la sortie de K^+ suite à une activation de KCNN4.

4.4.4.2. Canaux cationiques non sélectif (NSCC)

TRPC6

PIEZO1 n'est pas le seul NSCC présent dans le GR. C'est également le cas de TRPC6 (Transcient Receptor Potential Channel 6), un membre de la famille des canaux TRP (Föller et al., 2008) détecté au niveau protéique dans l'erythrocyte. Il est impliqué dans la fuite cationique et notamment calcique, à l'origine des mécanismes de senescence.

TRPV2

TRPV2 (TRP vanilloid 2) est un autre membre de la famille TRP exprimé dans le GR et impliqué dans l'homéostasie calcique (Belkacemi et al., 2021). Son activation par le cannabidiol induit une activation de KCNN4 par entrée de Ca^{2+} et une déshydratation du GR.

NMDAR

Les canaux ligand dépendants NMDAR (Nmethyl-D-Aspartate Receptors) ont été décrit dans le GR (Makhro et al., 2013) et sont impliqués dans l'homéostasie calcique. Leur activation induit une augmentation transitoire de Ca^{2+} induisant une déshydratation aggravant le phénotype de la drépanocytose.

NSVDC

Enfin le canal cationique non sélectif voltage dépendant (NSVDC), est responsable du phénomène de repolarisation observé en conditions de Low Ionic Strenght (LIS). En solution LIS, le Na^{+} est remplacé par du sucrose et l'incubation du GR dans cette solution induit une forte dépolarisation de la membrane vers +75mV qui retourne à une valeur normale (-10mV) au bout de 60 min (Moersdorf et al., 2013) en partie due à NSVDC qui est activé à partir de +30mV. Ce canal est perméable au Na+, K+ et Ca2+ et serait important pour le maintien du potentiel de membrane (Kaestner et al., 2000). NSVDC pourrait être impliqué dans la restauration du volume après activation de PIEZO1 et KCNN4 dans la circulation sanguine (Monedero Alonso et al., 2021) bien que ce mécanisme soit encore hypothétique.

4.5. Couplage PIEZO1 KCNN4 dans le GR

L'existence de perméabilités cationiques monovalentes ou divalentes activées par un stress mécanique du Globule rouge, est connue depuis longtemps. Une des premières études à ce sujet montre une augmentation de l'influx calcique après un stress mécanique (Larsen et al., 1981). Cet influx est notamment visible en absence d'ATP puisque la pompe PMCA ATPase permet de recycler très rapidement le Ca^{2+} en sa présence. Plus tard, il a été montré qu'un stress mécanique pouvait induire un influx de Na^{+} et un efflux de K^{+} similaire (Johnson and Gannon, 1990). Il a alors été observé que cette perméabilité était transitoire et donnait lieu à un efflux de K^{+} uniquement en présence de Ca^{2+} extracellulaire (Johnson and Tang, 1992). Les changements physiques induits par les différents protocoles de stimulation (chambre de microcirculation) restaient difficiles à étudier. L'existence de composés chimiques induisant une courbure de la membrane plasmique ont notamment été utilisés mais n'ont pas pu induire à eux seuls une perméabilité cationique (Johnson, 1994).

A partir du moment où PIEZO1 a été décrit dans les GR, la question d'un lien fonctionnel avec KCNN4 s'est rapidement posée. Avant cela, une étude clef montrait que les déformations de la membrane plasmique des globules rouges pouvait induire une activation de KCNN4 (Dyrda et al., 2010). En 2015 Cahalan *et al.* posent les jalons du lien fonctionnel unissant PIEZO1 et KCNN4 via l'augmentation du calcium intracellulaire (Cahalan et al., 2015). Dans la microcirculation sanguine, les chocs mécaniques et stress hydrostatiques subis par le GR pourraient entraîner l'ouverture de PIEZO1 et provoquer un influx calcique. Cette entrée de Ca^{2+} induit une activation subséquente de KCNN4 qui va alors dissiper le gradient de K^{+}, créant un déséquilibre cationique. Cela va engendrer une sortie d'H_2O osmotiquement liée qui déshydratant le GR. Cette perte d'eau permettrait l'adaptation locale du volume pour faciliter le passage des GR dans les microcapillaires (Danielczok et al., 2017) (Figure 11). Physiologiquement, l'existence d'un tel phénomène suscite un débat quand on sait que le GR ne régule pas son volume. Le GR devrait se déshydrater extrêmement rapidement au vu du nombre de passages dans la microcirculation et dans les fentes spléniques. Toutes ces micro déshydrations, hypothétiques, ne sont pas compensées et pourraient jouer un rôle dans la senescence programmée (Rogers and Lew, 2021).

Si le rôle physiologique du couplage fonctionnel PIEZO1-KCNN4 reste l'objet de débats, en revanche, ce couplage est impliqué dans la pathologie érythrocytaire où il est la cause d'une anémie hémolytique : la Xérocytose Héréditaire, qui sera l'objet de la prochaine section.

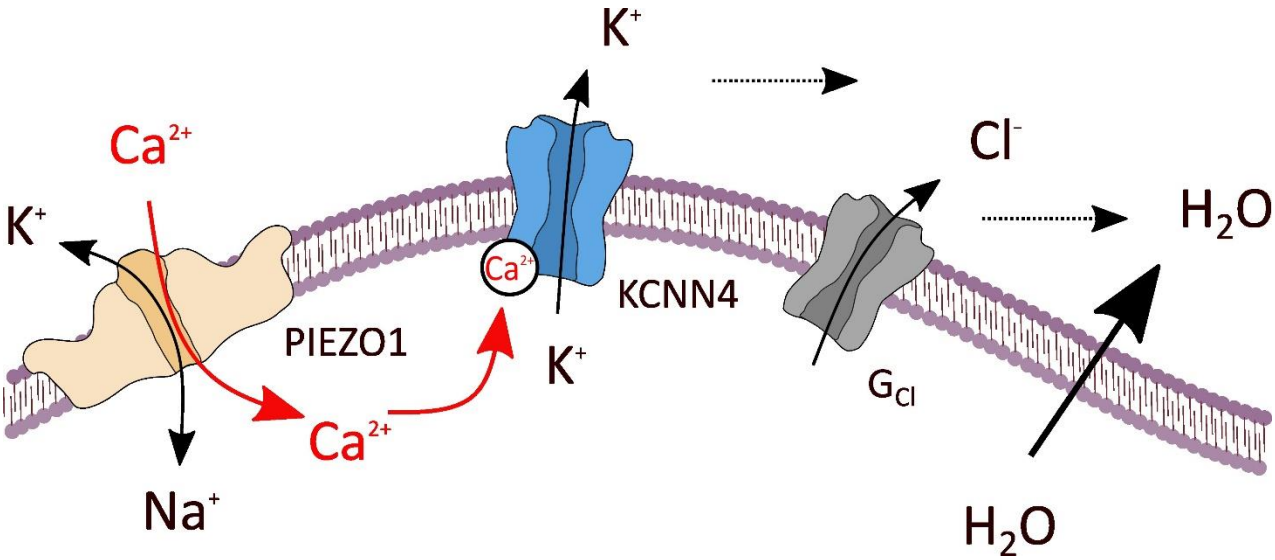

Figure 11 : Modèle proposé du couplage PIEZO1 – KCNN4 dans le GR humain en conditions physiologiques.

PIEZO1 est activé à la suite d'une perturbation mécanique dans la circulation sanguine. Son ouverture permet un influx calcique qui active le canal KCNN4. KCNN4 engendre alors un efflux net de K^+ suivi de Cl^- par une conductance notée G_{Cl}. Cette sortie nette de KCl entraine une perte d'eau osmotiquement lié, déshydratant le GR.

5. Anémie Hémolytique héréditaire lié à un défaut de perméabilité

5.1. Généralités

Selon l'OMS, une anémie est une affection au cours de laquelle le nombre de GR ou le taux d'Hb est inférieur à la normale. Il y a anémie si les taux d'Hb sont inférieur à 13 g/dL chez l'homme et 11.5 g/dL chez la femme. On distingue 2 catégories d'anémies :

- Anémie centrale :
    - Carence en fer
    - Maladie inflammatoire
    - Déficit en érythropoïétine (EPO)
    - Dysfonctionnement du tissus hématopoïétique (ex : Anémie de Blackfan-Diamond (BFD)
- Anémie périphérique :
    - Hémorragie
    - Destruction anormale des GR : Anémie Hémolytique.

Les anémies hémolytiques sont des maladies rares induites par une hémolyse aiguë ou chronique des GR. Les symptômes sont très hétérogènes avec des anémies sévères nécessitant des transfusions régulières et des anémies très bien compensées pouvant passer inaperçu durant la vie de l'individu. Elle peut être régénérative ou arégénérative selon la capacité de compensation du tissu hématopoïétique. Une anémie hémolytique est extra-corpusculaire lorsqu'elle est causée par un facteur extérieur ou intra-corpusculaire si le défaut est interne du GR. Les anémies intra-corpusculaires sont congénitales car elles sont induites par la mutation d'un gène entraînant différentes anomalies (Tableau 3).

Anomalie	Maladie	Gène(s) muté(s)
Hémoglobine	Drépanocytose	HBB
	Thalassémie (alpha, beta)	HBB ou HBA
Enzymatique	Déficit en G6PD	G6PD
	Déficit en PK	PKM
	Déficit en 5’ nucléotidase 3A	NT5C3A
Structure	Ovalocytose	SLC4A1
	Sphérocytose	ANK1, SPTB, SPTA1, SLC4A1, EPB42
	Elliptocytose	EPB41, SPTA1, SPTB
	Pyropoïkilocytose	SPTA1
Perméabilité	Stomatocytose déshydratée (Xérocytose) DHS (Dehydrated Stomatocytocis)	PIEZO1 (DHS1), KCNN4 (DHS2)
	Stomatocytose Hyperhydratée	RHAG
	Cryohydrocytose/South East Asian Ovalocytosis (SAO)	SLC4A1
	Pseudohyperkaliémie	ABCB6

Tableau 3 : Liste des principales anémies hémolytiques intra-corpusculaires et les gènes associés.

(Andolfo et al., 2016 ; “Anémie hémolytique,” 2011)

5.2. Xérocytose Héréditaire

La Xérocytose Héréditaire (XH ou Stomatocytose Déshydratée : DHS) est une anémie hémolytique congénitale autosomique dominante qui touche 1:50000 individus. Elle est caractérisée par une déshydratation des GR (Miller et al., 1971). Cette déshydratation est induite par une augmentation de la perméabilité cationique (Albuisson et al., 2013; Caulier et al., 2020; Rapetti-Mauss et al., 2015) et notamment par une perte de K^+ excessive. Cela entraine une fragilisation du GR dont l'espérance de vie est réduite. Génétiquement, la XH est causée par des mutations gain de fonctions sur le canal PIEZO1 (Zarychanski et al., 2012) ou sur le canal KCNN4 (Glogowska et al., 2015; Rapetti-Mauss et al., 2015; Rivera et al., 2017) . Dans la majorité des cas, c'est PIEZO1 qui est muté avec plus de 69 mutations faux-sens recensées. Toutes ne sont pas caractérisées d'un point de vue fonctionnel mais les mutations listées dans le Tableau 5 sont toutes associées à un phénotype de XH. Concernant KCNN4, 11 mutations ont été recensées dans la littérature (Tableau 4) dont 6 sont décrites comme gain de fonction. La cause primaire de cette déshydratation est le couplage entre PIEZO1 et KCNN4. Les mutations de PIEZO1 entraîneraient une réponse au stimulus mécanique accrue ou prolongée, induisant une plus forte entrée de Ca^{2+} et donc une activation de KCNN4 permettant la sortie de K^+. Les mutations de KCNN4, quant à elles, induisent une augmentation de la sensibilité Ca^{2+} et/ou une augmentation de la conductance du canal. Que ce soit en présence de mutations de PIEZO1 ou KCNN4, l'effecteur final de la déshydratation est KCNN4 puisque c'est son activation qui provoque la perte massive de KCl et donc d'eau (Rapetti-Mauss et al., 2017).

Nucléotide	Acide aminé	Reference
nr	P204R	(Utsugisawa et al., 2017)
c.664G > C	V222L	(Allegrini et al., 2022)
nr	A279T	(Utsugisawa et al., 2017)
c.845T > A	V282E	(Glogowska et al., 2015)
c.844G > A	V282M	(Glogowska et al., 2015)
c.940T > C	S314P	(Fermo et al., 2020)
c.965C > T	A322V	(Mansour-Hendili et al., 2021)
c.983A > G	H328R	(Andolfo et al., 2021)
c.1018C > A	H340N	(Allegrini et al., 2022)
c.1055G > A	R352H	(Rapetti-Mauss et al., 2015)
c.G1104 (TG/GT)	DelV369-K373	(Picard et al., 2019)

Tableau 4 : Liste des mutations faux-sens de KCNN4 associé à une Xérocytose Héréditaire.

(Andolfo et al., 2018; More et al., 2020; Picard et al., 2019). Seule la mutations deV369-L379 n'est pas faux-sens mais est un frame-shift (décalage de phase) qui induit une délétion de 28pb correspondant à 11pb de l'exon 7 et de 17 l'intron suivant. nr : non renseigné.

Nucléotide	Acide aminé	Référence
c.608T > C	L203P	(Andolfo et al., 2021)
c.1001C > T	A334V	(Andolfo et al., 2021)
c.1013C > A	S338Y	(Picard et al., 2019)
c.1369C > T	R457C	(Russo et al., 2018)
c.1447G>A	V483M	(Andolfo et al., 2021)
c.1792G > A	V598M	(Rapetti-Mauss et al., 2017)
c.1792G > C	V598L	(Picard et al., 2019)
c.1795G > C	V599L	(More et al., 2020)
c.1813A > G	M605V	(Andolfo et al., 2021)
c.1815G > A	M605I	(Picard et al., 2019)
c.2005G > T	D669Y	(Andolfo et al., 2018)
c.2042 T > C	F681S	(Rapetti-Mauss et al., 2017)
c.2152G > A	G718S	(Andolfo et al., 2013)
c.2344G > A	G782S	(Andolfo et al., 2013)
c.2423G > A	R808Q	(Andolfo et al., 2013)
c.2896G > A	V966M	(Kedar et al., 2019)
c.2915G > A	R972H	(More et al., 2020)
c.3350C > T	S1117L	(Andolfo et al., 2013)
c.3935C > T	A1312V	(Andolfo et al., 2021)
c.4069A > G	I1357V	(Picard et al., 2019)
c.4071C > G	I1357M	(Picard et al., 2019)
c.4073G > C	R1358P	(Albuisson et al., 2013)
c.4082A > G	Q1361R	(Kager et al., 2018)
c.4481A > C	E1494A	(Andolfo et al., 2021)
c.4556A > C	Q1519P	(Picard et al., 2019)
c.5195C > T	T1732M	(Andolfo et al., 2021)
c.5389C > T	R1797C	(Russo et al., 2018)
c.5694G > C	E1898D	(Russo et al., 2018)
c.5728G > A	E1910L	(Picard et al., 2019)
c.5773C > T	R1925W	(Picard et al., 2019)
c.5828G > A	R1943Q	(Glogowska et al., 2017)
c.5835C > G	F1945L	(Andolfo et al., 2021)
c.5981C > T	S1994F	(Picard et al., 2019)
c.5981C>G	S1994C	(Andolfo et al., 2021)
c.6007G > A	A2003T	(Picard et al., 2019)
c.6008C > A	A2003D	(Andolfo et al., 2013)
c.6016G > A	V2006I	(Picard et al., 2019)
c.6058G > A	A2020T	(Albuisson et al., 2013)
c.6059C > T	A2020V	(Andolfo et al., 2013)
c.6067C > G	L2023V	(Risinger et al., 2018)
c.6205G>A	V2069M	(Andolfo et al., 2021)
c.6262C > G	R2088G	(Glogowska et al., 2017)
c.6328C > T	R2110W	(Russo et al., 2018)
c.6329G > A	R2110Q	(Picard et al., 2019)
c.6380C > T	T2127M	(Andolfo et al., 2013)
c.6451 T > C	C2151R	(Picard et al., 2019)
c.6479C > T	P2160I	(Picard et al., 2019)
c.6574C > A	L2192I	(Picard et al., 2019)
c.6601G > T	V2201F	(Picard et al., 2019)
c.6674 T > G	M2225R	Zarychanski 2012
c.6796G > A	V2266I	(Russo et al., 2018)
c.6829C > A	I2277M	(Picard et al., 2019)
c.6905G > A	R2302H	(Glogowska et al., 2017)
c.6922C > G	Q2308E	(Picard et al., 2019)
c.7180G > A	G2394S	(Andolfo et al., 2021)
c.7219G > C	E2407Q	(Andolfo et al., 2021)
c.7297G > C	G2433R	(Picard et al., 2019)
c.7367G > A	R2456H	(Zarychanski et al., 2012a)
c.7372 T > C	F2458L	(More et al., 2020)
c.7381G > A	E2461K	(Kedar et al., 2019)
c.7391A > C	H2464P	(Picard et al., 2019)
c.7420G > A	V2474M	(Picard et al., 2019)
c.7463G > A	R2488Q	(Andolfo et al., 2013)
c.7467G > C	Q2489D	(Picard et al., 2019)
c.7471C > T	R2491W	(Picard et al., 2019)
c.7505A > G	K2502R	(Del Orbe Barreto et al., 2016)
c.7529C > T	P2510L	(Shefer Averbuch et al., 2018)
c.7558A > G	K2520E	(Andolfo et al., 2021)

Tableau 5 : Liste des 69 mutations faux-sens de PIEZO1 associé à une Xérocytose Héréditaire.

La majorité des mutations listées dans ce tableau ne sont pas caractérisées d'un point de vue fonctionnel mais sont associées un phénotype clinique de type DHS soit seules soit combinées entre elles.

D'un point de vue clinique le phénotype des XH est très hétérogène. Deux patients sur trois présentent une anémie complètement compensée, la surcharge en fer est fréquente, des évènement thrombotiques peuvent survenir après splénectomie qui n'est donc pas recommandée (Picard et al., 2019). L'étude rétrospective de Picard *et al.* sur 126 patients XH montre que les mutations KCNN4 sont associées à un phénotype plus sévère que les mutations PIEZO1. Pourtant, les mesures d'Ektacytométrie associent plus souvent une déshydratation aux mutations PIEZO1, contrairement aux mutations KCNN4. Cette contradiction est d'autant plus frappante puisque c'est KCNN4 qui est le médiateur final de la déshydratation. Cette différence a permis de séparer la XH en deux sous-groupes : Stomatocytose Déshydratée de type 1 (DHS1 : mutations PIEZO1) et Stomatocytose Déshydratée de type 2 (DHS2 : mutations KCNN4). La DHS1 étant associée à une déshydratation alors que la DHS2 ne l'est pas (Andolfo et al., 2016; Fermo et al., 2017).

Cela suggère que la pathologie pourrait résulter de conséquences de ces mutations sur d'autres tissus que le GR. Etant donné les rôles de PIEZO1 dans un grand nombre de tissus, des mutations gain de fonction pourraient entrainer des effets collatéraux et complexifier davantage le tableau clinique de la pathologie. De la même manière pour KCNN4, les mutations sont rarement associées à une déshydratation du GR mais le phénotype de l'anémie est néanmoins parfois très sévère.

Au-delà de son rôle dans le GR, PIEZO1 est exprimé dans les progéniteurs érythroïdes précoces (Caulier et al., 2020) où son activation retarde l'érythropoïèse. Cela ajoute une complexité supplémentaire à la pathologie mais explique difficilement pourquoi les mutations PIEZO1 sont associées à une hémolyse bien compensée. En effet, outre son effet hémolytique, PIEZO1 aurait un effet central, diminuant la production de GR. PIEZO1 est également associé à l'hyperferritinémie souvent retrouvée chez les patients XH. Cette surcharge en fer peut être provoquée par 3 causes :
(1) des transfusions de sang, mais l'hyperferritinémie est souvent décelée au moment du diagnostic donc avant tout traitement.
(2) Une hémolyse chronique, souvent compensée chez les mutants PIEZO1.
(3) Implication de PIEZO1 dans le métabolisme du fer. En effet, il a été démontré que les niveaux d'hepcidine, une hormone secrétée par le foie permettant de réguler le métabolisme du fer, étaient réduits chez les patients XH. Ce mécanisme serait directement imputable aux mutations gain de fonction de PIEZO1 qui joueraient sur l'expression de l'hepcidine par le biais de la voie de signalisation BMP/SMAD et ce de manière Ca^{2+} dépendante (Andolfo et al., 2020).

Enfin, une observation intéressante concerne la Dysplasie lymphatique congénitale. C'est une maladie due à des mutation perte de fonction de PIEZO1 (Fotiou et al., 2015; Lukacs et al., 2015). Il est surprenant de constater que les caractéristiques cliniques des patients porteurs de mutations perte de fonction de PIEZO1 sont parfois retrouvées avec les mutations gain de fonction, notamment

concernant les œdèmes périnataux que l'on peut observer aussi dans la XH (Andolfo et al., 2013; Grootenboer et al., 1998) ou encore la présence de stomatocytes. Cela démontre la complexité du rôle de PIEZO1 et suggère que le phénotype déshydratation des GR induit par ses mutations gain de fonction n'est peut-être pas le seul en cause dans la XH.

De la même façon, les mutations gain de fonction de KCNN4 pourraient jouer un rôle dans les précurseurs des GR, notamment dans les réticulocytes (Picard et al., 2020). En effet, le MCV des réticulocytes (rMCV) est diminué en cas de mutations KCNN4 contrairement aux mutations PIEZO1 où il n'y a pas de changement. Ces indices réticulocytaires peuvent alors être très utiles pour poser un diagnostic d'anémie hémolytique XH associé à une mutation de KCNN4.

L'expression de *KCNN4* est également corrélée à la différenciation érythrocytaire comme démontré à partir CD34+ isolée de sang total de volontaires sains (Andolfo et al., 2015). Après mise en culture, ex vivo, avec érythropoïétine (EPO), au bout de14 jours de traitement, une augmentation de la quantité d'ARN messager de *KCNN4* a été mesurée. Avant cela, l'ARN messager de *KCNN4* avait pu être détecté dans des cellules souche embryonnaires différenciées en cellules hématopoïétiques (Vandorpe et al., 1998).

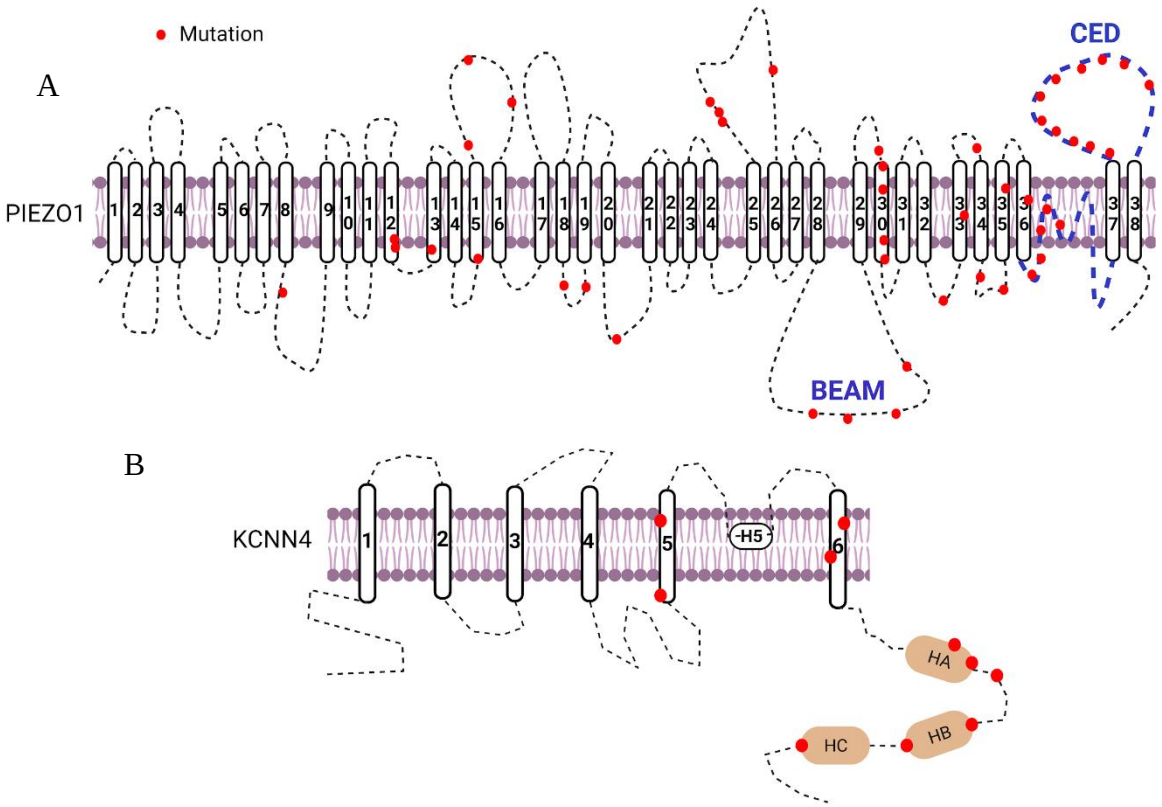

Figure 12 : Structure 2D de PIEZO1 et KCNN4 avec les mutations retrouvées dans la XH.

Les mutations connues sont placées approximativement au niveau des domaines correspondants (points rouges) (The UniProt Consortium, 2023). Le détail des mutations est donné dans les tableaux 4 et 5.

La grande majorité des mutations de PIEZO1 sont localisées dans la partie C-terminale de la protéine qui permet la formation du pore du canal. C'est le cas des deux premières mutations de PIEZO1 décrites dans la XH en 2012 (Zarychanski et al., 2012a): M2225R et R2456H. Par ailleurs, c'est la première description d'une mutation sur un canal mécanosensible, associée à une pathologie. Elle a permis de donner une cause génétique à la XH, déjà décrite auparavant (An and Mohandas, 2008; Flatt and Bruce, 2009; Grootenboer et al., 1998; Miller et al., 1971). Par la suite, d'autres mutations de PIEZO1 ont été décrites: A2020T, R1358P, 7479_7484dup et E2496ELE (Albuisson et al., 2013; Bae et al., 2013; Glogowska et al., 2017). Albuisson et son équipe ont réalisé la première étude fonctionnelle et déterminé le caractère gain de fonction des mutations de PIEZO1. Ils ont introduit les différentes mutations dans hPIEZO1 qu'ils ont ensuite exprimé dans des cellules HEK293T afin d'analyser l'activité du canal en patch-clamp (cellule entière). Ils n'ont pas mis en évidence de changement de la sensibilité mécanique ni de l'amplitude du courant mais une augmentation importante du temps d'inactivation. La forme sauvage du canal s'active de façon transitoire malgré la persistance du stimulus. Ici, les mutations modifient cette propriété de PIEZO1 qui ne se referme plus

aussi rapidement, son temps d'inactivation τ est rallongé. Ce τ est obtenu à partir d'une régression exponentielle de phase d'inactivation (Figure 13A).

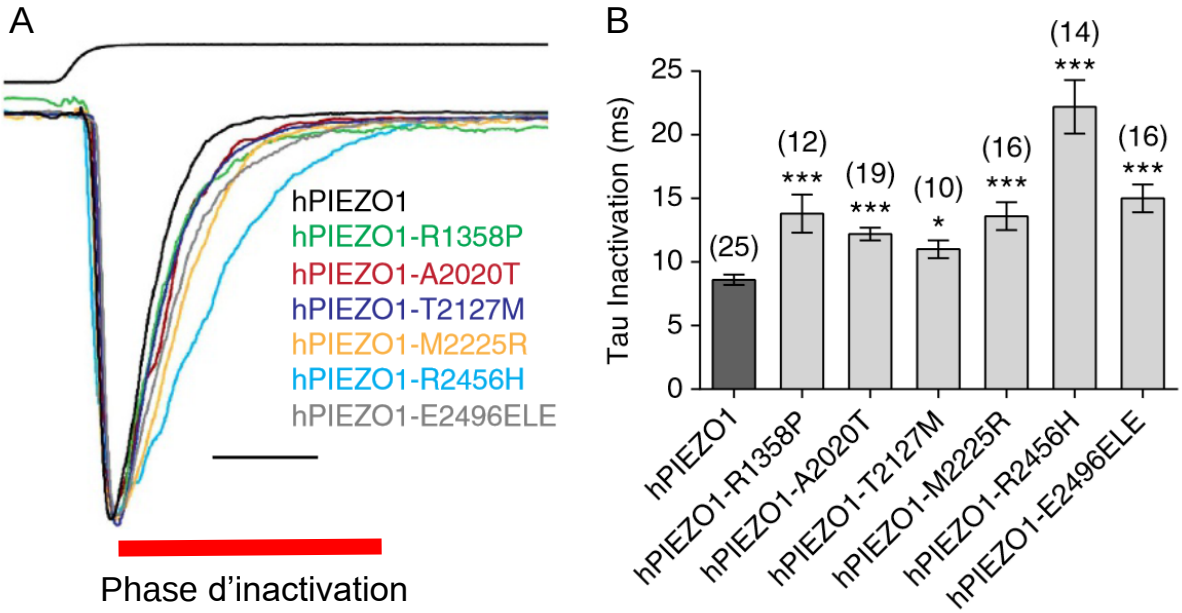

Figure 13 : Les mutations gains de fonction de PIEZO1 augmentent le temps d'inactivation.

(A) Tracés représentatifs de PIEZO1 WT (noir) ou mutés (couleur) obtenus après stimulation mécanique. (B) τ constante d'inactivation de PIEZO1 WT ou muté. Adapté de (Albuisson et al., 2013).

De la même manière pour KCNN4, les mutations sont majoritairement retrouvées dans la partie C-terminale et plus particulièrement au niveau des domaines de liaison de la calmoduline. La première mutation décrite est R352H où l'arginine du domaine de liaison à la CaM est substituée par une histidine (Glogowska et al., 2015; Rapetti-Mauss et al., 2015). Cela entraine une augmentation de la sensibilité calcique : KCNN4 s'active pour des concentrations de Ca^{2+} plus faibles et donc plus souvent chez ces patients. Deux mutations ont ensuite été décrites et sont localisées au niveau du pore du canal : V282E et V282M (Glogowska et al., 2015; Rapetti-Mauss et al., 2016; Rivera et al., 2017). La Valine 282 est un résidu clé dans le mécanisme d'ouverture du canal (4.4.2.2) (Garneau et al., 2009) et la mutation V282M rend le canal insensible au Ca^{2+} qui devient un canal de fuite.

Objectifs de la thèse

Chez les patients atteints de XH, il est proposé que les mutations gain de fonction sur PIEZO1 conduisent à une hyperactivité du couplage entre PIEZO1 et KCNN4, ce qui entraîne une déshydratation importante des globules rouges, cause d'anémie hémolytique. Dans le cas des mutations gain de fonction sur KCNN4, c'est l'effecteur même de la déshydratation qui serait hyperactif. On observe un tableau clinique très hétérogène chez les patients atteints. Ceux-ci peuvent avoir des anémies modérées à sévères, une hémolyse plus ou moins compensée nécessitant ou non des transfusions sanguines. Comme mentionné précédemment, cette hétérogénéité n'est pas bien comprise et représente un obstacle majeur dans le diagnostic de cette maladie. De plus, depuis la caractérisation initiale de la cause génétique des XH, il a été décrit à de multiples reprises dans la littérature que les mutations de PIEZO1 ou KCNN4 n'induisaient pas les mêmes conséquences. En particulier, les XH associées aux mutations PIEZO1 sont corrélées à une déshydratation des GRs, ce qui est rarement le cas pour les mutations de KCNN4. Ces observations sont paradoxales car KCNN4 est l'effecteur final conduisant à la déshydratation dans la XH. Ainsi il existe encore de nombreuses inconnues dans cette pathologie érythrocytaire. Ma thèse s'est donc intéressée à étudier le couplage fonctionnel entre PIEZO1 et KCNN4 afin de mieux comprendre son rôle dans la pathologie érythrocytaire.

Cette thèse s'articule autour de deux grands axes :

1. Caractérisation de nouvelles mutations de PIEZO1 et KCNN4 identifiées chez des patients atteints d'anémie hémolytique héréditaire.
2. Comprendre comment le couple PIEZO1/KCNN4 est régulée dans le GR en conditions physiologiques et pathologiques.

Chapitre 1 :

Caractérisation des mutations de PIEZO1 et KCNN4 dans la Xérocytose Héréditaire

Outils utilisés

Afin d'étudier les GR de patients porteurs de mutations KCNN4 ou PIEZO1, nous avons utilisé différentes approches. Nous avons mesuré les contenus en eau, potassium, sodium et calcium ; la résistance osmotique (RO) ; l'expression protéique quand cela était possible ; ainsi que l'activité électrique concernant les mutations de KCNN4 avec la technique de patch-clamp. Les prélèvements de sang de patients étaient accompagnés, quand cela était possible, de prélèvements issus de volontaires sains (témoins). Dès la réception, le sang a été lavé trois fois dans une solution de Ringer (mM) : NaCl (145), KCl (5), MgSO4 (2), $CaCl_2$ (1), HEPES (10) pH 7.4 et la couche leucocytaire a été retirée par aspiration.

L'évolution des contenus ioniques et hydriques est suivie au cours du temps après ajout de différentes drogues : yoda1 (2µM) pour activer le canal PIEZO1, vanadate (5mM) pour inhiber la PMCA, senicapoc (4µM) pour inhiber le canal KCNN4 et GsMTx4 (5µM) pour inhiber le canal PIEZO1. Afin de mesurer les contenus en eau, potassium et sodium spécifiquement, de l'ouabaïne (0.5mM) est utilisée pour bloquer la pompe NaK. Cela empêche la NaK de gommer toutes différences de contenus potassiques ou sodiques. Chaque expérience est faite en triplicata sauf pour les mesures de Ca^{2+}. Les valeurs de contenus en eau sont données en *Eau / P.S corr* (Poids sec corrigé) et correspondent au ratio entre le poids du culot de GR et le poids du culot sec (après chauffage à 80°C), en prenant en compte le volume d'eau entre les cellules. Le contenu en Na^+ et K^+ intracellulaire est extrait à partir de culot sec de GR et est donné en *µmol/g P.S.*

Les mesures de Résistance Osmotique (RO) sont toutes réalisées à partir du sang total avant lavage. La RO permet de connaitre indirectement l'état d'hydratation des GR, en soumettant ces derniers à différentes tonicités de NaCl, afin de provoquer une hémolyse par entrée d'eau. La courbe de RO est donnée par le % d'hémolyse en fonction de la concentration en NaCl relative (0.1-1) (une valeur de 1 correspondant à un milieu isotonique alors qu'une valeur de 0.1 correspond à un milieu hypotonique). Des GR déshydratés résisteront mieux à la lyse dans un milieu hypotonique au contraire de GR hyperhydratés. On parlera de décalage vers la droite ou la gauche de la courbe de RO selon que la résistance osmotique augmente ou diminue. Un décalage de la courbe vers la gauche sera signe de déshydratation. Une mesure importante est l'IC50, c'est-à-dire la tonicité relative de NaCl induisant 50% d'hémolyse, qui servira de point de comparaison. On notera toutefois que des défauts de structure de la membrane ou du cytosquelette peuvent modifier cette RO (Cueff et al., 2010). En effet, une diminution de la déformabilité peut être à l'origine d'une diminution de la résistance osmotique car le GR lyse pour une entrée d'eau plus faible.

Les mesures de Ca^{2+} sont réalisées avec une approche fluorimétrique (Fluo4-AM) à l'aide d'un cytomètre en flux. Le culot de GR lavé est chargé avec du Fluo4-AM à 37°C pendant 30min dans du ringer sans Ca^{2+}. À la suite de quoi les GR sont placés dans une solution de ringer + Ca^{2+} ± yoda1 et/ou vanadate. L'intensité de la fluorescence (a.u) est mesurée toutes les 10 min, de même que le FSC-H (Forward Scatter – H), paramètre reflétant la taille des GR.

L'utilisation de yoda1 permet d'activer PIEZO1 et modifier les contenus ioniques (Na^+, K^+ et Ca^{2+}) dans l'objectif de mettre en évidence des différences d'activité d'un PIEZO1 muté.

Le vanadate, bien que non spécifique, inhibe la PMCA. Cette inhibition bloque la sortie de Ca^{2+} ATP dépendante entrainant une augmentation de Ca^{2+} intracellulaire. L'objectif est de mettre en évidence des changements de comportement des GR mutés par rapport aux témoins en réponse au vanadate. L'hypothèse est que des mutations PIEZO1 gain de fonction engendrent un influx calcique plus importante que le témoin et donc une déshydratation des GR plus importante via l'activation de KCNN4. La mesure de la fluorescence calcique en réponse au vanadate permet de mettre en évidence l'influx Ca^{2+} au travers de PIEZO1, mais d'autre perméabilités calciques peuvent être impliquées. En présence de mutations de KCNN4, une activité accrue de ce canal pour des quantité de Ca^{2+} plus faibles, engendrerait la déshydratation des GR malgré une perméabilité calcique inchangée.

Dans le cas de mutations de KCNN4, des mesures de la sensibilité calcique par électrophysiologie (patch-clamp configuration cellule entière) ont été réalisées dans des cellules HEK293T. Pour cela, la densité de courant de KCNN4 à 0 mV (pA/pF (0 mV)) a été mesurée avec différentes concentrations de Ca^{2+} intracellulaire (0.01, 0.1, 0.25, 0.5, 1 µM). Les milieux extracellulaires et intracellulaires (intra pipette) utilisés sont les suivants :

- Extracellulaire (mM) : NaCl (145), CaCl2 (2), KCl (5), MgCl2 (1), and HEPES (10), pH 7.4 ajusté avec NaOH.
- Intra pipette (mM) : KCl (145), MgCl2 (1), HEPES (1), and EGTA (1), pH 7.2 ajusté avec KOH. Les concentrations en Ca^{2+} libre sont ajustées avec du $CaCl_2$ en utilisant le logiciel web : Ca-EGTA Calculator v1.3.

Les niveaux d'expression protéique ont également été mesurés quand cela était possible. Il est pratiquement impossible d'utiliser les GR tel quels pour le WB du fait de la présence d'Hb en abondance. Nous réalisons donc des « ghosts » par lyse des GR dans un milieu hypo-osmotique. Cette lyse provoque une sortie massive d'Hb et d'autres constituants intracellulaires. La qualité des conditions de lyse influe sur la qualité des ghosts, avec plus ou moins de perte du matériel protéique, notamment des protéines membranaires.

Résultats et discussions

Vue d'ensemble des mutations présentées

Protéine	Mutation (+ autres protéines mutées)	Altération génétique	Intervalle Prélèvement – Manip	Référence
KCNN4	**H340N**	c. 1018C > A	48h	(Allegrini et al., 2022)
			48h	
KCNN4	**V222L**	c. 664G > C	48h	(Allegrini et al., 2022)
			72h	
PIEZO1	**Intron 9**	c.1107+1G > C	24h	Figure 14
			24h	
PIEZO1	R2088G	c.6262C > G	24h	Figure 15
PIEZO1	G782S R808Q V598L Patient G et R2456H Patient Y	c.1792G > C (V598L) c.2344G > A (G782S) c.2423G > A (R808Q) c.7367G > A (R2456H)	48h	Figure 16 + (Yamaguchi et al., 2021)
PIEZO1	V598M	c.1792G > A	24h	Figure 17 + (Yamaguchi et al., 2021)
PIEZO1	**T1201M** (+ SPTB1, RHAG, SLC4A1)	c.3602C>T	24h	(Allegrini et al., 2023)
PIEZO1	A2003T/ R2491W	c.6007G > A/ c.7471C > T	24h	Figure 18
PIEZO1	R2456H Patient P	c.7367G > A	48h	Figure 19
PIEZO1	**R2508C** Patient Q	c. 7522C > T	48h	Figure 20
PIEZO1	**S1994Y** (+ALAS2, ADKA, PKLR)	c.5978C > A	24h	Figure 21
PIEZO1	**R2491-E2492 dup**	c.7472_7477dup	72h	Figure 22
PIEZO1	**R1955C**	c.5863C>T	48h	Figure 23
PIEZO1	**A1003V**	c.3008C>T	24h	Figure 24
PIEZO1	**del**	c.326-7-326+8 del CCinsAT	48h	Figure 25
KCNN4	**G50R**	c.148G > A	24h	Figure 26
KCNN4	**V369-K373 del**	c.G1104 (TG/GT)	24h	Figure 27
KCNN4	**H340N**	c. 1018C > A	24h	Figure 28
			48h	

Tableau 6 : Récapitulatif des mutations étudiées au cours de cette thèse.

L'intervalle prélèvement – manip correspond au temps entre le prélèvement de l'échantillon sanguin et l'arrivée de ce dernier au laboratoire pour manipulations. Lorsque plusieurs lignes sont présentes pour une mutation cela signifie qu'il y a eu plusieurs prélèvements étudiés. En gras sont représentées les mutations qui n'avaient pas encore été caractérisées. La mutation H340N a fait l'objet de 2 prélèvements chez deux patients différents, l'étude des 2 prélèvements du 1er patient a fait l'objet d'une publication en même temps que la mutation KCNN4 V222L. Les références renvoient aux figures et publications correspondantes réalisées au cours de ma thèse.

Durant ces 4 années de thèse, les GR de 14 patients porteurs de mutations sur PIEZO1 et 5 porteurs de mutations sur KCNN4, suivis pour anémie hémolytique, ont été étudiés. Au total ce sont 8 mutations de PIEZO1 et 4 mutations de KCNN4 que nous caractérisons pour la première fois (représentées en gras dans le Tableau 6). Les mutations de KCNN4 V222L et H340N ainsi que les mutations de PIEZO1 T1201M, G782S-R808Q-V598L et V598M ont fait l'objet de 3 publications qui sont incluses dans cette thèse (voir références Tableau 6). Pour la mutation PIEZO1 G782S-R808Q-V598L un autre prélèvement a été étudié mais n'est pas dans la publication, il est présenté indépendamment dans une section dédiée. De même pour PIEZO1 V598M je présente les analyses faites sur les GR d'un autre patient que celui mentionné dans la publication.

Les résultats bruts des expériences de perméabilité réalisées sur les GR des patients sont présentés dans la section suivante. Une conclusion et discussion générale de ces résultats est ensuite exposée.

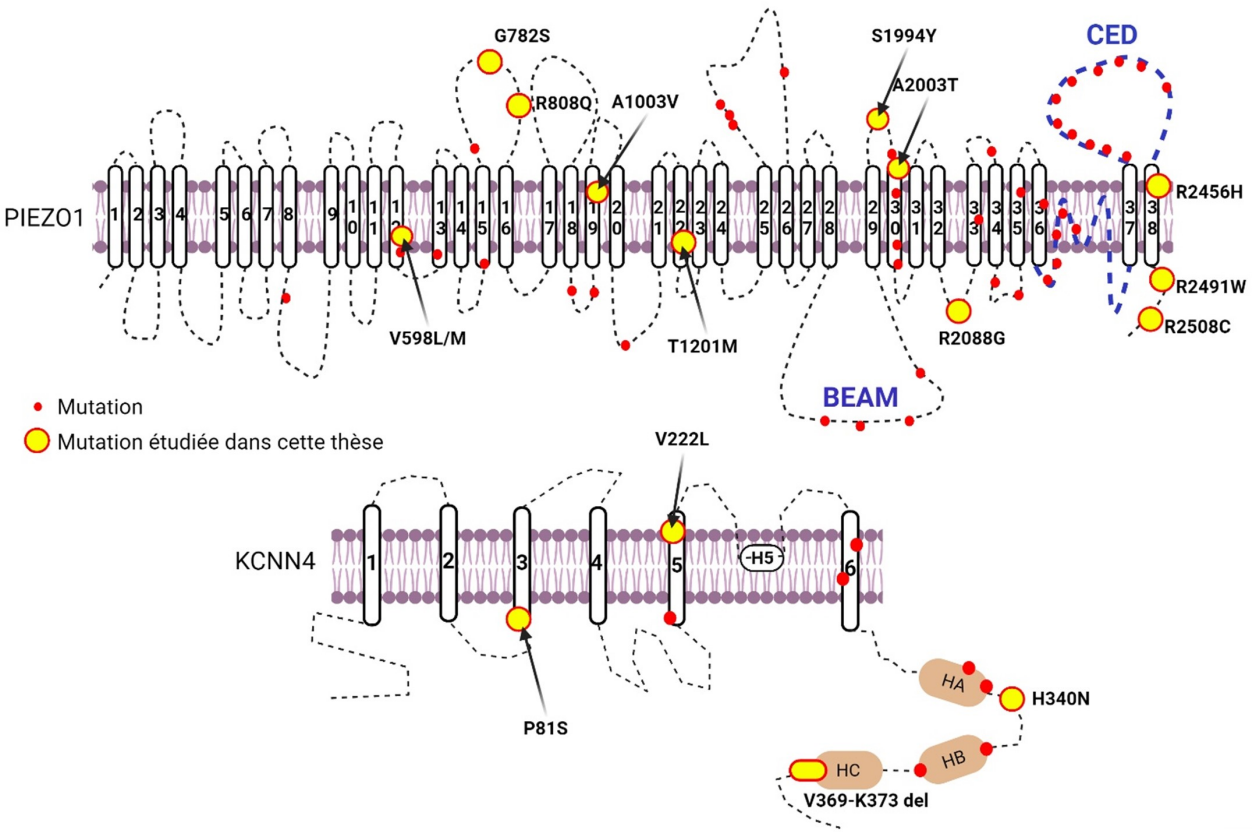

Figure 12B : Topologie de PIEZO1 et KCNN4 avec les mutations étudiées.

PIEZO1 et KCNN4 sont représentés sous forme secondaire avec leurs TM numérotés. Chaque mutation est placée approximativement (point rouge) et les mutations étudiées dans cette thèse sont mentionnées (point jaune).

PIEZO1 Intron 9

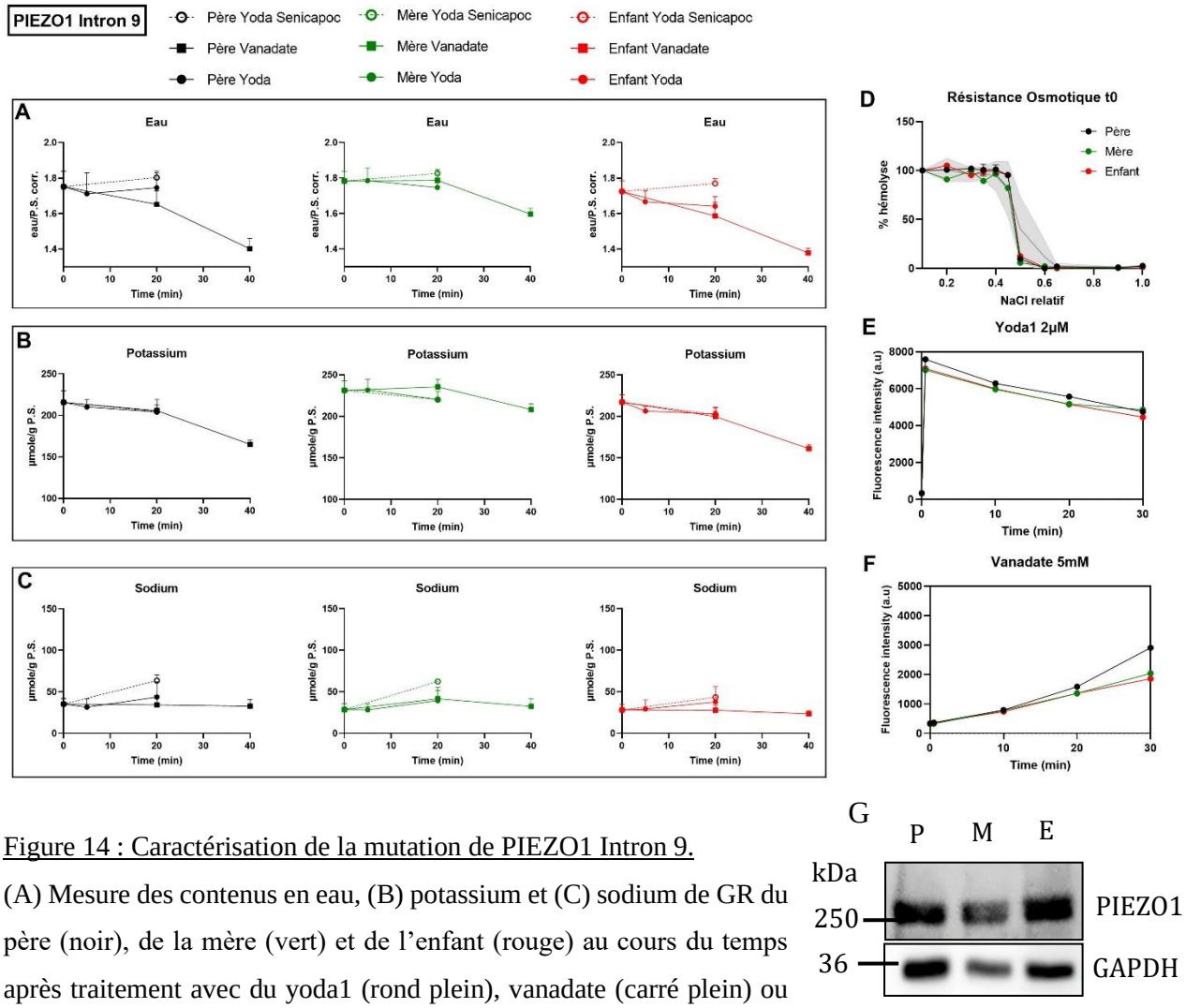

Figure 14 : Caractérisation de la mutation de PIEZO1 Intron 9.

(A) Mesure des contenus en eau, (B) potassium et (C) sodium de GR du père (noir), de la mère (vert) et de l'enfant (rouge) au cours du temps après traitement avec du yoda1 (rond plein), vanadate (carré plein) ou yoda1 + senicapoc (rond vide). (D) Résistance osmotique avec la courbe moyenne +/- SD de tous les témoins (gris clair). (E) Mesure de la fluorescence calcique (Fluo4-AM) au cours du temps après traitement au yoda1 ou vanadate (F). (G) Western blot à partir de ghost de GR du père (P), de la mère (M) et de l'enfant (E).

La mutation de PIEZO1 intron 9 correspond à l'altération génétique c.1107+1G > C qui entraine un probable saut de l'exon de 9 de *PIEZO1*.

Elle a fait l'objet de deux caractérisations à la suite de deux prélèvements à 3 mois d'intervalle. Le patient adressé au service d'hématologie est un enfant. A chaque fois, un prélèvement de sang issus de la mère et du père a été acheminé dans les mêmes conditions. Sur l'ensemble des deux prélèvements, à t0, aucune différence statistique de contenu en eau n'est observable entre le père (1.75±0.08), la mère (1.78±0.05) et l'enfant (1.73±0.06) malgré une tendance à la diminution par

rapport à l'ensemble des témoins (1.81±0.10) (Figure 14A). De la même façon, les contenus potassiques et sodiques sont similaires (Figure 14B, C). Après 40 min de traitement avec du vanadate, une déshydration est mesurable chez le père (1.40±0.06), la mère (1.59±0.03), l'enfant (1.38±0.03) et l'ensemble des témoins (1.54±0.17), corrélée à une perte de K^+ plus importante chez le père (delta K^+ = -42.9) et l'enfant (delta K^+ = -50) par rapport et la mère (-17.6). La résistance osmotique effectuée sur le sang total n'est pas différente entre les 3 individus et est dans la gamme de l'ensemble des témoins (Figure 14D). Les mesures de fluorescence calcique réalisées après incubation avec la sonde fluo4-AM ne permettent pas de mettre en évidence des différences de contenu calcique à t0 pour le père (380±59), la mère (318±2) et l'enfant (344.6±18.28). Le traitement avec yoda1 induit une forte augmentation de la fluorescence calcique quasi-immédiate et de façon similaire pour les 3 individus (Figure 14E). La réponse au vanadate est également la même (Figure 14F). Un western blot à partir de ghosts de GR a été réalisé afin de comparer l'expression de PIEZO1. Aucune différence du niveau d'expression n'est observable.

Après deux mesures ayant donné des résultats similaires, le patient et son père pourrait avoir une fuite calcique plus élevé mais il est difficile d'incriminer la mutation PIEZO1 intron 9.

PIEZO1 R2088G

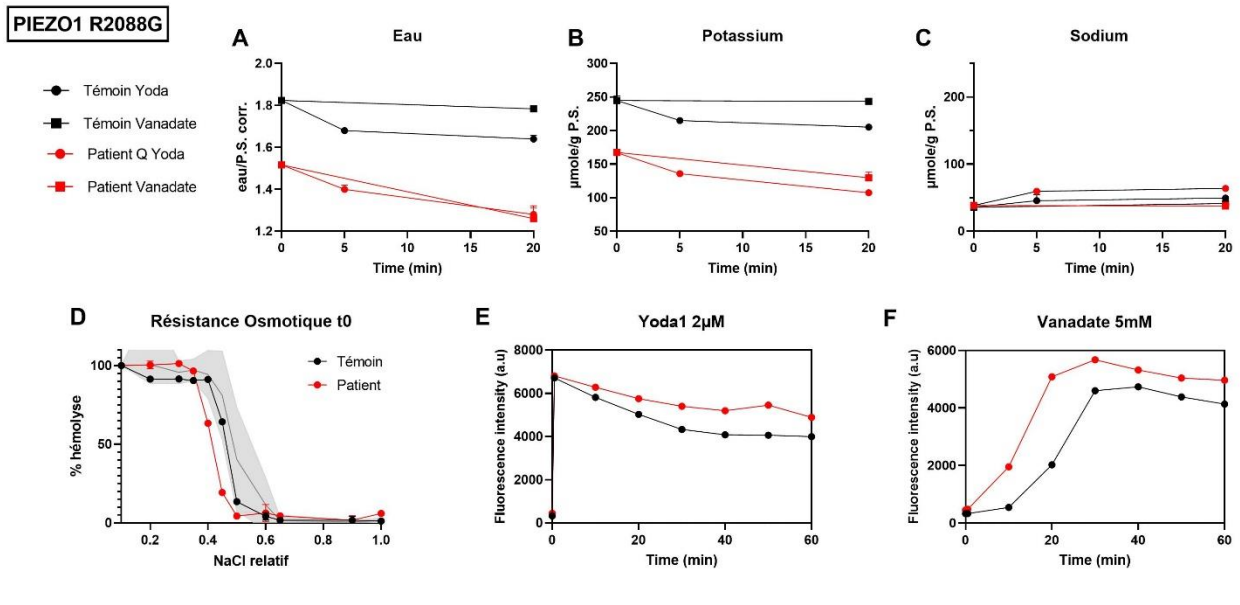

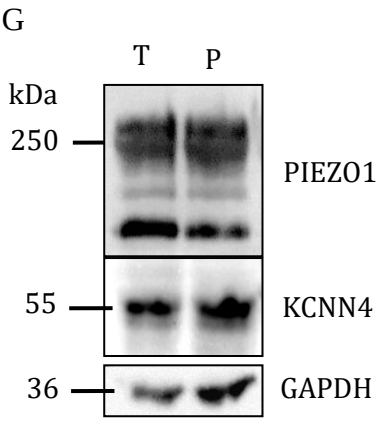

Figure 15 : Caractérisation de la mutation de PIEZO1 R2088G.

(A) Mesure des contenus en eau, (B) potassium et (C) sodium de GR d'un témoin (noir), et du patient (rouge) au cours du temps après traitement avec du yoda1 (rond plein) et vanadate (carré plein). (D) Résistance osmotique avec la courbe moyenne +/- SD de tous les témoins (gris clair). (E) Mesure de la fluorescence calcique (Fluo4-AM) au cours du temps après traitement au yoda1 ou vanadate (F). (G) WB à partir de ghosts de GR de témoin (T) et patient R2088G (P).

Nous avons eu accès à un prélèvement de sang issus d'un patient porteur de la mutation PIEZO1 R2088G ainsi que celui d'un volontaire sain. Les mesures de contenus en eau révèlent une forte déshydratation du patient (1.52±0.02) par rapport au témoin (1.82±0.02) (Figure 15A) qui est associée à une diminution importante du contenu en potassium (166.93±5.05 vs 244.7±6.6) (Figure 15B). Cette perte de potassium n'est pas compensée par un gain de sodium (38.4±0.8 vs 35.8±2.6) induisant une déshydratation par perte nette de cations (Figure 15C). La RO est fortement décalée à gauche par rapport au témoin et à l'ensemble des témoins (Figure 16D) confirmant la déshydratation mesurée. Le niveau de fluorescence calcique du patient est plus élevé que le témoin (451 vs 326) mais est compris dans la gamme de l'ensemble des témoins (402.2±80.35). Au bout de 20min de traitement avec du vanadate, on observe une forte déshydratation des GR du patient (1.26±0.06) au contraire du témoin (1.78±0.007) et tous les témoins (1.74±0.02) (Figure 15A). Au niveau de la fluorescence calcique, on observe une plus forte augmentation de Ca^{2+} après traitement au vanadate chez le patient

par rapport au témoin (Figure 15F). Le blocage de la pompe PMCA entraine une accumulation de Ca^{2+} dans le GR dû aux fuites calciques. Ces dernières pourraient être plus importantes chez le patient, causées directement par PIEZO1 R2088G. Cette augmentation d'activité n'est pas associée à une augmentation du niveau protéique de PIEZO1 (Figure 15G).

La mutation R2088G de PIEZO1 induit un phénotype clair de déshydratation par diminution du contenu potassique et semble être directement associée à une augmentation de la perméabilité calcique qui est très prononcée après ajout de vanadate.

La mutation R2088G a déjà été caractérisée par le passé (Glogowska et al., 2017) comme étant gain de fonction. Celle-ci entraine une diminution du seuil d'activation du canal sans changer le temps d'inactivation. En d'autres termes, PIEZO1 R2088G s'ouvre plus fréquemment, mais se ferme aussi rapidement que le PIEZO1 sauvage. Cela peut se traduire par des ouvertures transitoires fréquentes de PIEZO1 R2088G dans la circulation sanguine entrainant de rapides influx calciques. Ces derniers entrainent alors des activations de KCNN4 provoquant la déshydratation du GR. Il n'est alors pas impossible de voir s'activer PIEZO1 R2088G dans des conditions de très faible stress, là où un PIEZO1 sauvage ne s'activerait pas. En effet, dans nos conditions, les GR ne subissent pas de réels stress mécaniques sauf lors des centrifugations et des mesures de fluorescence calcique avec le cytomètre en flux. Pourtant, même en absence de stimulation mécanique de PIEZO1, il est intéressant de voir que le vanadate induit un influx calcique et une déshydratation très importante. Cela s'apparente alors à une fuite calcique constitutive.

PIEZO1 G782S R808Q V598L et R2456H

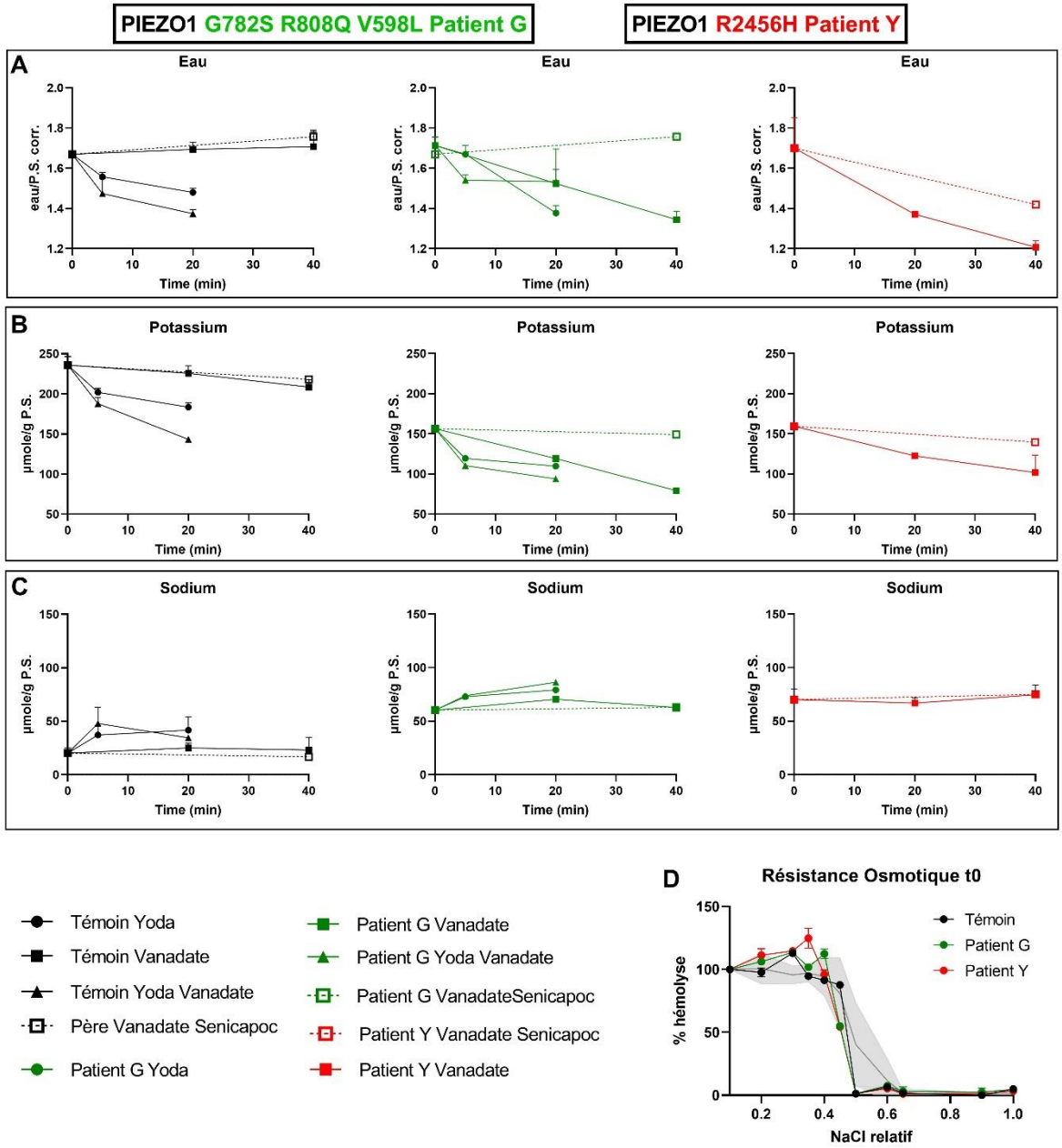

Figure 16 : Caractérisation de la triple mutation de PIEZO1 G782S R808Q V598L (Patient G) et d'une mutation R2456H (Patient Y).

(A) Mesure des contenus en eau, (B) potassium et (C) sodium de GR d'un témoin (noir), du patient G (vert) et du patient Y (rouge) au cours du temps après traitement avec du yoda1 (rond plein), vanadate (carré plein), yoda1 + vanadate (triangle plein) et vanadate + senicapoc (carré vide). (D) Résistance osmotique avec la courbe moyenne +/- SD de tous les témoins (gris clair).

Ce cas fait référence à deux patients (patient G et patient Y). Une triple mutation de PIEZO1 (G782S, R808Q, V598L) a été identifié chez le patient G et une mutation récurrente R2456H chez le patient Y. Etant donné que les prélèvements ont été acheminés dans les mêmes conditions et que nous les avons traités en parallèle, j'ai choisi de présenter ces deux patients sur une même figure. Toutefois, un autre patient porteur de R2456H sera présenté par la suite.

Nous observons une légère déshydratation non significative des GR pour le patient G (1.71±0.045) et le patient Y (1.70±0.15) par rapport à l'ensemble des témoins (1.81±0.10) (Figure 29A). Les GR du témoin de prélèvement sont également déshydratés (1.67±0.0). On remarque également une diminution importante du contenu potassique chez les patient G (156.43±1.62) et patient Y (159.46±3.45) en comparaison du témoin (235.82±10.76) (Figure 16B) qui est compensée par une augmentation du contenu en sodium (patient G : 60.25±0.71 vs patient Y : 70.10±9.7 vs témoin : 20.31±4.9) (Figure 16B, C). Ces différences de contenu cationique sont également visibles par rapport aux témoins génériques (Figure 29B, C). La RO est augmentée avec un décalage vers la gauche marqué pour le patient G et patient Y (Figure 16D, Figure 29D). Le vanadate induit une activation importante de KCNN4 chez les deux patients témoignant d'une fuite calcique plus importante

En conclusion, les deux mutations présentées ici ont un phénotype pathogène dans le GR qui se manifeste par des changements de contenus en K^+ et Na^+ non corrélé à une déshydratation. Les GR du patient G et Y ont un comportement proche suggérant un effet similaire des mutations. Une activité accrue de PIEZO1 devrait dissiper les gradients de Na^+ et K^+ et induire une entrée de Ca^{2+}, à l'origine d'une perte d'eau dépendante de KCNN4. Ici les gradients de K^+ et Na^+ sont effectivement dissipés et l'effet du vanadate indique indirectement une augmentation de la fuite Ca^{2+} mais nous ne mettons pas en évidence de perte d'eau significative sur ces prélèvements.

Le patient G porteur de la mutation PIEZO1 G782S-R808Q-V598L présenté ici est le même que dans la publication qui est incluse dans une section ci-dessous (Yamaguchi et al., 2021). Au moment de la publication seules les mutations G782S et R808Q avaient été identifiées chez ce patient G. La mutation V598L de PIEZO1 a été identifiée après une seconde analyse NGS. Lors de l'étude du patient G PIEZO1 G782S-R808Q-V598L dans l'article Yamaguchi *et al.*, 2021, nous avions mis en évidence une déshydratation de ses GR. Le fait que ce résultat ne soit pas exactement reproduit pourrait provenir de variabilités expérimentales ou de changements de mode de vie du patient (ces deux aspects seront discutés par la suite).

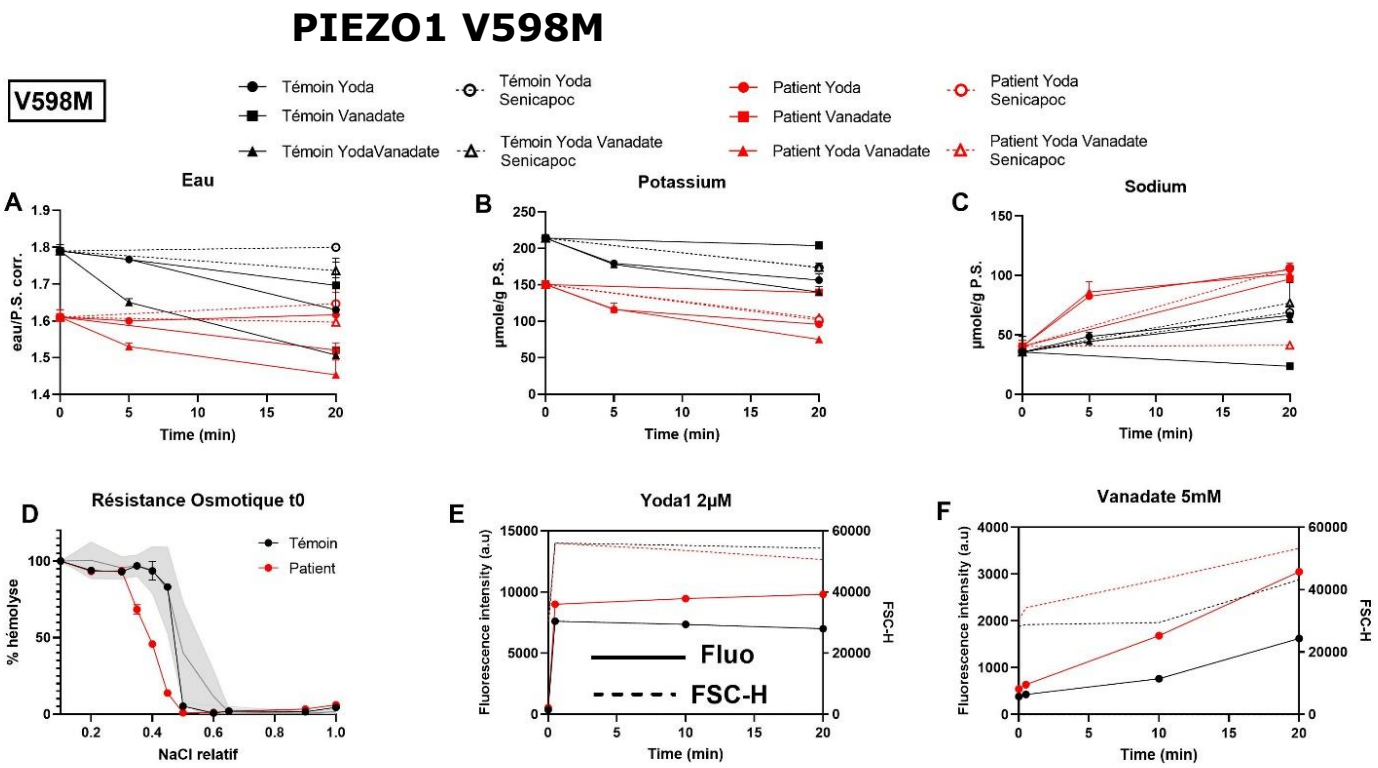

Figure 17 : Caractérisation de la mutation de PIEZO1 V598M.

(A) Mesure des contenus en eau, (B) potassium et (C) sodium de GR d'un témoin (noir), et du patient (rouge) au cours du temps après traitement avec du yoda1 (rond plein), vanadate (carré plein), yoda1 + vanadate (triangle plein), yoda1 + senicapoc (rond vide) et yoda1 + vanadate + senicapoc (triangle vide). (D) Résistance osmotique avec la courbe moyenne +/- SD de tous les témoins (gris clair). (E) Mesure de la fluorescence calcique (Fluo4-AM) (trait plein) et FSC-H (trait pointillé) au cours du temps après traitement au yoda1 ou vanadate (F).

Un patient porteur de la mutation PIEZO1 V598M a été prélevé en même temps qu'un volontaire sain. Le contenu en eau à t0 est diminué par rapport au témoin (1.61±0.02 vs 1.79±0.02) (Figure 17A) et est statistiquement plus faible que l'ensemble des témoins (Figure 29A). Ceci est associé à une baisse du contenu potassique non compensé par un gain de sodium (Figure 17B, C). La réponse au vanadate et yoda1 est de même amplitude que le témoin. On note toutefois une entrée de sodium à 20min induite par le yoda1, plus forte chez le patient que chez le témoin. La courbe de résistance osmotique des GR du patient V598M est décalée vers la gauche signifiant une augmentation de la RO confirmant la déshydratation (Figure 17D). Le contenu calcique à t0 mesuré par fluorescence est plus haut chez le patient que le témoin (544 vs 385) et l'ensemble des témoins (402.2±80.35) suggérant une perméabilité calcique augmentée. Cela se vérifie avec l'utilisation de vanadate qui induit une augmentation de la fluorescence calcique au moins 2 fois plus importante chez le patient (3053) que le témoin (1625) à 20min (Figure 17F).

La mutation V598M a déjà été décrite (Gnanasambandam et al., 2018; Rapetti-Mauss et al., 2017) comme gain de fonction dans les GR chez un autre patient. Elle induit un clair phénotype de déshydratation associé à une perte de potassium via l'activation du canal KCNN4 (voir l'article ci-joint Yamaguchi et al., 2021) que nous confirmons ici. Sur le second cas présenté ici, cette mutation semble induire une fuite calcique de PIEZO1, qui serait une conséquence des mutations de la partie N-terminale (Rapetti-Mauss et al., 2017), et serait à l'origine d'une activité constitutive de PIEZO1 en absence de stimuli mécanique. Cette fuite calcique est à l'origine de l'activation de KCNN4 induisant une déshydratation par perte de KCl des GR du patient. Il est intéressant de comparer le phénotype de la mutation V598M avec celui de la triple mutation G782S, R808Q, V598L (patient G) puisque dans les deux cas un même résidu est muté avec une déshydratation visible bien que plus faible avec la mutation V598L+G782R +R808Q du patient G.

PIEZO1 A2003T/R2491W

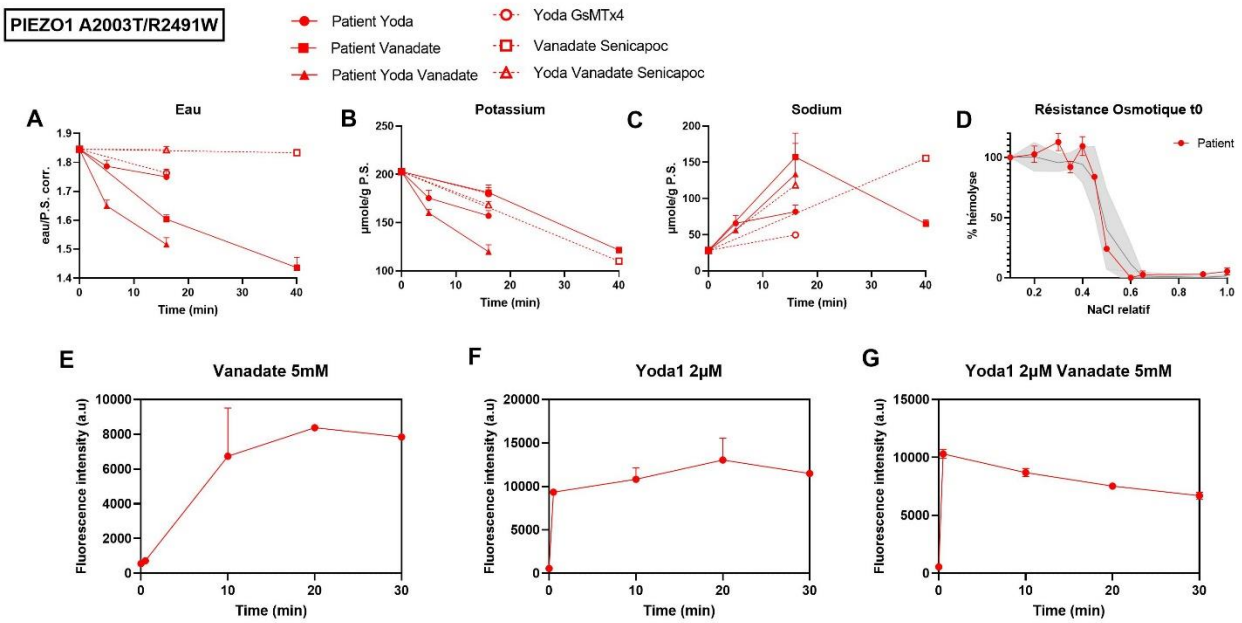

Figure 18 : Caractérisation de la double mutation de PIEZO1 A2003T/R2491W.

(A) Mesure des contenus en eau, (B) potassium et (C) sodium de GR du patient (rouge) au cours du temps après traitement avec du yoda1 (rond plein), vanadate (carré plein), yoda1 + vanadate (triangle plein), yoda1 + GsMTx4, vanadate + senicapoc (carré vide) et yoda1 + vanadate + senicapoc (tringle vide). (D) Résistance osmotique avec la courbe moyenne +/- SD de tous les témoins (gris clair). (E) Mesure de la fluorescence calcique (Fluo4-AM) au cours du temps après traitement au vanadate, yoda1 (F) ou yoda1 + vanadate (G). (H) WB à partir de ghost de patient en comparaison d'un témoin.

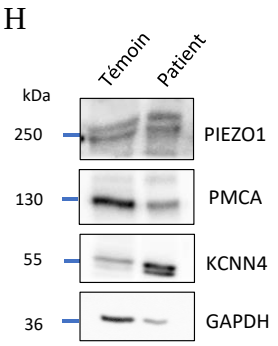

Le prélèvement sanguin du patient portant les mutations A2003T/R2491W a été fait en absence de volontaire sain et les mesures seront comparées à l'ensemble des témoins. Le contenu en eau n'est pas différent de la moyenne de tous les témoins (patient : 1.84±0.01 vs témoins : 1.81±0.10). On remarque un contenu potassique diminué chez le patient (202.79±1.35) de façon significative par rapport à l'ensemble des témoins (237.2±25.5) sans changement de contenu sodique (Figure 29B, C). On observe une déshydratation senicapoc-sensible induite par le vanadate au bout de 20 min (1.60±0.01) contrairement aux témoins (1.74±0.02) (Figure 18A). De manière surprenante, le senicapoc n'a pas eu d'effet sur la perte de potassium médiée par le vanadate (Figure 18B). Ceci n'a pas de réelle explication si ce n'est une erreur expérimentale. L'utilisation de yoda1 induit une déshydratation (1.75±0.02) qui n'est pas significativement différente du contrôle (1.72±0.04). La

résistance osmotique est dans la norme de l'ensemble des témoins. La fluorescence calcique basale des GR du patient (560) est plus élevée que la moyenne générale (402±80.3) mais sans contrôle il est difficile d'exclure un biais expérimental. On remarque une intensité de fluorescence calcique en réponse au vanadate plus forte (8382) que la moyenne (2167±1707) qui correspondrait à une fuite calcique largement augmentée chez le patient. La mesure des niveaux d'expression de PIEZO1, PMCA et KCNN4 montre que l'expression de KCNN4 est largement augmentée chez le patient par rapport à un témoin, au contraire de la PMCA. En revanche, aucun changement d'expression de PIEZO1 n'est observé. De façon intéressante, les niveaux de GAPDH sont largement diminués chez le patient (Figure 18H).

En conclusion, cette mutation n'est pas phénotypique au regard d'une déshydratation mais altère la perméabilité K^+ et Ca^{2+} des GR. On note toutefois que la diminution du niveau d'expression de la PMCA est corrélée à une augmentation du niveau basal de fluorescence calcique, ce qui témoigne d'une altération de l'homéostasie calcique. Ces deux mutations A2003T/R2491W dans la partie C-terminale du canal ont déjà été mentionnées (Andolfo et al., 2013; Picard et al., 2019) et caractérisées (Caulier et al., 2020). Elles sont associées à un fort phénotype érythrocytaire (diminution du taux d'Hb, augmentation du nombre de Réticulocytes). Cela suggère que de légères modifications de la perméabilité cationique sont suffisante pour induire un phénotype clinique sévère.

PIEZO1 R2456H

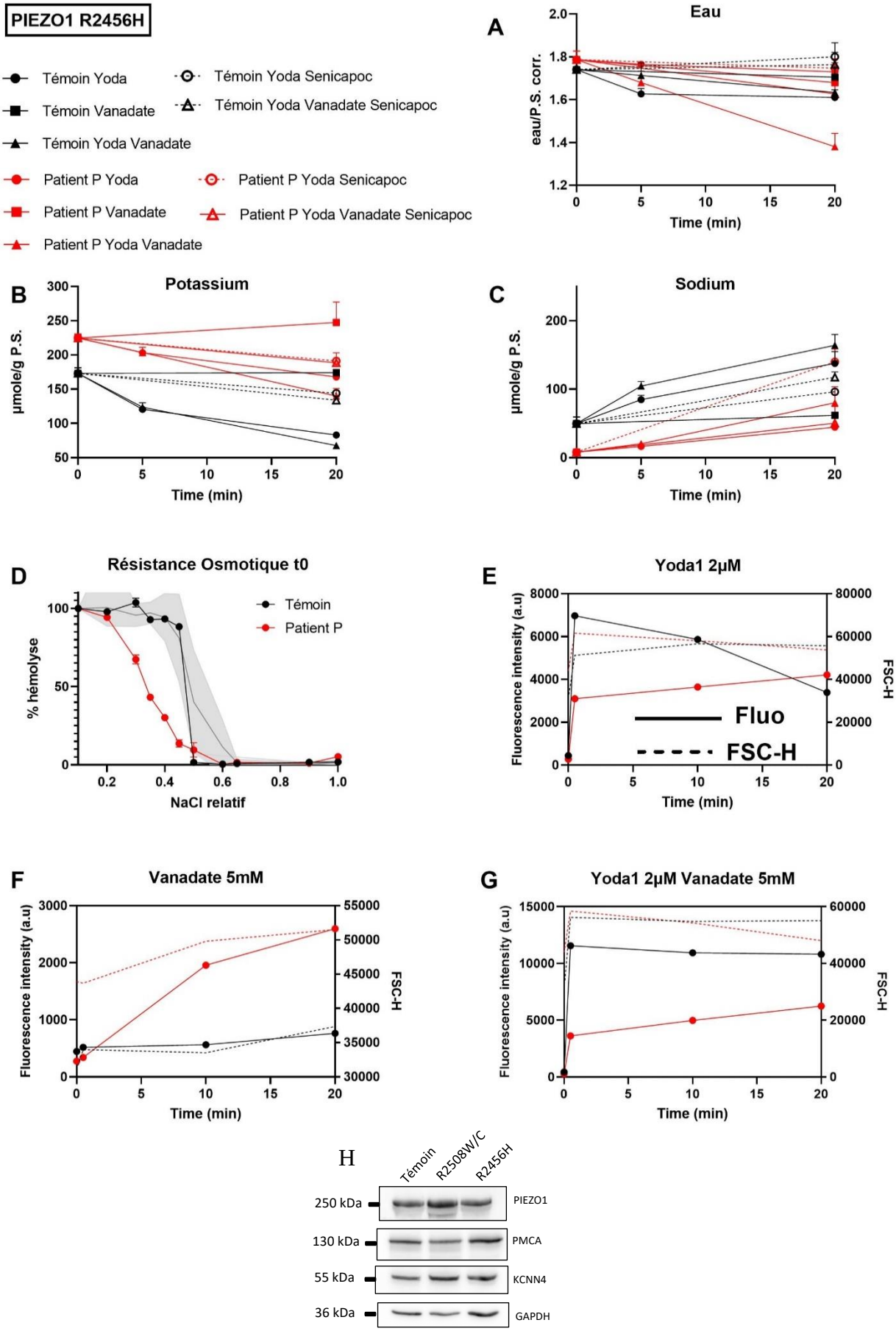

Figure 19 : Caractérisation de la mutation de PIEZO1 R2456H (patient P).

(A) Mesure des contenus en eau, (B) potassium et (C) sodium de GR d'un témoin (noir), et du patient P (rouge) au cours du temps après traitement avec du yoda1 (rond plein), vanadate (carré plein), yoda1 + vanadate (triangle plein), yoda1 + senicapoc (rond vide) et yoda1 + vanadate + senicapoc (triangle vide). (D) Résistance osmotique avec la courbe moyenne +/- SD de tous les témoins (gris clair). (E) Mesure de la fluorescence calcique (Fluo4-AM) (trait plein) et FSC-H (trait pointillé) au cours du temps après traitement au yoda1, vanadate (F) ou yoda1 + vanadate (G). (H) WB à partir de ghosts de témoin, patient P et patient Q.

Nous avons reçu un prélèvement de sang du patient P porteur de cette mutation R2456H ainsi que d'un patient Q porteur de la mutation R2508C, avec un témoin prélevé et acheminé dans les mêmes conditions. Par mesure de clarté j'ai choisi de présenter séparément les deux mutations mais le témoin sera le même dans les deux conditions.

La mesure de contenu hydrique ne révèle pas de changement significatif par rapport au témoin (Figure 19A). Les GR du patient ont une quantité de K^+ intracellulaire augmentée (224.7±5.6) par rapport au témoin (173.05±8.14) (Figure 19B) mais dans la norme de tous les témoins (237.2±25.5). En revanche, le niveau de Na^+ intracellulaire est diminué (8.03±2.39) en comparaison du témoin (49.75±9.6) (Figure 19C) qui est, quant à lui, supérieur à la moyenne global (29.85±15). Concernant la RO, on observe une forte augmentation de la résistance osmotique (Figure 19D). Le niveau de fluorescence calcique basal du patient est plus faible (276) que le témoin (446). La morphologie des GR du patient est modifiée (FSC-H : 43906) par rapport au témoin (FSC-H : 31107). L'influx calcique provoqué par le yoda1 et yoda1 + vanadate est plus faible chez le patient que le témoin (Figure 19E, 20G). La réponse au vanadate, quant à elle est largement augmentée avec un influx calcique drastique corrélé à une augmentation de la FSC-H (Figure 19F). Les niveaux d'expression protéique de PIEZO1 et KCNN4 sont similaires chez le patient P et le témoin (Figure 19H).

En conclusion, PIEZO1 R2456H a un phénotype mitigé avec une diminution marqué du Na^+ intracellulaire et une RO largement augmentée par rapport à l'ensembles des témoins. La FSC-H augmentée suggère une forme altérée des GR de ce patient. Ces derniers pourraient alors être plus fragiles face aux stress physiques subit dans la circulation et lyserait plus rapidement. La mutation R2456H de PIEZO1 est une des premières mutations décrites dans la Xérocytose Héréditaire (Zarychanski et al., 2012) et induit un allongement du délai d'inactivation du canal (Albuisson et al., 2013) (Figure 13A).

PIEZO1 R2508C

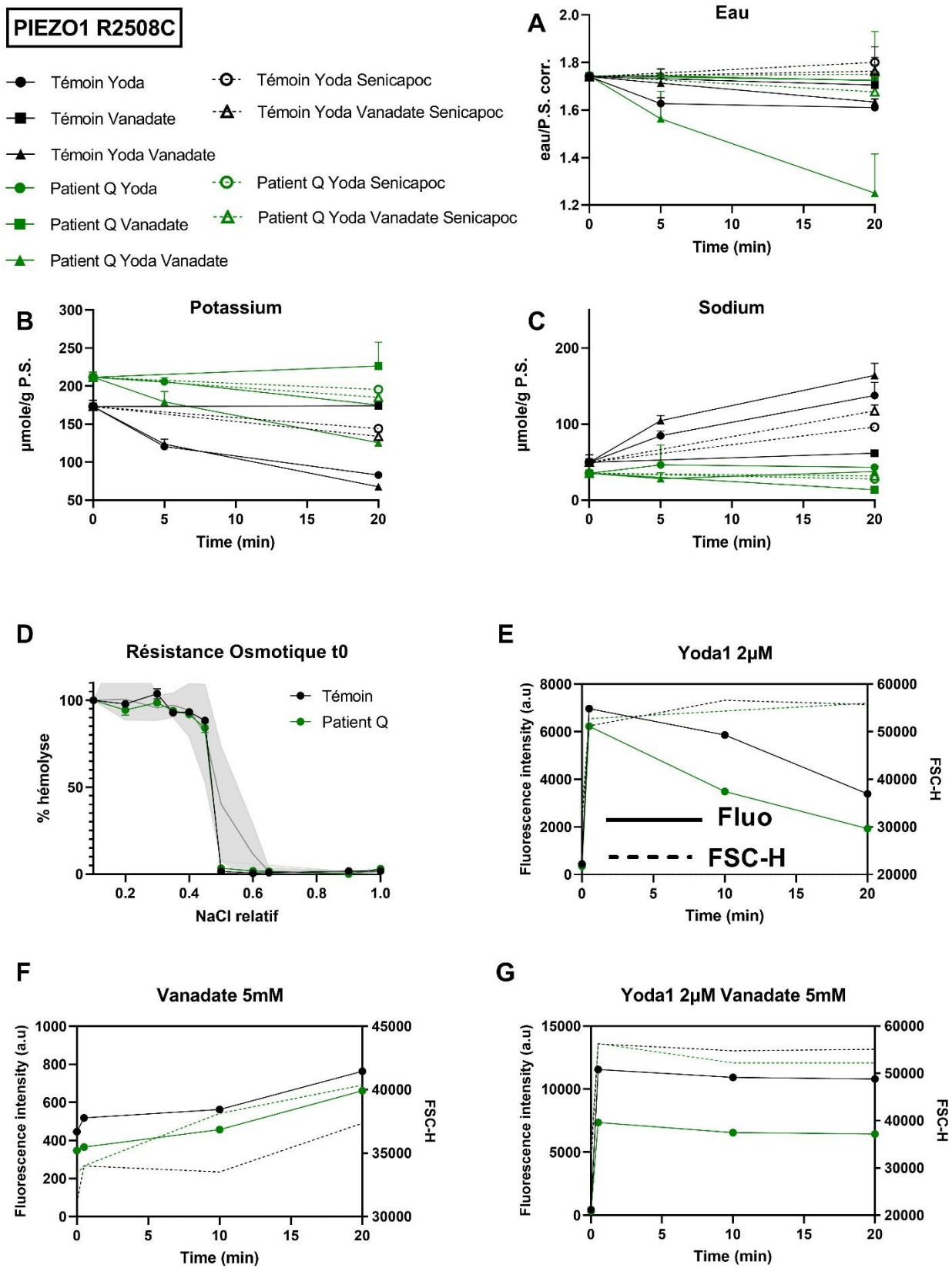

Figure 20 : Caractérisation de la mutation de PIEZO1 R2508C (patient Q).

(A) Mesure des contenus en eau, (B) potassium et (C) sodium de GR d'un témoin (noir), et du patient Q (vert) au cours du temps après traitement avec du yoda1 (rond plein), vanadate (carré plein), yoda1 + vanadate (triangle plein), yoda1 + senicapoc (rond vide) et yoda1 + vanadate + senicapoc (triangle vide). (D) Résistance osmotique avec la courbe moyenne +/- SD de tous les témoins (gris clair). (E) Mesure de la fluorescence calcique (Fluo4-AM) (trait plein) et FSC-H (trait pointillé) au cours du temps après traitement au yoda1, vanadate (F) ou yoda1 + vanadate (G).

Le contenu en eau des GR du patient Q est dans la norme (1.79±0.45) par rapport à l'ensemble des témoins (Figure 20A). Comme mentionné pour le patient P muté R2456H, le contenu potassique est diminué par rapport aux témoins génériques (Figure 20B). La résistance osmotique est normale (Figure 20D) de même que la fluorescence calcique basale (347 vs 402±80.3) ainsi que la taille (FSC-H patient Q : 33386 vs FSC-H témoin : 31107). Le patient Q semble moins bien répondre que le témoin en ce qui concerne l'influx calcique provoqué par le yoda1 et/ou vanadate (Figure 20E, F, G). Les niveaux d'expression protéique de PIEZO1 sont similaires chez le témoin et le patient Q (Figure 19H).

Contrairement à la mutation R2456H étudiée en parallèle, la mutation R2508C de PIEZO1 n'induit pas d'anomalie de la RO mais un déficit en potassium intracellulaire.

PIEZO1 S1994Y

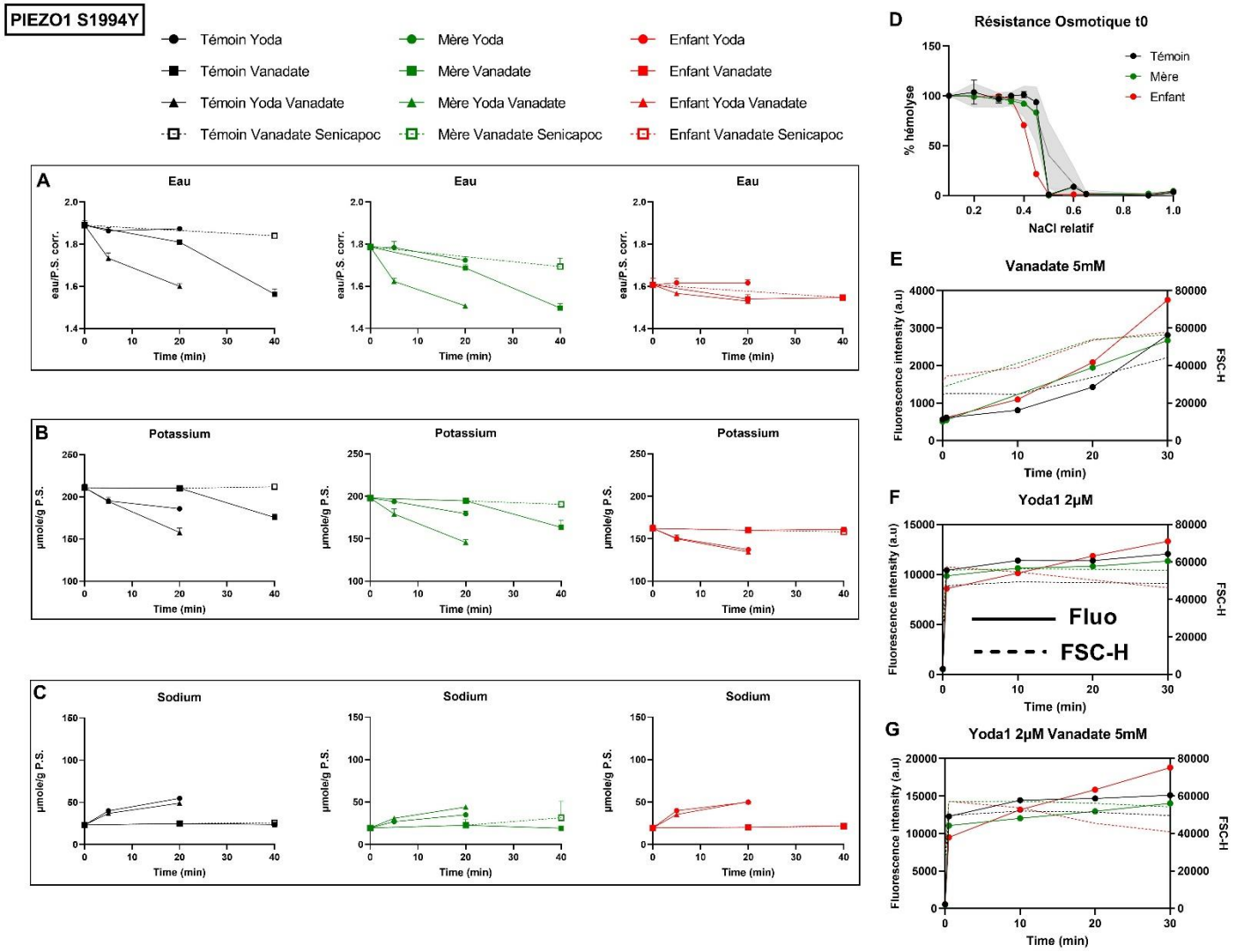

Figure 21 : Caractérisation de la mutation de PIEZO1 S1994Y.

(A) Mesure des contenus en eau, (B) potassium et (C) sodium de GR d'un témoin (noir), de la mère (vert) et de l'enfant (rouge) au cours du temps après traitement avec du yoda1 (rond plein), vanadate (carré plein), yoda1 + vanadate (triangle plein) et vanadate + senicapoc (carré vide). (D) Résistance osmotique avec la courbe moyenne +/- SD de tous les témoins (gris clair). (E) Mesure de la fluorescence calcique (Fluo4-AM) (trait plein) et FSC-H (trait pointillé) au cours du temps après traitement au yoda1, vanadate (F) ou yoda1 + vanadate (G).

L'étude de la mutation S1994Y, identifiée chez un enfant, a été réalisé en parallèle de l'étude des GR de sa mère et d'un témoin. L'enfant est également porteur de mutations sur les gènes *ALAS2*, *ADKA* et *PKLR*. *ALAS2* code pour la 5'-aminolevulinate synthase 2 dont les mutations sont impliquées dans l'anémie sidéroblastique liée à l'X et la protoporphyrie érythropoïétique liée à l'X. *ADKA* code pour une adénylate kinase et *PKLR* code pour le pyruvate kinase dont les mutations sont associées au déficit en pyruvate kinase du GR provoquant une anémie.

Les contenus en eau des GR de l'enfant sont significativement diminués par rapport à ceux de la mère et du témoin (1.61±0.03 vs 1.79±0.01 vs 1.89±0.02) (Figure 21A) de même que par rapport à l'ensemble des témoins (1.81±0.10) (Figure 29A). Cette déshydratation est associée à une diminution du contenu en potassium (162.21±3.82) par rapport au témoin (210.84±4.29) (Figure 21B) mais n'est pas compensée par un gain de sodium (19.52±0.55 vs 23.30±0.66). Le vanadate induit une déshydratation à 40 min chez le témoin (1.57±0.02) et la mère (1.50±0.02) qui est reversé par le senicapoc chez le témoin (1.84±0.01) et partiellement chez la mère (1.69±0.04). De façon surprenante, le vanadate a très peu d'effet sur les GR de l'enfant, peut-être dû à un contenu en K^+ basal déjà très diminué ne permettant pas plus de diminution (gradient K^+ moindre que dans les contrôles) (Figure 21A). Le décalage vers la gauche de la courbe de RO permet de confirmer la déshydratation mesurée chez l'enfant (Figure 21D). Concernant les niveaux de calcium, la fluorescence calcique basale est similaire entre l'enfant (560), la mère (508) et le témoin (560). On note toutefois une taille des GR augmentée chez l'enfant (FSC-H : 31311) en comparaison du témoin (FSC-H : 24417). La réponse calcique à la suite du traitement avec yoda1 et/ou vanadate est la même (Figure 21E, F, G).

La mutation S1994Y est donc associée à une déshydratation marquée corrélée à une diminution du contenu potassique et une augmentation de la RO. Cependant ce patient est également porteur d'autres mutations sur les gènes *ALAS2*, *ADKA* et *PKLR*, eux-mêmes impliqué dans des anémies hémolytiques. Il n'est donc pas impossible que la mutation S1994Y de PIEZO1 soit indépendante du phénotype observé même si la perméabilité ionique est largement affectée suggérant un rôle de PIEZO1. D'autre part, on ne peut pas exclure que les autres mutations décelées puissent avoir un effet synergique avec PIEZO1 S1994Y et aggraver le phénotype. Cela nécessite une caractérisation plus poussée de cette mutation dans un système d'expression hétérologue par exemple. Une autre mutation S1994F avait déjà été identifiée dans une famille avec des mesures d'Ektacytométrie typiques de déshydratation des GR et est prédite comme pathogène par des algorithmes (Picard et al., 2019).

PIEZO1 R2491-E2492 dup

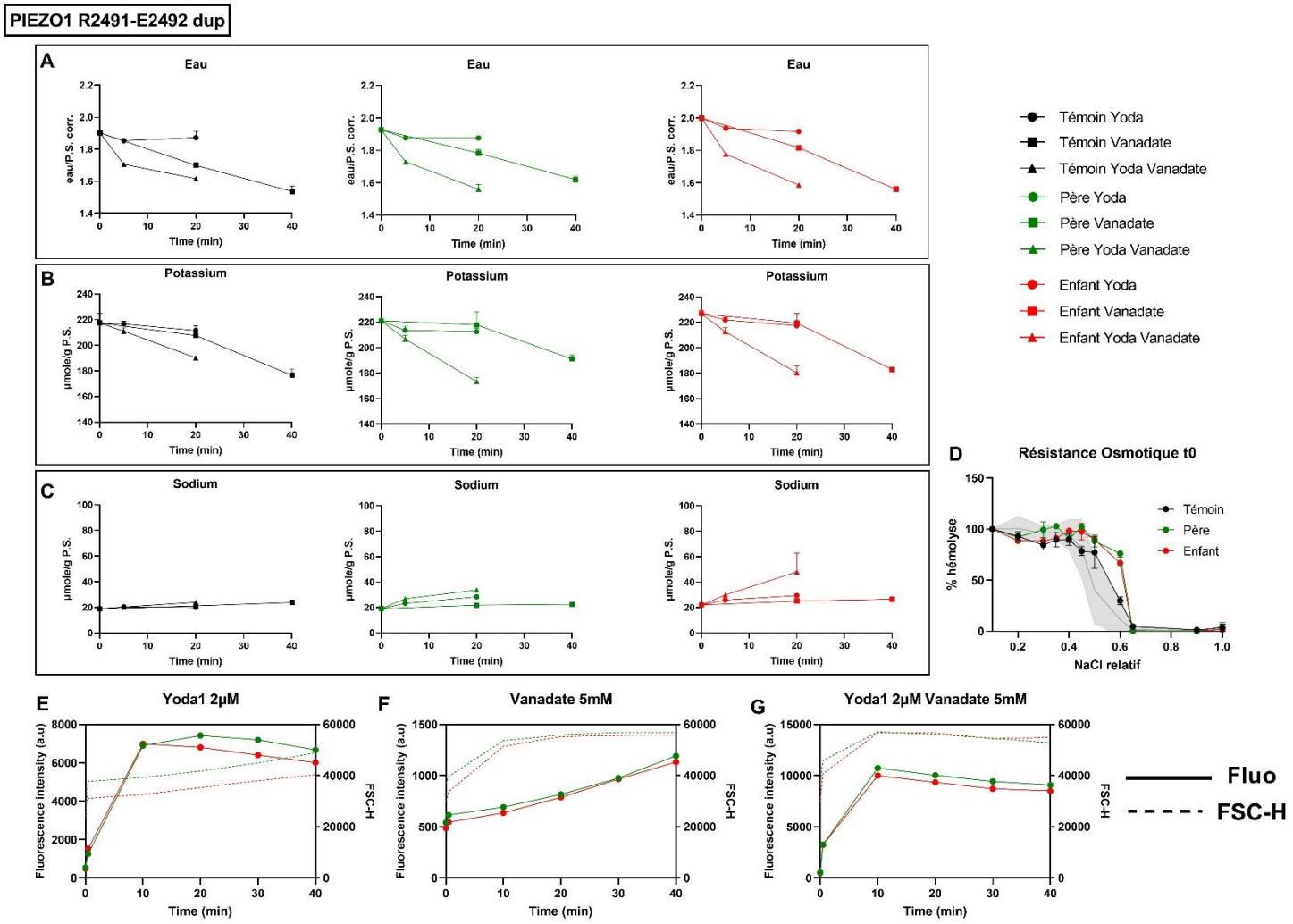

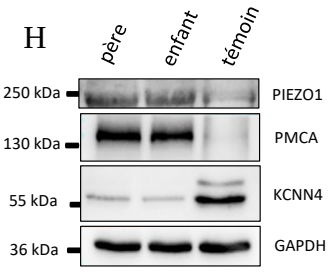

Figure 22 : Caractérisation de la mutation de PIEZO1 R2491-E2492 dup.

(A) Mesure des contenus en eau, (B) potassium et (C) sodium de GR d'un témoin (noir), du père (vert) et de l'enfant (rouge) au cours du temps après traitement avec du yoda1 (rond plein), vanadate (carré plein) et yoda1 + vanadate (triangle plein). (D) Résistance osmotique avec la courbe moyenne +/- SD de tous les témoins (gris clair). (E) Mesure de la fluorescence calcique (Fluo4-AM) (trait plein) et FSC-H (trait pointillé) au cours du temps après traitement au yoda1, vanadate (F) ou yoda1 + vanadate (G). (H) WB à partir de ghosts du témoin, père et enfant.

La mutation PIEZO1 R2491-E2492 dup correspond à l'altération génétique c.7472_7477dup.

Nous avons reçu un prélèvement de sang de l'enfant porteur de cette mutation ainsi que de son père également porteur de la mutation et d'un témoin. Le contenu en eau des GR à t0 du patient est plus important (2.00±0.026) que le témoin (1.90±0.013) et le père (1.92±0.01) (Figure 22A). La quantité de potassium interne est cependant inchangée dans les GR du patient (226.79±2.54) par rapport au

témoin à t0 (217.39±7.38) (Figure 22B) ainsi que par rapport à l'ensemble des témoins (237.2±25.5). Les contenus sodiques sont également normaux (Figure 22C) à t0. Les réponses au vanadate et yoda1 sont similaires entre les 3 conditions. On note un décalage vers la droite de la courbe de résistance osmotique chez l'enfant et son père confirmant une hyperhydratation des GR de l'enfant mais pas pour le père (Figure 22D). Aussi, on peut supposer une fragilité plus importante des GR sans lien avec le contenu en eau. Au niveau des contenus calciques, à t0 la fluorescence est plus élevée chez le père (540) que chez l'enfant (489) qui se trouve dans la gamme des témoins. Cela est associé à une taille plus grande des GR du père (FSC-H : 36739) par rapport à ceux de l'enfant (FSC-H : 29813). Le père et l'enfant répondent de la même façon à une stimulation par yoda1 et/ou vanadate (Figure 22F, G, H). L'analyse de l'expression protéique par WB est difficilement interprétable au vu du comportement du témoin. On peut voir que ce-dernier n'exprime pas ou peu de PMCA de même que PIEZO1. En revanche le père et l'enfant ont une expression de KCNN4 très faible (Figure 22H). Cela irait dans le sens d'une hyperhydratation.

En conclusion, cette mutation PIEZO1 R2491-E2492 dup est associée à une hyperhydratation accompagnée d'une diminution de la RO et associée à une diminution d'expression de KCNN4 des GR de l'enfant. Nous n'observons pas de gain de soluté et donc l'hyperhydratation ne provient pas d'un défaut de perméabilité ionique mais éventuellement d'un nombre de réticulocytes important. On peut penser que la mutation R2491-E2492 dup est perte de fonction car cela rejoint le phénotype des GR de souris, invalidées pour PIEZO1, qui sont plus gros par hyperhydratation (Cahalan et al., 2015). Ou encore, chez l'humain, les mutations perte de fonction retrouvées dans la dysplasie lymphatique sont associées à une hyperhydratation des GR. Toutefois, il convient de replacer ces mesures dans un contexte ou l'intervalle entre le prélèvement et l'arrivée des GR dans notre laboratoire a été de 72h. C'est un temps particulièrement long quand on sait que la majorité des prélèvements arrivent en 24h-48h. Cela n'enlève en rien l'effet de la mutation par rapport au témoin mais au vu du comportement assez extrême de ce-dernier (RO à limite droite : Figure 22D) il n'est pas impossible que le phénotype de la mutation ait été aggravé par le transport.

PIEZO1 R1955C

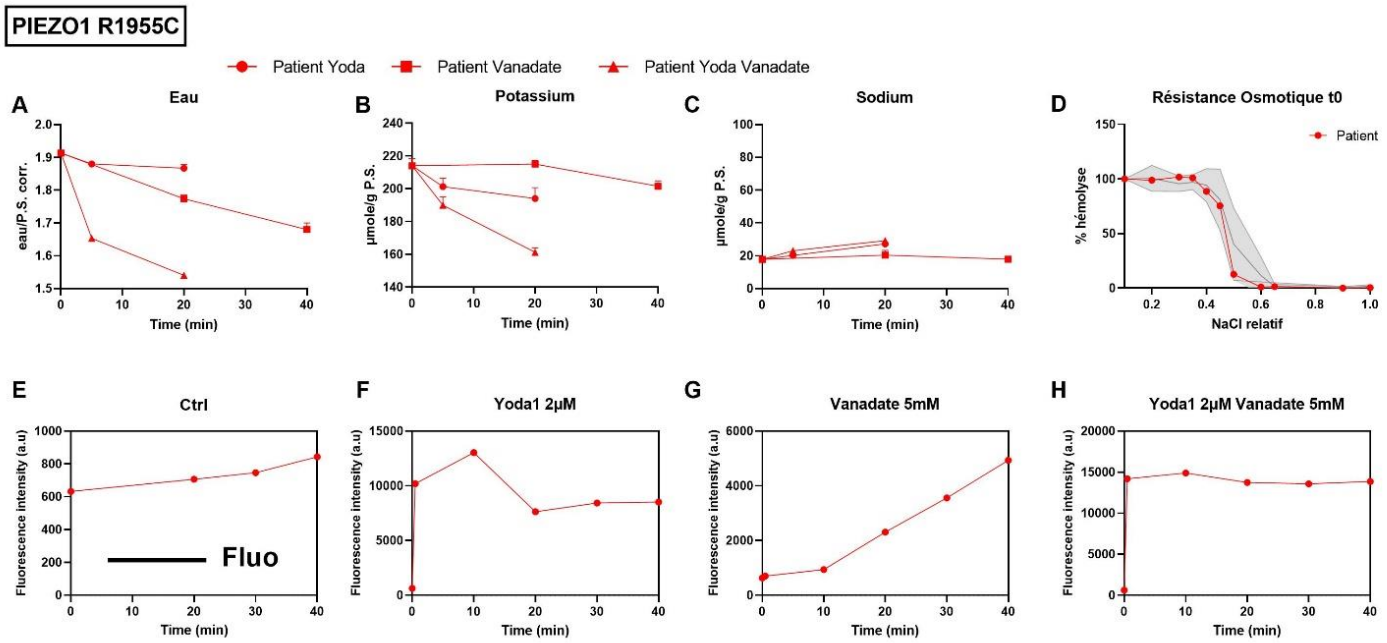

Figure 23 : Caractérisation de la mutation de PIEZO1 R1955C.

(A) Mesure des contenus en eau, (B) potassium et (C) sodium de GR du patient (rouge) au cours du temps après traitement avec du yoda1 (rond plein), vanadate (carré plein) et yoda1 + vanadate (triangle plein). (D) Résistance osmotique avec la courbe moyenne +/- SD de tous les témoins (gris clair). (E) Mesure de la fluorescence calcique (Fluo4-AM) (trait plein) au cours du temps sans traitement ou après traitement au yoda1 (F), vanadate (G) ou yoda1 + vanadate (H).

La mutation PIEZO1 R1955C a été identifiée chez un patient dont nous avons eu un prélèvement sanguin en absence de prélèvement témoin. Les contenus en eau, potassium et sodium ne sont pas statistiquement différents des témoins (Figure 29A, B, C) et la courbe de résistance osmotique est dans la norme (Figure 23D). Le niveau de calcium à t0 est plus élevé que les témoins (632 vs 402.2±80.35) de même qu'après 20min de traitement au yoda1 + vanadate (13748 vs 9751±2468) (Figure 29H). On peut voir que la fluorescence calcique augmente légèrement avec le temps sans aucun traitement (632 à t0 vs 706 à t20) (Figure 23E). Cette augmentation reste cependant négligeable par rapport à l'augmentation induit par le yoda1 et/ou vanadate.

A ce stade on ne peut pas conclure sur le phénotype de la mutation PIEZO1 R1955C dans les GR de ce patient. On note toutefois une altération de la perméabilité calcique qui ne semble pas être corrélée à une augmentation d'activité de PIEZO1.

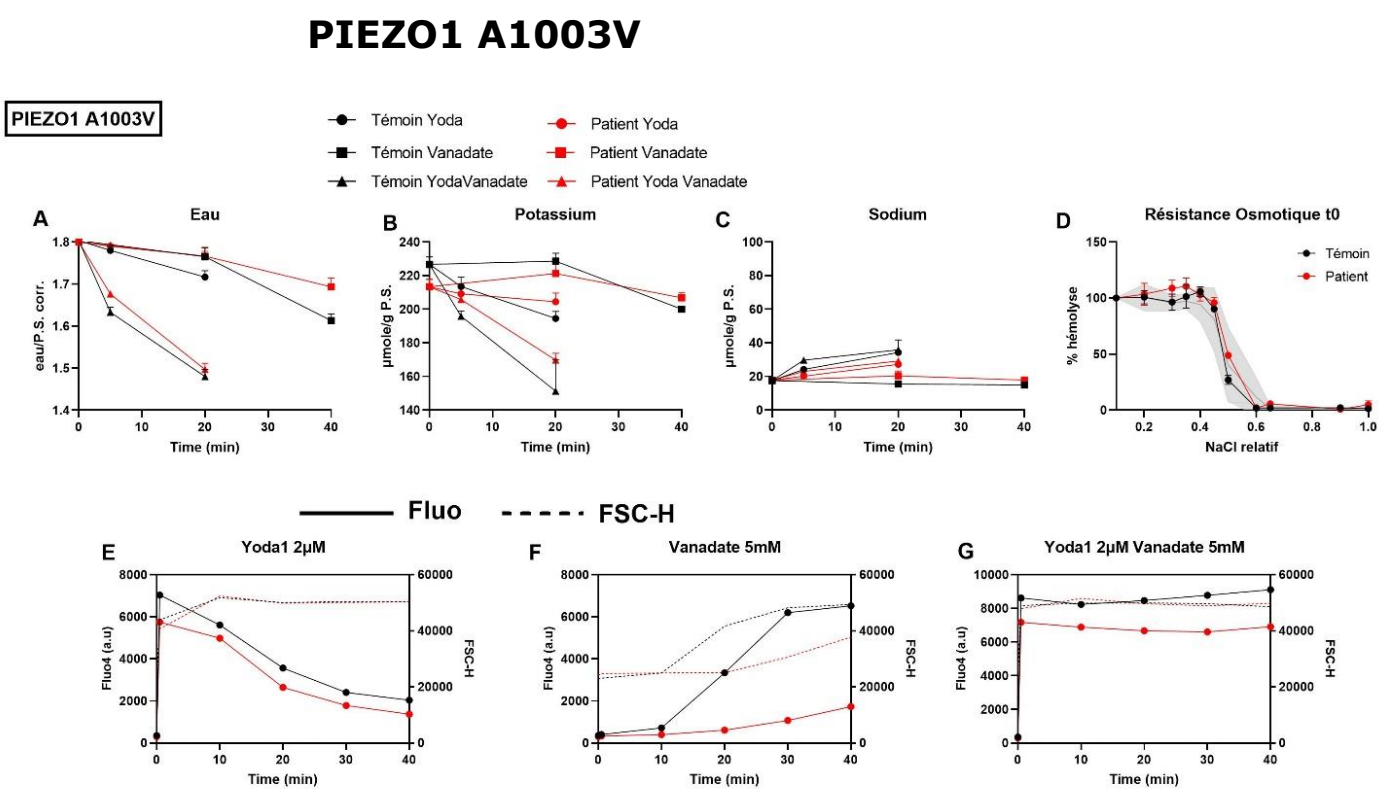

Figure 24 : Caractérisation de la mutation de PIEZO1 A1003V.

(A) Mesure des contenus en eau, (B) potassium et (C) sodium de GR d'un témoin (noir) et du patient (rouge) au cours du temps après traitement avec du yoda1 (rond plein), vanadate (carré plein) et yoda1 + vanadate (triangle plein). (D) Résistance osmotique avec la courbe moyenne +/- SD de tous les témoins (gris clair). (E) Mesure de la fluorescence calcique (Fluo4-AM) (trait plein) et FSC-H (trait pointillé) au cours du temps après traitement au yoda1, vanadate (F) ou yoda1 + vanadate (G).

Le contenu en eau du patient n'est pas différent du témoin (1.80±0.010 vs 1.80±0.017) (Figure 24A) malgré un contenu potassique légèrement réduit (213.41±4.4 vs 226.69±4.44) (Figure 24B). Le contenu sodique est normal (Figure 24C) de même que la résistance osmotique (Figure 24D). La morphologie des GR du patient (FSC-H : 24137) est semblable à celle du témoin (FSC-H : 22835). On note une réponse calcique au yoda1, vanadate et yoda1 + vanadate à 20 min plus faible que l'ensembles des témoins (yoda1 t20 : 2646 vs 5551±2063 ; vanadate : 611 vs 2167±1707 ; yoda1 + vanadate : 6670 vs 9751±2467) (Figure 29F, G, H).

En conclusion, il est difficile de corréler l'anémie du patient à un défaut de la perméabilité ionique des GR, qui se comportent comme l'ensemble des témoins. On notera toutefois une perméabilité calcique diminuée qui nécessitera une confirmation avec un deuxième prélèvement. La mutation PIEZO1 A1003V est une nouvelle mutation qui n'a jamais été décrite ou mentionnée.

PIEZO1 del

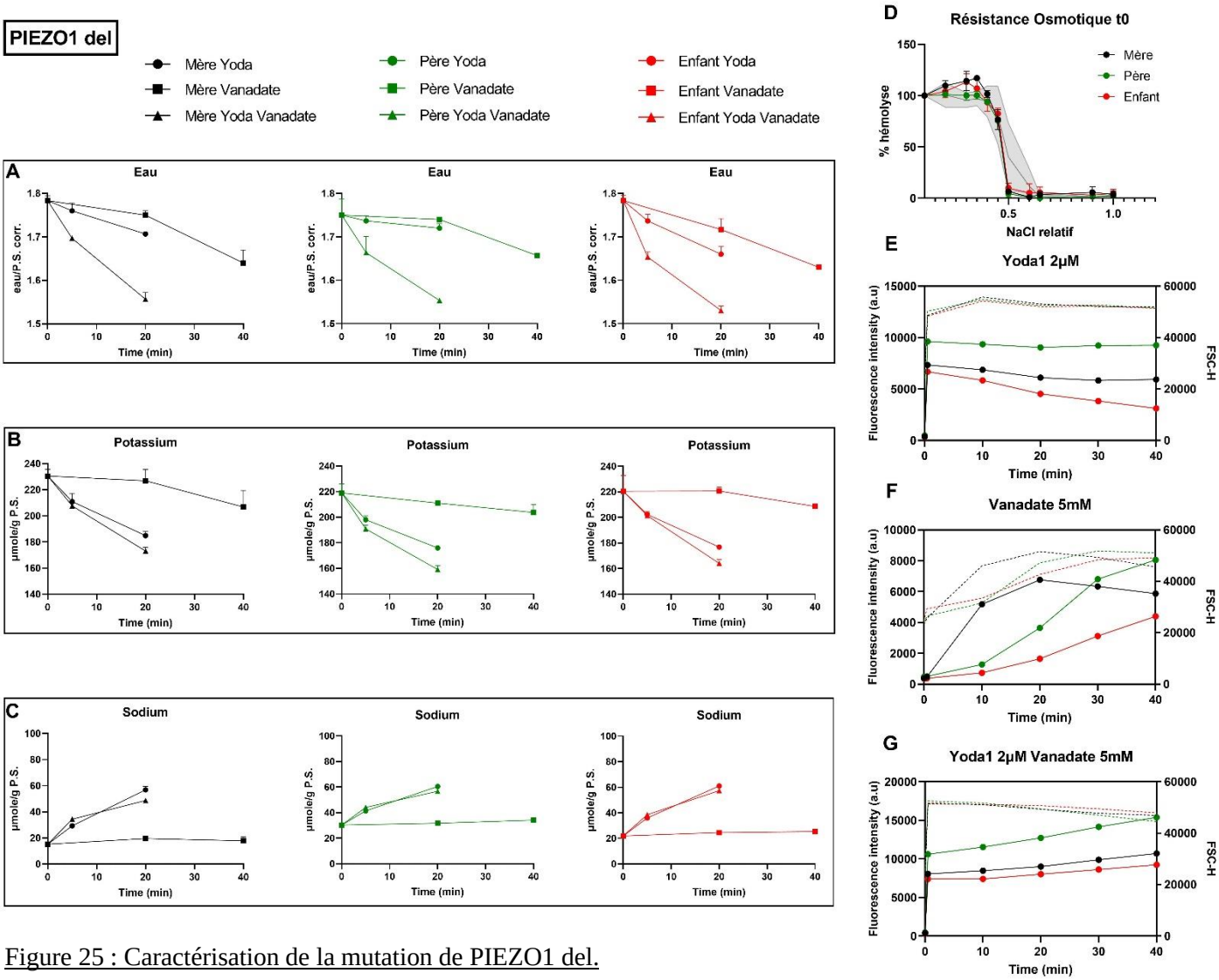

Figure 25 : Caractérisation de la mutation de PIEZO1 del.

(A) Mesure des contenus en eau, (B) potassium et (C) sodium de GR de la mère (noir), du père (vert) et de l'enfant (rouge) au cours du temps après traitement avec du yoda1 (rond plein), vanadate (carré plein) et yoda1 + vanadate (triangle plein). (D) Résistance osmotique avec la courbe moyenne +/- SD de tous les témoins (gris clair). (E) Mesure de la fluorescence calcique (Fluo4-AM) (trait plein) et FSC-H (trait pointillé) au cours du temps après traitement au yoda1, vanadate (F) ou yoda1 + vanadate (G). (H) WB à partir de ghosts de l'enfant, de la mère et du père.

La mutation PIEZO1 del correspond à cette altération génétique : c.326-7-326+8 del CCinsAT.

Nous avons reçu des échantillons sanguins de la mère, du père et de l'enfant chez qui la mutation a été identifiée suivi depuis sa naissance et nécessitant des transfusions régulières. Aucun changement de contenu hydrique ou ionique n'a été observé entre les 3 individus et en comparaison de l'ensemble

des témoins (Figure 25A, B, C et Figure 29A, B, C). La RO est normale chez l'enfant et ses parents et ne témoigne pas d'un défaut de perméabilité ou de déformabilité (Figure 25D). Les contenus calciques mesurés par fluorescence à t0 sont dans la norme (402.2±80.35) pour l'enfant (350), sa mère (387) ou son père (477) (Figure 29E). La morphologie basale est également similaire (enfant FSC-H : 24656 ; mère FSC-H : 23387 ; père FSC-H : 24051). L'influx calcique engendré par les traitements au yoda1 et/ou vanadate est plus faible chez l'enfant par rapport à ses parents (Figure 25E, F, G) et par rapport à l'ensemble des témoins à 20min (Figure 29E, F, G).

En conclusion, la mutation PIEZO1 del n'est pas phénotypique d'une déshydration ou d'un défaut de perméabilité ionique des GR. Nos critères ne nous ont pas permis de mettre en évidence une quelconque différence. Le phénotype clinique sévère de l'enfant n'est pas lié à un défaut de perméabilité ionique ou hydrique. On ne peut pas exclure d'autres effet de PIEZO1 del, indépendants de son rôle de canal ionique, comme des effets sur la structure du GR ou des effets sur les précurseurs érythroïdes.

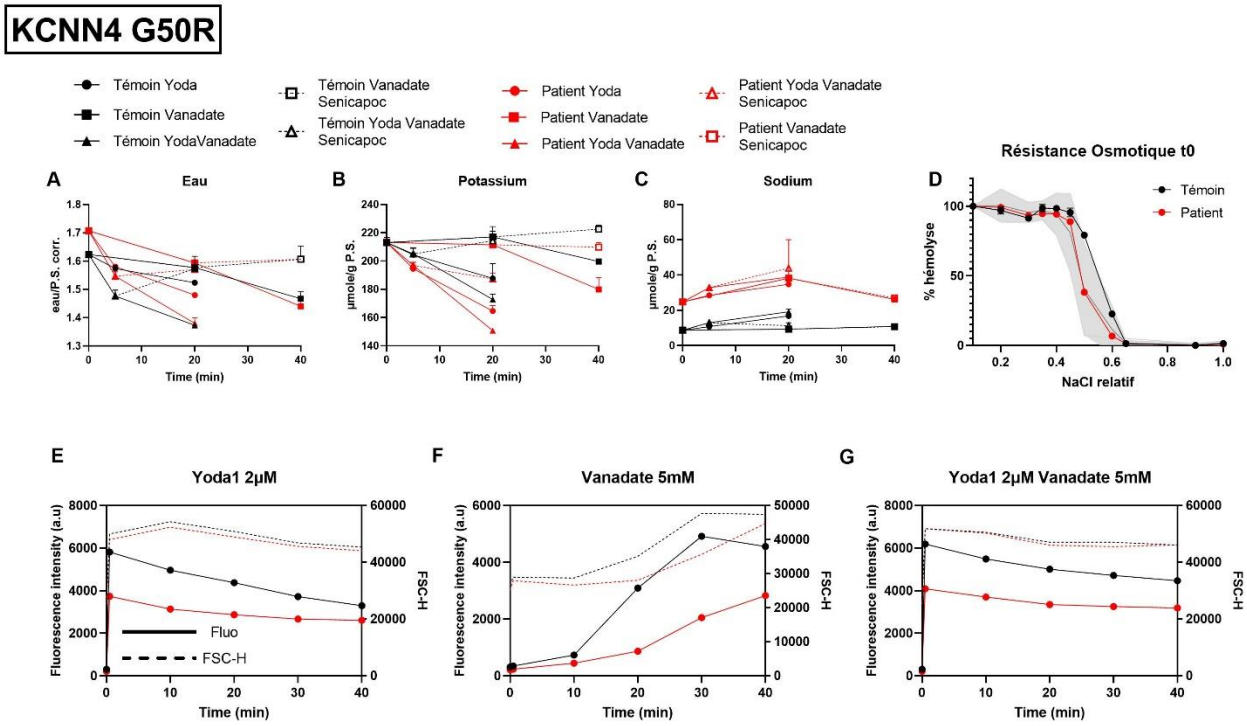

Figure 26 : Caractérisation de la mutation de KCNN4 G50R.

(A) Mesure des contenus en eau, (B) potassium et (C) sodium de GR d'un témoin (noir) et du patient (rouge) au cours du temps après traitement avec du yoda1 (rond plein), vanadate (carré plein), yoda1 + vanadate (triangle plein), vanadate + senicapoc (carré vide) et yoda1 + vanadate + senicapoc (trinagle vide). (D) Résistance osmotique avec la courbe moyenne +/- SD de tous les témoins (gris clair). (E) Mesure de la fluorescence calcique (Fluo4-AM) (trait plein) et FSC-H (trait pointillé) au cours du temps après traitement au yoda1, vanadate (F) ou yoda1 + vanadate (G). (H) Densité de courant (pA/pF) à 0mV de HEK293T transfectées avec KCNN4 WT ou muté en fonction de la $[Ca^{2+}]_i$ (cellule entière).

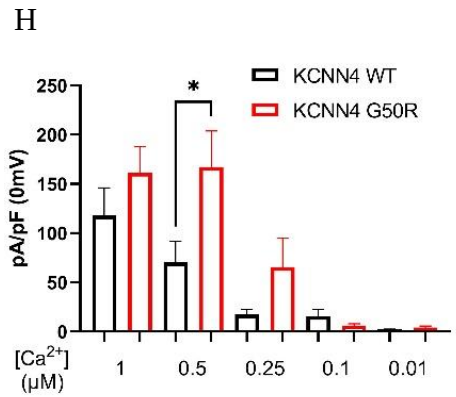

KCNN4 G50R est une mutation nouvelle qui n'a jamais été décrite ou mentionnée dans la littérature scientifique. Le patient porteur de cette mutation G50R a été prélevé en même temps qu'un témoin auquel les résultats ont été comparés.

Le contenu en eau du patient (1.71±0.001) est plus élevé que le témoin (1.62±0.001) mais plus faible que l'ensemble des témoins (1.81±0.10) (Figure 26A et Figure 29A). Il n'y a pas de changement de contenu potassique (Figure 26B) mais des contenus sodiques différents (témoin : 8.72±0.8 vs patient :

24.74±0.23) (Figure 26C). Au vu de ces résultats on pourrait dire que le patient a un gain de sodium mais lorsque l'on compare à l'ensemble des témoins, il n'y a pas de changement (29.85±15). Cela soulève un point important concernant la variabilité des témoins qui fera l'objet d'une discussion dans la dernière section de ce chapitre. La courbe de résistance osmotique est similaire à la moyenne de tous les témoins (Figure 26D) confirmant l'absence de défaut d'hydratation des GR (Figure 26D). Les niveaux de fluorescence calcique à t0 sont légèrement plus faibles chez le patient (219) par rapport au témoin (311) et l'ensemble des témoins (402.2±80.35) contrairement à la taille FSC-H qui est similaire chez le patient (25213) et le témoin (26825). On peut remarquer des réponses au yoda1 et/ou vanadate plus faible chez le patient avec une fluorescence au bout de 20 min de vanadate chez le patient (869) en comparaison du témoin (3092) (Figure 26E, F, G). Le mutant KCNN4 G50R a ensuite été exprimé dans des HEK293T afin de mesurer l'activité du canal en fonction de la concentration calcique intracellulaire. De manière surprenante, KCNN4 G50R a une densité courant significativement augmentée pour 0.5µM Ca^{2+} (167.1±104.1, n=8) que le canal sauvage (70.34±80.99, n=12) (Figure 26H).

En conclusion, KCNN4 G50R n'est pas phénotypique d'un point de vue de la perméabilité ionique et hydrique dans les GR de ce patient. Cependant, la sensibilité au Ca^{2+} est légèrement augmenté dans les cellules HEK293T ce qui va dans le sens d'un gain de fonction ce qui contraste avec l'absence d'effet sur la perméabilité des GR. Le résidu glycine 50 de KCNN4 est localisé à la jonction entre la première boucle intracellulaire et le premier domaine transmembranaire. Sa substitution en arginine (R), un résidu chargé positivement, pourrait expliquer un changement d'activité mais également altérer la structure du canal. Le lien entre cette mutation et l'augmentation de la sensibilité calcique que nous observons nécessite de futures investigations.

KCNN4 delV369-K373

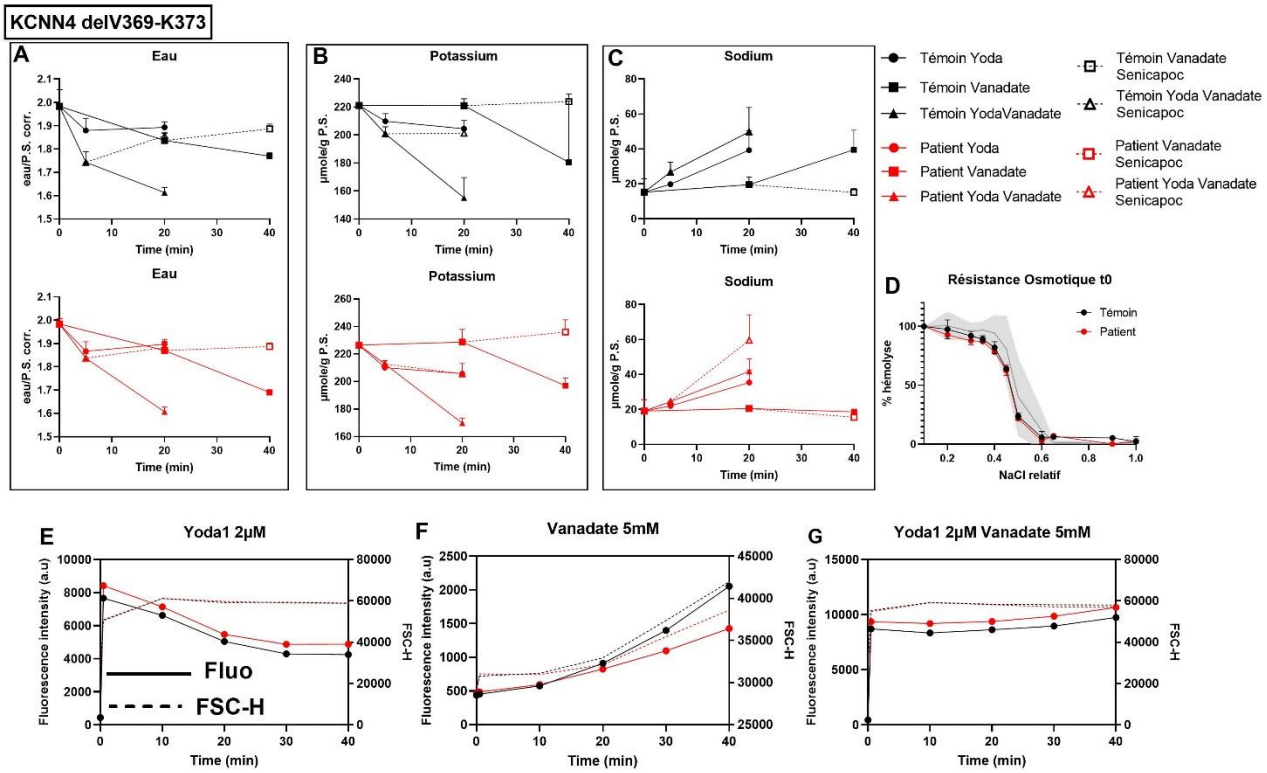

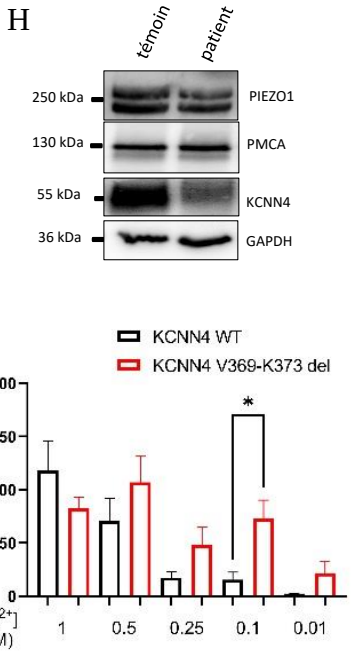

Figure 27 : Caractérisation de la mutation de KCNN4 delV369-K373.

(A) Mesure des contenus en eau, (B) potassium et (C) sodium de GR d'un témoin (noir) et du patient (rouge) au cours du temps après traitement avec du yoda1 (rond plein), vanadate (carré plein), yoda1 + vanadate (triangle plein), vanadate + senicapoc (carré vide) et yoda1 + vanadate + senicapoc (trinagle vide). (D) Résistance osmotique avec la courbe moyenne +/- SD de tous les témoins (gris clair). (E) Mesure de la fluorescence calcique (Fluo4-AM) (trait plein) et FSC-H (trait pointillé) au cours du temps après traitement au yoda1, vanadate (F) ou yoda1 + vanadate (G). (H) WB à partir de ghosts de patient et témoin. (I) Densité de courant (pA/pF) à 0mV de HEK293T transfectées avec KCNN4 WT ou muté en fonction de la $[Ca^{2+}]_i$ (cellule entière).

Ce cas fait référence à une mutation de KCNN4 déjà mentionnée (Picard et al., 2019) qui consiste en une délétion de 18 pb, identifiée entre l'exon 7 et l'intron du gène *KCNN4*, chez 3 patients avec une anémie marquée. Il a été suggéré que ce défaut puisse mener à la délétion de 5 aa dans le domaine de

liaison à la CaM en C-terminal. Les conséquences fonctionnelles d'une telle mutation n'ont jamais été testées.

Nous avons eu accès au prélèvement sanguin d'un patient portant la mutation KCNN4 V369-K373 del accompagné d'un prélèvement témoin. A t0, la mesure du contenu en eau des GR du patient (1.98±0.03) n'est pas différente par rapport au témoin (1.98±0.07) mais est statistiquement augmentée en comparaison de l'ensemble des témoins (Figure 27A, Figure 29A). Les mesures de potassium et sodium ne révèlent aucune différence entre le patient et le témoin (Figure 27B, C). La courbe de RO du patient est dans la gamme des témoins (Figure 27D). Les niveaux de base de fluorescence calcique sont similaires entre le patient (455) et le témoin (439). La morphologie est également inchangée (patient FSC-H : 455 vs témoin FSC-H : 29242). On ne note pas de différence de réponse au yoda1 et/ou vanadate sur l'influx calcique. Un WB réalisé sur les ghosts de patient et témoin révèlent une diminution importante de l'expression de KCNN4 chez le patient (Figure 27H). Nous avons ensuite transposé cette altération génétique au niveau protéique en supposant qu'elle corresponde à une délétion de 5 aa de KCNN4 dans la partie C-terminal. La mesure de l'activité de cette mutation de KCNN4 en patch-clamp, montre une augmentation statistique de la densité de courant moyenne (pA/pF) à 0mV par rapport à KCNN4 WT avec 0.1µM de $[Ca^{2+}]_i$, (72.55±46.85, n=7 vs 15.5±20.22, n=8). Cela suggère une augmentation de la sensibilité calcique du canal muté.

En conclusion, KCNN4 delV369-K373 n'induit pas de déshydratation du GR. Nous observons une hyperhydratation des GR mais cette mesure non corrélée à un changement de la RO. Cette hyperhydratation pourrait très bien être causée par un nombre important de réticulocytes, plus gros que les GR, faussant les résultats. Néanmoins cette mutation induit une augmentation de la sensibilité au calcium de KCNN4 dans les cellules HEK293T. Ceci a déjà été observé avec les deux autres mutations de KCNN4 (V222L et H340N) (Allegrini et al., 2022). L'effet traductionnel exact de la délétion de 18 pb entre l'exon 7 et intron 7 de KCNN4 V369-K373 del n'est pas connu. Nous sommes partis de l'hypothèse selon laquelle cette délétion induirait une perte de 5 aa du domaine C-terminal (Picard et al., 2019). Nous avons donc mesuré l'activité électrique d'un KCNN4 dont les 5aa correspondants ont été retirés. Il est tout à fait envisageable que l'effet de cette délétion conduise à l'absence d'expression de la protéine mutée, comme suggéré par le WB. D'autre part, l'interpretation de ces résultats doit être faite avec précaution au vu du comportement du témoin (hyperhydraté). Il n'est pas impossible que les conditions de transport aient pu modifier nos mesures.

KCNN4 H340N

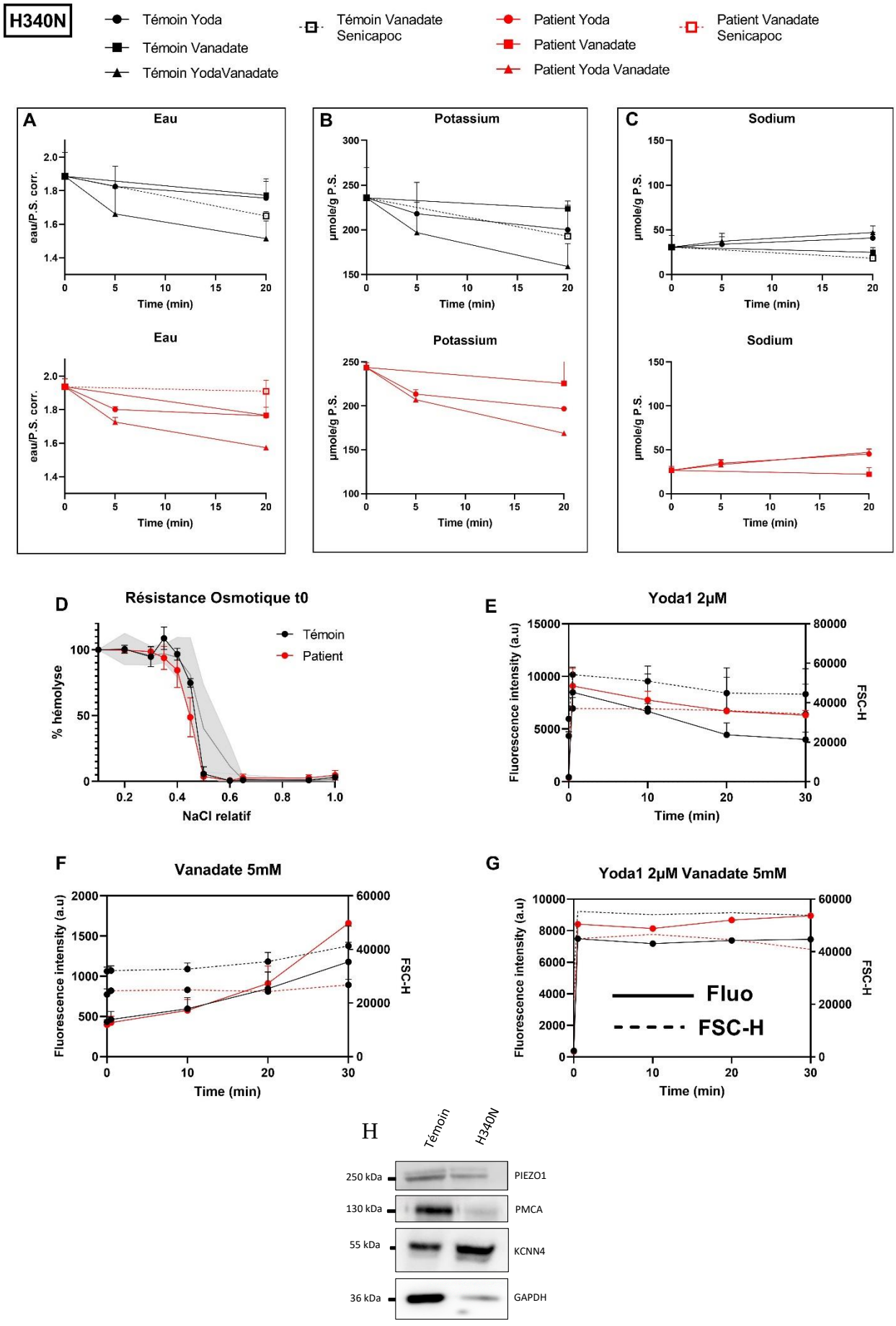
H340N
Témoin Yoda
Témoin Vanadate
Témoin YodaVanadate
Témoin Vanadate Senicapoc
Patient Yoda
Patient Vanadate
Patient Yoda Vanadate
Patient Vanadate Senicapoc
A
Eau
eau/P.S. corr.
Time (min)
B
Potassium
µmole/g P.S.
C
Sodium
D
Résistance Osmotique t0
Témoin
Patient
% hémolyse
NaCl relatif
E
Yoda1 2µM
Fluorescence intensity (a.u)
FSC-H
F
Vanadate 5mM
G
Yoda1 2µM Vanadate 5mM
Fluo
FSC-H
H
Témoin
H340N
250 kDa
PIEZO1
130 kDa
PMCA
55 kDa
KCNN4
36 kDa
GAPDH

Figure 28 : Caractérisation de la mutation de KCNN4 H340N.

(A) Mesure des contenus en eau, (B) potassium et (C) sodium de GR d'un témoin (noir), et du patient (rouge) au cours du temps après traitement avec du yoda1 (rond plein), vanadate (carré plein) ou yoda1 + vanadate (carré vide). (D) Résistance osmotique avec la courbe moyenne +/- SD de tous les témoins (gris clair). (E) Mesure de la fluorescence calcique (Fluo4-AM) au cours du temps après traitement au yoda1, vanadate (F) ou yoda1 + vanadate (G). (H) WB à partir de ghosts de témoin et patient.

Nous avons eu accès aux prélèvements sanguins de deux patients porteurs de cette mutation. Les deux prélèvements du premier patient ont déjà fait l'objet d'une publication au cours de cette thèse (Allegrini et al., 2022) présentée en fin de chapitre. Dans cette section il sera question de deux prélèvements du second patient.

Le contenu en eau des GR du patient H340N est augmenté (1.93±0.05) par rapport aux témoins (1.76±0.08) et la moyenne générale (1.807±0.10) suggérant une hyperhydratation (Figure 28A). Cela est associé à un gain de potassium (237.2±25.5 vs 205.26±2.96) qui n'est cependant pas significatif (Figure 28B). Les contenus en sodium sont similaires (Figure 28C). La RO révèle un léger décalage vers la gauche (Figure 19D) qui est confirmé avec des analyses plus poussées (Figure 29D) où l'IC50 (NaCl relatif pour 50% d'hémolyse) du patient est en dessous de l'ensemble des témoins. Les contenus calciques ne révèlent pas de différences notables (Figure 28E, F, G). L'analyse de ghosts de GR par WB montre une diminution des niveaux de PMCA ainsi que GAPDH chez le patient en comparaison du témoin (Figure 28H). C'est une observation déjà faite pour la mutation PIEZO1 A2003T/R2491W qui reste sans explication.

En conclusion, KCNN4 H340N semble induire une hyperhydratation des GR. On note toutefois une augmentation de RO qui est surprenante au vu des contenus en eau et K^+ puisque dans un cas d'hyperhydratation on aurait pu s'attendre à une diminution de la résistance osmotique (décalage vers la droite de la courbe). Cela suggère plutôt un changement de structure du GR. De plus, de la même façon que pour KCNN4 del, les résultats peuvent être faussés par un nombre important de réticulocytes bien que la RO devrait également être modifiée. Le phénotype érythrocytaire de cette mutation H340N ne montre pas d'anomalie de la perméabilité. Ces résultats sont en accord avec les mesures réalisées sur le précédent patient porteur de cette mutation chez qui nous n'avons pas observé de déshydratation des GR malgré une sensibilité calcique augmentée de KCNN4 H340N dans les cellules HEK293T (Allegrini et al., 2022).

Conclusion générale sur les mutations étudiées.

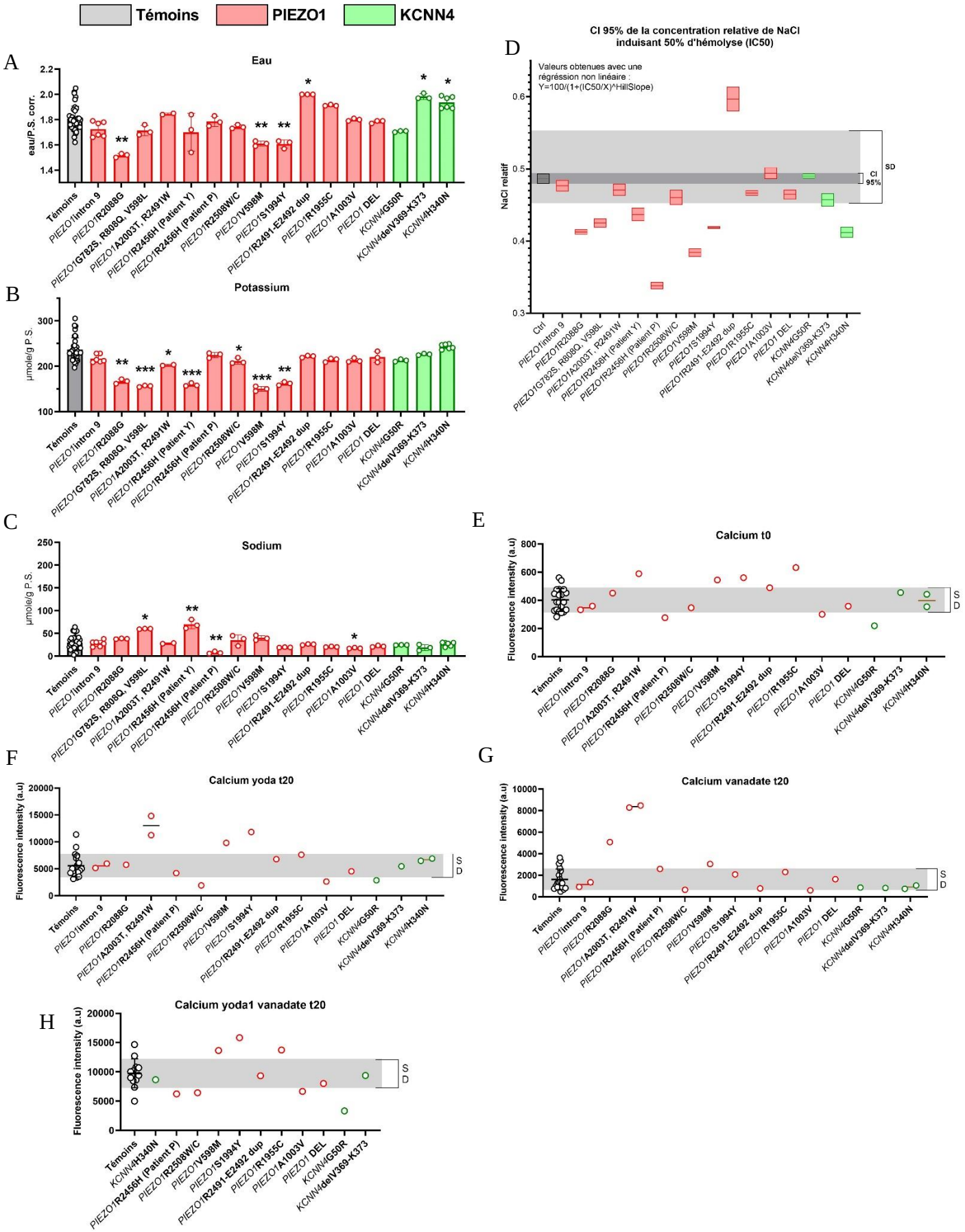

Figure 29 : Bilan de l'effet des mutations PIEZO1 et KCNN4 par rapport à l'ensemble des témoins.

(A) Mesure des contenus en eau, (B) potassium et (C) sodium, réalisées en triplicatas. Comparaison par rapport aux témoins réalisé avec un test « Kruskal-Wallis test, uncorrected Dunn's test », * : $p<0.05$, ** : $p<0.01$, *** : $p<0.001$. (D) Intervalle de confiance à 95% de la valeur de NaCl relatif permettant d'obtenir 50% d'hémolyse. Obtenu par régression linéaire à partir des courbes de résistance osmotiques. En gris foncé est représenté l'IC50 des témoins et en gris clair est représenté par la déviation standard (SD) qui a été extrapolée à partir des courbes de RO des témoins. (E, F, G, H) Mesure de la fluorescence calcique (Fluo4-AM) basale (E), 20 min après traitement au yoda1 (F), vanadate (G) et yoda1 + vanadate (H).

Certaines mutations sont associées à un phénotype pathogène dans le GR que l'on définit selon plusieurs critères : (1) changement du contenu hydrique, (2) changement de la perméabilité ionique (K^+, Na^+ et Ca^{2+}), (3) changement de la résistance osmotique et (4) réponse augmentée avec traitement avec yoda1±vanadate. On peut ainsi classer les mutations d'après leur degré de sévérité selon qu'elles réunissent 0 ou plusieurs de ces critères :

- 4 critères : PIEZO1 V598M, S1994Y et R2088G.
- 3 critères : aucune mutation
- (2) + (4) : A2003T-R2491W et
- (2) + (3) : PIEZO1 G782S-R808Q-V598L, R2456H.
- (1) + (3) : KCNN4 H340N.
- 1 critères : PIEZO1 R2491-E2492 dup (1), R2508C (2), A1003V (2), R1955C (2) (2), V369-K373 del (1).
- 0 critère : PIEZO1 intron 9, DEL.
  KCNN4 G50R

Les mutations les plus pathogènes sont associées à un phénotype de déshydratation avec diminution significative du contenu en eau (PIEZO1 R2088G, V598M et S1994Y (Figure 29A)) corrélée à une diminution significative du contenu potassique non compensé par un gain de sodium (Figure 29B, C). C'est un phénotype classique de déshydratation médiée par une activation de KCNN4. En effet, l'activation de KCNN4 se traduit par un efflux net de potassium sans influx de sodium. Ce phénotype est retrouvé seulement avec les mutations de PIEZO1. Dans le cas de certaines mutations comme PIEZO1 G782S-R808Q-V598L et R2456H (Patient Y) on observe une perte significative de potassium (Figure 29B) compensée par un gain significatif de sodium (Figure 29C) qui se traduit par une absence de déshydratation significative alors que la RO est augmentée. Ceci suggère l'intervention d'autres facteurs que la déshydratation dans les modifications de RO comme des défauts de structure.

De façon intéressante, les mutations PIEZO1 R2491-E2492 dup, KCNN4 H340N et V369-K373 del sont associées à une hyperhydratation des GR. Ce gain d'eau est corrélé à une diminution de la RO uniquement pour PIEZO1 R2491-E2492dup. Le comportement atypique des mutations KCNN4 H340N et V369-K373 del peut provenir d'un nombre important de réticulocytes pouvant fausser les résultats. Un volume apparent plus élevé des GR avec mutations KCNN4 avait aussi été observé dans la description de la mutation princeps (R352H) (Rapetti-Mauss et al., 2015)

Deux mutations, PIEZO1 R2456H (Patient P) et A1003V sont associées à une perte significative de sodium (Figure 29C) sans changement du contenu en eau ou potassium. PIEZO1 R2456H (Patient P) a une RO extrêmement augmentée alors que ce n'est pas le cas pour PIEZO1 A1003V. La mutation R2456H du patient P semble induire une augmentation de la perméabilité Na^+ de PIEZO1 sans changement des perméabilités K^+ et Ca^{2+}. Le changement drastique de RO non corrélé à une déshydratation suggère une altération de la déformabilité.

Le cas de la mutation R2456H est assez surprenant, avec deux patients porteurs mais des phénotypes différents. Chez le patient P et Y le contenu en eau est inchangé mais les contenus ioniques sont complètement différents. Les GR du patient Y ont moins de K^+ et plus de Na^+ contrairement à ceux du patient P qui ont beaucoup moins de Na^+. La RO du patient Y est moins augmentée que le patient P. En revanche même si les observations diffèrent, pour des raisons expérimentales ou de variabilité individuelle, dans les deux cas la mutation altère les propriétés des GR.

Concernant le Ca^{2+}, on note une augmentation de la fluorescence calcique à t0 pour PIEZO1 A2003T-R2491W, V598M, S1994Y et R1955C. Cette augmentation est corrélée à une déshydratation pour PIEZO1 V598M et S1994Y au contraire des deux autres mutations qui n'induisent pas de modification de la perméabilité ionique et hydrique. Le cas de PIEZO1 A2003T/R2491W est assez particulier puisque on observe des réponses calciques, après traitement au yoda1 et/ou vanadate, au-dessus de toutes les autres mutations et témoins. PIEZO1 A2003T/R2491W pourrait modifier la perméabilité calcique mais l'absence d'autres effets (déshydratation, RO, etc…) laisse à penser que ces différences sont dues à un biais expérimental, d'autant plus que nous n'avions pas de témoin à tester en parallèle.

Xérocytose Héréditaire : Différences de comportement des mutations du domaine extracellulaire N-terminal de PIEZO1, entre les Globule Rouges et les cellules HEK293T.

Contexte

C'est une étude que nous avons réalisée en collaboration avec Rémy Peyronnet afin de mieux comprendre comment les mutations de PIEZO1 dans la XH altèrent la physiologie du GR. Nous nous sommes focalisés sur 3 cas de patient porteurs de mutation de PIEZO1 dans la partie N-terminale (V598M, F681S, G782S/R808Q). Nous avons montré que les GR de ces patients sont significativement déshydratés par rapport aux témoins indiquant l'effet pathogène de ces mutations de PIEZO1. Cependant, nos résultats montrent que ces mutations exprimées dans des cellules HEK293T n'affectent pas systématiquement le fonctionnement du canal. En effet, les mutations V598M, F681S et R808Q n'induisent aucun changement d'activité de PIEZO1 au contraire de PIEZO1 G782S qui montre des courants plus forts que PIEZO1 WT. Cela montre que l'étude des mutations de PIEZO1 dans les HEK293T ne relate pas toujours le phénotype observé dans les GR. Une des explications de ce phénomène concerne l'environnement lipidique qui diffère entre les cellules HEK293T et les GR. Or, on sait que cet environnement à une influence sur les propriétés de PIEZO1, notamment par la composition en acide gras et cholestérol.

frontiers in Physiology

BRIEF RESEARCH REPORT
published: 18 October 2021
doi: 10.3389/fphys.2021.736585

Hereditary Xerocytosis: Differential Behavior of PIEZO1 Mutations in the N-Terminal Extracellular Domain Between Red Blood Cells and HEK Cells

*Yohei Yamaguchi[1,2†], Benoit Allegrini[3], Raphaël Rapetti-Mauss[3], Véronique Picard[4], Loïc Garçon[5], Peter Kohl[1,2,6], Olivier Soriani[3], Rémi Peyronnet[1,2] and Hélène Guizouarn[3]**

[1] Institute for Experimental Cardiovascular Medicine, University Heart Center Freiburg, Bad Krozingen, Germany, [2] Medical Center and Faculty of Medicine, University of Freiburg, Freiburg im Breisgau, Germany, [3] Université Côte d'Azur, CNRS, INSERM, Institut de Biologie Valrose, Nice, France, [4] Université Paris Sud-Paris Saclay, Faculté de Pharmacie, Service d'Hématologie Biologique, Hôpital Bicêtre, APHP, Le Kremlin-Bicêtre, France, [5] Université Picardie Jules Verne, EA 4666, Service d'Hématologie Biologique, CHU, Amiens, France, [6] CIBSS – Centre for Integrative Biological Signalling Studies, University of Freiburg, Freiburg im Breisgau, Germany

OPEN ACCESS

Edited by:
Richard Van Wijk, Utrecht University, Netherlands

Reviewed by:
Emile Van Den Akker, Sanquin Research, Netherlands
Roberta Russo, University of Naples Federico II, Italy

***Correspondence:**
Hélène Guizouarn
helene.guizouarn@univ-cotedazur.fr

†Present address:
Yohei Yamaguchi, Department of Physiology, Asahikawa Medical University, Hokkaido, Japan

Specialty section:
This article was submitted to Red Blood Cell Physiology, a section of the journal Frontiers in Physiology

Received: *05 July 2021*
Accepted: *02 September 2021*
Published: *18 October 2021*

Citation:
Yamaguchi Y, Allegrini B, Rapetti-Mauss R, Picard V, Garçon L, Kohl P, Soriani O, Peyronnet R and Guizouarn H (2021) Hereditary Xerocytosis: Differential Behavior of PIEZO1 Mutations in the N-Terminal Extracellular Domain Between Red Blood Cells and HEK Cells. Front. Physiol. 12:736585. doi: 10.3389/fphys.2021.736585

Hereditary Xerocytosis, a rare hemolytic anemia, is due to gain of function mutations in PIEZO1, a non-selective cation channel activated by mechanical stress. How these PIEZO1 mutations impair channel function and alter red blood cell (RBC) physiology, is not completely understood. Here, we report the characterization of mutations in the N-terminal part of the protein (V598M, F681S and the double mutation G782S/R808Q), a part of the channel that was subject of many investigations to decipher its role in channel gating. Our data show that the electrophysiological features of these PIEZO1 mutants expressed in HEK293T cells are different from previously characterized PIEZO1 mutations that are located in the pore or at the C-terminal extracellular domain of the protein. Although RBC with PIEZO1 mutations showed a dehydrated phenotype, the activity of V598M, F681S or R808Q in response to stretch was not significantly different from the WT channels. In contrast, the G782S mutant showed larger currents compared to the WT PIEZO1. Interestingly, basal activity of all the mutated channels was not significantly altered at the opposite of what was expected according to the decreased water and cation contents of resting RBC. In addition, the features of mutant PIEZO1 expressed in HEK293 cells do not always correlate with the observation in RBC where PIEZO1 mutations induced a cation leak associated with an increased conductance. Our work emphasizes the role of the membrane environment in PIEZO1 activity and the need to characterize RBC permeability to assess pathogenicity to PIEZO1 mutants associated with erythrocyte diseases.

Keywords: PIEZO1, KCNN4, hereditary xerocytosis, stomatocytosis, red blood cell

INTRODUCTION

Gain-of-function mutations in PIEZO1 have been linked to Dehydrated Hereditary Stomatocytosis (DHSt), a rare red blood cell (RBC) disease also known as hereditary xerocytosis (Zarychanski et al., 2012; Albuisson et al., 2013; Andolfo et al., 2013). PIEZO1 is a non-selective cation channel, activated by mechanical stimuli, that has been proposed to link mechanical forces to RBC calcium permeability (Coste et al., 2012; Cahalan et al., 2015). Once activated, PIEZO1 mediates a cation current that decreases toward basal values even during persistent mechanical stimulation (inactivation). In RBC, this transient activation of PIEZO1 in response to membrane stretch increases intracellular calcium concentration and stimulates the Ca^{2+} activated K^+ channel, KCNN4 (or Gardos channel), that allows K^+ to leave the cell. The high anion conductance of RBC membrane allows Cl^- flux, leading to a net KCl efflux. This loss of osmolytes from the cytosol is accompanied by water leaving the cell, resulting in RBC dehydration. Gain-of-function mutations in PIEZO1 have thus been associated with RBC dehydration through excessive KCNN4 stimulation (Rapetti-Mauss et al., 2017).

In DHSt patients with PIEZO1 gain of function mutations, RBC are dehydrated and show a typical leftward shift in osmotic gradient ektacytometry (i.e., toward increased deformability at lower osmolality values), attesting changes in the water content equilibrium (Andolfo et al., 2013; Picard et al., 2019; Pérès et al., 2021). The increasing use of sequencing in diagnosis has resulted in identification of a collection of mutations in *PIEZO1*. Characterizing the electrophysiological features of new PIEZO1 mutations, discovered by genetic screening of patients with suspected DHSt, is necessary to understand the link between the genotype and the RBC phenotype.

Here, we report electrophysiological features of five different PIEZO1 mutations, identified in three independent index cases with typical DHSt clinical and biological phenotypes [as described in previous publications (Andolfo et al., 2013; Rapetti-Mauss et al., 2017)]. In contrast to the majority of PIEZO1 mutations associated to DHSt so far, the present mutations are located at the N-terminal part of the protein. This part of the protein is not yet structurally resolved, however, it is made up of clusters of alpha helices, that may function as membrane tension sensors (Zhao et al., 2018). Recent structural studies proposed that this domain is organized as a repetitive pattern of 4 helices connected by intracellular and extracellular loops similar to the 6 repeats of 4 helices that shape the extended arm of each subunit of the channel (Guo and MacKinnon, 2017). Interestingly, the electrophysiological features of here assessed PIEZO1 mutants (expressed in HEK293 cells) are different from previously characterized PIEZO1 mutations that are located in the pore or at the C-terminal extracellular domain of the protein.

MATERIALS AND METHODS

Blood samples: Human blood samples were obtained with written informed consent from four hereditary xerocytosis patients from previously described families (Andolfo et al., 2013) and six unrelated healthy control subjects. Blood withdrawn into EDTA collecting tubes was used directly for ektacytometry in a hospital laboratory and sent to the research laboratory within 24 h. Osmotic gradient ektacytometry was performed on fresh blood samples as previously described (Cynober et al., 1996). In brief, red blood cells in a 4% polyvinylpyrrolidone solution of gradually increasing osmolality (from 60 to 450 mOsm) were submitted to continuous flow using a first generation ektacytometer (Bayer Diagnostics, Tarrytown, NY, United States) and osmolar parameters as well as maximal elongation index were recorded. Upon reception at the research lab, blood was washed three times in saline solution containing (in mM): NaCl (145), KCl (5), $MgSO_4$ (2), $CaCl_2$ (1), HEPES (10) pH 7.4 and any buffy coat was removed by aspiration. RBC Na^+, K^+ and water content were measured as previously described (Rapetti-Mauss et al., 2015).

HEK293T cell experiments: HEK293T cells were transiently transfected with pIRES-eGFP plasmids containing the following PIEZO1 constructs: the control PIEZO1 channel WT, V598M, F681S, G782S, R808Q, or G782S/R808Q. Transfection was conducted using jetPEI transfection reagent (Polyplus-transfection) and experiments were carried on 48 to 72 h after transfection. pIRES-eGFP containing human WT PIEZO1 DNA was a kind gift from B. Coste. Mutations in the WT PIEZO1 were introduced by PCR with pfu Turbo DNA polymerase and primers overlapping the mutation by 15 nucleotides downstream and upstream. The obtained constructs were sequenced to check for correct mutations (Beckman Coulter Genomics, Takeley, United Kingdom).

To quantify PIEZO1 expression at the plasma membrane, HEK293T cells transfected with the different plasmids or not transfected (NT) were labeled with biotin using Pierce cell surface protein isolation kit according to manufacturer's procedures (Pierce Thermo Fisher). 48 h after transfection, cells at 80% confluence were washed twice with ice-cold Phosphate Buffered Saline (PBS) and incubated for 30 min on ice with sulfo-NHS-SS-biotin in PBS. Labeled proteins were immunodetected by Western blot, using anti-PIEZO1 antibody 1/1,000 (Proteintech 15939-1-AP) and anti Na^+/K^+ ATPase ß1 subunit 1/1,000 (Sigma Aldrich) was used as an internal loading standard. The intensity of biotinylated Na^+/K^+ ATPase (I_{NaK}) and PIEZO1 (I_P) lanes were quantified using Fiji software (Schindelin et al., 2012). A normalizing factor (Nf = I_{NaK} in lanes with WT PIEZO1/I_{NaK} in lanes with mutant PIEZO1) was calculated to normalize the PIEZO1 signal. The ratio ($I_{pmutant} \times Nf$)/I_{pWT} was calculated and plotted for five different Western blots corresponding to three different preparations of HEK293T cell lysates.

Electrophysiology: stretch-activated currents of PIEZO1 WT and mutants in HEKT293 cells, 48–72 h after transfection, were recorded in cell-attached configuration. Current recordings were done using an Axopatch 200B Microelectrode Amplifier (Axon Instruments). Currents were induced by stepwise negative pipette pressure (0 to −80 mmHg, Δ10 mmHg, 500 ms), applied using a high-speed pressure clamp (ALA Scientific Instruments). Average pipette resistance was 1.3 ± 0.3 MΩ. Peak current-pressure relationship of stretch-activated currents elicited at −80 mV were

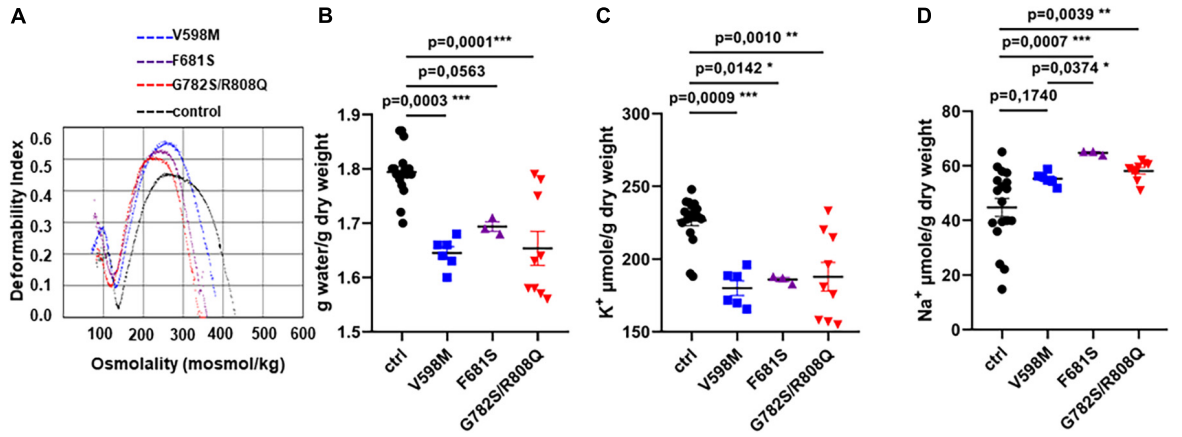

FIGURE 1 | (A) Ektacytometry profiles of RBC from three independent index-cases with clinical and biological phenotypes typical of hereditary xerocytosis, which were previously described. **(B)** water, **(C)** K^+, and **(D)** Na^+ content of control or mutant RBC, measured in resting conditions 24 h after blood withdrawal. Statistical analyzes of the data were done with a Kruskal and Wallis test followed by a Dunn's post-test. The *p* value is given on each figure. There were no significant differences ($p < 0.05$) between mutants except the Na^+ content between V598M and F681S, $p = 0.03$.

fitted with a Boltzmann equation. Currents were acquired at 20 kHz sampling rate, and low-pass filtered at 1 kHz. Recordings were analyzed with pCLAMP 10.6 software (Axon Instruments) using solutions already described for characterizing PIEZO1 channels (Peyronnet et al., 2013). The bath solution contained (in mM): KCl (155), $MgCl_2$ (3), EGTA (5), HEPES (10); pH buffered to 7.2 using KOH, measured osmolality ≈ 320 mOsm L^{-1}. The solution was stored at room temperature. Pipette solution, contained (in mM): NaCl (150), KCl (5), HEPES (10), $CaCl_2$ (2), pH buffered to 7.4 using NaOH, ≈ 305 mOsm L^{-1}.

RESULTS

We first analyzed RBC from three patients who carried the following PIEZO1 substitutions: V598M, F681S and the double mutation G782S/R808Q, respectively. Patients' RBC ektacytometry curves were typical of DHSt (**Figure 1A**), showing a leftward shift of the maximum elongation index indicative of cell dehydration (already shown for V598M and F681S in Rapetti-Mauss et al., 2017). Indeed, patients' RBC water content was about 10% lower for V598M and G782S/R808Q mutations, compared to WT RBC (**Figure 1B**). A significantly lower K^+ content was observed for all three mutants, with a high variability for G782S/R808Q (**Figure 1C**). Na^+ content was significantly higher (∼10–15%) in the F681S and the double mutant (**Figure 1D**). When observed, this Na^+ increase did not fully compensate the K^+ loss, and there is a decrease in monovalent cation content ($Na^+ + K^+$), which correlates with the RBC dehydration. It was shown in our previous work, that patients' RBC cation leak is associated with a rise in cell membrane conductance (Rapetti-Mauss et al., 2017): a transient current following Goldman-Hodgkin-Katz law was observed in patients' RBC, which is not observed in control RBC (recorded in whole cell configuration). This current is thought to be indicative of increased PIEZO1 activity in RBC with the PIEZO1 mutations V598M, F681S and G782S/R808Q. The increased current may result either from a higher stretch sensitivity, a greater conductance of mutant PIEZO1, an increased presence of channels in the cell membrane, or a mix of these factors. Thus far, the stretch-sensitivity of the PIEZO1-mutants has not been characterized.

To analyze the functional consequences of these PIEZO1 mutations, HEK293 cells were transiently transfected with pIRES-eGFP vector containing either the control human PIEZO1 (WT), the mutants V598M, F681S, G782S/R808Q as in RBC or G782S and R808Q alone.

The expression and location at the plasma membrane of WT and mutant PIEZO1 protein were assessed by quantification of biotinylated PIEZO1, and related to the expression of the ß1 subunit of Na^+/K^+ ATPase. There was no significant difference between WT and mutant PIEZO1 levels (**Figures 2A,B**) in protein expression at the plasma membrane. A representative WB of total and biotinylated PIEZO1 signal with a quantification of PIEZO1 signal is shown in **Supplementary Figures 1A,B**. An immunofluorescence labeling of PIEZO1 in HEK293 transfected cells illustrated the transfection efficiency (**Supplementary Figure 2**). Thus, mutant protein trafficking and targeting to the HEK293 plasma membrane was similar to WT. Of note, we did not detect endogenous PIEZO1 protein by Western blot in our HEK293 cell line.

Stretch-activated currents of each PIEZO1 mutant were measured using stepwise application of negative pressure in cell-attached configuration. The peak current in V598M, F681S and R808Q was not significantly different from WT (**Figure 2C**), while in G782S and G782S/R808Q it was significantly larger at pipette pressures ranging from −40 to −80 mmHg. Representative current traces for each construct are shown in **Figure 3A**. In the absence of negative pipette pressure, the current levels of WT and mutant PIEZO1 channels were not significantly different (**Figure 2D**), suggesting no change in constitutive current activity of mutated channels in HEK293 cells.

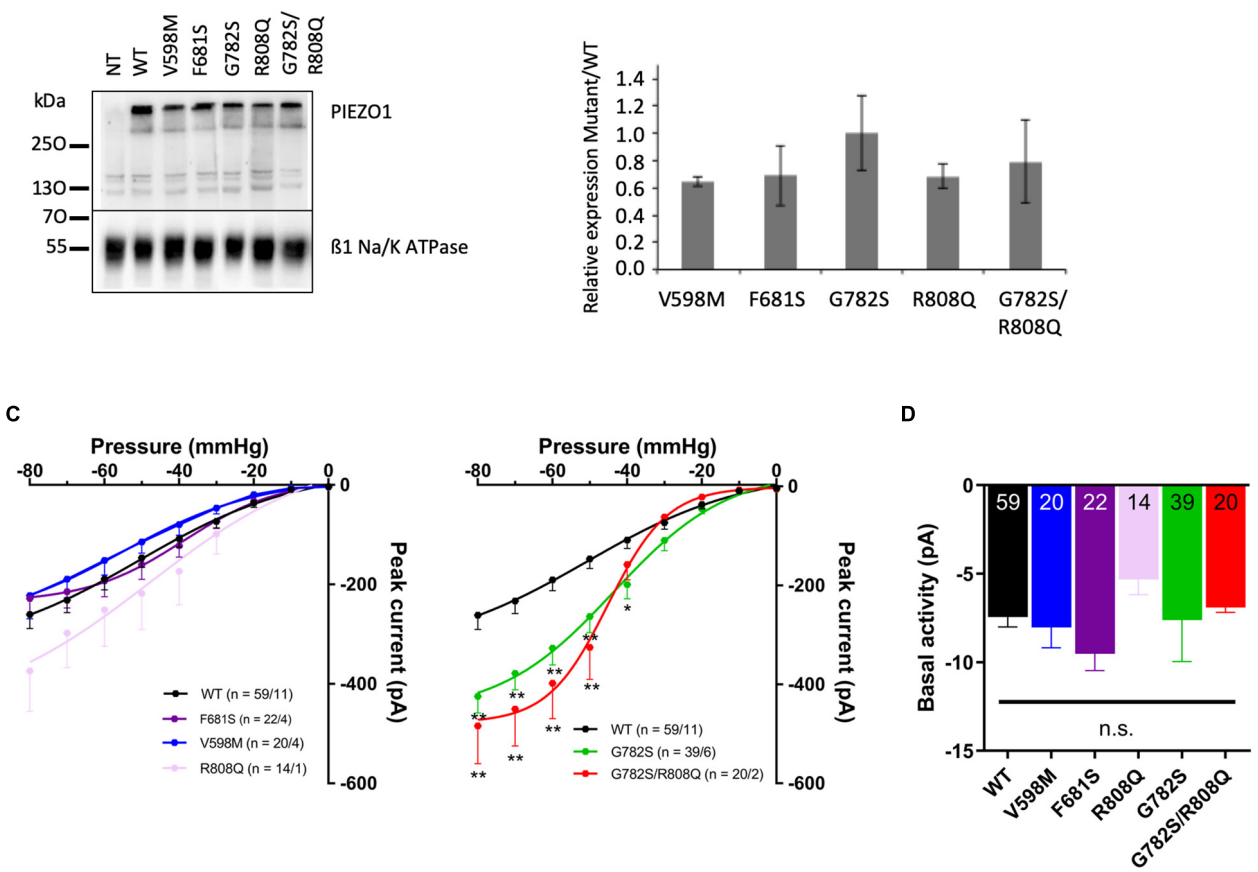

FIGURE 2 | (A) Representative Western blot (WB) from three different cell labeling done on three different batches of transfected cells. **(B)** Quantification of PIEZO1 mutant expression related to WT. A ratio of Na^+/K^+ ATPase signal for each mutant versus WT was calculated for each WB and the PIEZO1 signal was corrected according to this internal standard. The plot illustrates the ratio Mutant/WT PIEZO1 calculated after five different WB (means ± sem). Statistical analyzes were done with Kruskal and Wallis test and differences were not significant ($p > 0.05$). **(C)** Stretch-activated currents of PIEZO1 WT and mutants, expressed in HEK293T cells, recorded in cell-attached configuration. Bars represent the mean ± sem, and the number of cells tested/the number of cell transfections is shown as n in the figures. $^{**}p < 0.01$; $^{*}p < 0.05$ vs. WT, two-way analysis of variance with Bonferroni's *post hoc*. **(D)** Basal activity of PIEZO1. Basal activity calculated from the current traces without additional negative pipette pressure application, showing no significant differences between eGFP without PIEZO1, WT, and mutant constructs. Bars represent the mean ± sem, and the number of cells tested is shown in the bottom of the bars. n.s., not significantly different, one-way analysis of variance with Bonferroni's *post hoc*.

The inactivation kinetics of channels, as well as their near steady-state currents, were not statistically different in WT and mutants (**Figures 3B,C**).

DISCUSSION

Data presented here show that the Na^+ and K^+ permeability of patients' RBC was increased in the three cases of PIEZO1 mutations (V598M, F681S, G782S/R808Q) and these RBC are slightly dehydrated due to chronic activation of KCNN4, as shown in our previous publication (Rapetti-Mauss et al., 2017). The properties of these RBC are similar to the ones recently described for the D669Y PIEZO1 mutant (Pérès et al., 2021). The D669Y PIEZO1 RBC have an increased cation conductance and slight dehydration likely due to more frequent activation of KCNN4. Hence, these PIEZO1 mutants are likely to induce a constitutive Na^+, K^+, and Ca^{2+} leak in RBC. Moreover, in previously published patch-clamp experiments on RBC carrying the V598M PIEZO1 mutant (in whole cell and cell-attached configurations), a constitutive cation leak, increased conductance and increased spontaneous activity were observed (Rapetti-Mauss et al., 2017; Gnanasambandam et al., 2018). To characterize mutant PIEZO1 features, they were expressed in HEK293 cells.

Once expressed in HEK293 cells, peak current and kinetics in response to stretch of PIEZO1 mutants V598M, F681S, and R808Q did not differ significantly from WT. Only the PIEZO1 constructs containing G782S either alone or as double mutation G782S/R808Q showed an increased peak current but no

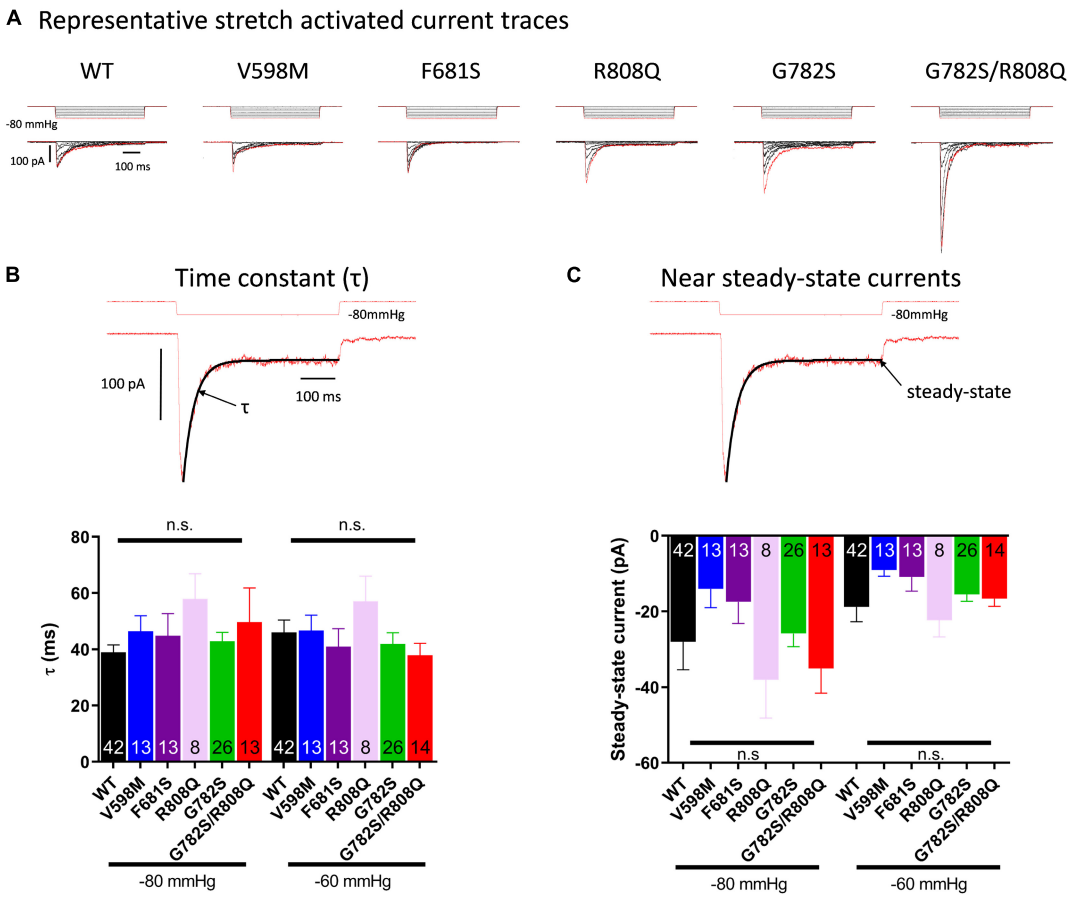

FIGURE 3 | (A) Representative traces of currents induced by stepwise negative pipette pressure (0 to −80 mmHg, Δ10 mmHg) recorded in HEK293T cells expressing WT and mutants. Stretch-activated currents of PIEZO1 WT and mutants-expressing HEK293T cells recorded in cell-attached configuration. **(B)** Inactivation time constant (τ) of currents from PIEZO1 WT and mutants. The top trace shows a representative current fitted by an exponential decay at −60 and −80 mmHg. τ is obtained from the fit. **(C)** Near steady-state currents from PIEZO1 WT and mutants. The steady-state current values were obtained from the fit at the end of the pressure pulse. Currents recorded in cell-attached configuration.

significant change in inactivation kinetics compared to the WT (**Figure 3**). In the presence of the double mutation G782S/R808Q only the G782S mutation changed PIEZO1 response to stretch, suggesting a negligible effect of the R808Q substitution in this response. Translated to RBC, only the G782S mutation showing an increased peak current, would be expected to rise intracellular Ca^{2+} and Na^{2+}, and lose K^{+}, as PIEZO1 is a cation non-selective channel. The increase in Ca^{2+} could induce an additional K^{+} leak through KCNN4 activation and lead to the observed RBC dehydration.

These data show that there are different responses in RBC and expression systems. Such cell type-dependence of the behavior of PIEZO1 mutants may be explained by differences in cell shape, lipid composition, and surface tension of RBC and HEK293 cells, as the position of the mutated amino acids in PIEZO1 suggests a role for these residues in membrane tension sensing, which may be affected by membrane composition and lipid or cytoskeleton interactions. In HEK293 cells, the cytoskeleton is indeed altering PIEZO1 gating (Cox et al., 2016). Lipid bilayer forces drive conformational changes in PIEZO1, and cholesterol-PIEZO1 interactions have been proposed to control the spatiotemporal activity of the ion channel (Cox et al., 2016; Buyan et al., 2020; Ridone et al., 2020). Moreover fatty acid composition of the bilayer also modulates PIEZO1 mechanical response (Romero et al., 2019). The different status of PIEZO1 in HEK293 cells and RBC is confirmed further by the effect of Yoda1, a PIEZO1 activator, which activates the channel in resting RBC and other cell types (Li et al., 2014; Rapetti-Mauss et al., 2017; Blythe et al., 2019; Atcha et al., 2021), whereas in HEK293 cells Yoda1-effects on PIEZO1 activation are observed only in the presence of additional membrane stretch (Syeda et al., 2015; Botello-Smith et al., 2019). Although HEK293 cells constitute a powerful expression system extensively used to study stretch-activated channels (and channels in general), these above considerations together with the results presented here question the relevance of using HEK293 cells to study the gating of mechano-sensitive channel from RBC. Of note, in a previous study, the pressure sensitivity of V598M PIEZO1 mutant expressed in HEK293 cells was shown

to slightly increase compared to WT (Gnanasambandam et al., 2018). This discrepancy with our present results would suggest an even more complex regulation of PIEZO1 activity depending on the different experimental conditions among diverse laboratories, such as (i) different cellular clones, (ii) stages of cellular cycle, (iii) cellular senescence, and (iv) number of replicates.

The mutations are in the more distal part of the arms of the channel where it connects with the membrane curvature. According to the dome mechanism (Lin et al., 2019), changes in this domain might alter tension sensitivity of the channel (Haselwandter and MacKinnon, 2018). The specificity of RBC cytoskeleton (Svetina, 2020) and PIEZO1 interaction with spectrin (Dumitru et al., 2021) are likely responsible for differential sensitivity of the arms of the channel compared to HEK293 cells. The PIEZO1/spectrin relation is emphasized by the recent study showing a coinheritance of PIEZO1 and spectrin mutations in a cohort of 155 patients with clinical suspicion of hereditary anemia (Andolfo et al., 2021).

Although electrophysiological features of PIEZO1 mutants expressed in HEK293 cells may differ from RBC, expression systems remain helpful for studying PIEZO1. Differences in PIEZO1 electrophysiological features between the two cell types might furthermore point out residues involved in channel regulation by its environment.

Our data suggest that a direct analysis of patients' RBC electrophysiological features is required to assess specifically the RBC pathogenicity of PIEZO1 mutations. The use of automated patch-clamp devices to test PIEZO1 in RBC may be a promising strategy to analyze the increasing number of PIEZO1 mutations identified in patients with suspected DHSt (Rotordam et al., 2018).

DATA AVAILABILITY STATEMENT

The original contributions presented in the study are included in the article/**Supplementary Material**, further inquiries can be directed to the corresponding author.

AUTHOR CONTRIBUTIONS

YY and RP performed patch clamp experiments on HEK293T cells. BA, RR-M, OS, and HG performed experiments on red blood cells. VP and LG took care of patients and provided blood samples. VP did the ektacytometry. PK, RP, RR-M, and OS supervised electrophysiology studies. HG supervised the study and wrote the manuscript. All authors analyzed data and improved the manuscript.

FUNDING

YY was supported by Japan Society for the Promotion of Science (JSPS) Overseas Challenge Program for Young Researchers. PK and RP are affiliated with SFB1425, funded by the German Research Foundation (DFG #422681845). HG, BA, RR-M, OS, and LG benefit from an ANR grant ANR-19-CE14-0049-01.

SUPPLEMENTARY MATERIAL

The Supplementary Material for this article can be found online at: https://www.frontiersin.org/articles/10.3389/fphys.2021.736585/full#supplementary-material

REFERENCES

Albuisson, J., Murthy, S. E., Bandell, M., Coste, B., Louis-Dit-Picard, H., Mathur, J., et al. (2013). Dehydrated hereditary stomatocytosis linked to gain-of-function mutations in mechanically activated PIEZO1 ion channels. *Nat. Commun.* 4:1884. doi: 10.1038/ncomms3440

Andolfo, I., Alper, S. L., De Franceschi, L., Auriemma, C., Russo, R., De Falco, L., et al. (2013). Multiple clinical forms of dehydrated hereditary stomatocytosis arise from mutations in PIEZO1. *Blood* 121, 3925–3935, S1-S12. doi: 10.1182/blood-2013-02-482489

Andolfo, I., Martone, S., Rosato, B. E., Marra, R., Gambale, A., Forni, G. L., et al. (2021). Complex modes of inheritance in hereditary red blood cell disorders: a case series study of 155 patients. *Genes (Basel)* 12:958. doi: 10.3390/genes12070958

Atcha, H., Jairaman, A., Holt, J. R., Meli, V. S., Nagalla, R. R., Veerasubramanian, P. K., et al. (2021). Mechanically activated ion channel Piezo1 modulates macrophage polarization and stiffness sensing. *Nat. Commun.* 12:3256. doi: 10.1038/s41467-021-23482-5

Blythe, N. M., Muraki, K., Ludlow, M. J., Stylianidis, V., Gilbert, H. T. J., Evans, E. L., et al. (2019). Mechanically activated Piezo1 channels of cardiac fibroblasts stimulate p38 mitogen-activated protein kinase activity and interleukin-6 secretion. *J. Biol. Chem.* 294, 17395–17408. doi: 10.1074/jbc.ra119.009167

Botello-Smith, W. M., Jiang, W., Zhang, H., Ozkan, A. D., Lin, Y. C., Pham, C. N., et al. (2019). A mechanism for the activation of the mechanosensitive Piezo1 channel by the small molecule Yoda1. *Nat. Commun.* 10:4503.

Buyan, A., Cox, C. D., Barnoud, J., Li, J., Chan, H. S. M., Martinac, B., et al. (2020). Piezo1 forms specific, functionally important interactions with phosphoinositides and cholesterol. *Biophys. J.* 119, 1683–1697. doi: 10.1016/j.bpj.2020.07.043

Cahalan, S. M., Lukacs, V., Ranade, S. S., Chien, S., Bandell, M., and Patapoutian, A. (2015). Piezo1 links mechanical forces to red blood cell volume. *Elife* 4:e07370.

Coste, B., Xiao, B., Santos, J. S., Syeda, R., Grandl, J., Spencer, K. S., et al. (2012). Piezo proteins are pore-forming subunits of mechanically activated channels. *Nature* 483, 176–181. doi: 10.1038/nature10812

Cox, C. D., Bae, C., Ziegler, L., Hartley, S., Nikolova-Krstevski, V., Rohde, P. R., et al. (2016). Removal of the mechanoprotective influence of the cytoskeleton reveals PIEZO1 is gated by bilayer tension. *Nat. Commun.* 7:10366. doi: 10.1038/ncomms10366

Cynober, T., Mohandas, N., and Tchernia, G. (1996). Red cell abnormalities in hereditary spherocytosis: relevance to diagnosis and understanding of the variable expression of clinical severity. *J. Lab. Clin. Med.* 128, 259–269. doi: 10.1016/s0022-2143(96)90027-x

Dumitru, A. C., Stommen, A., Koehler, M., Cloos, A. S., Yang, J., Leclercqz, A., et al. (2021). Probing PIEZO1 localization upon activation using high-resolution atomic force and confocal microscopy. *Nano Lett.* 21, 4950–4958. doi: 10.1021/acs.nanolett.1c00599

Gnanasambandam, R., Rivera, A., Vandorpe, D. H., Shmukler, B. E., Brugnara, C., Snyder, L. M., et al. (2018). Increased red cell KCNN4 activity in sporadic hereditary xerocytosis associated with enhanced single channel pressure sensitivity of PIEZO1 mutant V598M. *Hemasphere* 2:e55. doi: 10.1097/hs9.0000000000000055

Guo, Y. R., and MacKinnon, R. (2017). Structure-based membrane dome mechanism for Piezo mechanosensitivity. *Elife* 6:e33660. doi: 10.7554/eLife.33660.028

Haselwandter, C. A., and MacKinnon, R. (2018). Piezo's membrane footprint and its contribution to mechanosensitivity. *Elife* 7:e41968. doi: 10.7554/eLife.41968.019

Li, J., Hou, B., Tumova, S., Muraki, K., Bruns, A., Ludlow, M. J., et al. (2014). Piezo1 integration of vascular architecture with physiological force. *Nature.* 515, 279–282. doi: 10.1038/nature13701

Lin, Y. C., Guo, Y. R., Miyagi, A., Levring, J., MacKinnon, R., and Scheuring, S. (2019). Force-induced conformational changes in PIEZO1. *Nature* 573, 230–234. doi: 10.1038/s41586-019-1499-2

Pérès, L., Monedero Alonso, D., Nudel, M., Figeac, M., Bruge, J., Sebda, S., et al. (2021). Characterisation of Asp669Tyr Piezo1 cation channel activity in red blood cells: an unexpected phenotype. *Br. J. Haematol.* 194, e51–e55. doi: 10.1111/bjh.17467

Peyronnet, R., Martins, J. R., Duprat, F., Demolombe, S., Arhatte, M., Jodar, M., et al. (2013). Piezo1-dependent stretch-activated channels are inhibited by Polycystin-2 in renal tubular epithelial cells. *EMBO Rep.* 14, 1143–1148. doi: 10.1038/embor.2013.170

Picard, V., Guitton, C., Thuret, I., Rose, C., Bendelac, L., Ghazal, K., et al. (2019). Clinical and biological features in PIEZO1-hereditary xerocytosis and gardos-channelopathy: a retrospective series of 126 patients. *Haematologica* 104, 1554–1564. doi: 10.3324/haematol.2018.205328

Rapetti-Mauss, R., Lacoste, C., Picard, V., Guitton, C., Lombard, E., Loosveld, M., et al. (2015). A mutation in the gardos channel is associated with hereditary xerocytosis. *Blood* 126, 1273–1280. doi: 10.1182/blood-2015-04-642496

Rapetti-Mauss, R., Picard, V., Guitton, C., Ghazal, K., Proulle, V., Badens, C., et al. (2017). Red blood cell Gardos channel (KCNN4): the essential determinant of erythrocyte dehydration in hereditary xerocytosis. *Haematologica* 102, e415–e418. doi: 10.3324/haematol.2017.171389

Ridone, P., Pandzic, E., Vassalli, M., Cox, C. D., Macmillan, A., Gottlieb, P. A., et al. (2020). Disruption of membrane cholesterol organization impairs the activity of PIEZO1 channel clusters. *J. Gen. Physiol.* 152:e201912515. doi: 10.1085/jgp.201912515

Romero, L. O., Massey, A. E., Mata-Daboin, A. D., Sierra-Valdez, F. J., Chauhan, S. C., Cordero-Morales, J. F., et al. (2019). Dietary fatty acids fine-tune Piezo1 mechanical response. *Nat. Commun.* 10:1200. doi: 10.1038/s41467-019-09055-7

Rotordam, G. M., Fermo, E., Becker, N., Barcellini, W., Brüggemann, A., Fertig, N., et al. (2018). A novel gain-of-function mutation of Piezo1 is functionally affirmed in red blood cells by high-throughput patch clamp. *Haematologica* 104, e179–e183. doi: 10.3324/haematol.2018.201160

Schindelin, J., Arganda-Carreras, I., Frise, E., Kaynig, V., Longair, M., Pietzsch, T., et al. (2012). Fiji: an open-source platform for biological-image analysis. *Nat. Methods* 9, 676–682. doi: 10.1038/nmeth.2019

Svetina, S. (2020). Theoretical bases for the role of red blood cell shape in the regulation of its volume. *Front. Physiol.* 11:544. doi: 10.3389/fphys.2020.00544

Syeda, R., Xu, J., Dubin, A. E., Coste, B., Mathur, J., Huynh, T., et al. (2015). Chemical activation of the mechanotransduction channel Piezo1. *Elife* 4:e07369. doi: 10.7554/eLife.07369.008

Zarychanski, R., Schulz, V. P., Houston, B. L., Maksimova, Y., Houston, D. S., Smith, B., et al. (2012). Mutations in the mechanotransduction protein PIEZO1 are associated with hereditary xerocytosis. *Blood* 120, 1908–1915. doi: 10.1182/blood-2012-04-422253

Zhao, Q., Zhou, H., Chi, S., Wang, Y., Wang, J., Geng, J., et al. (2018). Structure and mechanogating mechanism of the Piezo1 channel. *Nature* 554, 487–492. doi: 10.1038/nature25743

Conflict of Interest: The authors declare that the research was conducted in the absence of any commercial or financial relationships that could be construed as a potential conflict of interest.

Publisher's Note: All claims expressed in this article are solely those of the authors and do not necessarily represent those of their affiliated organizations, or those of the publisher, the editors and the reviewers. Any product that may be evaluated in this article, or claim that may be made by its manufacturer, is not guaranteed or endorsed by the publisher.

Intérêt du séquençage de nouvelle génération (NGS) pour décrypter l'association des défauts moléculaires érythrocytaires dans les troubles du globule rouge : phénotypes cliniques et érythrocytaires des patients présentant des mutations héréditaires de *PIEZO1, Spectrin ß1, RhAG et SLC4A1*.

Contexte

Dans cet article nous avons étudié les GR d'un enfant diagnostiqué avec une anémie régénérative dont la cytologie et l'Ektacytométrie suggéraient l'association de différentes pathologies de la membrane du globule rouge. Un recours au séquençage nouvelle génération (NGS) réalisé sur 93 gènes cibles, impliqués dans des défauts érythrocytaires, a permis de mettre en évidence des mutations faux sens sur 4 gènes : *PIEZO1, SLC4A1, RhAG et Spectrine β1*. Les mutations sur *PIEZO1* et *SPTB1* ont été transmises par la mère et les mutations sur SLC4A1 et RhAG ont été transmises par le père. Chaque mutation était classée non significative (VUS : « variant of unknown significance »). Afin de comprendre l'effet de ces mutations nous avons caractérisé la perméabilité des GR du patient et de ses parents. Nous avons constaté que l'enfant et le père avaient des GR hyperhydratés avec une inversion des contenus Na^+ et K^+ alors que les GR de la mère étaient normaux. Nos résultats n'ont pas permis de mettre en évidence de défauts apparents de la mutations PIEZO1. En revanche, ils confirment que la mutation de SLC4A1, déjà décrite par le passé, est responsable d'une fuite cationique de ces GR qui se manifeste lorsque les GR sont stockés au froid (Cryohydrocytose).

Blood Cells, Molecules and Diseases 103 (2023) 102780

Contents lists available at ScienceDirect

Blood Cells, Molecules and Diseases

journal homepage: www.elsevier.com/locate/bcmd

Next generation sequencing (NGS) interest in deciphering erythrocyte molecular defects' association in red cell disorders: Clinical and erythrocyte phenotypes of patients with mutations inheritance in *PIEZO1*, *Spectrin ß1*, *RhAG* and *SLC4A1*

Benoit Allegrini [a], Ludivine David NGuyen [b], Morgane Mignotet [a], Catherine Etchebest [e,f], Odile Fenneteau [b], Jessica Platon [c], Anne Lambilliotte [g,1], Hélène Guizouarn [a,f,*,1], Lydie Da Costa [b,c,d,e,**,1]

[a] *Université Côte d'Azur, CNRS, Inserm, Institut Biologie Valrose, Nice, France*
[b] *AP-HP, Service Hématologie Biologique, Hôpital R. Debré, Paris, France*
[c] *HEMATIM EA4666, Université Picardie Jules Vernes, Amiens, France*
[d] *Université Paris, Paris, France*
[e] *Inserm U1134, France*
[f] *Laboratory of Excellence for RBCs, LABEX GR-Ex, 75015 Paris, France*
[g] *CHU Lille, Service Hématologie Pédiatrique, Lille, France*

ARTICLE INFO

Editor: Lionel Blanc

Keywords:
Red blood cell membrane
Cryohydrocytosis
PIEZO1
RHAG
SPTB
SLC4A1

ABSTRACT

We report here an instructive case referred at 16 months-old for exploration of hemolysis without anemia (compensated anemia with reticulocytosis). The biology tests confirmed the hemolysis with increased total and indirect bilirubin. The usual hemolysis diagnosis tests were normal (DAT, G6PD, PK, Hb electrophoresis) except cytology and ektacytometry suggesting an association of multiple red blood cell (RBC) membrane disorders. This led us to propose a molecular screening analysis using targeted-Next Generation Sequencing (t-NGS) with a capture technique on 93 genes involved in RBC and erythropoiesis defects. We identified 4 missense heterozygous allelic variations, all of them were described without any significance (VUS) in the *SLC4A1*, *RhAG*, *PIEZO1* and *SPTB* genes. The study of the familial cosegregation and research functional tests allowed to decipher the role of at least two by two genes in the phenotype and the hemolytic disease of this young patient. Specialized t-NGS panel (or virtual exome/genome sequencing) in a disease-referent laboratory and the motivated collaboration of clinicians, biologists and scientists should be the gold standard for improving the diagnosis of the patients affected with RBC diseases or rare inherited anemias.

1. Introduction

Hereditary hemolytic anemias are rare human disorders characterized by highly variable symptoms, from severe to well compensated anemia with iron overload as a major drawback. Alterations of red blood cell (RBC) membrane proteins are one of the main causes of this condition [1]. These alterations either affect structural interactions between membrane proteins and cytoskeleton or affect RBC permeability. Mutations in SPTA1 (α-spectrin), SPTB (β-spectrin), SLC4A1 (band 3), ANK1 (ankyrin) or EPB42 (protein 4.2) are the most frequent and are associated with impaired RBC membrane scaffolding. Less frequently, the mutations impair membrane transport function, which is the hallmark of hereditary stomatocytosis (HSt). RBC have an increased Na^+ and K^+ permeability that is either associated to overhydration (OHSt) or dehydration (DHSt) depending on the nature of transporters whose activity is impaired [2,3]. Up to now, 6 different membrane transporters have been involved in HSt when they are mutated: SLC4A1, RhAG, SLC2A1, ABCB6, PIEZO1 and KCNN4 [2–5]. Mutations in *SLC4A1*,

* Correspondence to: H. Guizouarn, Université Côte d'Azur, CNRS, Inserm, Institut Biologie Valrose, Nice, France.
** Correspondence to: L. Da Costa, AP-HP, Service Hématologie Biologique, Hôpital R. Debré, Paris, France.
E-mail address: helene.guizouarn@univ-cotedazur.fr (H. Guizouarn).
[1] Same participation.

https://doi.org/10.1016/j.bcmd.2023.102780
Received 24 April 2023; Received in revised form 6 July 2023; Accepted 13 July 2023
Available online 20 July 2023

Table 1
Hematological data for the proband and his parents compared to published data describing patient with SLC4A1 p.(Ser762Arg) [6].

	Normal range (adult)	Normal range (child)	Mother		Father		Proband			SLC4A1-Ser762Arg [6]	
Age (year)			37		38		1	5		Adult	
Time after blood withdraw			0	24 h	0	24 h	0	0	24 h	0	2 h
RBC* 10^6/µl	4.5–6.2 (male) 4–5.4 (female)	4.36–4.96 (6 month – 2 years-old) 4.37–4.97 (2–6 years-old)	4.7	4.87	4.07	4.05	3.39	3.45			
Hemoglobin g/dl	13–18 (male) 12–16 (female)	11.1–12.9 (6 month – 2 years-old) 11.5–12.9 (2–6 years-old)	16.4	16.6	13.4	14.6	10.5	10.3	11.2	15.4	15.3
Ht %	40–54 (male) 35–47 (female)	33–37.8 (6 month – 2 years-old) 34–38.8 (2–6 years-old)	46.6	48.7	36.8	42.4	27.2	27.8	38.3	39.3	44.1
MCH pg/cell	23–33		34.9	34.1	32.9	36.0	31.0	29.9			
MCV fl	80–100	72.9–79.3 (6 month–2 years-old) 74.3–80.9 (2–6 years-old)	99	100	90	104.7	80	81	106.4	95.1	105.5
MCHC g/dl	32–36	32.8–35 (6 month–6 years-old)	35.2	34.1	36.4	34.4	38.6	37.1	29.2	39.2	34.7
Morphology				Rare Stom Howel Jolly	Stom Howel Jolly	Stom++, Ovalo, Ovalo-Stom Howel Jolly Target RBC	Stom, Ellipto, Ovalo	Stom		Stom, Sphero	
Reticulocyte 10^6/ml (0.6–1.7 %)	20–120	20–120	127	132.5	95	176	171	194	189	5.2 %	
Bilirubin (direct) mg/l	1–12 (0–3)				25		15 (4)	44			
Haptoglobin	0.3–2						<0.08				
LDH U/l	225–600				255		327	268			
Ferritin ng/ml	30–400		170		446		83	89	325	1877	
EMA# %	<16 %			−5.6		39.8			32.5		
Ektacytometry Omin (mOsml/kg)	Day 0: 130–167 Day +1: 131–167			148		156			171		
DImax	Day 0: 0.53–0.581 Day +1: 0.524–0.58			0.56		0.439			0.431		
Hyper (mOsml/kg)	Day 0: 388–449 Day +1: 386–439			403		372			468		

Hematocrit (Ht), mean cell volume (MCV), mean corpuscular hemoglobin concentration (MCHC). Stomatocytes (Stom), Elliptocytes (Ellipto), Spherocytes (Sphero), Ovalocytes (Ovalo). *Complete blood count for proband was: White Blood Cells 15.35 × 10^9/L (normal value for 6 months of age: 6.4–16.4 × 10^9/L) and platelets 372 × 10^9/L (normal value for 6 months of age:150–450 × 10^9/L). #MIF of the patient: 7612; MIF of the 3 age-matched controls: 11278. Normal hemoglobin electrophoresis: 93,6 % Hb A, 2,7 % Hb A2, 3,7 % Hb F.
Normal values in infants from Lainey, E et al., Revue francophone des laboratoires, 2009(416), 49–59.

SLC2A1 and *RhAG* have been associated mostly to OHSt [6–9] whereas mutations in *PIEZO1* and *KCNN4* are linked to DHSt [10–14]. *ABCB6* mutations induce pseudo-hyperkalemia [15].

With the development of sequencing technologies, we have access to more and more genetic data related to RBC disorders and a recent genetic study of 155 patients with this condition showed multi locus inheritance in 15 % of the cases [16]. However, the impact of combined mutations on the RBC phenotype is largely unpredictable. Although very useful, the algorithms cannot predict the effects of combined mutations in genes that are independently associated with RBC pathologies. Correlating mutations and phenotypes remains highly challenging and clinicians with geneticists are often facing undecidable situations. To ensure the link between protein alteration and RBC disorders, the analysis of RBC functional properties together with the functional study of the altered protein are essential to complete the clinic and the genetic.

Here we present a case study with missense mutations in 4 different genes, all involved in RBC membrane disorders: *RhAG*, *SLC4A1*, *PIEZO1* and *SPTB*. The genetic study of the family showed that both parents transmitted two mutations (*RhAG* and *SLC4A1* from the father and *SPTB* and *PIEZO1* from the mother). RBC membrane permeability, clinical and hematological parameters indicated that *SLC4A1* missense mutation was largely responsible for the observed phenotype.

2. Methods

2.1. Patient and hematology

Patient was followed-up in Jeanne de Flandres hospital (Lille, France) for RBC membrane disorder and was referred to Hematology Diagnostic laboratory (AP-HP) for phenotypic and genotypic explorations.

Blood smears were examined and blind diagnostics were validated independently by two cytologists. The EMA-test was performed according to the recommendation [17] [18]. Blood samples were analyzed by ektacytometry within 24 h after blood sample collection on LoRRca MaxSis (Mechatronics instruments BV®, Netherland) as previously described [18–21].

2.2. Genotype

Genomic DNA was extracted from lymphocytes. Written informed consent was obtained in accordance with the ethical standards of the

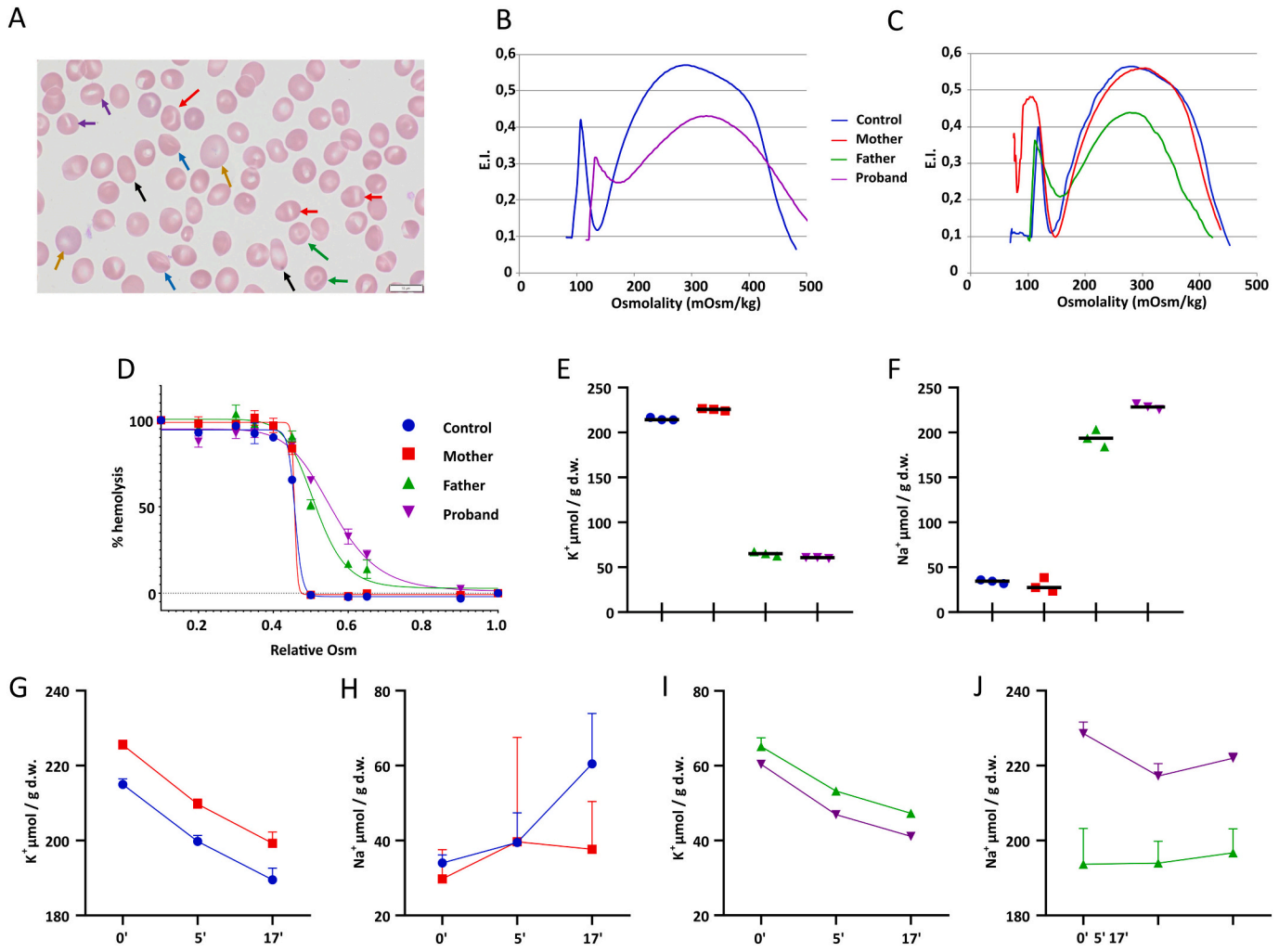

Fig. 1. A - Blood smear after May-Grunwald-Giemsa coloration at ×50 magnificence from the proband: Anisocytosis and poikilocytosis with macrocytosis due in part to the high reticulocyte count (polychromatophilia) (yellow arrows). Important poikilocytosis due to RBC morphology anomalies: elliptocytes (black arrows), ovalocytes and ovalostomatocytes (red arrows), stomatocytes (purple arrows), target RBCs (green arrows), codocytes (blue arrows).
B. Ektacytometry curve from the patient compared to an age-matched control: Decreased RBC deformability with decreased DImax, right shift of both the Omin and hyper points in the proband's RBC (purple curve) compared to the normal ektacytometry curve of the age-matched control (blue curve).
C. Ektacytometry curve from the mother's RBC, the father's RBC compared to a control
Green curve: father's RBC, red curve: mother's RBC, blue curve: control RBC.
D. Osmotic resistance curves from control, patient, proband's mother and proband's father blood.
Upon reception of blood samples in EDTA collecting tubes, 24 h after withdrawal, RBC osmotic resistance determination was done. Blue curve: control, red curve: mother (PIEZO1 + SPTB1 mutations), green curve: father (SLC4A1 + RhAG mutations), purple curve: proband (PIEZO1 + SPTB1 + SLC4A1 + RhAG mutations).
E–F: respectively K^+ and Na^+ contents (µmol/g dry weight) of control, proband's mother, proband's father and proband RBC.
Blood withdrawn into EDTA collecting tubes was used in research laboratory within 24 h. The Na^+ and K^+ contents of RBC were measured after blood washing in saline buffer just after reception. Control RBC in blue, mother's RBC in red, father's RBC in green and proband's RBC in purple. Data are triplicates done on a single shipment.
G–H: respectively K^+ and Na^+ contents (µmol/g dry weight) of control and proband's mother following RBC stimulation by 2 µM Yoda1; I-J K^+ and Na^+ contents of proband and proband's father following RBC stimulation by 2 µM Yoda1.
The Na^+ and K^+ contents of RBC were measured after blood washing in saline buffer, as a function of time following 2 µM Yoda1 addition. Activation of PIEZO1, the stress-activated, non-selective cation conductance, induces a Na^+ uptake and a K^+ loss in RBC [33]. RBC suspension 25 % hematocrit, 0.5 mM ouabain and 2 µM Yoda1 (Sigma-Aldrich, stock solutions in DMSO, 100 mM for Ouabain and 0.5 mM for Yoda1). Data are means±sem of 3 measurements done on a single RBC shipment. Control RBC in blue, mother's RBC in red, father's RBC in green and proband's RBC in purple.

Declaration of Helsinki. We used a Roche "NimbleGen SeqCap EZ" library and an illumina flowcell (Flowcell standard 2*150) with a library of 144 genes including 93 genes for RBC disorders. The sequences were run on a Miseq or a Nextseq in the genetic platform R. Debré hospital, Paris. Sequences were analyzed on CLC Biomedical Work Bench (Qiagen) and allelic variations were read with Qiagen Clinical Insight (QCI) [22,23]. Each allelic variation was verified by Sanger technique.

2.3. Ion and water content measurements

Blood withdrawn into EDTA collecting tubes was used in research laboratory 24 h after collection. Upon reception, osmotic resistance determination was done. For ion and water content determination, blood was washed 3 times in saline solution containing (in mM): NaCl (145), KCl (5), MgSO4 (2), CaCl2 (1), Hepes (10) pH 7.4 (buffered with NaOH 1 N) and any buffy coat was removed by aspiration. RBC Na^+ and K^+ contents were measured as previously described [11]. Yoda1,

ouabain (Sigma-Aldrich) and Senicapoc (MedChemExpress) stock solutions in DMSO were added at desired concentrations to RBC suspension 25 % hematocrit.

2.4. Bioinformatic analysis

Molecular graphics and analyses performed with UCSF Chimera, developed by the Resource for Biocomputing, Visualization, and Informatics at the University of California, San Francisco, with support from NIH P41-GM103311. Contacts were calculated with the Structure Analysis/Find Clash/Contact Chimera Tool.

3. Results and discussion

The proband was admitted to emergency unit for fever at 16-month-old with history of neonatal jaundice. Pyelonephritis was diagnosed but the blood count was remarkable with compensated anemia and RBC morphologic abnormalities without jaundice nor splenomegaly. The father was a 38 years-old man with history of jaundice and anemia at 12 years-old. He underwent cholecystectomy and splenectomy at 17 years-old. He carried an unusual RBC membrane pathology with Gilbert syndrome. The mother was a 37 years-old woman with no history of anemia or jaundice. Table 1 summarized hematological data. Hemolysis has been diagnosed and the usual etiology was ruled out (erythrocyte enzyme deficiency, immune anemia, hemoglobinopathies). 24 h after blood withdraw, proband RBC were macrocytic, hypochromic, showing increased RDW at 25 % (normal value <15 %). The hemolysis was a so-called compensated hemolysis with no anemia but a bone marrow regeneration as shown on the increased reticulocyte count to compensate the peripheral RBC destruction. It was the same significance as a hemolytic anemia and the etiology should be investigated. The RBC morphology (Fig. 1A) with anisocytosis, hypochromia, polychromatophilia and an important poikilocytosis reflecting the large panel of morphological anomalies, suggested an association of different RBC membrane disorders: elliptocytic RBC, evoking hereditary elliptocytosis, macrocytic and ovalocytic RBC, evoking South-east Asian Ovalocytosis (SAO), stomatocytes, evoking HSt, codocytes and anomaly of the hemoglobin repartition, evoking hemoglobinopathy (which was lately eliminated), and Howell Jolly bodies, which may result from a defect in splenic function or maturation in a non-splenectomized infant. We had no arguments for a hereditary spherocytosis (HS), meanwhile the EMA-test was positive. The ektacytometry was abnormal with a dramatic decrease in the RBC deformability compared to an age-matched normal control (Fig. 1B, Table 1). Proband's mother exhibited rare stomatocytes, Howell Jolly bodies, in association with a normal ektacytometry curve and EMA test not in favor of a HS (Fig. 1C, Table 1). The complete erythrocyte record did not suggest any RBC membrane pathology. The father's blood count exhibited a compensated anemia with a normal Hb level but reticulocytosis. RBC morphology showed stomatocytes with ovalocytes-SAO like and Howell Jolly bodies because of splenectomy. Osmotic gradient ektacytometry showed an important reduction of RBC deformability and a left shift to lower osmolarities of the deformability profile. The EMA test was positive.

We hypothesized a composite RBC membrane pathology and molecular screening analysis was done (gene list in Supplemental Table 1). Four heterozygous allelic variations in four different genes were identified: *SLC4A1* p.(Ser762Arg), *RHAG* p.(Ala248Thr), *PIEZO1* p.(Thr1201Met) and *SPTB* p.(Ala1884Val) (Supplemental Table 2-Fig. 1). All of them were classified of unknown significance according to the ACMG-AMP recommendations [24,25]. Familial molecular screening was performed. The father had transmitted the *SLC4A1* and *RHAG* allelic variations, while the mother had transmitted the *PIEZO1* and the *SPTB* ones.

Each of these four proteins can be responsible for RBC disorder when individually mutated: PIEZO1, RhAG and SLC4A1 could alter cation permeability [8–10,13,26,27]; SPTB and SLC4A1 could alter membrane cytoskeleton interaction [28,29].

In order to decipher the impact of the different mutations on RBC permeability, experiments were carried on to measure, water, Na^+ and K^+ contents. Proband's and father's RBC osmotic resistance were shifted to the right compared to control or mother's RBC suggesting RBC hyperhydration induced by RhAG+SLC4A1 mutations and/or structure defects [30] (Fig. 1D). The Na^+ and K^+ contents were dramatically altered for RBC with either RhAG+SLC4A1 (father) or RhAG+SLC4A1 + SPTB+PIEZO1 (proband) mutations (Fig. 1E-F). There was an inversion of the Na^+/K^+ gradient with intracellular Na^+ raising up to 194 μmol/g d.w for the RhAG+SLC4A1 mutations and 229 μmol/g d.w for RBC with the 4 mutations RhAG+SLC4A1 + SPTB1 + PIEZO1 and K^+ content decreasing to 65 μmol/g d.w for the double mutant and to 60 μmol/g d.w. for the quadruple mutant. In contrast, the Na^+ and K^+ contents of RBC with SPTB+PIEZO1 mutations (mother) were similar to control RBC. The addition of SPTB+PIEZO1 to RhAG+SLC4A1 mutations did not prevent the cation gradient alteration induced by RhAG+SLC4A1 mutations.

To assess the effect of PIEZO1 mutation on RBC permeability, RBC were stimulated by Yoda1, the chemical activator of PIEZO1 [31]. Yoda1 induced a similar K^+ loss in WT or SPTB+PIEZO1 mutated RBC (Fig. 1G–H) as in RhAG+SLC4A1 or RhAG+SLC4A1 + SPTB+PIEZO1 mutated RBC (Fig. 1I–J), suggesting no functional effect of PIEZO1 p.(Thr1201Met) mutation on RBC Na^+ and K^+ permeability. Moreover, mother's RBC morphology and deformability were not altered suggesting the SPTB Ala1884Val and PIEZO1 Thr1201Met mutations were silent on RBC physical features as well as permeability.

The SLC4A1 mutation p.(Ser762Arg) has been previously shown to induce a Na^+ and K^+ leak in RBC and it was associated with cryohydrocytosis, a form of OHSt [6]. This cation leak is temperature dependent with a maximum at temperatures below 20 °C. Ser762Arg substitution converts SLC4A1 into a non-selective cation conductance dissipating Na^+ and K^+ electrochemical gradients. This leads to increased Na^+ and decreased K^+ contents that is observed when blood is at room temperature. This cation leak can be compensated in vivo by hyperactivity of the pump Na^+/K^+ ATPase. For comparison the hematological data from the first identified patient carrying SLC4A1-p.(Ser762Arg) mutation were shown in Table 1 [6]. For this patient as for the proband and proband's father, MCV which is in the normal range or slightly above just after blood withdraw, increased with the delay of the analysis, unmasking the Na^+ and K^+ leak where it is hardly compensated by pump activity. Hence, the *SLC4A1* mutation present in proband and proband's father can explain the non-selective Na^+ K^+ leak leading to net Na^+ uptake and RBC swelling at room temperature. The positive EMA test for proband's and father's RBC suggested a reduced expression of SLC4A1 in plasma membrane or a reduced access of the mutated protein to the dye. The SLC4A1 mutation by inducing a cation leak through the transport site of the protein that abolished its anion exchange activity might produce conformational changes able to alter eosin-maleimide binding. Moreover, it was observed that other single point mutations in SLC4A1 converting the protein into a cation conductance [32], had a decreased expression level in RBC membrane [9]. In accordance with the positive EMA test, ektacytometry on proband's and father's RBC indicated a reduced deformability. In addition to the change in SLC4A1 transport features, this suggested an alteration of membrane scaffolding induced by Ser762Arg mutation. Hence, SLC4A1 Ser762Arg mutation can lead to complex RBC alterations evoking spherocytosis as well as OHSt that might depend on the energy status of RBC allowing to compensate more or less efficiently the cold induced cation leak. It is noteworthy that stomatocytes as well as spherocytes were observed on blood smear from the first patient and he was treated by splenectomy for spherocytosis. In the present case, the differences in ektacytometry curves between proband's and father's RBC emphasized the duality of SLC4A1 Ser762Arg mutation modifying both, permeability and structural features of RBC membrane with varying efficiency.

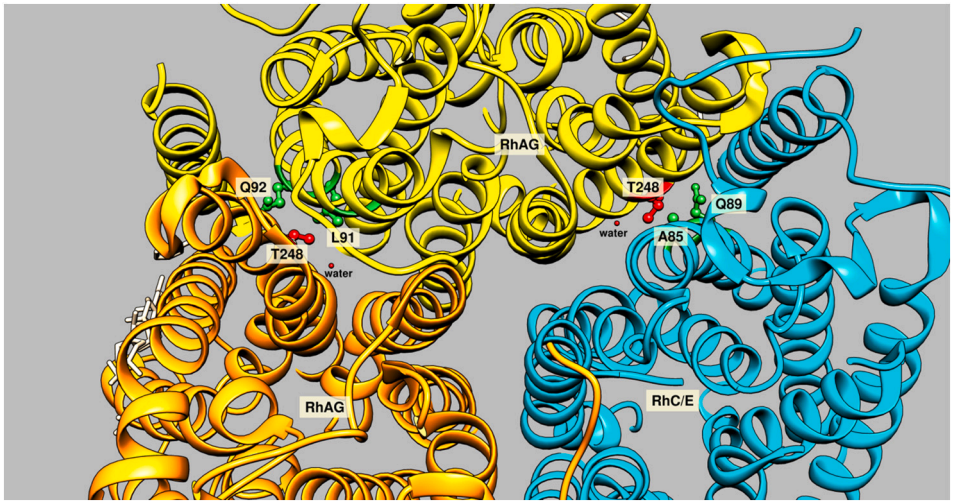

Fig. 2. Model of RhAG/CE with Ala248Thr substitution based on the RhAG/CE wild-type X-ray structure (pdb:8CSX).
The two RhAG monomers are coloured in yellow and orange respectively, RhCE is in cyan. The backbone is represented in cartoon. Residue 248 has been substituted for Thr using Chimera mutate tool (Pettersen EF, et al. J Comput Chem. 2004 Oct;25(13):1605–12).
The conformation of the Thr mutant side chain represented here in ball-and-stick, corresponds to the rotamer having no unfavourable overlap with the rest of the complex. The 3D model indicates that residue 248 is in contact with highly conserved Leu91-Gln92 residues in adjacent monomer.

Different mutations in RhAG have also been linked to increased cation conductance in RBC, dissipating the Na^+ and K^+ gradients [8]. These previously described RhAG mutations (Ile61Arg and Phe65Ser) associated with OHSt led to structural changes of the protein increasing the size of the pore which could explain the change in permeability, the mutated protein dissipating Na^+ and K^+ gradient across plasma membrane. The present mutation RhAG p.(Ala248Thr) would unlikely influence directly the transport activity of the protein since Ala248, located in transmembrane helix 8, is not facing towards the pore of the protein. However, it might alter the trimer formation and per se the function because it is involved in inter-monomer contacts with highly conserved Glutamine residues (Fig. 2). RBC WT or carrying the different mutations were labeled with specific antibodies against RhAG (Supplemental Fig. 2). The staining index was similar between father's, mother's and proband's RBC, indicating a similar immunodetection of RhAG WT or mutated in RBC membrane between family members. This staining index was lower in control RBC suggesting differences in RhAG immunoreactivity between individuals that was not related to the mutation Ala248Thr. Thus, this mutation did not reduce the expression of the RhAG protein. If we cannot conclude about the correct interactions between RhAG monomers nor with other membrane or cytoskeletal proteins, it appears unlikely the present RhAG mutation altered RBC cation permeability or mechanical properties. Strikingly, the SLC4A1 p.(Ser762Arg) mutation alone per se can lead to the observed phenotype: the addition of RhAG or RhAG+PIEZO1 + SPTB mutation(s) did not potentiate nor prevent the reversion of Na^+ and K^+ gradient that can be observed in RBC carrying only SLC4A1 p.(Ser762Arg) mutation as in the patient described previously [6].

4. Conclusion

This study of the familial co-segregation and research functional tests allowed to decipher the role of at least two by two genes in the phenotype and the hemolytic disease of the patient. After a long investigation, only the SLC4A1 allelic variation was responsible for the phenotype of cold induced cation leaky RBC associated with fragility and compensated hemolytic anemia. To our knowledge, this is the second case of SLC4A1 p.(Ser762Arg) mutation described so far and this gene allelic variation should now with our study be classified as pathogenic (class 5) since we confirmed with fundamental research and functional tests its pathogenic effect on RBC. The consequences of this mutation on RBC fragility might be misdiagnosed as a hereditary spherocytosis, likely due to altered SLC4A1 structure, masking a real OHSt induced by the cation leaky mutated SLC4A1 that is noticeable few hours after blood withdraw. The new described RhAG, SPTB1 and PIEZO1 mutations do not further impair the phenotype. SPTB1 p.(Ala1884Val) combined with PIEZO1 p.(Thr1201Met) do not induce significant RBC disorder.

This case study emphasized the need for specialized t-NGS panel (or whole exome/genome sequencing) in a disease-referent laboratory and the motivated collaboration of clinicians, biologists and scientists that should be the gold standard for improving the diagnosis of the patients affected with RBC condition or rare inherited anemias.

Author statements

No data set were generated by this study. Raw data should be available on request to the corresponding authors.

CRediT authorship contribution statement

LDC and HG design the study. LDNG performed and analyzed the ektacytometry and LDNG and JP performed the molecular characterization of the samples. OF and LDC analyzed blood smear. LDC analyzed and validated the ektacytometry and gene mutations screening analysis. AL diagnosed the case, supervised hematological analysis and took care of patients. BA, HG and MM performed osmotic resistance test, Na^+ and K^+ content measurements. CE modelized RhAG mutations. BA, AL, HG, CE and LDC analyzed and collected all the data. AL, HG and LDC wrote the article.

Funding

This research was funded by Agence Nationale de la Recherche ANR 19-CE14 0049.

Declaration of competing interest

The authors declare no conflict of interest.

Acknowledgement

We are grateful to the patient and his family and to the medical staff around this patient. We acknowledge the flow cytometry area (Dr E. Lainey, A. Bonnel, J-M Renard) for the EMA test performed and all the technicians from the cytology area (R. Rooben Balasoupramanien, M. Boirie, M. Cand, I. Contassot, J-L. Delecourt, C. Dieuxyssies, A. Galimard, G. Jalladaud, M. Pellois, A. Rose) into the Hematology diagnostic lab in 2016.

Appendix A. Supplementary data

Supplementary data to this article can be found online at https://doi.org/10.1016/j.bcmd.2023.102780.

References

[1] J. Narla, N. Mohandas, Red cell membrane disorders, Int. J. Lab. Hematol. 39 (Suppl. 1) (2017) 47–52.
[2] C. Badens, H. Guizouarn, Advances in understanding the pathogenesis of the red cell volume disorders, Br. J. Haematol. 174 (2016) 674–685.
[3] J.F. Flatt, L.J. Bruce, The molecular basis for altered cation permeability in hereditary stomatocytic human red blood cells, Front. Physiol. 9 (2018) 367.
[4] I. Andolfo, R. Russo, A. Gambale, A. Iolascon, New insights on hereditary erythrocyte membrane defects, Haematologica 101 (2016) 1284–1294.
[5] P.G. Gallagher, Disorders of erythrocyte hydration, Blood 130 (2017) 2699–2708.
[6] H. Guizouarn, F. Borgese, N. Gabillat, P. Harrison, J.S. Goede, C. McMahon, G. W. Stewart, L.J. Bruce, South-east Asian ovalocytosis and the cryohydrocytosis form of hereditary stomatocytosis show virtually indistinguishable cation permeability defects, Br. J. Haematol. 152 (2011) 655–664.
[7] J.F. Flatt, H. Guizouarn, N.M. Burton, F. Borgese, R.J. Tomlinson, R.J. Forsyth, S. A. Baldwin, B.E. Levinson, P. Quittet, P. Aguilar-Martinez, J. Delaunay, G. W. Stewart, L.J. Bruce, Stomatin-deficient cryohydrocytosis results from mutations in SLC2A1: a novel form of GLUT1 deficiency syndrome, Blood 118 (2011) 5267–5277.
[8] L.J. Bruce, H. Guizouarn, N.M. Burton, N. Gabillat, J. Poole, J.F. Flatt, R.L. Brady, F. Borgese, J. Delaunay, G.W. Stewart, The monovalent cation leak in overhydrated stomatocytic red blood cells results from amino acid substitutions in the Rh-associated glycoprotein, Blood 113 (2009) 1350–1357.
[9] L.J. Bruce, H.C. Robinson, H. Guizouarn, F. Borgese, P. Harrison, M.J. King, J. S. Goede, S.E. Coles, D.M. Gore, H.U. Lutz, R. Ficarella, D.M. Layton, A. Iolascon, J. C. Ellory, G.W. Stewart, Monovalent cation leaks in human red cells caused by single amino-acid substitutions in the transport domain of the band 3 chloride-bicarbonate exchanger, AE1, Nat. Genet. 37 (2005) 1258–1263.
[10] J. Albuisson, S.E. Murthy, M. Bandell, B. Coste, H. Louis-Dit-Picard, J. Mathur, M. Fénéant-Thibault, G. Tertian, J.P. de Jaureguiberry, P.Y. Syfuss, S. Cahalan, L. Garçon, F. Toutain, P. Simon Rohrlich, J. Delaunay, V. Picard, X. Jeunemaitre, A. Patapoutian, Dehydrated hereditary stomatocytosis linked to gain-of-function mutations in mechanically activated PIEZO1 ion channels, Nat. Commun. 4 (2013) 1884.
[11] R. Rapetti-Mauss, C. Lacoste, V. Picard, C. Guitton, E. Lombard, M. Loosveld, V. Nivaggioni, N. Dasilva, D. Salgado, J.P. Desvignes, C. Béroud, P. Viout, M. Bernard, O. Soriani, H. Vinti, V. Lacroze, M. Feneant-Thibault, I. Thuret, H. Guizouarn, C. Badens, A mutation in the Gardos channel is associated with hereditary xerocytosis, Blood 126 (2015) 1273–1280.
[12] E. Glogowska, K. Lezon-Geyda, Y. Maksimova, V.P. Schulz, P.G. Gallagher, Mutations in the Gardos channel (KCNN4) are associated with hereditary xerocytosis, Blood 126 (2015) 1281–1284.
[13] R. Zarychanski, V.P. Schulz, B.L. Houston, Y. Maksimova, D.S. Houston, B. Smith, J. Rinehart, P.G. Gallagher, Mutations in the mechanotransduction protein PIEZO1 are associated with hereditary xerocytosis, Blood 120 (2012) 1908–1915.
[14] I. Andolfo, R. Russo, F. Manna, B.E. Shmukler, A. Gambale, G. Vitiello, G. De Rosa, C. Brugnara, S.L. Alper, L.M. Snyder, A. Iolascon, Novel Gardos channel mutations linked to dehydrated hereditary stomatocytosis (xerocytosis), Am. J. Hematol. 90 (2015) 921–926.
[15] I. Andolfo, S.L. Alper, J. Delaunay, C. Auriemma, R. Russo, R. Asci, M.R. Esposito, A.K. Sharma, B.E. Shmukler, C. Brugnara, L. De Franceschi, A. Iolascon, Missense mutations in the ABCB6 transporter cause dominant familial pseudohyperkalemia, Am. J. Hematol. 88 (2013) 66–72.
[16] I. Andolfo, S. Martone, B.E. Rosato, R. Marra, A. Gambale, G.L. Forni, V. Pinto, M. Göransson, V. Papadopoulou, M. Gavillet, M. Elalfy, A. Panarelli, G. Tomaiuolo, A. Iolascon, R. Russo, Complex modes of inheritance in hereditary red blood cell disorders: a case series study of 155 patients, Genes (Basel) 12 (2021).
[17] F. Girodon, L. Garçon, E. Bergoin, M. Largier, J. Delaunay, M. Fénéant-Thibault, M. Maynadié, G. Couillaud, S. Moreira, T. Cynober, Usefulness of the eosin-5′-maleimide cytometric method as a first-line screening test for the diagnosis of hereditary spherocytosis: comparison with ektacytometry and protein electrophoresis, Br. J. Haematol. 140 (2008) 468–470.
[18] L. Da Costa, L. Suner, J. Galimand, A. Bonnel, T. Pascreau, N. Couque, O. Fenneteau, N. Mohandas, S.o.H.a.P.I.S. group, F.S.o.H. (SFH), Diagnostic tool for red blood cell membrane disorders: assessment of a new generation ektacytometer, Blood Cells Mol. Dis. 56 (2016) 9–22.
[19] N. Mohandas, P.G. Gallagher, Red cell membrane: past, present, and future, Blood 112 (2008) 3939–3948.
[20] N. Mohandas, J.A. Chasis, S.B. Shohet, The influence of membrane skeleton on red cell deformability, membrane material properties, and shape, Semin. Hematol. 20 (1983) 225–242.
[21] N. Mohandas, J.A. Chasis, Red blood cell deformability, membrane material properties and shape: regulation by transmembrane, skeletal and cytosolic proteins and lipids, Semin. Hematol. 30 (1993) 171–192.
[22] C. Kopanos, V. Tsiolkas, A. Kouris, C.E. Chapple, M. Albarca Aguilera, R. Meyer, A. Massouras, VarSome: the human genomic variant search engine, Bioinformatics 35 (2019) 1978–1980.
[23] D. Baux, C. Van Goethem, O. Ardouin, T. Guignard, A. Bergougnoux, M. Koenig, A. F. Roux, MobiDetails: online DNA variants interpretation, Eur. J. Hum. Genet. 29 (2021) 356–360.
[24] L.M. Amendola, G.P. Jarvik, M.C. Leo, H.M. McLaughlin, Y. Akkari, M.D. Amaral, J.S. Berg, S. Biswas, K.M. Bowling, L.K. Conlin, G.M. Cooper, M.O. Dorschner, M. C. Dulik, A.A. Ghazani, R. Ghosh, R.C. Green, R. Hart, C. Horton, J.J. Johnston, M. S. Lebo, A. Milosavljevic, J. Ou, C.M. Pak, R.Y. Patel, S. Punj, C.S. Richards, J. Salama, N.T. Strande, Y. Yang, S.E. Plon, L.G. Biesecker, H.L. Rehm, Performance of ACMG-AMP variant-interpretation guidelines among nine laboratories in the Clinical Sequencing Exploratory Research Consortium, Am. J. Hum. Genet. 99 (2016) 247.
[25] S. Richards, N. Aziz, S. Bale, D. Bick, S. Das, J. Gastier-Foster, W.W. Grody, M. Hegde, E. Lyon, E. Spector, K. Voelkerding, H.L. Rehm, A.L.Q.A. Committee, Standards and guidelines for the interpretation of sequence variants: a joint consensus recommendation of the American College of Medical Genetics and Genomics and the Association for Molecular Pathology, Genet Med 17 (2015) 405–424.
[26] I. Andolfo, S.L. Alper, L. De Franceschi, C. Auriemma, R. Russo, L. De Falco, F. Vallefuoco, M.R. Esposito, D.H. Vandorpe, B.E. Shmukler, R. Narayan, D. Montanaro, M. D'Armiento, A. Vetro, I. Limongelli, O. Zuffardi, B.E. Glader, S.L. Schrier, C. Brugnara, G.W. Stewart, J. Delaunay, A. Iolascon, Multiple clinical forms of dehydrated hereditary stomatocytosis arise from mutations in PIEZO1, Blood, 121 (2013) 3925–3935, S3921-3912.
[27] A. Iolascon, L. De Falco, F. Borgese, M. Esposito, R. Avvisati, P. Izzo, C. Piscopo, H. Guizouarn, A. Biondani, A. Pantaleo, L. De Franceschi, A novel erythroid anion exchange variant (Gly796Arg) of hereditary stomatocytosis associated with dyserythropoiesis, Haematologica 94 (2009) 1049–1059.
[28] L. Da Costa, J. Galimand, O. Fenneteau, N. Mohandas, Hereditary spherocytosis, elliptocytosis, and other red cell membrane disorders, Blood Rev. 27 (2013) 167–178.
[29] S. Perrotta, P.G. Gallagher, N. Mohandas, Hereditary spherocytosis, Lancet 372 (2008) 1411–1426.
[30] A. Cueff, R. Seear, A. Dyrda, G. Bouyer, S. Egée, A. Esposito, J. Skepper, T. Tiffert, V.L. Lew, S.L. Thomas, Effects of elevated intracellular calcium on the osmotic fragility of human red blood cells, Cell Calcium 47 (2010) 29–36.
[31] R. Syeda, J. Xu, A.E. Dubin, B. Coste, J. Mathur, T. Huynh, J. Matzen, J. Lao, D. C. Tully, I.H. Engels, H.M. Petrassi, A.M. Schumacher, M. Montal, M. Bandell, A. Patapoutian, Chemical activation of the mechanotransduction channel Piezo1, Elife 4 (2015).
[32] H. Guizouarn, S. Martial, N. Gabillat, F. Borgese, Point mutations involved in red cell stomatocytosis convert the electroneutral anion exchanger 1 to a nonselective cation conductance, Blood 110 (2007) 2158–2165.
[33] R. Rapetti-Mauss, V. Picard, C. Guitton, K. Ghazal, V. Proulle, C. Badens, O. Soriani, L. Garçon, H. Guizouarn, Red blood cell Gardos channel (KCNN4): the essential determinant of erythrocyte dehydration in hereditary xerocytosis, Haematologica 102 (2017) e415–e418.

Nouveaux variants de KCNN4 associés à une anémie : Stomatocytose sans déshydratation des globules rouge.

Contexte

Dans cet article nous décrivons deux nouvelles mutations de KCNN4 impliquées dans la Xérocytose Héréditaire (V222L et H340N). Exprimées dans des cellules HEK293T, les mutations V222L et H340N de KCNN4 sont gain de fonction avec une sensibilité calcique augmentée par rapport à la forme sauvage du canal. En revanche, nous n'observons pas de déshydratation des GR des patients porteurs de l'une ou l'autre de ces mutations. Le phénotype est très hétérogène au niveau clinique chez les patients porteurs de V222L et H340N avec des anémies asymptomatiques à sévères. Ces résultats remettent en question le rôle des mutations gain de fonction de KCNN4 dans la perméabilité hydrique et la survie du GR dans la circulation sanguine.

frontiers | Frontiers in Physiology

ORIGINAL RESEARCH
published: 08 August 2022
doi: 10.3389/fphys.2022.918620

New KCNN4 Variants Associated With Anemia: Stomatocytosis Without Erythrocyte Dehydration

*B. Allegrini[1], S. Jedele[2], L. David Nguyen[3,4], M. Mignotet[1], R. Rapetti-Mauss[1], C. Etchebest[2], O. Fenneteau[4], A. Loubat[1], A. Boutet[5], C. Thomas[6], J. Durin[7], A. Petit[7], C. Badens[8,9], L. Garçon[10,11], L. Da Costa[3,4,10] and H. Guizouarn[1]**

[1]Université Côte d'Azur, CNRS, INSERM, iBV, Nice, France, [2]Université Paris Cité and Université des Antilles, Inserm, BIGR, Paris, France, [3]Université Paris Cité, Paris, France, [4]AP-HP, Service d'Hématologie Biologique, Hôpital R. Debré, Paris, France, [5]Hôpital Saint Nazaire, Saint-Nazaire, France, [6]CHU Nantes, Service Oncologie-hématologie et Immunologie Pédiatrique, Nantes, France, [7]Sorbonne Université, AP-HP, Hôpital Armand Trousseau, Service d'Hématologie Oncologie Pédiatrique, Paris, France, [8]Aix Marseille Univ, INSERM, MMG, Marseille, France, [9]AP-HM, Department of Genetic, Marseille, France, [10]Université Picardie Jules Verne, Unité EA4666 Hematim, Amiens, France, [11]CHU Amiens, Service d'Hématologie Biologique, Amiens, France*

OPEN ACCESS

Edited by:
Egee Stéphane, UMR8227 Laboratoire de Biologie Intégrative des Modèles Marins, France

Reviewed by:
Reinhart Reithmeier, University of Toronto, Canada
John Stanley Gibson, University of Cambridge, United Kingdom

***Correspondence:**
H. Guizouarn
helene.guizouarn@univ-cotedazur.fr

Specialty section:
This article was submitted to Red Blood Cell Physiology, a section of the journal Frontiers in Physiology

Received: *12 April 2022*
Accepted: *27 May 2022*
Published: *08 August 2022*

Citation:
Allegrini B, Jedele S, David Nguyen L, Mignotet M, Rapetti-Mauss R, Etchebest C, Fenneteau O, Loubat A, Boutet A, Thomas C, Durin J, Petit A, Badens C, Garçon L, Da Costa L and Guizouarn H (2022) New KCNN4 Variants Associated With Anemia: Stomatocytosis Without Erythrocyte Dehydration. Front. Physiol. 13:918620. doi: 10.3389/fphys.2022.918620

The K^+ channel activated by the Ca^{2+}, KCNN4, has been shown to contribute to red blood cell dehydration in the rare hereditary hemolytic anemia, the dehydrated hereditary stomatocytosis. We report two *de novo* mutations on *KCNN4*, We reported two *de novo* mutations on *KCNN4*, V222L and H340N, characterized at the molecular, cellular and clinical levels. Whereas both mutations were shown to increase the calcium sensitivity of the K^+ channel, leading to channel opening for lower calcium concentrations compared to WT KCNN4 channel, there was no obvious red blood cell dehydration in patients carrying one or the other mutation. The clinical phenotype was greatly different between carriers of the mutated gene ranging from severe anemia for one patient to a single episode of anemia for the other patient or no documented sign of anemia for the parents who also carried the mutation. These data compared to already published KCNN4 mutations question the role of KCNN4 gain-of-function mutations in hydration status and viability of red blood cells in bloodstream.

Keywords: Hereditary Xerocytosis, Stomatocytosis, red blood cell, Gardos, KCNN4

INTRODUCTION

The rare disease dehydrated hereditary stomatocytosis (DHSt or hereditary xerocytosis, HX) is an autosomal dominant hemolytic anemia, characterized by an alteration of the cation permeability of red blood cell (RBC) (Badens and Guizouarn, 2016; Gallagher, 2017; Flatt and Bruce, 2018). In 2012, the identification of *PIEZO1* mutations in families suffering DHSt paved the way toward the genetic cause of this long-known hemolytic anemia (Zarychanski et al., 2012; Albuisson et al., 2013; Andolfo et al., 2013). Three years later, with the identification of mutations in *KCNN4*, another genetic cause of DHSt was claimed: "two genetic causes for a single RBC pathology" (Grygorczyk and Mohandas, 2015). KCNN4 is a Ca^{2+}-activated K^+ channel (also named SK4 or Gardos channel in RBC) (Gárdos et al., 1977; Maher and Kuchel, 2003) and PIEZO1 is a non-selective cation channel, permeable to Na^+ and K^+ and divalent cations Ca^{2+} and Mg^{2+} (Gnanasambandam et al., 2015) activated by mechanical stimuli (Coste et al., 2012). Numerous gain-of-function mutations in *PIEZO1* were identified in families with DHSt (Picard et al., 2019; More et al., 2020) and some of them were shown to modify the channel gating leading to longer open state that should increase Ca^{2+} concentration in

RBC (Albuisson et al., 2013; Cahalan et al., 2015; Danielczok et al., 2017; Glogowska et al., 2017). This Ca^{2+} concentration rise can activate KCNN4, which leads to RBC dehydration (Syeda et al., 2015). The large anion conductance of erythrocyte membrane allows the loss of K^+ when intracellular Ca^{2+} increase opens KCNN4. This KCl loss is accompanied by osmotically linked water. The Ca^{2+}-induced K^+ loss, named the Gardos effect, is of primary importance in RBC physiology (Gárdos et al., 1977; Maher and Kuchel, 2003). These cells do not regulate their volume. Hence, the dehydration resulting from KCNN4 activation is irreversible and this is expected to alter the RBC rheological properties. In sickle cell disease, the Gardos effect contributes to RBC sickling, the S-S hemoglobin having a greater tendency to polymerize following dehydration than A-A hemoglobin (Brugnara et al., 1993; De Franceschi et al., 1994). This mechanism has also been proposed to participate in the senescence of RBC. In a recent study, Rogers and Lew suggested that successive micro-activations of KCNN4 slowly dehydrate the RBC contributing to its densification, a marker of senescence (Rogers and Lew, 2021). In the case of PIEZO1 gain-of-function mutations linked to DHSt, a chronic stimulation of KCNN4 is considered as the cause of the observed RBC dehydration. In patients' RBC with different PIEZO1 mutations, KCNN4 activation appears as the sole effector of this dehydration (Rapetti-Mauss et al., 2017).

In patients' RBC carrying KCNN4 mutations, the channel conductance was increased (Rapetti-Mauss et al., 2016; Rivera et al., 2017; Fermo et al., 2020). Moreover, the mutations changed channel gating mainly by modifying its Ca^{2+} sensitivity (Garneau et al., 2009; Rapetti-Mauss et al., 2016).

Despite leading to a more active channel, the gain-of-function mutations in *KCNN4* are not systematically linked to RBC dehydration, and routine hematological tests failed to clearly diagnose DHSt (Picard et al., 2021). Nonetheless, these *KCNN4* mutations are associated with anemia that is often severe, especially in childhood and fetal life (Rapetti-Mauss et al., 2015).

Our present study was designed to reinforce our knowledge about KCNN4 mutations and DHSt. Two *de novo* KCNN4 mutations were identified in two unrelated families leading to the amino acid substitution V222L and H340N. This later had already been reported in a genetic screen but had not been functionally characterized (Andolfo et al., 2021). The two mutations were characterized by expression in HEK293T cells and it was observed that they changed the channel gating by calcium. Confirming previous observation with the majority of the KCNN4 mutations, our data did not correlate KCNN4 gain-of-function mutations with RBC dehydration, raising the question of classifying this pathology as a DHSt. Moreover, it emphasized the difficulty to diagnose altered RBC permeability facing KCNN4 mutations and the great variability in RBC phenotypes associated with KCNN4 gain-of-function mutations.

MATERIALS AND METHODS

Patients: Patients had been referred to our Hematology Diagnostic laboratory (AP-HP) for phenotypic and genotypic explorations. The lab is quality certified for molecular screening analysis for "targeted-NGS red cell and erythropoiesis defects" (Cofrac Iso15189) and labelized "Reference Medical Biological Laboratory" for red cell membrane diagnosis (LBMR July 2021). The patients exhibited chronic hemolytic anemia/hemolysis signs or had been followed up for uncharacterized red blood cell membrane disorder.

Red cell and reticulocyte indices, EMA test, and Ektacytometry: All blood samples were collected on EDTA and shipped at 4°C after blood was drawn along with a blood smear. Samples should be delivered to our laboratory within 48h after blood collection. RBC indices including hemoglobin concentration, hematocrit, mean cell volume (MCV), mean corpuscular hemoglobin concentration (MCHC), mean hemoglobin content (MHC), RBC volume distribution (RDW), and reticulocyte count and distribution have been measured for each sample using a hematological analyzer (XN, Sysmex, Kobe, Japan). Blood smears stained with May Grümwald Giemsa (MGG) were carefully examined and blind diagnostics of RBC morphology abnormalities were validated independently by two cytologists prior to additional analysis. The EMA test has been performed according to the recommendation (Girodon et al., 2008; Da Costa et al., 2016) with modification (Da Costa et al., 2016). The mean fluorescence intensity (MFI) for each sample was compared to three age-matched controls collected on the same day. A ratio of the mean fluorescence for patient RBC to the mean fluorescence for the three controls was derived (mean of three age-matched control MFI–patient MFI/mean of three age-matched control MFI). Ektacytometry LoRRca MaxSis (Mechatronics instruments BV®, Zwaag, Netherland) has been performed as previously described (Mohandas and Chasis, 1993; Mohandas and Gallagher, 2008; Da Costa et al., 2016). Blood samples (minimum of 100 µl) were analyzed by ektacytometry freshly and in any case before 48h after blood sample collection. Briefly, samples were subjected to increasing shear stress and an osmotic gradient and the laser diffraction pattern through the RBC suspension were recorded. The RBC shape goes from circular to elliptical as shear stress increases. From these measurements, a deformability or elongation index for the cells can be derived. Three distinct features of the osmotic gradient ektacytometry profiles are the Omin, the DImax, and the O' or hyperpoints. The Omin point corresponds to the osmolarity at the minimal deformability in hypoosmolar area or at the osmolarity when 50% of the RBC hemolyzed during the regular osmotic resistance test. It reflects the surface-to-area ratio. DImax corresponds to the maximal deformability index or elongation index (EI). The hyperpoint or O' corresponds to the osmolarity at half of the DImax and reflects the hydration state of the cells. Ektacytometry enables simultaneous analysis of three major RBC properties, RBC cell geometry, viscosity, and deformability, under the osmoscan application of the ektacytometer.

Genotype characterization: Genomic DNA was extracted from blood lymphocytes. Written informed consent was obtained from affected individuals and/or parents prior to inclusion in this study, which was performed in accordance with the ethical standards of the Declaration of Helsinki. The targeted New Generation Sequencing (t-NGS), developed in the

lab, is a Roche "NimbleGen SeqCap EZ" library and an illumina flowcell (Flowcell standard 2*150) with a library of 187 genes including 93 genes for red cell disorders and erythropoiesis defects. Among them 21 genes were for red cell membrane disorders. The sequences have been run on a Miseq or a Nextseq in a genetic platform (Pr A. Verloes, Genetic Department, R. Debré hospital, Paris). Sequences have been analyzed on CLC Biomedical Work Bench and allelic variations have been interpreted with Qiagen Clinical Insight (QCI), Alamut visual (Sophia Genetics), and Varsome (Kopanos et al., 2019; Baux et al., 2021).

Red cell cation content and volume measurements: Fresh venous blood was obtained by venipuncture in EDTA collecting tubes from informed patients and healthy volunteers. Blood samples were received in the laboratory within 24–48 h traveling at room temperature. For vanadate experiments: blood was washed four times at room temperature in a medium containing (in mM): NaCl (145), KCl (5), $MgSO_4$ (2), $CaCl_2$ (1), and Hepes/NaOH, pH 7.4 (10). Red cell suspension was then incubated at room-temperature 25% hematocrit with 0.5 mM ouabain, and 5 mM vanadate was added alone or with 4 µM Senicapoc. A few minutes before sampling time, 400 µl of cell suspension was taken to fill three nylon tubes that were centrifuged for 10 min at 4°C, 20 000 g at the exact sampling time. The pellet of red cells was extracted and immediately weighted. Then, dry weight was measured after overnight heating (80°C). Water content was calculated with a correction of 3.64% corresponding to the trapped medium between packed cells. Intracellular ions were extracted from dried pellets by overnight incubation at 4°C in 5 ml milliRho water (Millipore). Two percent perchloric acid was then added to precipitate proteins, samples were centrifuged for 10 min 20 000 g, and supernatant was collected for Na^+ and K^+ quantification by flame spectroscopy with an Eppendorf ELEX6361.

Intracellular Ca^{2+} measurement: RBCs were washed two times (800 g, 5 min, and 4°C) in Ringer without Ca^{2+} to remove buffy coat by aspiration. Four microliters of packed RBC were loaded with 2.5 µl of 1 mM Fluo-4 AM stock solution in 500 µl Ringer without Ca^{2+}, 37°C, and 30 min. The Fluo4-loaded RBC suspension was directly used to quantify intracellular Ca^{2+} concentration (25 µl of RBC suspension in 975 µl Ringer without Ca^{2+} in FACS tubes) by measuring fluorescence with a FACS Fortessa BD. Internal RBC fluorescence was assessed on RBC treated without Fluo-4 AM. For vanadate experiments, the Fluo4-loaded RBC suspension was diluted 40 times in Ringer with 1 mM Ca^{2+} and 5 mM vanadate at time 0 and intracellular fluorescence was measured with FACS Fortessa BD as a function of time.

HEK293T cells transfection: HEK293T cells were grown in DMEM glutamax (Gibco) 10% FBS penicillin–streptomycin. Cells were co-transfected with WT or point-mutated pcDNA3-KCNN4-HA and pIRES-eGFP (ratio 10:1) using $CaPO_4$. WT pcDNA3-KCNN4-HA was a kind gift of Len Kaczmarek laboratory. Sixteen hours later, cells were washed twice with PBS, and patch clamp was done on fluorescently labeled cells. Point mutations were done by PCR on pcDNA3-KCNN4-HA with the proofreading DNA polymerase pfu-Turbo and primers covering 16 nucleotides upstream and downstream the single point mutation C1018 A for H340N or G649C for V222L. The pcDNA3-KCNN4-HA H340N or V222L clones used in the study were sequenced entirely.

Protein expression assay: HEK293T cells were grown to 70% confluence in DMEM glutamax 10% FBS penicillin–streptomycin in 60 mm Petri dishes (Starsted) and transfected with CaPO4 with 5 µg of DNA: pcDNA3-KCNN4-HA WT, V222L, or H340N per 5 ml cell culture. Transfected medium was removed after 6h. After 24h of expression, cells were biotinylated following manufacturer instructions (Pierce cell surface protein assay), and then lysed. The lysate was loaded on avidin-agarose beads (Pierce cell surface protein assay) to isolate the biotinylated fraction. Total fraction and biotinylated fraction were subjected to SDS-PAGE western blot. Migration of proteins was made at 120 V during 90 min in 10% acrylamide gel. Proteins were then transferred to PVDF using wet transfer protocol for 1h at 100 V and blocked in blocking solution (BS: 5% low-fat milk in TBS-tween 0.1%). Immunolabelling was done using primary antibodies: anti-KCNN4 (Proteintech, Rabbit, 1: 1,000), anti-Ecadherin (Cell Signaling, Mouse, 1:5,000), and anti-GAPDH (Calbiochem, Mouse, 1:200,000) for 1 h 30 min at room temperature in BS and HRP coupled secondary antibodies for 50 min at RT using: anti-rabbit (1:2,000, DAKO) and anti-mouse (1:5,000, DAKO). HRP-labeled proteins were revealed with Enhanced Chemiluminescent solution (Millipore) with a Fusion FX EDGE.

Patch-clamp electrophysiology: Glass pipettes (Brand, Wertheim, Germany) with final resistance of 3–5 MΩ were made on a horizontal pipette puller (P-97, Sutter Instrument, Navato, CA). All patch-clamp experiments were performed with a PC-controlled EPC9 patch-clamp amplifier (HEKA, Lambrecht/Pfalz, Germany). Currents were acquired and analyzed with Pulse and Pulsefit software (HEKA).

Currents were measured in whole-cell configuration with bath solution (mM): NaCl (145), $CaCl_2$ (2), KCl (5), $MgCl_2$ (1), and HEPES (10), pH 7.4 adjusted with NaOH. Pipette solution (mM): KCl (145), $MgCl_2$ (1), HEPES (1), and EGTA (1), pH 7.2 adjusted with KOH. Free Ca^{2+} concentrations were adjusted by adding $CaCl_2$ using Ca-EGTA Calculator v1.3. Currents were measured at room temperature using a ramp protocol from -120 to +80 mV from a holding potential of -60 mV (sampling frequency 10 kHz; filtered 5 kHz).

KCNN4/CaM complex modeling: Three full-length models of the KCNN4/Calmodulin (CaM) complex were constructed by assembling KCNN4 C-ter helices (residues 376 to 415, PDB ID: 6D42) (Ji et al., 2018) to the three cryo-EM structures catching the main part of the channel in three distinct conformational states (inactivated, activated/closed, and activated/open) with CaM and Ca^{2+} ions (PDB IDs: 6CNM, 6CNN, and 6CNO, respectively) (Lee and MacKinnon, 2018). Missing CaM N-lobe in the first structure was modeled by adding the N-lobe of the second structure and changing some torsion angles in CaM linker region, so that the CaM N-lobe is kept in solvent as described in the associated publication. Missing loops and residues were modeled using MODELLER (Webb and Sali, 2016) and residue protonation states were predicted at pH 7 using PROPKA

TABLE 1 | Hematologic data collected from publications describing patients with V282M or R352H KCNN4 mutation ([1]Andolfo et al. 2015,[2]Waldstein et al. 2021,[3]Rapetti-Mauss et al. 2015) and from the new patients with V222L or H340N KCNN4 mutations.

Parameters	Normal range	V282M Worcester[1]		R352H Naples[1]			R352H Milan[1]		R352H American[2]			R352H Marseille[3]		R352H Paris[3]		V222L Nantes	H340N Paris	
		III.5	IV.5	F		Child	Father	Child (F)	Mother	Daughter	Son	Mother	Child (M)	Mother	Child (M)	Proband A (F)	Proband B (M)	
				Pre-splen	Post-splen													
Age (years)	—	56	21	13	40	10	40	1	61	39	34		0.4	25	2	3.5	4.2	0.75	1.3	4.3
Hb (g/dl)	11.5–16.5	13.3	12.5	10.4	9	10.5	10.5	9.9	10.5	11.1	9.3	8.5	9.8	11	10.4	7.5	8.9	7.7	12.3	13.7
RBC (10^{12}/L)	3.8–5.8	3.9	3.3	3	2.5	3.6										2.72	3.11	2.4	4.23	
Hct (%)	37–47	37	35.6	30.5	28.5	31.3										22.5	25.4	21.6		
MCV (fL)	76–96	103	96	101	112	86	108	81.5	106.5	99.9	98.8	109	87.9	93.1	86.9	82.8	81.7	90	77.3	79.6
MCH (pg/cell)	27–32	–	33.7	34.3	35.4	28.8	35.8	29.1								27.6	28.6	32	29.1	
MCHC (g/dl)	30–35	–	36.1	34	31.6	33.5	33	35.7	34.1	33.9	32.9	35.4	35.6	36.1	36.5	33.3	35	35.6	37.6	
RDW (%)	11.5–15.5	–	14.7	–	14.5	4.1			15	16.1	21.2					14.8	14.1	–	10.1	
Retics %	0.5–2	6.5	12.2	11.8	17.7	6.3			12.6	6.7	>22					ND	ND	6.44	1.98	
Retic absolute count (10^3/µl)	20–80	254	403	358	450	229						255	263	249	363	ND	ND	155		71.6

(F) refers to female and (M) to male.

(Olsson et al., 2011; Søndergaard et al., 2011). Models of V222L and H340N KCNN4 mutants were obtained by replacing the side-chain of the mutated residue. Resulting structures were embedded in pure symmetric POPC membranes with 150 mM of KCl using CHARMM-GUI Membrane Builder server (Wu et al., 2014) and further relaxed using 1 µs molecular dynamics simulations carried out with GROMACS (Abraham et al., 2015). Models were represented using PyMol (Shrödinger L., DeLano W.2020).

Residue conservation: Residue conservation analysis was based on the comparison of 3944 sequences collected from the NCBI non-redundant protein sequence database using blastp tool with human KCNN4 sequence (UniProt ID: O15554) as input query. Only sequences with sizes lower than 900 residues or with query coverage values higher than 66% were kept. Synthetic constructs were removed. Multiple alignments and associated weblogos were obtained using the EBI clustal omega tool (Sievers et al., 2011) and Weblogo server (Crooks et al., 2004). Conservation frequency of the KCNN4 residues was calculated as the occurrence ratio of the KCNN4 residue at the given position in the multiple sequence alignment.

RESULTS

Clinical Description of the Cases

Two subjects from two unrelated families were enrolled in this study after informed consent. The proband A had history of severe anemia requiring transfusion every 5–6 weeks since the age of 2 months when anemia was diagnosed. There was no splenomegaly, iron chelation was started at the age of 3 years. Blood withdrawal for permeability measurements was done on two occasions 3 months after the last transfusion.

The proband B was born after an uneventful pregnancy from non-consanguineous parents and delivery at 40 weeks by caesarean operation. At 9 months in a routine examination, he presented icterus and pallor requiring hematologic investigation in hospital. Results are presented in **Table 1**. Hemoglobin electrophoresis was normal (HbF 3.3%), G6PD and PK were normal, with no sign of infection, and Coombs test was negative. Bone marrow examination showed erythroid hyperplasia with discrete dyserythropoiesis. He was transfused and a steroid therapy had been started for 3 months. At the end of the steroid therapy, hemoglobin was stabilized. Growth and psychomotor development were normal and 4 years later, hematological parameters were normal (**Table 1**).

Genetics

Two allelic variations have been identified in *KCNN4* gene (NM_002250.2) in two unrelated probands: 1) proband A carried a heterozygous missense allelic variation in exon 3 of *KCNN4*: c.664G > C; *p*.(Val222Leu) (**Figure 1A**), variant without significance [VUS or Class 3 (Richards et al., 2015; Amendola et al., 2016)], sift damaging, Mutation Taster disease causing, absent from the database. The variation has been inherited from the mother. 2) proband B carried a heterozygous missense allelic variation in exon 6 of *KCNN4*: c.1018C > A; *p*.(His340Asn)

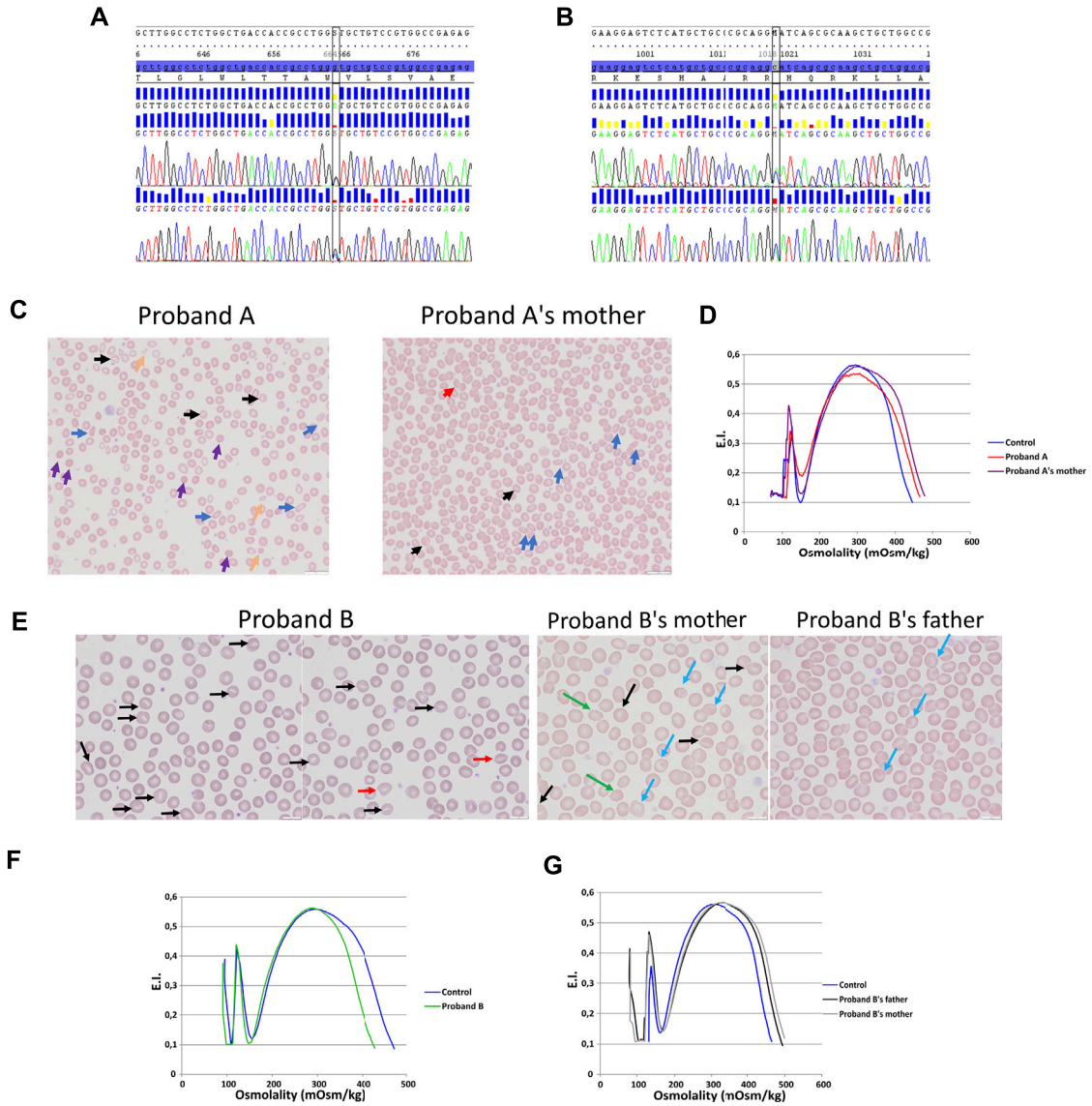

FIGURE 1 | Blood smear, ektacytometry and genetics. DNA sequencing on proband A **(A)** and proband B **(B)**. **(C)**: Blood smear on proband A with her mother (mutation KCNN4 V222L). **(D)**: Ektacytometry on proband A with her mother and control. **(E)**: blood smear done on proband B RBC (mutation KCNN4 H340N) and his father and mother. Ektacytometry on proband B **(F)** and proband B's mother's and father's RBC **(G)**.

(rs76935412) (**Figure 1B**), likely pathogenic (class 4, Varsome *in silico* prediction) variant, sift damaging, Mutation Taster disease causing, level pathogenic, MetaLR damaging, allele frequencies of 0.16%. The variation has been inherited from the mother.

Hematological Parameters

Table 1 compared hematological data coming from the new cases with H340N or V222L KCNN4 mutations with previously described RBC from patients carrying the R352H or V282M KCNN4 mutations. Anemia is a common feature of the different cases. This anemia is compensated in the family with V282M mutation showing a normal level of hemoglobin associated with hyper-reticulocytosis. The other cases exhibited a severe anemia not compensated by high reticulocytosis. The mutation H340N KCNN4 was correlated with a single episode of anemia which had not been further observed. In contrast, proband A with V222L KCNN4 mutation exhibited a severe uncompensated anemia associated with major dyserythropoiesis that could not be explained genetically, but a defect in iron/heme metabolism has been suggested.

MCHC is in the normal range or only few deciles above maximum. However, the MCHC has been reported at 37.6 g/dL in proband B at the time ektacytometry was performed (1.3 years) away from the hemolytic crisis (9 months). The size of RBC is most of the time larger than control (macrocytosis), while normal in probands A and B. These observations might result from the hyper-reticulocytosis: the maximum MCV is increased by 6–18% which could result from a 5–17% reticulocytes.

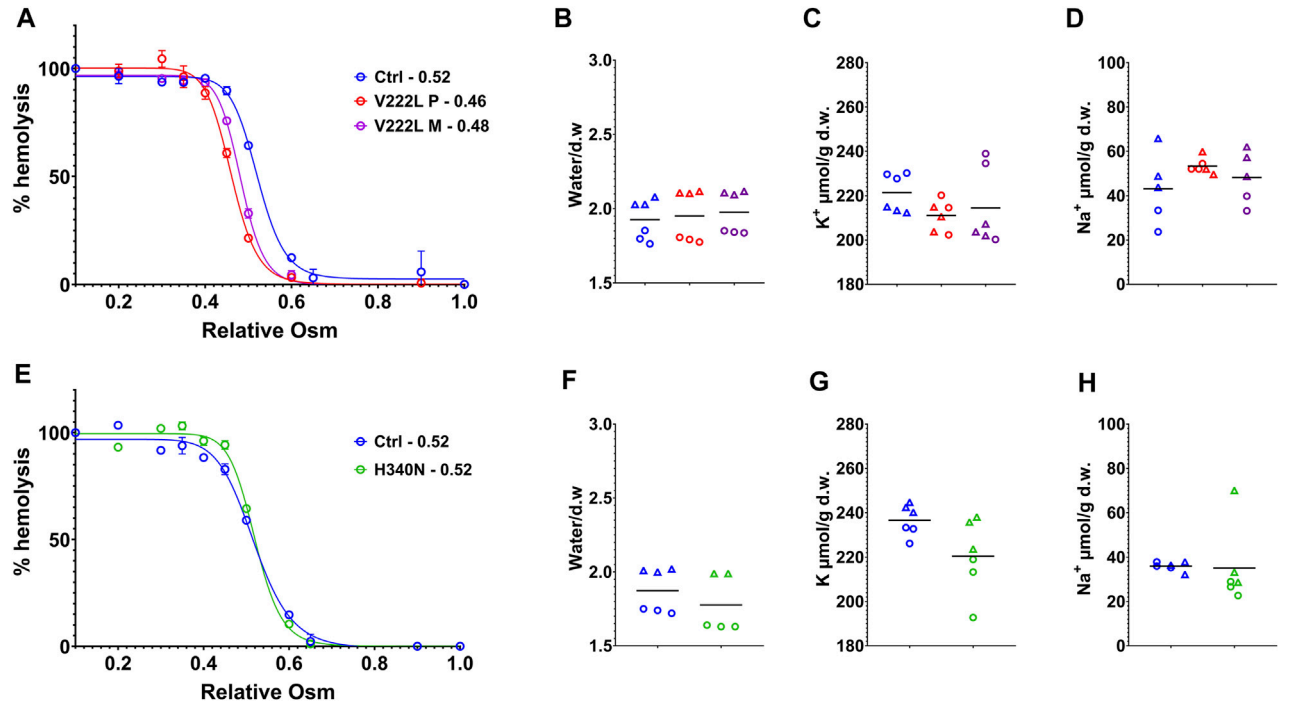

FIGURE 2 | Control vs. mutated RBC analysis. RBC analysis was made on patients and control blood collected at the same time and traveled together to the laboratory. **(A,E)**: Osmotic resistance analysis made on total blood represented as percentage hemolysis function of relative NaCl concentration. Data are means ± SD illustrating one experiment done in triplicate on one blood shipment for each family. **(A)** Control in blue, V222L proband A in red and proband A's mother in purple; **(E)** control in blue, H340N proband B in green. **(B,C,D,F,G,H)**: RBC were washed in Ringer (1 mM Ca^{2+}), dried, and weighted for water content expressed in g of water/g of dry weight **(B,F)**, then solubilized for K^+ **(C,G)** and Na^+ **(D,H)** content measurements expressed in µmol/g of dry weight. Data showed the results coming from experiments performed on two blood shipments for each patient with corresponding controls (each experiment in triplicate, hence, six symbols of the same color per condition). Circles or triangles correspond to paired samples in the same shipment. From left to right along *x* axis in each plot: control (blue), proband A V222L (red), and proband A's mother (purple) **(B,C,D)** and control (blue), proband B, and H340N (green) **(F,G,H)**. The bars represent the median. Statistical analyses were made with a Mann–Whitney test when comparing two conditions or Kruskal–Wallis if more than two. Neither of both gave statistical differences for any conditions.

Blood smear showed anisopoikilocytosis (**Figure 1C**), with rare spherocytes (purple arrows), rare elliptocytes (blue arrows), rare stomatocytes (black arrows), few RBC fragments (yellow arrows), and erythroblastemia for proband A with V222L KCNN4 mutation. Proband A's mother's blood smear did not show noticeable erythrocyte anomaly, except rare elliptocytes and very rare stomatocytes (**Figure 1C**). The ektacytometry indicated altered RBC deformability for proband A without any shift in osmotic resistance (**Figure 1D**). Omin point was normal while hyperpoint was shifted to the right. Proband A's mother's RBC deformability was normal and hyperpoint exhibited the same shift to the right as her daughter. For proband B, blood smear strikingly exhibited few stomatocytes [black and red (smile feature) arrows] (**Figure 1E**). The ektacytometry indicated normal deformability with a shift to the left of the hyperpoint in accordance with the increased MCHC at 37.6 g/dL in proband B at the time of the study (**Figure 1F**). The mother and the father exhibited normal ektacytometry curves (**Figure 1G**) and the mother, who carried the same allelic variation as his son, exhibited only rare stomatocytes, rare target cells (blue arrows), and acanthocytes (green arrows), while the father exhibited only few target cells (blue arrows) (**Figure 1E**).

Red Blood Cell Permeability

RBC water, K^+- and Na^+-ion contents were measured following RBC washing in saline buffer containing calcium, 48h after blood collection in EDTA tubes. **Figure 2** illustrates data coming from experiments corresponding to two different shipments of either proband A or proband B blood samples collected at different times. Osmotic resistance curves for proband A as for the mother with V222L mutation were slightly shifted to the left compared to control (**Figure 2A**). However, this shift is in the normal range and there was no change in water content between control and mutant (**Figure 2B**). The K^+ and Na^+ contents of RBC with V222L KCNN4 were not significantly different from control despite a tendency to increased Na^+ content correlated with decreased K^+ content in one blood sample (**Figures 2C,D**). Osmotic resistance curves showed no significant difference between control and H340N mutants (**Figure 2E**). This is correlated with no significant change in water content (**Figure 2F**). The K^+ and Na^+ contents were also similar between control and H340N mutants (**Figures 2G,H**). Hence, it was not possible to detect any significant change in water, K^+, and Na^+ permeability in RBC carrying KCNN4 mutations V222L or H340N compared to WT. Similar results were observed

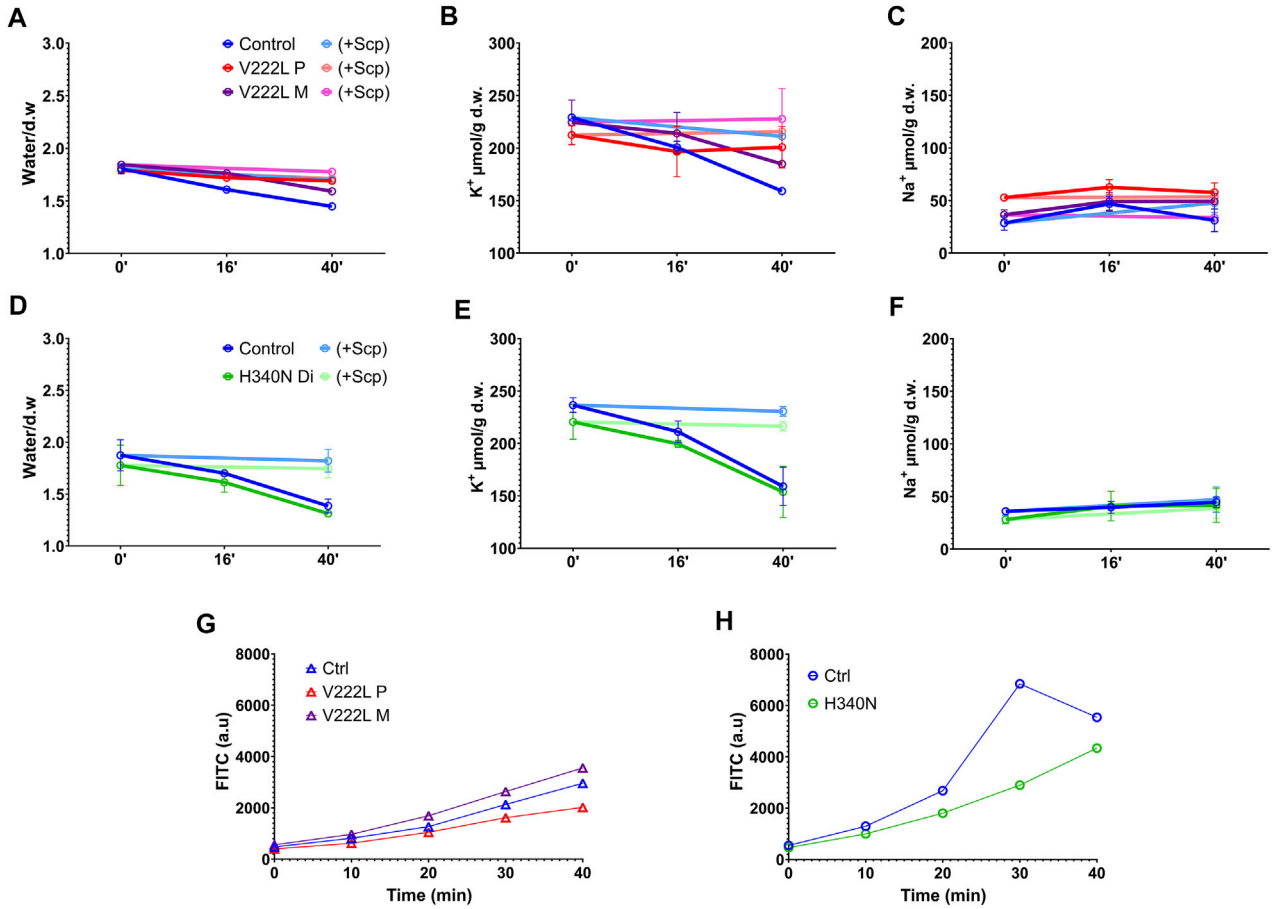

FIGURE 3 | RBC ion, water, and Ca^{2+} contents in response to vanadate. Washed RBCs were submitted to 5 mM Vanadate with or without 4 µM Senicapoc treatment in the presence of 0.5 mM ouabain. Water, K^+, and Na^+ contents were measured at different time points (0′, 16′ and 40′). Water content **(A,D)**, K^+ content **(B,E)**, and Na^+ content **(C,F)** are represented for control in blue, V222L proband A in red and proband A's mother in purple: panel **(A,B,C)**, and control in blue, H340N proband B in green: panel **(D,E,F)**. Bright colors represented Senicapoc effect compared to untreated conditions. Data are given as mean ± SD of triplicate experiments done on either a single blood shipment for proband A [panel **(A,B,C)**] or two different blood shipments for proband B [panel **(D,E,F)**]. **(G,H)**: Fresh RBCs were washed in Ringer without calcium and incubated with 5 µM Fluo-4AM 30min at 37°C. Fluo-4AM-loaded RBCs were then incubated in Ringer solution with 1 mM Ca^{2+} and 5 mM vanadate. Fluorescence was measured with a FACS as a function of time. Data are given as FITC in arbitrary units, median of a single experiment, 10,000 events. The fluorescence linked to basal intracellular Ca^{2+} concentration was in arbitrary units, mean ± s.e.m.: 750 ± 9 for proband A, 1,167 ± 6 for proband A's mother, and 839 ± 6 for control and 528 ± 5 for proband B compared to 533 ± 7 for control.

previously in RBC with R352H mutated KCNN4 (Andolfo et al., 2015; Glogowska et al., 2015; Rapetti-Mauss et al., 2015).

In order to unmask a possible difference in the activation of mutated KCNN4 compared to WT, control and mutant RBCs were challenged with vanadate, inhibitor of the Ca^{2+}-ATPase pump. Blocking Ca^{2+} pump leads to intracellular Ca^{2+} increase that in turn activates KCNN4. This activation resulted in K^+ loss that can be blocked by Senicapoc, inhibitor of KCNN4. A significant dehydration correlated with K^+ loss was observed in control RBC 40 min after vanadate addition that was blocked by Senicapoc (**Figures 3A**,**BD**,**E**), confirming the involvement of KCNN4 in RBC water loss. The K^+ drop was marked after 16 min with vanadate and negligible before 16 min. Vanadate did not change RBC Na^+ content (**Figures 3C**,**F**). Following incubation with vanadate, the K^+ content decreased in RBC with either V222L or H340N KCNN4 mutations, and this K^+ loss was blocked by addition of Senicapoc. Following the same scheme as R352H KCNN4, a greater Ca^{2+} sensitivity of V222L and H340N mutants was expected to increase K^+ loss within 16 min incubation with vanadate (Rapetti-Mauss et al., 2015). However, there was no difference between control and mutant RBC 16 min after vanadate addition. Strikingly, the K^+ loss and dehydration were even reduced compared to control for proband A with V222L KCNN4 mutation (**Figures 3B**,**C**).

Intracellular Ca^{2+} rise following Ca^{2+} pump inhibition with vanadate depends on the Ca^{2+} leak allowing progressive Ca^{2+} uptake. Hence, the absence of differential activation of mutated KCNN4 compared to WT in RBC incubated with vanadate could be explained by variations in intracellular Ca^{2+} concentration between samples. Using the fluorescent probe Fluo4, intracellular Ca^{2+} concentration was measured in the

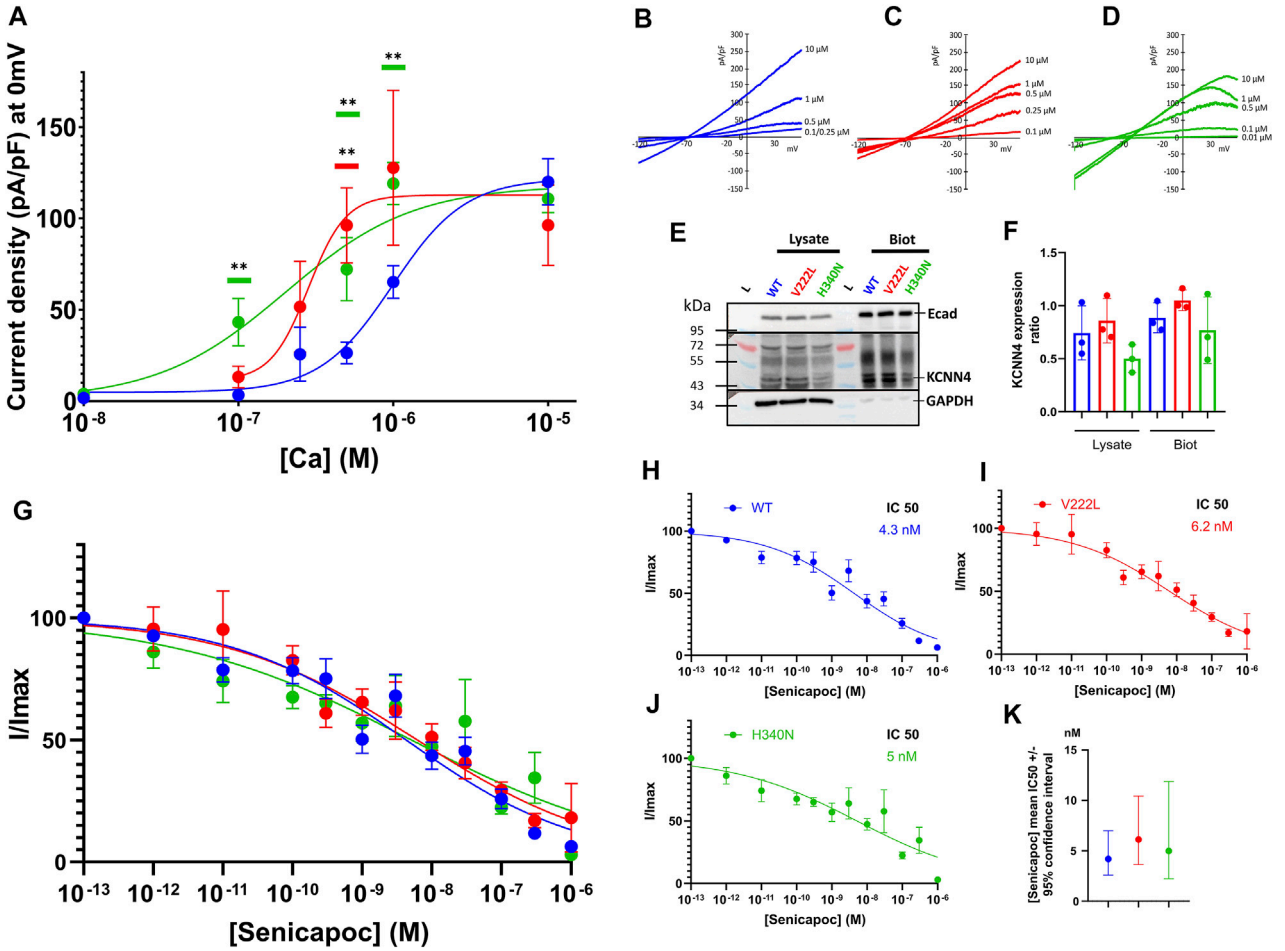

FIGURE 4 | Calcium sensitivity of KCNN4 mutations V222L and H340N in HEK293T cells. **(A)** Current density (pA/pF) was measured in response to $(Ca^{2+})_i$ for KCNN4 WT (blue), V222L (red), and H340N (green). Experimental values were fitted with a variable slope model (Hill equation) ($Y = Y_{min} + (X^{hillslope})*(Y_{max}- Y_{min})/(X^{hillslope} + EC50^{Hillslope}$). The resulting EC50 corresponds to the $(Ca^{2+})_i$ at which half of the max current is reached. **(B–D)** Representative I/V curves for WT, V222L, and H340N at different Ca^{2+} concentrations (0.01–0.1–0.25–0.5–1, and 10 μM). Statistical analysis against WT at different Ca^{2+} concentrations was performed using a Kruskal–Wallis test followed by an uncorrected Dunn's test, $n = 7–12$ (*: $p < 0.05$; **: $p < 0.01$). **(E)** Representative western blot showing total (Lysate) or only surface (Biot) protein expression of KCNN4 WT, V222L, and H340N in HEK293T-transfected cells. Total fraction corresponded to cell lysate and biotinylated fraction corresponded to membrane proteins. We used GAPDH as housekeeping for total fraction quantification (lysate) and E-cadherin for biotinylated fraction quantification. In KCNN4 labeling, the three bands between 43 kDa and 55 kDa corresponded to different glycosylated states of the protein. In lysate, the band at 72 kDa is non-specific. **(F)** Ratio KCNN4/GAPDH in lysate and KCNN4/ECadherin (biotinylation) were calculated from three independent Western Blots, taking the total KCNN4 signal. No significantly increased expression with V222L and H340N compared to WT KCNN4 was observed. Only H340N tended to have a reduced expression. Kruskal–Wallis test was used to determine statistical significance against WT. **(G)** Senicapoc sensitivity of KCNN4 WT or mutated. Normalized currents were measured in response to [Senicapoc] for WT (blue), V222L (red), and H340N (green). Experimental values were fitted with variable slope model (Hill equation): $Y = 100/(1 + (IC50/X)^{hillslope})$. The resulting IC50 corresponded to 50% inhibition by Senicapoc; the mean value ±95% confidence interval of IC50 is represented in **(K)**, $n = 15–21$. For clarity purposes, fits are represented alone for each condition **(H,I,J)**. Statistical analyses were performed using a Kruskal–Wallis test followed by an uncorrected Dunn's test, $n = 15–21$.

different RBC incubated with vanadate (**Figures 3G,H**). Vanadate increased similarly intracellular calcium concentration in control and patients' RBC in the different experiments.

KCNN4 Expression in HEK293T Cells

To study the effect of KCNN4 mutations on the channel activity, HEK293T cells were transfected with either WT KCNN4 or H340N KCNN4 or V222L KCNN4. It is observed that the maximal current intensity is not changed by the mutations (**Figures 4A–D**). However, the two mutants V222L and H340N were more sensitive to Ca^{2+} compared to WT with an IC50 = 0.28 and 0.20 μM, respectively (0.99 μM for WT). The expression at the plasma membrane of the different constructs was assessed by western blotting of biotinylated proteins. Immunodetection of E-cadherin was used as a reference for expression of endogenous membrane protein to compare the different conditions. All the constructs were similarly expressed at the plasma membrane (**Figures 4E,F**), ruling out an effect of the mutations on protein addressing the HEK293T plasma membrane. The mutants were sensitive to Senicapoc, blocker of KCNN4, showing a sensitivity similar to the WT (**Figures 4G–K**).

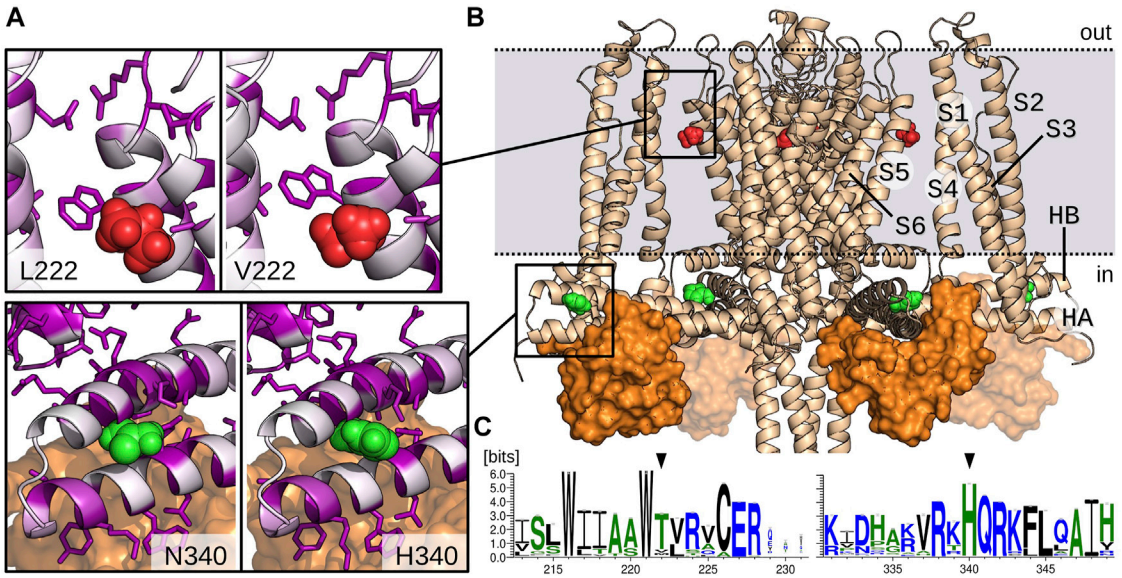

FIGURE 5 | Model of KCNN4 showing V222 and H340 amino acids location. **(A)** Zoom on V222 (red) and H340 (green) environment in the activated/closed KCNN4/CaM model. Mutant models (L222 and N340) are presented in the left windows. KCNN4 residues are colored according to their conservation frequency (white to purple) in the multiple sequence alignment. Side chains of residues with a conservation percentage greater than 70% are represented. **(B)** Model of KCNN4/CaM complex based on cryo-EM structures. For clarity, only KCNN4 and C-lobes (orange surface) of the four CaM molecules are shown. Dashed lines delineate the position of plasma membrane upper and lower leaflets. **(C)** Weblogos of the KCNN4 sequence segments encompassing positions 222 and 340 (black arrows).

KCNN4 Structure Analysis

The two mutations are located in very different regions of the channel (**Figures 5A,B**). The multiple sequence analysis also showed drastic different profiles for V222L and H340N mutations in terms of conservation. Indeed, the weblogo established from this alignment (**Figure 5C**) designates H340 as a highly conserved residue (99%), in contrast the Valine in position 222 is poorly conserved (8%). This last position is actually mainly occupied by Threonine (83%). Leucine residue can be found but extremely rarely in the superfamily of KCNN4 (0.9%).

The 3D structure shows that H340 is located in the binding site with the constitutively bound calmodulin (CaM) C-lobe (**Figure 5B**), More precisely, H340 is carried by the intracellular HB helix, in the region facing the HA helix and close to the peripheral helices S2–S3 linker. H340 is in contact with residues E321, M324, F325, and H328 of HA and A336 and L343 of HB. V222 is located in the transmembrane part of the channel, in the middle of the interface bridging the S1/S4 peripheral helices with the S5/S6 helices that constitute the pore domain. V222 is in contact with both L154 and L157 situated in the peripheral S4 helix and with the conserved residue V266 from helix S6. It is also close to the interface between S1 and S5 helices involving highly conserved residues, i.e., V41 (87%) and E45 (93%) on one side and residues W221 (99%) and R228 (99%) on the other side.

Preliminary results obtained for the mutated modeled structures relaxed with molecular dynamics simulations did not show major changes in the environment of the residue, most local contacts being preserved. However, this does not preclude long range effects as observed through slight displacements of helices for the two mutants along the molecular dynamic simulations.

DISCUSSION

At the molecular level, it was shown that the KCNN4 mutations V222L and H340N altered the Ca^{2+} sensitivity of the K^+ channel and could be classified as gain-of-function mutations. The IC50 is shifted toward lower intracellular Ca^{2+} concentrations suggesting that the mutated channels might be activated with a lower Ca^{2+} increase compared to WT channels. The functional changes observed for the two mutants may originate from two mechanisms: the first one involving V222L could be due to the fine regulation that exists between the peripheral helices and the pore helices during the transport; in contrast, the second one involving H340N may participate in the activation process itself, by changing the interplay between CaM and the channel. In this last case, it is important to note that other mutations (R352, A322, and S314) in CaM C-lobe-binding site have been reported.

Clinically, these two new KCNN4 mutations blurred a bit more the phenotype of KCNN4 gain-of-function mutations. From **Table 1**, it appears that KCNN4 gain-of-function mutations are associated with more or less compensated hemolytic anemia. For proband A with V222L mutation, the anemia seemed related to dyserythropoiesis and strikingly the mother carrying the same mutation had no history of anemia. For proband B with H340N mutation,

the anemia was transient and again the mother carrying this mutation had never been followed for hematological disorder. The complete response observed under steroids, however, challenges the responsibility of the KCNN4 mutation alone in the pathophysiology of this transient anemia. This questions the role of these two KCNN4 gain-of-function mutations in proband A's constitutive or proband B's transient anemia. The hematologic disorder might result from the combination between the presence of KCNN4 gain-of-function mutations and a secondary trigger such as an infection, or a cumulative mutation on another gene involved in erythropoiesis, not included in the 93 "RBC genes" of the t-NGS library, or structural allelic variation not identified in t-NGS. A previous article reported the H340N KCNN4 mutation in a genetic study enrolling 155 patients with suspected hereditary anemia (Andolfo et al., 2021). This KCNN4 mutation was identified in two patients from different kindred and it was associated with either a SPTA1 mutation or two independent mutations on LARS2 and ABCB6. Unfortunately, no hematological or clinical data were given and we could not compare it with the present cases. Considering proband A (V222L mutation), the non-regenerative anemia may be due to either a non-identified intercurrent cause, or a role of KCNN4 during erythropoiesis, as described for PIEZO1-related DHSt (Caulier et al., 2020).

At the cell level, neither V222L nor H340N KCNN4 gain-of-function mutations did correlate with altered RBC hydration status: 48 h after withdrawal in EDTA collecting tubes, the osmotic resistance curves were within normal range. When assessed, the MCHC was normal or slightly above the maximal value, and the water, $Na^{+,}$ and K^+ contents were not significantly different from WT. Previous data with other KCNN4 mutations reported by us or others in different publications also failed to correlate KCNN4 mutations with RBC dehydration (Andolfo et al., 2015; Fermo et al., 2015; Rapetti-Mauss et al., 2015; Fermo et al., 2017; Waldstein et al., 2021).

The higher Ca^{2+} sensitivity of H340N and V222L KCNN4 as well as the other characterized mutants S314P and R352H (Rapetti-Mauss et al., 2015; Rivera et al., 2017; Fermo et al., 2020) suggested that these channels would be more often activated in RBC challenged with increasing Ca^{2+} concentration. This higher Ca^{2+} sensitivity of mutated KCNN4 was expected to induce RBC shrinking due to net KCl loss accompanied by water loss that is not compensated in human RBC which does not regulate their volume. It could be argued that to observe KCNN4 activity, Ca^{2+} has to be present in extracellular medium and its concentration should increase in the cell (Dyrda et al., 2010). In ektacytometry experiments as in osmotic resistance measurements, there was no Ca^{2+} in extracellular medium and the water uptake or the elongation resulted in no change or at worse a decrease in intracellular Ca^{2+} (due to water uptake). These experimental conditions do not promote KCNN4 activation. We have previously shown that osmotic resistance curves done on RBC carrying R352H KCNN4 mutation treated with the anticoagulant heparin, within hours following withdrawal, were shifted to the left compared to WT, indicating RBC dehydration (Rapetti-Mauss et al., 2015). A similar shift to the left on ektacytometry curves done on RBC with R352H or A322V KCNN4 was observed in another laboratory, indicating experimental conditions allowing KCNN4 activation in patient RBC compared to control WT (Mansour-Hendili et al., 2021). Moreover, at the time ektacytometry analysis was done on proband B, a shift to the left of the curve indicated dehydration that was corroborated by increased MCHC (**Table 1** age 1.3 years). Hence, there might be a situation where the RBC carrying KCNN4 mutations would appear dehydrated. To unmask the consequences of KCNN4 gain-of-function mutations on RBC water homeostasis, Ca^{2+} must be present in extracellular medium and the RBC energy depleted: without ATP, the Ca^{2+} pump activity decreases and intracellular Ca^{2+} slowly increases leading to the activation of KCNN4. Gain-of-function KCNN4 mutations will result in a more rapid activation of the channel compared to WT. Thus, depending on 1) the energy status of RBC following blood withdrawal and 2) the presence of Ca^{2+} in medium, mutated KCNN4 could be activated and patient RBC dehydration could be observed. The fact that in EDTA collecting tubes within 24–48 h of withdrawal, patient RBC was within normal range for water content, suggested KCNN4 activity was kept silent in bloodstream. Alternatively, we can hypothesize that the RBC where KCNN4 was activated were dramatically dehydrated and immediately removed from circulation and could not be observed in blood samples. However, blood smear clearly indicated altered RBC shapes (**Figure 1**) that were even more visible when patients were splenectomized (Rapetti-Mauss et al., 2015). In addition, the ektacytometry indicated in some patients an increased RBC fragility (diminution of the maximum and increase in the minimum elongation index, proband A **Figure 1**). Nonetheless, these altered shapes or RBC fragility could not be linked to changes in RBC hydration status, or K^+ and Na^+ contents. This questions the relevance of connecting the hydration status and RBC fragility in case of KCNN4 gain-of-function mutations.

Moreover, it reinforces the phenotype distinction between KCNN4 gain-of-function mutations and gain-of-function mutations in PIEZO1. In similar experimental condition (EDTA collecting tubes), PIEZO1-mutated RBC is most of the time dehydrated and ektacytometry or osmotic resistance curves show a leftward shift of the curves compared to control (Rapetti-Mauss et al., 2017; Picard et al., 2019; More et al., 2020; Andolfo et al., 2021). The RBC dehydration linked to PIEZO1 gain-of-function mutations was explained by a more frequent stimulation of KCNN4 (Albuisson et al., 2013), leading to a new RBC volume homeostasis. The role of PIEZO1 in RBC volume homeostasis was confirmed by the observation that mice or zebrafish RBC knockdown for *piezo1* was hyperhydrated compared to WT RBC (Faucherre et al., 2014; Cahalan et al., 2015). Moreover, a patient with combined *PIEZO1* mutations correlated with decreased expression of the protein exhibited overhydrated RBC (Andolfo et al., 2015).

The present data combined with the previous publications reinforce the difficulty to link hemolytic anemia to KCNN4 gain-of-function mutations. The activity of the mutated channel appeared to be most of the time under strict control, kept silent in RBC with one notable exception, the V282M mutation that yields a constitutive K^+ leaky channel that is clearly associated with RBC dehydration (Rivera et al., 2017). Since 2015, and taking into account the new mutations reported

here, 11 different KCNN4 mutations have been identified in independent kindreds (P204R, A279T, S314P, V222L, V282/M or E, H340N, R352H, and delV369-L373) (Andolfo et al., 2015; Glogowska et al., 2015; Rapetti-Mauss et al., 2015; Fermo et al., 2017; Utsugisawa et al., 2017; Picard et al., 2019; Fermo et al., 2020; Andolfo et al., 2021; Mansour-Hendili et al., 2021). According to the different patients studied so far, using the RBC hydration status to diagnose a DHSt associated to KCNN4 mutations is perhaps misleading. The dehydration seems to be a signature of PIEZO1 gain-of-function mutations and exceptionally of KCNN4 mutation, when the mutation converts the channel into a constitutive K^+ leak (the V282M mutation is the only one documented so far). Nonetheless, the presence of a gain-of-function mutated Gardos channel in RBC can dramatically impair RBC viability by a mechanism that remains to be identified. This fragility might involve other KCNN4 functions than permeability or require additional events. The susceptibility for a given KCNN4 gain-of-function mutation to lead to hemolysis appears more dramatic in early life, which is a classical feature of constitutional RBC membrane hemolytic anemia. More experimental data will be needed to better understand the physiological role of KCNN4 and how the mutations alter its function in RBC.

DATA AVAILABILITY STATEMENT

The data presented in the study are deposited in the SRA repository, accession number PRJNA853732.

ETHICS STATEMENT

The studies involving human participants were reviewed and approved by Comité de protection des personnes Ile de France. Written informed consent to participate in this study was provided by the participants' legal guardian/next of kin.

AUTHOR CONTRIBUTIONS

BA, LDN, MM, RR-M, OF, LDC, and HG did the experiments on blood samples. SJ and CE performed the bioinformatic analysis of the channel. AL supervised the calcium fluorometry. AB, CT, JD, and AP were the clinicians who followed the patients. All the authors analyzed the data and reviewed the manuscript.

ACKNOWLEDGMENTS

The authors are extremely grateful to the patients and their parents who contributed to this research by providing blood samples during the time course of their medical care. We thank the LabEx GR-Ex that sponsored the clinical study (Clinical Trials.gov reference: NCT03541525). All patients having given their informed consent were eligible and inclusion samples were collected prospectively.

REFERENCES

Abraham, M. J., Murtola, T., Schulz, R., Páll, S., Jeremy, C., and Hess, S. B. (2015). GROMACS: High Performance Molecular Simulations through Multi-Level Parallelism from Laptops to Supercomputers. *SoftwareX* 1-2, 19–25. doi:10.1016/j.softx.2015.06.001

Albuisson, J., Murthy, S. E., Bandell, M., Coste, B., Louis-Dit-Picard, H., Mathur, J., et al. (2013). Dehydrated Hereditary Stomatocytosis Linked to Gain-Of-Function Mutations in Mechanically Activated PIEZO1 Ion Channels. *Nat. Commun.* 4, 1884. doi:10.1038/ncomms2899

Amendola, L. M., Jarvik, G. P., Leo, M. C., McLaughlin, H. M., Akkari, Y., Amaral, M. D., et al. (2016). Performance of ACMG-AMP Variant-Interpretation Guidelines Among Nine Laboratories in the Clinical Sequencing Exploratory Research Consortium. *Am. J. Hum. Genet.* 99, 247. doi:10.1016/j.ajhg.2016.06.001

Andolfo, I., Alper, S. L., De Franceschi, L., Auriemma, C., Russo, R., De Falco, L., et al. (2013). Multiple Clinical Forms of Dehydrated Hereditary Stomatocytosis Arise from Mutations in PIEZO1. *Blood* 121, 3925–3935. doi:10.1182/blood-2013-02-482489

Andolfo, I., Martone, S., Rosato, B. E., Marra, R., Gambale, A., Forni, G. L., et al. (2021). Complex Modes of Inheritance in Hereditary Red Blood Cell Disorders: A Case Series Study of 155 Patients. *Genes. (Basel)* 12, 958. Epub 20210623. doi:10.3390/genes12070958

Andolfo, I., Russo, R., Manna, F., Shmukler, B. E., Gambale, A., Vitiello, G., et al. (2015). Novel Gardos Channel Mutations Linked to Dehydrated Hereditary Stomatocytosis (Xerocytosis). *Am. J. Hematol.* 90, 921–926. doi:10.1002/ajh.24117

Badens, C., and Guizouarn, H. (2016). Advances in Understanding the Pathogenesis of the Red Cell Volume Disorders. *Br. J. Haematol.* 174, 674–685. Epub 2016/06/29. doi:10.1111/bjh.14197

Baux, D., Van Goethem, C., Ardouin, O., Guignard, T., Bergougnoux, A., Koenig, M., et al. (2021). MobiDetails: Online DNA Variants Interpretation. *Eur. J. Hum. Genet.* 29, 356–360. Epub 20201107. doi:10.1038/s41431-020-00755-z

Brugnara, C., de Franceschi, L., and Alper, S. L. (1993). Inhibition of Ca(2+)-dependent K+ Transport and Cell Dehydration in Sickle Erythrocytes by Clotrimazole and Other Imidazole Derivatives. *J. Clin. Invest.* 92, 520–526. doi:10.1172/jci116597

Cahalan, S. M., Lukacs, V., Ranade, S. S., Chien, S., Bandell, M., and Patapoutian, A. (2015). Piezo1 Links Mechanical Forces to Red Blood Cell. *Elife* 4, e07370. doi:10.7554/eLife.07370

Caulier, A., Jankovsky, N., Demont, Y., Ouled-Haddou, H., Demagny, J., Guitton, C., et al. (2020). PIEZO1 Activation Delays Erythroid Differentiation of Normal and Hereditary Xerocytosis-Derived Human Progenitor Cells. *Haematologica* 105 (3), 610–622. doi:10.3324/haematol.2019.218503

Coste, B., Xiao, B., Santos, J. S., Syeda, R., Grandl, J., Spencer, K. S., et al. (2012). Piezo Proteins Are Pore-Forming Subunits of Mechanically Activated Channels. *Nature* 483, 176–181. doi:10.1038/nature10812

Crooks, G. E., Hon, G., Chandonia, J. M., and Brenner, S. E. (2004). WebLogo: a Sequence Logo Generator. *Genome Res.* 14, 1188–1190. doi:10.1101/gr.849004

Da Costa, L., Suner, L., Galimand, J., Bonnel, A., Pascreau, T., Couque, N., et al. (2016). Diagnostic Tool for Red Blood Cell Membrane Disorders: Assessment of a New Generation Ektacytometer. *Blood Cells Mol. Dis.* 56, 9–22. Epub 20150916. doi:10.1016/j.bcmd.2015.09.001

Danielczok, J. G., Terriac, E., Hertz, L., Petkova-Kirova, P., Lautenschläger, F., Laschke, M. W., et al. (2017). Red Blood Cell Passage of Small Capillaries Is Associated with Transient Ca. *Front. Physiol.* 8, 979. Epub 2017/12/05. doi:10.3389/fphys.2017.00979

De Franceschi, L., Saadane, N., Trudel, M., Alper, S. L., Brugnara, C., and Beuzard, Y. (1994). Treatment with Oral Clotrimazole Blocks Ca(2+)-Activated K+ Transport and Reverses Erythrocyte Dehydration in Transgenic SAD Mice. A Model for Therapy of Sickle Cell Disease. *J. Clin. Invest.* 93, 1670–1676. doi:10.1172/jci117149

Dyrda, A., Cytlak, U., Ciuraszkiewicz, A., Lipinska, A., Cueff, A., Bouyer, G., et al. (2010). Local Membrane Deformations Activate Ca^{2+}-dependent K^+ and Anionic Currents in Intact Human Red Blood Cells. *PLoS One* 5 (2), e9447. doi:10.1371/journal.pone.0009447

Faucherre, A., Kissa, K., Nargeot, J., Mangoni, M. E., and Jopling, C. (2014). Piezo1 Plays a Role in Erythrocyte Volume Homeostasis. *Haematologica* 99, 70–75. doi:10.3324/haematol.2013.086090

Fermo, E., Bogdanova, A., Petkova-Kirova, P., Zaninoni, A., Marcello, A., Makhro, A., et al. (2015). Gardos Channel Mutation Is Associated with Hereditary Dehydrated Stomatocytosis: a Complex Channelopathy. *Blood* 126, 3333. doi:10.1182/blood.v126.23.3333.3333

Fermo, E., Bogdanova, A., Petkova-Kirova, P., Zaninoni, A., Marcello, A. P., Makhro, A., et al. (2017). 'Gardos Channelopathy': a Variant of Hereditary Stomatocytosis with Complex Molecular Regulation. *Sci. Rep.* 11 (7), 1744. Epub 20170511. doi:10.1038/s41598-017-01591-w

Fermo, E., Monedero-Alonso, D., Petkova-Kirova, P., Makhro, A., Pérès, L., Bouyer, G., et al. (2020). Gardos Channelopathy: Functional Analysis of a Novel KCNN4 Variant. *Blood Adv.* 12 22 (4), 6336–6341. doi:10.1182/bloodadvances.2020003285

Flatt, J. F., and Bruce, L. J. (2018). The Molecular Basis for Altered Cation Permeability in Hereditary Stomatocytic Human Red Blood Cells. *Front. Physiol.* 9, 367. Epub 2018/04/16. doi:10.3389/fphys.2018.00367

Gallagher, P. G. (2017). Disorders of Erythrocyte Hydration. *Blood* 12 (130), 2699–2708. Epub 2017/10/19. doi:10.1182/blood-2017-04-590810

Gárdos, G., Szász, I., and Sarkadi, B. (1977). Effect of Intracellular Calcium on the Cation Transport Processes in Human Red Cells. *Acta Biol. Med. Ger.* 36, 823–829.

Garneau, L., Klein, H., Banderali, U., Longpré-Lauzon, A., Parent, L., and Sauvé, R. (2009). Hydrophobic Interactions as Key Determinants to the KCa3.1 Channel Closed Configuration. An Analysis of KCa3.1 Mutants Constitutively Active in Zero Ca^{2+}. *J. Biol. Chem.* 284, 389–403. doi:10.1074/jbc.m805700200

Girodon, F., Garçon, L., Bergoin, E., Largier, M., Delaunay, J., Fénéant-Thibault, M., et al. (2008). Usefulness of the Eosin-5'-Maleimide Cytometric Method as a First-Line Screening Test for the Diagnosis of Hereditary Spherocytosis: Comparison with Ektacytometry and Protein Electrophoresis. *Br. J. Haematol.* 140, 468–470. Epub 20071219. doi:10.1111/j.1365-2141.2007.06944.x

Glogowska, E., Lezon-Geyda, K., Maksimova, Y., Schulz, V. P., and Gallagher, P. G. (2015). Mutations in the Gardos Channel (KCNN4) Are Associated with Hereditary Xerocytosis. *Blood* 126, 1281–1284. doi:10.1182/blood-2015-07-657957

Glogowska, E., Schneider, E. R., Maksimova, Y., Schulz, V. P., Lezon-Geyda, K., Wu, J., et al. (2017). Novel Mechanisms of PIEZO1 Dysfunction in Hereditary Xerocytosis. *Blood* 10130, 1845–1856. Epub 2017/07/17. doi:10.1182/blood-2017-05-786004

Gnanasambandam, R., Bae, C., Gottlieb, P. A., and Sachs, F. (2015). Ionic Selectivity and Permeation Properties of Human PIEZO1 Channels. *PLoS One* 10, e0125503. doi:10.1371/journal.pone.0125503

Grygorczyk, R., and Mohandas, N. (2015). More Than One Way to Shrink. *Blood* 126, 1263–1264. doi:10.1182/blood-2015-07-657916

Ji, T., Corbalán-García, S., and Hubbard, S. R. (2018). Crystal Structure of the C-Terminal Four-Helix Bundle of the Potassium Channel KCa3.1. *PLoS One* 13, e0199942. Epub 2018/06/28. doi:10.1371/journal.pone.0199942

Kopanos, C., Tsiolkas, V., Kouris, A., Chapple, C. E., Albarca Aguilera, M., Meyer, R., et al. (2019). VarSome: the Human Genomic Variant Search Engine. *Bioinformatics* 35, 1978–1980. doi:10.1093/bioinformatics/bty897

Lee, C. H., and MacKinnon, R. (2018). Activation Mechanism of a Human SK-Calmodulin Channel Complex Elucidated by Cryo-EM Structures. *Science* 360, 508–513. doi:10.1126/science.aas9466

Maher, A. D., and Kuchel, P. W. (2003). The Gárdos Channel: a Review of the Ca2+-Activated K+ Channel in Human Erythrocytes. *Int. J. Biochem. Cell. Biol.* 35, 1182–1197. doi:10.1016/s1357-2725(02)00310-2

Mansour-Hendili, L., Egée, S., Monedero-Alonso, D., Bouyer, G., Godeau, B., Badaoui, B., et al. (2021). Multiple Thrombosis in a Patient with Gardos Channelopathy and a New KCNN4 Mutation. *Am. J. Hematol.* 96, E318–E321. Epub 20210602. doi:10.1002/ajh.26245

Mohandas, N., and Chasis, J. A. (1993). Red Blood Cell Deformability, Membrane Material Properties and Shape: Regulation by Transmembrane, Skeletal and Cytosolic Proteins and Lipids. *Semin. Hematol.* 30, 171–192.

Mohandas, N., and Gallagher, P. G. (2008). Red Cell Membrane: Past, Present, and Future. *Blood. Nov.* 112, 3939–3948. doi:10.1182/blood-2008-07-161166

More, T. A., Dongerdiye, R., Devendra, R., Warang, P. P., and Kedar, P. S. (2020). Mechanosensitive Piezo1 Ion Channel Protein (PIEZO1 Gene): Update and Extended Mutation Analysis of Hereditary Xerocytosis in India. *Ann. Hematol.* 99, 715–727. Epub 20200228. doi:10.1007/s00277-020-03955-1

Olsson, M. H., Søndergaard, C. R., Rostkowski, M., and Jensen, J. H. (2011). PROPKA3: Consistent Treatment of Internal and Surface Residues in Empirical pKa Predictions. *J. Chem. Theory Comput.* 7, 525–537. Epub 20110106. doi:10.1021/ct100578z

Picard, V., Guitton, C., Mansour-Hendili, L., Jondeau, B., Bendélac, L., Denguir, M., et al. (2021). Rapid Gardos Hereditary Xerocytosis Diagnosis in 8 Families Using Reticulocyte Indices. *Front. Physiol.* 11, 602109. doi:10.3389/fphys.2020.602109

Picard, V., Guitton, C., Thuret, I., Rose, C., Bendelac, L., Ghazal, K., et al. (2019). Clinical and Biological Features in PIEZO1-Hereditary Xerocytosis and Gardos-Channelopathy: A Retrospective Series of 126 Patients. *Haematologica* 104 (8), 1554–1564. doi:10.3324/haematol.2018.205328

Rapetti-Mauss, R., Lacoste, C., Picard, V., Guitton, C., Lombard, E., Loosveld, M., et al. (2015). A Mutation in the Gardos Channel Is Associated with Hereditary Xerocytosis. *Blood* 126, 1273–1280. doi:10.1182/blood-2015-04-642496

Rapetti-Mauss, R., Picard, V., Guitton, C., Ghazal, K., Proulle, V., Badens, C., et al. (2017). Red Blood Cell Gardos Channel (KCNN4): the Essential Determinant of Erythrocyte Dehydration in Hereditary Xerocytosis. *Haematologica* 102, e415–e418. Epub 2017/06/15. doi:10.3324/haematol.2017.171389

Rapetti-Mauss, R., Soriani, O., Vinti, H., Badens, C., and Guizouarn, H. (2016). Senicapoc: a Potent Candidate for the Treatment of a Subset of Hereditary Xerocytosis Caused by Mutations in the Gardos Channel. *Haematologica* 101, e431–e435. Epub 2016/07/21. doi:10.3324/haematol.2016.149104

Richards, S., Aziz, N., Bale, S., Bick, D., Das, S., Gastier-Foster, J., et al. (2015). Standards and Guidelines for the Interpretation of Sequence Variants: a Joint Consensus Recommendation of the American College of Medical Genetics and Genomics and the Association for Molecular Pathology. *Genet. Med.* 17, 405–424. Epub 20150305. doi:10.1038/gim.2015.30

Rivera, A., Vandorpe, D., Gallagher, D., Fikry, C., Kuypers, F., Brugnara, C., et al. (2017). Erythrocytes from Hereditary Xerocytosis Patients Heterozygous for KCNN4 V282M Exhibit Increased Spontaneous Gardos Channel-like Activity Inhibited by Senicapoc. *Am. J. Hematol.* 92 (6), E108–E110. Epub 2017 Apr 29. doi:10.1002/ajh.24716

Rogers, S., and Lew, V. L. (2021). Up-down Biphasic Volume Response of Human Red Blood Cells to PIEZO1 Activation during Capillary Transits. *PLoS Comput. Biol.* 17, e1008706. Epub 20210303. doi:10.1371/journal.pcbi.1008706

Sievers, F., Wilm, A., Dineen, D., Gibson, T. J., Karplus, K., Li, W., et al. (2011). Fast, Scalable Generation of High-Quality Protein Multiple Sequence Alignments Using Clustal Omega. *Mol. Syst. Biol.* 7, 539. Epub 20111011. doi:10.1038/msb.2011.75

Søndergaard, C. R., Olsson, M. H., Rostkowski, M., and Jensen, J. H. (2011). Improved Treatment of Ligands and Coupling Effects in Empirical Calculation and Rationalization of pKa Values. *J. Chem. Theory Comput.* 7, 2284–2295. Epub 20110609. doi:10.1021/ct200133y

Syeda, R., Xu, J., Dubin, A. E., Coste, B., Mathur, J., Huynh, T., et al. (2015). Chemical Activation of the Mechanotransduction Channel Piezo1. *Elife* 4, e07369. doi:10.7554/eLife.07369

Utsugisawa, T., Iwasaki, T., Aoki, T., Okamoto, Y., Kawakami, T., Ogura, H., et al. (2017). The Flow Cytometric Osmotic Fragility Test Is an Effective Screening Method for Dehydrated Hereditary Stomatocytosis. *Blood* 130, 929. doi:10.1182/blood.v130.suppl_1.929.929

Waldstein, S., Arnold-Croop, S., Carrel, L., and Eyster, M. E. (2021). Diagnosing Dehydrated Hereditary Stomatocytosis Due to a KCNN4 Gardos Channel Mutation: Understanding Challenges through Study of a Multi-Generational Family. *eJHaem* 2, 485–487. Epub 13 july 2021. doi:10.1002/jha2.267

Webb, B., and Sali, A. (2016). Comparative Protein Structure Modeling Using MODELLER. *Curr. Protoc. Bioinforma.* 54, 5.6.1–5.6.37. Epub 20160620. doi:10.1002/cpps.20

Wu, E. L., Cheng, X., Jo, S., Rui, H., Song, K. C., Dávila-Contreras, E. M., et al. (2014). CHARMM-GUI Membrane Builder toward Realistic Biological Membrane Simulations. *J. Comput. Chem.* 35, 1997–2004. Epub 20140807. doi:10.1002/jcc.23702

Zarychanski, R., Schulz, V. P., Houston, B. L., Maksimova, Y., Houston, D. S., Smith, B., et al. (2012). Mutations in the Mechanotransduction Protein PIEZO1 Are Associated with Hereditary Xerocytosis. *Blood* 120, 1908–1915. doi:10.1182/blood-2012-04-422253

Conflict of Interest: The authors declare that the research was conducted in the absence of any commercial or financial relationships that could be construed as a potential conflict of interest.

Publisher's Note: All claims expressed in this article are solely those of the authors and do not necessarily represent those of their affiliated organizations, or those of the publisher, the editors, and the reviewers. Any product that may be evaluated in this article, or claim that may be made by its manufacturer, is not guaranteed or endorsed by the publisher.

Discussion générale

Variabilité et limites des outils

Variabilité

La Xérocytose Héréditaire est caractérisée par une forte hétérogénéité au niveau clinique mais aussi au niveau cellulaire. Notamment, les mutations de PIEZO1 sont plus souvent associées à une déshydratation des GR contrairement aux mutations de KCNN4. De plus, les patients porteurs d'une même mutation peuvent avoir des GR avec un phénotype différent, dû à la variabilité interindividuelle. D'autre part, lorsque l'on compare des prélèvements effectués chez un même patient, à plusieurs mois ou années d'intervalle, on peut parfois noter des différences de comportement des GR. Enfin, nous avons également observé une forte variabilité des GR de témoins, ce qui peut parfois compliquer l'interprétation de nos résultats.

Il est important de faire la distinction entre les variabilités évoquées ci-dessus et les facteurs extérieurs qui pourraient influer sur nos mesures. Les conditions de prélèvements (tube EDTA, sans Ca^{2+}), le temps d'acheminement vers notre laboratoire (24h, 48, 72h) ou la température pendant le transport sont autant de facteurs, potentiellement à l'origine d'une variabilité (Minetti et al., 2013). L'utilité du prélèvement témoin est d'avoir un contrôle sur ces derniers. Une solution serait d'utiliser ces facteurs externes en dénominateur commun et de comparer uniquement les prélèvements effectués et acheminés dans les mêmes conditions.

En revanche, même si les facteurs externes sont identiques, on peut parfois mesurer de fortes différences entre les témoins. Cela rejoint la notion de variabilité interindividuelle qui est indépendante de la maladie. Chaque témoin est par définition asymptomatique mais nos mesures peuvent parfois déceler de légères anomalies des GR lorsque nous les comparons à l'ensemble des témoins (déshydratation, contenu ionique altéré, réponse calcique anormale). Ceci peut s'expliquer notamment par l'existence de traits thalassémique, beta ou alpha (forme hétérozygote de la maladie) répandus dans le bassin méditerranéen. Dans ce cas particulier, les GR plus petits sont complètement viables et ne donnent pas lieu à une anémie mais auront des contenus en eau plus faibles. Par exemple le cas des témoins acheminés avec les prélèvements du patient PIEZO1 G782S-R808Q-V598M ou muté KCNN4 G50R montre bien une diminution importante du contenu en eau par rapport à la moyenne ce qui rend difficile la comparaison avec le patient. Il se pourrait alors que ces témoins soient porteurs d'une anomalie non décelée. A l'inverse, certains témoins auront un contenu en eau plus important comme c'est le cas du témoin de PIEZO1 R2491-E2492 dup et KCNN4 V369-K373 del.

De plus les GR reflètent les 3 à 4 dernier mois avant prélèvement du sang. La durée de vie moyenne des GR étant de 120 jours, les stress environnementaux qu'ils subissent pendant cet intervalle de temps exerceront une influence directe sur nos résultats. Par exemple, un séjour à la montagne de quelques semaines ou encore une alimentation modifiée sont suffisants pour modifier les propriétés des GR (Bogdanova et al., 2020).

Un autre exemple de variabilité interindividuelle concerne l'âge des patients, qui sont souvent des enfants. Il est tout à fait envisageable qu'un enfant en phase de croissance, qui a des besoins énergétiques plus importants, ait des GR avec un métabolisme et un comportement différent d'un adulte. D'autre part, il est évidemment impossible d'avoir des enfants volontaires sains et donc les mesures sur lesquelles nous définissons nos standards sont toutes issus de témoins adultes. Nous ne pouvons donc pas exclure que les mesures réalisées sur les GR d'un enfant ne correspondent pas exactement aux mesures faites chez un adulte.

Un exemple frappant de variabilité interindividuelle concerne la mutation PIEZO1 R2456H portée par deux patients différents (P et Y). Les GR des deux patients se comportent de façon anormale mais les mesures que nous faisons divergent de façon surprenante. Cet exemple montre parfaitement que l'effet des mutations de PIEZO1 (ou KCNN4) se manifestent différemment selon l'individu.

Alors comment savoir si une différence entre un témoin et un patient est due à un facteur externe (acheminement du sang, etc…), à des variabilités interindividuelles ou à une réelle pathogénicité de la mutation ? Il n'est pas toujours possible d'avoir accès à d'autre prélèvements pour confirmer les observations. C'est une limitation importante qui peut complexifier l'étude des GR humain, notamment dans le cas de maladies rare comme la XH.

Limites des outils

L'interprétation des mesures réalisées sur des GR doit être faite avec précaution. L'étude de ces cellules est soumise à de nombreux artefact qui peuvent grandement fausser les résultats obtenus (Minetti et al., 2013). On peut citer : (1) la température qui influe sur les contenus hydriques et ioniques notamment en modifiant l'activité des transporteurs ATP dépendants, (2) la composition des milieux utilisés pour les différentes mesures (présence de glucose, Ca^{2+}, etc…) ou (3) les outils de mesures utilisés.

Concernant la limite des outils, je parlerai ici des mesures de fluorescence calcique des GR. C'est un outil extrêmement intéressant car nous avons accès à des cinétiques rapides et non à un état d'équilibre mais les résultats sont parfois difficilement interprétables. Les mesures de Ca^{2+} dépendent d'une sonde fluorescente (Fluo4-AM) dont la fluorescence est mesurée par cytomètre en flux. La charge

des GR avec cette sonde est la principale étape limitante et dépend du nombre de GR. En pratique, lors du pipetage du culot de GR, il est impossible de savoir précisément combien de GR sont présents dans un volume donné. Par exemple, des GR plus petits occuperont moins d'espace et seront plus nombreux dans un même volume. Le cytomètre en flux est un bon outil pour contrôler le nombre de GR, qui est directement corrélé au flux (évènements/secondes). La fluorescence calcique que l'on mesure dépend directement de la charge de Fluo4-AM et donc du nombre de sondes dans chaque GR. Lorsque l'on regarde la fluorescence basale calcique de GR témoins, la variabilité est assez faible avec une moyenne±SD de 402.2±80.35 a.u.

Après stimulation on observe de fortes variations (yoda1 t20 = 5551±2065 ; vanadate t20 = 1614±966.1 ; yoda1 + vanadate = 9752±2468). Le yoda1 induit systématiquement une augmentation massive de la fluorescence quasi instantanée au moment où les GR sont ajoutés au milieu. Dans chaque figure où est représentée la mesure de fluorescence calcique en fonction du temps, après ajout de yoda1, le temps 0 min correspond à la fluorescence basale en l'absence de yoda1. Ensuite un temps (0.2 min) est utilisé pour la première valeur de fluorescence qui est lue en présence de yoda1. En pratique, avec un cytomètre en flux, il est impossible d'avoir une mesure au moment où le yoda1 est ajouté. La mesure de fluorescence est réalisée au minimum 3 secondes après ajout du yoda1. C'est une limite puisque nous n'avons pas accès à la phase exponentielle d'augmentation de la fluorescence qui correspond à ces 3 secondes incompressibles (le temps entre l'ajout des GR dans le milieu avec yoda1, le placement du tube dans la machine et la lecture de la fluorescence). Cette phase pourrait nous apporter davantage d'information sur le fonctionnement de yoda1 et par extension de PIEZO1. Il faut noter néanmoins, que l'on observe une assez bonne corrélation entre la déshydratation et l'augmentation de la perméabilité calcique pour les mutations PIEZO1 V598M et S1994Y. De la même façon pour les mutations KCNN4 où nous n'observons pas de déshydratation, la perméabilité calcique n'est pas altérée. Ce sont des résultats rassurants qui montre que cet outil de mesure du Ca^{2+} est fiable mais nécessitera tout de même des optimisations.

Les Western Blot que nous avons réalisés à partir de ghosts de GR révèlent parfois des différences importantes d'expression de certaines protéines entre les patients et témoins. Ces différences sont intéressantes mais le fait que nous ne pouvons pas systématiquement reproduire le résultat avec un autre prélèvement, rend l'interprétation difficile. On ne peut pas exclure des biais car chaque étape de cette technique peut s'avérer limitante :

1. Lyse hypo-osmotique des GR où du matériel protéique peut être perdu.
2. Solubilisation des ghosts des GR. Les protéines membranaires sont très sensibles au tampon de solubilisation utilisé.
3. Migration, transfert, blocage.

4. Spécificité des anticorps.

Concernant PIEZO1, le poids moléculaire que nous mesurons (255kDa) semble être cohérent avec le poids attendu (233-286kDa). Cependant, parfois nous allons observer une absence complète d'expression de PIEZO1 alors que le GR réagi bien au yoda1 avec une perte de K^+, un gain de Na^+ et de Ca^{2+} (Figure 17). Comme discuté dans la partie résultat, cette perte de PIEZO1 pourrait provenir de l'étape 1 mentionnée ci-dessus. Il est important de rappeler que la transformation de GR en ghost passe par une lyse hypo-osmotique qui peut induire des pertes du matériel protéique, potentiellement membranaire. Toutefois, il parait improbable qu'une protéine membranaire spécifique soit perdue durant le processus de lyse et que d'autres protéines ne le soient pas.
Concernant la PMCA et KCNN4 les résultats sont parfois surprenants. Avec la mutation PIEZO1 R2491-E2492 dup on observe une baisse importante des niveaux de KCNN4 qui est corrélée à une hyperhydratation des GR du patient. En revanche dans le cas de la mutation KCNN4 H340N on observe une quasi-absence de PMCA alors que les GR sont hyperhydratés. Dans ce cas précis, l'absence de PMCA devrait favoriser un état de déshydratation car le Ca^{2+} intracellulaire est moins bien régulé. Cela montre que les résultats de WB doivent être interprétés avec beaucoup de précaution.

Dans le cas où un défaut de la membrane du GR est suspecté et que toutes autres causes d'anémies ont pu être exclues, la technique de NGS (Next generation sequencing) est utilisée. Cette technique, dans ce cas, est ciblée sur 93 gènes codant pour des protéines étant impliquées dans diverses altérations de la membrane du GR et permet de déceler des mutations. Parmi ces gènes figurent *PIEZO1* et *KCNN4* dont les mutations identifiées doivent être caractérisées pour définir la cause de la pathologie. Cependant on ne corrèle pas toujours la présence d'une mutation PIEZO1 ou KCNN4 avec un défaut de perméabilité du GR. Dans ce cas, soit la mutation identifiée est fortuite et n'a pas de rôle dans la pathologie, soit elle a un rôle qui n'est pas encore défini. On peut imaginer des rôles de structure de PIEZO1 et KCNN4 dont les mutations pourraient être à l'origine de changements morphologiques indépendants de leur rôle de canaux ioniques. De plus, toutes les protéines de membranes ne sont pas ciblées par cette technique NGS. C'est notamment le cas de la PMCA qui est absente des gènes cibles.

Différences entre les mutations de PIEZO1 et KCNN4.

Observations

Nous n'avons pas observé de phénotype de déshydration des GR avec les mutations KCNN4 étudiées (G50R, H340N, V222L, V369-K373 del). Elles s'ajoutent aux 5 mutations de KCNN4 déjà caractérisées précédemment: V282M, V282E, S314P, A322V et R352H (Andolfo et al., 2015; Fermo et al., 2020, 2017; Glogowska et al., 2015; Mansour-Hendili et al., 2021; Rapetti-Mauss et al., 2015; Rivera et al., 2017). La mutation V282E a été identifiée à posteriori et son effet sur la perméabilité des GR des patients n'a jamais été mesurée.

- S314P est une mutation récemment identifiée et caractérisée (Fermo et al., 2020). Les GR avec la mutation S314P ne montrent pas de signes clairs de déshydratation malgré un phénotype gain de fonction sur l'activité de KCNN4.

- A322V est également une mutation récemment identifiée et caractérisée (Mansour-Hendili et al., 2021). Cette mutation induit une augmentation de la sensibilité calcique de KCNN4, mesuré avec la méthode CCCP (carbonylcyanide-m-chloro-phenyl-hydrazone, mesure du pH pour déterminer le potentiel de membrane). En revanche, la mesure des contenus hydriques n'a pas montré de déshydratation mais une surface projetée plus importante des GR mutés a été mesurée en microscopie.

- R352H est une des première mutation identifiée sur KCNN4 (Andolfo et al., 2015; Fermo et al., 2017; Rapetti-Mauss et al., 2015). Dans un premier temps, Rapetti-Mauss *et al.* montrent que la RO est augmentée uniquement lorsque les GR mutés sont incubés à 37°C pendant 24h de façon à dépléter les stocks d'ATP, associée à une perte de K^+. Ils montrent également que KCNN4 R352H a une sensibilité calcique augmentée (EC50 0.21µM R352H vs 1µM WT). Ensuite Andolfo *et al.* montrent que la RO est normale mais l'Ektacytométrie est légèrement atypique. Cette RO a été faite après 24h d'incubation à 4°C et donc les stocks d'ATP étaient préservés. Enfin, chez une autre famille, Fermo *et al.* montrent que la RO est normale de même que l'Ektacytométrie mais l'amplitude du courant de KCNN4 R352H est augmentée.

- V282M est l'exception qui confirme la règle puisque c'est la seule mutation de KCNN4 associée clairement à une déshydratation avec une RO augmentée et une Ektacytométrie décalée vers la gauche (Andolfo et al., 2015; Rivera et al., 2017). Cependant, l'effet de V282M est plus complexe avec des comportements de GR XH suggérant une perte de fonction lorsque

ceux-ci sont exposés à une augmentation de la concentration calcique ou après traitement avec du vanadate (Rivera et al., 2019).

L'étude rétrospective de *Picard et al.* sur un large panel de patient avec des mutation PIEZO1 ou KCNN4 confirme cette tendance (Picard et al., 2019). On constate que les mutations de KCNN4 retrouvées dans la XH ne sont pas associées à une déshydratation et ont un profil d'Ektacytométrie normal, malgré une anémie plus sévère que les patient PIEZO1. Bien que KCNN4 soit l'effecteur final de la déshydration, si la concentration calcique n'est pas suffisante il ne s'activera pas. La mutation V282M est la seule induisant un phénotype clair de déshydratation. Dans ce cas, KCNN4 devient pratiquement un canal de fuite et n'est donc plus soumis à une régulation calcique (Rapetti-Mauss et al., 2016). La mutation R352H provoque une déshydratation uniquement après 24H 37°C. Les mutations de KCNN4 décrites dans cette thèse ne permettent pas d'observer d'anomalie de perméabilité des GR, d'après nos mesures (G50R, V222L, S314P, H340N, V369-K373 del) malgré un phénotype gain de fonction dans les cellules HEK293T. Étant donné la difficulté à réaliser des mesures électrophysiologiques de KCNN4 dans les GR, ces mesures sont souvent réalisées dans un modèle d'expression hétérologue. L'études de mutations, faites dans un autre modèle, peut ne pas refléter exactement la réalité du GR (voir article Yamaguchi et al. 2022).

Explications

Le fait que nous n'observons pas d'effet dans le GR des mutations de KCNN4 malgré un effet évident sur le canal peut être expliqué de différentes façon :

1. Le biais du survivant. L'absence de déshydratation mesurable des GR n'est pas forcément synonyme d'absence d'effet des mutations de KCNN4. La population de GR est grandement hétérogène aussi bien chez les témoins sains que les patients (Bogdanova et al., 2020). Cette hétérogénéité a plusieurs origines dont notamment (1) l'âge des GR, (2) le fait que tous les GR ne soient pas issus d'un même précurseur érythroïde et (3) les stress environnementaux subis par un GR pendant ses 120 jours de vie. Il existe donc des populations de GR dont les caractéristiques ne sont pas les mêmes. Ainsi, il est possible qu'uniquement une, ou plusieurs, populations spécifiques de GR soient affectées par des mutations gain de fonction de KCNN4. Dès l'apparition de conditions favorables à l'activation de KCNN4, les GR pourraient être déshydratés et lysés de façon très rapide. De cette façon, au moment du prélèvement, ce ne sont que les GR viables, où KCNN4 n'est pas activable, qui sont récupérés et que l'on utilise pour mesurer les contenus hydriques et ioniques : c'est le biais du survivant. En revanche, un contre argument important est que nous observons des altérations de la morphologie des GR sur frottis sanguin.

Cela suggère que de nombreux GR sont affectés mais restent viables jusqu'à la survenue d'un évènement déclencheur de l'hémolyse.

2. Contamination par des Réticulocytes. Une augmentation du nombre de réticulocytes est fréquente en cas d'anémie hémolytique compensée. Ces cellules étant plus grosses que les GR, un nombre important de ces dernières pourrait masquer une déshydratation des GR lors de nos mesures. Néanmoins, il a été montré que les mutations de KCNN4 entrainaient une diminution de la taille des réticulocytes contrairement aux mutation PIEZO1 (Picard et al., 2020). Dans cette étude, en cas de mutation de KCNN4 le VCM (volume corpusculaire moyen) des réticulocytes est paradoxalement plus faible que celui des GR. La méthode de mesure du VCM est différent d'une mesure de contenu en eau. Il est alors difficile de parler de déshydratation des réticulocytes en cas de mutation KCNN4. Un rôle de KCNN4 dans la structure de la membrane et du cytosquelette serait à privilégier.

3. L'âge du patient qui rejoint partiellement le point numéro 1. Il est possible que les effets des mutations de KCNN4 sur les GR soient visibles uniquement sur une courte période de vie du patient en particulier dans la période péri-natale qui est souvent le moment où les mutations sont diagnostiquées.

4. Il faut un influx calcique suffisant pour activer KCNN4. Il n'est pas impossible que l'influx calcique provoqué par l'ouverture d'un PIEZO1 sauvage, soit trop faible pour un KCNN4 muté et induire une déshydratation.

Du côté de PIEZO1, pourquoi ses mutations sont-elles plus souvent associées à une déshydratation des GR que les mutations de KCNN4 ? Une explication intéressante provient du rôle de PIEZO1 dans le métabolisme, mis en évidence à de nombreuses reprises :

- Dans les GR soumis à déformation, le métabolisme glycolytique est augmenté, avec une augmentation de la consommation d'ATP (Kuchel and Shishmarev, 2017).
- Chez les patients mutés PIEZO1 dans la XH, une diminution de la quantité de 2,3DPG, une glycolyse augmentée et une hausse de l'affinité de l'Hb pour l'O_2 sont observés (Kiger et al., 2021).
- Enfin une récente analyse protéomique chez des patient XH mutés PIEZO1 a montré que plusieurs processus biologique du GR étaient modifiés (Andolfo et al., 2023). Notamment, ils observent une modification de l'expression de transporteurs ATP dépendants comme la

PCMA1 ou PMCA4. De façon intéressante, ils observent une augmentation de kinases (WNK1 et OSR1) impliqué dans l'activation du cotransport NKCC1 (cf. 4.3.2). Ils montrent également une colocalisation de PIEZO1 et de l'AE1. L'activité de l'AE1 pourrait alors être modulé par la présence de PIEZO1 connu pour altérer son environnement lipidique.

Lorsqu'une mutation gain de fonction touche PIEZO1, elles engendrent une augmentation des perméabilités Ca^{2+}, Na^{+} et K^{+} qui doivent être compensées par une augmentation de l'activité de la PMCA et NaK. Cela se traduit par une consommation accrue d'ATP dont le stock doit être maintenu par une augmentation de la glycolyse. Etant donné l'importance du métabolisme dans la fonction et la survie du GR (cf. Introduction 2.3), une glycolyse trop importante induite par PIEZO1 aura un effet délétère sur la survie du GR. Sur le long terme, ce stress métabolique s'accumule et entraine une déshydratation progressive mais lente qui ne conduit pas forcément à la destruction du GR mais peut le fragiliser. Cette hypothèse permet d'expliquer pourquoi les patients mutés PIEZO1 ont un phénotype de déshydratation important malgré un tableau clinique moins sévère que les patients mutés KCNN4. En effet, contrairement aux mutations de PIEZO1, il est possible que les mutations de KCNN4 entrainent une déshydratation si soudaine et importante que le GR soit directement lysé. Cet évènement pourrait se produire uniquement dans la circulation sanguine et ne serait pas visible ex vivo. Il serait intéressant de comparer l'âge moyens des GR de patient mutés PIEZO1 ou KCNN4. Dans le cas où l'hypothèse de fonctionnement des mutations gains de fonction de PIEZO1 est correcte on s'attendrait à un raccourcissement homogène de l'espérance de vie de tous les GR. En revanche, pour KCNN4, seuls certains GR seraient atteints et l'espérance de vie serait modifiée de façon hétérogène.

Chapitre 2 :

Régulation du canal KCNN4 par la pompe calcique ATP dépendante : PMCA.

Contexte

Ce deuxième chapitre se détache de l'aspect clinique et part d'un constat simple que nous faisons concernant le GR humain : la déshydratation induite par KCNN4 n'est pas directement corrélée à la concentration de Ca^{2+} intracellulaire. Bien que celle-ci augmente drastiquement à la suite d'une activation chimique de PIEZO1, KCNN4 ne s'active pas, et ce à cause d'un contrôle négatif exercé par la pompe calcique ATP dépendante PMCA. D'après nos résultats dans les cellules HEK293T, ce contrôle est indépendant du Ca^{2+} et de l'activité de la PMCA. En revanche il est favorisé par une double interaction : (1) moléculaire, rapprochant KCNN4 et PMCA et (2) fonctionnelle impliquant une régulation inhibitrice de KCNN4 par le domaine C-terminal de la pompe. Ces résultats mettent en lumière un tout nouveau mécanisme de régulation de KCNN4 dans le GR et apporte des éléments de compréhension sur les mécanismes de déshydratation dans la Xérocytose Héréditaire.

Article : Régulation de l'effet Gardos par la pompe calcique : découplage du canal PIEZO1 de la déshydratation érythrocytaire.

"The Ca^{2+}pump sheds new light on Gardos effect: uncoupling PIEZO1 from erythrocyte dehydration."

Benoit Allegrini[1], Morgane Mignotet[1], Olivier Soriani[1], Hélène Guizouarn[1*]

[1]Université Côte d'Azur, CNRS, Inserm, Institut Biologie Valrose, Nice, France.

[*] Corresponding author

Key points

1/ PIEZO1 activity can be uncoupled from red blood cell dehydration.

2/ A new partner in the Gardos effect: KCNN4 is controlled by a molecular interaction with the calcium pump ATP2B4.

Abstract

KCNN4, a Ca^{2+}-activated K^+ channel, is a major modulator of Red Blood Cell (RBC) volume homeostasis. Activation of KCNN4, following Ca^{2+} increase, leads to RBC dehydration, a mechanism known as the "Gardos effect" described seventy years ago. This dehydration is irreversible in human RBC and must be tightly controlled, otherwise hemolysis can occur leading to disease. In this study, we investigated the regulation of KCNN4 activity related to changes in Ca^{2+} homeostasis and demonstrated that KCNN4-mediated dehydration was not correlated to Ca^{2+} level increase. Using electrophysiology, immunoprecipitation, proximity ligation assay, we found that KCNN4 and the Ca^{2+} pump PMCA4b are tightly interacting with each other, allowing the C-terminal domain of PMCA4b to regulate KCNN4 activity, independent of the Ca^{2+} extrusion activity of the pump. Finally, this regulation was not restricted to KCNN4 since we found that KCNN2 was similarly regulated by the calcium pump.

Introduction

KCNN4 is a Ca^{2+}- activated K^+ channel, first described as the Gardos channel in red blood cells (RBC) [1,2]. KCNN4 is an actor of RBC volume homeostasis as its activation by intracellular Ca^{2+} increase induces an irreversible dehydration, the Gardos effect. The identification of PIEZO1[3] in RBC membrane, the non-selective cationic conductance mechanically gated enabled to establish a link between RBC deformation and dehydration. The model is the following, when PIEZO1 opens upon mechanical stimulation, it allows Ca^{2+} entry due to high external to internal Ca^{2+} concentration ratio. This Ca^{2+} increase leads to KCNN4 activation allowing K^+ efflux followed by Cl^- and H_2O resulting in RBC dehydration. This functional coupling between the two channels is the molecular mechanism involved in the rare human disease, hereditary xerocytosis [4,5], where gain of function mutations in PIEZO1 are associated with hyperactivity of KCNN4 and a change in water homeostasis, patients' RBC being dehydrated compared to control RBC [6]. The role of PIEZO1-KCNN4 functional coupling via Ca^{2+}increase in RBC water homeostasis is reinforced by studies on mice RBC KO for *piezo1* that are slightly overhydrated, as well as what is observed in human RBC carrying loss of function mutations in PIEZO1 that have a greater cell volume [7].

While the calcium dependent PIEZO1-KCNN4 functional coupling found RBC disorder, the question of its physiological relevance is still pending. On the basis of PIEZO1-KCNN4 functional coupling, a mechanism linking RBC membrane deformation to water efflux fitting RBC to narrow capillaries and blood stream constraints has been proposed[8]. However, it should be noticed that human RBC are unable to regulate their volume. Meaning once KCl and water are lost through KCNN4 activation, the RBC will remain dehydrated. This change in water homeostasis alters RBC rheological properties

and the activation of KCNN4 is associated with impaired RBC deformability [9]. Computational modeling to investigate the changes experienced by RBC during capillary transit opening PIEZO1 has shown that cell volume changes are infinitesimal and incompatible with a functional role in capillary flow [10,11]. This study suggests that PIEZO1 stimulation in blood flow might not lead to sustained KCNN4 activation. The present study was designed to better understand the regulation of KCNN4 activity in RBC related to changes in Ca^{2+} homeostasis. RBC Ca^{2+} homeostasis relies on the activity of Ca^{2+} channels (such as PIEZO1, TRPV2, TRPC6, VDCC), resulting in intracellular Ca^{2+} increase and Ca^{2+} pump, which effluxes Ca^{2+} utilizing ATP hydrolysis energy (For review [12]). RBC express two different Ca^{2+} ATPases, PMCA4b (encoded by *ATP2B4*) which is the most abundant and PMCA1 (*ATP2B1*) to a lesser extent [13,14].

We investigated the Ca^{2+} dependency of the functional coupling PIEZO1-KCNN4 in RBC and reconstituted the system in HEK293T transfected cells. Our results show that massive intracellular Ca^{2+} increase through PIEZO1 activation did not stimulate KCNN4 in RBC. We show that the activity of KCNN4 is controlled by the Ca^{2+} ATPase PMCA4b through a mechanism involving a molecular interaction between the channel and the C-terminal end of the pump. This control by the Ca^{2+} pump is not restricted to KCNN4 but also observed with another member of the Ca^{2+} dependent K^+ channel family, KCNN2. This is the first characterization of a control of Ca^{2+} dependent K^+ channels by molecular interaction with a Ca^{2+} pump. This mechanism is thought to finely tune KCNN4 activity in RBC where PMCA4b/KCNN4 coupling appears as a new pharmacological target to maintain RBC volume homeostasis.

Methods

Red blood cells:

Fresh venous blood was obtained by venipuncture in EDTA collecting tubes from healthy volunteers.

Na^+, K^+ and water content measurements:

Blood was washed 4 times (800 g, 5 minutes, 4°C, swinging rotor) in Ringer medium containing (in mM): NaCl (145) KCl (5) MgSO4 (2) CaCl2 (1) Hepes/NaOH pH 7.4 (10). Red cell suspension was then incubated at room temperature 25% hematocrit with 0.5 mM ouabain, and Yoda1 (2 µM, Sigma) or vanadate (5 mM) was added alone or with 4 µM Senicapoc (Medchemexpress). A few minutes before sampling time, 400 µl of cell suspension were taken to fill 3 nylon tubes that were centrifuged for 10 minutes at 4°C, 20 000 g at the exact sampling time. The pellet of red cells was extracted and immediately weighted. Then, dry weight was measured after overnight heating (80°C). Water content

was calculated with a correction of 3.64% corresponding to trapped medium between packed cells. Intracellular ions were extracted from dried pellets by overnight incubation at 4°C in 5 ml milliRho water (Millipore). 2% perchloric acid was then added to precipitate proteins, samples were centrifuged 10 minutes 20 000 g and supernatant was collected for Na^+ and K^+ quantification by flame spectroscopy with a Solaar AA spectrometer.

Vanadate stock solution preparation: Na_3VO_4 (Sigma) was solubilized at 100 mM in mQ water pH 10 adjusted with HCl, heated until clear and cooled. Yoda1, Oubain and Senicapoc were prepared in DMSO stock solutions 1000 times concentrated.

Ca^{2+}measurements:

RBC were washed 2 times in Ringer without Ca^{2+} to remove buffy coat by aspiration. 4µl of packed RBC were loaded with 2.5 µl of 1 mM Fluo4 AM stock solution in 500 µl Ringer without Ca^{2+}, 37°C, 30 minutes. The Fluo4 loaded RBC suspension was directly used to quantify intracellular Ca^{2+} concentration (25 µl of RBC suspension in 975 µl Ringer medium (control) or Ringer medium with different drugs (Yoda1: 2 µM, vanadate: 5 mM, 4-Br-A23187 5 µM (Millipore) from stock solution in DMSO 5 mM) by measuring fluorescence with a FACS Fortessa BD. Internal RBC fluorescence was assessed on RBC treated without Fluo4 AM. To avoid any changes in intracellular water content while measuring Ca^{2+} associated fluorescence in presence of Ca^{2+} ionophore 4-Br-A23187 experiments were carried on in high K^+ medium (90 mM KCl+ 55 mM NaCl instead of 145 mM NaCl in Ringer solution) to achieve electro-chemical equilibrium for K^+. The opening of KCNN4 in this medium did not lead to net K^+ movement and there was no dehydration that could alter Ca^{2+} concentration measurements. It was checked that the change in RBC morphology induced by vanadate or Yoda1 addition did not significantly modify RBC fluorescence by doing the experiments in Ringer without Ca^{2+}.

Plasmid constructs:

pcDNA3-hKCNN4-HA was a kind gift of Len Kaczmarek laboratory. pcDNA3-hKCNN2 was a kind gift from Neil V. Marrion, Bristol University. peGFP-hPMCA4b and peGFP-hPMCA4bct120 were a gift from Emanuel Strehler (Addgene plasmid # 47589 ; http://n2t.net/addgene:47589; RRID:Addgene_47589 and Addgene plasmid # 47593; http://n2t.net/addgene:47593; RRID:Addgene_47593). Three single point mutations had been detected in peGFP-hPMCA4b and hPMCA4bct120, two of them leading to amino acid substitution (c:2675A>G, p:K442R and c:3368

C>T, p:P673L). These two mutations were corrected by two successive PCR on the plasmids deposited in Addgene with oligo-nucleotides overlapping 15 nucleotides upstream and downstream the wrong base using KAPA high fidelity polymerase kit (Roche). Point mutation D452A was done by PCR on peGFP-hPMCA4b (corrected for mutations on the Addgene plasmid) with the proofreading KAPA high fidelity polymerase and primers covering 16 nucleotides upstream and downstream Asp452. CTer PMCA4b-HA was constructed by amplifying on peGFP-PMCA4b with KAPA high fidelity the 120 C-terminal amino-acids of PMCA4b with forward primer: AAGTGGTACCATGCTGCGCCGAGGCCAGAT introducing a KpnI restriction site and reverse primer: CTAGCTCGAGAACTGATGTCTCTAGGCTCT introducing a HA tag and XhoI restriction site. The PCR product was cloned in pcDNA3 KpnI-XhoI. All constructs were sequenced to check for correct DNA sequences.

HEK293T cells transfection:

HEK293T cells were grown in DMEM glutamax (Gibco) 10% FBS penicillin-streptomycin. Cells at ~70% confluence were transfected using CaPO4 with 1 µg of plasmid DNA per ml of culture medium (0.5 + 0.5 µg of plasmid DNA in case of co-transfection). 16 hours later, cells were washed twice with PBS. For patch-clamp experiments, peGFP was co-transfected with constructs that did not carry fluorescent tag to select fluorescent cells as transfected cells.

K562 cells were grown in RPMI1640 10% FBS penicillin-streptomycin.

Protein expression assay:

HEK293T cells were grown to 70% confluence in DMEM glutamax 10% FBS penicillin-streptomycin in 60mm petri dishes (Starsted). 24h after transfection, cells were biotinylated following manufacturer instructions (Pierce cell surface protein assay) then lysed. The lysate was loaded on avidin-agarose beads (Pierce cell surface protein assay) to isolate the biotinylated fraction. Total fraction and biotinylated fraction were subjected to SDS-PAGE western blot. Migration of proteins was made at 120V during 90 min in 8% acrylamide gel. Proteins were then transferred to PVDF using wet transfer protocol for 1h at 100V and blocked in blocking solution (BS: 5% low-fat milk in TBS-tween 0.1%). Immunolabelling was done using primary antibodies: anti-KCNN4 (Proteintech, Rabbit, 1:1000), anti-pan PMCA 5F10 (Invitrogen, Mouse, 1:1000) and anti-ECadherin (Mouse, BD 1:5000) for 1h30 at room temperature in BS and HRP coupled secondary antibodies for 50min at RT

using: anti-rabbit (1:2000, DAKO) and anti-mouse (1:5000, DAKO). HRP labelled proteins were revealed with Enhanced Chemiluminescent solution (Millipore) with a Fusion FX EDGE.

Immunoprecipitation:

Pierce co-immunoprecipitation kit was used following manufacturer instructions. 10 µg of primary antibodies anti-PMCA (5F10 mouse monoclonal Invitrogen) were covalently bound to agarose beads. Empty beads were used as control. HEK293T cells were lysed in IP-lysis buffer and lysate was precleared on dedicated agarose beads. 1 mg of cleared lysate was loaded on immunoglobulin beads or control beads and incubated overnight at 4°C under gentle shaking. Unbound fraction was collected prior to extensive washes of the columns. Elution (50 µl) was subjected to SDS-Page and Western Blot as described above. Anti KCNN4 (1:1000, Proteintech rabbit); anti KCNN2 (Alomone rabbit); anti GFP (1:1000, Cell Signaling rabbit) or anti GFP (). For immunoprecipitation with vanadate, 5 mM vanadate was added to cell lysate during immunoprecipitation with agarose-IgG coupled beads over-night at 4°C.

Proximity ligation assay:

The DuoLink PLA (Olink Bioscience) was used to detect interaction between KCNN4 and PMCA or PMCA4b in HEK293T cells and RBC. HEK293T cells were transfected or not with pEGFP-hPMCA4b and/or pcDNA3-HA-hKCNN4 (0.5µg DNA/mL of DMEM) using $CaPO_4$ during 8 hours then seeded on poly-Lysine (40µg/mL)-coated microscope slides and grown until 70% confluency. Cells were washed with PBS1X, fixed with paraformaldehyde 4% 10min, permeabilized 10min with triton×100 (0.03%). Blocking of unspecific antigen was done with blocking solution from kit during 1h at 37°C. Cells were immunolabeled with primary antibodies anti KCNN4 (1:200, rabbit, Proteintech) and anti-PMCA4b (1:200, mouse, JA3 Millipore) in kit solution O/N at 4°C. Next steps were done according to manufacturer instruction (Duolink). For RBCs, fresh blood drawn was washed in Ringer without Ca^{2+} then, 20µL of pellet was fixed for 30min at RT in 1mL PBS1X containing 4% PFA and 0.05% glutaraldehyde. Fixed RBC were stored at 4°C until use. PLA was done in suspension with 20µL of previously-fixed RBC. RBC were immunolabeled with primary antibodies anti KCNN4 (1:200, rabbit, Proteintech) and anti-panPMCA (1:200, mouse, Invitrogen) in kit solution O/N at 4°C. Except for centrifugation steps (1 min at 1000rpm) to pellet the cells and remove supernatant, the rest was done according to manufacturer instruction in the same conditions as HEK293T cells. PLA images were captured using an inverted Zeiss Axio Observer Z1 microscope

(Zeiss) x64, Cyan5 filter for PLA dot (far red) and DAPI filter for nucleus. Confocal L880 Zeiss microscope, x64 were used for illustration. For quantification, PLA dots per cells were quantified using Image J software and compared to control condition: non-transfected HEK293T cells or RBC with only secondary antibodies.

Electrophysiology:

Glass pipettes (Brand, Wertheim, Germany) with final resistance of 3-5 MΩ were made on a horizontal pipette puller (P-97, Sutter Instrument, Navato, CA). All patch-clamp experiments were performed with a PC-controlled EPC9 patch-clamp amplifier (HEKA, Lambrecht/Pfalz, Germany). Currents were acquired and analyzed with Pulse and Pulsefit software (HEKA).

Currents were measured in whole-cell configuration with bath solution in mM: 150 NaCl, 5 KCl, 1 $CaCl_2$, 1 $MgCl_2$, 10 HEPES at pH 7,4 and inside: 150 KCl, 5 NaCl, 1 $MgCl_2$ 1 EGTA, 10 HEPES, 0,03 $CaCl_2$ to reach 10 nM of free Ca^{2+} at pH 7,2. Free Ca2+ concentrations were adjusted by adding $CaCl_2$ using Ca-EGTA Calculator v1.3. Currents were measured at room temperature using a ramp protocol from -120 to +80 mV from a holding potential of -60 mV (sampling frequency 10 kHz; filtered 5 kHz).

Statistical analysis:

For one comparison, Mann and Whitney test was used. For multiple comparisons, Kruskall and Wallis test was applied with a post-hoc Dunn's correction when comparing each condition or Uncorrected Dunn's test when comparing only against one condition. For grouped analysis two-way ANOVA with Dunnet's post hoc test was used. Statistical differences are given as follows: *: $p<0.05$; ** : $p<0.01$; *** : $p<0.001$. For electrophysiological analysis, current below <5pA/pF were removed as a cut off considering that KCNN4 was not present in the recording.

Results

There is no linear correlation between intracellular Ca^{2+} concentration and RBC dehydration:

We compared water, K^+ and Na^+ contents of RBC in different experimental conditions expected to increase intracellular Ca^{2+} concentration. Yoda1 was used to stimulate PIEZO1 which dissipates the cation electrochemical gradient, allowing K^+ loss together with Na^+ and Ca^{2+} uptake. Vanadate was used to inhibit the Ca^{2+} ATPase pump, which is very active in RBC to maintain a Ca^{2+} concentration around 100 nM against Ca^{2+} leaks and the mM range of extracellular calcium concentration [15,16].

Figure 1 illustrates the RBC water contents, K^+ and Na^+ variations and Ca^{2+} contents in control condition, treated by 2 µM Yoda1 and/or 5 mM vanadate. RBC were significantly dehydrated when treated by Yoda1+vanadate or after 40 minutes vanadate (Figure 1A). After 20 minutes, Yoda1 or vanadate, alone, did not induce significant RBC dehydration. When observed, the dehydration was correlated to a K^+ loss not compensated by Na^+ uptake (Figure 1B). In the presence of Yoda1 alone, the K^+ loss was not significantly different from the Na^+ uptake (figure 1B, p=0.17), and RBC volume was kept stable. However, with Yoda1 + vanadate the K^+ loss was not compensated by a Na^+ uptake, leading to RBC dehydration. The excess K^+ loss was due to KCNN4 activation as shown by the inhibition of RBC dehydration with KCNN4 blocker Senicapoc, confirming our previous data [6]. Figure 1C illustrates intracellular Ca^{2+} contents in the experimental conditions shown in figure 1 A-B. The Ca^{2+} concentration dramatically increased in RBC as soon as Yoda1 was added to RBC suspension and the addition of vanadate led to a sustained elevation of intracellular Ca^{2+}. Vanadate alone induced a slow increase of intracellular Ca^{2+} concentration due to calcium inward leaks [17]. Surprisingly, the 12-fold increase in intracellular Ca^{2+} observed after 20 minutes of Yoda1 did not significantly stimulate KCNN4 (fig.1A-B). In contrast, a lower 6-fold increase Ca^{2+} level at 40 minutes vanadate, was sufficient to activate KCNN4 (fig. 1 A-B). These results suggested that there was no linear correlation between Ca^{2+} level increase and KCNN4 activation in RBC. To further assess the effect of vanadate on KCNN4 activity independent of PIEZO1 activation, we used the Ca^{2+} ionophore 4Br-A23187. Following ionophore addition, the intracellular Ca^{2+} reached a plateau within 10 minutes that was similar in presence or absence of vanadate. Despite the apparent similar Ca^{2+} level, the K^+ loss and RBC dehydration were larger in presence of vanadate (suppl. figure 1).

The Ca^{2+} pump regulates KCNN4 activity:

These data suggested that the Ca^{2+} pump activity could impair KCNN4 functioning. There are two different Ca^{2+} pump isoforms expressed in RBC plasma membrane: the main one is PMCA4b whereas PMCA1 is present in lower amount [18]. To assess the ability of calcium pump to regulate KCNN4 activity, we reconstituted the system in HEK293T cell model. HEK293T cells were co-transfected

with PIEZO1 and KCNN4 with or without PMCA4b. As shown in figure 2, in absence of PIEZO1 stimulation and without sufficient amount of intracellular Ca^{2+}, no KCNN4 current was observed (figure 2C-D). Within 40 seconds following PIEZO1 stimulation by Yoda1 a current was recorded corresponding to KCNN4 activity: the Ca^{2+} influx mediated by PIEZO1 stimulation was able to activate KCNN4 (figure 2F-G). This current was blocked by Senicapoc (suppl. figure 2). The PIEZO1-mediated KCNN4 activation was inhibited upon co-expression of PMCA4b (Figure 2F-G). To rule out the possibility that this decrease in response was related to the KCNN4 protein amount or surface expression, we compared the expression of KCNN4.

Using Western blot on total proteins or biotinylated proteins for surface expression, we found that KCNN4 was expressed in similar manner at the plasma membrane, in presence of PIEZO1 +/- PMCA4b (figure 2A-B). As the reduction of the current was not associated to a reduced number of channels, it could result from a faster decreased Ca^{2+} concentration related to PMCA4b activity. To overcome this possibility, intracellular Ca^{2+} was clamped at 1 µM and KCNN4 activity was measured in HEK293T cells expressing KCNN4 alone or with PMCA4b (Figure 3). Whereas the calcium concentration was constant, KCNN4 current measured at 0 mV was again reduced in presence of PMCA4b (Figure 3A-B). This confirmed a calcium-independent effect of PMCA4b observed on PIEZO1-mediated KCNN4 activity. The inhibition of KCNN4 activity by PMCA4b expression could also result from local Ca^{2+} pumping out around KCNN4. To test whether the activity of PMCA could interfere with KCNN4 activity, we used two different constructs of PMCA4b: the PMCA4b-ct120 where 120 C-terminal amino-acids were deleted and the point mutated PMCA4b-D452A. The PMCA4b-ct120 is a constitutively active Ca^{2+} pump [19] whereas the D452A mutation prevents a phosphorylation on D452 and leads to an inactive Ca^{2+} pump[20]. Figure 3A-B shows that the constitutively active PMCA4b-ct120 was no longer able to inhibit KCNN4 activity in contrast to the inactive PMCA4b-D452A. The inhibitory effect of PMCA4b on KCNN4 appeared to be independent of Ca^{2+}pump activity. This observation was confirmed by the experiments done in presence of ATP to insure energy supply throughout recording (Figure 2E-H and 3C). The difference between control and PMCA4b condition was equivalent in the presence or absence of 2mM ATP in pipette solution. In addition, KCNN4 current was measured in HEK293T cells co-expressing PMCA4b incubated with vanadate. The presence of vanadate removed PMCA4b inhibition on KCNN4 current (Figure 3D).

We then reproduced these experiments on native currents. We used the erythroleukemia K562 cell line which endogenously expressed KCNN4 and PMCA4b (Suppl. Figure 3A). Confirming our results in heterologous system, we observed that the endogenous Ca^{2+} dependent K^+ current was increased when vanadate was added in the pipette with 10µM free Ca^{2+} (Suppl. figure 3B). If the Ca^{2+} pump activity of PMCA4b was not involved, its C-terminal part seemed to be the main effector of

KCNN4 inhibition since PMCA4b-ct120 had no inhibitory effect on the channel. We expressed the PMCA4b C-terminal end alone (CterPMCA4b-HA) with KCNN4 in HEK293T cells. In this condition, CterPMCA4b-HA was able to inhibit KCNN4 current but to a lesser extent compared to the full length PMCA4b (Figure 3 A-B). Hence, the inhibition of KCNN4 by PMCA4b seemed related to the structure of the pump as its C-terminal part was necessary to inhibit KCNN4.

KCNN4 and PMCA4b are in close proximity:

To address this hypothesis, a proximity ligation assay (PLA) was done on either RBC or HEK293T cell expressing KCNN4 and different PMCA4b constructs. As shown on figure 4 (A-D) a proximity between KCNN4 and PMC4Ab was detected in HEK293T cells as in RBC. In addition, co-immunoprecipitation was done on HEK293T cells expressing KCNN4 with PMCA4b or the truncated pump PMCA4b-ct120. The immunoprecipitation of PMCA4b was able to specifically drag KCNN4 in HEK293T transfected cells (Figure 4E-F). Interestingly, in HEK293T cells, PMCA4b-ct120 was still interacting with KCNN4 as shown by co-IP (Figures 4E). A tight molecular interaction between KCNN4 and PMCA4b was independent on the C-terminal end of PMCA4b whereas this domain was involved in the regulation of KCNN4 activity.

We then wondered whether other members of the Ca^{2+} dependent K^+ channel family could also be regulated by PMCA4b. We used our heterologous expression system HEK293T cells transfected with KCNN2, a small conductance member of the family, with or without PMCA4b. As for KCNN4, KCNN2 current was reduced in presence of PMCA4b (Figure 5).

Discussion

The coupling between KCNN4 and PMCA4b underlies the Gardos effect is not directly correlated with the intracellular Ca^{2+}increase.

First, we showed that the functional coupling between PIEZO1 and KCNN4 described in RBC could be reconstituted in HEK293T cells. In experimental condition with 10 nM Ca^{2+} in the pipette, the stimulation of PIEZO1 by Yoda1 was able to stimulate KCNN4 opening as what was previously described in RBC [3,6,21]. The Ca^{2+} entry resulting from PIEZO1 activation was able to activate KCNN4 in HEK293T cells.

Second, to test the calcium dependency of this regulation, we partially activated PIEZO1 with lower non-saturating concentration of Yoda1 in RBC. At low non-saturating Yoda1 concentrations, but sufficient to activate PIEZO1 as shown by the changes in Na^+ and K^+ contents as well as calcium uptake, the RBC dehydration did not occur. This demonstrates that PIEZO1 activation might not lead

to KCNN4 stimulation. This challenges the dogma of RBC dehydration induced by mechanical stress confirming our recently published observation[22].

Based on our present data, we propose a model explaining the molecular events that lead to the uncoupling of PIEZO1 stimulation and KCNN4 activation in RBC. The calcium ATPase PMCA4b is part of this mechanism, inhibiting PIEZO1-KCNN4 Ca^{2+}-mediated coupling. This new regulating mechanism of KCNN4 is efficient in RBC and reproduced in the HEK293T cells. In control RBC, we observed a rapid and strong Ca^{2+} concentration increase, induced by Yoda1, an agonist of PIEZO1[23,24], without significant dehydration, meaning KCNN4 had not been activated. In contrast, vanadate, a blocker of the Ca^{2+} pump PMCA, induced a KCNN4-mediated dehydration with lower elevation of Ca^{2+} than Yoda1 condition. Moreover, adding vanadate to Yoda1 allowed a sustained Ca^{2+} increase correlated to dehydration. A similar effect of vanadate was also observed with the calcium ionophore 4Br-A23187. In RBC devoid of any intracellular Ca^{2+} stores, 4Br-A23187 is expected to equilibrate calcium across plasma membrane according to its electrochemical gradient, shunting the effect of the calcium pump. The intracellular Ca^{2+} fluorescence between RBC treated by 4Br-A23187 alone or together with vanadate plateaued at similar level, suggesting that the intracellular calcium concentration was equivalent in both conditions (Suppl. figure 1). Hence, the increased activity of KCNN4 observed with addition of vanadate might not be due to higher availability of Ca^{2+}. Altogether, these results suggested a control of KCNN4 activity in RBC by the Ca^{2+}-ATPase.

In HEK293T cells we provided evidence for a direct inhibitory interaction of KCNN4 by PMCA4b. It was observed that the inhibitory effect of PMCA4b was independent of its Ca^{2+} pumping out activity: a similar inhibition was observed with the inactive PMCA4b D452A. The addition of ATP did not modify the shape of inhibition suggesting a control by the calcium pump independent of Ca^{2+} efflux efficiency. The inhibition involved the C-terminal soluble part of PMCA4b that is necessary and close to be sufficient to recapitulate the effect of PMCA over-expression. Its deletion from the protein abolished PMCA-induced KCNN4 inhibition whereas its expression as soluble part was able to block partially but significantly KCNN4 activity. The solubility of this domain that is free to move in the cytoplasm could explain a lower inhibiting efficiency compared to full length PMCA. PMCA and KCNN4 being both integral membrane proteins, have reduced ability to diffuse, which increase their relative local concentration and subsequently their interaction. In the case of KCNN4 and C-terminal end of PMCA4b, one of the partners is cytosolic increasing its degree of freedom in the cytoplasm reducing its apparent affinity for KCNN4. The regulatory interaction between KCNN4 and the C-terminal end of PMCA4b might be optimized by the molecular interactions between KCNN4

and other domains of PMCA4b. This could explain why PMCA4b C-terminal end inhibited only partially KCNN4 compared to the full length PMCA4b which is in close proximity to KCNN4.

Interestingly, the vanadate removed PMCA4b control on KCNN4. Vanadate blocks the Ca^{2+} pump in the E2P state, phosphorylated unable to transport Ca^{2+} [25-27]. In this conformational state the first two α helices of the pump are re-oriented in plasma membrane. The molecular interaction between the Ca^{2+} pump and KCNN4 was still observed in presence of vanadate: this inhibitor did not prevent co-immunoprecipitation between PMCA4b and KCNN4 meaning the E2P state was still able to interact with KCNN4. However, this conformation removed the molecular control of the PMCA4b C-terminal end on KCNN4 activity. Hence, PMCA4b and KCNN4 might form a molecular complex in which the C-terminal end of PMCA4b would be able to modulate KCNN4 activity in a PMCA4b conformation-dependent manner.

The structure of PMCA4b has not yet been solved, however, its spatial organization might be modelized according to the structure of the Sarcoplasmic Endoplasmic Reticulum Ca^{2+} pump (SERCA), another P-type ATPase[26]. Five structural domains are proposed: a membrane spanning domain consisting of 10 α helices, and 4 cytoplasmic domains, the A (Actuator) domain formed by the loop between transmembrane helices (TM) 2 and 3, the P (Phosphorylation) and N (Nucleotide binding) domains between TM 4 and 5 and the R (Regulatory) domain consisting of the C-terminal part of the protein that has two calmodulin binding domains and a PDZ recognizing domain[20,28]. The Calmodulin (CaM) binding domains in PMCA C-terminal region adjust pump activity to Ca^{2+} concentration[13,29]. In low Ca^{2+} concentration media, PMCA4b is autoinhibited by its C-terminal end which blocks catalytic domain. Upon Ca^{2+} increase, CaM-Ca^{2+} complexes are formed and CaM C-lobe binds first to CaM-binding domain of PMCA4b. Then CaM N-lobe can access to its site and provoke the detachment of PMCA C-terminal part from the catalytic domain, enhancing PMCA4b catalytic activity. KCNN4 is a homo-tetramer which gating is controlled by CaM[30-33]. Each KCNN4 monomer is constitutively bound to CaM C-lobe. Ca^{2+} binding to CaM allows a conformational change with the N-lobe moving toward and adjacent channel monomer and each CaM cross-links two adjacent KCNN4 monomers which in turn opens the channel. A role of CaM as an intermediate between PMCA4b and control of KCNN4 activity was tempting. However, the fact that KCNN4 inhibition was not dependent on PMCA4b activity suggested that the active conformation of PMCA4b controlled by CaM is not required for the modulation. In order to prevent KCNN4 activation, the free N-lobe of the constitutively KCNN4-bound CaM should be engaged with another interaction. However, the CaM interaction with PMCA4b is driven by its C-lobe at first not the N-lobe. These specific molecular interactions would rule out a role of CaM in the inhibitory mechanism linking PMCA4b and KCNN4.

Finally, we showed that PMCA4b dependent regulation is not restricted to KCNN4 but can be extended to other channels as we demonstrated for KCNN2 another member of the Ca^{2+} dependent K^+ channel family. This enlarges the possible physiological consequences of this regulation notably in neurons. KCNN2 contributes to neuronal excitability, brain rhythmic activity, synaptic transmission and, interplay with the endoplasmic Ca^{2+} pump has been observed[34,35]. Our present data suggest the channel could directly interact with the Ca^2 pump providing a new regulatory mechanism of KCNN2 activity in these cells. KCNN2 and KCNN4 activity are also well documented in cancer cells where they trigger their migration[36-38]. Recent studies have shown that PMCA4b expression is decreased in some cancer cells favoring migration and metastasis[39]. The mechanism of reduced Ca^{2+} dependent K^+ channel activity by interaction with PMCA4b we described, could contribute to control the pro-metastatic role of these channels in cancer cells.

Going back to RBC, PMCA appears as a key player in their volume homeostasis. Our results show that the stimulation of a mechanosensitive Ca^{2+} channel would not necessarily activate the Gardos channel. There is a 3-member partnership between Ca^{2+} channels-KCNN4-Ca^{2+} pump in RBC membrane that could tightly control KCNN4 which activation, by inducing irreversible water loss, might be deleterious. Hence PMCA4b is able to uncouple PIEZO1 activity from Gardos channel activation. This control by PMCA4b on KCNN4 activity would also prevent dehydration following any Ca^{2+} channel activation. Recent studies have shown a link between *ATP2B4* polymorphism and RBC hydration status. In mice knockdown for *atp2b4*, RBC have increased hemoglobin concentration (greater MCHC, Mean Corpuscular Hemoglobin Concentration) compared to WT mice that could indicate a loss of KCNN4 control by the calcium pump in addition to the observed Ca^{2+} increase in these RBC [40]. Moreover, a minor haplotype in ATP2B4 associated to reduced PMCA4b expression in human RBC is also correlated to increased MCHC suggesting a greater KCNN4 activity in these cells[14].

Conclusion

We proposed a mechanism that controls KCNN4 activity in RBC by a molecular inhibitory interaction with PMCA4b (figure 6). This inhibitory interaction is dependent on Ca^{2+} pump conformation, it is removed when PMCA4b is in E2P state. This mechanism uncouples Ca^{2+} entry and KCNN4 activation preventing RBC dehydration when PIEZO1 is stimulated. It is therefore tempting to target this interaction to reduce the Gardos effect in patient suffering from xerocytosis or sickle cell disease, to prevent dehydration and hemolysis.

Authorship Contributions

MM, BA and HG performed experiments, most of molecular biology experiments were done by MM, BA did the electrophysiology under OS and RRM supervision and did the PLA with FB. All the authors collected and analyzed the data. HG and BA wrote the manuscript and all the authors corrected the manuscript.

Acknowledgements

This work was granted by the French National Agency for Research, ANR, (ANR-19-CE14-0049). We thank Agnes Loubat at the cytometry facility for Ca^{2+} measurements and the PRISM facility for microscopy experiments (Baptiste Monterroso and Sameh Ben-Aïcha). We are grateful to Guillaume Sandoz for helpful comments and discussion.

Conflict of Interest Disclosures

The authors declare no conflict of interest.

References

1. GARDOS G. The function of calcium in the potassium permeability of human erythrocytes. Biochim Biophys Acta. 1958;30(3):653-654.

2. Hoffman JF, Joiner W, Nehrke K, Potapova O, Foye K, Wickrema A. The hSK4 (KCNN4) isoform is the Ca2+-activated K+ channel (Gardos channel) in human red blood cells. Proc Natl Acad Sci U S A. 2003;100(12):7366-7371.

3. Cahalan SM, Lukacs V, Ranade SS, Chien S, Bandell M, Patapoutian A. Piezo1 links mechanical forces to red blood cell volume. Elife. 2015;4.

4. Archer NM, Shmukler BE, Andolfo I, et al. Hereditary xerocytosis revisited. Am J Hematol. 2014;89(12):1142-1146.

5. More TA, Dongerdiye R, Devendra R, Warang PP, Kedar PS. Mechanosensitive Piezo1 ion channel protein (PIEZO1 gene): update and extended mutation analysis of hereditary xerocytosis in India. Ann Hematol. 2020;99(4):715-727.

6. Rapetti-Mauss R, Picard V, Guitton C, et al. Red blood cell Gardos channel (KCNN4): the essential determinant of erythrocyte dehydration in hereditary xerocytosis. Haematologica. 2017;102(10):e415-e418.

7. Andolfo I, De Rosa G, Errichiello E, et al. Hypomorphic Variants in Congenital Lymphatic Dysplasia Cause Shape and Hydration Alterations of Red Blood Cells. Front Physiol. 2019;10:258.

8. Danielczok JG, Terriac E, Hertz L, et al. Red Blood Cell Passage of Small Capillaries Is Associated with Transient Ca. Front Physiol. 2017;8:979.

9. Kuck L, Peart JN, Simmonds MJ. Calcium dynamically alters erythrocyte mechanical response to shear. Biochim Biophys Acta Mol Cell Res. 2020;1867(11):118802.

10. Rogers S, Lew VL. PIEZO1 and the mechanism of the long circulatory longevity of human red blood cells. PLoS Comput Biol. 2021;17(3):e1008496.

11. Rogers S, Lew VL. Up-down biphasic volume response of human red blood cells to PIEZO1 activation during capillary transits. PLoS Comput Biol. 2021;17(3):e1008706.

12. Bogdanova A, Makhro A, Wang J, Lipp P, Kaestner L. Calcium in red blood cells-a perilous balance. Int J Mol Sci. 2013;14(5):9848-9872.

13. Niggli V, Carafoli E. The Plasma Membrane Ca(2+) ATPase: Purification by Calmodulin Affinity Chromatography, and Reconstitution of the Purified Protein. Methods Mol Biol. 2016;1377:57-70.

14. Zámbó B, Várady G, Padányi R, et al. Decreased calcium pump expression in human erythrocytes is connected to a minor haplotype in the ATP2B4 gene. Cell Calcium. 2017;65:73-79.

15. Romero PJ, Romero EA. New vanadate-induced Ca2+ pathway in human red cells. Cell Biol Int. 2003;27(11):903-912.

16. Tiffert T, Lew VL. Kinetics of inhibition of the plasma membrane calcium pump by vanadate in intact human red cells. Cell Calcium. 2001;30(5):337-342.

17. Schatzmann HJ, Luterbacher S, Stieger J, Wüthrich A. Red blood cell calcium pump and its inhibition by vanadate and lanthanum. J Cardiovasc Pharmacol. 1986;8 Suppl 8:S33-37.

18. Bryk AH, Wiśniewski JR. Quantitative Analysis of Human Red Blood Cell Proteome. J Proteome Res. 2017;16(8):2752-2761.

19. Enyedi A, Verma AK, Filoteo AG, Penniston JT. A highly active 120-kDa truncated mutant of the plasma membrane Ca2+ pump. J Biol Chem. 1993;268(14):10621-10626.

20. Kühlbrandt W. Biology, structure and mechanism of P-type ATPases. Nat Rev Mol Cell Biol. 2004;5(4):282-295.

21. Rapetti-Mauss R, Soriani O, Vinti H, Badens C, Guizouarn H. Senicapoc: a potent candidate for the treatment of a subset of hereditary xerocytosis caused by mutations in the Gardos channel. Haematologica. 2016;101(11):e431-e435.

22. Lohia R, Allegrini B, Berry L, et al. Pharmacological activation of PIEZO1 in human red blood cells prevents Plasmodium falciparum invasion. Cell Mol Life Sci. 2023;80(5):124.

23. Syeda R, Xu J, Dubin AE, et al. Chemical activation of the mechanotransduction channel Piezo1. Elife. 2015;4.

24. Botello-Smith WM, Jiang W, Zhang H, et al. A mechanism for the activation of the mechanosensitive Piezo1 channel by the small molecule Yoda1. Nat Commun. 2019;10(1):4503.

25. Saffioti NA, de Sautu M, Ferreira-Gomes MS, et al. E2P-like states of plasma membrane Ca. Biochim Biophys Acta Biomembr. 2019;1861(2):366-379.

26. Clausen JD, Bublitz M, Arnou B, et al. Crystal Structure of the Vanadate-Inhibited Ca(2+)-ATPase. Structure. 2016;24(4):617-623.

27. Xu C, Rice WJ, He W, Stokes DL. A structural model for the catalytic cycle of Ca(2+)-ATPase. J Mol Biol. 2002;316(1):201-211.

28. Krebs J. Structure, Function and Regulation of the Plasma Membrane Calcium Pump in Health and Disease. Int J Mol Sci. 2022;23(3).

29. Falchetto R, Vorherr T, Brunner J, Carafoli E. The plasma membrane Ca2+ pump contains a site that interacts with its calmodulin-binding domain. J Biol Chem. 1991;266(5):2930-2936.

30. Lee CH, MacKinnon R. Activation mechanism of a human SK-calmodulin channel complex elucidated by cryo-EM structures. Science. 2018;360(6388):508-513.

31. Ji T, Corbalán-García S, Hubbard SR. Correction: Crystal structure of the C-terminal four-helix bundle of the potassium channel KCa3.1. PLoS One. 2018;13(10):e0205540.

32. Ji T, Corbalán-García S, Hubbard SR. Crystal structure of the C-terminal four-helix bundle of the potassium channel KCa3.1. PLoS One. 2018;13(6):e0199942.

33. Sforna L, Megaro A, Pessia M, Franciolini F, Catacuzzeno L. Structure, Gating and Basic Functions of the Ca2+-activated K Channel of Intermediate Conductance. Curr Neuropharmacol. 2018;16(5):608-617.

34. Sun J, Liu Y, Baudry M, Bi X. SK2 channel regulation of neuronal excitability, synaptic transmission, and brain rhythmic activity in health and diseases. Biochim Biophys Acta Mol Cell Res. 2020;1867(12):118834.

35. Cueni L, Canepari M, Luján R, et al. T-type Ca2+ channels, SK2 channels and SERCAs gate sleep-related oscillations in thalamic dendrites. Nat Neurosci. 2008;11(6):683-692.

36. Vandier C, Velge-Roussel F. Regulation of human dendritic cell immune functions by ion channels. Curr Opin Immunol. 2018;52:27-31.

37. Todesca LM, Maskri S, Brömmel K, et al. Targeting K. Cell Physiol Biochem. 2021;55(S3):131-144.

38. Rapetti-Mauss R, Nigri J, Berenguier C, et al. SK2 channels set a signalling hub bolstering CAF-triggered tumourigenic processes in pancreatic cancer. Gut. 2023;72(4):722-735.

39. Naffa R, Hegedűs L, Hegedűs T, et al. Plasma membrane Ca. J Physiol. 2023.

40. Lessard S, Gatof ES, Beaudoin M, et al. An erythroid-specific ATP2B4 enhancer mediates red blood cell hydration and malaria susceptibility. J Clin Invest. 2017;127(8):3065-3074.

Figures and Legends

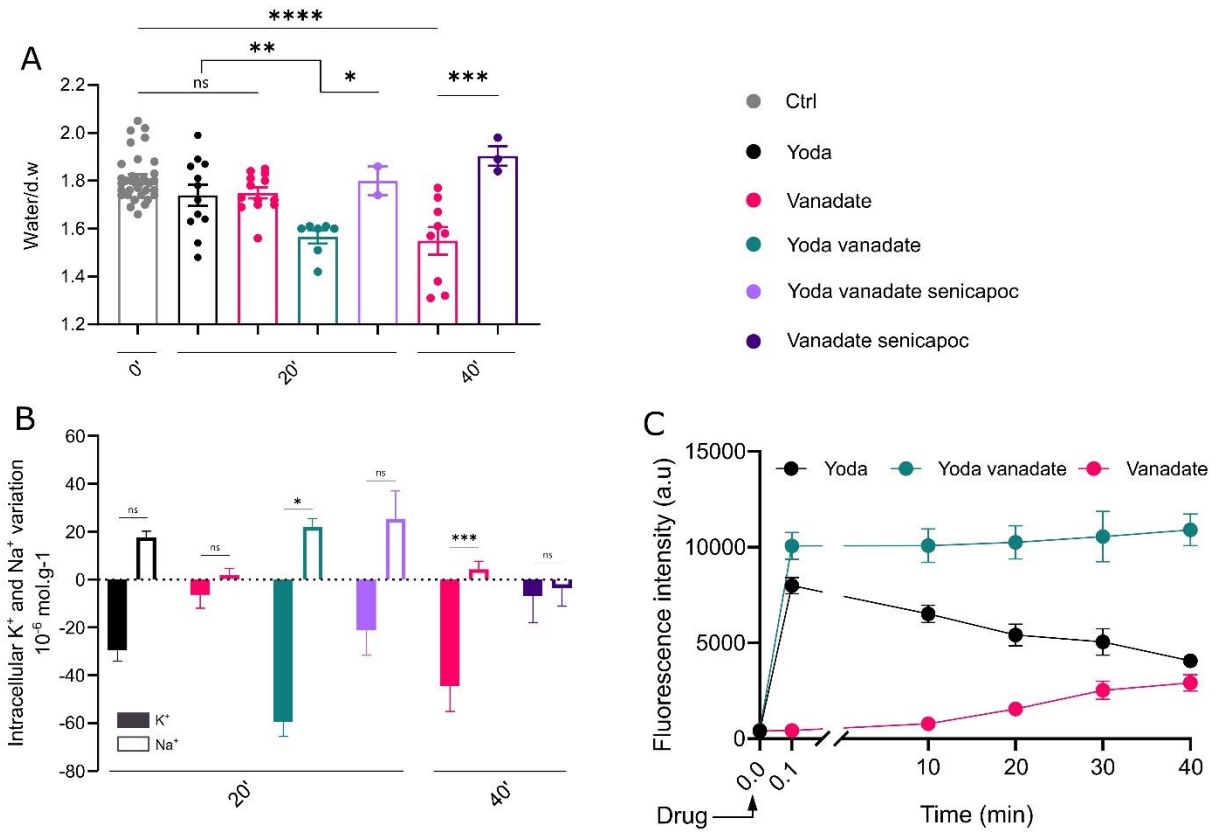

Figure 1: Water contents, Na^+ and K^+ variations and Ca^{2+} contents of RBC in different experimental conditions.

Water (A) and variations in K^+, Na^+ (B) contents (absolute values) were measured on washed RBC treated with 2 µM Yoda1 +/- 5 mM Vanadate or 5 mM Vanadate alone. Senicapoc (2 µM) was added to block KCNN4. In A) water content was plotted at t=0 (control) and t=20 minutes for Yoda1± Vanadate treated RBC and 40 minutes for Vanadate treated RBC. The variation in Na^+ and K^+ contents were calculated between t=0 and t=20 minutes (Yoda1 ± Vanadate) or 40 minutes (Vanadate). Mean ± sem Na^+ and K^+ contents at t=0 were in µmol/g dry weight: Na^+=30.2±2.6 K^+=237.5±4.4, n=37. (C) fluorescence in arbitrary units associated to intracellular Ca^{2+} content measured by flow cytometry with Fluo4-AM probe. Ca^{2+} content was measured overtime after addition of 2 µM Yoda1 +/- Vanadate (5 mM) or Vanadate (5 mM) alone. Data are means ± sem of n=37 (control), n=15 (Yoda1), n=10 (Yoda1+vanadate), n=2 (Yoda+vanadate+senicapoc) and n=16 (Vanadate) experiments at t=20 minutes; n=12 (vanadate) and n=3 (vanadate+senicapoc) for experiments at 40 minutes. * p<0.05, ** p<0.01, ***p<0.001 and ****p<0.0001.

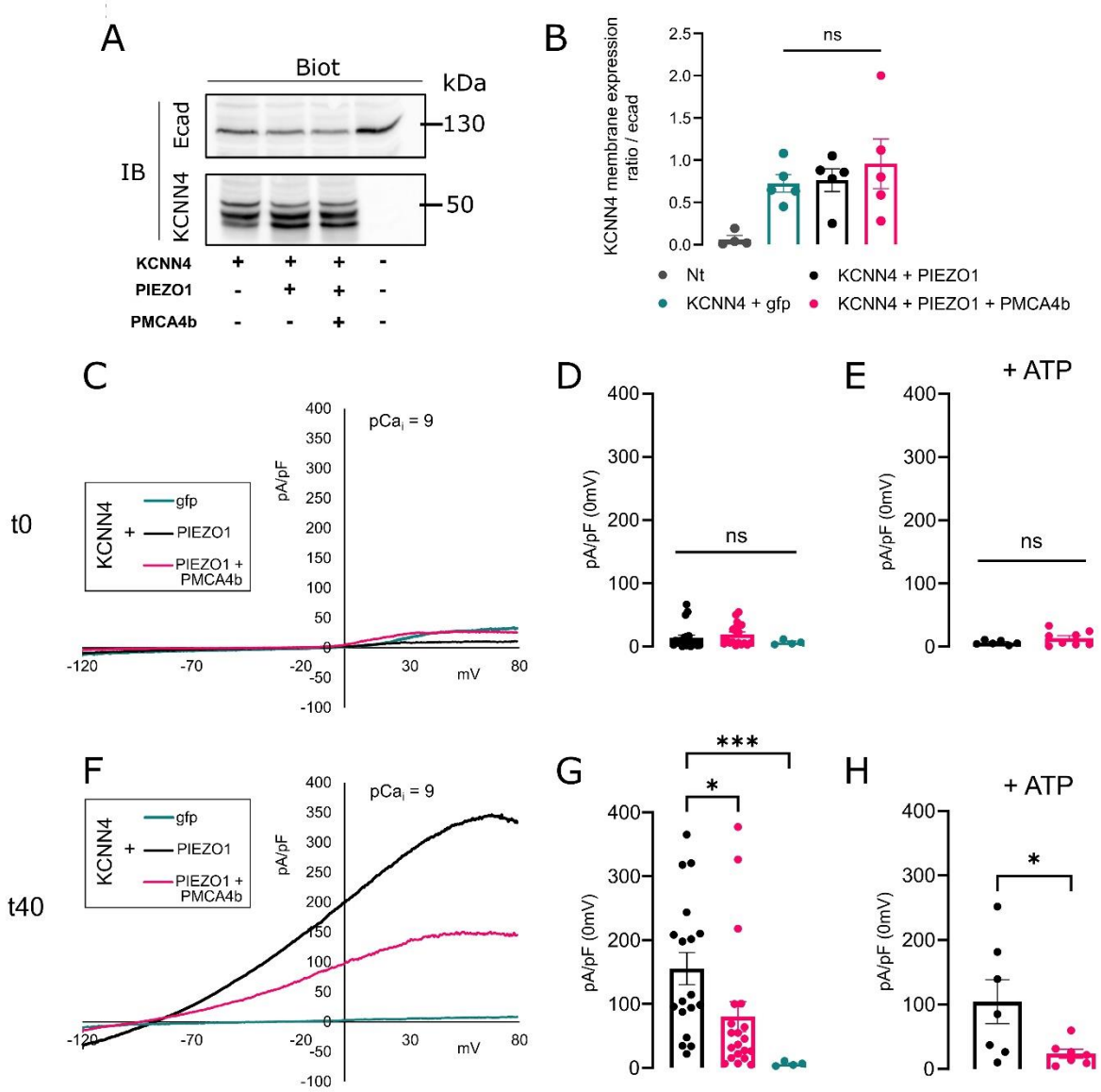

Figure 2: Electrophysiological recordings of PIEZO1-mediated KCNN4 current on HEK293T cells transfected with KCNN4, PIEZO1 and PMCA4b.

(A-B) Expression of KCNN4 at the plasma membrane when PIEZO1 or PIEZO1+PMCA4b were co-transfected. (A) Representative western blot and (B) quantitative analysis of 3 different Western blots done on 3 different transfection assays showing proteins addressed at the plasma membrane, only biotinylated proteins were detected. KCNN4 is glycosylated and appeared as multiple bands arround 50 kDa. KCNN4 expression level was normalized to the level of E-cadherin. Data are means ± sem, n=3. (C) Representative traces in different co-transfection conditions: KCNN4 alone (green), + PIEZO1 (black), + PMCA4b (pink) in whole cell configuration at t=0 and t=40 s (E) after 15 µM Yoda1 addition. Associated current density (pA/pF) at 0mV measured at t=0 (D) or t=40 s (F) after Yoda1 addition without ATP inside (left panels) or with 1 mM ATP (right panels). n=4 (KCNN4 + GFP) to n=18(KCNN4 + PIEZO1 + PMCA4b) cells coming from different batches of transfection. Data are means ± sem. * $p<0.05$ and *** $p<0.001$.

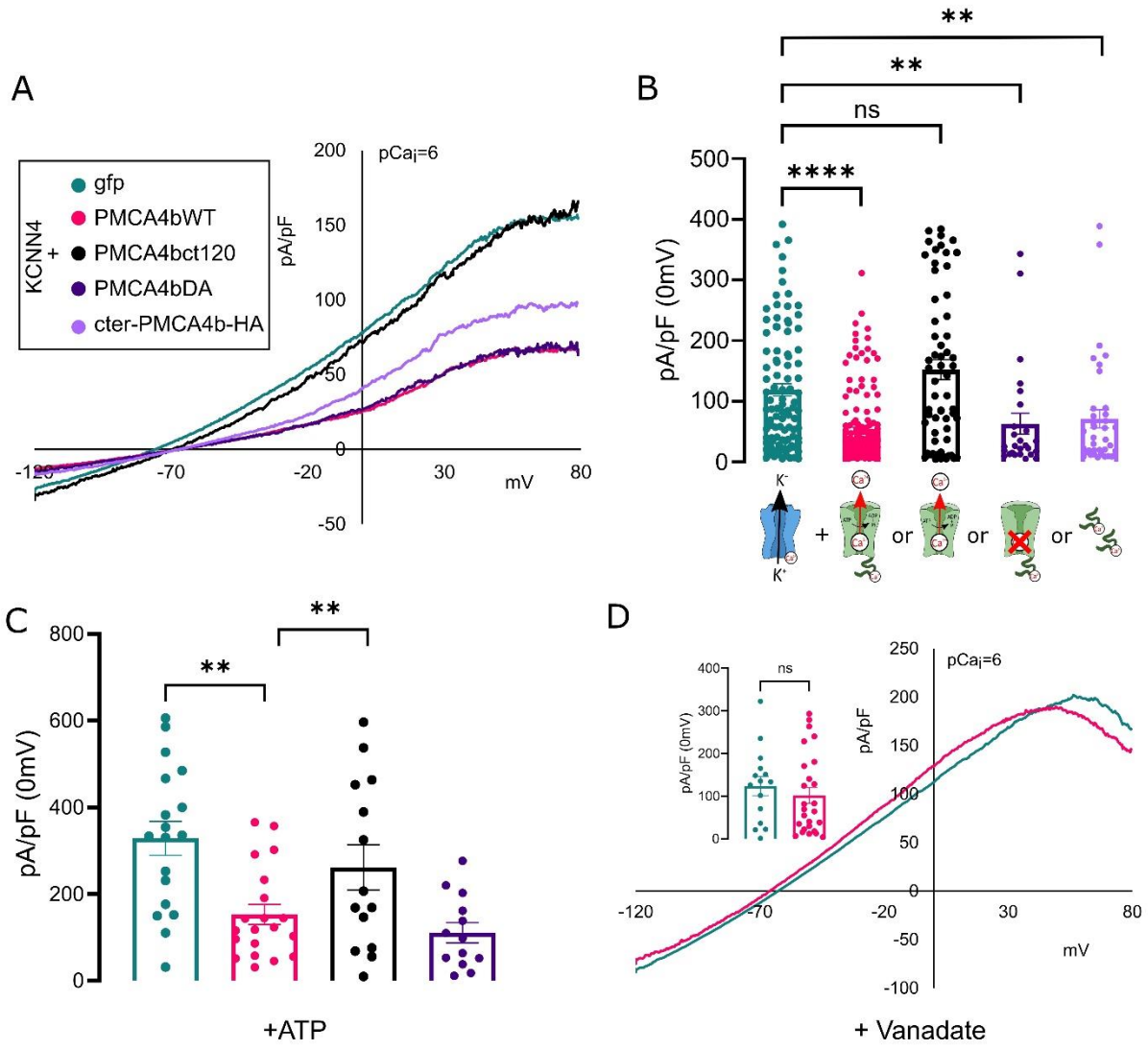

Figure 3: Electrophysiology on HEK293T cells expressing KCNN4 with or without PMCA4b WT or mutated in presence of 1 µM Ca^{2+}.

A) Representative current traces observed in HEK293T cells expressing KCNN4 with GFP (green) or with different PMCA4b constructs: WT (pink), deleted of the C terminal end (PMCA4bCT120, black), mutated D452A (sapphire) or soluble PMCA4b C-terminal end (purple). B) Corresponding current density in pA/pF measured at 0 mV, n=111 KCNN4+GFP, n=133 KCNN4+PMCA4b WT, n=73 KCNN4+PMCA4bCT120, n=24 KCNN4+PMCA4b D452A and n=39 KCNN4+soluble PMCA4b C-terminal end. C) Current density measured in presence of 1 mM ATP for HEK293T cells expressing KCNN4+GFP (green), KCNN4+PMA4b WT (pink), KCNN4+PMCA4bCT120 (black), KCNN4+mutated D452A (sapphire). D) representative traces and current density in pA/pF in presence of 5 mM Vanadate incubated for 20 minutes in extracellular bath. Data are means ± sem. ** p<0.01 and ****p<0.0001.

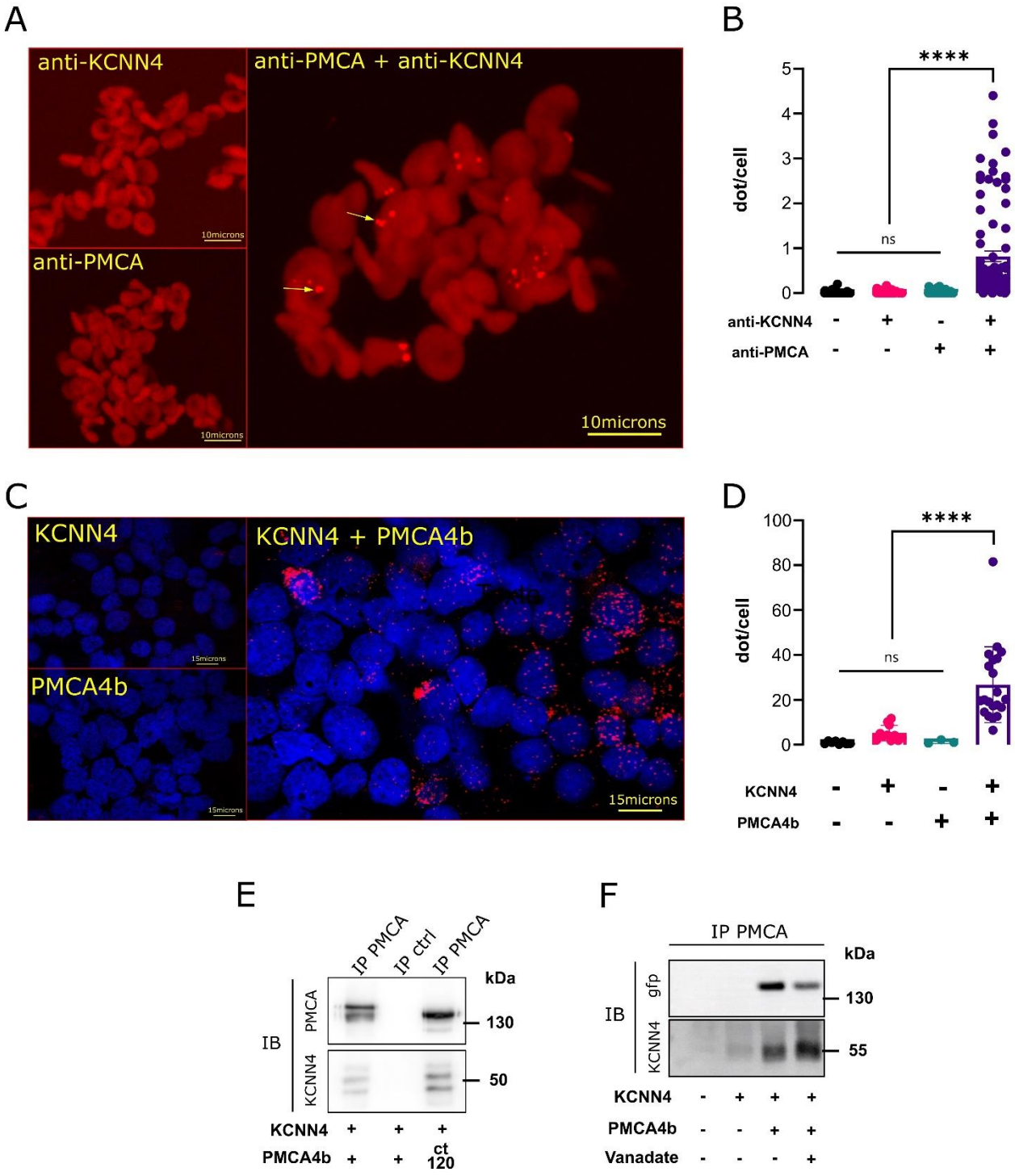
A
anti-KCNN4
anti-PMCA
anti-PMCA + anti-KCNN4
10microns
10microns
10microns
B
****
ns
dot/cell
0
1
2
3
4
5
anti-KCNN4 - + - +
anti-PMCA - - + +
C
KCNN4
PMCA4b
KCNN4 + PMCA4b
15microns
15microns
15microns
D
****
ns
dot/cell
0
20
40
60
80
100
KCNN4 - + - +
PMCA4b - - + +
E
IP PMCA
IP ctrl
IP PMCA
kDa
IB
PMCA
KCNN4
130
50
KCNN4 + + +
PMCA4b + + ct 120
F
IP PMCA
kDa
IB
gfp
KCNN4
130
55
KCNN4 - + + +
PMCA4b - - + +
Vanadate - - - +

Figure 4: Proximity ligation assay and immunoprecipitation.

Representative pictures of proximity ligation assay on RBC (A) or on HEK293T cells co-expressing KCNN4 and PMC4Ab (B) done with both antibodies anti-KCNN4 and anti-PMCA or with only anti-PMCA or anti-KCNN4. Quantification of PLA dots per cell in different experimental conditions for RBC (C) and HEK293T cells expressing KCNN4 and PMCA4b (D). Data are means ± sem, n=2 experiments for HEK293T transfected cells and n=4 for RBC. E-F) immunoprecipitation of PMCA4b in HEK293T cells control (GFP transfection), transfected with KCNN4 alone, KCNN4+PMCA4b WT (F) or KCNN4+PMCA4bCT120 (E). Eluted fractions were revealed on WB with anti-PMCA and anti KCNN4 (E) or with anti GFP (PMCA4b is fused to GFP) and anti KCNN4 (F). IP control was done on empty agarose beads. Representative WB, n= 4.

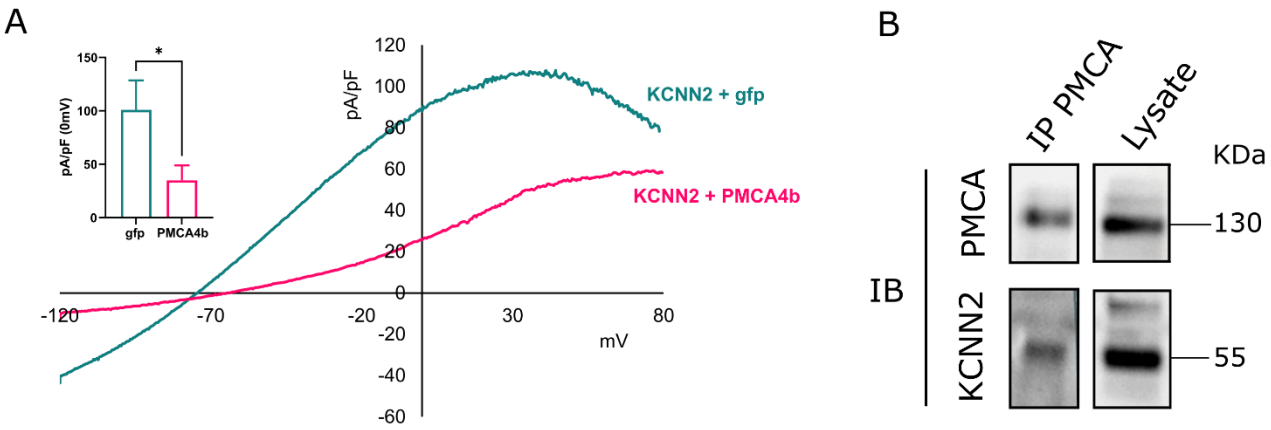

Figure 5: KCNN2 control by PMCA4b in HEK293T cells.

(A) Representative traces of currents in HEK293T cells expressing KCNN2 in presence (magenta) or absence (indigo) of PMCA4b and statistical analysis in insert (Bar plot with Mean +/- SEM, n=7 for KCNN2 + gfp, n=11 for KCNN2 + PMCA4b, * : $p<0.05$ with a Mann-Whitney test) . (B) Immunoprecipation of KCNN2 and PMCA4b in HEK293T cells transfected with both proteins. Eluted fractions were revealed on WB with anti-PMCA and anti KCNN2.

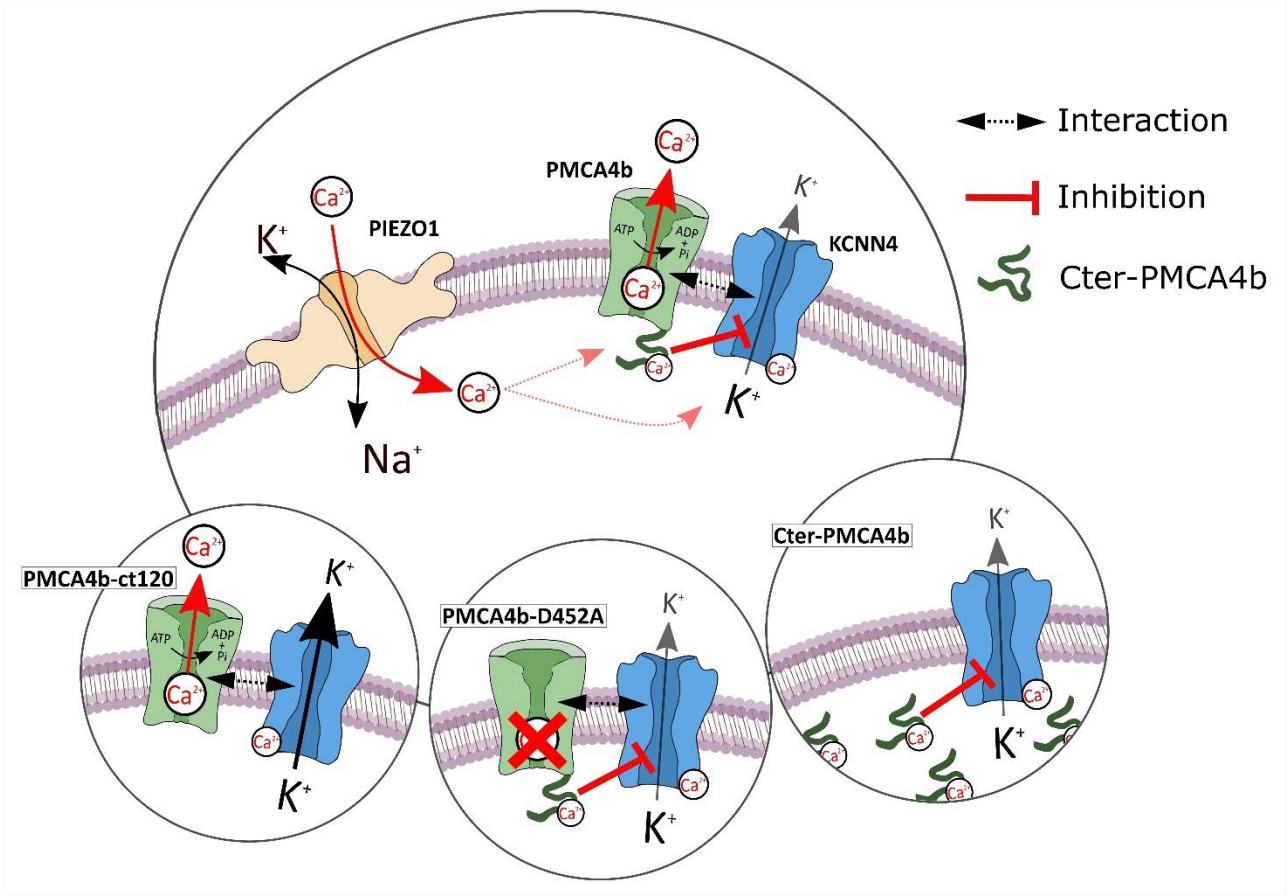

Figure 6: Schema recapitulating the control by PMCA4b on KCNN4 transport activity.

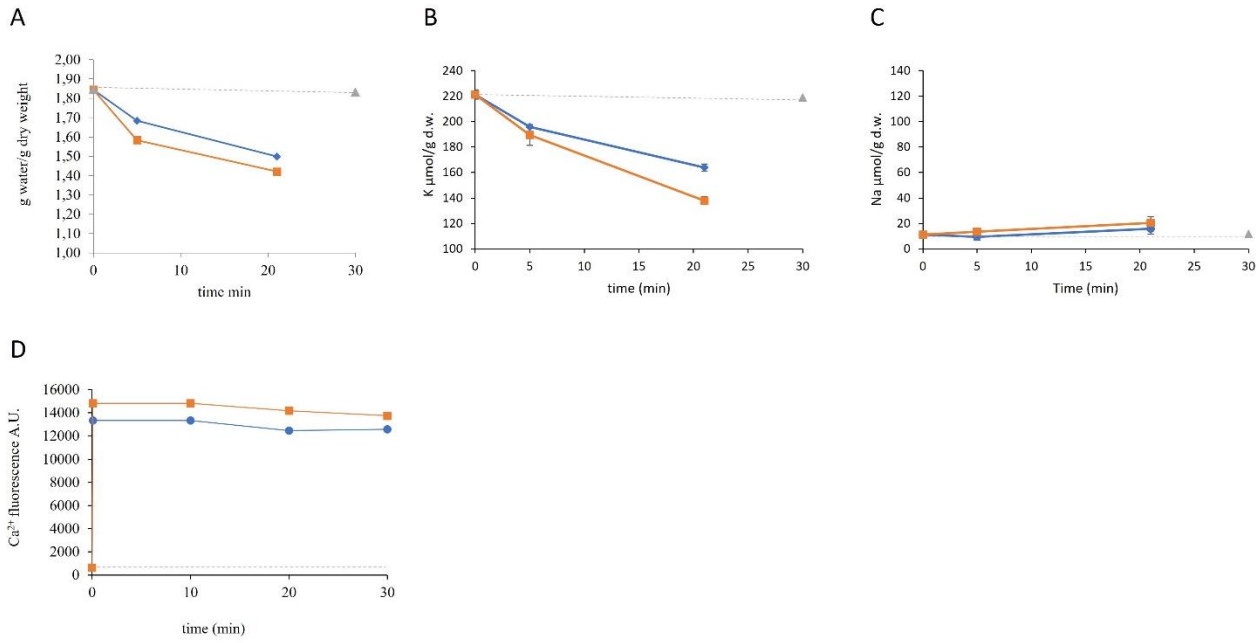

Supplemental Figure 1: Effect of 4Br-A23187 and vanadate on water and ion permeability. Effect of 4Br-A23187 (5 µM) (Blue) and 4Br-A23187 + Vanadate (5mM) (Orange) on water (A), K+ (B), Na+ (C) contents and Ca2+ fluorescence (D). Controls measurement are given with grey dash line (triangle) for comparison. Means±S.D. of 3 samples from the same experiment that was done 2 times. Error bars are within symbols when not visible.

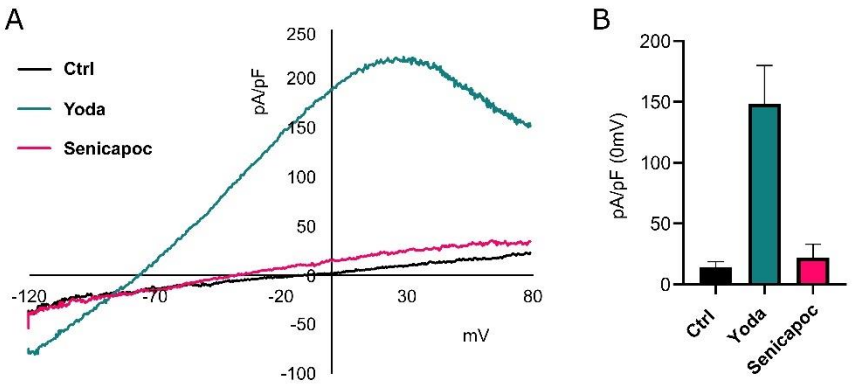

Supplemental figure 2: Functional coupling between KCNN4 and PIEZO1 in HEK293T cells.
Representative traces of KCNN4 current before (ctrl, black), after PIEZO1 activation by Yoda1 (indigo) and inhibition of KCNN4 by Senicapoc (magenta) measured in HEK293T cells with patch-clamp in whole-cell configuration with 0.001µM Ca2+ free inside (A). Corresponding statistical analyses (B).

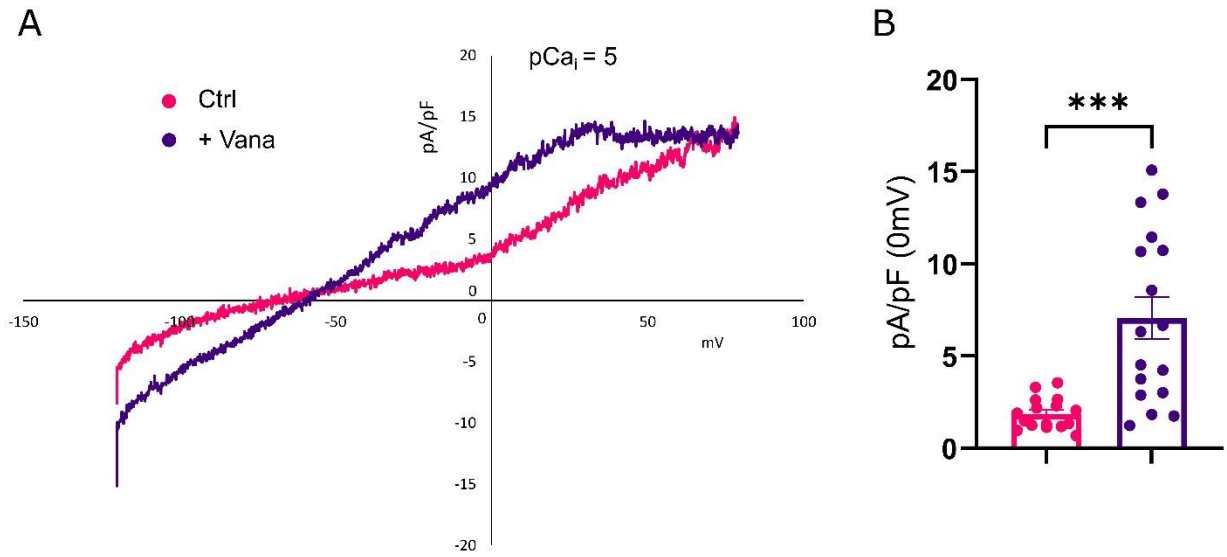

Supplemental figure 3: Effect of vanadate on K562 endogenous current.
Representative traces of endogenous K562 cells current with (purple) or without (magenta) 5 mM Vanadate in the pipette, measured with path-clamp in whole-cell configuration with 10 µM Ca2+ free inside (A). Corresponding statistical analyses (B).

Conclusion

Le GR humain est étudié depuis de nombreuses années sur pratiquement tous ses aspects. Du fait de sa simplicité d'accès, il a été un excellent modèle d'étude de la perméabilité ionique et hydrique. Malgré cela, nous sommes encore loin d'avoir déchiffré toutes les subtilités de la perméabilité des GR. Il existe un équilibre hydrique, ionique et oncotique entre le milieu interne et externe qui garantit le volume du GR. Cependant, les nombreuses perméabilités ioniques qui existent dans la membrane du GR sont autant de possibilités d'altérer cet équilibre. Deux exemples, présentés dans cette thèse, sont PIEZO1 et KCNN4, dont l'activation conduit à la déshydratation du GR. La déshydratation est un évènement irréversible dans le GR humain, qui est dépourvu de mécanismes de régulation de son volume. Il en possède pourtant la majorité des acteurs mais pour une raison encore mal comprise, ces derniers ne sont pas ou peu actifs. Bien qu'encore débattue, l'activation physiologique du couple PIEZO1-KCNN4 dans la circulation serait responsable d'infimes déshydratation facilitant le passage des GR dans les microcapillaires. En revanche, en conditions pathologiques le rôle de ce couple est mieux connu. En effet, les mutations gains de fonction de PIEZO1 ou KCNN4 sont responsables de la Xérocytose Héréditaire (Stomatocytose déshydratée), une anémie hémolytique dont la première cause établie était la déshydratation par perte excessive de K^+. Rapidement, des divergences de phénotypes cliniques et cellulaires associés aux mutations PIEZO1 et KCNN4, ont été décrites. Cela a conduit à la séparation en deux maladies avec des tableaux cliniques différents : la Stomatocytose déshydratée de type 1, causée par les mutations de PIEZO1, associées à des anémies bien compensées et la Stomatocytose déshydratée de type 2, causée par les mutations de KCNN4, associée à des anémies sévères. Le comportement des GR de patients mutés PIEZO1 ou KCNN4 est fondamentalement différent. Nous observons plus fréquemment un phénotype de déshydratation des GR associé à une mutation PIEZO1 mais très rarement avec une mutation KCNN4.

Les travaux présentés dans cette thèse permettent de mieux comprendre comment le couplage PIEZO1-KCNN4 est régulé dans le GR humain. Dans un premier axe, j'ai présenté la caractérisation de mutations de PIEZO1 et KCNN4 associées à une anémie hémolytique et dans un deuxième axe, j'ai décrit un nouveau mécanisme régulateur de KCNN4 impliquant la pompe calcique ATP dépendante PMCA.

Dans le premier axe nous rapportons les effets cellulaires de 15 mutations PIEZO1 et 4 mutations de KCNN4. 8 mutations de PIEZO1 et 4 mutations de KCNN4 n'avaient jamais été caractérisées au niveau cellulaire. Nos résultats confirment les différences de phénotype érythrocytaire entre les mutations PIEZO1 et KCNN4. C'est-à-dire une absence de déshydratation des GR des patients porteurs de mutations de KCNN4 malgré un phénotype gain de fonction dans un modèle d'expression

hétérologue. A l'inverse, les mutations de PIEZO1 sont associées à un défaut de perméabilité ionique et hydrique lorsqu'elles sont pathogènes.

Nos travaux sur les mutations de KCNN4 remettent en question la classification en « Stomatocytose Déshydratée ». Nous observons effectivement des stomatocytes ainsi que d'autres anomalies de la morphologie du GR mais aucune déshydratation. Cela suggère un autre rôle de KCNN4 dans cette maladie, peut-être lié à la structure et non à la perméabilité du GR, qui mérite une attention particulière.
De plus, ces travaux mettent en évidence les difficultés à trouver un bon modèle pour étudier le fonctionnement des protéines membranaires du GR humain. En effet, nous mesurons de fortes disparités de comportement des mutations de PIEZO1 entre les cellules HEK293T et le GR ce qui remet en cause la pertinence de ce modèle pour évaluer les spécificités fonctionnelles des canaux ioniques exprimés dans les GR. Cela souligne l'importance de l'environnement lipidique et protéique sur le comportement des canaux ioniques dont PIEZO1.

Dans le second axe, nous mettons en lumière un nouveau mécanisme de régulation du canal KCNN4 par la PMCA4b. Nos résultats montrent que la PMCA4b inhibe KCNN4 dans les GR et dans les HEK293T. Cette inhibition nécessite la présence de la partie C-terminale de la PMCA4b, est indépendante du Ca^{2+} ainsi que de l'activité d'efflux de la pompe et est bloquée par l'ajout de Vanadate. Les deux protéines sont également en interaction, soit directement par un domaine de la PMCA4b qui n'est pas le C-terminal, soit indirectement par un ou plusieurs intermédiaires. Ce nouveau mécanisme serait important dans le GR pour empêcher l'activation de KCNN4 par une augmentation de la concentration calcique. Il agirait comme une sécurité supplémentaire et préserverait le GR d'une déshydratation. La suite logique de ces travaux visera à identifier quels sont les domaines impliqués dans l'interaction et comment le C-ter exerce-t-il son effet sur KCNN4. D'autre part, il existe de nombreuses isoformes de PMCA, il serait intéressant de savoir si toutes les isoformes sont capables d'un tel mécanisme. Ce mécanisme de régulation pourrait bien être conservé dans la famille des canaux SK, dans d'autre contexte que celui du GR.
Une question importante est de savoir si ce mécanisme joue un rôle dans la XH. Des défauts d'expression de la PMCA4b ont déjà été corrélés à certains polymorphismes du gène *ATP2B4*. De plus nous avons mis en évidence une diminution d'expression de la PMCA dans les GR de certains patients mutés PIEZO1 ou KCNN4. Dans quelle mesure, la PMCA joue-t-elle un rôle dans cette pathologie ? Est-ce que la régulation de KCNN4 par la PMCA est impliquée dans la XH ? Ce sont autant de questions qui méritent des études approfondies.

Matériels et Méthodes

Western Blot

Les protéines ont été dénaturées dans du tampon Laemmli (SDS, BME) et chargées sur le gel. Afin de visualiser les hauts poids moléculaires tels que PIEZO1, des gels contenant 8 % de polyacrylamide ont été utilisés. Les migrations ont été faites pendant 1h30 à 120V à température ambiante. Ensuite, les protéines ont été transférées sur une membrane de PVDF préalablement activée avec de l'éthanol à 100 %. Le transfert a été réalisé en semi-sec pendant 30 minutes à 250mA par gel ou en liquide pendant 1h à 100V.Les membranes ont ensuite été bloquées avec le milieu de blocage (MB : lait pauvre en graisses dilué à 5 % avec du milieu de lavage (ML : TBS tween 0,1 %) pendant au moins 1h à température ambiante. Les différents anticorps ont été incubés pendant 1h30 à température ambiante ou toute la nuit à 4 degrés Celsius dans du MB : anti-KCNN4 (Proteintech, Lapin, 1:1000), anti-pan PMCA 5F10 (Invitrogen, Souris, 1:1000), anti-GAPDH (Souris, Millipore, 1:200000) and PIEZO1 (Lapin, Proteintech 1:1000). Ensuite, il y a eu trois lavages successifs de 15 minutes dans du ML. Les anticorps secondaires couplés à HRP ont été incubés pendant 45 minutes à température ambiante dans du MB : anti-lapin (1:2000, DAKO) and anti-souris (1:5000, DAKO . Après lavages des membranes dans du ML, les substrats de la peroxydase (Enhanced Chemoluminescence) ont été ajoutés à la membrane pendant quelques secondes en fonction des protéines à révéler. La révélation s'est faite avec une machine Fusion Edge en mode manuel avec des temps d'exposition suffisants pour observer un signal non saturé. Ensuite, les images sans les marqueurs ont été quantifiées avec le logiciel ImageJ en utilisant la fonction de mesure de la densité de pixels et rapportées à un gène de ménage.

Proximity Ligation Assay (PLA)

Le kit Duolink PLA (Olink Bioscience) a été utilisé pour détecter l'interaction entre KCNN4 et PMCA ou PMCA4b dans les cellules HEK293T et les globules rouges (RBC). Les cellules HEK293T ont été transfectées ou non avec pEGFP-hPMCA4b et/ou pcDNA3-HA-hKCNN4 (0,5 µg d'ADN/mL de DMEM) en utilisant du CaPO4 pendant 8 heures, puis ensemencées sur des lames de microscopie préalablement revêtues de poly-Lysine (40 µg/mL) et cultivées jusqu'à ce qu'elles atteignent une confluence de 70 %. Les cellules ont été lavées avec du PBS1X, fixées avec du paraformaldéhyde à 4 % pendant 10 minutes, puis perméabilisées pendant 10 minutes avec du triton×100 (0,03 %). Le blocage de l'antigène non spécifique est effectué avec la solution de blocage du kit pendant 1 heure à 37 °C. Les cellules ont été immunomarquées avec les anticorps primaires anti-KCNN4 (1 :200, lapin, Proteintech) et anti-PMCA4b (1 :200, souris, Millipore MABN1801) dans la solution du kit pendant une nuit à 4 °C. Les étapes suivantes sont réalisées selon les instructions du fabricant (Duolink).

Pour les GR, du sang frais prélevé est lavé dans une solution de Ringer sans Ca^{2+} (mM) : NaCl (145), KCl (5), MgSO4 (2), CaCl2 (1), HEPES (10) pH 7.4. Puis 20 µL du culot est fixé pendant 30 minutes à température ambiante dans 1 mL de PBS1X contenant 4 % de PFA et 0,05 % de glutaraldéhyde. Les GR fixés sont conservés à 4 °C jusqu'à leur utilisation. La technique PLA est réalisée en suspension avec 20 µL de GR précédemment fixés. Les GR sont immunomarqués avec les anticorps primaires anti-KCNN4 (1 :200, lapin, Proteintech) et anti-panPMCA (1 :200, souris, Invitrogen) dans la solution du kit pendant une nuit à 4 °C. À l'exception des étapes de centrifugation (1 minute à 1000 tr/min) pour récupérer les cellules et éliminer le surnageant, le reste est réalisé selon les instructions du fabricant dans les mêmes conditions que pour les cellules HEK293T. Les images du PLA ont été capturées à l'aide d'un microscope inversé Zeiss Axio Observer Z1 (Zeiss) x64, avec un filtre Cyan5 pour les points PLA (rouge lointain) et un filtre DAPI pour le noyau. Des microscopes confocaux L880 Zeiss, x64 ont été utilisés pour l'illustration. Pour la quantification, les points PLA par cellule ont été quantifiés à l'aide du logiciel Image J et comparés à la condition témoin : cellules HEK293T non transfectées ou GR avec uniquement les anticorps secondaires.

Culture Cellulaire

Les cellules HEK293T ont été cultivées dans du DMEM glutamax (Gibco) avec 10 % de sérum de veau fœtal (FBS) et de la pénicilline-streptomycine. Les cellules ont été co-transfectées avec les plasmides pcDNA3-KCNN4-HA WT ou mutés ponctuellement et pIRES-eGFP (rapport 10:1) en utilisant du $CaPO_4$. Le plasmide pcDNA3-KCNN4-HA WT a été gracieusement offert par le laboratoire de Len Kaczmarek. Seize heures plus tard, les cellules ont été lavées deux fois avec du PBS, puis les mesures de courant en patch-clamp ont été réalisés sur les cellules fluorescentes.

Les mutations ponctuelles ont été effectuées par PCR sur le plasmide pcDNA3-KCNN4-HA avec la polymérase ADN à correction d'épreuves pfu-Turbo et des amorces couvrant 16 nucléotides en amont et en aval de la mutation ponctuelle. Les clones utilisés dans l'étude ont été entièrement séquencés.

Mesure du contenu hydrique et ionique dans les GR

Du sang veineux frais a été prélevé par ponction veineuse dans des tubes de collecte contenant de l'EDTA, auprès de patients informés et de volontaires en bonne santé. Les échantillons de sang ont été reçus au laboratoire dans les 24 à 72 heures, transportés à température ambiante. Le sang a été lavé quatre fois à température ambiante dans un milieu contenant (en mM) : NaCl (145), KCl (5), MgSO4 (2), CaCl2 (1) et Hepes/NaOH, pH 7.4. La suspension de GR a ensuite été incubée à

température ambiante avec un hématocrite de 25 % avec 0.5 mM d'ouabaïne. Les différentes drogues ont été ajoutées à ce moment : yoda1 (2 µM), vanadate (5 mM), senicapoc (0.4 µM) et GsMTx4 (5 µM). Quelques minutes avant l'heure d'échantillonnage, 400 µl de la suspension cellulaire ont été prélevés pour remplir trois tubes en nylon qui ont été centrifugés pendant 10 minutes à 4°C, à 20 000 g au moment exact de l'échantillonnage. Le culot des GR a été extrait et pesé immédiatement. Ensuite, le poids sec a été mesuré après une nuit de chauffage (80°C). La teneur en eau a été calculée avec une correction de 3,64 % correspondant au milieu piégé entre les GR tassées. Les ions intracellulaires ont été extraits des culots secs par incubation pendant la nuit à 4°C dans 5 ml d'eau milliRho (Millipore). Ensuite, 2 % d'acide perchlorique ont été ajoutés pour précipiter les protéines, les échantillons ont été centrifugés pendant 10 minutes à 20 000 g, et le surnageant a été prélevé pour quantifier les concentrations en Na^+ et K^+ par spectroscopie de flamme avec un Eppendorf ELEX6361.

Mesure du Calcium

Les GR ont été lavés deux fois (800 g, 5 min, à 4°C) dans du Ringer sans Ca^{2+}. Quatre microlitres de globules rouges concentrés ont été chargés avec 2,5 µl d'une solution mère de Fluo-4 AM à 1 mM dans 500 µl de Ringer sans Ca^{2+}, à 37°C, pendant 30 minutes. La suspension de GR chargés de Fluo-4 a été directement utilisée pour quantifier la concentration intracellulaire de Ca^{2+} (25 µl de suspension de globules rouges dans 975 µl de Ringer avec Ca^{2+} dans des tubes FACS), en mesurant la fluorescence à l'aide d'un FACS Fortessa BD. La fluorescence interne a été évaluée sur des GR traités sans Fluo-4 AM. Pour les expériences avec le yoda1 et le vanadate, la suspension de GR chargés de Fluo-4 a été diluée 40 fois dans du Ringer contenant 1 mM de Ca^{2+} ± 2 µM de yoda1 et/ou 5 mM de vanadate au temps 0 min, et la fluorescence intracellulaire a été mesurée à l'aide du FACS Fortessa BD en fonction du temps.

Mesure de la Résistance Osmotique

La résistance Osmotique est un moyen de constater indirectement l'état d'hydratation des GRs. Ces derniers sont soumis à des concentrations décroissantes de NaCl et constante de pH afin d'induire l'hémolyse. L'hémoglobine libérée lors de ce phénomène peut être quantifiée par spectrométrie afin de déterminer la concentration de NaCl pour lequel on atteint 50% d'hémolyse. Un GR déshydraté lysera pour des concentrations de NaCl plus faibles alors qu'un GR hyperhydraté lysera pour des concentrations des NaCl plus importantes. Des modifications de la résistance osmotique peuvent aussi témoigner d'altération de structure indépendamment de défaut d'hydratation.

Protocole : Des solution de travail avec des concentrations relatives de NaCl allant de 1 à 0.1 par incrément de 0.1, sont préparées à partir d'une solution stock de NaCl 10% (NaCl 1.54M, Na_2HPO4 0.096M, NaH_2PO4 0.020M) correspondant à 3,312 mosm. 10µL de sang total homogénéisé est ajouté à 1mL de solution de travail pour chaque concentration de NaCl puis mélangé délicatement. Après 30min d'incubation à température ambiante (RT), le sang est remis en suspension et centrifugé 5min à 2000 rpm. La Densité Optique (DO) est lue à partir de 100 µL de surnageant à 540nm avec un lecteur de microplaque FluoStar Optima.

Statistiques

Pour une comparaison entre deux conditions, le test de Mann-Whitney a été utilisé. Pour des comparaisons multiples, le test de Kruskal-Wallis a été appliqué avec une correction post-hoc de Dunn lorsque chaque condition étaient comparées entre elles, ou un test de Dunn non corrigé lorsque chaque condition était comparée à une condition contrôle. Pour l'analyse groupée, le test ANOVA à deux facteurs avec un test post-hoc de Dunnett a été utilisé. Les différences statistiques sont indiquées comme suit : * : $p<0.05$; ** : $p<0.01$; *** : $p<0.001$.

Electrophysiologie

Principe

Le gradient électrochimique est utilisé par les ions comme une Force Electromotrice (FEM). L'ouverture d'un canal est donnée par sa conductance unitaire γ qui se transpose au niveau de la cellule entière par la conductance globale G (G et γ en Siemens, S). Plus l'ouverture est grande, plus γ est grand et donc par extension G et plus le flux ionique passant par le canal ionique sera grand. De plus, les canaux ioniques peuvent sélectivement faire passer une espèce ionique contrairement à une vanne qui ne fait pas la distinction, c'est la sélectivité.

En électrophysiologie, la loi électrique la plus importante est la loi d'Ohm. La différence de potentiel entre deux points liés électriquement (U) en volt (V) est donné par le courant (I) en ampère (A) et la conductance (G) en siemens (S) qui s'avère être l'inverse de la résistance (R) en Ohm (Ω).

$$U = R.I$$

ou

$$I = \frac{U}{R} \; et \; comme \; R = \frac{1}{G} \; alors \; I = U.G$$

Équation 4 : Loi de Ohm.

U : différence de potentiel (V), R : résistance (Ω), I : courant (A). G : conductance (S).

U, la différence de potentiel, est l'équivalent de la FEM dans un modèle de membrane cellulaire et dépend de l'espèce ionique : FEM = Er – Ei (cf. Chapitre 1 : 4.1). Plus la valeur absolue de la FEM est grande et plus le courant de l'ion sera grand :

$$I = G.FEM$$

On parle ici de courant I macroscopique qui est la résultante de la somme des courants unitaires. En réalité, G, la conductance globale est de fait la résultante des conductances unitaires γ, du nombre de canaux ioniques présent N et de leur probabilité d'ouverture Po.

On a ainsi : $G = n.Po.\gamma$

Donc : $I = n.Po.\gamma.(Er - Ei)$

Le courant va donc dépendre de la FEM qui peut être positive ou négative en fonction de l'ion. Par convention :

- SI FEM > 0 on parle de courant cationique sortant ou anionique entrant.
- Si FEM < 0 on parle de courant cationique entrant ou anionique sortant.

Mesure de courant : technique de patch clamp.

Afin de mesurer l'activité des canaux ioniques d'une cellule, j'ai utilisé la technique de Patch Clamp en configuration : « Cellule entière ». Cette technique permet de mesurer un courant électrique déterminé par un mouvement d'ions chargé de part et d'autre de la membrane plasmique.

L'étude des canaux ionique peut se réaliser de multiples manières qu'elles soient directes ou indirectes. La technique de patch développée par Neher et Sakmann (Neher and Sakmann, 1976;

Sakmann and Neher, 1984) permet de mesurer directement des courants électriques, de l'ordre du pico Ampère, induit par un mouvement ionique. Cette technique a notamment permis de mesurer les premiers courants ioniques dans un GR en 1981 (Hamill et al., 1981).

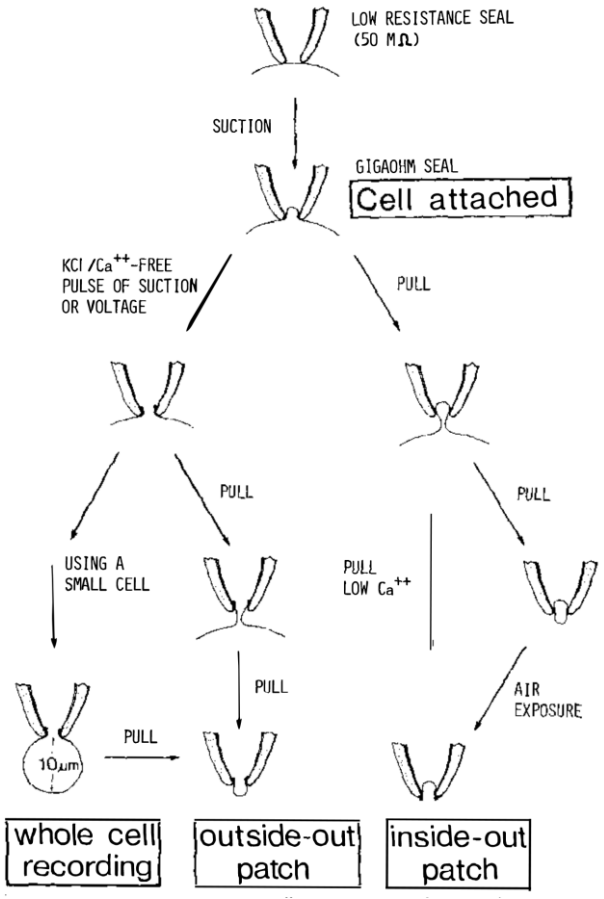

Figure 30 Configuration obtenues avec la technique de patch-clamp.
(Sakmann and Neher, 1984)

Plusieurs configurations de patch-clamp existent (Figure 30):

- Cellule attachée ou « cell-attached » qui correspond au moment où la membrane est aspirée dans la pipette et forme ce qu'on appelle un « giga-seal ». C'est-à-dire un scellement hermétique faisant grimper la résistance à des valeurs de l'ordre du giga Ohm. C'est une configuration utilisée pour mesurer des conductances unitaires. Le milieu intra-pipette ne communique pas avec l'intérieur de la cellule.

- Cellule entière ou « whole-cell », est obtenue en appliquant une pression négative dans la pipette ce qui induit une aspiration. De cette façon, le giga-seal est rompu, la membrane de la cellule adhère aux parois de la pipette, qui communique directement avec le milieu intracellulaire. C'est une configuration qui permet de mesurer l'activité de l'ensemble des canaux ioniques présent à la membrane de la cellule.
- Externe-dehors ou « outside-out » est obtenu à partir de la configuration cellule-entière en retirant délicatement la pipette de la cellule. De cette façon, la membrane de la cellule qui adhère à la pipette se rompt et se referme sur elle-même tout en restant accrochée à la pipette. C'est une configuration utilisée pour mesurer des courants unitaires en contrôlant les milieux interne et externe. La face externe de la membrane est en contact du milieu extérieur et la face interne en contact du milieu intra-pipette.
- Interne-dehors ou « inside-out » est obtenu à partir de la configuration cellule attachée en retirant délicatement la pipette de la cellule. La membrane se rompt et se referme avec la face interne dirigée vers le milieu extérieur et la face externe vers le milieu intra-pipette.

Protocole

Les pipettes de verre (Brand, Wertheim, Allemagne) avec une résistance finale comprise entre 3 et 5 mΩ ont été faite avec une étireuse de pipette horizontale (P-97, Sutter Instrument, Navato, CA). Les courants sont mesurés sur un amplificateur Axon et une digidata 1440 sur le logiciel clampex 10.5. Les cellules atteignant une résistance d'au moins 1GΩ en cellule-attachée sont gardées. Après passage en configuration cellule-entière, la cellule est soumise à un protocole de rampe allant de -120mV à +80mV pendant 150ms et toutes les 2.5s avec un potentiel de maintien à -60mV. Les courants sont échantillonnés à 10kHz et filtrés à 5kHz. La densité de courant de KCNN4 à 0 mV (pA/pF (0 mV)) a été mesurée, à l'état stable, avec différentes concentrations de Ca^{2+} intracellulaire (0.01, 0.1, 0.25, 0.5, 1 µM). Les milieux extracellulaire et intracellulaire (intra pipette) utilisés sont les suivants :

- Extracellulaire (mM) : NaCl (145), CaCl2 (2), KCl (5), MgCl2 (1), and HEPES (10), pH 7.4 ajusté avec NaOH.
- Intra pipette (mM) : KCl (145), MgCl2 (1), HEPES (1), and EGTA (1), pH 7.2 ajusté avec KOH. Les concentrations en Ca^{2+} libre sont ajustées avec du $CaCl_2$ en utilisant le logiciel web : Ca-EGTA Calculator v1.3.

Références

Albert, S., Wolf, P.L., Pryjma, I., Vazquez, J., 1966. Erythropoiesis in the Human Thymus. Am. J. Clin. Pathol. 45, 460–464. https://doi.org/10.1093/ajcp/45.4.460

Albuisson, J., Murthy, S.E., Bandell, M., Coste, B., Louis-dit-Picard, H., Mathur, J., Fénéant-Thibault, M., Tertian, G., de Jaureguiberry, J.-P., Syfuss, P.-Y., Cahalan, S., Garçon, L., Toutain, F., Simon Rohrlich, P., Delaunay, J., Picard, V., Jeunemaitre, X., Patapoutian, A., 2013. Dehydrated hereditary stomatocytosis linked to gain-of-function mutations in mechanically activated PIEZO1 ion channels. Nat. Commun. 4, 1884. https://doi.org/10.1038/ncomms2899

Allegrini, B., Jedele, S., David Nguyen, L., Mignotet, M., Rapetti-Mauss, R., Etchebest, C., Fenneteau, O., Loubat, A., Boutet, A., Thomas, C., Durin, J., Petit, A., Badens, C., Garçon, L., Da Costa, L., Guizouarn, H., 2022. New KCNN4 Variants Associated With Anemia: Stomatocytosis Without Erythrocyte Dehydration. Front. Physiol. 13.

Allegrini, B., NGuyen, L.D., Mignotet, M., Etchebest, C., Fenneteau, O., Platon, J., Lambilliotte, A., Guizouarn, H., Da Costa, L., 2023. Next generation sequencing (NGS) interest in deciphering erythrocyte molecular defects' association in red cell disorders: Clinical and erythrocyte phenotypes of patients with mutations inheritance in PIEZO1, Spectrin ß1, RhAG and SLC4A1. Blood Cells. Mol. Dis. 102780. https://doi.org/10.1016/j.bcmd.2023.102780

Alvarez, J., García-Sancho, J., 1987. An estimate of the number of Ca2+-dependent K+ channels in the human red cell. Biochim. Biophys. Acta 903, 543–546. https://doi.org/10.1016/0005-2736(87)90062-9

An, X., Lecomte, M.C., Chasis, J.A., Mohandas, N., Gratzer, W., 2002. Shear-response of the spectrin dimer-tetramer equilibrium in the red blood cell membrane. J. Biol. Chem. 277, 31796–31800. https://doi.org/10.1074/jbc.M204567200

An, X., Mohandas, N., 2008. Disorders of red cell membrane. Br. J. Haematol. 141, 367–375. https://doi.org/10.1111/j.1365-2141.2008.07091.x

Andolfo, I., Alper, S.L., De Franceschi, L., Auriemma, C., Russo, R., De Falco, L., Vallefuoco, F., Esposito, M.R., Vandorpe, D.H., Shmukler, B.E., Narayan, R., Montanaro, D., D'Armiento, M., Vetro, A., Limongelli, I., Zuffardi, O., Glader, B.E., Schrier, S.L., Brugnara, C., Stewart, G.W., Delaunay, J., Iolascon, A., 2013. Multiple clinical forms of dehydrated hereditary stomatocytosis arise from mutations in PIEZO1. Blood 121, 3925–3935, S1-12. https://doi.org/10.1182/blood-2013-02-482489

Andolfo, I., Martone, S., Rosato, B.E., Marra, R., Gambale, A., Forni, G.L., Pinto, V., Göransson, M., Papadopoulou, V., Gavillet, M., Elalfy, M., Panarelli, A., Tomaiuolo, G., Iolascon, A., Russo, R., 2021. Complex Modes of Inheritance in Hereditary Red Blood Cell Disorders: A Case Series Study of 155 Patients. Genes 12, 958. https://doi.org/10.3390/genes12070958

Andolfo, I., Monaco, V., Cozzolino, F., Rosato, B.E., Marra, R., Cerbone, V., Pinto, V.M., Forni, G.L., Unal, S., Iolascon, A., Monti, M., Russo, R., 2023. Proteome alterations in erythrocytes with PIEZO1 gain-of-function mutations. Blood Adv. bloodadvances.2022008673. https://doi.org/10.1182/bloodadvances.2022008673

Andolfo, I., Rosato, B.E., Manna, F., Rosa, G.D., Marra, R., Gambale, A., Girelli, D., Russo, R., Iolascon, A., 2020. Gain-of-function mutations in PIEZO1 directly impair hepatic iron metabolism via the inhibition of the BMP/SMADs pathway. Am. J. Hematol. 95, 188–197. https://doi.org/10.1002/ajh.25683

Andolfo, I., Russo, R., Gambale, A., Iolascon, A., 2016. New insights on hereditary erythrocyte membrane defects. Haematologica 101, 1284–1294. https://doi.org/10.3324/haematol.2016.142463

Andolfo, I., Russo, R., Manna, F., Shmukler, B.E., Gambale, A., Vitiello, G., De Rosa, G., Brugnara, C., Alper, S.L., Snyder, L.M., Iolascon, A., 2015. Novel Gardos channel mutations linked to dehydrated hereditary stomatocytosis (xerocytosis): KCNN4 mutations in dehydrated hereditary stomatocytosis. Am. J. Hematol. 90, 921–926. https://doi.org/10.1002/ajh.24117

Andolfo, I., Russo, R., Rosato, B.E., Manna, F., Gambale, A., Brugnara, C., Iolascon, A., 2018. Genotype-phenotype correlation and risk stratification in a cohort of 123 hereditary stomatocytosis patients. Am. J. Hematol. 93, 1509–1517. https://doi.org/10.1002/ajh.25276

Andrews, D.A., Yang, L., Low, P.S., 2002. Phorbol ester stimulates a protein kinase C–mediated agatoxin-TK–sensitive calcium permeability pathway in human red blood cells. Blood 100, 3392–3399. https://doi.org/10.1182/blood.V100.9.3392

Anémie hémolytique : définition, symptômes, causes, personnes à risques [WWW Document], 2011. . https://www.passeportsante.net/. URL https://www.passeportsante.net/fr/Maux/Problemes/Fiche.aspx?doc=anemie_hemolytique_pm (accessed 6.29.23).

Aribi, M., Merzouk, H., Haddouche, M., Benyoucef, M., Taleb, A., Kendouci-Tani, M., Merzouk, S.A., Meziane, A., 2010. Clinical evaluation of lipids, lipoproteins and red blood cells sodium and potassium in patients with different grades of hypertension. Clin. Biochem. 43, 942–947. https://doi.org/10.1016/j.clinbiochem.2010.05.012

Armsby, C.C., Brugnara, C., Alper, S.L., 1995. Cation transport in mouse erythrocytes: role of K(+)-Cl- cotransport in regulatory volume decrease. Am. J. Physiol. 268, C894-902. https://doi.org/10.1152/ajpcell.1995.268.4.C894

Bae, C., Gnanasambandam, R., Nicolai, C., Sachs, F., Gottlieb, P.A., 2013. Xerocytosis is caused by mutations that alter the kinetics of the mechanosensitive channel PIEZO1. Proc. Natl. Acad. Sci. 110, E1162–E1168. https://doi.org/10.1073/pnas.1219777110

Barbosa, N.S.V., Lima, E.R.A., Boström, M., Tavares, F.W., 2015. Membrane Potential and Ion Partitioning in an Erythrocyte Using the Poisson–Boltzmann Equation. J. Phys. Chem. B 119, 6379–6388. https://doi.org/10.1021/acs.jpcb.5b02215

Baunbæk, M., Bennekou, P., 2008. Evidence for a random entry of Ca2+ into human red cells. Bioelectrochemistry, Red Blood Cells 2007 73, 145–150. https://doi.org/10.1016/j.bioelechem.2008.04.006

Begenisich, T., Nakamoto, T., Ovitt, C.E., Nehrke, K., Brugnara, C., Alper, S.L., Melvin, J.E., 2004. Physiological roles of the intermediate conductance, Ca2+-activated potassium channel Kcnn4. J. Biol. Chem. 279, 47681–47687. https://doi.org/10.1074/jbc.M409627200

Belkacemi, A., Fecher-Trost, C., Tinschert, R., Flormann, D., Malihpour, M., Wagner, C., Meyer, M.R., Beck, A., Flockerzi, V., 2021. The TRPV2 channel mediates Ca2+ influx and the Δ9-THC-dependent decrease in osmotic fragility in red blood cells. Haematologica 106, 2246–2250. https://doi.org/10.3324/haematol.2020.274951

Benesch, R., Benesch, R.E., 1967. The effect of organic phosphates from the human erythrocyte on the allosteric properties of hemoglobin. Biochem. Biophys. Res. Commun. 26, 162–167. https://doi.org/10.1016/0006-291x(67)90228-8

Bessis, M., 1958. [Erythroblastic island, functional unity of bone marrow]. Rev. Hematol. 13, 8–11.

Bianconi, E., Piovesan, A., Facchin, F., Beraudi, A., Casadei, R., Frabetti, F., Vitale, L., Pelleri, M.C., Tassani, S., Piva, F., Perez-Amodio, S., Strippoli, P., Canaider, S., 2013. An estimation of the number of cells in the human body. Ann. Hum. Biol. 40, 463–471. https://doi.org/10.3109/03014460.2013.807878

Bogdanova, A., Kaestner, L., Simionato, G., Wickrema, A., Makhro, A., 2020. Heterogeneity of Red Blood Cells: Causes and Consequences. Front. Physiol. 11, 392. https://doi.org/10.3389/fphys.2020.00392

Bogdanova, A., Makhro, A., Wang, J., Lipp, P., Kaestner, L., 2013. Calcium in Red Blood Cells—A Perilous Balance. Int. J. Mol. Sci. 14, 9848–9872. https://doi.org/10.3390/ijms14059848

Borgese, F., Garcia-Romeu, F., Motais, R., 1987. Control of cell volume and ion transport by beta-adrenergic catecholamines in erythrocytes of rainbow trout, Salmo gairdneri. J. Physiol. 382, 123–144. https://doi.org/10.1113/jphysiol.1987.sp016359

Botello-Smith, W.M., Jiang, W., Zhang, H., Ozkan, A.D., Lin, Y.-C., Pham, C.N., Lacroix, J.J., Luo, Y., 2019. A mechanism for the activation of the mechanosensitive Piezo1 channel by the small molecule Yoda1. Nat. Commun. 10, 4503. https://doi.org/10.1038/s41467-019-12501-1

Bouyer, G., Cueff, A., Egée, S., Kmiecik, J., Maksimova, Y., Glogowska, E., Gallagher, P.G., Thomas, S.L.Y., 2011. Erythrocyte peripheral type benzodiazepine receptor/voltage-dependent anion channels are upregulated by Plasmodium falciparum. Blood 118, 2305–2312. https://doi.org/10.1182/blood-2011-01-329300

Bruce, L.J., Robinson, H.C., Guizouarn, H., Borgese, F., Harrison, P., King, M.-J., Goede, J.S., Coles, S.E., Gore, D.M., Lutz, H.U., Ficarella, R., Layton, D.M., Iolascon, A., Ellory, J.C., Stewart, G.W., 2005. Monovalent cation leaks in human red cells caused by single amino-acid substitutions in the transport domain of the band 3 chloride-bicarbonate exchanger, AE1. Nat. Genet. 37, 1258–1263. https://doi.org/10.1038/ng1656

Bryk, A.H., Wiśniewski, J.R., 2017. Quantitative Analysis of Human Red Blood Cell Proteome. J. Proteome Res. 16, 2752–2761. https://doi.org/10.1021/acs.jproteome.7b00025

Cahalan, S.M., Lukacs, V., Ranade, S.S., Chien, S., Bandell, M., Patapoutian, A., 2015. Piezo1 links mechanical forces to red blood cell volume. eLife 4, e07370. https://doi.org/10.7554/eLife.07370

Canessa, M., Fabry, M.E., Suzuka, S.M., Morgan, K., Nagel, R.L., 1990. Na+/H+ exchange is increased in sickle cell anemia and young normal red cells. J. Membr. Biol. 116, 107–115. https://doi.org/10.1007/BF01868669

Caride, A.J., Filoteo, A.G., Penniston, J.T., Strehler, E.E., 2007. THE PLASMA MEMBRANE CA2+ PUMP ISOFORM 4A DIFFERS FROM ISOFORM 4B IN THE MECHANISM OF CALMODULIN BINDING AND ACTIVATION KINETICS. IMPLICATIONS FOR CA2+ SIGNALING. J. Biol. Chem. 282, 25640–25648. https://doi.org/10.1074/jbc.M701129200

Caulier, A., Jankovsky, N., Demont, Y., Ouled-Haddou, H., Demagny, J., Guitton, C., Merlusca, L., Lebon, D., Vong, P., Aubry, A., Lahary, A., Rose, C., Gréaume, S., Cardon, E., Platon, J., Ouadid-Ahidouch, H., Rochette, J., Marolleau, J.-P., Picard, V., Garçon, L., 2020. PIEZO1 activation delays erythroid differentiation of normal and hereditary xerocytosis-derived human progenitor cells. Haematologica 105, 610–622. https://doi.org/10.3324/haematol.2019.218503

Caulier, A., Rapetti-Mauss, R., Guizouarn, H., Picard, V., Garçon, L., Badens, C., 2018. Primary red cell hydration disorders: Pathogenesis and diagnosis. Int. J. Lab. Hematol. 40 Suppl 1, 68–73. https://doi.org/10.1111/ijlh.12820

Chasis, J.A., Mohandas, N., 2008. Erythroblastic islands: niches for erythropoiesis. Blood 112, 470–478. https://doi.org/10.1182/blood-2008-03-077883

Christophersen, P., Bennekou, P., 1991. Evidence for a voltage-gated, non-selective cation channel in the human red cell membrane. Biochim. Biophys. Acta BBA - Biomembr. 1065, 103–106. https://doi.org/10.1016/0005-2736(91)90017-3

Cooper, R.A., 1978. Influence of increased membrane cholesterol on membrane fluidity and cell function in human red blood cells. J. Supramol. Struct. 8, 413–430. https://doi.org/10.1002/jss.400080404

Cosgrove, J., Hustin, L.S.P., de Boer, R.J., Perié, L., 2021. Hematopoiesis in numbers. Trends Immunol. 42, 1100–1112. https://doi.org/10.1016/j.it.2021.10.006

Coste, B., Mathur, J., Schmidt, M., Earley, T.J., Ranade, S., Petrus, M.J., Dubin, A.E., Patapoutian, A., 2010. Piezo1 and Piezo2 are essential components of distinct mechanically-activated cation channels. Science 330, 55–60. https://doi.org/10.1126/science.1193270

Coste, B., Xiao, B., Santos, J.S., Syeda, R., Grandl, J., Spencer, K.S., Kim, S.E., Schmidt, M., Mathur, J., Dubin, A.E., Montal, M., Patapoutian, A., 2012. Piezo proteins are pore-forming subunits of mechanically activated channels. Nature 483, 176–181. https://doi.org/10.1038/nature10812

Cox, C.D., Bae, C., Ziegler, L., Hartley, S., Nikolova-Krstevski, V., Rohde, P.R., Ng, C.-A., Sachs, F., Gottlieb, P.A., Martinac, B., 2016. Removal of the mechanoprotective influence of the cytoskeleton reveals PIEZO1 is gated by bilayer tension. Nat. Commun. 7, 10366. https://doi.org/10.1038/ncomms10366

Cueff, A., Seear, R., Dyrda, A., Bouyer, G., Egée, S., Esposito, A., Skepper, J., Tiffert, T., Lew, V.L., Thomas, S.L.Y., 2010. Effects of elevated intracellular calcium on the osmotic fragility of human red blood cells. Cell Calcium 47, 29–36. https://doi.org/10.1016/j.ceca.2009.11.002

Danielczok, J.G., Terriac, E., Hertz, L., Petkova-Kirova, P., Lautenschläger, F., Laschke, M.W., Kaestner, L., 2017. Red Blood Cell Passage of Small Capillaries Is Associated with Transient Ca2+-mediated Adaptations. Front. Physiol. 8, 979. https://doi.org/10.3389/fphys.2017.00979

Del Orbe Barreto, R., Arrizabalaga, B., De la Hoz Rastrollo, A.B., García-Orad, A., Gonzalez Vallejo, I., Bento, C., Villegas, A., García-Ruiz, J.C., 2016. Hereditary xerocytosis, a misleading anemia. Ann. Hematol. 95, 1545–1546. https://doi.org/10.1007/s00277-016-2716-9

Delgado, T.C., Castro, M.M., Geraldes, C.F., Jones, J.G., 2004. Quantitation of erythrocyte pentose pathway flux with [2-13C]glucose and 1H NMR analysis of the lactate methyl signal. https://doi.org/10.1002/mrm.20096

Drew, C., Ball, V., Robinson, H., Clive Ellory, J., Gibson, J.S., 2004. Oxygen sensitivity of red cell membrane transporters revisited. Bioelectrochemistry Amst. Neth. 62, 153–158. https://doi.org/10.1016/j.bioelechem.2003.07.003

Duhm, J., Otto Göbel, B., 1984. Role of the furosemide-sensitive Na+/K+ transport system in determining the steady-state Na+ and K+ content and volume of human erythrocytesin vitro andin vivo. J. Membr. Biol. 77, 243–254. https://doi.org/10.1007/BF01870572

Dunham, E.T., Glynn, I.M., 1961. Adenosinetriphosphatase activity and the active movements of alkali metal ions. J. Physiol. 156, 274–293. https://doi.org/10.1113/jphysiol.1961.sp006675

Dyrda, A., Cytlak, U., Ciuraszkiewicz, A., Lipinska, A., Cueff, A., Bouyer, G., Egée, S., Bennekou, P., Lew, V.L., Thomas, S.L.Y., 2010. Local membrane deformations activate Ca2+-dependent K+ and anionic currents in intact human red blood cells. PloS One 5, e9447. https://doi.org/10.1371/journal.pone.0009447

Elliott, S., Pham, E., Macdougall, I.C., 2008. Erythropoietins: a common mechanism of action. Exp. Hematol. 36, 1573–1584. https://doi.org/10.1016/j.exphem.2008.08.003

Ellory, J.C., Gibson, J.S., Stewart, G.W., 1998. Pathophysiology of Abnormal Cell Volume in Human Red Cells. Cell Vol. Regul. 123, 220–239. https://doi.org/10.1159/000059915

Enyedi, A., Verma, A.K., Filoteo, A.G., Penniston, J.T., 1993. A highly active 120-kDa truncated mutant of the plasma membrane Ca2+ pump. J. Biol. Chem. 268, 10621–10626. https://doi.org/10.1016/S0021-9258(18)82243-8

Evans, E.L., Cuthbertson, K., Endesh, N., Rode, B., Blythe, N.M., Hyman, A.J., Hall, S.J., Gaunt, H.J., Ludlow, M.J., Foster, R., Beech, D.J., 2018. Yoda1 analogue (Dooku1) which antagonizes Yoda1-evoked activation of Piezo1 and aortic relaxation. Br. J. Pharmacol. 175, 1744–1759. https://doi.org/10.1111/bph.14188

Fairbanks, G., Steck, T.L., Wallach, D.F., 1971. Electrophoretic analysis of the major polypeptides of the human erythrocyte membrane. Biochemistry 10, 2606–2617. https://doi.org/10.1021/bi00789a030

Falchetto, R., Vorherr, T., Brunner, J., Carafoli, E., 1991. The plasma membrane Ca2+ pump contains a site that interacts with its calmodulin-binding domain. J. Biol. Chem. 266, 2930–2936.

Fan, J., Tian, R., Yang, X., Wang, H., Shi, Y., Fan, X., Zhang, J., Chen, Y., Zhang, K., Chen, Z., Li, L., 2022. KCNN4 Promotes the Stemness Potentials of Liver Cancer Stem Cells by Enhancing Glucose Metabolism. Int. J. Mol. Sci. 23, 6958. https://doi.org/10.3390/ijms23136958

Fanger, C.M., Rauer, Heiko, Neben, A.L., Miller, M.J., Rauer, Heike, Wulff, H., Rosa, J.C., Ganellin, C.R., Chandy, K.G., Cahalan, M.D., 2001. Calcium-activated Potassium Channels Sustain Calcium Signaling in T Lymphocytes: SELECTIVE BLOCKERS AND MANIPULATED CHANNEL EXPRESSION LEVELS *. J. Biol. Chem. 276, 12249–12256. https://doi.org/10.1074/jbc.M011342200

Farquhar, J.W., Ahrens, E.H., 1963. EFFECTS OF DIETARY FATS ON HUMAN ERYTHROCYTE FATTY ACID PATTERNS*. J. Clin. Invest. 42, 675–685.

Faucherre, A., Kissa, K., Nargeot, J., Mangoni, M.E., Jopling, C., 2014. Piezo1 plays a role in erythrocyte volume homeostasis. Haematologica 99, 70–75. https://doi.org/10.3324/haematol.2013.086090

Faucherre, A., Nargeot, J., Mangoni, M.E., Jopling, C., 2013. piezo2b Regulates Vertebrate Light Touch Response. J. Neurosci. 33, 17089–17094. https://doi.org/10.1523/JNEUROSCI.0522-13.2013

Fermo, E., Bogdanova, A., Petkova-Kirova, P., Zaninoni, A., Marcello, A.P., Makhro, A., Hänggi, P., Hertz, L., Danielczok, J., Vercellati, C., Mirra, N., Zanella, A., Cortelezzi, A., Barcellini, W., Kaestner, L., Bianchi, P., 2017. 'Gardos Channelopathy': a variant of hereditary Stomatocytosis with complex molecular regulation. Sci. Rep. 7, 1744. https://doi.org/10.1038/s41598-017-01591-w

Fermo, E., Monedero-Alonso, D., Petkova-Kirova, P., Makhro, A., Pérès, L., Bouyer, G., Marcello, A.P., Longo, F., Graziadei, G., Barcellini, W., Bogdanova, A., Egee, S., Kaestner, L., Bianchi, P., 2020. Gardos channelopathy: functional analysis of a novel KCNN4 variant. Blood Adv. 4, 6336–6341. https://doi.org/10.1182/bloodadvances.2020003285

Finkelstein, A., Cass, A., 1967. Effect of cholesterol on the water permeability of thin lipid membranes. Nature 216, 717–718. https://doi.org/10.1038/216717a0

Flatt, J., Bruce, L., 2009. The hereditary stomatocytosis. Haematologica 94, 1039–41. https://doi.org/10.3324/haematol.2009.010041

Flynn, F., Maizels, M., 1949. Cation control in human erythrocytes. J. Physiol. 110, 301–318. https://doi.org/10.1113/jphysiol.1949.sp004440

Föller, M., Kasinathan, R.S., Koka, S., Lang, C., Shumilina, E., Birnbaumer, L., Lang, F., Huber, S.M., 2008. TRPC6 Contributes to the Ca2+ Leak of Human Erythrocytes. Cell. Physiol. Biochem. 21, 183–192. https://doi.org/10.1159/000113760

Fotiou, E., Martin-Almedina, S., Simpson, M.A., Lin, S., Gordon, K., Brice, G., Atton, G., Jeffery, I., Rees, D.C., Mignot, C., Vogt, J., Homfray, T., Snyder, M.P., Rockson, S.G., Jeffery, S., Mortimer, P.S., Mansour, S., Ostergaard, P., 2015. Novel mutations in PIEZO1 cause an autosomal recessive generalized lymphatic dysplasia with non-immune hydrops fetalis. Nat. Commun. 6, 8085. https://doi.org/10.1038/ncomms9085

Fowler, V.M., 1996. Regulation of actin filament length in erythrocytes and striated muscle. Curr. Opin. Cell Biol. 8, 86–96. https://doi.org/10.1016/s0955-0674(96)80052-4

Friedrich, E.E., Hong, Z., Xiong, S., Zhong, M., Di, A., Rehman, J., Komarova, Y.A., Malik, A.B., 2019. Endothelial cell Piezo1 mediates pressure-induced lung vascular hyperpermeability via disruption of adherens junctions. Proc. Natl. Acad. Sci. U. S. A. 116, 12980–12985. https://doi.org/10.1073/pnas.1902165116

Funder, J., Wieth, J.O., 1966. Chloride and Hydrogen Ion Distribution between Human Red Cells and Plasma. Acta Physiol. Scand. 68, 234–245. https://doi.org/10.1111/j.1748-1716.1966.tb03423.x

Gardos, G., 1958. The function of calcium in the potassium permeability of human erythrocytes. Biochim. Biophys. Acta 30, 653–654. https://doi.org/10.1016/0006-3002(58)90124-0

Gardos, G., 1956. The permeability of human erythrocytes to potassium. Acta Physiol. Acad. Sci. Hung. 10, 185–189.

Garneau, L., Klein, H., Banderali, U., Longpré-Lauzon, A., Parent, L., Sauvé, R., 2009. Hydrophobic interactions as key determinants to the KCa3.1 channel closed configuration. An analysis of KCa3.1 mutants constitutively active in zero Ca2+. J. Biol. Chem. 284, 389–403. https://doi.org/10.1074/jbc.M805700200

Gautier, E.-F., Ducamp, S., Leduc, M., Salnot, V., Guillonneau, F., Dussiot, M., Hale, J., Giarratana, M.-C., Raimbault, A., Douay, L., Lacombe, C., Mohandas, N., Verdier, F., Zermati, Y., Mayeux, P., 2016. Comprehensive Proteomic Analysis of Human Erythropoiesis. Cell Rep. 16, 1470–1484. https://doi.org/10.1016/j.celrep.2016.06.085

Gautier, E.-F., Leduc, M., Cochet, S., Bailly, K., Lacombe, C., Mohandas, N., Guillonneau, F., El Nemer, W., Mayeux, P., 2018. Absolute proteome quantification of highly purified

populations of circulating reticulocytes and mature erythrocytes. Blood Adv. 2, 2646–2657. https://doi.org/10.1182/bloodadvances.2018023515

Ge, J., Li, W., Zhao, Q., Li, N., Chen, M., Zhi, P., Li, R., Gao, N., Xiao, B., Yang, M., 2015. Architecture of the mammalian mechanosensitive Piezo1 channel. Nature 527, 64–69. https://doi.org/10.1038/nature15247

Ghanshani, S., Wulff, H., Miller, M.J., Rohm, H., Neben, A., Gutman, G.A., Cahalan, M.D., Chandy, K.G., 2000. Up-regulation of the IKCa1 Potassium Channel during T-cell Activation: MOLECULAR MECHANISM AND FUNCTIONAL CONSEQUENCES *. J. Biol. Chem. 275, 37137–37149. https://doi.org/10.1074/jbc.M003941200

Glogowska, E., Lezon-Geyda, K., Maksimova, Y., Schulz, V.P., Gallagher, P.G., 2015. Mutations in the Gardos channel (KCNN4) are associated with hereditary xerocytosis. Blood 126, 1281–1284. https://doi.org/10.1182/blood-2015-07-657957

Glogowska, E., Schneider, E.R., Maksimova, Y., Schulz, V.P., Lezon-Geyda, K., Wu, J., Radhakrishnan, K., Keel, S.B., Mahoney, D., Freidmann, A.M., Altura, R.A., Gracheva, E.O., Bagriantsev, S.N., Kalfa, T.A., Gallagher, P.G., 2017. Novel mechanisms of PIEZO1 dysfunction in hereditary xerocytosis. Blood 130, 1845–1856. https://doi.org/10.1182/blood-2017-05-786004

Gnanasambandam, R., Rivera, A., Vandorpe, D.H., Shmukler, B.E., Brugnara, C., Snyder, L.M., Andolfo, I., Iolascon, A., Silveira, P.A., Hamerschlak, N., Gottlieb, P., Alper, S.L., 2018. Increased Red Cell KCNN4 Activity in Sporadic Hereditary Xerocytosis Associated With Enhanced Single Channel Pressure Sensitivity of PIEZO1 Mutant V598M: HemaSphere 2, e55. https://doi.org/10.1097/HS9.0000000000000055

Gokhin, D.S., Fowler, V.M., 2016. Feisty filaments: actin dynamics in the red blood cell membrane skeleton. Curr. Opin. Hematol. 23, 206–214. https://doi.org/10.1097/MOH.0000000000000227

Gottlieb, P.A., Bae, C., Sachs, F., 2012. Gating the mechanical channel Piezo1: a comparison between whole-cell and patch recording. Channels Austin Tex 6, 282–289. https://doi.org/10.4161/chan.21064

Grootenboer, S., Schischmanoff, P.O., Cynober, T., Rodrigue, J.C., Delaunay, J., Tchernia, G., Dommergues, J.P., 1998. A genetic syndrome associating dehydrated hereditary stomatocytosis, pseudohyperkalaemia and perinatal oedema. Br. J. Haematol. 103, 383–386. https://doi.org/10.1046/j.1365-2141.1998.00992.x

Grygorczyk, R., Schwarz, W., 1983. Properties of the Ca2+-activated K+ conductance of human red cells as revealed by the patch-clamp technique. Cell Calcium 4, 499–510. https://doi.org/10.1016/0143-4160(83)90025-8

Grygorczyk, R., Schwarz, W., Passow, H., 1984. Ca2+-activated K+ channels in human red cells. Comparison of single-channel currents with ion fluxes. Biophys. J. 45, 693–698. https://doi.org/10.1016/S0006-3495(84)84211-3

Guizouarn, H., Allegrini, B., 2020. Erythroid glucose transport in health and disease. Pflüg. Arch. - Eur. J. Physiol. 472, 1371–1383. https://doi.org/10.1007/s00424-020-02406-0

Guizouarn, H., Motais, R., Garcia-Romeu, F., Borgese, F., 2000. Cell volume regulation: the role of taurine loss in maintaining membrane potential and cell pH. J. Physiol. 523, 147–154. https://doi.org/10.1111/j.1469-7793.2000.t01-1-00147.x

Guo, Y.R., MacKinnon, R., 2017. Structure-based membrane dome mechanism for Piezo mechanosensitivity. eLife 6, e33660. https://doi.org/10.7554/eLife.33660

Haines, P.G., Jarvis, H.G., King, S., Noormohamed, F.H., Chetty, M.C., Fisher, J., Hill, P., Nicolaou, A., Stewart, G.W., 2001. Two further British families with the "cryohydrocytosis" form of hereditary stomatocytosis. Br. J. Haematol. 113, 932–937. https://doi.org/10.1046/j.1365-2141.2001.02792.x

Halperin, J.A., Brugnara, C., Tosteson, M.T., Van Ha, T., Tosteson, D.C., 1989. Voltage-activated cation transport in human erythrocytes. Am. J. Physiol.-Cell Physiol. 257, C986–C996. https://doi.org/10.1152/ajpcell.1989.257.5.C986

Hamill, O.P., Marty, A., Neher, E., Sakmann, B., Sigworth, F.J., 1981. Improved patch-clamp techniques for high-resolution current recording from cells and cell-free membrane patches. Pflugers Arch. 391, 85–100. https://doi.org/10.1007/BF00656997

Han, B.-G., Nunomura, W., Takakuwa, Y., Mohandas, N., Jap, B.K., 2000. Protein 4.1R core domain structure and insights into regulation of cytoskeletal organization. Nat. Struct. Biol. 7, 871–875. https://doi.org/10.1038/82819

Hao, J., Delmas, P., 2011. Recording of mechanosensitive currents using piezoelectrically driven mechanostimulator. Nat. Protoc. 6, 979–990. https://doi.org/10.1038/nprot.2011.343

Hao, J., Ruel, J., Coste, B., Roudaut, Y., Crest, M., Delmas, P., 2013. Piezo-electrically driven mechanical stimulation of sensory neurons. Methods Mol. Biol. Clifton NJ 998, 159–170. https://doi.org/10.1007/978-1-62703-351-0_12

Hatem, A., Poussereau, G., Gachenot, M., Pérès, L., Bouyer, G., Egée, S., 2023. Dual action of Dooku1 on PIEZO1 channel in human red blood cells. Front. Physiol. 14.

Hattangadi, S.M., Wong, P., Zhang, L., Flygare, J., Lodish, H.F., 2011. From stem cell to red cell: regulation of erythropoiesis at multiple levels by multiple proteins, RNAs, and chromatin modifications. Blood 118, 6258–6268. https://doi.org/10.1182/blood-2011-07-356006

Hegedűs, T., Chaubey, P.M., Várady, G., Szabó, E., Sarankó, H., Hofstetter, L., Roschitzki, B., Stieger, B., Sarkadi, B., 2015. Inconsistencies in the red blood cell membrane proteome analysis: generation of a database for research and diagnostic applications. Database 2015, bav056. https://doi.org/10.1093/database/bav056

Hilpert, P., Fleischmann, R.G., Kempe, D., Bartels, H., 1963. The Bohr effect related to blood and erythrocyte pH. Am. J. Physiol.-Leg. Content 205, 337–340. https://doi.org/10.1152/ajplegacy.1963.205.2.337

Hodgkin, A.L., Katz, B., 1949. The effect of sodium ions on the electrical activity of the giant axon of the squid. J. Physiol. 108, 37–77.

Hoffman, J.F., Joiner, W., Nehrke, K., Potapova, O., Foye, K., Wickrema, A., 2003. The hSK4 (KCNN4) isoform is the Ca2+-activated K+ channel (Gardos channel) in human red blood cells. Proc. Natl. Acad. Sci. U. S. A. 100, 7366–7371. https://doi.org/10.1073/pnas.1232342100

Hoffman, J.F., Laris, P.C., 1974. Determination of membrane potentials in human and Amphiuma red blood cells by means of a fluorescent probe. J. Physiol. 239, 519–552. https://doi.org/10.1113/jphysiol.1974.sp010581

Huber, S.M., Duranton, C., Henke, G., Sand, C. van de, Heussler, V., Shumilina, E., Sandu, C.D., Tanneur, V., Brand, V., Kasinathan, R.S., Lang, K.S., Kremsner, P.G., Hübner, C.A., Rust, M.B., Dedek, K., Jentsch, T.J., Lang, F., 2004. Plasmodium Induces Swelling-activated ClC-2 Anion Channels in the Host Erythrocyte *. J. Biol. Chem. 279, 41444–41452. https://doi.org/10.1074/jbc.M407618200

Ibrahim, S., Chaigne, J., Dakik, H., Fourbon, Y., Corset, L., Lecomte, T., Raoul, W., Guéguinou, M., 2021. SK4 oncochannels regulate calcium entry and promote cell migration in KRAS-mutated colorectal cancer. Cell Calcium 96, 102384. https://doi.org/10.1016/j.ceca.2021.102384

Ishii, T.M., Silvia, C., Hirschberg, B., Bond, C.T., Adelman, J.P., Maylie, J., 1997. A human intermediate conductance calcium-activated potassium channel. Proc. Natl. Acad. Sci. 94, 11651–11656. https://doi.org/10.1073/pnas.94.21.11651

Jagannathan-Bogdan, M., Zon, L.I., 2013. Hematopoiesis. Development 140, 2463–2467. https://doi.org/10.1242/dev.083147

James, P., Maeda, M., Fischer, R., Verma, A.K., Krebs, J., Penniston, J.T., Carafoli, E., 1988. Identification and primary structure of a calmodulin binding domain of the Ca2+ pump of human erythrocytes. J. Biol. Chem. 263, 2905–2910.

Jansen, J., Qiao, M., Hertz, L., Wang, X., Fermo, E., Zaninoni, A., Colombatti, R., Bernhardt, I., Bianchi, P., Kaestner, L., 2021. Mechanistic ion channel interactions in red cells of patients with Gárdos channelopathy. Blood Adv. 5, 3303–3308. https://doi.org/10.1182/bloodadvances.2020003823

Jarolim, P., Murray, J.L., Rubin, H.L., Taylor, W.M., Prchal, J.T., Ballas, S.K., Snyder, L.M., Chrobak, L., Melrose, W.D., Brabec, V., Palek, J., 1996. Characterization of 13 novel band 3 gene defects in hereditary spherocytosis with band 3 deficiency. Blood 88, 4366–4374.

Ji, P., Murata-Hori, M., Lodish, H.F., 2011. Formation of mammalian erythrocytes: Chromatin condensation and enucleation. Trends Cell Biol. 21, 409–415. https://doi.org/10.1016/j.tcb.2011.04.003

Ji, T., Corbalán-García, S., Hubbard, S.R., 2018. Crystal structure of the C-terminal four-helix bundle of the potassium channel KCa3.1. PloS One 13, e0199942. https://doi.org/10.1371/journal.pone.0199942

Jiang, F., Yin, K., Wu, K., Zhang, M., Wang, S., Cheng, H., Zhou, Z., Xiao, B., 2021. The mechanosensitive Piezo1 channel mediates heart mechano-chemo transduction. Nat. Commun. 12, 869. https://doi.org/10.1038/s41467-021-21178-4

Jiang, W., Wijerathne, T.D., Zhang, H., Lin, Y.-C., Im, W., Lacroix, J.J., Luo, Y.L., 2023. Rationale design of novel PIEZO1 modulators. Biophys. J. 122, 396a. https://doi.org/10.1016/j.bpj.2022.11.2163

Johnson, R.M., 1994. Membrane stress increases cation permeability in red cells. Biophys. J. 67, 1876–1881. https://doi.org/10.1016/S0006-3495(94)80669-1

Johnson, R.M., Gannon, S.A., 1990. Erythrocyte cation permeability induced by mechanical stress: a model for sickle cell cation loss. Am. J. Physiol. 259, C746-751. https://doi.org/10.1152/ajpcell.1990.259.5.C746

Johnson, R.M., Tang, K., 1992. Induction of a Ca2+-activated K+ channel in human erythrocytes by mechanical stress. Biochim. Biophys. Acta BBA - Biomembr. 1107, 314–318. https://doi.org/10.1016/0005-2736(92)90418-L

Joiner, W.J., Khanna, R., Schlichter, L.C., Kaczmarek, L.K., 2001. Calmodulin Regulates Assembly and Trafficking of SK4/IK1 Ca2+-activated K+ Channels*. J. Biol. Chem. 276, 37980–37985. https://doi.org/10.1074/jbc.M104965200

Joiner, W.J., Wang, L.-Y., Tang, M.D., Kaczmarek, L.K., 1997. hSK4, a member of a novel subfamily of calcium-activated potassium channels. Proc. Natl. Acad. Sci. 94, 11013–11018. https://doi.org/10.1073/pnas.94.20.11013

Joshi, R., Gilligan, D.M., Otto, E., McLaughlin, T., Bennett, V., 1991. Primary structure and domain organization of human alpha and beta adducin. J. Cell Biol. 115, 665–675. https://doi.org/10.1083/jcb.115.3.665

Kaestner, L., Bogdanova, A., Egee, S., 2020. Calcium Channels and Calcium-Regulated Channels in Human Red Blood Cells. Adv. Exp. Med. Biol. 1131, 625–648. https://doi.org/10.1007/978-3-030-12457-1_25

Kaestner, L., Christophersen, P., Bernhardt, I., Bennekou, P., 2000. The non-selective voltage-activated cation channel in the human red blood cell membrane: reconciliation between two conflicting reports and further characterisation. Bioelectrochemistry, Bioelectrochemistry and biophysics of red blood cells and red blood cell membranes 52, 117–125. https://doi.org/10.1016/S0302-4598(00)00110-0

Kager, L., Jimenez Heredia, R., Hirschmugl, T., Dmytrus, J., Krolo, A., Müller, H., Bock, C., Zeitlhofer, P., Dworzak, M., Mann, G., Holter, W., Haas, O., Boztug, K., 2018. Targeted mutation screening of 292 candidate genes in 38 children with inborn haematological cytopenias efficiently identifies novel disease-causing mutations. Br. J. Haematol. 182, 251–258. https://doi.org/10.1111/bjh.15389

Kamajaya, A., Kaiser, J., Lee, J., Reid, M., Rees, D.C., 2014. The structure of a conserved Piezo channel domain reveals a novel beta sandwich fold. Struct. Lond. Engl. 1993 22, 1520–1527. https://doi.org/10.1016/j.str.2014.08.009

Kasahara, M., Hinkle, P.C., 1977. Reconstitution and purification of the D-glucose transporter from human erythrocytes. J. Biol. Chem. 252, 7384–7390.

Kedar, P.S., Harigae, H., Ito, E., Muramatsu, H., Kojima, S., Okuno, Y., Fujiwara, T., Dongerdiye, R., Warang, P.P., Madkaikar, M.R., 2019. Study of pathophysiology and molecular

characterization of congenital anemia in India using targeted next-generation sequencing approach. Int. J. Hematol. 110, 618–626. https://doi.org/10.1007/s12185-019-02716-9

Khan, A.A., Hanada, T., Mohseni, M., Jeong, J.-J., Zeng, L., Gaetani, M., Li, D., Reed, B.C., Speicher, D.W., Chishti, A.H., 2008. Dematin and Adducin Provide a Novel Link between the Spectrin Cytoskeleton and Human Erythrocyte Membrane by Directly Interacting with Glucose Transporter-1. J. Biol. Chem. 283, 14600–14609. https://doi.org/10.1074/jbc.M707818200

Kherd, A.A., Helmi, N., Balamash, K.S., Kumosani, T.A., AL-Ghamdi, S.A., Qari, M., Huwait, E.A., Yaghmoor, S.S., Nabil, A., AL-Ghamdi, M.A., Moselhy, S.S., 2017. Changes in erythrocyte ATPase activity under different pathological conditions. Afr. Health Sci. 17, 1204–1210. https://doi.org/10.4314/ahs.v17i4.31

Kiger, L., Oliveira, L., Guitton, C., Bendélac, L., Ghazal, K., Proulle, V., Galacteros, F., Junot, C., Fenaille, F., Roméo, P.-H., Garçon, L., Picard, V., 2021. Piezo1-xerocytosis red cell metabolome shows impaired glycolysis and increased hemoglobin oxygen affinity. Blood Adv. 5, 84–88. https://doi.org/10.1182/bloodadvances.2020003028

Kim, E., DeMarco, S.J., Marfatia, S.M., Chishti, A.H., Sheng, M., Strehler, E.E., 1998. Plasma membrane Ca2+ ATPase isoform 4b binds to membrane-associated guanylate kinase (MAGUK) proteins via their PDZ (PSD-95/Dlg/ZO-1) domains. J. Biol. Chem. 273, 1591–1595. https://doi.org/10.1074/jbc.273.3.1591

Kim, S.E., Coste, B., Chadha, A., Cook, B., Patapoutian, A., 2012. The role of Drosophila Piezo in mechanical nociception. Nature 483, 209–212. https://doi.org/10.1038/nature10801

Kosk-Kosicka, D., Bzdega, T., 1988. Activation of the erythrocyte Ca2+-ATPase by either self-association or interaction with calmodulin. J. Biol. Chem. 263, 18184–18189. https://doi.org/10.1016/S0021-9258(19)81342-X

Kosk-Kosicka, D., Inesi, G., 1985. Cooperative calcium binding and calmodulin regulation in the calcium-dependent adenosine triphosphatase purified from the erythrocyte membrane. FEBS Lett. 189, 67–71. https://doi.org/10.1016/0014-5793(85)80843-7

Krapivinsky, G., Krapivinsky, L., Stotz, S.C., Manasian, Y., Clapham, D.E., 2011. POST, partner of stromal interaction molecule 1 (STIM1), targets STIM1 to multiple transporters. Proc. Natl. Acad. Sci. U. S. A. 108, 19234–19239. https://doi.org/10.1073/pnas.1117231108

Krebs, J., 2022. Structure, Function and Regulation of the Plasma Membrane Calcium Pump in Health and Disease. Int. J. Mol. Sci. 23, 1027. https://doi.org/10.3390/ijms23031027

Krebs, J., 2017. The Plasma Membrane Calcium Pump (PMCA): Regulation of Cytosolic Ca2+, Genetic Diversities and Its Role in Sub-plasma Membrane Microdomains. Adv. Exp. Med. Biol. 981, 3–21. https://doi.org/10.1007/978-3-319-55858-5_1

Kuchel, P.W., Shishmarev, D., 2017. Accelerating metabolism and transmembrane cation flux by distorting red blood cells. Sci. Adv. 3, eaao1016. https://doi.org/10.1126/sciadv.aao1016

Kuhlman, P.A., Hughes, C.A., Bennett, V., Fowler, V.M., 1996. A New Function for Adducin: CALCIUM/CALMODULIN-REGULATED CAPPING OF THE BARBED ENDS OF ACTIN FILAMENTS (*). J. Biol. Chem. 271, 7986–7991. https://doi.org/10.1074/jbc.271.14.7986

Lacroix, J.J., Botello-Smith, W.M., Luo, Y., 2018. Probing the gating mechanism of the mechanosensitive channel Piezo1 with the small molecule Yoda1. Nat. Commun. 9, 2029. https://doi.org/10.1038/s41467-018-04405-3

Lange, T., Jungmann, P., Haberle, J., Falk, S., Duebbers, A., Bruns, R., Ebner, A., Hinterdorfer, P., Oberleithner, H., Schillers, H., 2006. Reduced number of CFTR molecules in erythrocyte plasma membrane of cystic fibrosis patients. Mol. Membr. Biol. 23, 317–323. https://doi.org/10.1080/09687860600738304

Larsen, F.L., Katz, S., Roufogalis, B.D., Brooks, D.E., 1981. Physiological shear stresses enhance the Ca 2+ permeability of human erythrocytes. Nature 294, 667–668. https://doi.org/10.1038/294667a0

Lassen, U.V., Sten-Knudsen, O., 1968. Direct measurements of membrane potential and membrane resistance of human red cells. J. Physiol. 195, 681–696. https://doi.org/10.1113/jphysiol.1968.sp008482
Lee, A., Zhou, H., Scheuer, T., Catterall, W.A., 2003. Molecular determinants of Ca2+/calmodulin-dependent regulation of Cav2.1 channels. Proc. Natl. Acad. Sci. 100, 16059–16064. https://doi.org/10.1073/pnas.2237000100
Lee, C.-H., MacKinnon, R., 2018. Activation mechanism of a human SK-calmodulin channel complex elucidated by cryo-EM structures. Science 360, 508–513. https://doi.org/10.1126/science.aas9466
Leidl, K., Liebisch, G., Richter, D., Schmitz, G., 2008. Mass spectrometric analysis of lipid species of human circulating blood cells. Biochim. Biophys. Acta BBA - Mol. Cell Biol. Lipids 1781, 655–664. https://doi.org/10.1016/j.bbalip.2008.07.008
Lessard, S., Gatof, E.S., Beaudoin, M., Schupp, P.G., Sher, F., Ali, A., Prehar, S., Kurita, R., Nakamura, Y., Baena, E., Ledoux, J., Oceandy, D., Bauer, D.E., Lettre, G., 2017. An erythroid-specific ATP2B4 enhancer mediates red blood cell hydration and malaria susceptibility. J. Clin. Invest. 127, 3065–3074. https://doi.org/10.1172/JCI94378
Lew, V.L., Tiffert, T., 2017. On the Mechanism of Human Red Blood Cell Longevity: Roles of Calcium, the Sodium Pump, PIEZO1, and Gardos Channels. Front. Physiol. 8, 977. https://doi.org/10.3389/fphys.2017.00977
Lew, V.L., Tsien, R.Y., Miner, C., Bookchin, R.M., 1982. Physiological [Ca2+]i level and pump-leak turnover in intact red cells measured using an incorporated Ca chelator. Nature 298, 478–481. https://doi.org/10.1038/298478a0
Lewis, A.H., Grandl, J., 2021. Stretch and poke stimulation for characterizing mechanically activated ion channels. Methods Enzymol. 654, 225–253. https://doi.org/10.1016/bs.mie.2020.12.024
Lewis, A.H., Grandl, J., 2015. Mechanical sensitivity of Piezo1 ion channels can be tuned by cellular membrane tension. eLife 4. https://doi.org/10.7554/eLife.12088
Lewis, I.A., Campanella, M.E., Markley, J.L., Low, P.S., 2009. Role of band 3 in regulating metabolic flux of red blood cells. Proc. Natl. Acad. Sci. U. S. A. 106, 18515–18520. https://doi.org/10.1073/pnas.0905999106
Li, J., Hou, B., Tumova, S., Muraki, K., Bruns, A., Ludlow, M.J., Sedo, A., Hyman, A.J., McKeown, L., Young, R.S., Yuldasheva, N.Y., Majeed, Y., Wilson, L.A., Rode, B., Bailey, M.A., Kim, H.R., Fu, Z., Carter, D.A., Bilton, J., Imrie, H., Ajuh, P., Dear, T.N., Cubbon, R.M., Kearney, M.T., Prasad, R.K., Evans, P.C., Ainscough, J.F., Beech, D.J., 2014. Piezo1 integration of vascular architecture with physiological force. Nature 515, 279–282. https://doi.org/10.1038/nature13701
Li, X., Matsuoka, Y., Bennett, V., 1998. Adducin preferentially recruits spectrin to the fast growing ends of actin filaments in a complex requiring the MARCKS-related domain and a newly defined oligomerization domain. J. Biol. Chem. 273, 19329–19338. https://doi.org/10.1074/jbc.273.30.19329
Liu, S.C., Derick, L.H., Palek, J., 1987. Visualization of the hexagonal lattice in the erythrocyte membrane skeleton. J. Cell Biol. 104, 527–536. https://doi.org/10.1083/jcb.104.3.527
Llinás, R., Sugimori, M., Lin, J.W., Cherksey, B., 1989. Blocking and isolation of a calcium channel from neurons in mammals and cephalopods utilizing a toxin fraction (FTX) from funnel-web spider poison. Proc. Natl. Acad. Sci. U. S. A. 86, 1689–1693. https://doi.org/10.1073/pnas.86.5.1689
Lohia, R., Allegrini, B., Berry, L., Guizouarn, H., Cerdan, R., Abkarian, M., Douguet, D., Honoré, E., Wengelnik, K., 2023. Pharmacological activation of PIEZO1 in human red blood cells prevents Plasmodium falciparum invasion. Cell. Mol. Life Sci. 80, 124. https://doi.org/10.1007/s00018-023-04773-0
Low, P.S., 1986. Structure and function of the cytoplasmic domain of band 3: center of erythrocyte membrane—peripheral protein interactions. Biochim. Biophys. Acta BBA - Rev. Biomembr. 864, 145–167. https://doi.org/10.1016/0304-4157(86)90009-2

Low, P.S., Rathinavelu, P., Harrison, M.L., 1993. Regulation of glycolysis via reversible enzyme binding to the membrane protein, band 3. J. Biol. Chem. 268, 14627–14631.

Lukacs, V., Mathur, J., Mao, R., Bayrak-Toydemir, P., Procter, M., Cahalan, S.M., Kim, H.J., Bandell, M., Longo, N., Day, R.W., Stevenson, D.A., Patapoutian, A., Krock, B.L., 2015. Impaired PIEZO1 function in patients with a novel autosomal recessive congenital lymphatic dysplasia. Nat. Commun. 6, 8329. https://doi.org/10.1038/ncomms9329

Lux, S.E., John, K.M., Kopito, R.R., Lodish, H.F., 1989. Cloning and characterization of band 3, the human erythrocyte anion-exchange protein (AE1). Proc. Natl. Acad. Sci. U. S. A. 86, 9089–9093. https://doi.org/10.1073/pnas.86.23.9089

Madácsy, T., Varga, Á., Papp, N., Tél, B., Pallagi, P., Szabó, V., Kiss, A., Fanczal, J., Rakonczay, Z., Tiszlavicz, L., Rázga, Z., Hohwieler, M., Kleger, A., Gray, M., Hegyi, P., Maléth, J., 2022. Impaired regulation of PMCA activity by defective CFTR expression promotes epithelial cell damage in alcoholic pancreatitis and hepatitis. Cell. Mol. Life Sci. 79, 265. https://doi.org/10.1007/s00018-022-04287-1

Makhro, A., Hänggi, P., Goede, J.S., Wang, J., Brüggemann, A., Gassmann, M., Schmugge, M., Kaestner, L., Speer, O., Bogdanova, A., 2013. N-methyl-d-aspartate receptors in human erythroid precursor cells and in circulating red blood cells contribute to the intracellular calcium regulation. Am. J. Physiol.-Cell Physiol. 305, C1123–C1138. https://doi.org/10.1152/ajpcell.00031.2013

Mangialavori, I.C., Ferreira-Gomes, M.S., Saffioti, N.A., González-Lebrero, R.M., Rossi, R.C., Rossi, J.P.F.C., 2013. Conformational Changes Produced by ATP Binding to the Plasma Membrane Calcium Pump *. J. Biol. Chem. 288, 31030–31041. https://doi.org/10.1074/jbc.M113.494633

Mansour-Hendili, L., Egée, S., Monedero-Alonso, D., Bouyer, G., Godeau, B., Badaoui, B., Lunati, A., Noizat, C., Aissat, A., Kiger, L., Mekki, C., Picard, V., Moutereau, S., Fanen, P., Bartolucci, P., Garçon, L., Galactéros, F., Funalot, B., 2021. Multiple thrombosis in a patient with Gardos channelopathy and a new KCNN4 mutation. Am. J. Hematol. 96, E318–E321. https://doi.org/10.1002/ajh.26245

Marty, A., 1981. Ca-dependent K channels with large unitary conductance in chromaffin cell membranes. Nature 291, 497–500. https://doi.org/10.1038/291497a0

Maruyama, Y., Nishiyama, A., Teshima, T., 1986. Two Types of Cation Channels in the Basolateral Cell Membrane of Human Salivary Gland Acinar Cells. Jpn. J. Physiol. 36, 219–223. https://doi.org/10.2170/jjphysiol.36.219

Mei, Y., Liu, Y., Ji, P., 2021. Understanding terminal erythropoiesis: An update on chromatin condensation, enucleation, and reticulocyte maturation. Blood Rev. 46, 100740. https://doi.org/10.1016/j.blre.2020.100740

Messana, I., Orlando, M., Cassiano, L., Pennacchietti, L., Zuppi, C., Castagnola, M., Giardina, B., 1996. Human erythrocyte metabolism is modulated by the O2-linked transition of hemoglobin. FEBS Lett. 390, 25–28. https://doi.org/10.1016/0014-5793(96)00624-2

Miller, D.R., Rickles, F.R., Lichtman, M.A., La Celle, P.L., Bates, J., Weed, R.I., 1971. A New Variant of Hereditary Hemolytic Anemia With Stomatocytosis and Erythrocyte Cation Abnormality. Blood 38, 184–204. https://doi.org/10.1182/blood.V38.2.184.184

Minetti, G., Egée, S., Mörsdorf, D., Steffen, P., Makhro, A., Achilli, C., Ciana, A., Wang, J., Bouyer, G., Bernhardt, I., Wagner, C., Thomas, S., Bogdanova, A., Kaestner, L., 2013. Red cell investigations: Art and artefacts. Blood Rev. 27, 91–101. https://doi.org/10.1016/j.blre.2013.02.002

Moersdorf, D., Egee, S., Hahn, C., Hanf, B., Ellory, C., Thomas, S., Bernhardt, I., 2013. Transmembrane Potential of Red Blood Cells Under Low Ionic Strength Conditions. Cell. Physiol. Biochem. 31, 875–882. https://doi.org/10.1159/000350105

Mohandas, N., Gallagher, P.G., 2008. Red cell membrane: past, present, and future. Blood 112, 3939–3948. https://doi.org/10.1182/blood-2008-07-161166

Monedero Alonso, D., Pérès, L., Hatem, A., Bouyer, G., Egée, S., 2021. The Chloride Conductance Inhibitor NS3623 Enhances the Activity of a Non-selective Cation Channel in Hyperpolarizing Conditions. Front. Physiol. 12.

Montel-Hagen, A., Kinet, S., Manel, N., Mongellaz, C., Prohaska, R., Battini, J.-L., Delaunay, J., Sitbon, M., Taylor, N., 2007. Induction of GLUT1 during Erythropoiesis Triggers a Switch from Glucose to DHA Uptake in Vitamin C-Defective Mammals. Blood 110, 1705. https://doi.org/10.1182/blood.V110.11.1705.1705

More, T.A., Dongerdiye, R., Devendra, R., Warang, P.P., Kedar, P.S., 2020. Mechanosensitive Piezo1 ion channel protein (PIEZO1 gene): update and extended mutation analysis of hereditary xerocytosis in India. Ann. Hematol. 99, 715–727. https://doi.org/10.1007/s00277-020-03955-1

Motais, R., Guizouarn, H., Borgese, F., 2003. The Swelling-Sensitive Osmolyte Channel, in: Bernhardt, I., Ellory, J.C. (Eds.), Red Cell Membrane Transport in Health and Disease. Springer, Berlin, Heidelberg, pp. 153–171. https://doi.org/10.1007/978-3-662-05181-8_7

Mousavi, S.A.R., Dubin, A.E., Zeng, W.-Z., Coombs, A.M., Do, K., Ghadiri, D.A., Keenan, W.T., Ge, C., Zhao, Y., Patapoutian, A., 2021. PIEZO ion channel is required for root mechanotransduction in Arabidopsis thaliana. Proc. Natl. Acad. Sci. 118, e2102188118. https://doi.org/10.1073/pnas.2102188118

Nans, A., Mohandas, N., Stokes, D.L., 2011. Native Ultrastructure of the Red Cell Cytoskeleton by Cryo-Electron Tomography. Biophys. J. 101, 2341–2350. https://doi.org/10.1016/j.bpj.2011.09.050

Narla, A., Mohandas, N., 2020. Staying hydrated is important also for erythroblasts. Haematologica 105, 528–529. https://doi.org/10.3324/haematol.2019.233999

Neher, E., Sakmann, B., 1976. Single-channel currents recorded from membrane of denervated frog muscle fibres. Nature 260, 799–802. https://doi.org/10.1038/260799a0

Nonomura, K., Lukacs, V., Sweet, D.T., Goddard, L.M., Kanie, A., Whitwam, T., Ranade, S.S., Fujimori, T., Kahn, M.L., Patapoutian, A., 2018. Mechanically activated ion channel PIEZO1 is required for lymphatic valve formation. Proc. Natl. Acad. Sci. 115, 12817–12822. https://doi.org/10.1073/pnas.1817070115

Oceandy, D., Cartwright, E.J., Emerson, M., Prehar, S., Baudoin, F.M., Zi, M., Alatwi, N., Venetucci, L., Schuh, K., Williams, J.C., Armesilla, A.L., Neyses, L., 2007. Neuronal Nitric Oxide Synthase Signaling in the Heart Is Regulated by the Sarcolemmal Calcium Pump 4b. Circulation 115, 483–492. https://doi.org/10.1161/CIRCULATIONAHA.106.643791

Ohanian, V., Wolfe, L.C., John, K.M., Pinder, J.C., Lux, S.E., Gratzer, W.B., 1984. Analysis of the ternary interaction of the red cell membrane skeletal proteins, spectrin, actin, and 4.1. Biochemistry 23, 4416–4420. https://doi.org/10.1021/bi00314a027

Ohya, S., Matsui, M., Kajikuri, J., Kito, H., Endo, K., 2022. Downregulation of IL-8 and IL-10 by the Activation of Ca2+-Activated K+ Channel KCa3.1 in THP-1-Derived M2 Macrophages. Int. J. Mol. Sci. 23, 8603. https://doi.org/10.3390/ijms23158603

Okunade, G.W., Miller, M.L., Pyne, G.J., Sutliff, R.L., O'Connor, K.T., Neumann, J.C., Andringa, A., Miller, D.A., Prasad, V., Doetschman, T., Paul, R.J., Shull, G.E., 2004. Targeted Ablation of Plasma Membrane Ca2+-ATPase (PMCA) 1 and 4 Indicates a Major Housekeeping Function for PMCA1 and a Critical Role in Hyperactivated Sperm Motility and Male Fertility for PMCA4*. J. Biol. Chem. 279, 33742–33750. https://doi.org/10.1074/jbc.M404628200

Percy, A.K., Schmell, E., Earles, B.J., Lennarz, W.J., 1973. Phospholipid biosynthesis in the membranes of immature and mature red blood cells. Biochemistry 12, 2456–2461. https://doi.org/10.1021/bi00737a014

Peters, L.L., Shivdasani, R.A., Liu, S.-C., Hanspal, M., John, K.M., Gonzalez, J.M., Brugnara, C., Gwynn, B., Mohandas, N., Alper, S.L., Orkin, S.H., Lux, S.E., 1996. Anion Exchanger 1 (Band 3) Is Required to Prevent Erythrocyte Membrane Surface Loss but Not to Form the Membrane Skeleton. Cell 86, 917–927. https://doi.org/10.1016/S0092-8674(00)80167-1

Picard, V., Guitton, C., Mansour-Hendili, L., Jondeau, B., Bendélac, L., Denguir, M., Demagny, J., Proulle, V., Galactéros, F., Garçon, L., 2020. Rapid Gardos Hereditary Xerocytosis Diagnosis in 8 Families Using Reticulocyte Indices. Front. Physiol. 11, 602109. https://doi.org/10.3389/fphys.2020.602109

Picard, V., Guitton, C., Thuret, I., Rose, C., Bendelac, L., Ghazal, K., Aguilar-Martinez, P., Badens, C., Barro, C., Bénéteau, C., Berger, C., Cathébras, P., Deconinck, E., Delaunay, J., Durand, J.-M., Firah, N., Galactéros, F., Godeau, B., Jaïs, X., de Jaureguiberry, J.-P., Le Stradic, C., Lifermann, F., Maffre, R., Morin, G., Perrin, J., Proulle, V., Ruivard, M., Toutain, F., Lahary, A., Garçon, L., 2019. Clinical and biological features in *PIEZO1* -hereditary xerocytosis and Gardos channelopathy: a retrospective series of 126 patients. Haematologica 104, 1554–1564. https://doi.org/10.3324/haematol.2018.205328

Picart, C., Discher, D.E., 1999. Actin Protofilament Orientation at the Erythrocyte Membrane. Biophys. J. 77, 865–878. https://doi.org/10.1016/S0006-3495(99)76938-9

Prole, D.L., Taylor, C.W., 2013. Identification and Analysis of Putative Homologues of Mechanosensitive Channels in Pathogenic Protozoa. PLOS ONE 8, e66068. https://doi.org/10.1371/journal.pone.0066068

Puckeridge, M., Chapman, B.E., Conigrave, A.D., Grieve, S.M., Figtree, G.A., Kuchel, P.W., 2013. Stoichiometric relationship between Na(+) ions transported and glucose consumed in human erythrocytes: Bayesian analysis of (23)Na and (13)C NMR time course data. Biophys. J. 104, 1676–1684. https://doi.org/10.1016/j.bpj.2013.03.019

Qin, L., He, T., Chen, S., Yang, D., Yi, W., Cao, H., Xiao, G., 2021. Roles of mechanosensitive channel Piezo1/2 proteins in skeleton and other tissues. Bone Res. 9, 1–17. https://doi.org/10.1038/s41413-021-00168-8

Radin, I., Richardson, R.A., Coomey, J.H., Weiner, E.R., Bascom, C.S., Li, T., Bezanilla, M., Haswell, E.S., 2021. Plant PIEZO homologs modulate vacuole morphology during tip growth. Science 373, 586–590. https://doi.org/10.1126/science.abe6310

Rana, A.P., Ruff, P., Maalouf, G.J., Speicher, D.W., Chishti, A.H., 1993. Cloning of human erythroid dematin reveals another member of the villin family. Proc. Natl. Acad. Sci. U. S. A. 90, 6651–6655. https://doi.org/10.1073/pnas.90.14.6651

Ranade, S.S., Qiu, Z., Woo, S.-H., Hur, S.S., Murthy, S.E., Cahalan, S.M., Xu, J., Mathur, J., Bandell, M., Coste, B., Li, Y.-S.J., Chien, S., Patapoutian, A., 2014. Piezo1, a mechanically activated ion channel, is required for vascular development in mice. Proc. Natl. Acad. Sci. 111, 10347–10352. https://doi.org/10.1073/pnas.1409233111

Rapetti-Mauss, R., Lacoste, C., Picard, V., Guitton, C., Lombard, E., Loosveld, M., Nivaggioni, V., Dasilva, N., Salgado, D., Desvignes, J.-P., Béroud, C., Viout, P., Bernard, M., Soriani, O., Vinti, H., Lacroze, V., Feneant-Thibault, M., Thuret, I., Guizouarn, H., Badens, C., 2015. A mutation in the Gardos channel is associated with hereditary xerocytosis. Blood 126, 1273–1280. https://doi.org/10.1182/blood-2015-04-642496

Rapetti-Mauss, R., Picard, V., Guitton, C., Ghazal, K., Proulle, V., Badens, C., Soriani, O., Garçon, L., Guizouarn, H., 2017. Red blood cell Gardos channel (KCNN4): the essential determinant of erythrocyte dehydration in hereditary xerocytosis. Haematologica 102, e415–e418. https://doi.org/10.3324/haematol.2017.171389

Rapetti-Mauss, R., Soriani, O., Vinti, H., Badens, C., Guizouarn, H., 2016. Senicapoc: a potent candidate for the treatment of a subset of hereditary xerocytosis caused by mutations in the Gardos channel. Haematologica 101, e431–e435. https://doi.org/10.3324/haematol.2016.149104

Richter, S., Hamann, J., Kummerow, D., Bernhardt, I., 1997. The monovalent cation “leak” transport in human erythrocytes: an electroneutral exchange process. Biophys. J. 73, 733–745.

Risinger, M., Glogowska, E., Chonat, S., Zhang, K., Dagaonkar, N., Joiner, C.H., Quinn, C.T., Kalfa, T.A., Gallagher, P.G., 2018. Hereditary xerocytosis: Diagnostic considerations. Am. J. Hematol. 93, E67–E69. https://doi.org/10.1002/ajh.24996

Rivera, A., Vandorpe, D.H., Shmukler, B.E., Andolfo, I., Iolascon, A., Archer, N.M., Shabani, E., Auerbach, M., Hamerschlak, N., Morton, J., Wohlgemuth, J.G., Brugnara, C., Snyder, L.M., Alper, S.L., 2019. Erythrocyte ion content and dehydration modulate maximal Gardos channel activity in KCNN4 V282M/+ hereditary xerocytosis red cells. Am. J. Physiol. Cell Physiol. 317, C287–C302. https://doi.org/10.1152/ajpcell.00074.2019

Rivera, A., Vandorpe, D.H., Shmukler, B.E., Gallagher, D.R., Fikry, C.C., Kuypers, F.A., Brugnara, C., Snyder, L.M., Alper, S.L., 2017. Erythrocytes from hereditary xerocytosis patients heterozygous for KCNN4 V282M exhibit increased spontaneous Gardos channel-like activity inhibited by senicapoc: RIVERA ET AL. Am. J. Hematol. 92, E108–E110. https://doi.org/10.1002/ajh.24716

Rogers, S., Lew, V.L., 2021. PIEZO1 and the mechanism of the long circulatory longevity of human red blood cells. PLOS Comput. Biol. 17, e1008496. https://doi.org/10.1371/journal.pcbi.1008496

Romac, J.M.-J., Shahid, R.A., Swain, S.M., Vigna, S.R., Liddle, R.A., 2018. Piezo1 is a mechanically activated ion channel and mediates pressure induced pancreatitis. Nat. Commun. 9. https://doi.org/10.1038/s41467-018-04194-9

Romero, L.O., Massey, A.E., Mata-Daboin, A.D., Sierra-Valdez, F.J., Chauhan, S.C., Cordero-Morales, J.F., Vásquez, V., 2019. Dietary fatty acids fine-tune Piezo1 mechanical response. Nat. Commun. 10, 1200. https://doi.org/10.1038/s41467-019-09055-7

Rowe, C.E., Allison, A.C., Lovelock, J.E., 1960. Synthesis of lipids by different human blood cell types. Biochim. Biophys. Acta 41, 310–314. https://doi.org/10.1016/0006-3002(60)90014-7

Rumsey, S.C., Kwon, O., Xu, G.W., Burant, C.F., Simpson, I., Levine, M., 1997. Glucose transporter isoforms GLUT1 and GLUT3 transport dehydroascorbic acid. J. Biol. Chem. 272, 18982–18989. https://doi.org/10.1074/jbc.272.30.18982

Russo, R., Andolfo, I., Manna, F., Gambale, A., Marra, R., Rosato, B.E., Caforio, P., Pinto, V., Pignataro, P., Radhakrishnan, K., Unal, S., Tomaiuolo, G., Forni, G.L., Iolascon, A., 2018. Multi-gene panel testing improves diagnosis and management of patients with hereditary anemias. Am. J. Hematol. 93, 672–682. https://doi.org/10.1002/ajh.25058

Sakmann, B., Neher, E., 1984. Patch clamp techniques for studying ionic channels in excitable membranes. Annu. Rev. Physiol. 46, 455–472. https://doi.org/10.1146/annurev.ph.46.030184.002323

Schatzmann, H.J., 1966. ATP-dependent Ca++-Extrusion from human red cells. Experientia 22, 364–365. https://doi.org/10.1007/BF01901136

Schuh, K., Cartwright, E.J., Jankevics, E., Bundschu, K., Liebermann, J., Williams, J.C., Armesilla, A.L., Emerson, M., Oceandy, D., Knobeloch, K.-P., Neyses, L., 2004. Plasma membrane Ca2+ ATPase 4 is required for sperm motility and male fertility. J. Biol. Chem. 279, 28220–28226. https://doi.org/10.1074/jbc.M312599200

Shefer Averbuch, N., Steinberg-Shemer, O., Dgany, O., Krasnov, T., Noy-Lotan, S., Yacobovich, J., Kuperman, A.A., Kattamis, A., Ben Barak, A., Roth-Jelinek, B., Chubar, E., Shabad, E., Dufort, G., Ellis, M., Wolach, O., Pazgal, I., Abu Quider, A., Miskin, H., Tamary, H., 2018. Targeted next generation sequencing for the diagnosis of patients with rare congenital anemias. Eur. J. Haematol. 101, 297–304. https://doi.org/10.1111/ejh.13097

Shimizu, S., Narita, M., Tsujimoto, Y., 1999. Bcl-2 family proteins regulate the release of apoptogenic cytochrome c by the mitochondrial channel VDAC. Nature 399, 483–487. https://doi.org/10.1038/20959

Shoshan-Barmatz, V., De Pinto, V., Zweckstetter, M., Raviv, Z., Keinan, N., Arbel, N., 2010. VDAC, a multi-functional mitochondrial protein regulating cell life and death. Mol. Aspects Med., VDAC, a multi-functional mitochondrial protein regulating both cell life and death 31, 227–285. https://doi.org/10.1016/j.mam.2010.03.002

Skals, M., Jensen, U.B., Ousingsawat, J., Kunzelmann, K., Leipziger, J., Praetorius, H.A., 2010. Escherichia coli alpha-hemolysin triggers shrinkage of erythrocytes via K(Ca)3.1 and

TMEM16A channels with subsequent phosphatidylserine exposure. J. Biol. Chem. 285, 15557–15565. https://doi.org/10.1074/jbc.M109.082578

Smallwood, J.I., Gügi, B., Rasmussen, H., 1988. Regulation of erythrocyte Ca2+ pump activity by protein kinase C. J. Biol. Chem. 263, 2195–2202.

Soares, M.P., Hamza, I., 2016. Macrophages and Iron Metabolism. Immunity 44, 492–504. https://doi.org/10.1016/j.immuni.2016.02.016

Solis, A.G., Bielecki, P., Steach, H.R., Sharma, L., Harman, C.C.D., Yun, S., de Zoete, M.R., Warnock, J.N., To, S.D.F., York, A.G., Mack, M., Schwartz, M.A., Dela Cruz, C.S., Palm, N.W., Jackson, R., Flavell, R.A., 2019. Mechanosensation of cyclical force by PIEZO1 is essential for innate immunity. Nature 573, 69–74. https://doi.org/10.1038/s41586-019-1485-8

Sprague, R.S., Ellsworth, M.L., Stephenson, A.H., Kleinhenz, M.E., Lonigro, A.J., 1998. Deformation-induced ATP release from red blood cells requires CFTR activity. Am. J. Physiol. 275, H1726-1732. https://doi.org/10.1152/ajpheart.1998.275.5.H1726

Strehler, E.E., James, P., Fischer, R., Heim, R., Vorherr, T., Filoteo, A.G., Penniston, J.T., Carafoli, E., 1990. Peptide sequence analysis and molecular cloning reveal two calcium pump isoforms in the human erythrocyte membrane. J. Biol. Chem. 265, 2835–2842.

Subczynski, W.K., Pasenkiewicz-Gierula, M., Widomska, J., Mainali, L., Raguz, M., 2017. High cholesterol/low cholesterol: Effects in biological membranes Review. Cell Biochem. Biophys. 75, 369–385. https://doi.org/10.1007/s12013-017-0792-7

Sun, W., Chi, S., Li, Yuheng, Ling, S., Tan, Y., Xu, Y., Jiang, F., Li, J., Liu, C., Zhong, G., Cao, D., Jin, X., Zhao, D., Gao, X., Liu, Z., Xiao, B., Li, Yingxian, 2019. The mechanosensitive Piezo1 channel is required for bone formation. eLife 8, e47454. https://doi.org/10.7554/eLife.47454

Sutherland, H.G., Albury, C.L., Griffiths, L.R., 2019. Advances in genetics of migraine. J. Headache Pain 20, 72. https://doi.org/10.1186/s10194-019-1017-9

Syeda, R., Florendo, Maria.N., Cox, Charles.D., Kefauver, J., Santos, Jose.S., Martinac, B., Patapoutian, A., 2016. Piezo1 channels are inherently mechanosensitive. Cell Rep. 17, 1739–1746. https://doi.org/10.1016/j.celrep.2016.10.033

Syeda, R., Xu, J., Dubin, A.E., Coste, B., Mathur, J., Huynh, T., Matzen, J., Lao, J., Tully, D.C., Engels, I.H., Petrassi, H.M., Schumacher, A.M., Montal, M., Bandell, M., Patapoutian, A., 2015. Chemical activation of the mechanotransduction channel Piezo1. eLife 4, e07369. https://doi.org/10.7554/eLife.07369

Syme, C.A., Hamilton, K.L., Jones, H.M., Gerlach, A.C., Giltinan, L., Papworth, G.D., Watkins, S.C., Bradbury, N.A., Devor, D.C., 2003. Trafficking of the Ca2+-activated K+ channel, hIK1, is dependent upon a C-terminal leucine zipper. J. Biol. Chem. 278, 8476–8486. https://doi.org/10.1074/jbc.M210072200

Takakuwa, Y., Mohandas, N., 1988. Modulation of erythrocyte membrane material properties by Ca2+ and calmodulin. Implications for their role in regulation of skeletal protein interactions. J. Clin. Invest. 82, 394–400. https://doi.org/10.1172/JCI113611

Thomas, S.L.Y., Bouyer, G., Cueff, A., Egée, S., Glogowska, E., Ollivaux, C., 2011. Ion channels in human red blood cell membrane: Actors or relics? Blood Cells. Mol. Dis. 46, 261–265. https://doi.org/10.1016/j.bcmd.2011.02.007

Tiffert, T., Bookchin, R.M., Lew, V.L., 2003. Calcium Homeostasis in Normal and Abnormal Human Red Cells, in: Bernhardt, I., Ellory, J.C. (Eds.), Red Cell Membrane Transport in Health and Disease. Springer, Berlin, Heidelberg, pp. 373–405. https://doi.org/10.1007/978-3-662-05181-8_15

Tiffert, T., Lew, V.L., 1997. Cytoplasmic calcium buffers in intact human red cells. J. Physiol. 500, 139–154. https://doi.org/10.1113/jphysiol.1997.sp022005

Tiffert, T., Spivak, J.L., Lew, V.L., 1988. Magnitude of calcium influx required to induce dehydration of normal human red cells. Biochim. Biophys. Acta 943, 157–165. https://doi.org/10.1016/0005-2736(88)90547-0

Ursitti, J.A., Wade, J.B., 1993. Ultrastructure and immunocytochemistry of the isolated human erythrocyte membrane skeleton. Cell Motil. Cytoskeleton 25, 30–42. https://doi.org/10.1002/cm.970250105

Utsugisawa, T., Iwasaki, T., Aoki, T., Okamoto, Y., Kawakami, T., Ogura, H., Kanno, H., 2017. The Flow Cytometric Osmotic Fragility Test Is an Effective Screening Method for Dehydrated Hereditary Stomatocytosis. Blood 130, 929–929. https://doi.org/10.1182/blood.V130.Suppl_1.929.929

van Meer, G., Voelker, D.R., Feigenson, G.W., 2008. Membrane lipids: where they are and how they behave. Nat. Rev. Mol. Cell Biol. 9, 112–124. https://doi.org/10.1038/nrm2330

van Wijk, R., van Solinge, W.W., 2005. The energy-less red blood cell is lost: erythrocyte enzyme abnormalities of glycolysis. Blood 106, 4034–4042. https://doi.org/10.1182/blood-2005-04-1622

Vandorpe, D.H., Shmukler, B.E., Jiang, L., Lim, B., Maylie, J., Adelman, J.P., de Franceschi, L., Cappellini, M.D., Brugnara, C., Alper, S.L., 1998. cDNA cloning and functional characterization of the mouse Ca2+-gated K+ channel, mIK1. Roles in regulatory volume decrease and erythroid differentiation. J. Biol. Chem. 273, 21542–21553. https://doi.org/10.1074/jbc.273.34.21542

Vera, J.C., Rivas, C.I., Fischbarg, J., Golde, D.W., 1993. Mammalian facilitative hexose transporters mediate the transport of dehydroascorbic acid. Nature 364, 79–82. https://doi.org/10.1038/364079a0

Verkleij, A.J., Zwaal, R.F., Roelofsen, B., Comfurius, P., Kastelijn, D., van Deenen, L.L., 1973. The asymmetric distribution of phospholipids in the human red cell membrane. A combined study using phospholipases and freeze-etch electron microscopy. Biochim. Biophys. Acta 323, 178–193. https://doi.org/10.1016/0005-2736(73)90143-0

Verma, A.K., Filoteo, A.G., Stanford, D.R., Wieben, E.D., Penniston, J.T., Strehler, E.E., Fischer, R., Heim, R., Vogel, G., Mathews, S., 1988. Complete primary structure of a human plasma membrane Ca2+ pump. J. Biol. Chem. 263, 14152–14159. https://doi.org/10.1016/S0021-9258(18)68198-0

Wang, J., Jiang, J., Yang, X., Zhou, G., Wang, L., Xiao, B., 2022. Tethering Piezo channels to the actin cytoskeleton for mechanogating via the cadherin-β-catenin mechanotransduction complex. Cell Rep. 38, 110342. https://doi.org/10.1016/j.celrep.2022.110342

Wang, S., Cao, S., Arhatte, M., Li, D., Shi, Y., Kurz, S., Hu, J., Wang, L., Shao, J., Atzberger, A., Wang, Z., Wang, C., Zang, W., Fleming, I., Wettschureck, N., Honoré, E., Offermanns, S., 2020. Adipocyte Piezo1 mediates obesogenic adipogenesis through the FGF1/FGFR1 signaling pathway in mice. Nat. Commun. 11, 2303. https://doi.org/10.1038/s41467-020-16026-w

Wang, Y., Chi, S., Guo, H., Li, G., Wang, L., Zhao, Q., Rao, Y., Zu, L., He, W., Xiao, B., 2018. A lever-like transduction pathway for long-distance chemical- and mechano-gating of the mechanosensitive Piezo1 channel. Nat. Commun. 9, 1300. https://doi.org/10.1038/s41467-018-03570-9

Wieschhaus, A., Khan, A., Zaidi, A., Rogalin, H., Hanada, T., Liu, F., De Franceschi, L., Brugnara, C., Rivera, A., Chishti, A.H., 2012. Calpain-1 knockout reveals broad effects on erythrocyte deformability and physiology. Biochem. J. 448, 141–152. https://doi.org/10.1042/BJ20121008

Wiley, J.S., Cooper, R.A., 1974. A Furosemide-Sensitive Cotransport of Sodium plus Potassium in the Human Red Cell [WWW Document]. https://doi.org/10.1172/JCI107613

Wölwer, C.B., Pase, L.B., Russell, S.M., Humbert, P.O., 2016. Calcium Signaling Is Required for Erythroid Enucleation. PLoS ONE 11, e0146201. https://doi.org/10.1371/journal.pone.0146201

Wu, J., Lewis, A.H., Grandl, J., 2017. Touch, Tension, and Transduction – The Function and Regulation of Piezo Ion Channels. Trends Biochem. Sci. 42, 57–71. https://doi.org/10.1016/j.tibs.2016.09.004

Xu, P., Mo, X., Xia, R., Jiang, L., Zhang, C., Xu, H., Sun, Q., Zhou, G., Zhang, Y., Wang, Y., Xia, H., 2021. KCNN4 promotes the progression of lung adenocarcinoma by activating the AKT and ERK signaling pathways. Cancer Biomark. Sect. Dis. Markers 31, 187–201. https://doi.org/10.3233/CBM-201045

Yamaguchi, Y., Allegrini, B., Rapetti-Mauss, R., Picard, V., Garçon, L., Kohl, P., Soriani, O., Peyronnet, R., Guizouarn, H., 2021. Hereditary Xerocytosis: Differential Behavior of PIEZO1 Mutations in the N-Terminal Extracellular Domain Between Red Blood Cells and HEK Cells. Front. Physiol. 12.

Yan, M., Xu, M., Li, Z., An, Y., Wang, Z., Li, S., Chen, Y., Xia, Y., Wang, Liqiu, Wang, Longlong, Ji, S., Dong, W., Shi, J., Gao, C., 2022. TMEM16F mediated phosphatidylserine exposure and microparticle release on erythrocyte contribute to hypercoagulable state in hyperuricemia. Blood Cells. Mol. Dis. 96, 102666. https://doi.org/10.1016/j.bcmd.2022.102666

Yang, H., Kim, A., David, T., Palmer, D., Jin, T., Tien, J., Huang, F., Cheng, T., Coughlin, S.R., Jan, Y.N., Jan, L.Y., 2012. TMEM16F Forms a Ca2+-Activated Cation Channel Required for Lipid Scrambling in Platelets during Blood Coagulation. Cell 151, 111–122. https://doi.org/10.1016/j.cell.2012.07.036

Yang, L., Andrews, D.A., Low, P.S., 2000. Lysophosphatidic acid opens a Ca++ channel in human erythrocytes. Blood 95, 2420–2425. https://doi.org/10.1182/blood.V95.7.2420

Yoshida, H., Kawane, K., Koike, M., Mori, Y., Uchiyama, Y., Nagata, S., 2005. Phosphatidylserine-dependent engulfment by macrophages of nuclei from erythroid precursor cells. Nature 437, 754–758. https://doi.org/10.1038/nature03964

Zámbó, B., Várady, G., Padányi, R., Szabó, E., Németh, A., Langó, T., Enyedi, Á., Sarkadi, B., 2017. Decreased calcium pump expression in human erythrocytes is connected to a minor haplotype in the ATP2B4 gene. Cell Calcium 65, 73–79. https://doi.org/10.1016/j.ceca.2017.02.001

Zarychanski, R., Schulz, V.P., Houston, B.L., Maksimova, Y., Houston, D.S., Smith, B., Rinehart, J., Gallagher, P.G., 2012a. Mutations in the mechanotransduction protein PIEZO1 are associated with hereditary xerocytosis. Blood 120, 1908–1915. https://doi.org/10.1182/blood-2012-04-422253

Zarychanski, R., Schulz, V.P., Houston, B.L., Maksimova, Y., Houston, D.S., Smith, B., Rinehart, J., Gallagher, P.G., 2012b. Mutations in the mechanotransduction protein PIEZO1 are associated with hereditary xerocytosis. Blood 120, 1908–1915. https://doi.org/10.1182/blood-2012-04-422253

Zhao, C., Sun, Q., Tang, L., Cao, Y., Nourse, J.L., Pathak, M.M., Lu, X., Yang, Q., 2019. Mechanosensitive Ion Channel Piezo1 Regulates Diet-Induced Adipose Inflammation and Systemic Insulin Resistance. Front. Endocrinol. 10.

Zhao, Q., Zhou, H., Chi, S., Wang, Y., Wang, Jianhua, Geng, J., Wu, K., Liu, W., Zhang, T., Dong, M.-Q., Wang, Jiawei, Li, X., Xiao, B., 2018. Structure and mechanogating mechanism of the Piezo1 channel. Nature 554, 487–492. https://doi.org/10.1038/nature25743

Autres publications

Rapetti-Mauss, R., Berenguier, C., Allegrini, B., & Soriani, O. (2020**). Interplay between ion channels and the Wnt/β-catenin signaling pathway in cancers**. *Frontiers in Pharmacology*, *11*, 525020.

Guizouarn, H., & Allegrini, B. (2020). **Erythroid glucose transport in health and disease**. *Pflügers Archiv-European Journal of Physiology*, *472*(9), 1371-1383.

Jakob, D., Klesen, A., Allegrini, B., Darkow, E., Aria, D., Emig, R., ... & Peyronnet, R. (2021). **PIEZO1 and BKCa channels in human atrial fibroblasts: Interplay and remodelling in atrial fibrillation**. *Journal of Molecular and Cellular Cardiology*, *158*, 49-62.

Rapetti-Mauss, R., Nigri, J., Berenguier, C., Finetti, P., Tubiana, S. S., Labrum, B., ... & Soriani, O. (2023). **SK2 channels set a signalling hub bolstering CAF-triggered tumourigenic processes in pancreatic cancer**. *Gut*, *72*(4), 722-735.

Lohia, R., Allegrini, B., Berry, L., Guizouarn, H., Cerdan, R., Abkarian, M., ... & Wengelnik, K. (2023). **Pharmacological activation of PIEZO1 in human red blood cells prevents Plasmodium falciparum invasion**. *Cellular and Molecular Life Sciences*, *80*(5), 124.

Interplay between ion channels and the Wnt/β-catenin signaling pathway in cancers.

Rapetti-Mauss, R., Berenguier, C., Allegrini, B., & Soriani, O. (2020). *Frontiers in Pharmacology*, *11*, 525020.

Contexte :

C'est un article de revue rédigée en collaboration avec des membre de notre équipe, en rapport avec mon sujet de stage de Master 2. Il est ici question de l'association entre les canaux ioniques et les mécanismes cancéreux impliquant la voie Wnt/β-catenin. Cet axe de recherche est complètement novateur et suggère l'importance du potentiel de membrane dans l'activation de voies de signalisations.

frontiers in Pharmacology

REVIEW
published: 29 September 2020
doi: 10.3389/fphar.2020.525020

Interplay Between Ion Channels and the Wnt/β-Catenin Signaling Pathway in Cancers

Raphael Rapetti-Mauss, Camille Berenguier, Benoit Allegrini and Olivier Soriani*

Inserm, CNRS, iBV, Université Côte d'Azur, Nice, France

Increasing evidence point out the important roles of ion channels in the physiopathology of cancers, so that these proteins are now considered as potential new therapeutic targets and biomarkers in this disease. Indeed, ion channels have been largely described to participate in many hallmarks of cancers such as migration, invasion, proliferation, angiogenesis, and resistance to apoptosis. At the molecular level, the development of cancers is characterised by alterations in transduction pathways that control cell behaviors. However, the interactions between ion channels and cancer-related signaling pathways are poorly understood so far. Nevertheless, a limited number of reports have recently addressed this important issue, especially regarding the interaction between ion channels and one of the main driving forces for cancer development: the Wnt/β-catenin signaling pathway. In this review, we propose to explore and discuss the current knowledge regarding the interplay between ion channels and the Wnt/β-catenin signaling pathway in cancers.

Keywords: signaling pathways, drug targets, KCNQ1 channel, P2X7, cystic fibrosis transmembrane conductance regulator, hERG, transient receptor protein channels, ClC-2 channel

OPEN ACCESS

Edited by:
Sébastien Roger, Université de Tours, France

Reviewed by:
Irene Frischauf, Johannes Kepler University of Linz, Austria
Heike Wulff, University of California, Davis, United States

****Correspondence:***
Raphael Rapetti-Mauss
Raphael.RAPETTI-MAUSS@univ-cotedazur.fr

Specialty section:
This article was submitted to Pharmacology of Ion Channels and Channelopathies, a section of the journal Frontiers in Pharmacology

Received: *07 January 2020*
Accepted: *31 August 2020*
Published: *29 September 2020*

Citation:
Rapetti-Mauss R, Berenguier C, Allegrini B and Soriani O (2020) Interplay Between Ion Channels and the Wnt/β-Catenin Signaling Pathway in Cancers. Front. Pharmacol. 11:525020. doi: 10.3389/fphar.2020.525020

INTRODUCTION

Despite decades of intensive research on its physiopathology, cancer remains a leading cause of death worldwide according to the World Health Organisation. Traditional cancer treatments including radiation therapy, chemotherapy, and surgery have substantially improved patients' conditions. However, several challenges in curing cancer remain in front of us. Side effects generated by cancer treatments significantly impact patients quality of life; high patients intrinsic heterogeneity revealed treatments resistance, and finally the efficiency of treatment used for some types of cancer remains very low such as for pancreatic cancer. These circumstances highlight the urgent need to identify new therapeutic strategies in treating cancers.

Ion channels are transmembrane proteins allowing ions to cross biological membranes thereby generating electrical current and variation in membrane potential. Ion channels are classified in five main families, Potassium channels, Chloride channels, Sodium channels, Calcium channels that are selective for their specific ion, and non-selective ion channels that allow the passage of several species of ions. The functions attributed to ion channels were first confined to cell excitability and regulation of hydro-electrolytic balance. Interestingly, since the 1980's ion channels have also been described to be involved in controlling processes regulating cell behaviors such as proliferation,

migration, invasion and differentiation. In 1984, the pioneer work of DeCoursey describing the involvement of potassium channels in the proliferation of T lymphocytes (DeCoursey et al., 1984) opened new perspectives in studying the biology of ion channels. The first evidence for such functions of ion channels in cancer cells emerged in the late 1980's with studies describing that the pharmacological inhibition of ion channels reduces tumor cells proliferation (Yamashita et al., 1987; Lee et al., 1988; Pancrazio et al., 1989; Taylor and Simpson, 1992). Since then, the field has greatly expanded, and it has been shown that ion channels are involved in virtually all the hallmarks of cancers described by Hanahan et al. (Prevarskaya et al., 2010; Prevarskaya et al., 2018). Although the involvement of ion channels in cancer has been clearly described, how ion channels interact with cancer-related signaling pathways from a mechanistic point of view, and how the expression of ion channels is regulated in cancers is poorly understood. However, this issue has recently emerged in the literature and a growing number of reports tackle these questions. Cancer initiation and development is often associated to altered signaling pathway involved in cell and tissue homeostasis (Sanchez-Vega et al., 2018). Among these signaling pathways, the Wnt/β-catenin pathway emerged as the most associated pathway to ion channels in the literature. This review aims to summarize the current knowledge regarding the interplay between ion channels and the Wnt/β-catenin signaling pathway.

THE WNT SIGNALING PATHWAY

Since the first description of Wingless Int 1 (Wnt1) gene in virally induced breast tumors (Nusse and Varmus, 1982), the Wnt signaling pathway has been subjected to intense research, ranging from development to cancer. Its role in morphogenesis and adult stem cell renewal is closely linked to its involvement in cancer development (Nusse and Clevers, 2017). Mechanistically, Wnt signaling pathway can take mostly two directions: the canonical (Wnt/β-catenin), influencing cell-fate, proliferation, as well as self-renewal and the non-canonical (β-catenin-independent), Wnt/PCP, Wnt/Ca^{++}, Wnt/STOP, influencing planar polarity (Tree et al., 2002), Ca^{2+} homeostasis (Sheldahl et al., 2003), or protein stabilization (Davidson et al., 2009), respectively. Both are involved in cancer but canonical Wnt/β-catenin remains the most studied in a large variety of tissues.

In mammals, there are more than 19 Wnt ligands which are expressed in a tissue-specific manner. After their translation into proteins Wnt ligands are modified with attachment of a palmitoleic acid (palmitoylation) by the ER-resident acyl-transferase Porcupine (Kadowaki et al., 1996). This modification allows binding of Wnt ligand to the ER-transmembrane protein Evi/Wls, and therefore the transport to Golgi apparatus (Bänziger et al., 2006) assisted by the p24 protein (Buechling et al., 2011). Wnt ligands are either released by solubilisation (Mulligan et al., 2012), by exosomes (Gross et al., 2012), or in lipoproteins particles (Neumann et al., 2009) or linked to the plasma membrane. Importantly, after being secreted, Wnt ligands can form a gradient and act as directional growth factor, as it is the case in intestinal colonic crypts (Medema and Vermeulen, 2011)

Here we will focus on Wnt canonical pathway, which depends on β-catenin stability. In the absence of Wnt ligand (Wnt OFF state), cytosolic β-catenin is sequestrated by a destruction complex (DC) composed of the tumor suppressor Axin acting as scaffold protein, the tumor suppressor Adenomatous Polyposis Coli (APC), the glycogen synthase kinase 3β (GSK3β) and casein kinase 1α (CK1α). Inside this DC, β-catenin is bound to Axin and phosphorylated by the two constitutively active kinases GSK3β and CK1α at specific Serine and Threonine residues (Liu et al., 2002). Then, β-catenin is ubiquitylated by the F-box containing protein E3 ubiquitin ligase (β-TrCP) and addressed to the proteasome for degradation (Aberle et al., 1997; Latres et al., 1999).

Initiation of the Wnt canonical (β-catenin-dependent) pathway (Wnt ON state) is mediated by engagement of Frizzled (Fz) receptor and LRP5/6 co-receptor with Wnt ligands. Activation of the pathway leads to degradation complex relocation near Fz/LRP complexes, where LRP is phosphorylated by CK1α and GSK3β. The phosphorylation of LRP triggers Dishevelled (Dvl) protein polymerisation, thus inactivating the degradation complex (Metcalfe et al., 2010). Another study suggests a direct inhibition of GSK3β by the phosphorylated-LRP co-receptor (Stamos et al., 2014). Hence, β-catenin is not degraded, can accumulate in the cytoplasm and translocate into the nucleus. β-catenin then complexes with lymphoid enhanced factor (LEF) and T-cell factor (TCF) to act as a transcription factor activating target genes (Li et al., 2012). In the Wnt OFF state, TCF interacts with Groucho, preventing transcriptional activation of Wnt target genes (Cavallo et al., 1998). Interestingly, β-catenin plays a second role in maintaining epithelial junctions, by binding to the cytoplasmic tail of E-cadherin (Peifer et al., 1992). Thus, presence of epithelial junctions is a limiting factor for Wnt/β-catenin activity, and reciprocally (Huels et al., 2015).

The Wnt/β-catenin pathway is tightly regulated. For example, the two homologues E3 ubiquitin ligases ZNRF3/RNF43 can induce Fz receptor lysosomal degradation, thus inhibiting Wnt signaling. R-spondins are secreted proteins, interacting with their receptor LGR4-6, able to inhibit ZNRF3/RNF43 activity (de Lau et al., 2011). Furthermore, Hippo and Wnt pathway have been closely linked, since the Hippo transducer YAP/TAZ plays an integrative role inside the DC, allowing β-TrCP recruitment to the complex and subsequent β-catenin degradation (Azzolin et al., 2014). Others regulations are nicely reviewed by Zhan et al. (2017).

As mentioned above, Wnt canonical pathway is widely implicated in cancer diseases. The first mutations have been found in the APC gene, leading to Familiar Adenomatous Polyposis (Kinzler et al., 1991; Nishisho et al., 1991), and now found in the majority of colorectal cancers (Wood et al., 2007). Mutations of Axin1 are present in hepatocellular carcinoma (Satoh et al., 2000). Gain of function β-catenin mutations are reported in melanoma (Rubinfeld et al., 1997). Loss of function

mutations in Rnf43 or Znrf3 are found in pancreatic cancer (Wu et al., 2011) and adrenocortical carcinoma (Assié et al., 2014). Wnt signaling has also been implicated in cholangiosarcoma (Chan-On et al., 2013), leukemia (Wang et al., 2010) and in 50% of breast cancer cases (Lin et al., 2000).

WNT SIGNALING PATHWAY INTERPLAY WITH POTASSIUM CHANNELS

With more than 80 members, the potassium channel family is the widest group of ion channels. They participate in a multitude of biological processes from cell excitability to water and electrolyte homeostasis. They are especially essential in maintaining membrane resting potential. Increasing evidence point out the involvement of this family of ion channel in the physiopathology of cancers (Huang and Jan, 2014; Pardo and Stühmer, 2014). However, the molecular mechanisms sustaining potassium channels involvement in cancer are still unclear. This section reviews recent work that report the function of potassium channels in the Wnt/β-catenin pathway.

KCNQ1

The potassium channel KCNQ1, also called Kv7.1, belongs to the family of voltage-gated potassium channel. It is constituted by the assembly of four α subunits forming the pore of the channel. This channel can associate with ancillary subunits from the KCNE family which drastically change the channel features regarding the KCNE associated (Bendahhou et al., 2005; Jespersen et al., 2005). Association with KCNE1, shows a delay in KCNQ1 activation and in this case the complex KCNQ1/KCNE1 also called IKs, is essential to cardiac action potential repolarisation. With KCNE3 and KCNE2, KCNQ1 is no longer voltage-dependent and participates to transepithelial transport in nearly every epithelium. The effect of the last two members of the KCNE family on KCNQ1 are more discussed in the literature, however it appears that KCNE4 and KCNE5 mostly act as inhibitors of KCNQ1 activity (Abbott, 2014).

As aforementioned, KCNQ1 plays a key role in the physiology of epithelial transport. Transport mechanisms involve complex networks of ion channels and transporters, creating and dissipating ionic gradients required for the passage of water, electrolytes, nutrients or other substrates through the epithelium (Barrett and Keely, 2000). Thus, the Na^+/K^+ ATPase pump activity is the main force for transepithelial transport allowing Na^+ output against K^+ entry into the cell. In this context, K^+ channels provide two main functions: the maintenance of membrane potential and the basolateral recycling of K^+ that guarantees the maintenance of electrochemical gradients. In the colon, KCNQ1, associated with its regulatory subunit KCNE3, plays a fundamental role in Leiberkühn's crypts homeostasis by maintaining the electrical driving force required for apical secretion of Cl^- and water, and Na^+ absorption (Preston et al., 2010; Rapetti-Mauss et al., 2013).

Recently, studies found an unexpected link between KCNQ1 and epithelial cancers. In a first study, using mouse models, the authors have shown that the loss of KCNQ1 expression promotes the development of adenocarcinoma in the colon. They also showed that the low expression of KCNQ1 is associated with a poor survival prognosis in patients with Colorectal Cancer (CRC) showing hepatic metastases (Than et al., 2014). In line with these findings, another report has shown that in patients with stage II and III colon cancer, low expression of KCNQ1 is associated with poor survival prognosis. This channel therefore seems to be an interesting prognostic marker for the early stages of the disease as well as for the prediction of recurrences (den Uil et al., 2016). These studies also suggest that KCNQ1 acts as a tumor suppressor in CRC. Another study described the same function of KCNQ1 in Hepatocellular Carcinoma (HCC). They have shown using immunohistochemistry that HCC patients' samples show less KCNQ1 expression compared with normal liver tissues. Also, in patients with HCC, the high expression of KCNQ1 significantly correlates with a better patient's survival rate. Therefore, they reach the same conclusion as in CRC, KCNQ1 acts as a tumor suppressor in HCC (Fan et al., 2018).

It is clearly not trivial to explain the function of KCNQ1 as a tumor suppressor protein in epithelial cancers by its classical role in the physiology of epithelial transport. Therefore, could alternative functions of this channel underlie the observed correlations between KCNQ1 expression and cancers development? We and other have explored this issue to identify the molecular mechanism sustaining the tumor suppressor functions of KCNQ1 in CRC and HCC.

It appears that KCNQ1 expression is associated in CRC and HCC to epithelial cell plasticity (Rapetti-Mauss et al., 2017; Fan et al., 2018). Epithelial-to-Mesenchymal Transition (EMT) is a cellular process by which epithelial cells progressively and reversibly acquire mesenchymal features (Ye and Weinberg, 2015; Pastushenko and Blanpain, 2019). This process has largely been associated to cancer development and progression by allowing loss of epithelial structure and promoting cancer cell migration, invasion and drug resistance. In CRC, the expression of KCNQ1 in a panel of cell lines showing different degrees of EMT is associated with epithelial features. Conversely, the channel's expression is lowered in most mesenchymal cell lines. These data raise the hypothesis of a functional link between KCNQ1 and the cellular process of epithelial-to-mesenchymal transition in cancer cells. Interestingly, in CRC as well as in HCC, the rescue expression of KCNQ1 in cell lines that do not express this channel, restores the expression of epithelial markers such as E-cadherin, lowers the expression of mesenchymal markers such as N-cadherin and restores the ability of cell to form spheroids in 3D culture. Moreover, the molecular silencing of KCNQ1 in epithelial CRC cell line reduces the expression of E-cadherin, increases the expression of N-cadherin and impairs the ability to grow as a spheroid in 3D culture. Therefore, the expression of KCNQ1 seems to promote epithelial features.

An important event characterising EMT is the dislocation of adherens junctions (AJ) causing the loss of cohesion between adjacent cells and therefore disrupting the epithelial integrity. The

exploration of intestinal crypts by techniques coupling immunocytochemistry and in-situ immunisation (proximity ligation assay), provides data showing that KCNQ1 is directly associated with the β-catenin/E-cadherin complex in AJ in colonocytes. Interestingly, the same association between KCNQ1 and β-catenin has been established in hepatocyte cell lines. At the functional level, silencing of KCNQ1 expression in colon cell lines produces a disruption of the complex, as well as a loss of the integrity of epithelial architecture, which results in a decrease in epithelial electrical resistance. The study of the phosphorylation state of β-catenin in cell lines where KCNQ1 has been silenced by shRNA, indicates that KCNQ1 is necessary to retain β-catenin at the plasma membrane. Beside this observation it has been shown that pharmacological or molecular inhibition of KCNQ1 in CRC and in HCC, leads to a potentiation of the Wnt/β-catenin signaling pathway. Indeed, silencing of KCNQ1 in CRC induces the re-localisation of β-catenin in the cytosol and increases the expression of Wnt/β-catenin signaling pathway targets such as Cyclin D1 and C-jun. In HCC overexpression of KCNQ1 reduces Wnt target genes expression and Wnt activity using a Top/fop assay. These results indicate that KCNQ1 restricts the Wnt/β-catenin signaling pathway activity, stabilising β-catenin at the plasma membrane. These results reveal a new role for KCNQ1: in parallel with its function of transepithelial transport regulator, this channel plays a predominant role in maintaining the architectural integrity of the epithelium. These results shed new light on the correlation between the level of KCNQ1 expression and the clinical outcome of patients with CRC, since high levels of channel expression, together with the maintenance of adherens junctions guarantee the sequestration of β-catenin to the membrane, repression of the Wnt/β-catenin pathway, and finally reduces the commitment in the EMT process.

The stabilisation of the β-catenin/E-cadherin/KCNQ1 complex at the AJ constitutes an explanation to understand the role of KCNQ1 as a tumor suppressor in CRC and HCC. Would the latter only play an anchoring protein role for the β-catenin/E-cadherin complex, or is the KCNQ1-induced hyperpolarising potassium flow important in the stabilisation of the complex? In other words, do membrane potential variations influence β-catenin localisation and activity? The answer is provided by experiments in which CRC cells expressing KCNQ1 are experimentally depolarised by increasing the extracellular K^+ concentration 140mM K^+. This protocol causes a cytosolic accumulation of β-catenin, suggesting that the depolarisation induced by the silencing of the channel potentiates Wnt/β-catenin pathway. These results demonstrate the existence of a link between the electrical signature of the cancer cell and the signaling pathways that control cancer cells features. These data are consistent with a recent study that shows that the K-Ras/RAF/MAPK signaling pathway is directly controlled by membrane potential (Zhou et al., 2015).

There is only few information in the literature regarding how ion channel expression is regulated in the context of cancers. It has been observed that expression of KCNQ1 is decreased in both CRC and HCC. We have tempted to address this question and we reason that the link between KCNQ1 could be bidirectional. Is KCNQ1 expression repressed by Wnt activity? When the Wnt/β-catenin pathway is experimentally stimulated by pharmacological or molecular ways, we observed a decrease in KCNQ1 expression. We also identify that β-catenin as well as the TCF-4 transcription factor (member of the TCF/LEF family, which regulates the expression of the target genes of the Wnt pathway), bind directly to KCNQ1 promoter and cause the repression of its expression. These results thus reveal that KCNQ1 channel is a new target gene of Wnt pathway (Rapetti-Mauss et al., 2017).

By unveiling the bidirectional interaction between Wnt/β-catenin pathway and KCNQ1, these works reveal new functions of potassium channels in healthy tissue architecture, and their implication in the development of tumors. Thus, the fine understanding of these alternative functions could contribute to the characterisation of new markers, and innovative therapeutic targets. These data suggest that KCNQ1, by sequestering β-catenin at the AJ, restricts activation of Wnt signaling pathway and acts as a tumor suppressor in multiple epithelial cancers. The mechanism seems to be quite conserved suggesting a key role of KCNQ1 in epithelial homeostasis.

KCNH2

Another potassium channel has recently been associated to the Wnt/β-catenin pathway, KCNH2 also called hERG or Kv11.1 (Breuer et al., 2019). This channel is a voltage-gated potassium channel, which role in cancer cells has largely been studied especially by the groups of Arcangeli (Becchetti et al., 2019) and Soriani (Crottès et al., 2016). This channel is associated with β1-integrin when the channel is in its closed state, resulting in an increase of metastasis in breast cancer. Whereas, in the open state, the channel association with β1-integrin is decreased leading to a reduction in breast cancer metastasis (Becchetti et al., 2017).

A recent report described that an opener of hERG, the NS1643, reduces metastasis spread of breast tumor *in vivo* by attenuation of the Wnt/β catenin pathway signaling, suggesting that NS1643 mimics the dissociation between hERG and β1-integrin (Breuer et al., 2019). The authors observed that activating hERG channel stabilises β-catenin at the plasma membrane by inhibiting AKT (T308) and GSK3β (S9) phosphorylation. In this case the cytosolic fraction of β-catenin decreases favouring the association of β-catenin with E-cadherin. Therefore, NS1634 decreases Wnt pathway activity. This result suggests that the hyperproliferation induced by the opening of hERG reduces Wnt activity by retaining β-catenin at the plasma membrane. These data are consistent with the data from Arcangeli's lab showing that the open state of hERG lowers metastasis dissemination in breast cancer.

WNT SIGNALING PATHWAY INTERPLAY WITH CHLORIDE CHANNELS

Chloride channels regulate a variety of cell processes such as excitability and water and mucus secretion. Another important

aspect of these channels, especially in cancer, is their role in cell volume regulation and pH level regulation. As for the other ion channel families, different chloride channels have been described depending on their gating properties: calcium-activated, voltage-dependant, ligand-dependant. Although their role in cancer has been under study for the past years, their link with the Wnt/β-catenin pathway remains poorly investigated.

CFTR

Cystic Fibrosis Transmembrane Conductance Regulator (CFTR) is widely expressed in the apical epithelial membranes. CFTR is an anion channel regulating fluid transport and pH levels. Mutations of CFTR such as ΔF508 result in Cystic Fibrosis (CF) causing a wide range of symptoms linked to a defect in fluid transport across the epithelial membranes. The pulmonary symptoms are well-described, but the earliest symptoms concern the digestive system. In addition, CF patients are at high risk of developing gastrointestinal cancers (Yamada et al., 2018). The study from Strubberg et al. links for the first time the loss of functional CFTR and gastrointestinal cancer through the increase of the proliferation rate of crypt cells by activating Wnt/β-catenin pathway (Strubberg et al., 2018). Indeed, the authors show that loss of functional CFTR leads to an increase of intracellular pH (pHi) levels in crypt cells as Cl^- and $HCO3^-$ secretion is impaired. In addition, it has been shown in *Drosophila* species that alkaline pHi (negatively charged phospholipids at the inner leaflet) facilitates Dishevelled's interaction with the Wnt receptor Frizzled by addressing Dishevelled to the negatively charged phospholipids through its DEP domain (Simons et al., 2009). Strubberg et al. show that the same mechanism is occurring in Cftr KO cells. The inhibition of CFTR activity alkalinizes pHi in the crypt epithelium, enhancing Dishevelled-2's (Dvl-2) association at the plasma membrane and promoting binding between Fz and Dvl-2 and therefore facilitating Wnt signaling. Confirming these results, active β-catenin and LEF1 levels were higher in Cftr KO mice crypts than WT. Furthermore, CFTR has been shown to be a direct target of Wnt signaling as it exhibits an intestine-specific enhancer element positively regulated by TCF4 (Paul et al., 2007). All in all, loss of CFTR facilitates Wnt signaling in the intestinal crypt epithelium, increasing tumorigenesis and underlying the basis of increased risk of gastrointestinal cancers in CF patients.

The main cancer risk for CF patients is gastrointestinal (GI) cancers (Neglia et al., 1995). However, as new therapeutic strategies aim to enhance CF patients' life expectancy, and since the link between loss of functional CFTR and Wnt/β-catenin pathway has been assessed in GI cancers, other epithelial cancers could occur in CF patients following the same biological process.

CLCN2

Adherens junctions and tight junctions ensure epithelium integrity, providing a physical barrier. Adherens junctions further establish the apical-basal cell polarity. The importance of the chloride channel ClCN2, also called ClC-2, in the regulation of tight junctions' composition in the small intestine has been recently uncovered (Nighot and Blikslager, 2012). As ClCN2 seemed to be an important actor of epithelial integrity and maintenance of the tight junctions, Jin *et al.* questioned its involvement in adherens junctions (AJ) and its interaction with β-catenin (Jin et al., 2018). β-catenin binds E-cadherin in the adherens junctions. If the AJ are disrupted, β-catenin is freed from the membrane-bound E-cadherin, accumulates in the cytosol and translocates to the nucleus where it interacts with TCF/LEF1, activating the Wnt target genes.

ClCN2 is expressed physiologically in the colonic epithelium. Absence of ClCN2 alters AJ integrity, inducing an increase of nuclear β-catenin. The increase of nuclear β-catenin is linked to an upregulation of Wnt target genes. Moreover, the loss of ClCN2 alters colonic crypt homeostasis, increases proliferation and reduces differentiation of colonic cells.

Therefore, the loss of ClCN2 in colonic epithelium leads to the disruption of adherens junction and subsequent activation of Wnt pathway, promoting tumorigenicity. The involvement of other ClCs in the regulation of junctions and their link with Wnt/β-catenin pathway has not yet been assessed. However, a study showed that absence of a regulatory protein of Calcium-activated chloride channels (CaCCs)—such as ANO1, also called TMEM16A (Sala-Rabanal et al., 2015; Sala-Rabanal et al., 2017)—CLCA1, induces an increase of β-catenin in the nucleus (Li et al., 2017). However, this study only focuses on the consequence of a knock-out of CLCA1 and not its link with CaCC channels nor its direct or indirect interaction with Wnt/β-catenin pathway. These points remain to be understood to truly consider CLCA1 as a tumor suppressor *via* inhibition of Wnt pathway.

WNT SIGNALING PATHWAY INTERPLAY WITH OTHER CHANNELS

TRP Channels

Transient receptor protein (TRP) channels are cationic channels that generate Na^+ and Ca^{2+} influxes in response to a great variety of stimuli (Venkatachalam and Montell, 2007). Therefore, TRP channels enable individual cells to sense changes in their local environment, translating this information into signals that can be interpreted at a short time scale such as membrane potential and Ca^{2+} homeostasis (Shapovalov et al., 2016). Several works have revealed a functional link between TRP channels and Wnt/β-catenin pathway in cancers.

TRPV4

In gastric cancers, the Calcium receptor (CasR) is overexpressed. Its overexpression contributes to tumor growth, metastasis formation, and poor prognosis. Mechanistically, CasR stimulates TRPV4 channels. The TRPV4-dependent Ca^{2+} influx increases AKT activation, which in turn phosphorylates β-catenin on its residue Ser675 and thus activating β-catenin downstream signaling (Xie et al., 2017).

TRPM4

TRPM4 channels are overexpressed in prostate and colorectal cancers where they participate to migration and invasion (Gao and Liao, 2019). In prostate cancer cells, invalidation of TRPM4 increases GSK3β activity, leading to β-catenin degradation. In LnCAP prostate cancer cells, TRPM4-associated Ca^{2+} influx stimulates AKT1, which in turn increases the inhibitory Ser9 phosphorylation of GSK3β and the total amount of β-catenin (Sagredo et al., 2018). In this study, Sagredo et al. suggest that the effect of TRPM4 on AKT1 is probably mediated by an alteration in the calcium/calmodulin-EGFR axis, linking TRPM4 activity with the observed effects in β-catenin-related signaling pathways.

TRPM8

A recent study driven in prostate and breast cancer cell lines has proposed that Wnt ligand-induced signaling involves TRPM8 channels. The authors propose a model in which Wnt ligands bind to both their receptors and TRPM8 channels, inducing a rapid decrease in $[Ca^{2+}]i$, followed by a store-operated calcium entry (SOCE). The SOCE in turn triggers calcium-dependent potassium channels (KCNN4) leading to a large membrane hyperpolarization. This study indeed suggests that control of membrane potential by Wnt ligands is an early event of the Wnt signaling pathway (Ashmore et al., 2019).

TRPC5

TRPC5 is overexpressed, together with ATP-binding cassette, subfamily 1-member1 (ABCB1) in 5-Fluorouracil (5-FU), in CRC cells. ABCB1 is a transport protein involved in chemoresistance by mediating efflux of cytotoxic drugs. Enforcing TrpC5 expression increases in a Ca^{2+}-dependent manner nuclear accumulation of β-catenin and subsequent upregulation of Wnt target genes including ABCB1. These results suggest that TRPC5 may reinforce chemoresistance by regulating transporters controlled by the Wnt/β-catenin pathway (Wang et al., 2015).

Purinergic Ionotropic Receptors

P2RX7

The ionotropic ATP receptor P2RX7, (P2X7) is overexpressed in osteocarcinoma and participates to several cancer hallmarks including proliferation, migration, invasion and EMT. At the molecular level, P2X7 stimulation by receptor agonist (bzATP) increases GSK3β phosphorylation and further accumulation of β-catenin in the nucleus. Indeed, Wnt/β-catenin activation by P2X7 stimulation depends on PI3K/AKT stimulation. Interestingly, pharmacological inhibition of P2X7 decreased pro-tumoral behavior of cancer cells (Zhang et al., 2019).

Acid Sensing Ion Channels

ASIC1a: Acid sensing ion channels (Asic) are proton-gated Na^+/Ca^{2+} channels involved in a wide range of physiological features including pain perception and behavior (Hanukoglu and Hanukoglu, 2016). Asic1a is up-regulated in liver cancer tissues and cells lines and is associated to poor prognosis. KO of Asic1a inhibits liver cancer growth *in vivo* and *in vitro*, an effect that is underlied by cell cycle arrest and increased apoptosis. Jin et al. observed that low extracellular pH

TABLE 1 | Role of ion channels in regulating Wnt pathway activity in cancers.

(C) Cancers Type	Models	Channels	Effect of channels expression/activity on Wnt pathway	Mechanism	Expression in cancers	References
Colorectal Cancer	Cell lines, Rat colonic crypts	KCNQ1	↓ Wnt activity Wnt target genes	Stabilization of β-cat. at the plasma membrane	Down	Rapetti-Mauss et al., 2017
Hepatocellular Carcinoma	Cell lines	KCNQ1	↓ Wnt activity	Stabilization of β-cat at the plasma membrane	Down	Fan et al., 2018,
Breast cancer	Mouse models, Cell lines	hERG	↓ Wnt activity (Channel opened)	Stabilization of β-cat at the plasma membrane	Up	Breuer et al., 2019
Colorectal cancer	Mouse intestine	CFTR	↓ Wnt activity Wnt target genes	Modulation of the intracellular pH	Down	Strubberg et al., 2018
Colorectal cancer	Cell lines; Mouse models	ClC-2	↓ Wnt activity	Stabilization of β-cat at the plasma membrane	Down	Jin et al., 2018
Gastric cancer	Human sample, mouse model, Cell lines	TRPV4	↑ Wnt activity	Ca^{2+} → AKT → β-cat accumulation	Up	Xie et al., 2017
Prostate cancer	Cell lines	TRPM4	↑ Wnt activity	Ca^{2+} → AKT → β-cat accumulation	Up	Sagredo et al., 2018
Prostate cancer Breast cancer	Cell lines	TRPM8	↑ Wnt activity	Wnt ligands binding → calcium	Up	Ashmore et al., 2019
Colorectal cancer	Cell lines	TRPC5	↑ Wnt activity	Ca^{2+} → AKT → β-cat accumulation	Up	Wang et al., 2015
osteosarcoma	Cell lines	P2X7	↑ Wnt activity	AKT →GSK3 β → β-cat accumulation	Up	Zhang et al., 2019
Liver cancer	Human sample, Cell lines	ASIC1a	↑ Wnt activity	Modulation of β-cat phosphorylation and accumulation	Up	Jin et al., 2017

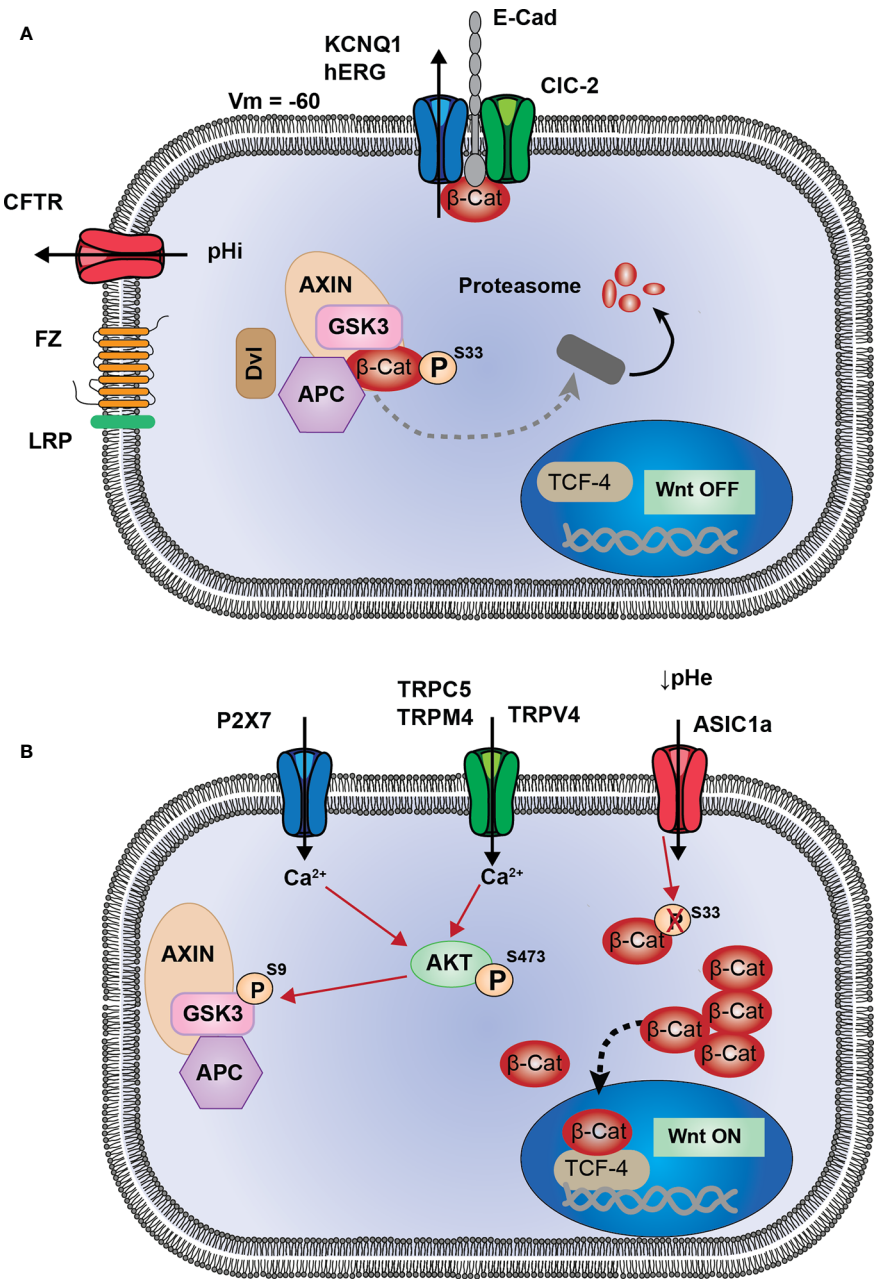

FIGURE 1 | Proposed model of interactions between ion channels and Wnt signaling. **(A)** KCNQ1 (or hERG) and ClC-2 are associated to E-cadherin and β-catenin at adherent junctions (AJ). Activity of these two channels maintain membrane potential hyperpolarized, which could be a favorable condition for AJ stability, and sequestration of β-catenin at the plasma membrane. CFTR activity maintains intracellular pH, preventing from pHi alkalinisation which induces Dishevelled-dependant inhibition of Destruction Complex (DC). These four channels participate in maintaining Wnt signaling in OFF-state, in which β-catenin is either degraded or sequestrated and cannot translocate into the nucleus to induce Wnt target genes. **(B)** Ca^{2+} entry through TRPC5, TRPM4, TRPV4 and P2X7 channels, induces AKT activation. Thus, AKT phosphorylates GSK3-β which becomes inhibited and subsequently allows the cytosolic accumulation of β-catenin. ASIC1a, by maintaining an acidic pH, decreases β-catenin phosphorylation and ubiquitination, preventing its degradation and inducing a cytosolic accumulation.

occurring in tumor microenvironment, increased Asic1a activity, which in turn decreases the Ser33 phosphorylation of β-catenin, leading to its accumulation in the nucleus, its combination with LEF/TCF promoting target gene transcription associated to liver cancer proliferation (Jin et al., 2017).

CONCLUSION AND FUTURE DIRECTIONS

In this review we have summarized the current work regarding the interplay between ion channels and the Wnt/β-catenin signaling pathway in cancers. The analysis of the literature

highlighted 10 ion channels associated to the Wnt pathway (**Table 1**). Among these channels four are associated to the repression of Wnt pathway (KCNQ1, hERG, CFTR, and ClCN-2, **Figure 1A**). The loss of activity or expression of these channels leads to an increase of Wnt activity and cancer progression. Supporting this, KCNQ1, CFTR and ClCN-2 have been described as tumor suppressors in CRC. Contrarily, six ion channels are overexpressed in cancers and promote the activity of Wnt pathway (TRPC5, TRPV4, TRPM4, TRPM8, P2RX7, and ASIC1a, **Figure 1B**).

Several conclusions can be drawn from this analysis of the literature. Firstly, the hyperpolarisation induced by the opening of potassium channel (background current from KCNQ1/KCNE3 in colonocytes or inducing the opening of hERG in breast cancer cells) leads to the restriction of Wnt activity by a similar mechanism, i.e. the sequestration of β-catenin at the plasma membrane and probably at the adherens junctions. Hyperpolarised plasma membrane seems to be important to prevent an over activation of the Wnt pathway and stabilise β-catenin at the plasma membrane. Therefore, the remaining question is: how can membrane potential act on β-catenin stability at the membrane? This is an outstanding question which will need more investigation to be answered. Secondly, regarding the Wnt-activating ion channels, the mechanism emerging from this analysis seems to mainly involve an increase in intracellular [Ca^{2+}] due to the overexpression or up regulation of cationic channels that mediate Ca^{2+} influx. The increase in intracellular [Ca^{2+}] shunts the canonical Wnt/β-catenin signaling cascade by activating AKT. AKT, in turn phosphorylates GSK3β on S9 causing its inhibition and finally the accumulation of β-catenin and the activation of Wnt pathway. Thirdly, as mentioned above, several ion channels are involved in the regulation of Wnt pathway, suggesting that interaction between them could exist. This is true especially regarding the case of KCNQ1, CFTR, and ClCN-2. It is interesting to note that KCNQ1 and ClCN-2 share the same mechanism to lower Wnt pathway activity. Both channels are associated to adherens junctions and contribute to stabilise β-catenin at the plasma membrane. This observation suggests a functional interaction between these channels which has not been investigated so far. Concerning KCNQ1 and CFTR, it is largely described that in colonic epithelium both channels are closely linked in the mechanism regulating the transepithelial transport of Cl^- and water. It seems credible that this functional link is conserved in the regulation of the Wnt pathway, both channels contributing to restrict its activity by two different, but complementary mechanisms, KCNQ1 controlling the stability of β-catenin at the plasma membrane and CFTR controlling the localization of Dvl. It will be interesting to study the effect of the simultaneous inhibition of both channels on Wnt activity.

Large research efforts have been made during the last 40 years to describe and understand the functions of ion channels in controlling cellular processes. Although the involvement of ion channels in processes participating in cancer development has largely been demonstrated, the precise mechanisms sustaining these abilities remain mainly unknown. Even if several functions of ion channels in signaling pathways can be explained by classical roles, such as regulation of cell volume or modulating the intracellular calcium concentration, other implication of this class of proteins are dictated by original mechanisms. Could ion channels be necessary in the regulation of classical signaling pathway and how? Can we insert ion channels in the notebook picture of signaling pathways beside tyrosine kinases receptors and G protein coupled receptors? Answering these questions are the arising challenges in the field of ion channels in cancer biology.

AUTHOR CONTRIBUTIONS

RR-M conceived the presented idea and supervised the project. RR-M, CB, BA, and OS wrote the manuscript. All authors contributed to the article and approved the submitted version.

FUNDING

This work was supported by the Foundation ARC (grant PJA 20181207701), "La Fondation pour la Recherche Médicale"—FRM—(PhD studentship to CB) (n° ECO201906008972) and the Cancéropole PACA (grant n° 2018-13) and Université Côte d'Azur (CSI-2018).

REFERENCES

Abbott, G. W. (2014). Biology of the KCNQ1 Potassium Channel. *New J. Sci.* 2014, 26. doi: 10.1155/2014/237431

Aberle, H., Bauer, A., Stappert, J., Kispert, A., and Kemler, R. (1997). beta-catenin is a target for the ubiquitin-proteasome pathway. *EMBO J.* 16, 3797–3804. doi: 10.1093/emboj/16.13.3797

Ashmore, J., Olsen, H., Sørensen, N., Thrasivoulou, C., and Ahmed, A. (2019). Wnts control membrane potential in mammalian cancer cells. *J. Physiol.* 597, 5899–5914. doi: 10.1113/JP278661

Assié, G., Letouzé, E., Fassnacht, M., Jouinot, A., Luscap, W., Barreau, O., et al. (2014). Integrated genomic characterization of adrenocortical carcinoma. *Nat. Genet.* 46, 607–612. doi: 10.1038/ng.2953

Azzolin, L., Panciera, T., Soligo, S., Enzo, E., Bicciato, S., Dupont, S., et al. (2014). YAP/TAZ incorporation in the β-catenin destruction complex orchestrates the Wnt response. *Cell* 158, 157–170. doi: 10.1016/j.cell.2014.06.013

Bänziger, C., Soldini, D., Schütt, C., Zipperlen, P., Hausmann, G., and Basler, K. (2006). Wntless, a conserved membrane protein dedicated to the secretion of Wnt proteins from signaling cells. *Cell* 125, 509–522. doi: 10.1016/j.cell.2006.02.049

Barrett, K. E., and Keely, S. J. (2000). Chloride secretion by the intestinal epithelium: molecular basis and regulatory aspects. *Annu. Rev. Physiol.* 62, 535–572. doi: 10.1146/annurev.physiol.62.1.535

Becchetti, A., Crescioli, S., Zanieri, F., Petroni, G., Mercatelli, R., Coppola, S., et al. (2017). The conformational state of hERG1 channels determines integrin association, downstream signaling, and cancer progression. *Sci. Signal.* 10 (473), eaaf3236. doi: 10.1126/scisignal.aaf3236

Becchetti, A., Petroni, G., and Arcangeli, A. (2019). Ion Channel Conformations Regulate Integrin-Dependent Signaling. *Trends Cell Biol.* 29, 298–307. doi: 10.1016/j.tcb.2018.12.005

Bendahhou, S., Marionneau, C., Haurogne, K., Larroque, M. M., Derand, R., Szuts, V., et al. (2005). In vitro molecular interactions and distribution of KCNE family with

KCNQ1 in the human heart. *Cardiovasc. Res.* 67, 529–538. doi: 10.1016/j.cardiores.2005.02.014

Breuer, E. K., Fukushiro-Lopes, D., Dalheim, A., Burnette, M., Zartman, J., Kaja, S., et al. (2019). Potassium channel activity controls breast cancer metastasis by affecting β-catenin signaling. *Cell Death Dis.* 10, 180. doi: 10.1038/s41419-019-1429-0

Buechling, T., Chaudhary, V., Spirohn, K., Weiss, M., and Boutros, M. (2011). p24 proteins are required for secretion of Wnt ligands. *EMBO Rep.* 12, 1265–1272. doi: 10.1038/embor.2011.212

Cavallo, R. A., Cox, R. T., Moline, M. M., Roose, J., Polevoy, G. A., Clevers, H., et al. (1998). Drosophila Tcf and Groucho interact to repress Wingless signalling activity. *Nature* 395, 604–608. doi: 10.1038/26982

Chan-On, W., Nairismägi, M. L., Ong, C. K., Lim, W. K., Dima, S., Pairojkul, C., et al. (2013). Exome sequencing identifies distinct mutational patterns in liver fluke-related and non-infection-related bile duct cancers. *Nat. Genet.* 45, 1474–1478. doi: 10.1038/ng.2806

Crottès, D., Rapetti-Mauss, R., Alcaraz-Perez, F., Tichet, M., Gariano, G., Martial, S., et al. (2016). SIGMAR1 Regulates Membrane Electrical Activity in Response to Extracellular Matrix Stimulation to Drive Cancer Cell Invasiveness. *Cancer Res.* 76, 607–618. doi: 10.1158/0008-5472.CAN-15-1465

Davidson, G., Shen, J., Huang, Y. L., Su, Y., Karaulanov, E., Bartscherer, K., et al. (2009). Cell cycle control of wnt receptor activation. *Dev. Cell.* 17, 788–799. doi: 10.1016/j.devcel.2009.11.006

de Lau, W., Barker, N., Low, T. Y., Koo, B. K., Li, V. S., Teunissen, H., et al. (2011). Lgr5 homologues associate with Wnt receptors and mediate R-spondin signalling. *Nature* 476, 293–297. doi: 10.1038/nature10337

DeCoursey, T. E., Chandy, K. G., Gupta, S., and Cahalan, M. D. (1984). Voltage-gated K+ channels in human T lymphocytes: a role in mitogenesis? *Nature* 307, 465–468. doi: 10.1038/307465a0

den Uil, S. H., Coupé, V. M., Linnekamp, J. F., van den Broek, E., Goos, J. A., Delis-van Diemen, P. M., et al. (2016). Loss of KCNQ1 expression in stage II and stage III colon cancer is a strong prognostic factor for disease recurrence. *Br. J. Cancer* 115, 1565–1574. doi: 10.1038/bjc.2016.376

Fan, H., Zhang, M., and Liu, W. (2018). Hypermethylated KCNQ1 acts as a tumor suppressor in hepatocellular carcinoma. *Biochem. Biophys. Res. Commun.* 503, 3100–3107. doi: 10.1016/j.bbrc.2018.08.099

Gao, Y., and Liao, P. (2019). TRPM4 channel and cancer. *Cancer Lett.* 454, 66–69. doi: 10.1016/j.canlet.2019.04.012

Gross, J. C., Chaudhary, V., Bartscherer, K., and Boutros, M. (2012). Active Wnt proteins are secreted on exosomes. *Nat. Cell Biol.* 14, 1036–1045. doi: 10.1038/ncb2574

Hanukoglu, I., and Hanukoglu, A. (2016). Epithelial sodium channel (ENaC) family: Phylogeny, structure-function, tissue distribution, and associated inherited diseases. *Gene* 579, 95–132. doi: 10.1016/j.gene.2015.12.061

Huang, X., and Jan, L. Y. (2014). Targeting potassium channels in cancer. *J. Cell Biol.* 206, 151–162. doi: 10.1083/jcb.201404136

Huels, D. J., Ridgway, R. A., Radulescu, S., Leushacke, M., Campbell, A. D., Biswas, S., et al. (2015). E-cadherin can limit the transforming properties of activating β-catenin mutations. *EMBO J.* 34, 2321–2333. doi: 10.15252/embj.201591739

Jespersen, T., Grunnet, M., and Olesen, S. P. (2005). The KCNQ1 potassium channel: from gene to physiological function. *Physiol. (Bethesda)* 20, 408–416. doi: 10.1152/physiol.00031.2005

Jin, C., Yuan, F. L., Gu, Y. L., Li, X., Liu, M. F., Shen, X. M., et al. (2017). Over-expression of ASIC1a promotes proliferation via activation of the β-catenin/LEF-TCF axis and is associated with disease outcome in liver cancer. *Oncotarget* 8, 25977–25988. doi: 10.18632/oncotarget.10774

Jin, Y., Ibrahim, D., Magness, S. T., and Blikslager, A. T. (2018). Knockout of ClC-2 reveals critical functions of adherens junctions in colonic homeostasis and tumorigenicity. *Am. J. Physiol. Gastrointest. Liver Physiol.* 315, G966–G979. doi: 10.1152/ajpgi.00087.2018

Kadowaki, T., Wilder, E., Klingensmith, J., Zachary, K., and Perrimon, N. (1996). The segment polarity gene porcupine encodes a putative multitransmembrane protein involved in Wingless processing. *Genes Dev.* 10, 3116–3128. doi: 10.1101/gad.10.24.3116

Kinzler, K. W., Nilbert, M. C., Su, L. K., Vogelstein, B., Bryan, T. M., Levy, D. B., et al. (1991). Identification of FAP locus genes from chromosome 5q21. *Science* 253, 661–665. doi: 10.1126/science.1651562

Latres, E., Chiaur, D. S., and Pagano, M. (1999). The human F box protein beta-Trcp associates with the Cul1/Skp1 complex and regulates the stability of beta-catenin. *Oncogene* 18, 849–854. doi: 10.1038/sj.onc.1202653

Lee, S. C., Deutsch, C., and Beck, W. T. (1988). Comparison of ion channels in multidrug-resistant and -sensitive human leukemic cells. *Proc. Natl. Acad. Sci. U. S. A.* 85, 2019–2023. doi: 10.1073/pnas.85.6.2019

Li, V. S., Ng, S. S., Boersema, P. J., Low, T. Y., Karthaus, W. R., Gerlach, J. P., et al. (2012). Wnt signaling through inhibition of β-catenin degradation in an intact Axin1 complex. *Cell* 149, 1245–1256. doi: 10.1016/j.cell.2012.05.002

Li, X., Hu, W., Zhou, J., Huang, Y., Peng, J., Yuan, Y., et al. (2017). CLCA1 suppresses colorectal cancer aggressiveness via inhibition of the Wnt/beta-catenin signaling pathway. *Cell Commun. Signal.* 15, 38. doi: 10.1186/s12964-017-0192-z

Lin, S. Y., Xia, W., Wang, J. C., Kwong, K. Y., Spohn, B., Wen, Y., et al. (2000). Beta-catenin, a novel prognostic marker for breast cancer: its roles in cyclin D1 expression and cancer progression. *Proc. Natl. Acad. Sci. U. S. A.* 97, 4262–4266. doi: 10.1073/pnas.060025397

Liu, C., Li, Y., Semenov, M., Han, C., Baeg, G. H., Tan, Y., et al. (2002). Control of beta-catenin phosphorylation/degradation by a dual-kinase mechanism. *Cell* 108, 837–847. doi: 10.1016/S0092-8674(02)00685-2

Medema, J. P., and Vermeulen, L. (2011). Microenvironmental regulation of stem cells in intestinal homeostasis and cancer. *Nature* 474, 318–326. doi: 10.1038/nature10212

Metcalfe, C., Mendoza-Topaz, C., Mieszczanek, J., and Bienz, M. (2010). Stability elements in the LRP6 cytoplasmic tail confer efficient signalling upon DIX-dependent polymerization. *J. Cell Sci.* 123, 1588–1599. doi: 10.1242/jcs.067546

Mulligan, K. A., Fuerer, C., Ching, W., Fish, M., Willert, K., and Nusse, R. (2012). Secreted Wingless-interacting molecule (Swim) promotes long-range signaling by maintaining Wingless solubility. *Proc. Natl. Acad. Sci. U. S. A.* 109, 370–377. doi: 10.1073/pnas.1119197109

Neglia, J. P., FitzSimmons, S. C., Maisonneuve, P., Schöni, M. H., Schöni-Affolter, F., Corey, M., et al. (1995). The risk of cancer among patients with cystic fibrosis. Cystic Fibrosis and Cancer Study Group. *N. Engl. J. Med.* 332, 494–499. doi: 10.1056/NEJM199502233320803

Neumann, S., Coudreuse, D. Y., van der Westhuyzen, D. R., Eckhardt, E. R., Korswagen, H. C., Schmitz, G., et al. (2009). Mammalian Wnt3a is released on lipoprotein particles. *Traffic* 10, 334–343. doi: 10.1111/j.1600-0854.2008.00872.x

Nighot, P. K., and Blikslager, A. T. (2012). Chloride channel ClC-2 modulates tight junction barrier function via intracellular trafficking of occludin. *Am. J. Physiol. Cell Physiol.* 302, C178–C187. doi: 10.1152/ajpcell.00072.2011

Nishisho, I., Nakamura, Y., Miyoshi, Y., Miki, Y., Ando, H., Horii, A., et al. (1991). Mutations of chromosome 5q21 genes in FAP and colorectal cancer patients. *Science* 253, 665–669. doi: 10.1126/science.1651563

Nusse, R., and Clevers, H. (2017). Wnt/β-Catenin Signaling, Disease, and Emerging Therapeutic Modalities. *Cell* 169, 985–999. doi: 10.1016/j.cell.2017.05.016

Nusse, R., and Varmus, H. E. (1982). Many tumors induced by the mouse mammary tumor virus contain a provirus integrated in the same region of the host genome. *Cell* 31, 99–109. doi: 10.1016/0092-8674(82)90409-3

Pancrazio, J. J., Viglione, M. P., Tabbara, I. A., and Kim, Y. I. (1989). Voltage-dependent ion channels in small-cell lung cancer cells. *Cancer Res.* 49, 5901–5906.

Pardo, L. A., and Stühmer, W. (2014). The roles of K(+) channels in cancer. *Nat. Rev. Cancer* 14, 39–48. doi: 10.1038/nrc3635

Pastushenko, I., and Blanpain, C. (2019). EMT Transition States during Tumor Progression and Metastasis. *Trends Cell Biol.* 29, 212–226. doi: 10.1016/j.tcb.2018.12.001

Paul, T., Li, S., Khurana, S., Leleiko, N. S., and Walsh, M. J. (2007). The epigenetic signature of CFTR expression is co-ordinated via chromatin acetylation through a complex intronic element. *Biochem. J.* 408, 317–326. doi: 10.1042/BJ20070282

Peifer, M., McCrea, P. D., Green, K. J., Wieschaus, E., and Gumbiner, B. M. (1992). The vertebrate adhesive junction proteins beta-catenin and plakoglobin and the Drosophila segment polarity gene armadillo form a multigene family with similar properties. *J. Cell Biol.* 118, 681–691. doi: 10.1083/jcb.118.3.681

Preston, P., Wartosch, L., Günzel, D., Fromm, M., Kongsuphol, P., Ousingsawat, J., et al. (2010). Disruption of the K+ channel beta-subunit KCNE3 reveals an important role in intestinal and tracheal Cl- transport. *J. Biol. Chem.* 285, 7165–7175. doi: 10.1074/jbc.M109.047829

Prevarskaya, N., Skryma, R., and Shuba, Y. (2010). Ion channels and the hallmarks of cancer. *Trends Mol. Med.* 16, 107–121. doi: 10.1016/j.molmed.2010.01.005

Prevarskaya, N., Skryma, R., and Shuba, Y. (2018). Ion Channels in Cancer: Are Cancer Hallmarks Oncochannelopathies? *Physiol. Rev.* 98, 559–621. doi: 10.1152/physrev.00044.2016

Rapetti-Mauss, R., O'Mahony, F., Sepulveda, F. V., Urbach, V., and Harvey, B. J. (2013). Oestrogen promotes KCNQ1 potassium channel endocytosis and postendocytic trafficking in colonic epithelium. *J. Physiol.* 591, 2813–2831. doi: 10.1113/jphysiol.2013.251678

Rapetti-Mauss, R., Bustos, V., Thomas, W., McBryan, J., Harvey, H., Lajczak, N., et al. (2017). Bidirectional KCNQ1:β-catenin interaction drives colorectal cancer cell differentiation. *Proc. Natl. Acad. Sci. U. S. A.* 114, 4159–4164. doi: 10.1073/pnas.1702913114

Rubinfeld, B., Robbins, P., El-Gamil, M., Albert, I., Porfiri, E., and Polakis, P. (1997). Stabilization of beta-catenin by genetic defects in melanoma cell lines. *Science* 275, 1790–1792. doi: 10.1126/science.275.5307.1790

Sagredo, A. I., Sagredo, E. A., Cappelli, C., Báez, P., Andaur, R. E., Blanco, C., et al. (2018). TRPM4 regulates Akt/GSK3-β activity and enhances β-catenin signaling and cell proliferation in prostate cancer cells. *Mol. Oncol.* 12, 151–165. doi: 10.1002/1878-0261.12100

Sala-Rabanal, M., Yurtsever, Z., Nichols, C. G., and Brett, T. J. (2015). Secreted CLCA1 modulates TMEM16A to activate Ca(2+)-dependent chloride currents in human cells. *Elife17* 4, e05875. doi: 10.7554/eLife.05875

Sala-Rabanal, M., Yurtsever, Z., Berry, K. N., Nichols, C. G., and Brett, T. J. (2017). Modulation of TMEM16A channel activity by the von Willebrand factor type A (VWA) domain of the calcium-activated chloride channel regulator 1 (CLCA1). *J. Biol. Chem.* 292, 9164–9174. doi: 10.1074/jbc.M117.788232

Sanchez-Vega, F., Mina, M., Armenia, J., Chatila, W. K., Luna, A., La, K. C., et al. (2018). Oncogenic Signaling Pathways in The Cancer Genome Atlas. *Cell* 173, 321–337.e310. doi: 10.1016/j.cell.2018.03.035

Satoh, S., Daigo, Y., Furukawa, Y., Kato, T., Miwa, N., Nishiwaki, T., et al. (2000). AXIN1 mutations in hepatocellular carcinomas, and growth suppression in cancer cells by virus-mediated transfer of AXIN1. *Nat. Genet.* 24, 245–250. doi: 10.1038/73448

Shapovalov, G., Ritaine, A., Skryma, R., and Prevarskaya, N. (2016). Role of TRP ion channels in cancer and tumorigenesis. *Semin. Immunopathol.* 38, 357–369. doi: 10.1007/s00281-015-0525-1

Sheldahl, L. C., Slusarski, D. C., Pandur, P., Miller, J. R., Kühl, M., and Moon, R. T. (2003). Dishevelled activates Ca2+ flux, PKC, and CamKII in vertebrate embryos. *J. Cell Biol.* 161, 769–777. doi: 10.1083/jcb.200211094

Simons, M., Gault, W. J., Gotthardt, D., Rohatgi, R., Klein, T. J., Shao, Y., et al. (2009). Electrochemical cues regulate assembly of the Frizzled/Dishevelled complex at the plasma membrane during planar epithelial polarization. *Nat. Cell Biol.* 11, 286–294. doi: 10.1038/ncb1836

Stamos, J. L., Chu, M. L., Enos, M. D., Shah, N., and Weis, W. I. (2014). Structural basis of GSK-3 inhibition by N-terminal phosphorylation and by the Wnt receptor LRP6. *Elife* 3, e01998. doi: 10.7554/eLife.01998

Strubberg, A. M., Liu, J., Walker, N. M., Stefanski, C. D., MacLeod, R. J., Magness, S. T., et al. (2018). Cftr Modulates Wnt/β-Catenin Signaling and Stem Cell Proliferation in Murine Intestine. *Cell Mol. Gastroenterol. Hepatol.* 5, 253–271. doi: 10.1016/j.jcmgh.2017.11.013

Taylor, J. M., and Simpson, R. U. (1992). Inhibition of cancer cell growth by calcium channel antagonists in the athymic mouse. *Cancer Res.* 52, 2413–2418.

Than, B. L., Goos, J. A., Sarver, A. L., O'Sullivan, M. G., Rod, A., Starr, T. K., et al. (2014). The role of KCNQ1 in mouse and human gastrointestinal cancers. *Oncogene* 33, 3861–3868. doi: 10.1038/onc.2013.350

Tree, D. R., Shulman, J. M., Rousset, R., Scott, M. P., Gubb, D., and Axelrod, J. D. (2002). Prickle mediates feedback amplification to generate asymmetric planar cell polarity signaling. *Cell* 109, 371–381. doi: 10.1016/S0092-8674(02)00715-8

Venkatachalam, K., and Montell, C. (2007). TRP channels. *Annu. Rev. Biochem.* 76, 387–417. doi: 10.1146/annurev.biochem.75.103004.142819

Wang, Y., Krivtsov, A. V., Sinha, A. U., North, T. E., Goessling, W., Feng, Z., et al. (2010). The Wnt/beta-catenin pathway is required for the development of leukemia stem cells in AML. *Science* 327, 1650–1653. doi: 10.1126/science.1186624

Wang, T., Chen, Z., Zhu, Y., Pan, Q., Liu, Y., Qi, X., et al. (2015). Inhibition of transient receptor potential channel 5 reverses 5-Fluorouracil resistance in human colorectal cancer cells. *J. Biol. Chem.* 290, 448–456. doi: 10.1074/jbc.M114.590364

Wood, L. D., Parsons, D. W., Jones, S., Lin, J., Sjöblom, T., Leary, R. J., et al. (2007). The genomic landscapes of human breast and colorectal cancers. *Science* 318, 1108–1113. doi: 10.1126/science.1145720

Wu, J., Jiao, Y., Dal Molin, M., Maitra, A., de Wilde, R. F., Wood, L. D., et al. (2011). Whole-exome sequencing of neoplastic cysts of the pancreas reveals recurrent mutations in components of ubiquitin-dependent pathways. *Proc. Natl. Acad. Sci. U. S. A.* 108, 21188–21193. doi: 10.1073/pnas.1118046108

Xie, R., Xu, J., Xiao, Y., Wu, J., Wan, H., Tang, B., et al. (2017). Calcium Promotes Human Gastric Cancer via a Novel Coupling of Calcium-Sensing Receptor and TRPV4 Channel. *Cancer Res.* 77, 6499–6512. doi: 10.1158/0008-5472.CAN-17-0360

Yamada, A., Komaki, Y., Komaki, F., Micic, D., Zullow, S., and Sakuraba, A. (2018). Risk of gastrointestinal cancers in patients with cystic fibrosis: a systematic review and meta-analysis. *Lancet Oncol.* 19, 758–767. doi: 10.1016/S1470-2045(18)30188-8

Yamashita, N., Hamada, H., Tsuruo, T., and Ogata, E. (1987). Enhancement of voltage-gated Na+ channel current associated with multidrug resistance in human leukemia cells. *Cancer Res.* 47, 3736–3741.

Ye, X., and Weinberg, R. A. (2015). Epithelial-Mesenchymal Plasticity: A Central Regulator of Cancer Progression. *Trends Cell Biol.* 25, 675–686. doi: 10.1016/j.tcb.2015.07.012

Zhan, T., Rindtorff, N., and Boutros, M. (2017). Wnt signaling in cancer. *Oncogene* 36, 1461–1473. doi: 10.1038/onc.2016.304

Zhang, Y., Cheng, H., Li, W., Wu, H., and Yang, Y. (2019). Highly-expressed P2X7 receptor promotes growth and metastasis of human HOS/MNNG osteosarcoma cells via PI3K/Akt/GSK3β/β-catenin and mTOR/HIF1α/VEGF signaling. *Int. J. Cancer* 145, 1068–1082. doi: 10.1002/ijc.32207

Zhou, Y., Wong, C. O., Cho, K. J., van der Hoeven, D., Liang, H., Thakur, D. P., et al. (2015). SIGNAL TRANSDUCTION. Membrane potential modulates plasma membrane phospholipid dynamics and K-Ras signaling. *Science* 349, 873–876. doi: 10.1126/science.aaa5619

Conflict of Interest: The authors declare that the research was conducted in the absence of any commercial or financial relationships that could be construed as a potential conflict of interest.

Erythroid glucose transport in health and disease

Guizouarn, H., & Allegrini, B. (2020).. *Pflügers Archiv-European Journal of Physiology*, *472*(9), 1371-1383.

Contexte :

C’est un article de revue rédigée avec ma directrice de thèse Hélène Guizouarn. Nous parlons ici du rôle de GLUT1 dans la pathophysiologie érythrocytaire.

Erythroid glucose transport in health and disease

Hélène Guizouarn & Benoit Allegrini

Pflügers Archiv - European Journal of Physiology

ISSN 0031-6768

Pflugers Arch - Eur J Physiol
DOI 10.1007/s00424-020-02406-0

Springer

Pflügers Archiv - European Journal of Physiology
https://doi.org/10.1007/s00424-020-02406-0

INVITED REVIEW

Erythroid glucose transport in health and disease

Hélène Guizouarn[1] · Benoit Allegrini[1]

Received: 6 February 2020 / Revised: 15 May 2020 / Accepted: 22 May 2020

Abstract
Glucose transport is intimately linked to red blood cell physiology. Glucose is the unique energy source for these cells, and defects in glucose metabolism or transport activity are associated with impaired red blood cell morphology and deformability leading to reduced lifespan. In vertebrate erythrocytes, glucose transport is mediated by GLUT1 (in humans) or GLUT4 transporters. These proteins also account for dehydroascorbic acid (DHA) transport through erythrocyte membrane. The peculiarities of glucose transporters and the red blood cell pathologies involving GLUT1 are summarized in the present review.

Keywords Erythrocyte · Glucose · GLUT1 · Red blood cell · Stomatocytosis

Introduction

What makes red blood cell glucose transport relevant to dedicate a review on this topic? Red blood cells could be described as corpuscles devoted to organism respiration, carrying and delivering oxygen to tissues and simultaneously transporting a significant part of the CO_2 produced in these tissues back to the lung. This simplified vision of erythrocyte physiology does not preclude the complexity of this cell, which is able to withstand considerable physical constraints throughout cardiovascular circulation and is interacting with various cells, but it helps to understand which role glucose plays in its physiology.

Binding, transporting and delivering oxygen is largely improved if this oxygen is not dissipated by metabolism. Red blood cells (RBCs), whether nucleated as in most vertebrates or not, like in mammals, are devoid of mitochondria and have developed to obtain energy only through glycolysis and pentose phosphate pathway (PPP) (Fig. 1). Glycolysis provides the ATP, essential to fuel the ion pumps Na^+/K^+ ATPase and calcium ATPase but also to control the phosphorylation of cytoskeleton a crucial determinant of RBC shape. In addition to ATP, glycolysis yields the nicotinamide adenine dinucleotide, NADH, a powerful reducing agent that prevents haem oxidation, keeping ferrous in its reduced Fe^{2+} state. RBCs are particularly exposed to reactive oxygen species (ROS), and besides NADH, their major defence against ROS is given by the anti-oxidant glutathione, which redox state depends on the PPP. The shuttle between glycolysis and pentose pathway is regulated by the enzyme glucose-6-phosphate dehydrogenase (G6PD) that diverts the glucose-6-phosphate from glycolysis to yield other hexose monophosphates (Fig. 1). This conversion allows the reduction of nicotinamide adenine dinucleotide phosphate, $NADP^+$, into NADPH that keeps glutathione in its reduced form. There is a correlation between RBC lifespan and the activity of G6PD, a reduced activity of G6PD leads to accumulation of ROS and lysis of RBCs. Another important metabolic pathway in RBC physiology is the Rapoport-Luebering shunt (RLS) that diverts the 1,3-diphosphoglycerate to provide 2,3-diphosphoglycerate (2,3 DPG). By binding haemoglobin, the 2,3 DPG modulates its affinity for oxygen, which is of particular importance for acclimation to oxygen pressure. In physiological condition, about 7% of glucose is metabolized through the PPP and the RLS bypasses 19% of the glycolytic flux in human RBCs [31, 111].

Hence, glucose metabolism provides the ATP, the reducing agents and the 2,3 DPG, which are essential for red blood cell physiology, the control of oxygen affinity for haemoglobin but also red blood cell shape and deformability. Maintaining a flexible disc shape and deformability of red blood cells, allowing circulation through narrow capillaries, are both dependent on glucose metabolism. For instance, a depletion of

This article is part of the special issue on Glucose Transporters in Health and Disease in Pflügers Archiv—European Journal of Physiology

✉ Hélène Guizouarn
helene.guizouarn@univ-cotedazur.fr

[1] Université Côte d'Azur, CNRS, Inserm, Institut de Biologie Valrose, 28 av. Valrose, 06100 Nice, France

Published online: 30 May 2020

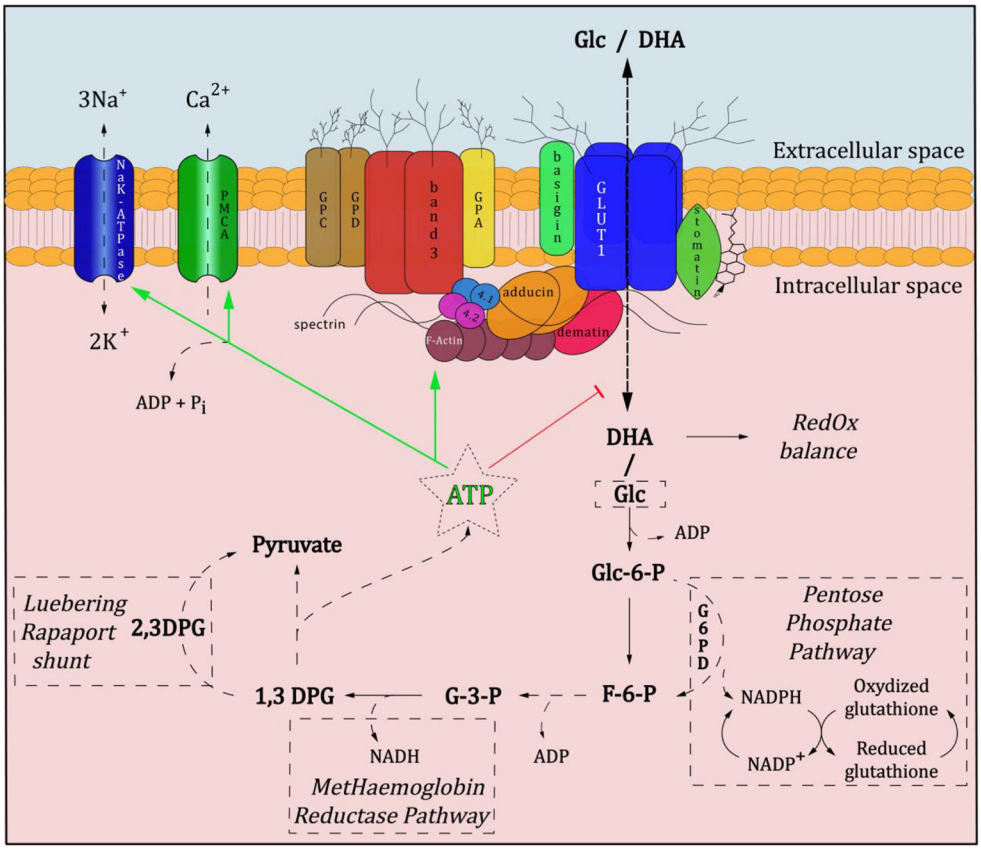

Fig. 1 GLUT1 function and interactions in red blood cell membrane. The main role of GLUT1 is to transport glucose following its chemical gradient. After entering the red blood cell, glucose is immediately turned into glucose-6-phosphate (Glc-6-P). Glc-6-P can either be used for glycolysis leading to ATP formation or proceed into the Pentose-P pathway via glucose-6-phosphate dehydrogenase. Glycolysis is partially drawn with important steps. A dotted arrow includes more than one step. Methaemoglobin reductase pathway uses NADH to maintain haem iron in its reduced (active) state. The Rapoport-Luebering shunt uses 1,3 DPG to produce 2,3 DPG which regulates haemoglobin binding affinity for oxygen. Normal glycolysis produces 2 molecules of ATP out of 1 molecule of glucose. Increasing intracellular ATP concentrations inhibit glucose uptake through GLUT1 tetramer, providing a negative feedback regulation. GLUT1 also transports dehydroascorbic acid (DHA, an oxidized form of vitamin C). Junctional complexes in red blood cell membrane are composed of GLUT1 associated to band 3 dimers through dematin, adducin and protein 4.1 and 4.2. Basigin, a transmembrane protein was shown to interact with GLUT1 [24]. Stomatin is linked to GLUT1 in a cholesterol-dependant manner. Other membrane proteins that are not shown can be associated to band 3 dimers (Kell, Kx, Duffy for instance) [88] Lux SE Blood 2016. The exact oligomeric status of GLUT1 bound to junctional complex is unknown; however, GLUT1 was detected as tetramers or dimers in red blood cell membranes] [48] Graybill C. et al. Biochemistry 2006. For clarity purposes, there are only two arrows symbolizing glucose and other solute permeabilities through the GLUT1 tetramer, but each monomer in itself constitutes transport pathway [48] Graybill C. et al. Biochemistry 2006. The complex is tethered to a flexible spectrin-based cytoskeleton tied by F-actin filaments.

glucose leads to red blood cell morphological changes that impair blood flow dynamics and transport functions [20, 130]. Moreover, a mechanical distortion of RBCs increases glycolysis [74]. As mentioned earlier, enzymatic defect in glucose metabolism such as G6PD deficiency causes a red blood cell condition characterized by accumulation of ROS that makes these cells more fragile and prone to lysis in response to oxidative stress (intake of fava beans, drugs or infections). Numerous enzyme abnormalities in erythrocyte glycolysis are thus linked to reduced red blood cell lifespan and more or less severe haemolysis [72, 124].

Red blood cells find glucose they need in plasma where its concentration is finely tuned around 0.7 to 1.1 g/l (4 to 6 mM) in humans. Glucose concentration is equilibrated between plasma and RBC cytosol, and as RBCs represent about 40% of blood volume, they are a significant reservoir for glucose throughout the human body. In contrast to human RBCs where glycogen metabolism in physiological condition is not significant [97, 98], in some other species, erythrocytes buffer glucose levels by absorbing and incorporating glucose into glycogen stores when glucose is high in plasma and by releasing glucose when the plasma concentration is low [49, 59].

This review will provide an overview on aspects of erythrocyte glucose permeability, focusing mainly on human glucose transporters as they have been the most studied and summarizing the present knowledge about red blood cell

pathologies linked to glucose transport defects. Pathologies related to deficiencies on glucose metabolism will not be considered in the present review.

Brief history of glucose permeability studies in red blood cells

Glucose permeability in erythrocytes from different species has been the subject of intense attention since the beginning of the twentieth century when cell culture was in its infancy, and red blood cells, easy to obtain, were the main object of membrane permeability studies. More than a century later, a research on PubMed with keywords "glucose", "erythrocyte" and "transport" yields more than 1700 registered publications from laboratories on each continent. The pioneer work of Kozawa, Klinghoffer, Wilbrandt or LeFevre studying glucose diffusion across red blood cells paved the way to the concept of a dedicated membrane carrier to drive glucose in the erythrocyte [73, 81, 135]. The carrier hypothesis was formulated through equation adapted from the Michaelis-Menten studies of enzyme saturation. Widdas and LeFevre independently determined for the first time a half saturation constant for a glucose carrier in human erythrocyte (7–17 mM) [82, 133]. The development of radioactive tracers provided the basis for extensive kinetic studies that have allowed to characterize the features of glucose transport protein within the erythrocyte membrane, defining conformational changes, glucose binding and modifier sites within the transporter. The studies leaded by Widdas, Naftalin and Carruthers, among many others, have greatly contributed to define kinetic models for glucose transport through the red blood cell membrane [17, 101, 134]. The molecular characterization of this transporter began in 1977 with the purification of the human glucose transporter from red blood cell membrane [65] and cloning from hepatocytes in 1985 [100] confirmed the cloned glucose transporter was the one expressed in human erythrocytes. This first identified glucose transporter was named GLUT1, SLC2A1 according to the HUGO committee for gene nomenclature of solute carriers. More recently, resolution of GLUT1 spatial organization, thanks to crystallography studies, allowed molecular dynamic simulations providing new ways to gain a deeper understanding of this glucose transporter [19, 32, 43].

Glucose transporters expressed in red blood cells

Erythroid glucose transporters belong to the SLC2 transporter family dedicated to facilitated sugar transport. It comprises 14 different isoforms characterized by substrate specificity and tissue distribution [57, 62, 99]. Two different isoforms of glucose transporter have been identified in erythrocyte of different species: GLUT1 and GLUT4, both class 1 glucose transporters. GLUT1 is expressed in human and a few other mammals' red blood cells (fruit bats, guinea pigs and higher primates). In the other mammalian erythrocytes studied so far, the glucose transport is mediated by GLUT4 [96]. Avian (pigeon [36]) and fish (Atlantic cod [26, 52]) erythrocytes also express the GLUT1 isoform. The GLUT isoform is different following the neonatal period of the mouse versus human red blood cells [96]. All studied mammalian newborn erythrocytes express GLUT1. However, GLUT1 is replaced by GLUT4 during the neonatal period in all studied mammals except in human erythrocytes, which continue to express high levels of GLUT1 [95]. Some dog species express both GLUT1 and GLUT4 transporters in adult red blood cells [106]. The presence of GLUT1 in these dog red blood cells would provide a stronger anti-oxidant protection by promoting vitamin C recycling [105].

GLUT1 in human red blood cells

Molecular features

The *GLUT1* gene on human chromosome 1 encodes a highly hydrophobic polypeptide of 492 amino-acids. The GLUT1 facilitates unidirectional glucose uptake or exit following the chemical gradient of glucose. Biochemical studies, molecular biology approaches (mutagenesis), homology modelling and, finally, crystallographic studies provided a spatial organization of the protein [7, 16, 21, 22, 32, 33, 48, 83, 116].

Like the other members of the sugar transporter family (MFS), GLUT1 is structured as a core fold that comprises 12 transmembrane segments organized into two folded domains of 6 helices of the amino-terminal domain and 6 helices of the carboxy-terminal domain (Fig. 2). These two folded domains delineate a cavity that is either open to the intracellular or the extracellular side of the membrane [32]. On the intracellular side, 4 helices play a crucial role in glucose transport regulation and contain an ATP binding site [84].

In the membrane of the red blood cell, the glucose transporter is organized as a GLUT1 homotetramer, each monomer being functionally independent. However, the oligomeric structure of GLUT1 modulates glucose transport activity, and there is a cooperative interaction between subunits [55]. The oligomeric status depends on reductant-sensitive, non-covalent interactions between monomers [143]. It is promoted by intra-monomer disulfide bonds between Cys 347 and 421 in the extracellular part of the protein (Fig. 2). Studies with other cells have shown that GLUT1 oligomeric status depends on the amount of transporters expressed at the plasma membrane [86].

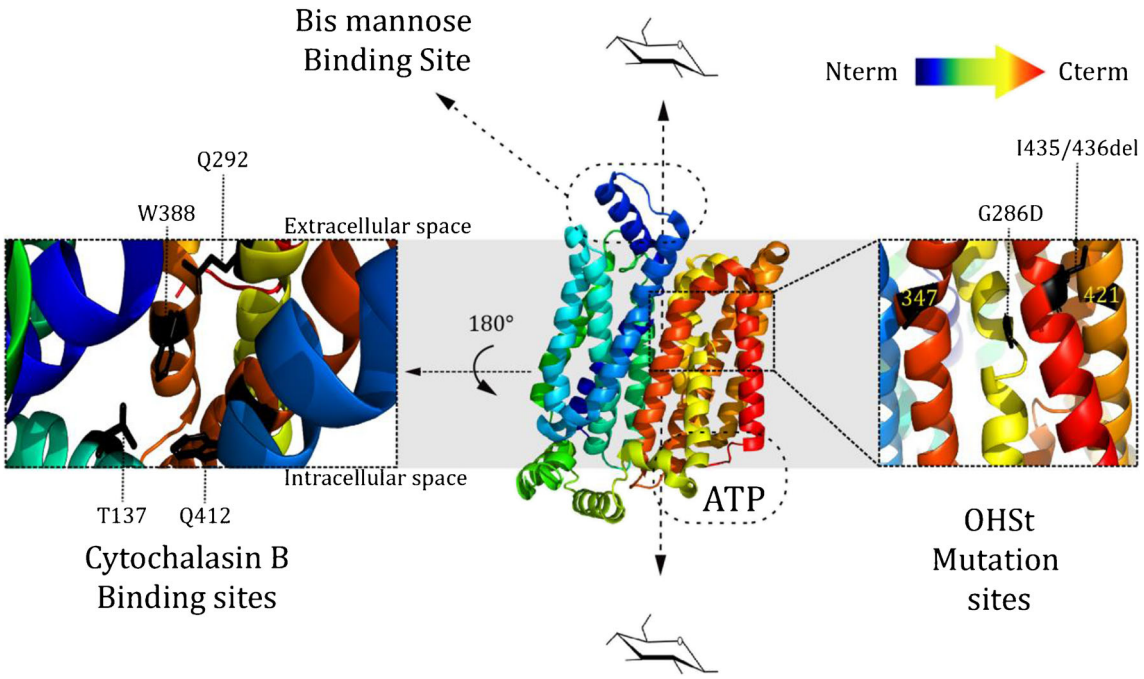

Fig. 2 GLUT1 crystal structure and ligand binding. Crystal structure of GLUT1 (SLC2A1) is given according to the protein data base (PDB: 4PYP), from N-terminus in blue to C-terminus in red. The interface between the two structural domains constituted by the 6 N-terminal helices, and the 6 C-terminal helices delineates glucose pathway. G286D and I435/436del mutations, described in a rare form of hereditary haemolytic anaemia, the overhydrated hereditary stomatocytosis (OHSt), are located in transmembrane segments 7 and 12, respectively. These two mutations abolished glucose transport and induced a leak of Na^+ and K^+. Cysteines 347 and 421 involved in GLUT1 oligomerizations are highlighted. Cytochalasin B binding involves T137, Q292, W388 and Q412 which are facing the pore. Bis-mannose binds an extracellular domain of GLUT1 and inhibits glucose transport. ATP negatively regulates GLUT1 transport through its intracellular part that is revealed by the tetramer formation.

GLUT1 in the protein network of the erythrocyte membrane

Biochemical and biophysical evidence have shown that GLUT1 interacts with various erythroid membrane proteins such as stomatin [113], adducin, dematin [67] and band 3, the erythroid anion exchanger 1 SLC4A1 [61] (Fig. 1). Proteins in the erythrocyte membrane are organized in structural complexes linking the transmembrane proteins to the cytoskeleton. The red blood cell deformability and mechanical property greatly depends on this membrane protein organization. Two main protein complexes around band 3 are observed: the ankyrin complex around band 3 tetramers that are linked to ankyrin and tether spectrin, and the actin junctional complex around band 3 dimers that binds to the spectrin-actin junction via protein 4.1, 4.2 and adducin [42, 88, 94]. GLUT1 is part of the junctional complex via interaction with adducin, dematin and band 3. Moreover, GLUT1 binds stomatin, an integral erythrocyte membrane protein that links cholesterol and is involved in membrane scaffolding [80]. The GLUT1/stomatin interaction has been shown to inhibit glucose uptake in different studies [139–141]. In Clone9 cells (rat hepatocytes), overexpression of stomatin results in a reduction of glucose transport that is not due to a decreased number of GLUT1 at the plasma membrane but rather to a decrease in the intrinsic activity of GLUT1 [140]. However, Kumar et al. found that stomatin interactions with GLUT1 did not alter glucose transport at least in adipocyte membranes [75] thus suggesting that additional components might interfere with GLUT1/stomatin complex to control GLUT1 transport activity. Whereas the exact role of stomatin in erythrocyte membrane is still in debate, it was proposed to be involved in the removal of misfolded or obsolete proteins from maturing reticulocytes [29, 71].

Very recent work has identified 3 different sub-populations of GLUT1 in the erythrocyte membrane suggesting that the transporter might interact with some yet unidentified partners thereby stabilizing these sub-populations. Indeed, at least two populations of GLUT1 in the red blood cell membrane are not associated with band 3 [70]. These complexes may involve known partners of GLUT1 but change their tethers to the spectrin-actin cytoskeleton. How supramolecular organization of GLUT1 interferes with glucose transport is unknown. However, recent data in HeLa cells suggest that glucose transport activation is correlated to the size of GLUT1 clusters: the smallest clusters are observed when glucose transport is stimulated [137]. A biophysical study has demonstrated the role of red blood cell skeletal dynamics in GLUT1 transport activity. The fluctuation of actin association/dissociation favours red blood cell glucose uptake by creating free space at the

endoplasmic side of GLUT1, allowing glucose release [3]. More generally, the cellular context around GLUT1 is involved in its transport properties [85].

Glucose transport in human red blood cells

Glucose transport through GLUT1 is by facilitated transport, meaning the net movement of glucose is driven by its concentration gradient across plasma membrane, from high to low sugar concentration. It differs from the sugar sodium co-transporter that is able to transport sugar against its chemical gradient using the energy obtained by dissipating the sodium gradient across the plasma membrane. Glucose transport in human red blood cell is very rapid, at 37 °C glucose equilibrium across membrane takes less than 2 s [87, 114]. This is due to the high number of glucose transporters in its membrane (10 to 20% of integral membrane proteins). Hence, kinetic studies to decipher the transport features of GLUT1 in erythrocytes have mostly been done at reduced temperature slowing down the processes to allow more accurate measurements. GLUT1 is characterized by a transport asymmetry meaning that the maximal velocity (Vmax) and sugar affinity (Km) for exit in sugar-free medium differs from the Vmax and Km for sugar entry into sugar free cells [15, 23]. This transport asymmetry is sensitive to temperature: at low temperature, the maximal velocity for sugar exit is 10-fold greater than the Vmax for sugar entry. This transport asymmetry is attenuated at body temperature (Vmax exit/Vmax entry ≈ 3 at 20 °C) [78, 87]. The transport asymmetry arises mainly from the proportion of inward- and outward-facing transporters and the affinities of the transporter for glucose in each conformation. At physiological temperatures, the transporter is similarly distributed between outward- and inward-facing conformations, and the affinity for glucose is about 2.5 times greater outside than inside. At low temperature, there is a higher proportion of inward-facing transporter, and the glucose affinity is similar for both conformations [87].

Another important property of glucose transport in red blood cells is the accelerated exchange, which means that glucose influx is accelerated in the presence of high glucose concentrations in erythrocyte; on the contrary, glucose efflux is accelerated by elevated extracellular glucose concentrations [78].

These kinetic features play an important function to either deliver glucose or refill glucose-depleted erythrocytes. Indeed, red blood cells are facing varying extracellular glucose concentrations throughout the body: in glucose consuming organs like the brain or placenta, erythrocytes are exposed to low extracellular glucose levels. The accelerated exchange impacts net glucose efflux from RBCs containing 5 mM glucose to serum with 2 mM glucose. In these conditions and with asymmetric transport (Vmax for glucose exit >Vmax for glucose entry), it was shown that an increased Vmax for exchange was correlated to a decreased half time of glucose exit from RBCs to serum. Thus, the accelerated exchange enhances glucose delivery from RBCs to glucose consuming organs. Moreover, in the initial absence of glucose in RBCs, it is observed that the Vmax for equilibration with extracellular glucose is accelerated by increasing transport asymmetry. This GLUT1 transport property favours a rapid glucose refilling of erythrocytes depleted in glucose, which emerge from glucose-consuming organs into regions with higher extracellular glucose [17].

Dehydroascorbic acid (DHA)

Another physiological important function of erythroid GLUTs is the transport of DHA, a precursor of vitamin C, which is a potent chelator of free radicals and acts as an anti-oxidant [112, 125].

The two erythroid glucose transporters GLUT1 and GLUT4 are both able to transport DHA; however, the transport efficiency greatly differs between the two proteins. DHA transport through GLUT4 is lower: in *Xenopus* oocytes expressing GLUT4, it is 2 to 4 times higher than control cells whereas it is 100 times higher in oocytes expressing GLUT1. A careful kinetic analysis of the transport of DHA and the glucose analogue 3-O-methyl-glucose in human erythrocytes has shown that both substrates compete for the same transport site in GLUT1 in human erythrocyte [114]. Previous work suggested that GLUT1 in human erythrocyte was more efficient in transporting DHA than glucose, and these transport properties were controlled by stomatin [96]. In this study, the stomatin/GLUT1 interaction was proposed to abolish the competition between glucose and DHA in GLUT1 substrate binding site and to enhance DHA transport. This conclusion was partly drawn from the observation of patients with a rare red blood cell condition, the overhydrated hereditary stomatocytosis (OHSt). These patients had a decreased red blood cell level of stomatin and glucose transport. On the other hand, DHA transport was increased.

Nevertheless, the GLUT1 transport rates are very high in the human erythrocyte membrane at physiological temperature, and both, DHA and glucose, are being equilibrated within seconds [114]. If stomatin does not modify GLUT1 transport properties, what could explain the reduced glucose and increased DHA uptakes in stomatin deficient red blood cells from OHSt patient compared with control? A decrease in erythrocyte stomatin expression is observed in OHSt either caused by mutations in RhAG, the rhesus-associated glycoprotein, or by mutations in GLUT1 [11, 40]. Glucose transport was abolished when GLUT1 mutations associated with OHSt were expressed in *Xenopus* oocytes hence ruling out that stomatin is fully responsible for decreased glucose uptake in OHSt red blood cells. Moreover, in red blood cells of patients with GLUT1 deficiency syndrome, a correlation between

decreased glucose transport and decreased DHA transport was observed [69]. Together, these studies suggest an influence of red blood cell metabolic activity as a determinant of glucose and DHA uptake kinetics rather than a modulation of the substrate selectivity by stomatin binding to GLUT1.

Transport regulation by substrate binding

Drugs that able to inhibit glucose transport have been identified very early such as phloretin and its derivatives [77]. Different compounds are able to covalently bind GLUT1; among them forskolin, cytochalasin B, impermeant bis-mannose and ATP have long been used to inhibit glucose transport [6, 14]. Cytochalasin B widely known for its inhibition of actin filament polymerization or forskolin, known for its activation of adenylate cyclase, are nonetheless direct modulators of GLUT1 activity [5, 47, 56, 121]. Binding of cytochalasin B and forskolin to GLUT1 has been demonstrated by photolabeling studies, and this binding competes with glucose transport. The binding site of cytochalasin B involves Trp residues 388 and 412 in the transmembrane segments (TM) 10 and 11, Thr137 in TM4 and Gln282 in TM7 [64] (Fig. 2). Mutation experiments on these residues decreased cytochalasin B binding as well as glucose transport. The binding of cytochalasin B to GLUT1 overlaps the glucose binding site thus blocking glucose transport. Forskolin binds to a site adjacent to the binding site of cytochalasin B in TM10 and also inhibits glucose transport [118, 127]. Bis mannose binds to an extracellular domain of the transport protein [6].

Glucose transport is also controlled by ATP binding on the intracellular ATP-binding site of the transporter. In the absence of intracellular ATP, the transport asymmetry fades, Vmax for sugar entry increases to reach Vmax for sugar exit. Hence, there is a coordination between the erythrocyte metabolic state, ATP level, and the activity of GLUT1: cytoplasmic ATP inhibits GLUT1-dependent glucose net uptake thereby slowing down glycolysis and ATP production [24, 25]. The structural basis for this ATP effect relies on the C-terminal cytoplasmic end of the protein. This nucleotide binding site is only accessible to ATP in the GLUT1 tetramer formation. The negative control of ATP on glucose transport is thus exerted on the most efficient transport conformation, the tetramer [54, 84].

Barbiturates can also inhibit glucose transport in red blood cells (albeit this requires concentrations 10 times higher than required for induction of anaesthesia) and are proposed to prevent GLUT1 conformational changes required for glucose transport [102].

More recent work has revealed other regulators of glucose transport through GLUT1 binding: caffeine [115], flavonoid from green tea or red wine [53, 107], oestradiol, genistein, tamoxifen [1] and androgens [103]. Caffeine binds to GLUT1 in the same site as ATP with a Ki = 3.5 mM. It mimics the action of ATP on glucose transport, and the magnitude of inhibition correlates with the level of the tetrameric form of GLUT1 that exposes the ATP binding site [51, 115]. Flavonoids effect on glucose transport depends on their concentration. At low concentration ($\leq \mu M$), flavonoids stimulate glucose uptake in RBCs, and, as their concentration raised, they inhibit glucose transport. This dual effect of flavonoids on glucose transport is mediated by two different binding sites in GLUT1 [107]. Glucose transport in RBCs is also inhibited by steroids binding to GLUT1 [34, 79]. A putative oestrogen binding site at the inner surface of GLUT1 is the target of oestrogen and its analogues as well as the modulators of oestrogen receptors, tamoxifen and Faslodex. It seems unlikely that physiological concentrations of oestradiol in women could affect glucose transport in RBCs where the Ki for oestradiol is 4.7 μM, which is ≈ 10 times higher than mean oestradiol concentration in serum (0.36 μM). In contrast, tamoxifen inhibits glucose transport with a Ki of 0.3 μM. This drug is widely used in the chemotherapy of breast cancer, and haemolytic anaemia is a side effect of this treatment. This has been attributed to a direct effect of the drug at high concentrations on the membrane structure of the erythrocytes by insertion in the lipid bilayer [28]. However, lower doses of tamoxifen might also affect glucose transport in RBCs and finally, the deformability and shape of these cells.

Among hormones, insulin and adrenaline play a critical role in controlling glucose transporters in different tissues. Human RBCs have insulin receptors responding to insulin stimulation by internalization [44, 45, 136]. These RBC insulin receptors are expressed in the foetal life of most studied mammalian species but disappear in adulthood except in humans [120]. Insulin on human RBCs decreased the affinity of GLUT1 for glucose without significantly modifying the Vmax [37]. These affinity changes are due to the downregulation of insulin receptors induced by insulin binding rather than by insulin occupancy of the receptors. A previous study also demonstrated an accelerated glucose efflux in RBCs stimulated by insulin [142]. However, there are no other evidences that insulin controls the capacity of RBCs to absorb glucose, and further studies did not show any physiological response to insulin in circulating RBCs [49]. It must be pointed out that the level of insulin receptors in the membrane of human RBCs declines with age, the older erythrocytes being unable to respond to insulin receptor stimulation [13]. This could explain the discrepancy between the different studies. Adrenaline was shown to enhance glucose release from glycogen stores in RBCs of rats [49] suggesting a control of glucose transporters GLUT4 by the stimulation of ß adrenergic receptors. In avian erythrocytes, a variety of catecholamines stimulates glucose transport (GLUT1), and this effect was not mimicked by the addition of cAMP. It was proposed that the stimulation of glucose transport by catecholamines in these RBCs was due to a decreased level of ATP [132]. To conclude, human RBCs

might not represent a significant resource to control glycaemia through insulin nor adrenaline signalling.

Independently of its role in red blood cell glucose transport, the search for specific inhibitors of GLUT1 has been enhanced by discovering the dependence of cancer cell metabolism on GLUT1 activity, and thus, specific inhibitors of GLUT1 such as Bay 876 have been developed for cancer therapy [119]. In addition to its potential therapeutic application, the development of drugs selectively targeting GLUT1 may lead to a better understanding of the transport mechanisms and the physiological and pathophysiological implication.

As mentioned in the introduction, any alteration of glucose transport in red blood cells may affect cell shape and deformability, hence oxygen delivery. Thus, particular interest should be paid on the wide variety of molecules from food to drugs that able to interact with GLUT1 and impair red blood cell function. This is particularly important for patients with existing red blood cell condition.

GLUT1 and red blood cell pathologies

GLUT1 mutations

Glucose transport deficiency has initially been identified in patients presenting neurological disorders. GLUT1 deficiency syndrome (GLUT1-DS), first described by De Vivo et al. in 1991, gathers conditions where glucose transport through the blood brain barrier and astrocytes is decreased [30]. Among the features of GLUT1-DS are infantile seizures, delayed development, microcephaly, hypoglycorrhachia (low glucose concentrations in cerebrospinal fluid) and decreased glucose uptake in erythrocytes [30, 68, 117, 138]. Indeed, GLUT1 is the main glucose transport expressed in neurons, and glucose serves as the primary energy substrate in these cells as in red blood cells.

Glucose transport deficiency in red blood cells is associated with a rare haemolytic anaemia, the overhydrated hereditary stomatocytosis (OHSt) [40]. This disorder is characterized by an increased red blood cell permeability to Na^+ and K^+. RBC membrane has a very low permeability to cations, and it keeps a high intracellular K^+ concentration and a low intracellular Na^+ concentration with a higher electrochemical force for Na^+ than for K^+. In case of OHSt, the increased cation permeability results in a Na^+ uptake that overcomes the K^+ loss, which promotes cell swelling [4, 39]. The intensity of the cation leak is sensitive to temperature, being increased at low temperature. Few years ago, we characterized 2 different GLUT1 mutations in patients with OHSt. These GLUT1 mutations are correlated to loss of stomatin in RBC membranes. The stomatin/GLUT1 interaction might be altered by OHSt GLUT1 mutations leading to loss of stomatin in mature red blood cell [40]. In addition to the red blood cell symptoms, patients experienced seizures, developmental delay, movement disorders and cataracts. The two different mutations associated to this phenotype are a single point mutation substituting the Gly in position 286 by an Asp and a deletion of 3 nucleotides resulting in the deletion of one of the two consecutive Ile (435 or 436) (Fig. 2). These mutations abolished the glucose transport and instead induced a Na^+ and K^+ leak dissipating the plasma membrane Na^+ and K^+ gradients. Gly286 in TM7 lies in the glucose binding site, and its substitution by Asp was proposed to form a salt bridge with Lys38 at the N-terminal part of the TM1 hence preventing glucose transport. Recent simulation of glucose transport highlighted the role of TM7 in glucose binding thus confirming the deleterious nature of the G286D substitution for glucose transport [43]. Ile435 or 436 is located in TM12, which forms extensive contacts with TM7. The substitution Gly286Asp and the deletion Ile435 or 436 induce a Na^+ and K^+ leak through GLUT1. A Na^+ and K^+ leak was also observed when two other red blood cell transmembrane proteins, the anion exchanger 1 SLC4A1 and the RHAG, are mutated [10, 11, 50]. Hence, specific mutations in GLUT1 as in these other erythrocyte membrane transporters are proposed to induce a cation leak dissipating Na^+ and K^+ gradient through the misfolded proteins. This cation leak associated with a decreased glucose transport challenges energy balance in red blood cells continuously compensating the cation leak by consuming ATP to power the Na^+/K^+ pump. These cells are fragile and prone to lysis explaining the observed haemolytic crisis (Fig. 3).

An abnormal red blood cell cation permeability was also observed with a deletion of 4 amino acids (Q282-S285del) in the pore region of GLUT-1, leading to a reduced glucose transport and subsequently altered calcium, sodium and potassium concentrations in human erythrocytes [129].

GLUT1 and malaria

Malaria is an infectious disease caused by a parasite of Plasmodium genus which contains several species. Among these species, the *Plasmodium falciparum* (P.f.) causes the most severe form of the disease with the highest complication rates and mortality in human. The parasite is transmitted to human by the bite of an infected mosquito. In the human body, it infects liver and red blood cells. The red blood cell life cycle of P.f. is responsible for recurrent fever and paroxysmal symptoms corresponding to red blood cell lysis after parasite multiplication. To infect the red blood cell, P.f. adheres to the cell membrane and then enters and proliferates. P.f. growth is dependent on glucose availability in red blood cell. A deficiency of G6PD has long been associated with a

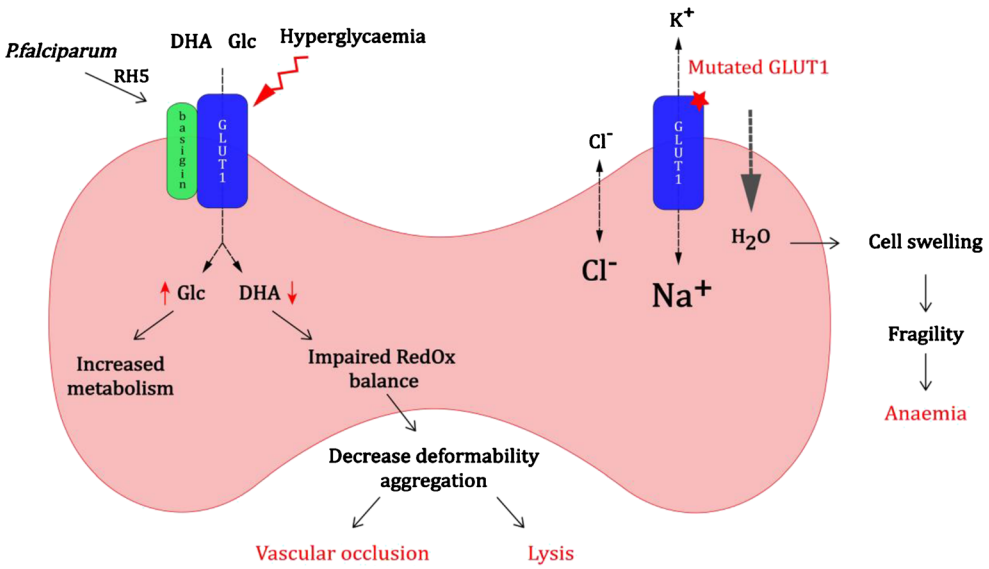

Fig. 3 Schema of GLUT1-related pathologies in human RBCs. Basigin is a transmembrane protein associated with GLUT1 and constitutes an entryway for *P. falciparum*. Basigin binds to RH5 protein in parasite membrane and initiates invasion processes. At physiological state, GLUT1 transports glucose and DHA (dehydroascorbic acid). In hyperglycaemia state, GLUT1 transports more glucose than DHA. Enhanced glucose uptake and fall in DHA level disturbs RedOx balance leading to hemorheological alterations (fragility and aggregation of RBCs) favouring vascular occlusion. Increased glucose concentration can overwhelm glycolysis and can induce glycosylation of various proteins such as haemoglobin (HbA1c). On the other hand, mutations of GLUT1 found in overhydrated hereditary stomatocytosis abolish glucose transport and induce Na^+, K^+ leakage. This leakage leads to NaCl uptake overwhelming KCl loss, water entry and thus swelling of the RBC. Overhydrated RBCs are fragile and have a reduced lifespan leading to anaemia.

reduced malaria infection risk, suggesting that the alteration of glucose metabolism in RBCs protects against malaria [89, 92]. Whereas the link between red blood cell metabolism and development of P.f. was extensively investigated, a more direct connection with GLUT1 transport activity has not been established. However, a recent study illustrates the interest of blocking GLUT1 to prevent P.f. development in red blood cells. Inhibition of glucose transport by WZB117 acting on the extracellular glucose binding site of GLUT1, alters the redox balance, enhances reactive oxygen species levels and parasite apoptosis, which in turn leads to the elimination of infected red blood cells [131].

In the search for a malaria vaccine, basigin, a member of the immunoglobulin family, is currently considered as a promising target [128]. Basigin is expressed in the erythrocyte membrane where it acts as a receptor for P.f. invasion (Fig. 3). Indeed, basigin binds the RH5 protein in the P.f. cell membrane, which is the only necessary membrane protein of the Plasmodium for erythrocyte invasion in all tested strains [27]. Basigin has been shown to bind monocarboxylate transporters but also GLUT1 [2]. In photoreceptors basigin/GLUT1 interaction stimulates glucose uptake. It has been suggested that drugs binding basigin could control basigin/GLUT1 interactions and glucose metabolism [2]. The role of the basigin/GLUT1 interaction in red blood cell glucose transport and metabolism as well as in P.f. infection deserves further investigation.

GLUT1 and diabetes

Diabetes mellitus, a condition characterized by elevated glucose concentrations in plasma, affects more than 400 million people worldwide. It may cause many complications including cardiovascular disease, stroke, retinopathy, neuropathy and renal failure. Indeed, diabetes mellitus is linked to vascular disease that is caused by alteration of the vascular endothelium but also by impaired hemorheological properties [38]. Associated to hyperglycaemia, oxidative stress is a recognized feature of diabetes mellitus [9], and both parameters affect RBCs. Hyperglycaemia induces an increased glycosylation of cytoskeleton and membrane proteins and glycation of haemoglobin. The amount of glycated haemoglobin (HbA1c) reflects the average plasma glucose concentration over the 3 previous months and is used as a biomarker of glycaemic status in diabetic patients [122]. HbA1c ranges between 4 and 6.5% in physiological condition and is inversely correlated to RBC deformability in type 2 diabetes mellitus [66]. Moreover, oxidative stress induces oxidation of lipids and proteins, leading to their denaturation [60]. These alterations of RBCs' components change their structure and function through a progressive decline in their deformability [8, 12, 35, 63, 66, 76, 104, 109]. The limited deformability observed in diabetes is associated with greater fragility and shortened lifespan of red blood cells leading to anaemia [76, 93, 108, 126]. In addition, these modified RBCs are prone to

aggregate, which causes micro-vascular occlusion and aggravate the vasculopathy [41].

As hyperglycaemia causes oxidative stress in endothelial cells but also in red blood cells, a link between diabetes vasculopathy and red blood cell vitamin C has been suggested [91]. This hypothesis relies on the observation that vitamin C deficiency in mice or humans is correlated to anaemia and haemolysis [18, 90]. More recently, a comprehensive study investigated the connection between GLUT1, DHA transport and diabetes [123]. It was observed that hyperglycaemia is inversely related to the ascorbate concentration in red blood cells and that the low ascorbate concentration was associated with strong haemolysis. Since ascorbate concentration comes from extracellular DHA uptake through GLUT1 in human red blood cell, the competition between DHA and glucose on GLUT1 appears attractive to explain reduced ascorbate content in RBCs thereby causing their increased fragility in diabetes. Nonetheless, hyperglycaemia could also alter GLUT1 expression in RBC membrane, or oxidative damage might change GLUT1 transport, hence reducing the DHA transport capacity as also suggested by the authors.

Chronic hyperglycaemia impairs the expression of glucose transporters in the plasma membrane of different cell types. However, in circulating RBCs, there is no possibility to adapt the expression of GLUT1 to the glycaemia. The regulation of GLUT1 expression at the plasma membrane of RBCs takes place during erythropoiesis. In children with type 1 diabetes, an almost half reduction of GLUT1 expression at the plasma membrane of RBCs has been observed compared with control [46]. However, this observation has not been reported in RBCs of diabetic adults (type 2 diabetes) where GLUT1 expression level in the plasma membrane was unchanged [110]. As mentioned earlier, the unbalanced redox status induces chemical modifications of RBC components, and GLUT1 has been proposed to be targeted by such modifications. Studying a Chinese population with type 2 diabetes, alteration of glucose transport kinetics has been observed in RBCs [58]. Whereas glucose efflux parameters were similar to control, the glucose entry was decreased. This was attributed to a molecular change of GLUT1 at the extracellular side of the protein in diabetic RBCs. This molecular change modifies the glucose access to transport site from the extracellular medium. Alternatively, the cytoskeleton and protein complexes around GLUT1 could also be chemically modified in diabetic RBCs. R. Asaro and co-authors proposed that glucose uptake could be controlled by skeletal/actin dynamics in normal RBCs [3]. It could be envisioned that RBC features interfering with skeletal/actin dynamics might affect glucose uptake through GLUT1 specifically in individuals with diabetes.

Conclusion

Summarizing glucose transport in red blood cells is challenging as this has been a subject of intense research activity for almost a century. The huge number of references renders it necessary to make a selection that may have excluded some contributions to the field. However, we tried to include a wide selection of references that allow to go deeper with regard to more specific aspects of glucose transport in red blood cells.

The contribution of GLUT1 in erythroid pathologies is either due to specific mutations altering its transport selectivity leading to a dissipation of the Na^+ and K^+ gradients across the plasma membrane or to its role in the energy supply of red blood cells. In this later case, glucose transport is challenged by metabolic condition such as diabetes or by an increased demand for glucose to facilitate the growth of Plasmodium in malaria. The complex organization of proteins in red blood cell membrane provides opportunities to modulate GLUT1 activity through specific protein-protein interactions that might not be observed in other membrane environments. Further studies deciphering the role of the protein or lipid environment in erythroid glucose transporter activity as well as its functional embedding in protein networks constitute a logical next step to gain a deeper understanding of this transporter in red blood cell physiology, pathophysiology and, potentially, therapy.

Availability of data and material Not applicable.
Code availability Not applicable.

Authors' contributions Both authors contributed to the writing.

Funding information This study was supported by the Public University and Centre National de la Recherche Scientifique.

Compliance with ethical standards

Conflicts of interest The authors declare that they have no conflict of interests.

Ethics approval Not applicable.

Consent to participate Not applicable.

Consent for publication Not applicable.

References

1. Afzal I, Cunningham P, Naftalin RJ (2002) Interactions of ATP, oestradiol, genistein and the anti-oestrogens, Faslodex (ICI 182780) and tamoxifen, with the human erythrocyte glucose transporter, GLUT1. Biochem J 365:707–719
2. Aït-Ali N, Fridlich R, Millet-Puel G, Clérin E, Delalande F, Jaillard C, Blond F, Perrocheau L, Reichman S, Byrne LC, Olivier-Bandini A, Bellalou J, Moyse E, Bouillaud F, Nicol X,

Dalkara D, van Dorsselaer A, Sahel JA, Léveillard T (2015) Rod-derived cone viability factor promotes cone survival by stimulating aerobic glycolysis. Cell 161:817–832
3. Asaro RJ, Zhu Q, Cabrales P, Carruthers A (2018) Do skeletal dynamics mediate sugar uptake and transport in human erythrocytes? Biophys J 114:1440–1454
4. Badens C, Guizouarn H (2016) Advances in understanding the pathogenesis of the red cell volume disorders. Br J Haematol 174:674–685
5. Baldwin SA, Baldwin JM, Gorga FR, Lienhard GE (1979) Purification of the cytochalasin B binding component of the human erythrocyte monosaccharide transport system. Biochim Biophys Acta 552:183–188
6. Basketter DA, Widdas WF (1978) Asymmetry of the hexose transfer system in human erythrocytes. Comparison of the effects of cytochalasin B, phloretin and maltose as competitive inhibitors. J Physiol 278:389–401
7. Blodgett DM, Graybill C, Carruthers A (2008) Analysis of glucose transporter topology and structural dynamics. J Biol Chem 283:36416–36424
8. Brown CD, Ghali HS, Zhao Z, Thomas LL, Friedman EA (2005) Association of reduced red blood cell deformability and diabetic nephropathy. Kidney Int 67:295–300
9. Brownlee M (2001) Biochemistry and molecular cell biology of diabetic complications. Nature 414:813–820
10. Bruce LJ, Robinson HC, Guizouarn H, Borgese F, Harrison P, King MJ, Goede JS, Coles SE, Gore DM, Lutz HU, Ficarella R, Layton DM, Iolascon A, Ellory JC, Stewart GW (2005) Monovalent cation leaks in human red cells caused by single amino-acid substitutions in the transport domain of the band 3 chloride-bicarbonate exchanger, AE1. Nat Genet 37:1258–1263
11. Bruce LJ, Guizouarn H, Burton NM, Gabillat N, Poole J, Flatt JF, Brady RL, Borgese F, Delaunay J, Stewart GW (2009) The monovalent cation leak in overhydrated stomatocytic red blood cells results from amino acid substitutions in the Rh-associated glycoprotein. Blood 113:1350–1357
12. Buys AV, Van Rooy MJ, Soma P, Van Papendorp D, Lipinski B, Pretorius E (2013) Changes in red blood cell membrane structure in type 2 diabetes: a scanning electron and atomic force microscopy study. Cardiovasc Diabetol 12:25
13. Camagna A, Rossetti L, De Pirro R, Di Franco M, Lauro R, Samoggia P, Caprari P, Salvo G (1987) Characterization of differences in insulin receptors from young and old red blood cells. J Endocrinol Investig 10:371–375
14. Carruthers A (1986) ATP regulation of the human red cell sugar transporter. J Biol Chem 261:11028–11037
15. Carruthers A, Melchior DL (1983) Asymmetric or symmetric? Cytosolic modulation of human erythrocyte hexose transfer. Biochim Biophys Acta 728:254–266
16. Carruthers A, Melchior DL (1984) A rapid method of reconstituting human erythrocyte sugar transport proteins. Biochemistry 23:2712–2718
17. Carruthers A, DeZutter J, Ganguly A, Devaskar SU (2009) Will the original glucose transporter isoform please stand up! Am J Physiol Endocrinol Metab 297:E836–E848
18. CHAZAN JA, MISTILIS SP (1963) The pathophysiology of scurvy. A report of seven cases. Am J Med 34:350–358
19. Chen LY, Phelix CF (2019) Extracellular gating of glucose transport through GLUT 1. Biochem Biophys Res Commun 511:573–578
20. Chien S (1987) Red cell deformability and its relevance to blood flow. Annu Rev Physiol 49:177–192
21. Chin JJ, Jung EK, Jung CY (1986) Structural basis of human erythrocyte glucose transporter function in reconstituted vesicles. J Biol Chem 261:7101–7104
22. Chin JJ, Jung EK, Chen V, Jung CY (1987) Structural basis of human erythrocyte glucose transporter function in proteoliposome vesicles: circular dichroism measurements. Proc Natl Acad Sci U S A 84:4113–4116
23. Cloherty EK, Heard KS, Carruthers A (1996) Human erythrocyte sugar transport is incompatible with available carrier models. Biochemistry 35:10411–10421
24. Cloherty EK, Hamill S, Levine K, Carruthers A (2001) Sugar transporter regulation by ATP and quaternary structure. Blood Cells Mol Dis 27:102–107
25. Cloherty EK, Levine KB, Carruthers A (2001) The red blood cell glucose transporter presents multiple, nucleotide-sensitive sugar exit sites. Biochemistry 40:15549–15561
26. Clow KA, Short CE, Hall JR, Gendron RL, Paradis H, Ralhan A, Driedzic WR (2016) High rates of glucose utilization in the gas gland of Atlantic cod (Gadus morhua) are supported by GLUT1 and HK1b. J Exp Biol 219:2763–2773
27. Crosnier C, Bustamante LY, Bartholdson SJ, Bei AK, Theron M, Uchikawa M, Mboup S, Ndir O, Kwiatkowski DP, Duraisingh MT, Rayner JC, Wright GJ (2011) Basigin is a receptor essential for erythrocyte invasion by Plasmodium falciparum. Nature 480:534–537
28. Cruz Silva MM, Madeira VM, Almeida LM, Custódio JB (2000) Hemolysis of human erythrocytes induced by tamoxifen is related to disruption of membrane structure. Biochim Biophys Acta 1464:49–61
29. de Gassart A, Geminard C, Fevrier B, Raposo G, Vidal M (2003) Lipid raft-associated protein sorting in exosomes. Blood 102:4336–4344
30. De Vivo DC, Trifiletti RR, Jacobson RI, Ronen GM, Behmand RA, Harik SI (1991) Defective glucose transport across the blood-brain barrier as a cause of persistent hypoglycorrhachia, seizures, and developmental delay. N Engl J Med 325:703–709
31. Delgado TC, Castro MM, Geraldes CF, Jones JG (2004) Quantitation of erythrocyte pentose pathway flux with [2-13C]glucose and 1H NMR analysis of the lactate methyl signal. Magn Reson Med 51:1283–1286
32. Deng D, Xu C, Sun P, Wu J, Yan C, Hu M, Yan N (2014) Crystal structure of the human glucose transporter GLUT1. Nature 510:121–125
33. Deng D, Sun P, Yan C, Ke M, Jiang X, Xiong L, Ren W, Hirata K, Yamamoto M, Fan S, Yan N (2015) Molecular basis of ligand recognition and transport by glucose transporters. Nature 526:391–396
34. Devés R, Krupka RM (1980) Testing transport systems for competition between pairs of reversible inhibitors. Inhibition of erythrocyte glucose transport by cytochalasin B and steroids. J Biol Chem 255:11870–11874
35. Diamantopoulos EJ, Kittas C, Charitos D, Grigoriadou M, Ifanti G, Raptis SA (2004) Impaired erythrocyte deformability precedes vascular changes in experimental diabetes mellitus. Horm Metab Res 36:142–147
36. Diamond DL, Carruthers A (1993) Metabolic control of sugar transport by derepression of cell surface glucose transporters. An insulin-independent recruitment-independent mechanism of regulation. J Biol Chem 268:6437–6444
37. Dustin ML, Jacobson GR, Peterson SW (1984) Effects of insulin receptor down-regulation on hexose transport in human erythrocytes. J Biol Chem 259:13660–13663
38. Fatehi-Hassanabad Z, Chan CB, Furman BL (2010) Reactive oxygen species and endothelial function in diabetes. Eur J Pharmacol 636:8–17
39. Flatt JF, Bruce LJ (2018) The molecular basis for altered cation permeability in hereditary stomatocytic human red blood cells. Front Physiol 9:367

40. Flatt JF, Guizouarn H, Burton NM, Borgese F, Tomlinson RJ, Forsyth RJ, Baldwin SA, Levinson BE, Quittet P, Aguilar-Martinez P, Delaunay J, Stewart GW, Bruce LJ (2011) Stomatin-deficient cryohydrocytosis results from mutations in SLC2A1: a novel form of GLUT1 deficiency syndrome. Blood 118:5267–5277
41. Foresto P, D'Arrigo M, Carreras L, Cuezzo RE, Valverde J, Rasia R (2000) Evaluation of red blood cell aggregation in diabetes by computerized image analysis. Medicina (B Aires) 60:570–572
42. Franco T, Low PS (2010) Erythrocyte adducin: a structural regulator of the red blood cell membrane. Transfus Clin Biol 17:87–94
43. Galochkina T, Ng Fuk Chong M, Challali L, Abbar S, Etchebest C (2019) New insights into GluT1 mechanics during glucose transfer. Sci Rep 9:998
44. Gambhir KK, Agarwal VR (1991) Red blood cell insulin receptors in health and disease. Biochem Med Metab Biol 45:133–153
45. Gambhir KK, Archer JA, Carter L (1977) Insulin radioreceptor assay for human erythrocytes. Clin Chem 23:1590–1595
46. Garg M, Thamotharan M, Becker DJ, Devaskar SU (2014) Adolescents with clinical type 1 diabetes display reduced red blood cell glucose transporter isoform 1 (GLUT1). Pediatr Diabetes 15:511–518
47. Gorga FR, Lienhard GE (1981) Equilibria and kinetics of ligand binding to the human erythrocyte glucose transporter. Evidence for an alternating conformation model for transport. Biochemistry 20:5108–5113
48. Graybill C, van Hoek AN, Desai D, Carruthers AM, Carruthers A (2006) Ultrastructure of human erythrocyte GLUT1. Biochemistry 45:8096–8107
49. Guarner V, Alvarez-Buylla R (1989) Erythrocytes and glucose homeostasis in rats. Diabetes 38:410–415
50. Guizouarn H, Martial S, Gabillat N, Borgese F (2007) Point mutations involved in red cell stomatocytosis convert the electroneutral anion exchanger 1 to a nonselective cation conductance. Blood 110:2158–2165
51. Gunnink LK, Busscher BM, Wodarek JA, Rosette KA, Strohbehn LE, Looyenga BD, Louters LL (2017) Caffeine inhibition of GLUT1 is dependent on the activation state of the transporter. Biochimie 137:99–105
52. Hall JR, Clow KA, Short CE, Driedzic WR (2014) Transcript levels of class I GLUTs within individual tissues and the direct relationship between GLUT1 expression and glucose metabolism in Atlantic cod (Gadus morhua). J Comp Physiol B 184:483–496
53. Hamilton KE, Rekman JF, Gunnink LK, Busscher BM, Scott JL, Tidball AM, Stehouwer NR, Johnecheck GN, Looyenga BD, Louters LL (2018) Quercetin inhibits glucose transport by binding to an exofacial site on GLUT1. Biochimie 151:107–114
54. Heard KS, Fidyk N, Carruthers A (2000) ATP-dependent substrate occlusion by the human erythrocyte sugar transporter. Biochemistry 39:3005–3014
55. Hebert DN, Carruthers A (1992) Glucose transporter oligomeric structure determines transporter function. Reversible redox-dependent interconversions of tetrameric and dimeric GLUT1. J Biol Chem 267:23829–23838
56. Helgerson AL, Carruthers A (1987) Equilibrium ligand binding to the human erythrocyte sugar transporter. Evidence for two sugar-binding sites per carrier. J Biol Chem 262:5464–5475
57. Holman GD (2018) Chemical biology probes of mammalian GLUT structure and function. Biochem J 475:3511–3534
58. Hu XJ, Peng F, Zhou HQ, Zhang ZH, Cheng WY, Feng HF (2000) The abnormality of glucose transporter in the erythrocyte membrane of Chinese type 2 diabetic patients. Biochim Biophys Acta 1466:306–314
59. Ingermann R, Virgin G (1987) Glycogen content and release of glucose from red blood cells of the sipunculan worm *Themiste dyscrita*. J Exp Biol 129:141–149
60. Jain SK (1989) Hyperglycemia can cause membrane lipid peroxidation and osmotic fragility in human red blood cells. J Biol Chem 264:21340–21345
61. Jiang W, Ding Y, Su Y, Jiang M, Hu X, Zhang Z (2006) Interaction of glucose transporter 1 with anion exchanger 1 in vitro. Biochem Biophys Res Commun 339:1255–1261
62. Joost HG, Thorens B (2001) The extended GLUT-family of sugar/polyol transport facilitators: nomenclature, sequence characteristics, and potential function of its novel members (review). Mol Membr Biol 18:247–256
63. Kamada T, McMillan DE, Yamashita T, Otsuji S (1992) Lowered membrane fluidity of younger erythrocytes in diabetes. Diabetes Res Clin Pract 16:1–6
64. Kapoor K, Finer-Moore JS, Pedersen BP, Caboni L, Waight A, Hillig RC, Bringmann P, Heisler I, Müller T, Siebeneicher H, Stroud RM (2016) Mechanism of inhibition of human glucose transporter GLUT1 is conserved between cytochalasin B and phenylalanine amides. Proc Natl Acad Sci U S A 113:4711–4716
65. Kasahara M, Hinkle PC (1977) Reconstitution and purification of the D-glucose transporter from human erythrocytes. J Biol Chem 252:7384–7390
66. Keymel S, Heiss C, Kleinbongard P, Kelm M, Lauer T (2011) Impaired red blood cell deformability in patients with coronary artery disease and diabetes mellitus. Horm Metab Res 43:760–765
67. Khan AA, Hanada T, Mohseni M, Jeong JJ, Zeng L, Gaetani M, Li D, Reed BC, Speicher DW, Chishti AH (2008) Dematin and adducin provide a novel link between the spectrin cytoskeleton and human erythrocyte membrane by directly interacting with glucose transporter-1. J Biol Chem 283:14600–14609
68. Klepper J, Leiendecker B (2007) GLUT1 deficiency syndrome–2007 update. Dev Med Child Neurol 49:707–716
69. Klepper J, Vera JC, De Vivo DC (1998) Deficient transport of dehydroascorbic acid in the glucose transporter protein syndrome. Ann Neurol 44:286–287
70. Kodippili GC, Putt KS, Low PS (2019) Evidence for three populations of the glucose transporter in the human erythrocyte membrane. Blood Cells Mol Dis 77:61–66
71. Komatsu T, Sato K, Otsuka Y, Arashiki N, Tanaka K, Tamahara S, Ono K, Inaba M et al (2010) Parallel reductions in stomatin and Na,KATPase through the exosomal pathway during reticulocyte maturation in dogs: stomatin as a genotypic and phenotypic marker of high K+ and low K+ red cells. J Vet Med Sci 72:893–901
72. Koralkova P, van Solinge WW, van Wijk R (2014) Rare hereditary red blood cell enzymopathies associated with hemolytic anemia - pathophysiology, clinical aspects, and laboratory diagnosis. Int J Lab Hematol 36:388–397
73. Kozawa S (1914) Beitdge zum arteigenen Verhalten der roten BlutkSrperchen 111. Artdiff erenzen in der Durclilissigkeit der roten Blutkijrperchen. Biorhem Z 60:231–256
74. Kuchel PW, Shishmarev D (2017) Accelerating metabolism and transmembrane cation flux by distorting red blood cells. Sci Adv 3:eaao1016
75. Kumar A, Xiao YP, Laipis PJ, Fletcher BS, Frost SC (2004) Glucose deprivation enhances targeting of GLUT1 to lipid rafts in 3T3-L1 adipocytes. Am J Physiol Endocrinol Metab 286: E568–E576
76. Kung CM, Tseng ZL, Wang HL (2009) Erythrocyte fragility increases with level of glycosylated hemoglobin in type 2 diabetic patients. Clin Hemorheol Microcirc 43:345–351
77. Lacko L, Burger M (1964) Effect of phlorizin on exchange and non-exchange transport of sugars in human Erythrocytes. Biochim Biophys Acta 79:563–567
78. Lacko L, Wittke B, Geck P (1973) The temperature dependence of the exchange transport of glucose in human erythrocytes. J Cell Physiol 82:213–218

79. Lacko L, Wittke B, Geck P (1975) Interaction of steroids with the transport system of glucose in human erythrocytes. J Cell Physiol 86(Suppl 2):673–680
80. Lapatsina L, Brand J, Poole K, Daumke O, Lewin GR (2012) Stomatin-domain proteins. Eur J Cell Biol 91:240–245
81. LeFEVRE PG (1948) Evidence of active transfer of certain non-electrolytes across the human red cell membrane. J Gen Physiol 31:505–527
82. LeFevre PG (1953) Further characterization of the sugar-transfer system in the red cell membrane by the use of phloretin. Fed Proc 12:84
83. Levine KB, Cloherty EK, Fidyk NJ, Carruthers A (1998) Structural and physiologic determinants of human erythrocyte sugar transport regulation by adenosine triphosphate. Biochemistry 37:12221–12232
84. Levine KB, Cloherty EK, Hamill S, Carruthers A (2002) Molecular determinants of sugar transport regulation by ATP. Biochemistry 41:12629–12638
85. Levine KB, Robichaud TK, Hamill S, Sultzman LA, Carruthers A (2005) Properties of the human erythrocyte glucose transport protein are determined by cellular context. Biochemistry 44:5606–5616
86. Looyenga B, VanOpstall C, Lee Z, Bell J, Lodge E, Wrobel K, Arnoys E, Louters L (2016) Determination of GLUT1 oligomerization parameters using bioluminescent Förster resonance energy transfer. Sci Rep 6:29130
87. Lowe AG, Walmsley AR (1986) The kinetics of glucose transport in human red blood cells. Biochim Biophys Acta 857:146–154
88. Lux SE (2016) Anatomy of the red cell membrane skeleton: unanswered questions. Blood 127:187–199
89. Luzzatto L, Usanga FA, Reddy S (1969) Glucose-6-phosphate dehydrogenase deficient red cells: resistance to infection by malarial parasites. Science 164:839–842
90. Maeda N, Hagihara H, Nakata Y, Hiller S, Wilder J, Reddick R (2000) Aortic wall damage in mice unable to synthesize ascorbic acid. Proc Natl Acad Sci U S A 97:841–846
91. Mann GV, Newton P (1975) The membrane transport of ascorbic acid. Ann N Y Acad Sci 258:243–252
92. Mbanefo EC, Ahmed AM, Titouna A, Elmaraezy A, Trang NT, Phuoc Long N, Hoang Anh N, Diem Nghi T, The Hung B, Van Hieu M, Ky Anh N, Huy NT, Hirayama K (2017) Association of glucose-6-phosphate dehydrogenase deficiency and malaria: a systematic review and meta-analysis. Sci Rep 7:45963
93. McMillan DE, Utterback NG, La Puma J (1978) Reduced erythrocyte deformability in diabetes. Diabetes 27:895–901
94. Mohandas N, Gallagher PG (2008) Red cell membrane: past, present, and future. Blood 112:3939–3948
95. Montel-Hagen A, Blanc L, Boyer-Clavel M, Jacquet C, Vidal M, Sitbon M, Taylor N (2008) The Glut1 and Glut4 glucose transporters are differentially expressed during perinatal and postnatal erythropoiesis. Blood 112:4729–4738
96. Montel-Hagen A, Kinet S, Manel N, Mongellaz C, Prohaska R, Battini JL, Delaunay J, Sitbon M, Taylor N (2008) Erythrocyte Glut1 triggers dehydroascorbic acid uptake in mammals unable to synthesize vitamin C. Cell 132:1039–1048
97. Moses SW, Bashan N, Gutman A (1972) Glycogen metabolism in the normal red blood cell. Blood 40:836–843
98. Moses SW, Bashan N, Gutman A, Ockerman PA (1974) Glycogen metabolism in glycogen-rich erythrocytes. Blood 44:275–284
99. Mueckler M, Thorens B (2013) The SLC2 (GLUT) family of membrane transporters. Mol Asp Med 34:121–138
100. Mueckler M, Caruso C, Baldwin SA, Panico M, Blench I, Morris HR, Allard WJ, Lienhard GE, Lodish HF (1985) Sequence and structure of a human glucose transporter. Science 229:941–945
101. Naftalin (2003) In: Bernhardt I, Ellory JC (eds) Glucose transport in *Red cell Membrane Transport*. Springer, pp 339–372
102. Naftalin RJ, Afzal I, Browning JA, Wilkins RJ, Ellory JC (2002) Effects of high pressure on glucose transport in the human erythrocyte. J Membr Biol 186:113–129
103. Naftalin RJ, Afzal I, Cunningham P, Halai M, Ross C, Salleh N, Milligan SR (2003) Interactions of androgens, green tea catechins and the antiandrogen flutamide with the external glucose-binding site of the human erythrocyte glucose transporter GLUT1. Br J Pharmacol 140:487–499
104. NeamȚu MC, CrăiȚoiu Ş, Avramescu ET, Margină DM, Băcănoiu MV, Turneanu D, Dănciulescu MR (2015) The prevalence of the red cell morphology changes in patients with type 2 diabetes mellitus. Romanian J Morphol Embryol 56:183–189
105. Ogawa E, Hishiyama N (2011) Japanese Shiba dogs possessing erythrocytes with high Glut-1 activity and high ascorbic acid recycling capacity. Comp Clin Pathol 21:639–644
106. Ogawa E, Neo S (2016) Akita dogs possess GLUT1 in erythrocytes, and Na, K-ATPase activity enables more efficient ascorbic acid recycling. J Vet Med Sci 78:1557–1561
107. Ojelabi OA, Lloyd KP, De Zutter JK, Carruthers A (2018) Red wine and greeen tea flavonoids are cis-allosteric activators and competitive inhibitors of glucose transporter 1 (GLUT1)-mediated sugar uptake. J Biol Chem 293:19823–19834
108. Parthasarathi K, Lipowsky HH (1999) Capillary recruitment in response to tissue hypoxia and its dependence on red blood cell deformability. Am J Phys 277:H2145–H2157
109. Peterson CM, Jones RL, Koenig RJ, Melvin ET, Lehrman ML (1977) Reversible hematologic sequelae of diabetes mellitus. Ann Intern Med 86:425–429
110. Porter-Turner MM, Skidmore JC, Khokher MA, Singh BM, Rea CA (2011) Relationship between erythrocyte GLUT1 function and membrane glycation in type 2 diabetes. Br J Biomed Sci 68:203–207
111. Puckeridge M, Chapman BE, Conigrave AD, Grieve SM, Figtree GA, Kuchel PW (2013) Stoichiometric relationship between Na(+) ions transported and glucose consumed in human erythrocytes: Bayesian analysis of (23)Na and (13)C NMR time course data. Biophys J 104:1676–1684
112. Rumsey SC, Kwon O, Xu GW, Burant CF, Simpson I, Levine M (1997) Glucose transporter isoforms GLUT1 and GLUT3 transport dehydroascorbic acid. J Biol Chem 272:18982–18989
113. Rungaldier S, Oberwagner W, Salzer U, Csaszar E, Prohaska R (2013) Stomatin interacts with GLUT1/SLC2A1, band 3/SLC4A1, and aquaporin-1 in human erythrocyte membrane domains. Biochim Biophys Acta 1828:956–966
114. Sage JM, Carruthers A (2014) Human erythrocytes transport dehydroascorbic acid and sugars using the same transporter complex. Am J Phys Cell Physiol 306:C910–C917
115. Sage JM, Cura AJ, Lloyd KP, Carruthers A (2015) Caffeine inhibits glucose transport by binding at the GLUT1 nucleotide-binding site. Am J Phys Cell Physiol 308:C827–C834
116. Salas-Burgos A, Iserovich P, Zuniga F, Vera JC, Fischbarg J (2004) Predicting the three-dimensional structure of the human facilitative glucose transporter glut1 by a novel evolutionary homology strategy: insights on the molecular mechanism of substrate migration, and binding sites for glucose and inhibitory molecules. Biophys J 87:2990–2999
117. Seidner G, Alvarez MG, Yeh JI, O'Driscoll KR, Klepper J, Stump TS, Wang D, Spinner NB, Birnbaum MJ, De Vivo DC (1998) GLUT-1 deficiency syndrome caused by haploinsufficiency of the blood-brain barrier hexose carrier. Nat Genet 18:188–191
118. Sergeant S, Kim HD (1985) Inhibition of 3-O-methylglucose transport in human erythrocytes by forskolin. J Biol Chem 260:14677–14682

119. Siebeneicher H, Cleve A, Rehwinkel H, Neuhaus R, Heisler I, Müller T, Bauser M, Buchmann B (2016) Identification and optimization of the first highly selective GLUT1 inhibitor BAY-876. ChemMedChem 11:2261–2271
120. Sinha MK, Ganguli S, Sperling MA (1981) Disappearance of erythrocyte insulin receptors during maturation in sheep. Diabetes 30:411–415
121. Sogin DC, Hinkle PC (1980) Binding of cytochalasin B to human erythrocyte glucose transporter. Biochemistry 19:5417–5420
122. Symeonidis A, Athanassiou G, Psiroyannis A, Kyriazopoulou V, Kapatais-Zoumbos K, Missirlis Y, Zoumbos N (2001) Impairment of erythrocyte viscoelasticity is correlated with levels of glycosylated haemoglobin in diabetic patients. Clin Lab Haematol 23:103–109
123. Tu H, Li H, Wang Y, Niyyati M, Leshin J, Levine M (2015) Low red blood cell vitamin C concentrations induce red blood cell fragility: a link to diabetes via glucose, glucose transporters, and Dehydroascorbic acid. EBioMedicine 2:1735–1750
124. van Wijk R, van Solinge WW (2005) The energy-less red blood cell is lost: erythrocyte enzyme abnormalities of glycolysis. Blood 106:4034–4042
125. Vera JC, Rivas CI, Fischbarg J, Golde DW (1993) Mammalian facilitative hexose transporters mediate the transport of dehydroascorbic acid. Nature 364:79–82
126. Virtue MA, Furne JK, Nuttall FQ, Levitt MD (2004) Relationship between GHb concentration and erythrocyte survival determined from breath carbon monoxide concentration. Diabetes Care 27: 931–935
127. Wadzinski BE, Shanahan MF, Seamon KB, Ruoho AE (1990) Localization of the forskolin photolabelling site within the monosaccharide transporter of human erythrocytes. Biochem J 272: 151–158
128. Warszawski S, Dekel E, Campeotto I, Marshall JM, Wright KE, Lyth O, Knop O, Regev-Rudzki N, Higgins MK, Draper SJ, Baum J, Fleishman SJ (2020) Design of a basigin-mimicking inhibitor targeting the malaria invasion protein RH5. Proteins 88: 187–195
129. Weber YG, Storch A, Wuttke TV, Brockmann K, Kempfle J, Maljevic S, Margari L, Kamm C, Schneider SA, Huber SM, Pekrun A, Roebling R, Seebohm G, Koka S, Lang C, Kraft E, Blazevic D, Salvo-Vargas A, Fauler M, Mottaghy FM, Münchau A, Edwards MJ, Presicci A, Margari F, Gasser T, Lang F, Bhatia KP, Lehmann-Horn F, Lerche H (2008) GLUT1 mutations are a cause of paroxysmal exertion-induced dyskinesias and induce hemolytic anemia by a cation leak. J Clin Invest 118:2157–2168
130. Weed RI, LaCelle PL, Merrill EW (1969) Metabolic dependence of red cell deformability. J Clin Invest 48:795–809
131. Wei M, Lu L, Sui W, Liu Y, Shi X, Lv L (2018) Inhibition of GLUTs by WZB117 mediates apoptosis in blood-stage Plasmodium parasites by breaking redox balance. Biochem Biophys Res Commun 503:1154–1159
132. Whitfield CF, Rannels SR, Morgan HE (1974) Acceleration of sugar transport in avian erythrocytes by catecholamines. J Biol Chem 249:4181–4188
133. WIDDAS WF (1953) An apparatus for recording erythrocyte volume changes in permeability studies. J Physiol 120:20–21P
134. Widdas WF (1988) Old and new concepts of the membrane transport for glucose in cells. Biochim Biophys Acta 947:385–404
135. WILBRANDT W, GUENSBERG E, LAUENER H (1947) Not available. Helv Physiol Pharmacol Acta 5:C20–C22
136. Wilson C, Peterson SW (1986) Insulin receptor processing as a function of erythrocyte age. A kinetic model for down-regulation. J Biol Chem 261:2123–2128
137. Yan Q, Lu Y, Zhou L, Chen J, Xu H, Cai M, Shi Y, Jiang J, Xiong W, Gao J, Wang H (2018) Mechanistic insights into GLUT1 activation and clustering revealed by super-resolution imaging. Proc Natl Acad Sci U S A 115:7033–7038
138. Yang H, Wang D, Engelstad K, Bagay L, Wei Y, Rotstein M, Aggarwal V, Levy B, Ma L, Chung WK, De Vivo DC (2011) Glut1 deficiency syndrome and erythrocyte glucose uptake assay. Ann Neurol 70:996–1005
139. Zhang JZ, Hayashi H, Ebina Y, Prohaska R, Ismail-Beigi F (1999) Association of stomatin (band 7.2b) with Glut1 glucose transporter. Arch Biochem Biophys 372:173–178
140. Zhang JZ, Abbud W, Prohaska R, Ismail-Beigi F (2001) Overexpression of stomatin depresses GLUT-1 glucose transporter activity. Am J Phys Cell Physiol 280:C1277–C1283
141. Zhu Y, Paszty C, Turetsky T, Tsai S, Kuypers FA, Lee G, Cooper P, Gallagher PG, Stevens ME, Rubin E, Mohandas N, Mentzer WC (1999) Stomatocytosis is absent in "stomatin"-deficient murine red blood cells. Blood 93:2404–2410
142. Zipper H, Mawe RC (1972) The exchange and maximal net flux of glucose across the human erythrocyte. I. the effect of insulin, insulin derivatives and small proteins. Biochim Biophys Acta 282: 311–325
143. Zottola RJ, Cloherty EK, Coderre PE, Hansen A, Hebert DN, Carruthers A (1995) Glucose transporter function is controlled by transporter oligomeric structure. A single, intramolecular disulfide promotes GLUT1 tetramerization. Biochemistry 34:9734–9747

Pharmacological activation of PIEZO1 in human red blood cells prevents Plasmodium falciparum invasion.

Lohia, R., Allegrini, B., Berry, L., Guizouarn, H., Cerdan, R., Abkarian, M., ... & Wengelnik, K. (2023). *Cellular and Molecular Life Sciences*, *80*(5), 124.

Contexte :

C’est un article réalisé en collaboration avec Kai Wengelnik. Nous avons étudié ici l’effet du Yoda1 et par extension, l’effet de l’activation de PIEZO1, sur l’infection des GR humain par le parasite *Plasmodium falciparum*.

Cellular and Molecular Life Sciences (2023) 80:124
https://doi.org/10.1007/s00018-023-04773-0

ORIGINAL ARTICLE

Pharmacological activation of PIEZO1 in human red blood cells prevents *Plasmodium falciparum* invasion

Rakhee Lohia[1] · Benoit Allegrini[2] · Laurence Berry[1] · Hélène Guizouarn[2] · Rachel Cerdan[1] · Manouk Abkarian[3] · Dominique Douguet[4] · Eric Honoré[4] · Kai Wengelnik[5]

Received: 3 February 2023 / Accepted: 30 March 2023

Abstract

An inherited gain-of-function variant (E756del) in the mechanosensitive cationic channel *PIEZO1* was shown to confer a significant protection against severe malaria. Here, we demonstrate in vitro that human red blood cell (RBC) infection by *Plasmodium falciparum* is prevented by the pharmacological activation of PIEZO1. Yoda1 causes an increase in intracellular calcium associated with rapid echinocytosis that inhibits RBC invasion, without affecting parasite intraerythrocytic growth, division or egress. Notably, Yoda1 treatment significantly decreases merozoite attachment and subsequent RBC deformation. Intracellular Na^+/K^+ imbalance is unrelated to the mechanism of protection, although delayed RBC dehydration observed in the standard parasite culture medium RPMI/albumax further enhances the resistance to malaria conferred by Yoda1. The chemically unrelated Jedi2 PIEZO1 activator similarly causes echinocytosis and RBC dehydration associated with resistance to malaria invasion. Spiky outward membrane projections are anticipated to reduce the effective surface area required for both merozoite attachment and internalization upon pharmacological activation of PIEZO1. Globally, our findings indicate that the loss of the typical biconcave discoid shape of RBCs, together with an altered optimal surface to volume ratio, induced by PIEZO1 pharmacological activation prevent efficient *P. falciparum* invasion.

Keywords Erythrocyte · Mechanosensitive ion channel · Piezo1 · Malaria · *Plasmodium falciparum*

Abbreviations

GOF	Gain-of-function
Hb	Haemoglobin
PKG	Protein kinase G
RBC	Red blood cell
SCD	Sickle cell disease

✉ Eric Honoré
honore@ipmc.cnrs.fr

✉ Kai Wengelnik
kai.wengelnik@umontpellier.fr

1 LPHI, University of Montpellier, CNRS UMR5294, Montpellier, France

2 iBV, Université Côte d'Azur, CNRS, INSERM, Nice, France

3 Centre de Biologie Structurale, CNRS UMR5048, INSERM U1054, University of Montpellier, Montpellier, France

4 IPMC, University Côte d'Azur, CNRS, INSERM, UMR7275, Labex ICST, Valbonne, France

5 LPHI, University of Montpellier, CNRS UMR5294, INSERM, Montpellier, France

Introduction

Malaria is caused by the cyclic infection and destruction of red blood cells (RBCs) by a protozoan parasite of the genus *Plasmodium*, the most deadly form being caused by *P. falciparum*. There is substantial variability in susceptibility to malaria in the human population and, in numerous cases this has been attributed to particular features of human RBCs. Sickle cell anaemia, caused by a point mutation in haemoglobin (Hb) leading to the production of HbS, is the most well-known condition conferring resistance to malaria [1]. Although having a drastic impact on well-being and survival, there is still continuous selection for these mutations in malaria endemic countries [2]. In addition, many other variations in RBC proteins and physiology were suggested to be linked to reduced susceptibility to malaria, including RBC dehydration caused by a variety of clinical or experimental conditions [3, 4].

PIEZO1 and PIEZO2 are mechanosensitive non-selective cationic channels, permeable to Na^+, K^+ and Ca^{2+} [5]. PIEZO1 is activated by a variety of mechanical stress, including local membrane stretch, whole cell indentation

Published online: 18 April 2023

or shear stress [6]. PIEZO1 and PIEZO2 homologs, which share 43% amino acid sequence identity, are conserved during evolution from plants, worm, fly, fish to human [5], while no orthologue is present in *Plasmodium* species or other apicomplexan parasites [7]. PIEZO1 and PIEZO2 are differentially expressed across different tissues and cell types, with only PIEZO1 present in RBCs [5, 8]. PIEZO1 and PIEZO2 are made of a remarkably large homotrimeric complex (about 900 kDa, including 114 transmembrane segments) with a curved shape, similar to a three blades propeller (or a triskelion) [9–13]. PIEZO1 curves the membrane, forming an inverted cone that reversibly flattens upon activation in response to mechanical stimulation [10, 14, 15].

Gain-of-function (GOF) *PIEZO1* mutations causing a delayed inactivation (i.e., prolonged opening), are linked to hereditary xerocytosis, a mild haemolytic anaemia associated with RBC dehydration [16–19]. Remarkably, mice carrying a xerocytosis mutation (mR2482H) either in all hematopoietic cells or specifically in erythrocytes show RBC dehydration and are protected from cerebral malaria caused by the rodent-specific parasite *Plasmodium berghei* [20, 21]. *Piezo1* R2482H mice show no damage of the blood–brain barrier, while wild type mice succumb to cerebral malaria leading to death within 5–7 days post infection. Along this line, another GOF *PIEZO1* variant (E756del), present in about 1/3 of the black population from Western Africa, also confers a significant resistance against severe malaria [20, 21]. Recently, it was confirmed that in children from Gabon, the *PIEZO1* E756del variant is strongly associated with protection against severe malaria in heterozygotes, independent of the protection conferred by the sickle cell trait (HbS) [21]. However, another report found no significant protection of the *PIEZO1* E756del variant against severe malaria in a Ghanaian study [22]. Whether or not the protective effect of *PIEZO1* E756del is linked to RBC dehydration and a decreased intracellular growth of *P. falciparum* is also disputed [20, 21, 23]. Moreover, additional evidence indicates that the beneficial effect of *PIEZO1* R2482H is not solely due to an effect on RBCs, but also involves the immune system [20]. *PIEZO1* E756del has also been shown to lead to iron overload by increasing RBC turnover through phagocytosis by macrophages, although whether or not this effect may be related to malaria protection is unknown [20, 24]. All together these data indicate that PIEZO1 GOF is protective against severe malaria, although the mechanisms implicated still remain unclear and controversial [20, 21, 23].

The pharmacology of PIEZO1 is still at its early ages. Yoda1 was identified by a high throughput screening of small molecules as an activator of mouse and human PIEZO1, without affecting PIEZO2 [25]. When analyzed in HEK 293T cells expressing either mouse or human PIEZO1, Yoda1 (in the micromolar range) causes enhanced opening of PIEZO1 in response to mechanical stimulation, together with a delayed inactivation [25]. Yoda1 acts as an activator of PIEZO1 (not as a true opener) by shifting its pressure-effect curve towards lower pressure values [25]. Two additional compounds Jedi1 and Jedi2 (chemically unrelated to Yoda1) similarly activate PIEZO1, although at a concentration in the millimolar range [26].

In mouse RBCs, Yoda1 causes a robust increase in intracellular calcium, without the requirement of a mechanical stimulation [8]. Notably, addition of 15 µM Yoda1 to RBCs leads to a dramatic change in cell shape, inducing echinocytosis within 30 s [8]. This change in cell shape is strictly dependent on the presence of Piezo1 since RBCs from knock out mice are not altered by Yoda1 [8]. Yoda1 induces mouse RBC dehydration through the secondary activation of the Ca^{2+}-dependent Gardos (KCNN4/KCa3.1) channel and consequent water loss by aquaporins [8, 27].

Although the link between inherited *PIEZO1* GOF variants and resistance against malaria is now well established, the mechanism(s) of protection still remain elusive and controversial [20, 21, 23]. In this study, taking advantage of an in vitro model of human RBC infection by *P. falciparum*, we aimed at exploring the antimalarial activity of PIEZO1 pharmacological activators and at determining which step of the infection cycle is PIEZO1 sensitive. Altogether, our findings show that the in vitro pharmacological activation of PIEZO1 in human RBCs prevents parasite invasion. PIEZO1 activation by Yoda1 or Jedi2 deforms the RBC membrane (echinocytosis) causing a loss of typical RBC discoid shape, anticipated to prevent merozoite attachment and internalization. Secondarily, RBC dehydration (that is delayed in the standard RPMI/albumax parasite culture medium) further contributes to enhance protection against malaria, as previously observed for the *PIEZO1* E756del GOF variant [4, 20, 21, 23]. Thus, our findings indicate that both membrane deformation and RBC dehydration contribute to decrease efficient *P. falciparum* invasion.

Results

The PIEZO1 activator Yoda1 increases intracellular calcium and causes transient echinocyte formation in human RBCs

We evaluated in vitro the effect of PIEZO1 activation by Yoda1 on human RBC infection by the malaria parasite *Plasmodium falciparum*. Parasite cultures are classically performed in a complex medium consisting of RPMI 1640 supplemented with albumax, allowing an optimal infection and host/parasite survival [28–30]. We first monitored intracellular calcium in Fluo4-AM loaded human RBCs in response to increasing concentrations of the PIEZO1 activator Yoda1 in the RPMI culture medium [8]. The calcium

response was biphasic at lower Yoda1 concentrations with an early transient component followed by a plateau, while maintained at higher concentrations similar to the calcium ionophore A23187 response (Fig. 1a). Taking advantage of video microscopy, we examined the change in RBC cell shape upon Yoda1 addition at increasing concentration of Yoda1. Human RBCs became echinocytic in a dose-dependent manner and within less than 30 s with 5 µM Yoda1 (Fig. 1b–d, Videos 1, 2, 3). We also followed the development of RBC morphology over more prolonged periods of time (up to 3 h) in the presence of Yoda1. Video-microscopy revealed that Yoda1 treated RBCs changed their shape over time from echinocytes to rounded cells (discocytes or stomatocytes) within about 2 h at all concentrations tested (Supplemental Fig. 1, Video 4).

Scanning electron microscopy images of RBC in the presence of 5 µM Yoda1 for 10 min further examined in detail the changes in cell shape (Fig. 1e, f). RBC readily changed to echinocytes in the presence of Yoda1 characterized by many tiny outward spikes. These changes were fully reversible upon wash out of Yoda1 (Fig. 1g–j).

Thus, our findings indicate that in the standard parasite RPMI culture medium (only containing 0.42 mM calcium), Yoda1 causes an increase in intracellular calcium associated with transient echinocyte formation. Notably, prolonged incubations of RBC cultures with Yoda1 did not induce cell lysis, with the exception of a mild haemolytic activity detected at the highest concentration tested (10 µM) after 24 h incubation (Supplemental Fig. 2). Accordingly, we used concentrations of Yoda1 ranging from 1 to 5 µM for RBC infection experiments described below.

Yoda1 induces delayed human RBC dehydration in the standard RPMI/albumax parasite culture medium

Next, we investigated whether RBC dehydration occurs in the RPMI medium, as previously reported for mouse RBCs cultured in a saline solution containing 2 mM calcium [8]. We used osmotic fragility assays to quantify RBC dehydration [8]. A leftward shift of the osmotic fragility curve indicates RBC dehydration. RBCs were cultured in the standard RPMI/albumax culture medium (containing 0.42 mM calcium) for up to 24 h with 1 µM Yoda1 to determine their osmotic fragility over time (Fig. 2a–e). Dehydration was observed in the presence of 1 µM Yoda1, but only after incubations of 6 h or longer. These results were confirmed using an independent assay based on the determination of intracellular water content (Fig. 2f). For comparison, when RBCs were incubated in a saline solution containing 2 mM calcium [8], significant dehydration was already observed for a 30 min long incubation with 1 µM Yoda1 (Supplemental Fig. 3).

In addition, we analyzed the intracellular sodium and potassium content of human RBCs in RPMI/albumax treated with 1 µM Yoda1 over a period of 24 h (Fig. 2g, h). At 1 µM Yoda1 an excess loss of K^+ with respect to a gain in Na^+ was consistently observed along with progressive dehydration over time.

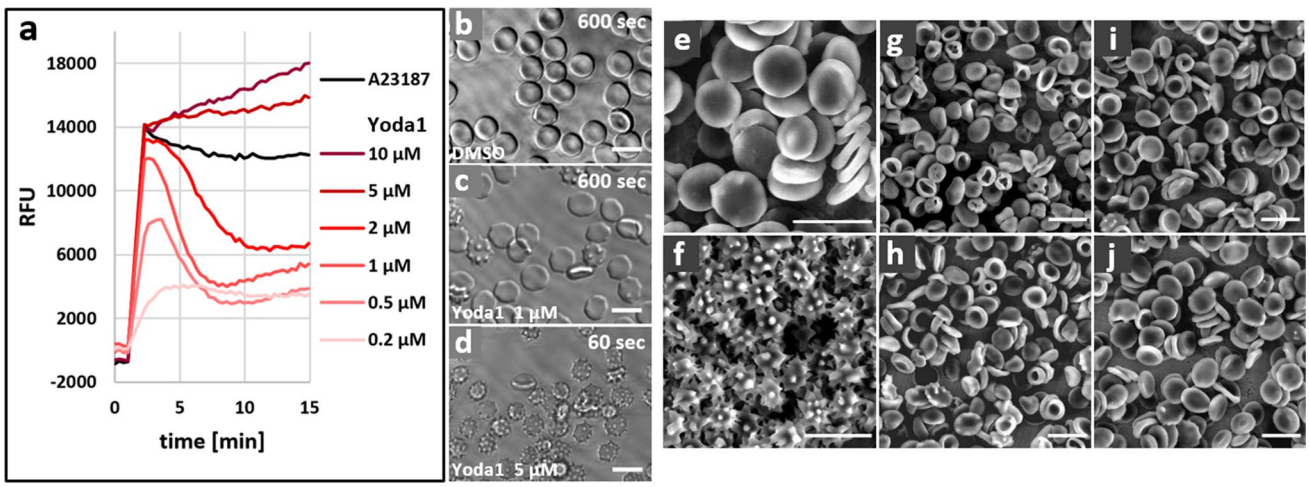

Fig. 1 Echinocytic effect of the PIEZO1 activator Yoda1 on human RBCs. **a** Kinetic analysis of the calcium signal elicited by the addition of Yoda1 at the indicated concentrations in RPMI medium. RBCs were loaded with Fluo4-AM and the calcium ionophore A23187 (2 µM) was used as positive control. Background readings of DMSO control samples were subtracted ($n=4$). **b** Morphological changes of RBCs over 10 min upon addition of 1 µM and 5 µM Yoda1. Stills of video microscopy (shown in supplemental data) for DMSO control (**b**, video 1) and 1 µM Yoda1 (**c**, video 2) after 10 min, and after 1 min for 5 µM Yoda1 (**d**, video 3). **e–j** Scanning electron microscopy images of RBCs. **e** DMSO mock treated, **f** in the presence of 5 µM Yoda1 after 10 min, **g–j** after treatment with 5 µM Yoda1 for 10 min, followed by washes and incubation in complete medium at 37 °C for 30 min (**g**), 2 h (**h**), 6 h (**i**), and 24 h (**j**)

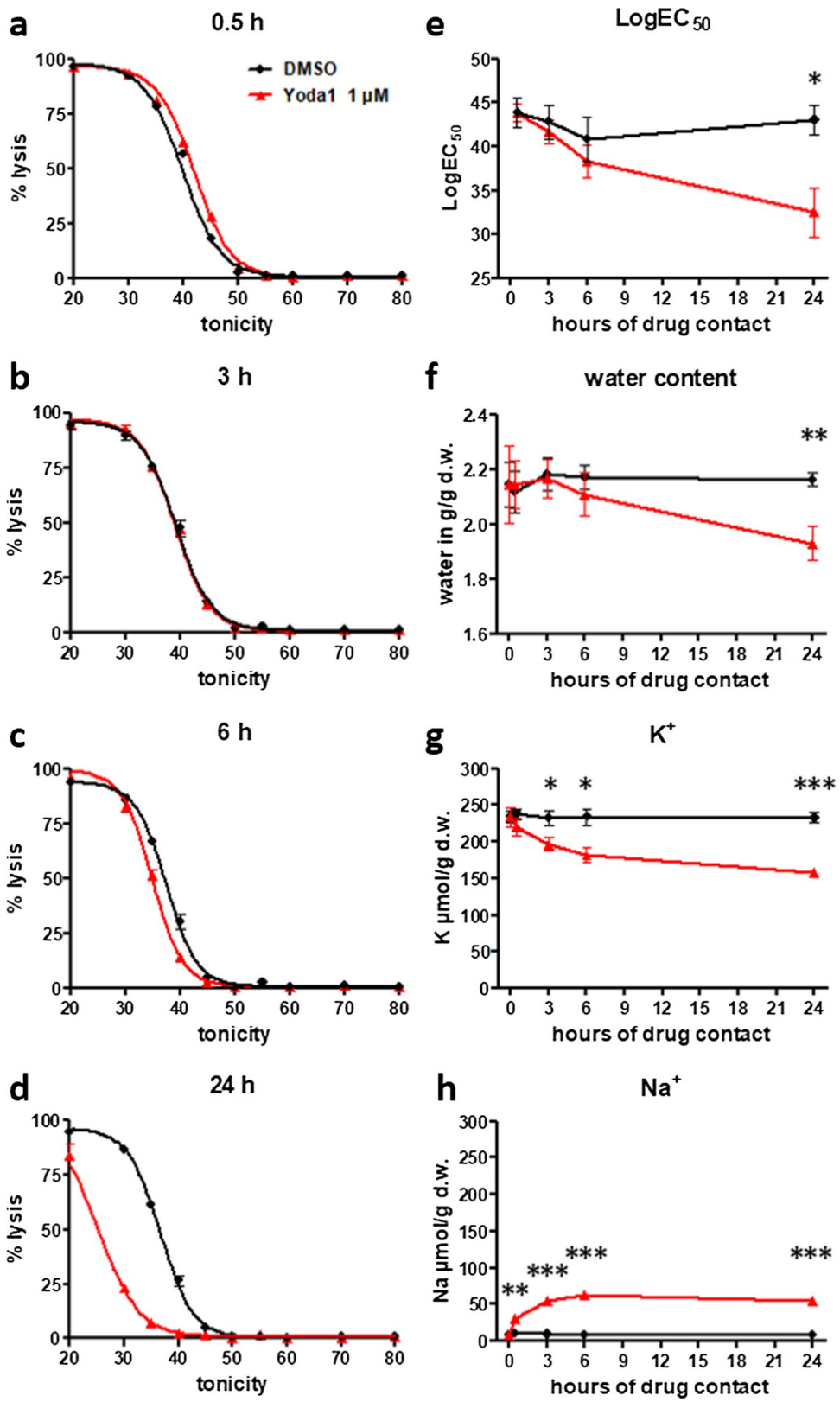

Fig. 2 The hydration- and cation status of Yoda1 treated human RBCs over time. **a–d** Osmotic fragility assays were performed on human RBCs that had been treated for the indicated times (0.5–24 h) at 37 °C in complete medium RPMI/albumax with 1 µM Yoda1 or DMSO vehicle ($n=4$). **e** Summary of the RBC hydration status over time. The $LogEC_{50}$ values were calculated form the curves in **a**–**d**. Shown are mean ± SEM, $n=4$. **f** Determination of the hydration status over time of treatment in RPMI/albumax ($n=3$). Intracellular K^+ (**g**) and Na^+ content (**h**) for RBC cultures that had been incubated for the indicated time in the presence of 1 µM Yoda1 or DMSO vehicle, $n=3$. Graph **e** to **h** show the mean ± SEM. $^*p<0.05$, $^{**}p<0.01$, $^{***}p<0.0001$

Thus, in RPMI a progressive change in Na^+ and K^+ content associated with delayed RBC dehydration is observed in the presence of 1 µM Yoda1 after an incubation period for more than 6 h, probably related to the low extracellular calcium concentration (0.42 mM) of the RPMI/albumax medium.

Low dose of Yoda1 prevents RBC invasion by *P. falciparum* merozoites

We investigated whether or not chemical activation of PIEZO1 with Yoda1 may influence *Plasmodium falciparum* infection of human RBCs using the standard parasite culture medium. Synchronized ring stage parasites were incubated for 60 h in the presence of different concentrations of Yoda1. All assays with parasites were performed in the standard RPMI/albumax parasite culture medium [29]. Notably, a dose-dependent decrease in parasitemia was observed with an IC_{50} value of about 500 nM Yoda1 (Fig. 3a). The protective effect of 1 µM Yoda1 was fully reversible upon wash, indicating that the protection against infection was not due to RBC damage (Fig. 3a, inset).

The observed reduction in parasitemia caused by Yoda1 could be due to selective lysis of infected RBCs, reduced growth and development of parasites, interference

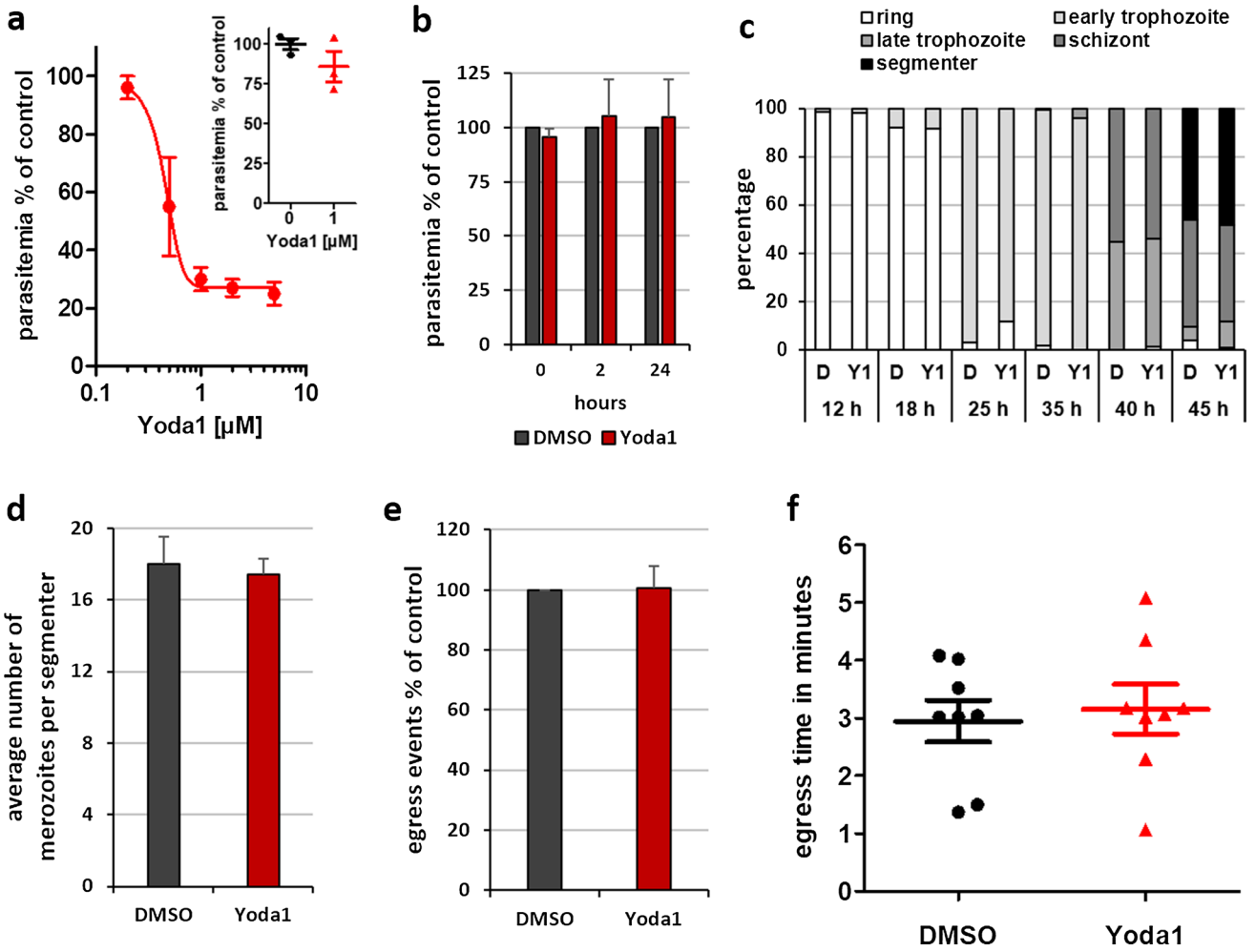

Fig. 3 Pharmacological activation of PIEZO1 reduces *P. falciparum* parasitemia but does not affect intra-erythrocytic growth and development in vitro. **a** Synchronized ring stage parasite cultures in RPMI/albumax were incubated for 60 h in the continuous presence of Yoda1 at different concentrations before determining the parasitemia by FACS analysis ($n=5$). The inset shows the reversibility of inhibition with 1 µM Yoda1. Uninfected RBCs were first pre-treated in RPMI/albumax with 1 µM Yoda1 for 10 min and then washed extensively before adding purified schizont/segmenter stage infected RBCs for culture in complete medium. Parasitemia was determined after incubation for 18 h ($n=3$). **b** Yoda1 (5 µM) was added to ring stage parasites (0–4 h post invasion) and parasitemia determined after 2 and 24 h incubation ($n=3$). **c** The progression through the intra-erythrocytic development in the presence of 5 µM Yoda1 was followed by Diff-Quick-stained thin smears. At 40 h, cultures were treated with PKG inhibitor C2 to block egress ($n=3$). **d** The number of merozoites formed per segmenter was counted on stained thin smears after 45 h culture in the presence of 5 µM Yoda1. Egress had been blocked by C2 treatment ($n=2$). **e** Relative number and **f** timing of egress events were determined from video microscopy analysis. Purified segmenter-stage parasites had been blocked before egress with C2. Upon removal of inhibitor by a rapid wash, parasites were added to RPMI/albumax containing 5 µM Yoda1 or DMSO vehicle and monitored in parallel allowing comparison of the total number of egress events and the relative time to first egress (after start of the video acquisition) between the two conditions ($n=2$). **a**–**f** Shown are mean values and SEM

with parasite egress from the infected RBC, reduction of RBC invasion, or to a combination of these effects. We observed no reduction in parasitemia when synchronised ring stage parasites were incubated with Yoda1 for 24 h (Fig. 3b), arguing against Yoda1-induced selective lysis of infected RBCs. Moreover, progression through the different stages of parasite maturation was not affected in the presence of Yoda1 (Fig. 3c). The same number of daughter cells were formed in the presence or absence of Yoda1 (Fig. 3d). Altogether, these results show that intracellular parasite development is not affected by Yoda1, indicating that either parasite egress or RBC invasion was affected.

We observed parasite egress by live microscopy in the presence of Yoda1. Highly synchronised late-stage parasite-infected RBCs were purified and allowed to mature to the segmenter stage (when daughter merozoites are fully formed and are close to egress) in the presence of the protein kinase G (PKG) inhibitor C2; this treatment reversibly blocks parasite egress from the host RBC [31]. The block of egress was then lifted in the presence of Yoda1 or of vehicle and both samples were observed in parallel by live microscopy. Counting the number of egress events (Fig. 3e) and determining the relative time of the first egress event revealed that there was no difference between the two samples (Fig. 3f). Thus, Yoda1 inhibits invasion of human RBCs by *P. falciparum*, but does not interfere with parasite growth or egress.

Yoda1 impairs parasite attachment to the RBC membrane

To analyze in closer detail which step in parasite invasion is impaired by Yoda1 we explored the initial cellular events occurring upon invasion of control and Yoda1-treated RBCs by *P. falciparum* merozoites using direct observation by video microscopy. Highly synchronized purified segmenter stage parasites were first blocked before egress by treatment with C2. Upon washing off the inhibitor, the infected RBCs were mixed with RBCs that had been pre-treated with Yoda1 or DMSO and then washed. From the analysis of the videos, we quantified the following events that occur in chronological order: (a) the number of RBCs that came close to and likely came in contact with released merozoites; (b) RBCs that deformed upon merozoite contact; (c) invasion events; and (d) echinocyte formation of RBCs as a consequence of completed parasite invasion (Fig. 4a, b, Video 5, Video 6). We observed a major reduction in the number of early RBC deformation, merozoite invasion and echinocyte formation in the presence of Yoda1.

We also determined whether or not the upstream event of merozoite attachment to RBCs would also be modified by Yoda1 treatment. We took advantage of the small molecule inhibitor of actin polymerisation, cytochalasin D (cytD) to allow attachment of merozoites to RBCs, while preventing parasite invasion [32, 33]. In the presence of cytD, pre-treatment of RBCs with Yoda1 followed by washes and recovery for 5 h resulted in a significant decrease in the attachment

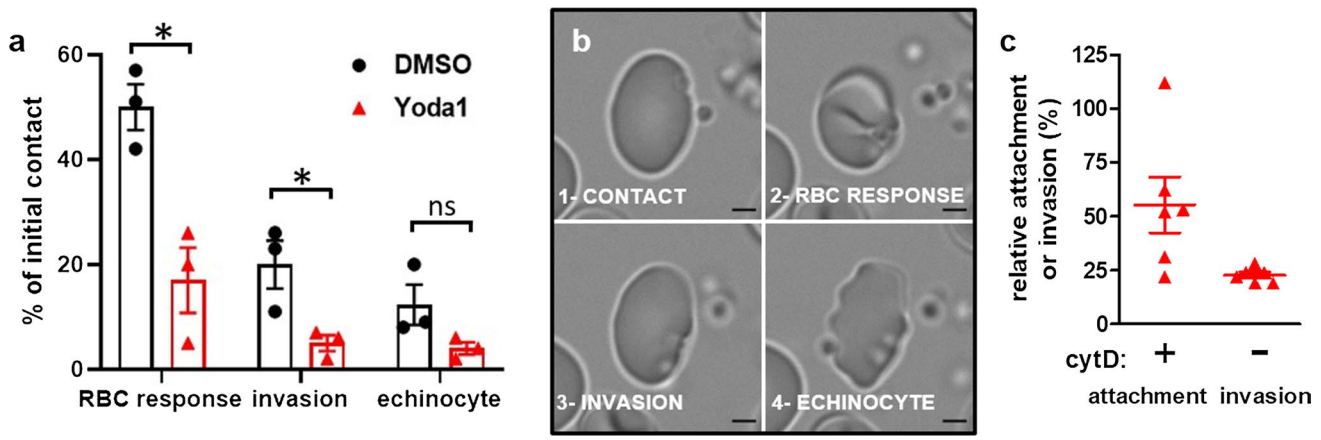

Fig. 4 Effect of Yoda1 on merozoite attachment and invasion. **a** Quantification of invasion events in the presence and absence of Yoda1. Highly synchronous purified parasites were mixed with RBC preparations that had been pre-treated for 10 min with 5 µM Yoda1 or DMSO 5 h prior to the experiment. Events subsequent to egress were observed by video microscopy and classified. Data are expressed with respect to the observed initial possible contact of merozoites with RBCs. Shown are the mean ± SEM of three independent experiments. *$p < 0.05$, *ns* not significant. **b** Still images of one RBC (DMSO condition, taken from video 5) representing the events that were quantified: merozoite contact, RBC response by deformation, invasion, and echinocyte formation. Scale bar 2 µm. Supplemental video 6 represents an example of the poor reponse of Yoda1-pretreated RBCs upon contact with merozoites. **c** Attachment of merozoites to RBCs pre-treated with 5 µM Yoda1 was quantified in the presence of 1 µM cytD and expressed as percentage of mock-treated control RBCs. In the presence of Yoda1 and in the absence of cytD we observed the reduction in parasitemia as described in Fig. 3A ($n = 6$, mean ± SEM, $p < 0.0001$ for both conditions)

of the parasite (Fig. 4c). Treatment with heparin that blocks adhesive events likely through interaction with the parasite invasion ligand MSP1 [34, 35], completely abolished attachment and invasion and was used as a control. Thus, invasion by merozoites appears to be blocked at the initial steps of merozoite attachment to the RBC by Yoda1.

Protection conferred by Yoda1 against *P. falciparum* invasion is independent of an altered intracellular Na^+/K^+ balance in human RBCs

We investigated whether or not changes in intracellular Na^+ and/or K^+ concentrations might contribute to the antimalarial properties of Yoda1. We experimentally modified the intracellular Na^+ and K^+ content of RBCs by pre-treatment in saline solutions with varying Na^+/K^+ concentrations in the presence of the ionophore nystatin (Fig. 5a). In the presence of 75 mM Na^+/75 mM K^+ and nystatin, Na^+ was elevated while K^+ was decreased, similar to the Yoda1 condition (Fig. 2g, h). This effect was enhanced with the 110 mM Na^+/40 mM K^+ and nystatin solution. These changes in intracellular cationic concentration persisted after a washout of 90 min in RPMI (Fig. 5a), i.e., around the time when RBCs would be invaded when cultured in the presence of purified parasites. Importantly, *P. falciparum* infection was not affected by the nystatin treatment with these modified ionic solutions (Fig. 5b), indicating that the antimalarial activity of Yoda1 is not mimicked by experimental conditions that similarly affect the intracellular Na^+/K^+ balance.

RBC dehydration contributes to Yoda1 mediated protection against *P. falciparum* infection

Previous findings indicated that dehydrated RBCs are less susceptible to *Plasmodium* infection [4, 20, 21, 23]. Normal RBCs that had been experimentally dehydrated or RBCs from donors with known hereditary conditions that result in dehydrated RBCs (including sickle cell disease) are greatly protected against *P. falciparum* infection. In the same line, Yoda1, as well as GOF *PIEZO1* mutations (slowing down channel inactivation) cause RBC dehydration in a defined minimal medium and was shown to confer resistance against cerebral malaria [8, 20, 23, 27]. Thus, we investigated to which extent RBC dehydration contributes to the antimalarial activity of Yoda1 in the RPMI/albumax medium [29].

We evaluated whether Yoda1-induced reduction in parasitemia depends on the duration of Yoda1 (1 µM) exposure, previously shown to induce delayed RBC dehydration (Fig. 2e, f). Yoda1 was added to RBC cultures in RPMI/albumax medium either 0.5, 3, or 24 h before starting the experiment by adding purified late stage parasites. Parasitemia was determined as before after 18 h and compared to mock-treated control cells (Fig. 5c).

The reduction in parasitemia initially observed after 30 min Yoda1 treatment of RBCs became significantly more pronounced for longer durations of incubation (Fig. 5c). Thus, the progressive dehydration of RBCs over time upon treatment with 1 µM Yoda1 (Fig. 2e, f) is anticipated to enhance the antimalarial effect of PIEZO1 activation [4, 20,

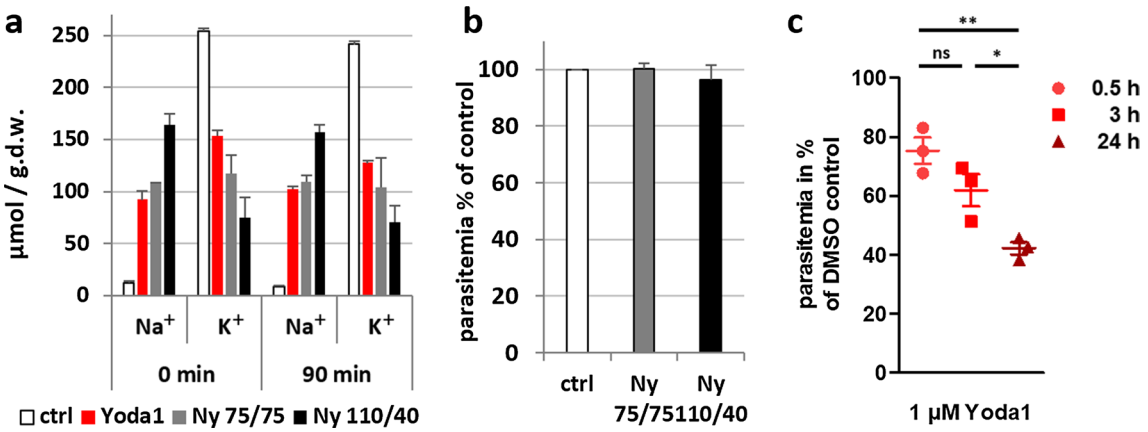

Fig. 5 Intracellular Na^+/K^+ balance in human RBCs upon Yoda1 treatment and effect on *P. falciparum* infection. **a** Na^+ and K^+ content was determined upon standard 10 min treatment with 5 µM Yoda1 either directly after treatment and washes or after further 90 min incubation in RPMI/albumax medium at 37 °C. Treatment of RBCs with the ionophore nystatin in saline solution containing either 75 mM Na^+ and 75 mM K^+ (Ny 75/75) or 110 mM Na^+ and 40 mM K^+ (Ny 110/40). The resulting intracellular Na^+ and K^+ concentrations were determined directly after washing and after a further incubation for 90 min at 37 °C in RPMI. **b** RBCs treated with nystatin in the two saline solutions were used for standard invasion assays with purified highly synchronous late-stage parasites. Results are expressed as percentage of untreated RBC controls ($n = 3$, mean ± SEM). **c** Effect of prolonged treatment with Yoda1 on parasite invasion. RBCs in RPMI/albumax medium were treated with 1 µM Yoda1 for 0.5, 3 or 20 h before purified late stage parasites were added. After 18 h of culture ring-stage parasitemia was determined and expressed as percentage of DMSO-treated controls. Results of three independent experiments performed in duplicates are shown (mean ± SEM). $*p < 0.05$, $**p < 0.01$, *ns* not significant

21, 23]. It should also be noted that RBCs recover a discoid shape after 3–24 h long Yoda1 incubation (Fig. 1e–j). However, in our standard assay conditions, the majority of parasite egress events and subsequent RBC invasion would have taken place within the first 3 h of the experiment, i.e., during the period where we did not measure detectable RBC dehydration. Thus, it is likely that additional mechanisms, besides RBC dehydration, may contribute to the observed reduction in parasitemia upon PIEZO1 activation by Yoda1.

Antimalarial effect of the PIEZO1 activator Jedi2

We investigated whether or not the antimalarial protection was similarly observed for the PIEZO1 activator Jedi2 that is chemically unrelated to Yoda1 [26]. The small molecule Jedi2 activates PIEZO1 at concentrations in the millimolar range [26]. Our calcium measurements indicated that Jedi2 elicited an increase in intracellular calcium, although weaker than Yoda1 (Supplemental Fig. 4). Similarly to Yoda1, in the presence of Jedi2, RBCs rapidly became echinocytes (Fig. 6a), in the absence of any haemolytic activity (Supplemental Fig. 2). In RPMI culture medium, we observed a time-dependent dehydration of RBCs with 1 mM Jedi2 similar to 1 µM Yoda1 (Figs. 2, 6b, Supplemental Fig. 5). This dehydration was confirmed by measuring RBC water content (Fig. 6c). Jedi2 treatment, similar to Yoda1 (Fig. 2g, h), also affected the intracellular Na^+ and K^+ balance (Fig. 6d, e). Again a more important loss of K^+ with respect to a gain in Na^+ could explain the observed dehydration after prolonged incubation.

When analyzed on parasite cultures, Jedi2 significantly and reversibly reduced *P. falciparum* parasitemia, similarly to Yoda1 (Fig. 6f, Jedi2). Washing out Jedi2 prior to infection by parasites completely re-established their competence for parasite invasion, as previously observed for 1 µM Yoda1 (Fig. 6f, Jedi wash; Fig. 3a inset).

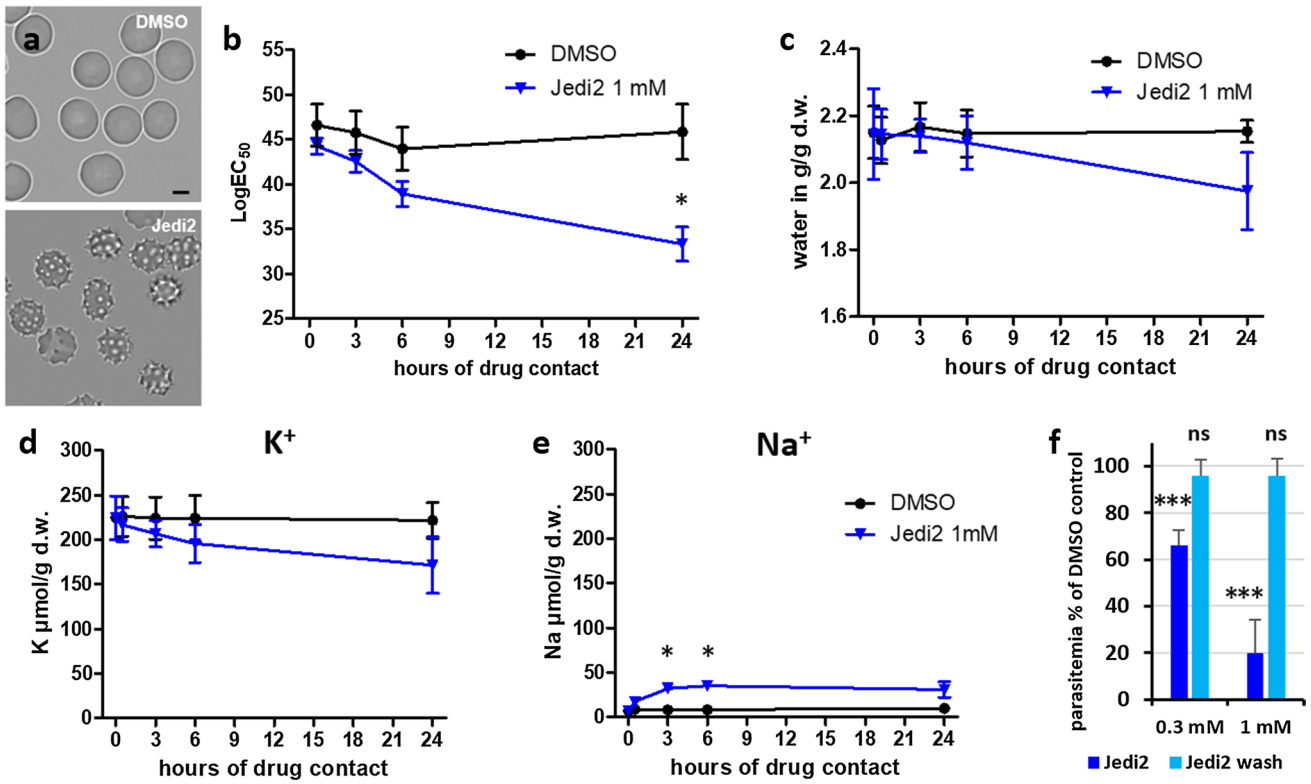

Fig. 6 Physiological effects of PIEZO1 activator Jedi2 on human RBCs. **a** Cell shape of the cells at 4 min after addition of compounds (DMSO vehicle and 1 mM Jedi2). Scale bar = 5 µm. **b** Hydration status of RBCs was determined by osmotic fragility assays (Supplemental Fig. 4) after the indicated time of contact of cells with 1 mM Jedi2 in RPMI/albumax medium ($n = 4$). **c** Quantification of hydration status ($n = 2$). **d**, **e** Intracellular K^+ and Na^+ concentrations for RBC cultures that had been incubated for the indicated time in the presence of 1 mM Jedi2 in RPMI/albumax ($n = 2$). **f** The effect of Jedi2 on parasitemia was observed either in the continuous presence of Jedi2 in complete medium (RPMI/albumax), or after a pre-treatment for 10 min in RPMI followed by extensive washes (wash) before adding synchronized schizont infected RBCs for culture in complete medium. Parasitemia was determined after incubation for 18 h and expressed as a percentage of mock-treated controls ($n = 3$). All graphs show mean ± SEM. $^*p < 0.05$, $^{***}p < 0.0001$, ns or without indication = not significant

Altogether, these findings indicate that the chemically unrelated PIEZO1 activators Yoda1 and Jedi2 similarly prevent in vitro parasitemia of human RBCs.

Discussion

Recent work demonstrates that polymorphisms in the *PIEZO1* gene causing a channel GOF, with a slower inactivation (i.e., increased channel opening), are associated with a protective effect against severe malaria both in humans and in a xerocytosis mouse model [20, 21]. However, the PIEZO1-dependent mechanisms at play conferring the resistance to severe malaria remain debated [20, 21, 23]. Our study focuses on the in vitro pharmacological activation of PIEZO1 in human RBCs and its impact on invasion, growth and development of the malaria parasite *P. falciparum*.

We show that both Yoda1 and Jedi2 PIEZO1 activators [25, 26], have a strong inhibitory effect on parasitemia (in the low micromolar range for Yoda1), reminiscent of the observed reduced multiplication rates in mice carrying *PIEZO1* GOF mutations [20]. Yoda1 does not affect parasite growth or development within RBCs, nor parasite egress from the infected RBCs. However, invasion of RBCs by *Plasmodium* merozoites is potently inhibited by Yoda1. The chemically unrelated PIEZO1 activators Yoda1 and Jedi2, similarly inhibit *P. falciparum* parasitemia (although at different concentrations), suggesting a PIEZO1-dependent mechanism (of note, Piezo1 orthologues are not present in the malaria parasite [7]). Yoda1 induces a major imbalance in intracellular Na^+ and K^+ content associated with RBC dehydration, although it is not the primary protection mechanism against malaria. Instead, we provide evidence that Yoda1 inhibits merozoite attachment, in parallel with a dramatic change in RBC shape associated with echinocytosis and formation of numerous spiky membrane projections. Altogether, our in vitro findings further support a role for PIEZO1 in the host RBC contributing to the resistance against severe malaria in vivo conferred by a GOF mutation in PIEZO1 [20, 21]. However, in the case of PIEZO1 GOF variants, echinocytosis was only rarely observed and instead significant RBC dehydration occurred [, 20, 23]. In the present study, RBCs cultured in the standard RPMI/albumax medium only showed significant dehydration after 6 h long drug application, while most of the invasion events were observed to occur within 3 h after the addition of purified *P. falciparum* infected cells to RBCs. Merozoite invasion occurs within minutes of mixing with RBCs in RPMI medium and is fully completed within 30 min at 37 °C [36]. Previous work demonstrated that other molecules causing echinocytosis of human RBCs, including sodium fluoride and phospholipase A2 (presumably unrelated to PIEZO1 activation) similarly prevented *P. falciparum* invasion [37]. These findings, together with our own observations, indicate that loss of the typical discoid shape of RBCs prevents optimal invasion by the malaria parasite.

Sickle cell disease (SCD) has long been recognized to confer a significant protection against malaria [38, 39]. In hypoxic conditions, RBCs from individuals carrying the heterozygote mutation HbS become shaped like sickles or crescent moons. However, RBC invasion is not altered in such conditions [40]. Instead, various alternative mechanisms were implicated in the resistance to malaria in individuals carrying the sickle cell trait, including weakened cytoadherence of infected RBCs, impaired haemoglobin digestion and increased splenic phagocytosis [39, 41, 42]. Thus, both PIEZO1 pharmacological activation (as well as PIEZO1 gain-of-function mutations [20, 21]) and SCD [38, 39] cause a change in the shape of RBCs and confer a significant protection against malaria, although apparently through distinct mechanisms.

Previous studies demonstrated that GOF mutations in *PIEZO1* cause xerocytosis, a mild haemolytic anaemia [16–19]. RBC dehydration was shown in xerocytosis patients [17, 27], in asymptomatic human carriers of a *PIEZO1* E756del polymorphism [20], as well as in an engineered *Piezo1* mouse model of xerocytosis [8, 20]. RBC dehydration arises through PIEZO1 mediated calcium influx leading to activation of the calcium-dependent K^+ channel Gardos and efflux of K^+ ions accompanied by water loss via aquaporins [8]. However, our data revealed that under standard *P. falciparum* in vitro culture conditions (in RPMI/albumax, only containing 0.42 mM calcium), RBCs are not significantly dehydrated upon treatment with the PIEZO1 activators Yoda1 or Jedi2 during the first 6 h of drug application. Delayed dehydration in this specific culture medium is likely due to the low extracellular calcium concentration used. Thus, the early protection mediated by PIEZO1 activators against malaria infection (at least in the RPMI medium) does not appear to primarily depend on RBC dehydration. Nevertheless, we observed an increased protection of PIEZO1 opening as a function of the duration of drug application, in parallel with RBC dehydration. Thus, PIEZO1 activation in RBCs by Yoda1 or Jedi2 is anticipated to confer protection against malaria by two independent mechanisms, one involving a loss of discoid shape due to echinocytosis [37] and an additional mechanism involving RBC dehydration [4, 20, 23]. Invasion of RBCs by *P. falciparum* merozoites is a complex process that has mainly been considered from the point of view of the invading parasite (reviewed in [43, 44]). The sequential events for successful invasion are: (1) attachment of the merozoite to the RBC by binding to specific RBC surface proteins triggering waves of RBC deformation; (2) reorientation of the parasite resulting in the apical pole facing the RBC; (3) discharge of apical organelles (micronemes and rhoptries) leading to the formation of a

moving junction; (4) invasion by active movement of the parasite using the moving junction as a fixation point for the activity of a parasite actin-myosin motor, leading *in fine* to the formation of a parasitophorous vacuole in which the parasite will develop during its intraerythrocytic growth [45, 46]. How RBC dehydration interferes with parasite invasion remains unclear [4, 20].

The deformation of the RBC during the initial interaction with the merozoite is anticipated to activate PIEZO1. However, no calcium signal in the RBC was reported during the pre-invasion stages (attachment and reorientation) when RBCs maximally deform upon initial merozoite contact (Video 5), suggesting that PIEZO1 activation is unlikely to occur at this stage [35, 47]. Binding of merozoites to human RBCs triggers important biophysical changes that will contribute to facilitate invasion [48]. Modelling has suggested that wrapping of the RBC membrane followed by reorganisation of the underlying cytoskeleton could account for the energetic steps required for the invasion process [49]. Upon contact with the parasite, a signalling pathway through a phosphorylation cascade causes altered viscoelastic properties of the host membrane [50]. A possibility is that these early events may prevent PIEZO1 opening at the very beginning of the invasion process (despite major membrane deformation), thus explaining the absence of a calcium signal at this stage where membrane movements are remarkably large [35, 47]. Moreover, in a quantitative phosphoproteomic analysis of the erythrocyte during the short phase of invasion, PIEZO1 was one of the few identified proteins showing increased phosphorylation upon merozoite attachment prior to invasion [51]. Another question is whether or not the intraerythrocytic parasite may also directly influence PIEZO1 activity within the host cell. Differential phosphorylation of PIEZO1 has been documented in parasitized RBCs [52]. However, the biological significance of PIEZO1 phosphorylation in infected RBCs is unclear at this stage.

Multiple questions remain open to better understand how the pharmacological activation of PIEZO1 confers a potent protection against malaria infection. Recent structural findings indicate that PIEZO1 negatively curves the membrane in the closed state [10, 11, 13, 15]. Upon activation in response to mechanical stimulation, the channel reversibly flattens [15]. How PIEZO1 activation and flattening may influence the shape of RBCs, thereby conditioning merozoite attachment and internalization is an intriguing question. Recent findings indicate that PIEZO1 is preferentially expressed at the RBC biconcave dimple, possibly explained by a curvature coupling between the negative curvature of PIEZO1 at the closed state and the curvature of the RBC membrane [53]. Intuitively, membrane flattening caused by PIEZO1 activation is in opposite direction to membrane internalization during invasion. Moreover, whether or not membrane depolarization (although the resting membrane potential of human RBCs is depolarized in the range of – 10 mV, close to the reversal potential of PIEZO1) and/or the increase in intracellular calcium (although blunted in our standard RPMI medium) are also involved in the mechanism of protection is unknown at this stage. In the same line, PIEZO1 opening in RBCs is anticipated to activate several downstream biochemical cascades (presumably calcium dependent), impacting various structural components of RBCs, including the cytoskeleton [54], as well as the lipid bilayer composition by influencing the cellular lipidome [55]. How these changes may contribute to the protection against malaria infection also needs to be investigated in future studies.

Altogether, our findings indicate that in the case of in vitro pharmacological activation of PIEZO1 by Yoda1 or Jedi2, the key protective event is an early loss of biconcave discoid shape of human RBCs, with secondarily a delayed RBC dehydration.

The *PIEZO1* E756del polymorphism is highly enriched in people of African origin [20]. Remarkably, this variant strongly associates with significant protection against severe malaria, although these heterozygote individuals have no detectable clinical symptoms caused by this deletion [21]. The mechanisms implicated in the protection conferred by the *PIEZO1* E756del against severe malaria appear to be complex and remain disputed [20, 21, 23]. It is likely that a combination of effects involving RBC dehydration [4, 20, 23], decreased expression of the cytoadherence molecule PfEMP-1 [21], and modulation of the immune system [20] mediate the PIEZO1-dependent protection against severe malaria. A recent report further indicates that PIEZO1 E756del opening by either Yoda1 or shear stress produce dehydration-dependent cell haemolysis, thereby inhibiting *P. falciparum* infection [23]. Moreover, 6–13% RBC from PIEZO1 E756del freshly drawn blood show distorted RBCs [23]. In addition, infected PIEZO1 E756del RBCs were also frequently misshaped and distorted. Thus, it is likely that a loss of discoid RBC shape may also contribute to the protection observed in PIEZO1 E756del carriers, although in this case RBC dehydration appears to be a dominant mechanism [20, 21, 23].

Host-directed therapeutic strategies for infectious diseases are becoming viable adjuncts to standard treatments (reviewed in [56]) and were also proposed for malaria [57]. Certain molecules targeting RBC proteins have antimalarial activities [58, 59]. Our in vitro findings now indicate that PIEZO1 pharmacological activation in human RBCs is sufficient to prevent invasion by *P. falciparum*. It is, therefore, tempting to speculate that pharmacological activation of PIEZO1 might constitute an original approach for the development of a future antimalarial treatment, without neglecting the widespread expression of PIEZO1 in human tissues.

Materials and methods

Chemicals

The following chemicals and their stock concentrations in DMSO (in square brackets) were used in this study: Yoda1 (Sigma–Aldrich) [20 mM], A23187 (Sigma–Aldrich) [2 mM], Jedi2 (Tocris)[100 mM], Nystatin (Sigma–Aldrich) [40 mg/ml]. The PKG inhibitor C2 was a generous gift of Oliver Billker [3 mM].

Biological material

Cell cultures of *P. falciparum* 3D7 strain (MRA-102 from MR4, BEI Resources) were performed as previously described [30] in human 0^+ or A^+ erythrocytes and complete medium, RPMI 1640 medium with 25 mM HEPES and 2 mM L-glutamine (Gibco), supplemented with 0.5% Albumax I (Gibco), 15 µg/ml hypoxanthine (Sigma–Aldrich) and 40 µg/ml gentamycin (Gibco) at 37 °C under a tri-gaseous mixture of 5% CO_2, 5% O_2 and 90% N_2. Culture conditions were generally static for culture maintenance or with gentle shaking to keep cells in suspension for experiments; this allowed to obtain higher multiplication rates and single infected RBCs. Parasites were synchronized by first purifying late-stage parasites using VarioMACS magnetic cell separator (CS columns, Miltenyi Biotec, Paris, France) [60] or centrifugation on a 63% Percoll/RPMI (GE Healthcare) cushion [61] before culture for 2–4 h with fresh RBCs to allow invasion, followed by a 5% sorbitol treatment to remove remaining late stages [62]. Human blood obtained as donations from anonymized individuals was provided by the local blood bank (Etablissement Français du Sang) under the approval number 21PLER2016-0103. Parasitemia was routinely monitored on thin blood smears fixed in methanol and stained with Diff-Quick™ (pH 7.2) (Dade Behring, France) or by SYBR Green staining and flow cytometry. For microscopic determination of parasitemia, at least 1000 cells were counted. Experiments were generally started with late stage parasites to eventually obtain ring stage parasitemia in the range of 1% and 10%.

Treatments with Yoda1 and Jedi2

Yoda1 and Jedi2 treatments were performed in two different ways: either in the presence of drug by adding Yoda1/Jedi2 directly to the parasite cultures in complete medium (drug-on experiments) or by pre-treating uninfected RBCs, washing and infection with parasites (drug-off experiments). For the latter, RBCs in RPMI were treated for 10 min at room temperature, washed three times in RPMI, re-suspended in complete medium and mixed with purified infected RBCs that were close to egress. To do so, late-stage parasites from synchronous cultures were purified either by passage over VarioMACS columns or by density centrifugation using a 63% Percoll/RPMI cushion. Pure infected RBCs were washed with complete medium, re-suspended in complete medium with 1.5 µM of the PKG inhibitor C2 [31], gazed and incubated at 37 °C for up to 5 h. This allows parasites to continue their development to segmenter stages but blocks egress until the inhibitor is removed by washing. These parasite preparations were then mixed with either Yoda1/Jedi2 pre-treated RBCs or with mock-treated RBCs. To treat ring stage parasites, purified late stage parasites were mixed with RBCs, incubated for 4 h and synchronized by 5% sorbitol treatment. Cultures were allowed to stabilize for 1 h before adding Yoda1. Individual experiments were generally performed in triplicates and parasitemia determined by FACS. Experiments were repeated at least three times with blood from different donors.

Parasitemia determination by FACS

Cultures were centrifuged and the cells fixed for at least 4 h at room temperature in 10 volumes of 4% paraformaldehyde (Electron Microscopy Sciences) in phosphate buffered saline (PBS). Preparations were then washed twice with PBS and incubated 30 min with 3.3 × SYBR Green (Thermo Fisher Scientific). DNA dye was removed by a simple wash in PBS and samples analysed on a FACS Canto (BD Biosciences) using processed uninfected RBCs as negative control.

Prolonged pre-treatment of RBCs with Yoda1 and Jedi2 and inhibition of parasite invasion

Total blood of different donors was washed three times in RPMI. 1 ml cultures at a haematocrit of 5% were prepared in triplicates and treated with drugs or vehicle (DMSO) and incubated in 12 well plates in standard culture conditions at 37 °C with shaking to keep cells in suspension. Treatment was done 24 h, 3 h and 0.5 h prior to the start of the experiment. Synchronised parasites at the schizont stage were purified to more than 90% purity using VarioMACS columns and put back into culture in the presence of 1.5 µM PKG inhibitor C2 for 4 h, what allows parasite development to the segmenter stage but reversibly blocks parasite egress. Parasites were collected by centrifugation at 300 *g* and re-suspended in complete medium. Ten µL suspension were then added per well of the pre-treated RBCs, and cultured under standard condition. After 18 h, 50 µL of culture were transferred to 96-well round bottom plates and fixed with an equal volume of 8% PFA in PBS for 3 h at RT. For FACS analysis, the cells were washed twice with 200 µL PBS and stained with 50 µL 5 × SYBR-Green solution for

30 min in the 96-well plate. Preparations were analyzed on a FACS-CANTO II cytometer (BD Biosciences). 100,000 events were recorded. Ring stage parastemia was determined using FlowJo software (vs10.8, Tree Star).

Haemolytic activity assays

Blood of different donors was obtained. Throughout these assays RPMI 1640 without phenol red (Gibco) was used. RBCs were washed twice in RPMI and suspensions at 5% haematocrit were prepared in complete medium (RPMI 0.5% albumax) and 100 µL samples were dispatched in round-bottom 96-well culture plates. Yoda1and Jedi2 were prepared in complete medium at double concentration, and 100 µL added to the wells containing 100 µL RBC suspensions in triplicates (2.5% final haematocrit) and mixed by pipetting. Final concentrations for Yoda1 were 10 µM, 5 µM, 2 µM and 1 µM and for Jedi2 1000 µM, 300 µM and 100 µM. Wells with DMSO were prepared for baseline determination (0.1% for Yoda1, 0.5% for Jedi2). Plates were incubated in standard conditions at 37 °C in 5% O_2, 5% CO_2. After 24 h, 2 µL of saponin (15%) were added to selected wells to obtain total lysis. RBCs were pelleted by centrifugation for 3 min at 1800 *g* and 150 µL of supernatant transferred to flat bottom 96-well plates. Haemoglobin released into the culture supernatant was quantified using a SPARK multifunctional microplate reader (TECAN) at 540 nm. Lysis was calculated after deduction of DMSO treated samples as percentage of total saponin-induced lysis.

Osmotic fragility assays

Osmotic fragility assays were performed as described [8] with minor modifications [4]. Briefly, blood from different donors was used the day of reception whenever possible. The blood was washed twice either in RPMI or in normal saline (NS, 149 mM NaCl, 2 mM HEPES, pH 7.4) depending on the following experimental conditions. One millilitre blood suspensions at 2.5% haematocrit were incubated with compounds for 30 min at 37 °C in RPMI or in NS supplemented with 4 mM KCl and 2 mM $CaCl_2$. Identical quantities of DMSO solvent served as controls. Ten µl of blood suspension were then added to U-bottom 96-well plates. Solutions of varying tonicity were generated by mixing NS (100%) with 2 mM HEPES, pH 7.4 (0%). 250 µl of these solutions were added to the diluted blood and incubated for 5 min at room temperature. Plates were then centrifuged at 1000 *g* for 3 min and 150 µl of the supernatant was transferred to flat bottom 96-well plates and spun again to remove air bubbles. Absorbance was measured using a SPARK multifunctional microplate reader (TECAN) at 415 nm. $LogEC_{50}$ values were determined by fitting the data to 4-parameter sigmoidal dose–response curves using Prism (GraphPad).

Hydration status of RBCs over time

Washed RBCs were pre-cultured for 24 h in our standard culture conditions in culture dishes in RPMI/albumax at 5% haematocrit in incubation chambers flushed with a gas mixture of 5% CO_2, 5% O_2, 90% N_2 and gentle shaking to keep cells in suspension. Then 1.5 ml of these cultures were treated with the indicated concentrations of Yoda1 or Jedi2 or corresponding volumes of DMSO as control. Cultures were transferred to 35 mm cell culture dishes and cultured as described above for up to 24 h. At the indicated time points, 250 µL of suspension was used to determine the hydration status by osmotic fragility assays.

Video microscopy

For the observation of the cell shape, RBCs were washed and re-suspended in complete medium and settled in a poly-L lysine (PLL) coated slide chamber (Ibidi µ-slide VI). Cells were washed thrice with complete medium to remove non-adherent cells and then flushed with complete medium containing either Yoda1 (1 µM or 5 µM) or DMSO and time–lapse video microscopy recorded with 63 × magnifications at a speed of 1 image/2 s. To observe the recovery of cell shape, RBCs in complete medium were treated with 10 µM Yoda1 (at this concentration, all RBCs become strong echinocytes), placed in glass bottom dishes (MatTek), and time–lapse video microscopy recorded with 63 × magnifications over 2 ½ h at 6 images/min. For the observation of egress and invasion events, late-stage parasites were purified on VarioMACS columns, washed and re-suspended in complete medium and incubated for up to 5 h in the presence of 1.5 µM PKG inhibitor C2 to block egress. For egress studies, parasites were washed twice and re-suspended in complete medium containing 5 µM Yoda1. For control samples 0.5% DMSO was used. 100 µl of each cell suspension was loaded into adjacent wells (Ibidi µ-8 well slide) and recorded in alternation. For invasion, washed parasites were mixed with RBCs that had been pre-treated with 5 µM Yoda1 or 0.5% DMSO for 10 min in RPMI, washed three times and incubated at 37 °C for 5 h. Samples were loaded in glass bottom dishes (MatTek). All events were imaged using an inverted brightfield microscope (Axioobserver, Zeiss), equipped with an incubation chamber set at 37 °C and 5% CO_2 and a CoolSNAP HQ2 CCD camera (Photometrics). Time-lapse experiments were performed, by automatic acquisition of designated fields using a 63 × Apochromat

objective (NA 1.4). Image treatment and analysis were performed using Zen software (Zeiss).

Scanning electron microscopy

For environmental scanning electron microscopy (ESEM), samples were fixed at room temperature with 2.5% glutaraldehyde in 0.1 M cacodylate buffer followed by 1% osmium tetroxide, and washed in water. A 10 µl drop of suspension was loaded on the sample carrier and imaged in a FEI Quanta200 FEG microscope in ESEM mode using the gaseous secondary electron detector. The stage was set-up at 2 °C, the acceleration voltage was 15 kV and the working distance 10 mm. Water was then progressively removed by cycles of decreasing pressure/injection of water, until reaching equilibrium at the dew point. The minimal final pressure in the chamber was 350 Pa. Pictures were taken with a dwell time of 6 µs.

Generation of RBCs with altered Na^+/K^+ content

To generate RBCs with a cellular Na^+ and K^+ content similar to the situation observed upon treatment with Yoda1, RBCs were incubated on ice in the presence of 40 µg/ml of the ionophore nystatin (Sigma–Aldrich) in a saline solution of either 75 mM NaCl/75 mM KCl or 110 mM NaCl/40 mM KCl in 5 mM Hepes pH 7.4 and 55 mM sucrose. Upon incubation during 20 min, cells were collected by centrifugation and washed twice for 20 min on ice with the identical solution containing 0.1% BSA to efficiently remove nystatin. The cellular Na^+/K^+ content was measured by spectroscopy with a Solaar spectrometer immediately after the washing and after an additional incubation of the RBCs for 90 min at 37 °C in RPMI.

Measurements of sodium, potassium and water

Fresh venous blood was washed three times at room temperature in RPMI and set at 30% haematocrit. Three aliquots of 1.5 ml were treated with 1 µM Yoda1 or DMSO (control) for 10 min at room temperature, then rinsed three times in RPMI. For Na^+ and K^+ content measurements, 500 µl of cell suspension were taken to fill 3 nylon tubes that were centrifuged for 10 min at 4 °C, 20,000 *g* at the end of Yoda1 washing ($t=0$) and up to 24 h incubation at 37 °C and 5% CO_2 in complete medium. The pellet of RBCs was extracted and weighed immediately. Dry weight was measured after overnight heating (80 °C). Water content was calculated with a correction of 3.64% corresponding to trapped medium between packed cells. Intracellular ions were extracted from dried pellets by overnight incubation at 4 °C in 5 ml milliRho water (Millipore). Na^+ and K^+ were measured by flame spectroscopy with a Solaar spectrometer.

RBC attachment assays

Merozoite attachment to RBCs was quantified in the presence of the inhibitor of actin polymerisation cytochalasin D (cytD) following the protocol of Paul et al. [33]. RBCs were washed twice in RPMI and treated with either 5 µM Yoda1 or DMSO vehicle for 10 min at RT. Preparations were then washed three times in RPMI and eventually re-suspended in complete medium (RPMI, 0.5% albumax) and cultured for 4–5 h in standard conditions. Schizont- and segmenter-infected RBCs were purified from highly synchronised parasite cultures by magnetic purification on MACS columns (Milteny), efficiently removing uninfected RBCs. Purified infected RBCs were cultured at 37 °C for 4–5 h in complete medium in the presence of 1.5 µM C2 to allow parasite maturation while blocking egress. C2 was removed by centrifuging and re-suspending cells in an equal volume of fresh complete medium. 100 µL of cell suspension were immediately added to 2 ml tubes containing 100 µL of Yoda1 or DMSO pre-treated RBC suspensions in the presence of 1 µM cytD (allowing attachment but inhibiting invasion), 200 µg/ml heparin (inhibiting attachment and invasion) or 0.1% DMSO vehicle (allowing invasion). Assays were done in triplicates at a final haematocrit of 2.5%. Tubes were gazed for 3 s with 5% O_2, 5% CO_2 and incubated for 3 h at 37 °C on a spinning wheel for mixing. Cells were fixed by adding to each tube 800 µL of a sucrose-stabilised solution (0.116 M) in PBS supplemented with 2% glutaraldehyde [32]. The starting parasitemia (3–6%) was determined by fixing cells immediately after addition of iRBCs. Samples were stored at 4 °C until later processing.

For quantification of attachment by FACS, 10^7 cells (200 µL fixed suspension) were transferred to microtubes, pelleted at 300 g for 90 s and blocked with 300 µL of a sucrose-stabilised solution (0.116 M) in PBS supplemented with 0.1 M glycine for 30 min at RT. Cells were washed twice with 500 µL PBS/sucrose and then incubated 30 min with 3.3 × SYBR Green (Thermo Fisher Scientific). DNA dye was removed by a simple wash in PBS/sucrose and samples analysed on a FACS-CANTO II cytometer (BD Biosciences) using processed uninfected RBCs as negative control. RBCs with attached merozoites (in the presence of cytD) are detected with a fluorescence signal identical to ring stage iRBCs (in the absence of cytD and heparin) while heparin treatment prevents attachment and invasion. Data were expressed as percentage of DMSO-treated control RBCs after subtraction of baseline measurements of parasitemia in the presence of heparin.

Calcium measurements

Assays were either preformed in saline solution (145 mM NaCl, 4 mM KCl, 0.15 mM $MgCl_2$, 10 mM glucose, 10 mM

HEPES, 2 mM $CaCl_2$) or in RPMI 1640 medium without phenol red (Gibco # 11835063) supplemented with 10 mM HEPES. RBCs were washed three times in the respective medium. 5×10^7 RBCs were labelled with 5 µM Fluo4-AM and incubated for 30 min at 37 °C. Cells were washed three times, re-suspended in the respective medium and incubated for de-esterification for 30 min at room temperature. Suspensions of 1×10^6 RBCs in 100 µL were distributed in 96-well plates. Baseline fluorescence measurements were taken over 2 min at 20 s intervals in a SPARK multifunctional microplate reader (TECAN) with excitation at 485 nm and emission at 535 nm. Assays were then started by adding 100 µL of double concentrated drugs in their respective medium and mixed using a multichannel pipette. Measurements were followed over 15–30 min. Fluorescent signals were calculated after subtraction of values of mock-treated samples.

Calcium measurements by video microscopy

RBCs were washed twice in RPMI and labelled for 30 min with 5 µM Fluo4-AM at 37 °C. After three washes with RPMI cells were re-suspended in complete medium and allowed to de-esterify at room temperature for 30 min. During this time cells were allowed to settle in poly-L lysine (PLL) coated slide chambers (Ibidi µ-slide VI). Non-adherent cells were removed by repeated washes. Alternate cycles of acquisitions every 4 s of brightfield and fluorescent signals were started before the addition of complete medium containing 5 µM Yoda1, 1 mM Jedi2 or DMSO vehicle and followed over about 5 min. Using Fiji software [63] relative fluorescent signals for defined areas of identical size covering individual RBCs were obtained. Background fluorescence was obtained by calculating the mean of five identical areas without cells and subtracted from all values.

Statistics and data analysis

Data analysis and plots were generated using Excel (Microsoft) and Prism (GraphPad). Osmotic fragility curves were generated by fitting the data to a four-parameter sigmoidal dose–response curve and $LogEC_{50}$ values were calculated. Statistical significance was determined by non-parametric Mann–Whitney test for $n > 3$, or by unpaired two-tailed *t*-test (GraphPad Prism). Means associated with the standard error of the mean (SEM) are illustrated on the figures.

Supplementary Information The online version contains supplementary material available at https://doi.org/10.1007/s00018-023-04773-0.

Acknowledgements The authors wish to thank Jordy Le Guet, Loic Dumas and Viviana Claveria for assistance with experiments, and Oliver Billker for supplying C2. We thank the Electron Microscopy facility of the University of Montpellier (MEA) for their assistance with ESEM microscopy and the imaging and cytometry facility MRI, member of the national infrastructure France-BioImaging supported by the French National Research Agency (ANR-10-INBS-04, Investments for the future).

Author contributions EH and KW designed the study. RL, LB, BA, HG and KW performed experiments. RL, LB, BA, HG, RC, MA, DD, EH and KW analysed the data. EH and KW wrote the paper. All authors read and approved the final manuscript.

Funding This research was supported by the Fondation Méditerranée Infection Marseille to R. Lohia, a prematuration grant of the Centre National de la Recherche Scientifique (PREMAT317) to K. Wengelnik and D. Douguet, the Agence Nationale de la Recherche under the "Investissements d'avenir" program (ANR-16-IDEX-0006) to K. Wengelnik and R. Cerdan, LabEx Numev (Convention ANR-10-LABX-0020) to M. Abkarian, and ANR-19-CE14-0049 to H. Guizouarn. E. Honoré thanks the Fondation pour la Recherche Médicale, the Agence Nationale de la Recherche (ANR-17-CE13-0012–02, ANR-19-CE14-0029–01 and ANR-20-CE14-0032–01) and the Human Frontier Science Program for funding this work. K. Wengelnik also thanks the Key Initiative MUSE Interdisciplinary Blood Science of the University of Montpellier for support.

Data availability All data generated or analyzed during this study are included in this published article and its supplementary information files.

Declarations

Conflict of interest The authors have no relevant financial or non-financial interests to disclose.

Ethical approval Human blood was provided by the local blood bank (Etablissement Français du Sang) and was obtained as donations from anonymized individuals under the approval number 21PLER2016-0103.

Consent to participate and consent for publication Not applicable.

References

1. Allison AC (1954) Protection afforded by sickle-cell trait against subtertian malareal infection. Br Med J 1:290–294. https://doi.org/10.1136/bmj.1.4857.290
2. Elguero E, Delicat-Loembet LM, Rougeron V, Arnathau C, Roche B, Becquart P, Gonzalez JP, Nkoghe D, Sica L, Leroy EM, Durand P, Ayala FJ, Ollomo B, Renaud F, Prugnolle F (2015) Malaria continues to select for sickle cell trait in Central Africa. Proc Natl Acad Sci USA 112:7051–7054. https://doi.org/10.1073/pnas.1505665112

3. Roberts DJ, Williams TN (2003) Haemoglobinopathies and resistance to malaria. Redox Rep 8:304–310. https://doi.org/10.1179/135100003225002998
4. Tiffert T, Lew VL, Ginsburg H, Krugliak M, Croisille L, Mohandas N (2005) The hydration state of human red blood cells and their susceptibility to invasion by *Plasmodium falciparum*. Blood 105:4853–4860. https://doi.org/10.1182/blood-2004-12-4948
5. Coste B, Mathur J, Schmidt M, Earley TJ, Ranade S, Petrus MJ, Dubin AE, Patapoutian A (2010) Piezo1 and Piezo2 are essential components of distinct mechanically activated cation channels. Science 330:55–60. https://doi.org/10.1126/science.1193270
6. Murthy SE, Dubin AE, Patapoutian A (2017) Piezos thrive under pressure: mechanically activated ion channels in health and disease. Nat Rev Mol Cell Biol 18:771–783. https://doi.org/10.1038/nrm.2017.92
7. Prole DL, Taylor CW (2013) Identification and analysis of putative homologues of mechanosensitive channels in pathogenic protozoa. PLoS ONE 8:e66068. https://doi.org/10.1371/journal.pone.0066068
8. Cahalan SM, Lukacs V, Ranade SS, Chien S, Bandell M, Patapoutian A (2015) Piezo1 links mechanical forces to red blood cell volume. Elife. https://doi.org/10.7554/eLife.07370
9. Ge J, Li W, Zhao Q, Li N, Chen M, Zhi P, Li R, Gao N, Xiao B, Yang M (2015) Architecture of the mammalian mechanosensitive Piezo1 channel. Nature 527:64–69. https://doi.org/10.1038/nature15247
10. Guo YR, MacKinnon R (2017) Structure-based membrane dome mechanism for Piezo mechanosensitivity. Elife. https://doi.org/10.7554/eLife.33660
11. Saotome K, Murthy SE, Kefauver JM, Whitwam T, Patapoutian A, Ward AB (2018) Structure of the mechanically activated ion channel Piezo1. Nature 554:481–486. https://doi.org/10.1038/nature25453
12. Wang L, Zhou H, Zhang M, Liu W, Deng T, Zhao Q, Li Y, Lei J, Li X, Xiao B (2019) Structure and mechanogating of the mammalian tactile channel PIEZO2. Nature 573:225–229. https://doi.org/10.1038/s41586-019-1505-8
13. Zhao Q, Zhou H, Chi S, Wang Y, Wang J, Geng J, Wu K, Liu W, Zhang T, Dong MQ, Li X, Xiao B (2018) Structure and mechanogating mechanism of the Piezo1 channel. Nature 554:487–492. https://doi.org/10.1038/nature25743
14. Haselwandter CA, MacKinnon R (2018) Piezo's membrane footprint and its contribution to mechanosensitivity. Elife. https://doi.org/10.7554/eLife.41968
15. Lin YC, Guo YR, Miyagi A, Levring J, MacKinnon R, Scheuring S (2019) Force-induced conformational changes in PIEZO1. Nature 573:230–234. https://doi.org/10.1038/s41586-019-1499-2
16. Albuisson J, Murthy SE, Bandell M, Coste B, Louis-Dit-Picard H, Mathur J, Feneant-Thibault M, Tertian G, de Jaureguiberry JP, Syfuss PY, Cahalan S, Garcon L, Toutain F, Simon Rohrlich P, Delaunay J, Picard V, Jeunemaitre X, Patapoutian A (2013) Dehydrated hereditary stomatocytosis linked to gain-of-function mutations in mechanically activated PIEZO1 ion channels. Nat Commun 4:1884. https://doi.org/10.1038/ncomms2899
17. Andolfo I, Alper SL, De Franceschi L, Auriemma C, Russo R, De Falco L, Vallefuoco F, Esposito MR, Vandorpe DH, Shmukler BE, Narayan R, Montanaro D, D'Armiento M, Vetro A, Limongelli I, Zuffardi O, Glader BE, Schrier SL, Brugnara C, Stewart GW, Delaunay J, Iolascon A (2013) Multiple clinical forms of dehydrated hereditary stomatocytosis arise from mutations in PIEZO1. Blood 121(3925–35):3925–3935. https://doi.org/10.1182/blood-2013-02-482489. (**S1-12**)
18. Bae C, Gnanasambandam R, Nicolai C, Sachs F, Gottlieb PA (2013) Xerocytosis is caused by mutations that alter the kinetics of the mechanosensitive channel PIEZO1. Proc Natl Acad Sci USA 110:E1162–E1168. https://doi.org/10.1073/pnas.1219777110
19. Zarychanski R, Schulz VP, Houston BL, Maksimova Y, Houston DS, Smith B, Rinehart J, Gallagher PG (2012) Mutations in the mechanotransduction protein PIEZO1 are associated with hereditary xerocytosis. Blood 120:1908–1915. https://doi.org/10.1182/blood-2012-04-422253
20. Ma S, Cahalan S, LaMonte G, Grubaugh ND, Zeng W, Murthy SE, Paytas E, Gamini R, Lukacs V, Whitwam T, Loud M, Lohia R, Berry L, Khan SM, Janse CJ, Bandell M, Schmedt C, Wengelnik K, Su AI, Honore E, Winzeler EA, Andersen KG, Patapoutian A (2018) Common PIEZO1 Allele in African populations causes RBC dehydration and attenuates *Plasmodium* infection. Cell 173:443–455. https://doi.org/10.1016/j.cell.2018.02.047. (**e12**)
21. Nguetse CN, Purington N, Ebel ER, Shakya B, Tetard M, Kremsner PG, Velavan TP, Egan ES (2020) A common polymorphism in the mechanosensitive ion channel PIEZO1 is associated with protection from severe malaria in humans. Proc Natl Acad Sci USA. https://doi.org/10.1073/pnas.1919843117
22. Thye T, Evans JA, Ruge G, Loag W, Ansong D, Agbenyega T, Horstmann RD, May J, Schuldt K (2022) Human genetic variant E756del in the ion channel PIEZO1 not associated with protection from severe malaria in a large Ghanaian study. J Hum Genet 67:65–67. https://doi.org/10.1038/s10038-021-00958-2
23. Glushakova S, Bezrukov L, Waters H, Kegawa Y, Blank PS, Zimmerberg J (2022) PIEZO1-dependent erythrocyte dehydration as the mechanism for selection of an allele protecting from severe malaria. BioRxiv. https://doi.org/10.1101/2022.03.31.486604
24. Ma S, Dubin AE, Zhang Y, Mousavi SAR, Wang Y, Coombs AM, Loud M, Andolfo I, Patapoutian A (2021) A role of PIEZO1 in iron metabolism in mice and humans. Cell 184:969–982. https://doi.org/10.1016/j.cell.2021.01.024. (**e13**)
25. Syeda R, Xu J, Dubin AE, Coste B, Mathur J, Huynh T, Matzen J, Lao J, Tully DC, Engels IH, Petrassi HM, Schumacher AM, Montal M, Bandell M, Patapoutian A (2015) Chemical activation of the mechanotransduction channel Piezo1. Elife. https://doi.org/10.7554/eLife.07369
26. Wang Y, Chi S, Guo H, Li G, Wang L, Zhao Q, Rao Y, Zu L, He W, Xiao B (2018) A lever-like transduction pathway for long-distance chemical- and mechano-gating of the mechanosensitive Piezo1 channel. Nat Commun 9:1300. https://doi.org/10.1038/s41467-018-03570-9
27. Rapetti-Mauss R, Picard V, Guitton C, Ghazal K, Proulle V, Badens C, Soriani O, Garcon L, Guizouarn H (2017) Red blood cell Gardos channel (KCNN4): the essential determinant of erythrocyte dehydration in hereditary xerocytosis. Haematologica 102:e415–e418. https://doi.org/10.3324/haematol.2017.171389
28. Ofulla AV, Okoye VC, Khan B, Githure JI, Roberts CR, Johnson AJ, Martin SK (1993) Cultivation of *Plasmodium falciparum* parasites in a serum-free medium. Am J Trop Med Hyg 49:335–340. https://doi.org/10.4269/ajtmh.1993.49.335
29. Schuster FL (2002) Cultivation of *Plasmodium* spp. Clin Microbiol Rev 15:355–364. https://doi.org/10.1128/cmr.15.3.355-364.2002
30. Trager W, Jensen JB (1976) Human malaria parasites in continuous culture. Science 193:673–675. https://doi.org/10.1126/science.781840
31. Collins CR, Hackett F, Strath M, Penzo M, Withers-Martinez C, Baker DA, Blackman MJ (2013) Malaria parasite cGMP-dependent protein kinase regulates blood stage merozoite secretory organelle discharge and egress. PLoS Pathog 9:e1003344. https://doi.org/10.1371/journal.ppat.1003344
32. Miller LH, Aikawa M, Johnson JG, Shiroishi T (1979) Interaction between cytochalasin B-treated malarial parasites and erythrocytes. Attachment and junction formation. J Exp Med 149:172–184. https://doi.org/10.1084/jem.149.1.172

33. Paul AS, Saha S, Engelberg K, Jiang RH, Coleman BI, Kosber AL, Chen CT, Ganter M, Espy N, Gilberger TW, Gubbels MJ, Duraisingh MT (2015) Parasite calcineurin regulates host cell recognition and attachment by apicomplexans. Cell Host Microbe 18:49–60. https://doi.org/10.1016/j.chom.2015.06.003
34. Boyle MJ, Richards JS, Gilson PR, Chai W, Beeson JG (2010) Interactions with heparin-like molecules during erythrocyte invasion by *Plasmodium falciparum* merozoites. Blood 115:4559–4568. https://doi.org/10.1182/blood-2009-09-243725
35. Weiss GE, Gilson PR, Taechalertpaisarn T, Tham WH, de Jong NW, Harvey KL, Fowkes FJ, Barlow PN, Rayner JC, Wright GJ, Cowman AF, Crabb BS (2015) Revealing the sequence and resulting cellular morphology of receptor-ligand interactions during *Plasmodium falciparum* invasion of erythrocytes. PLoS Pathog 11:e1004670. https://doi.org/10.1371/journal.ppat.1004670
36. Boyle MJ, Wilson DW, Richards JS, Riglar DT, Tetteh KK, Conway DJ, Ralph SA, Baum J, Beeson JG (2010) Isolation of viable *Plasmodium falciparum* merozoites to define erythrocyte invasion events and advance vaccine and drug development. Proc Natl Acad Sci USA 107:14378–14383. https://doi.org/10.1073/pnas.1009198107
37. Boampong JN, Manno S, Koshino I, Takakuwa Y (2007) Erythrocyte shape change prevents *Plasmodium falciparum* invasion. Membrane 32:95–102
38. Bunn HF (2013) The triumph of good over evil: protection by the sickle gene against malaria. Blood 121:20–25. https://doi.org/10.1182/blood-2012-08-449397
39. Taylor SM, Cerami C and Fairhurst RM (2013) Hemoglobinopathies: slicing the Gordian knot of *Plasmodium falciparum* malaria pathogenesis. PLoS Pathog 9:e1003327. https://doi.org/10.1371/journal.ppat.1003327
40. Pasvol G, Weatherall DJ and Wilson RJ (1978) Cellular mechanism for the protective effect of haemoglobin S against *P. falciparum* malaria. Nature 274:701–703. https://doi.org/10.1038/274701a0
41. Archer NM, Petersen N, Clark MA, Buckee CO, Childs LM and Duraisingh MT (2018) Resistance to *Plasmodium falciparum* in sickle cell trait erythrocytes is driven by oxygen-dependent growth inhibition. Proc Natl Acad Sci U S A 115:7350–7355. https://doi.org/10.1073/pnas.1804388115
42. Cyrklaff M, Sanchez CP, Kilian N, Bisseye C, Simpore J, Frischknecht F and Lanzer M (2011) Hemoglobins S and C interfere with actin remodeling in *Plasmodium falciparum*-infected erythrocytes. Science 334:1283–1286. https://doi.org/10.1126/science.1213775
43. Cowman AF, Tonkin CJ, Tham WH, Duraisingh MT (2017) The molecular basis of erythrocyte invasion by malaria parasites. Cell Host Microbe 22:232–245. https://doi.org/10.1016/j.chom.2017.07.003
44. Weiss GE, Crabb BS, Gilson PR (2016) Overlaying molecular and temporal aspects of malaria parasite invasion. Trends Parasitol 32:284–295. https://doi.org/10.1016/j.pt.2015.12.007
45. Gilson PR, Crabb BS (2009) Morphology and kinetics of the three distinct phases of red blood cell invasion by *Plasmodium falciparum* merozoites. Int J Parasitol 39:91–96. https://doi.org/10.1016/j.ijpara.2008.09.007
46. Riglar DT, Richard D, Wilson DW, Boyle MJ, Dekiwadia C, Turnbull L, Angrisano F, Marapana DS, Rogers KL, Whitchurch CB, Beeson JG, Cowman AF, Ralph SA, Baum J (2011) Super-resolution dissection of coordinated events during malaria parasite invasion of the human erythrocyte. Cell Host Microbe 9:9–20. https://doi.org/10.1016/j.chom.2010.12.003
47. Introini V, Crick A, Tiffert T, Kotar J, Lin YC, Cicuta P, Lew VL (2018) Evidence against a role of elevated intracellular Ca^{2+} during *Plasmodium falciparum* preinvasion. Biophys J 114:1695–1706. https://doi.org/10.1016/j.bpj.2018.02.023
48. Koch M, Wright KE, Otto O, Herbig M, Salinas ND, Tolia NH, Satchwell TJ, Guck J, Brooks NJ, Baum J (2017) *Plasmodium falciparum* erythrocyte-binding antigen 175 triggers a biophysical change in the red blood cell that facilitates invasion. Proc Natl Acad Sci USA 114:4225–4230. https://doi.org/10.1073/pnas.1620843114
49. Dasgupta S, Auth T, Gov NS, Satchwell TJ, Hanssen E, Zuccala ES, Riglar DT, Toye AM, Betz T, Baum J, Gompper G (2014) Membrane-wrapping contributions to malaria parasite invasion of the human erythrocyte. Biophys J 107:43–54. https://doi.org/10.1016/j.bpj.2014.05.024
50. Sisquella X, Nebl T, Thompson JK, Whitehead L, Malpede BM, Salinas ND, Rogers K, Tolia NH, Fleig A, O'Neill J, Tham WH, David Horgen F, Cowman AF (2017) *Plasmodium falciparum* ligand binding to erythrocytes induce alterations in deformability essential for invasion. Elife. https://doi.org/10.7554/eLife.21083
51. Zuccala ES, Satchwell TJ, Angrisano F, Tan YH, Wilson MC, Heesom KJ, Baum J (2016) Quantitative phospho-proteomics reveals the *Plasmodium* merozoite triggers pre-invasion host kinase modification of the red cell cytoskeleton. Sci Rep 6:19766. https://doi.org/10.1038/srep19766
52. Bouyer G, Reininger L, Ramdani G, L DP, Sharma V, Egee S, Langsley G, Lasonder E (2016) *Plasmodium falciparum* infection induces dynamic changes in the erythrocyte phospho-proteome. Blood Cells Mol Dis 58:35–44. https://doi.org/10.1016/j.bcmd.2016.02.001
53. Vaisey G, Banerjee P, North AJ, Haselwandter CA, MacKinnon R (2022) Piezo1 as a force-through-membrane sensor in red blood cells. Elife. https://doi.org/10.7554/eLife.82621
54. Li J, Hou B, Tumova S, Muraki K, Bruns A, Ludlow MJ, Sedo A, Hyman AJ, McKeown L, Young RS, Yuldasheva NY, Majeed Y, Wilson LA, Rode B, Bailey MA, Kim HR, Fu Z, Carter DA, Bilton J, Imrie H, Ajuh P, Dear TN, Cubbon RM, Kearney MT, Prasad KR, Evans PC, Ainscough JF, Beech DJ (2014) Piezo1 integration of vascular architecture with physiological force. Nature 515:279–282. https://doi.org/10.1038/nature13701
55. Buyan A, Cox CD, Barnoud J, Li J, Chan HSM, Martinac B, Marrink SJ, Corry B (2020) Piezo1 forms specific, functionally important interactions with phosphoinositides and cholesterol. Biophys J 119:1683–1697. https://doi.org/10.1016/j.bpj.2020.07.043
56. Zumla A, Rao M, Wallis RS, Kaufmann SH, Rustomjee R, Mwaba P, Vilaplana C, Yeboah-Manu D, Chakaya J, Ippolito G, Azhar E, Hoelscher M and Maeurer M (2016) Host-directed therapies for infectious diseases: current status, recent progress, and future prospects. Lancet Infect Dis 16:e47–63. https://doi.org/10.1016/S1473-3099(16)00078-5
57. Glennon EKK, Dankwa S, Smith JD and Kaushansky A (2018) Opportunities for host-targeted therapies for malaria. Trends Parasitol 34:843–860. https://doi.org/10.1016/j.pt.2018.07.011
58. Tubman VN, Mejia P, Shmukler BE, Bei AK, Alper SL, Mitchell JR, Brugnara C and Duraisingh MT (2016) The clinically tested gardos channel inhibitor senicapoc exhibits antimalarial activity. Antimicrob Agents Chemother 60:613–616. https://doi.org/10.1128/AAC.01668-15
59. Tiffert T, Ginsburg H, Krugliak M, Elford BC and Lew VL (2000) Potent antimalarial activity of clotrimazole in in vitro cultures of *Plasmodium falciparum*. Proc Natl Acad Sci U S A 97:331–336. https://doi.org/10.1073/pnas.97.1.331
60. Ahn SY, Shin MY, Kim YA, Yoo JA, Kwak DH, Jung YJ, Jun G, Ryu SH, Yeom JS, Ahn JY, Chai JY, Park JW (2008) Magnetic separation: a highly effective method for synchronization of cultured erythrocytic *Plasmodium falciparum*. Parasitol Res 102:1195–1200. https://doi.org/10.1007/s00436-008-0893-8
61. Saul A, Myler P, Elliott T, Kidson C (1982) Purification of mature schizonts of *Plasmodium falciparum* on colloidal silica gradients. Bull World Health Organ 60:755–759

62. Lambros C, Vanderberg JP (1979) Synchronization of *Plasmodium falciparum* erythrocytic stages in culture. J Parasitol 65:418–420
63. Schindelin J, Arganda-Carreras I, Frise E, Kaynig V, Longair M, Pietzsch T, Preibisch S, Rueden C, Saalfeld S, Schmid B, Tinevez JY, White DJ, Hartenstein V, Eliceiri K, Tomancak P, Cardona A (2012) Fiji: an open-source platform for biological-image analysis. Nat Methods 9:676–682. https://doi.org/10.1038/nmeth.2019

PIEZO1 and BKCa channels in human atrial fibroblasts: Interplay and remodelling in atrial fibrillation.

Jakob, D., Klesen, A., Allegrini, B., Darkow, E., Aria, D., Emig, R., ... & Peyronnet, R. (2021). *Journal of Molecular and Cellular Cardiology*, *158*, 49-62.

Contexte :

Cet article a été réalisé en collaboration avec l'équipe de Rémi Peyronnet. Nous avons étudié le couplage fonctionnel entre PIEZO1 et le canal BK (un autre membre de la famille des canaux potassique activés par le calcium) dans les fibroblastes dans un contexte pathologique : la fibrillation auriculaire. Nous avons montré que ces deux canaux sont couplés, sans interaction physique directe et que ce couplage est modulé dans les fibroblastes de patients.

Journal of Molecular and Cellular Cardiology 158 (2021) 49–62

Contents lists available at ScienceDirect

Journal of Molecular and Cellular Cardiology

journal homepage: www.elsevier.com/locate/yjmcc

Piezo1 and BK_{Ca} channels in human atrial fibroblasts: Interplay and remodelling in atrial fibrillation

Dorothee Jakob [a,b,1], Alexander Klesen [a,b,1], Benoit Allegrini [c], Elisa Darkow [a,b,d,e], Diana Aria [a,b,f], Ramona Emig [a,b,g], Ana Simon Chica [a,b], Eva A. Rog-Zielinska [a,b], Tim Guth [a,b], Friedhelm Beyersdorf [b,h], Fabian A. Kari [b,h], Susanne Proksch [b,f], Stéphane N. Hatem [i], Matthias Karck [j], Stephan R. Künzel [k], Hélène Guizouarn [c], Constanze Schmidt [l,m], Peter Kohl [a,b,g], Ursula Ravens [a,b], Rémi Peyronnet [a,b,*]

[a] Institute for Experimental Cardiovascular Medicine, University Heart Center Freiburg, Bad Krozingen, Medical Center - University of Freiburg, Germany
[b] Faculty of Medicine, University of Freiburg, Germany
[c] CNRS University Cote d'Azur laboratory Institut Biology Valrose, Nice, France
[d] Spemann Graduate School of Biology and Medicine (SGBM), University of Freiburg, Freiburg, Germany
[e] Faculty of Biology, University of Freiburg, Freiburg, Germany
[f] G.E.R.N. Tissue Replacement, Regeneration & Neogenesis, Department of Operative Dentistry and Periodontology, Medical Center - University of Freiburg, Germany
[g] CIBSS Centre for Integrative Biological Signalling Studies, Faculty of Biology, University of Freiburg, Germany
[h] Department of Cardiovascular Surgery, University Heart Center Freiburg Bad Krozingen, Medical Center - University of Freiburg, Germany
[i] Sorbonne University, Assistance Publique-Hôpitaux de Paris, GH Pitié-Salpètrière Hospital, INSERM UMR_S1166, Cardiology department, Institute of Cardiometabolism and Nutrition-ICAN, Paris, France
[j] Department of Cardiac Surgery, University of Heidelberg, Germany
[k] Institute of Pharmacology and Toxicology, Faculty of Medicine Carl Gustav Carus, Technische Universität Dresden, Germany
[l] Department of Cardiology, University of Heidelberg, Germany
[m] DZHK (German Center for Cardiovascular Research) partner site Heidelberg/Mannheim, University of Heidelberg, Germany

ARTICLE INFO

Keywords:
Stretch-activated ion channels
Mechano-sensing
Heart
Arrhythmia
Non-myocytes
Calcium
KCNMA1

ABSTRACT

Aims: Atrial Fibrillation (AF) is an arrhythmia of increasing prevalence in the aging populations of developed countries. One of the important indicators of AF is sustained atrial dilatation, highlighting the importance of mechanical overload in the pathophysiology of AF. The mechanisms by which atrial cells, including fibroblasts, sense and react to changing mechanical forces, are not fully elucidated. Here, we characterise stretch-activated ion channels (SAC) in human atrial fibroblasts and changes in SAC- presence and activity associated with AF.
Methods and results: Using primary cultures of human atrial fibroblasts, isolated from patients in sinus rhythm or sustained AF, we combine electrophysiological, molecular and pharmacological tools to identify SAC. Two electrophysiological SAC- signatures were detected, indicative of cation-nonselective and potassium-selective channels. Using siRNA-mediated knockdown, we identified the cation-nonselective SAC as Piezo1. Biophysical properties of the potassium-selective channel, its sensitivity to calcium, paxilline or iberiotoxin (blockers), and NS11021 (activator), indicated presence of calcium-dependent 'big potassium channels' (BK_{Ca}). In cells from AF patients, Piezo1 activity and mRNA expression levels were higher than in cells from sinus rhythm patients, while BK_{Ca} activity (but not expression) was downregulated. Both Piezo1-knockdown and removal of extracellular calcium from the patch pipette resulted in a significant reduction of BK_{Ca} current during stretch. No co-immunoprecipitation of Piezo1 and BK_{Ca} was detected.
Conclusions: Human atrial fibroblasts contain at least two types of ion channels that are activated during stretch: Piezo1 and BK_{Ca}. While Piezo1 is directly stretch-activated, the increase in BK_{Ca} activity during mechanical stimulation appears to be mainly secondary to calcium influx *via* SAC such as Piezo1. During sustained AF, Piezo1 is increased, while BK_{Ca} activity is reduced, highlighting differential regulation of both channels. Our data

* Corresponding author at: Institute for Experimental Cardiovascular Medicine, Elsässer Straße 2Q, Freiburg 79110, Germany.
E-mail address: remi.peyronnet@uniklinik-freiburg.de (R. Peyronnet).
[1] These authors contributed equally to the work.

https://doi.org/10.1016/j.yjmcc.2021.05.002
Received 14 May 2020; Received in revised form 18 April 2021; Accepted 4 May 2021
Available online 8 May 2021

support the presence and interplay of Piezo1 and BK_{Ca} in human atrial fibroblasts in the absence of physical links between the two channel proteins.

1. Introduction

Atrial Fibrillation (AF) is a supraventricular arrhythmia with increasing prevalence in countries with an aging population. Although AF is one of the most common cardiovascular causes of hospitalization [1–3], its pathophysiology is not fully elucidated, and it represents an unmet need for effective prevention and treatment. One hallmark of AF is its progressive nature. As AF becomes increasingly resistant over time to pharmacological or electrical attempts at conversion back to sinus rhythm (SR) [2], atrial tissue undergoes pronounced remodelling [2,4]. Structural and functional changes involve cell electrophysiological and tissue morphological alterations. Whilst electrical remodelling of atrial cardiomyocytes is characterised by a shortening of action potential duration and of effective refractory period, as well as by impaired adaptation of these parameters to changes in heart rate [5], fibrosis – a prominent feature of AF-related structural remodelling – may in parallel contribute to slowing of conduction. The combination of short effective refractory period and slow conduction favours maintenance of AF *via* re-entry mechanisms [6].

Many of the risk factors for AF, *e.g.* heart failure, hypertension, or valvulopathies, are accompanied by mechanical overload of the atria [7]. Since stretch enhances the susceptibility to AF induction [8,9], it has been suggested, that mechanical overload may contribute to initiation and perpetuation of AF *in vivo* [10–13]. In addition, acute stretch of control atrial tissue induces complex and regionally varying changes in action potential shape [10] and diastolic depolarizations that may trigger extrasystoles [9,14,15]. This 'mechano-electric feedback' [16,17] requires cells to be able to sense their mechanical environment, and to translate this into an electrophysiologically relevant signal.

Ample evidence points to an essential role of stretch-activated ion channels (SAC) as mechano-sensors in cardiomyocytes (for reviews see [18,19]). SAC are also present and functional in human atrial fibroblasts [20,21], but it is currently not known whether SAC function is altered in AF in the various human heart cells, especially in fibroblasts, which are key players in fibrosis. Therefore, the aim of this study was to compare SAC function in atrial fibroblasts from patients in SR or in sustained AF. The cation-nonselective SAC Piezo1 [22–24] forms a plausible candidate, in line with recently reported Piezo1 effects on remodelling of non-cardiac tissues [25]. A second candidate, the potassium-selective Ca^{2+}-activated channel of large conductance (BK_{Ca}), has been reported to respond to stretch, local Ca^{2+} concentration changes, transforming growth factor beta (TGF-β), and angiotensin II in several cardiac cell types [26–30]. BK_{Ca} is further known to modulate fibroblast proliferation [31], a critical event during pathological tissue remodelling in AF. Both Piezo1 and BK_{Ca} have previously been detected in human atrial fibroblasts [31–33].

In this study we report AF-related changes in Piezo1 and BK_{Ca} channel activity in human atrial fibroblasts, and establish functional interactions between the two channel types.

2. Material and methods

2.1. Tissue collection

Tissue samples were obtained from the right atrial appendage of patients undergoing open-heart surgery. Patients were either in SR, or in sustained AF (which includes patients with persistent, long-standing persistent and permanent AF, defined according to ESC Guidelines [34]). Tissue samples were processed by the Cardiovascular Biobank of the University Heart Center Freiburg Bad Krozingen (approved by the ethics committee of Freiburg University, No 393/16; 214/18) or the Clinical Center of the Medical Faculty Heidelberg (approved by the ethics committee of the University Heidelberg, S-017/2013). Upon excision in the operating theatre, tissue was placed in room-temperature cardioplegic solution (containing in [mmol/L]: NaCl 120, KCl 25, HEPES 10, glucose 10, $MgCl_2$ 1; pH 7.4, 300 mOsm/L) and immediately transported to the laboratory. Tissue was processed within 30 min of excision. Samples from 36 SR patients and 17 AF patients were used (mean age 64.8 ± 1.4 years [mean ± standard error of the mean, SEM], age range 38–83 years, 40 males, 13 females [Table 1]). No significant age differences between the two groups were observed. Left atrial diameter of AF patients was larger, compared to SR patients. All patients gave informed consent prior to inclusion in the study, and investigations

Table 1
Patient characteristics.

	SR	AF	*p* (AF *vs.* SR)
Number of patients (male/female)	36 (28 M/8 F)	17 (12 M/5 F)	
Age at time of surgery (years)	62.3 ± 10.7	70.2 ± 6.7	0.172
ASA Stage	3.5 ± 0.5	3.6 ± 0.5	0.440
BMI (kg/m^2)	27.5 ± 4.8	25.9 ± 4.4	0.244
Diabetes mellitus	8	2	
Hyperlipidaemia	15	5	
Arterial hypertension	21	6	
Blood pressure (mmHg)			
Systolic	129.1 ± 19.9	120.8 ± 16.5	0.154
Diastolic	73.3 ± 12.2	68.2 ± 15.1	0.202
Heart rate	79.7 ± 17.1	77.9 ± 20.7	0.747
Left atrial diameter (mm)	**35.5 ± 6.9**	**48.6 ± 6.3**	**<0.001**
Patients with dilated left atrium (%)[a]	**33**	**93**	
Patients with dilated right atrium (%)[b]	**0**	**78**	
Ejection fraction (%)	47.3 ± 16.5	45.3 ± 11.29	0.664
Surgical procedures			
Aorto-coronary venous bypass	14	7	
Aortic valve replacement/ reconstruction	11	8	
Mitral valve replacement/ reconstruction	4	6	
Pulmonary valve repl./ reconstruction	0	2	
Tricuspid valve repl./reconstruction	0	6	
Left ventricular assist device	2	0	
Heart transplantation	1	0	
Aortic aneurism	5	1	
Aortic arch replacement	1	1	
Mechanical conduit	3	0	
Number of patients receiving the following medication			
ACE Inhibitors	13	4	
AT1-receptor blocker	6	2	
β-Blocker	21	11	
Diuretics	11	8	
Aldosterone antagonists	1	1	
Nitrates	1	0	
Statins	16	10	
Anticoagulants	13	14	

ASA: American Society of Anaesthesiologists, BMI: body mass index, ACE: Angiotensin converting enzyme, AT1 receptor: Angiotensin II receptor type I; all data represented as mean ± SD. Bold: parameters being significantly different between AF and SR.

[a] Information available for 24 SR and 14 AF patients.

[b] Information available for 23 SR and 14 AF patients. The 2 patients used for Fig. S7 are not included.

conformed to the principles outlined in the Declaration of Helsinki.

2.2. Cell culture

The weight of the tissue samples was variable (50 to 200 mg). The epicardium and adipose tissue were carefully removed to avoid contamination with excess epicardial cells or adipocytes. The remaining myocardium was cut into blocks of about 1–4 mm^3. Tissue chunks were transferred into a 6-well plate, each well containing 2 mL of Dulbecco's Modified Eagle Medium (DMEM, Gibco, Germany), 10% foetal calf serum, and 1% penicillin/streptomycin (all Sigma-Aldrich, Germany), for incubation at 37 °C in an atmosphere of air supplemented with CO_2 to maintain 5% CO_2. Culture medium was changed twice a week. Prior to use, the surface of culture plates had been abraded using a scalpel blade to favour tissue attachment and cell propagation. This so-called 'outgrowth technique' [35] was used for functional experiments as it yields more reproducibly large numbers of viable cells, compared to enzymatic digestion.

After 7–10 days, cells started to migrate from the tissue chunks, reaching ~80% confluency after 20–28 days, when they had to be passaged to preserve viability. For passaging, culture medium was removed, and cells were washed with pre-warmed phosphate-buffered saline (PBS) solution, detached by adding 1 mL of 0.05% trypsin per 35-mm dish for 5–10 min at 37°C. After addition of 2 mL of culture medium per dish, the suspension was transferred into a 15 mL Falcon tube and centrifuged at 333 ×*g* for 5 min. The supernatant was carefully removed and discarded. The cell pellet was resuspended in 1 mL of pre-warmed culture medium; 10 µL of this cell suspension were counted in a Neubauer chamber. Then cells were seeded into culture flasks or dishes for further experiments. To achieve a uniform cell density, 25,000 cells were seeded per 35-mm dish. Cells were used for experimentation until passage 5 (*i.e.* for up to 6 weeks). For co-immunoprecipitation experiments, the recently developed [36] human atrial fibroblast cell line HAF-SRK01 (HAF) was also used. Culture conditions for HAF and primary cultures were identical.

For reference purposes we also used atrial fibroblasts that were freshly isolated by enzymatic dissociation [35]. In brief, the right atrial tissue samples were placed into Ca^{2+}-free modified 'Kraftbrühe' solution (in mmol/L: KCl 20, K_2HPO_4 10, glucose 25, D-mannitol 40, K-glutamate 70, ß-hydroxybutyrate 10, taurine 20, EGTA 10, pH 7.2) supplemented with albumin (0.1%) [37]. Fat and epicardial tissue were removed, and the remaining tissue was cut into pieces of 1–4 mm^3, followed by rinsing for 5 min with Ca^{2+}-free solution supplemented with taurine. The solutions were oxygenated with 100% O_2 at 37 °C and stirred. For digestion, tissue aliquots were transferred for 10 min into a Ca^{2+}-free solution (in mmol/L: NaCl 137, KH_2PO_4 5, $MgSO_4(7H_2O)$ 1, glucose 10, HEPES 5, pH 7.4) supplemented with taurine, albumin (0.1%), collagenase type V (200 U/mL) and proteinase XXIV (5.4 U/mL). The Ca^{2+} concentration was then increased to 0.2 mmol/L and the tissue was stirred for additional 20–30 min. An additional 10 min of incubation in the presence of collagenase was then performed to release the first cells. This step was repeated until complete digestion of the tissue was accomplished. Collected suspensions were centrifuged (7 × *g* for 2 min) to separate cardiomyocytes (in the pellet) from non-myocytes (in the supernatant). Cardiomyocytes were resuspended in 250 µL of lysis buffer (RLT, Qiagen, Germany) mixed with 10 µL of β-mercaptoethanol and frozen at −80 °C. Non-myocytes where centrifuged at 260 × *g* for 5 min. Cell pellets were resuspended in lysis buffer and frozen.

2.3. Immunocytochemistry

Primary cell culture characterisation: Cells were stained for vimentin (fibroblasts, myofibroblasts, endothelial cells; antibody from Progen, Germany), CD31 (endothelial cells; antibody from Pharmingen, USA), and α-smooth muscle actin (αSMA; myofibroblasts, smooth muscle cells; antibody from Abcam, USA). Cells were plated onto sterile glass coverslips, cultured as described above, incubated, and fixed before they reached full confluency. Cell-containing coverslips were washed twice in PBS, incubated in acetone at −20 °C for 5 min, and washed again with PBS. Blocking solution containing Polysorbat 20 ('Tween 20') and foetal calf serum were used to reduce non-specific binding during incubation with primary, and subsequently secondary, antibodies. Nuclei were labelled using Hoechst 33342 nuclear counter-stain. Images were acquired with a confocal or a wide-field fluorescence microscope. For quantifying αSMA content, a threshold was used to define stained and unstained cells. We used the 'Phansalkar' method in ImageJ to create a local threshold based on the minimum and maximum intensities of fluorescence in the proximity of every pixel [38]. Using this threshold, a macro was designed in ImageJ to identify green fluorescence and count all nuclei marked by Hoechst stain.

Piezo1 and BK_{Ca}immunocytochemistry: Cells were plated on fibronectin-coated glass coverslips (10 mm diameter), using 24-well plates seeded at 100,000 cells per well. Cells were fixed for 10 min using methanol (5%) and acetic acid at −20 °C. Fixed cells were washed with PBS at room temperature (RT) and permeabilized with Triton 0.3% in PBS for 15 min, then incubated during 2 h at RT in the following blocking buffer: PBS containing bovine serum albumin 4%, goat serum 1%, and triton 0.03%. Primary antibodies: anti-Piezo1 (proteintech, raised in rabbit, 1/300), anti-KCNMA1 (Abnova, Taipei, Taiwan, raised in mouse, 1/500), were incubated 1 h at RT in the blocking buffer. After several washes, secondary antibodies: anti-rabbit IgG AlexaFluor 647 (Invitrogen, Carlsbad, USA, raised in donkey, 1/1250) or anti-mouse IgG AlexaFluor 568 (Invitrogen, raised in donkey, 1/1250) were incubated 50 min at RT. Hoechst 33342 (Molecular Probes, Eugene, USA, 1/5000) was added before mounting with Polyvinyl alcohol mounting medium (with DABCO® antifade reagent, Fluka, Charlotte USA). Images were acquired with LSM 880 M (Carl Zeiss, Oberkochen, Germany) with Zen software, maximal z resolution in these conditions was 0.618 µm. Colocalisation was quantified using Pearson's R coefficient calculated with ImageJ coloc2 plugin.

2.4. Electrophysiology

The patch-clamp technique was used to characterise ion channel activity in primary cultures of atrial fibroblasts. Experiments were performed at RT (20 °C), using a patch-clamp amplifier (200B, Axon Instruments, USA) and a Digidata 1440A interface (Axon Instruments). Recorded currents were digitized at 3 kHz, low-pass filtered at 1 kHz, and analysed with pCLAMP10.3 software (Axon Instruments) and ORIGIN9.1 (OriginLab, USA).

Cell-attached patch-clamp recordings were performed using bath and pipette solutions previously described for characterising Piezo1 channels [39]. In short: pipette medium contained (in mmol/L): NaCl 150, KCl 5, $CaCl_2$ 2, HEPES 10 (pH 7.4 with NaOH); bath medium contained (in mmol/L): KCl 155, EGTA 5, $MgCl_2$ 3, and HEPES 10 (pH 7.2 with KOH). Average pipette resistance was 1.3 MΩ. Culture medium was removed and exchanged for the bath solution at least 5 min before the start of electrophysiological measurements to wash-out culture medium and streptomycin (a blocker of SAC) [40]. Membrane patches were stimulated with brief (500 ms) negative pressure pulses of increasing amplitude (from 0 up to −80 mmHg, in −10 mmHg increments unless otherwise stated), applied through the recording electrode using a pressure-clamp device (ALA High Speed Pressure Clamp-1 system; ALA Scientific, USA). To confirm channel identity, we applied the spider toxin peptide *Grammostola spatulata* mechanotoxin 4 (GsMTx4) L-isomer (10 µmol/L, H_2O as solvent, CSBio, Menlo Park, CA, USA), a known blocker of cation non-selective SAC, including Piezo1 [41] and potassium-selective ion channels such as BK_{Ca} [42]. The holding voltage for all experiments was −80 mV when recording Piezo1. Current-pressure curves were fitted with a standard Boltzmann function ($I = (I_{max} - I_{min})/(1 + e^{(P-P0.5)/k}) + I_{min}$), where I_{max} is the highest value of current during a pressure pulse, I_{min} is the lowest one, $P_{0.5}$ is the

pressure required to obtain half-maximal activation and k is the time constant.

BK_{Ca} channel activity in the absence of additional mechanical perturbation was recorded by depolarising the membrane (from −10 mV up to +60 mV, in 10 mV increments), holding each potential for 22 s. In some cases, the membrane was depolarised up to +80 mV for illustration purposes. The fraction of time during which a channel was open was measured to define the open probability of the channel. To confirm channel identity, the BK_{Ca} activator NS11021 (10 or 5 μmol/L, courtesy of Bo Bentzen, Denmark) as well as the BK_{Ca} blockers paxilline (3 μmol/L with 0.03% DMSO, Sigma-Aldrich, Germany) and iberiotoxin (100 nmol/L, Tocris, Bristol, UK) were used. To assess stretch responses of BK_{Ca}, membrane patches were held at +50 mV and stimulated with long (10 s) negative pressure pulses of increasing amplitude (−10 mmHg increments). To assess the possible relevance of extracellular Ca^{2+} on BK_{Ca} activation during stretch, a Ca^{2+}-free pipette solution was used. It contained (in mmol/L): NaCl 150, KCl 5, EGTA 6, HEPES 10 (pH 7.4 with NaOH). To further confirm channel identity, the dependence of BK_{Ca} channel activity on intracellular Ca^{2+} concentration was measured in the inside-out patch-clamp configuration. Patch excision was achieved by a fast upward displacement of the patch pipette. The bath medium (a nominally Ca^{2+}-free solution in these experiments) was supplemented with $CaCl_2$ to obtain Ca^{2+} concentrations of 1, 10 and 100 μmol/L.

In order to probe possible interactions between Piezo1 and BK_{Ca} activity, a protocol was used that first activated Piezo1 with a negative pressure pulse (−50 mmHg for 1 s) while holding the patch at −80 mV, and subsequently BK_{Ca} by releasing pressure back to 0 mmHg while clamping the patch to +50 mV (see Fig. 5A for illustration).

Gigaohm seal resistance was systematically checked before and after each protocol: seals having a resistance below 1 GΩ were rejected. If following a stretch protocol, the current did not return to baseline within 20 s, the recording was rejected.

2.5. Molecular biology

All reagents, kits and instruments used for molecular biology analysis were supplied by Thermo Fisher Scientific, Germany.

mRNA expression levels: Isolation of total RNA was performed using TRIzol Reagent, and frozen samples (made from freshly isolated cells, or from cultured cells for knockdown experiments) were processed according to the manufacturer's protocol. RNA concentration was quantified by spectrophotometry (ND-1000, Thermo Fisher Scientific, Germany) and synthesis of single-stranded cDNA was carried out as reported before [43] with the Maxima First Strand cDNA Synthesis Kit, using 3 μg of total RNA. Quantitative real-time polymerase chain reactions (RT-qPCR) was performed as described earlier [43]. Briefly, 10 μL were used per reaction, consisting of 0.5 μL cDNA, 5 μL TaqMan Fast Universal Master Mix and 6-carboxyfluorescein-labelled TaqMan probes and primers. Primers were analysed using the StepOnePlus (Applied Biosystems, Foster City, CA, USA) PCR system. The importin-8 housekeeping gene (IPO8), or glyceraldehyde 3-phosphate dehydrogenase (GAPDH), was used for normalisation. All RT-qPCR reactions were performed as triplicates and control experiments in the absence of cDNA were included. Means of triplicates were used for the $2 - \Delta Ct$ calculation, where $2 - \Delta Ct$ corresponds to the ratio of mRNA expression *versus* IPO8. Oligonucleotide sequences are available on request.

PCR-based detection of the Stress-Axis Regulated Exon (*STREX*)*:* Total RNA was isolated from freshly isolated fibroblasts and reverse transcribed into cDNA as described earlier. Primers were designed to flank the putative STREX sequence (forward: 5′ – CTGTCATGATGACATCACAGATC – 3′; reverse: 5′ – GTCAATCTGATCATTGCCAGG – 3′, Fig. 4E). PCR were performed to amplify the respective sequence from cDNA of isolated cells from 4 patients. PCR amplification was performed for 40 cycles, using the TaqMan Fast Advanced Master Mix (Cat. No. 4444557, ThermoFisher) according to the manufacturer's instructions. Subsequently, PCR products were separated by agarose gel electrophoresis and ethidium bromide was visualized by an E-BOX VX2 2.0 MP (Peqlab, Erlangen, Germany) documentation system.

Silencing of Piezo1: small interference RNA (siRNA)-mediated knockdown was achieved by transfection using HiPerFect (Qiagen, Venlo, The Netherlands) according to the manufacturer's instructions. Pools of 4 siRNA were applied at a final concentration of 8 nmol/L for Piezo1 and Piezo2 (SMARTpool, Dharmacon, Lafayette, USA); concentrations of scrambled controls (Dharmacon) were adjusted accordingly. Knockdown efficiency was assessed by RT-qPCR 48 h after transfection, and electrophysiological experiments were performed 72 h after transfection.

2.6. Co-immunoprecipitation

Cells were grown to confluence in 60 mm dishes, washed twice with ice-cold PBS, lysed with immuno-precipitation (IP)-lysis buffer (from IP Lysis kit Pierce) and supplemented with anti-protease (Roche, Basel, Switzerland). Co-immuno-precipitations were done following the manufacturer protocol (Pierce). For antibody immobilisation, 10 μg of mouse monoclonal anti-Piezo1 (MyBioSource, San Diego, USA), mouse anti-KCNMA1 (Abnova), mouse monoclonal anti-Na^+/K^+-ATPase β1 subunit (Sigma-Aldrich) were added to 50 μL of AminoLink Plus Coupling Resin (Creative Biolabs, New York, USA). Control was done with anti-mouse IgG (Sigma-Aldrich).

Co-immunoprecipitation eluates were subjected to 8% sodium dodecyl sulphate–polyacrylamide gel electrophoresis before transfer onto a Polyvinylidene fluoride membrane. Membrane was saturated with 5% low-fat milk in Tris-buffered saline containing Tween 0.1% during 1 h at RT and then probed with primary antibodies: anti-Piezo1 (rabbit, Proteintech, 1/1000), anti-KCNMA1 (rabbit, Bethyl, 1/1000), anti-Na^+/K^+-ATPase ß1 subunit (Sigma-Aldrich, 1/1000), over-night at 4 °C. Horseradish Peroxidase conjuguated anti-mouse IgG (Dako, 1/5000) and anti-rabbit IgG (Dako, 1/2000) were used as secondary antibodies. Blots were revealed with Enhanced Chemoluminescence (Millipore) reaction on a Fusion FX7 Edge 2019. Quantification was made with ImageJ software on 8-bit images after background subtraction (50 pixels rolling ball radius).

2.7. Statistical analysis

Unless otherwise indicated, values are expressed as mean ± SEM. N-numbers refer to the number of tissue donors, n-numbers to the number of cells assessed. Differences between groups with $n \geq 21$ and normally distributed data were evaluated by Student's *t*-test. For conditions with $n < 21$ and/or not normally distributed data, significance of the difference between means was tested with the nonparametric Mann-Whitney test. The Pearson's correlation coefficient was used to compare Piezo1 and BK_{Ca} localisation. A *p*-value <0.05 was taken to indicate a significant difference between means. Designation of significance: *: $p < 0.05$; **: $p < 0.01$; ***: $p < 0.001$; ns = not significant.

3. Results

3.1. Fibroblasts and myofibroblasts are the main constituents of right atrial outgrowth cell cultures

Cells obtained by the outgrowth technique from human right atrial appendage did not contain any cardiomyocytes. The majority (98%) of cells stained positive for vimentin, and 1% of the cells were positive for the endothelial cell marker CD31. Antibody functionality was verified in positive controls using human umbilical vein endothelial cell (HUVEC; Fig. S1A and B). Overall, results confirmed that the outgrowth technique yields predominantly fibroblasts-like cells with negligible contamination by endothelial cells. Vimentin-positive cells formed a mixed population of myofibroblasts and fibroblasts. Myofibroblasts constituted an

average of 17.9 ± 9.4% of all cells analysed (n > 37,000 cells, N = 11 SR patients), based on αSMA staining (Fig. S1C).

3.2. Piezo1 in right atrial fibroblasts of patients in SR

In cell-attached patch clamp recordings (holding potential −80 mV), SAC were observed in response to negative pressure pulses in the patch pipette (Fig. 1A). In this particular cell, inward current activated rather slowly at −40 mmHg, whereas at −80 mmHg, the current peaked rapidly and partially inactivated. Activation and inactivation patterns were variable. Therefore, in addition to peak-current amplitude, the average current (mean current calculated over the duration of the pulse of pressure) was analysed. Current-pressure curves had a sigmoidal shape, suggesting saturation at patch pipette pressures more negative than −60 mmHg (Fig. 1B). In n = 110 cells (all passages considered) from N = 11 patients in SR, the peak-current amplitude was −37.4 ± 2.8 pA at −60 mmHg and the average current amplitude was −19.9 ± 1.7 pA.

The current-voltage (I-V) relationship obtained from single channel activity (n = 9 cells from N = 3 SR patients) was linear, with a slope that yielded a channel conductance of 34.2 ± 1.6 pS (activity recorded at −30 mmHg pipette pressure or during deactivation, Fig. 1C). The reversal potential near 0 mV suggests the presence of a cation-nonselective SAC in human atrial fibroblasts. This was further tested by employing the blocker GsMTx4, which inhibited SAC activity: the average current at −60 mmHg was −42.5 ± 8.3 pA (n = 21; N = 3) in control conditions, *versus* −10.4 ± 2.0 pA (n = 24; N = 3) in the presence of GsMTx4 (Fig. 1D).

In order to test which SAC contributes to the observed current, Piezo1 was knocked down using a pool of siRNA. Under these conditions, stretch-induced current activity was strongly reduced at all pressure levels tested (Fig. 1E-F); at −60 mmHg, the average current was −15.8 ± 1.6 pA (n = 51; N = 3) in control cells transfected with non-targeting siRNA (Fig. S2A), *versus* −2.3 ± 0.4 pA in siPiezo1 transfected cells (n = 49; N = 3). These values correspond well with the observed 90% reduction in mRNA expression of Piezo1 (but not Piezo2) in siPiezo1-treated cells (Fig. S2B).

Altogether, these results indicate that the SAC activity recorded at −80 mV in human atrial fibroblasts is carried largely by Piezo1.

3.3. BK_{Ca} activity in right atrial fibroblasts of patients in SR

In cell-attached voltage clamp experiments without additional suction applied to the membrane, we recorded a distinct ion channel activity at voltages positive to +10 mV. The open probability of this outward current was strongly enhanced by increasing membrane

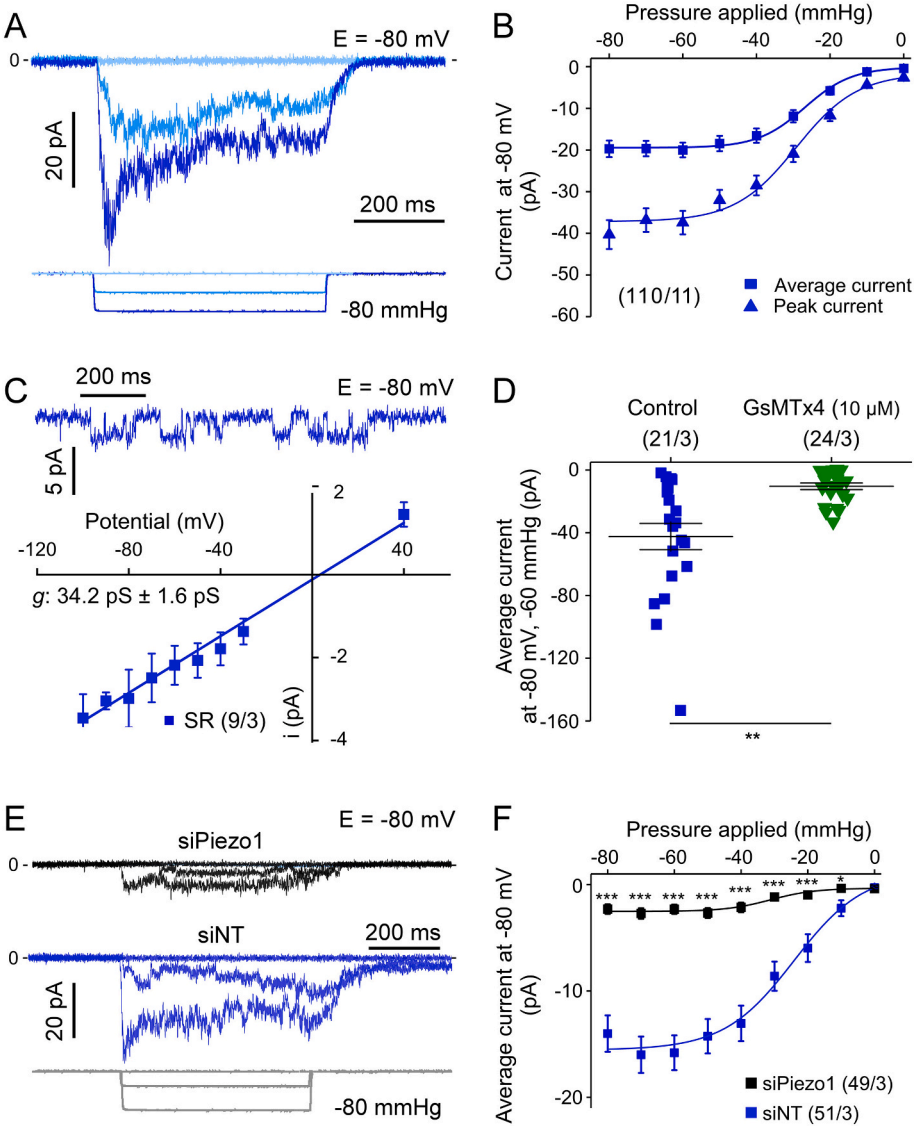

Fig. 1. Cation non-selective SAC activity, compatible with Piezo1, is present in human right atrial fibroblasts from patients in SR.
A: SAC activity, elicited by pulses of negative pressure in cell-attached mode. B: Average and peak-currents for all negative pipette pressures tested (from 0 to −80 mmHg); numbers in brackets state n of cells (here 110) and N of tissue donors (here 11) throughout all illustrations. C: Top: Single SAC channel activity, activated by a −30 mmHg pressure pulse. Bottom: I-V curve for single channel currents recorded at −30 mmHg or during deactivation, the slope of the straight line was calculated by linear regression (conductance g = 34.2 ± 1.6 pS). D: SAC activity at −60 mmHg under control conditions and with GsMTx4 L-isomer (10 µmol/L) in the pipette solution (cells from the same patients used for the two conditions). E: Representative traces of SAC activity with siRNA targeting Piezo1 (siPiezo1; black trace) and in presence of a non-targeting siRNA (siNT; blue trace). F: Summary of pressure-effects on average SAC current in cells transfected either with siNT or with a pool of 4 siRNA directed against Piezo1. All recordings, except for I–V curve, were obtained at −80 mV. Cells from passages 0 to 4. For all figures: asterisks indicate statistical significance, statistical analysis is described in the Section 2.7. (For interpretation of the references to colour in this figure legend, the reader is referred to the web version of this article.)

depolarisation (Fig. 2A-B). In addition to this pronounced voltage dependency, the conductance of channels was large, at 125.1 ± 4.9 pS (n = 60; N = 8; Fig. 2C). Based on these biophysical properties, we identified BK_{Ca} as a possible candidate underlying the current.

As means of further validation, we used pharmacological tools to either inhibit [44–46] or activate [47] BK_{Ca}. Paxilline and iberiotoxin strongly reduced the observed activity (Fig. 2D), while NS11021 caused a robust increase in open probability. The increase in open probability was attributable to an increase in the number of events and dwell time (see Fig. S3A and B). There was no significant difference in the conductance of the channel in the presence or absence of NS11021 (Fig. S3C). Interestingly, NS11021 caused a shift in potential dependence of dwell time to less positive potentials; this shift was even larger than that in open probability (Fig. S3B).

A key feature of BK_{Ca} channels is their Ca^{2+} sensitivity. We therefore tested the effects of various internal Ca^{2+} concentrations on channel activity (Fig. 2E and F). The inside-out patch configuration was used to expose the cytosolic side of the plasma membrane to increasing Ca^{2+} concentrations, ranging from a nominally Ca^{2+}-free environment to 100 µmol/L (pipette was Ca^{2+}-free). Upon increase of the Ca^{2+} concentration, a robust activation of the current was observed (from 5.6 ± 1.5 to 90.9 ± 26.0 pA; n = 11, N = 2).

Taken together, our results indicate the presence of BK_{Ca} channel activity in atrial fibroblasts from patients in SR.

3.4. *Piezo1 and BK_{Ca} activity in right atrial fibroblasts of patients in AF*

Piezo1 activity was detected in all AF and SR patients studied. The percentage of cells in which Piezo1 activity was detected was comparable in both patient populations (87%, n = 52, N = 5 in AF; 85%, n = 112, N = 10 in SR). Average Piezo1 current from cells at passage 0 (matched for cell culture time) was significantly higher in right atrial fibroblasts from patients in AF, compared to SR, at negative pressures of −40 mmHg or more (Fig. 3A and B).

While BK_{Ca} activity was observed in all patients, in some cells, we did not detect BK_{Ca} channel activity under our conditions (and no other channel activity could be measured in these 'silent' patches). The fraction of silent patches was larger in cells from AF than SR patients (60% *versus* 34%; n = 80, N = 5 for AF; n = 106, N = 10 for SR), all passages considered. In contrast to Piezo1, BK_{Ca} channels activity was significantly lower in fibroblasts from AF than SR patients for voltage clamp steps of +40 mV or more (Fig. 3C and D) even after excluding silent patches (not shown). The reduced open probability was due to a lower number of events in cells from AF tissue; mean dwell times were not significantly different in AF and SR (Fig. S4A and B).

The slopes of the I-V curves, both for Piezo1 or BK_{Ca} channels, were not different in cells from AF and SR patients (Fig. S4C and D). The distribution of cells exhibiting the various activation-inactivation patterns of Piezo1 currents was also not significantly different in cells from

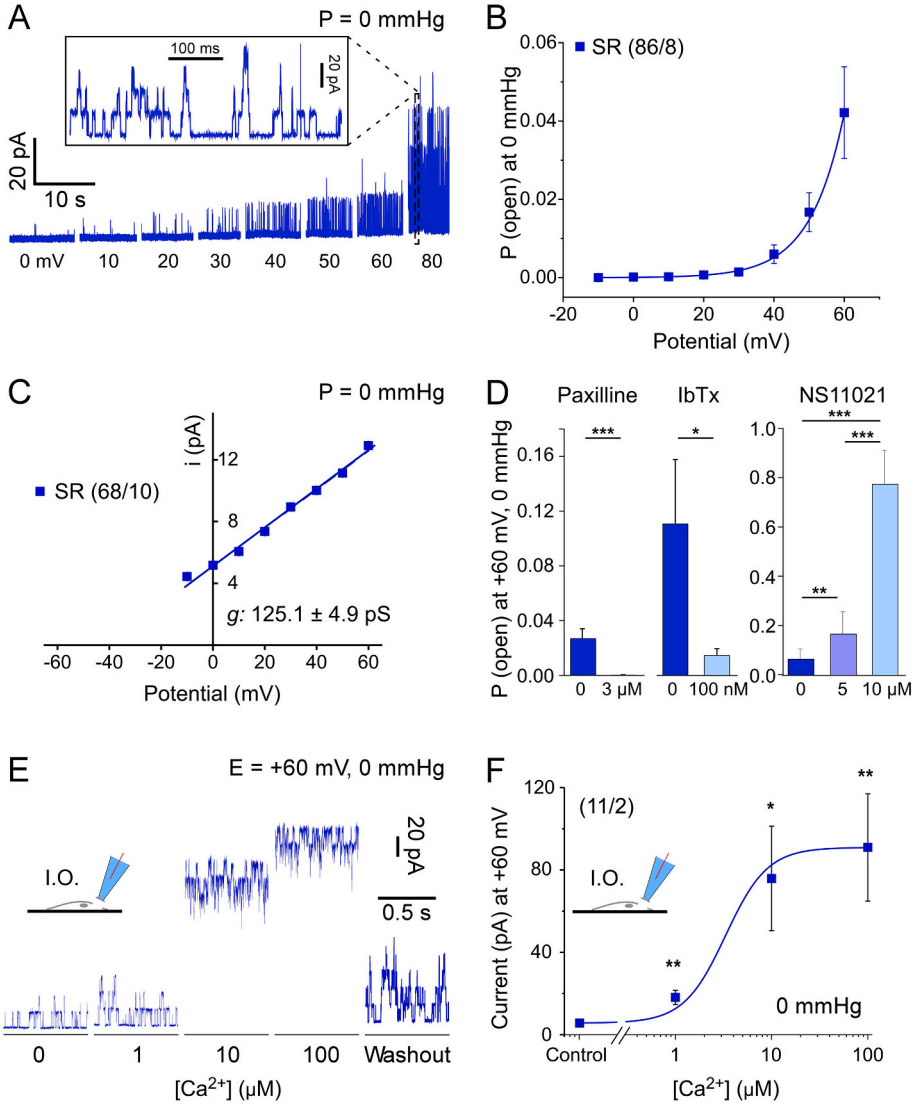

Fig. 2. Characterization of BK_{Ca} currents in right atrial fibroblasts from patients in SR.
A: Current traces in cell-attached patch clamp mode at different holding potentials in the absence of additional mechanical stimulation. Inset: expanded time scale for the trace at +80 mV. B: Open probability of BK_{Ca} channels at different potentials from −10 to +60 mV. C: I–V curve for single channel currents; straight line slope was calculated by linear regression (conductance g = 125.1 ± 4.9 pS). D: Open probability of single channels in control conditions and with 3 µmol/L paxilline (n = 26, N = 2 and n = 21, N = 2 respectively [same SR patients]); in control conditions and with iberiotoxin (IbTx) 100 nmol/L (n = 12, N = 2 and n = 15, N = 2 respectively [same SR patients]); and in control conditions with the BK_{Ca} channel activator NS11021 at 5 and 10 µmol/L (n = 14, N = 2; n = 11, N = 1; n = 18, N = 2, respectively [same SR patients]). Of note, the two controls used for paxilline and iberiotoxin (different patients) illustrate inter-patient variability. E: Original recording of BK_{Ca} channel activity at +60 mV in the inside-out configuration with increasing concentrations of Ca^{2+} applied to the cytosolic side of the membrane. F: Corresponding quantification of BK_{Ca} channel activity. Cells from passages 0 to 4.

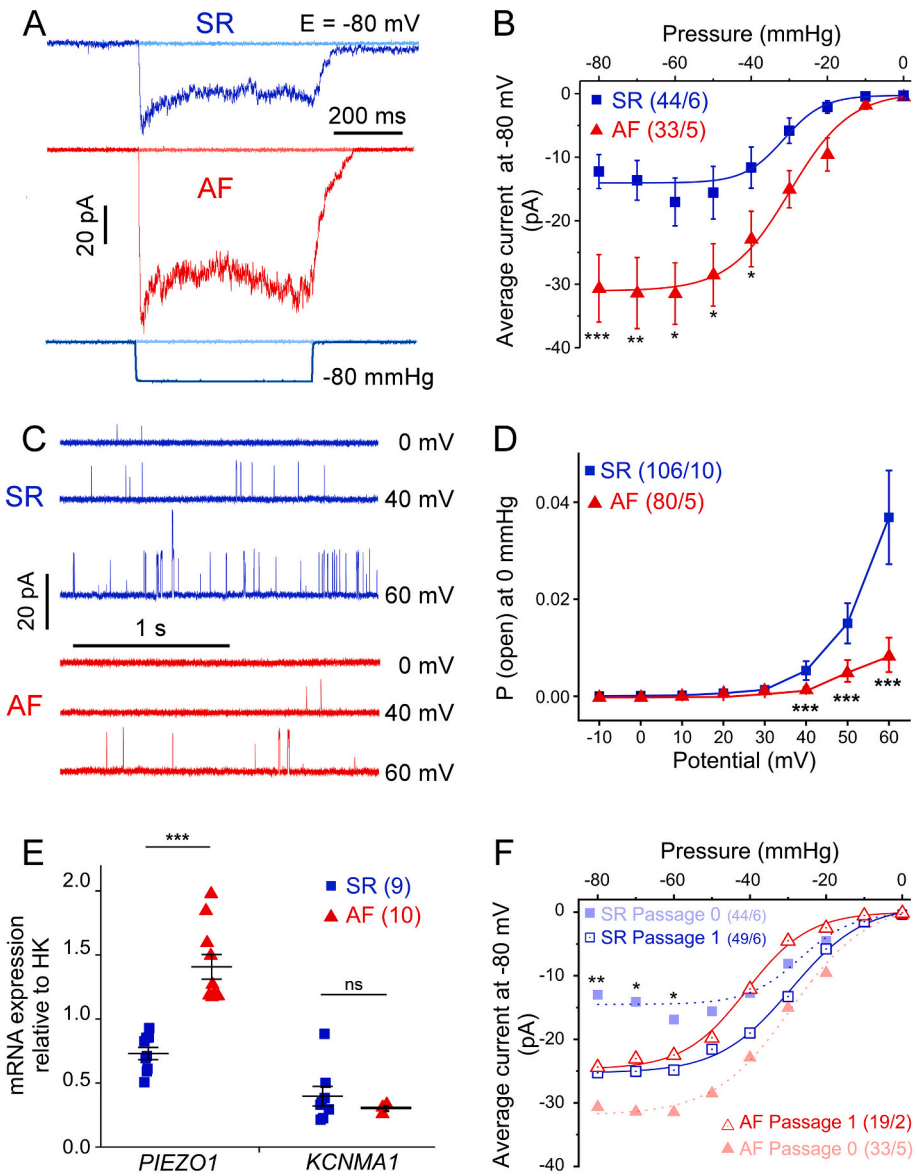

Fig. 3. Comparison of Piezo1 and BK_{Ca} channel activity and mRNA expression levels in atrial fibroblasts from patients in SR (blue) and AF (red).
A: Representative current traces (holding potential −80 mV) activated by 500-ms negative pressure pulse (−80 mmHg). B: Mean current-pressure curve for Piezo1, cells from passage 0 only. C: Representative traces of single BK_{Ca} channel activity in fibroblasts from an SR and AF patient at different holding potentials. D: Voltage dependence of open probability of BK_{Ca} channels from all patches studied (all passages). E: mRNA expression levels of Piezo1 and KCNMA1, normalised to the housekeeping gene (HK), in freshly isolated non-myocytes from patients in SR and patients in AF. F: Current-pressure relationship (average current; holding potential −80 mV) of cells from SR and AF patients at passage 0 (dotted lines; replotted for comparison from panel B) and passage 1 (solid lines). (For interpretation of the references to colour in this figure legend, the reader is referred to the web version of this article.)

AF compared to cells from SR patients (Fig. S4E). These results suggest that the observed differences in Piezo1 and BK_{Ca} activities of fibroblasts from AF tissue, compared to SR, are likely to be due to altered channel presence, rather than changes in individual channel properties.

To test the hypothesis that AF is associated with alterations in the expression of Piezo1 and BK_{Ca}, we measured the levels of mRNA encoding *PIEZO1* and *KCNMA1* [48,49] using RT-qPCR in human right atrial non-myocytes. Freshly isolated non-myocytes, obtained by enzymatic dissociation, were used to capture gene expression levels without any culture time, to be as close as possible to tissue conditions (Fig. 3E). Piezo1 expression levels in non-myocytes from AF patients were almost twice the level of SR cells. For BK_{Ca} channel expression, we did not observe significant differences between the AF and SR groups (Fig. 3E). For control purposes, the purity of the non-myocyte fraction, obtained with our enzymatic dissociation method, was checked by quantifying the expression of typical markers for non-myocytes and cardiomyocytes, *i.e.* vimentin and troponin, respectively (Fig. S5). Expression of vimentin was higher in batches containing isolated non-myocytes than in cardiomyocytes, whereas expression of troponin was higher in isolated myocytes, suggesting that the isolation protocol yielded a significant enrichment of the desired cell types.

Piezo1 (but not BK_{Ca}; see Fig. 6B) activity was found to remodel over culture time (Figs. 3F and S6). Piezo1 activity in cells from SR patients at passage 1 was significantly higher than in passage 0. No further increase of Piezo1 activity was detected at passage 2 (not shown). Cells from AF patients start off with a significantly higher level of Piezo1 than SR cells at passage 0. There is no further significant change in Piezo1 activity in cells from AF tissue (when comparing passage 1 to passage 0), and the initial difference in Piezo1-activity between cells from SR and AF patients is lost at passage 1 as SR cells become more AF-like in culture.

These results indicate that the two channels are differentially regulated in AF, with an increase in Piezo1 activity and expression, and a down-regulation of BK_{Ca} activity.

3.5. BK_{Ca} activation during stretch: Evidence for two mechanisms

BK_{Ca} channels have been described as mechano-sensitive [50], activated directly by membrane stretch [51]. This has been contrasted by the suggestion that they may respond to mechanical stimuli indirectly, by sensing changes in intracellular Ca^{2+}-concentration, caused by stretch-induced Ca^{2+} and/or Na^{+} entry through other SAC [52]. Therefore we tested whether BK_{Ca} channel activity in human atrial

fibroblasts is modified by stretch.

Fibroblasts from patients in SR were voltage-clamped to +50 mV in cell-attached mode and the patched membrane was simultaneously subjected to negative pressure pulses. The current traces in Fig. 4A show an increase of the typical large-conductance BK_{Ca} channel activity at negative pressures, compatible with stretch-dependent activation. In this particular patch, the maximum number of simultaneously open channels is 3.

The mean open probability of BK_{Ca} channels in the presence of 2 mmol/L Ca^{2+} in the pipette solution was significantly enhanced by increasing negative pressure (shown for n = 18 cells from N = 3 SR patients in Fig. 4B). Interestingly, without Ca^{2+} in the pipette solution, the stretch-dependent increase in BK_{Ca} channel open probability was significantly lower (n = 18 cells from the same N = 3 patients) but not entirely abolished at the highest negative pressure tested (−50 mmHg; Fig. 4B). The stretch-induced increase in open probability resulted mainly from a higher number of single channel events and increased dwell time, while single channel current amplitudes were not significantly different (Fig. 4C and D). As the stress-axis regulated exon (STREX) was described to be instrumental for BK_{Ca} stretch-activation, its presence was assessed in freshly isolated human atrial fibroblasts (Fig. 4E and F). PCR results demonstrate that STREX is present in most patients tested, although the BK_{Ca} splice variant without STREX is more abundantly expressed. Upon patch excision, the open probability increased (Fig. 4G and H), suggesting an inhibition of channel activity by the cytoskeleton, as previously shown for BK_{Ca} [53]. The data in Fig. 4B suggest that the majority of BK_{Ca}-activity during mechanical stimulation is dependent on external Ca^{2+}. We hypothesised that Ca^{2+} entry may be secondary to activation of other SAC. We therefore assessed Piezo1 and BK_{Ca} channel functional crosstalk (Fig. 5).

After activating Piezo1 with a 1 s-long pulse of negative pressure at a holding potential of −80 mV, suction was terminated and the holding potential switched to +50 mV. This yielded a large outward current that decayed slowly and, once the current amplitude had declined sufficiently, single channel activity could be resolved, compatible with BK_{Ca} activity (see inset in Fig. 5A). Piezo1 activity is known to rundown in response to repeated stimulation [54], so when the protocol was repeated, average inward current amplitudes declined dramatically as expected (Fig. 5A and B). Interestingly, the outward current observed upon depolarisation declined in a similar manner. With 0 mmol/L Ca^{2+} in the pipette solution, Piezo1 activity was comparable to control conditions (with Ca^{2+}), but hardly any BK_{Ca} activity was observed (Fig. 5C

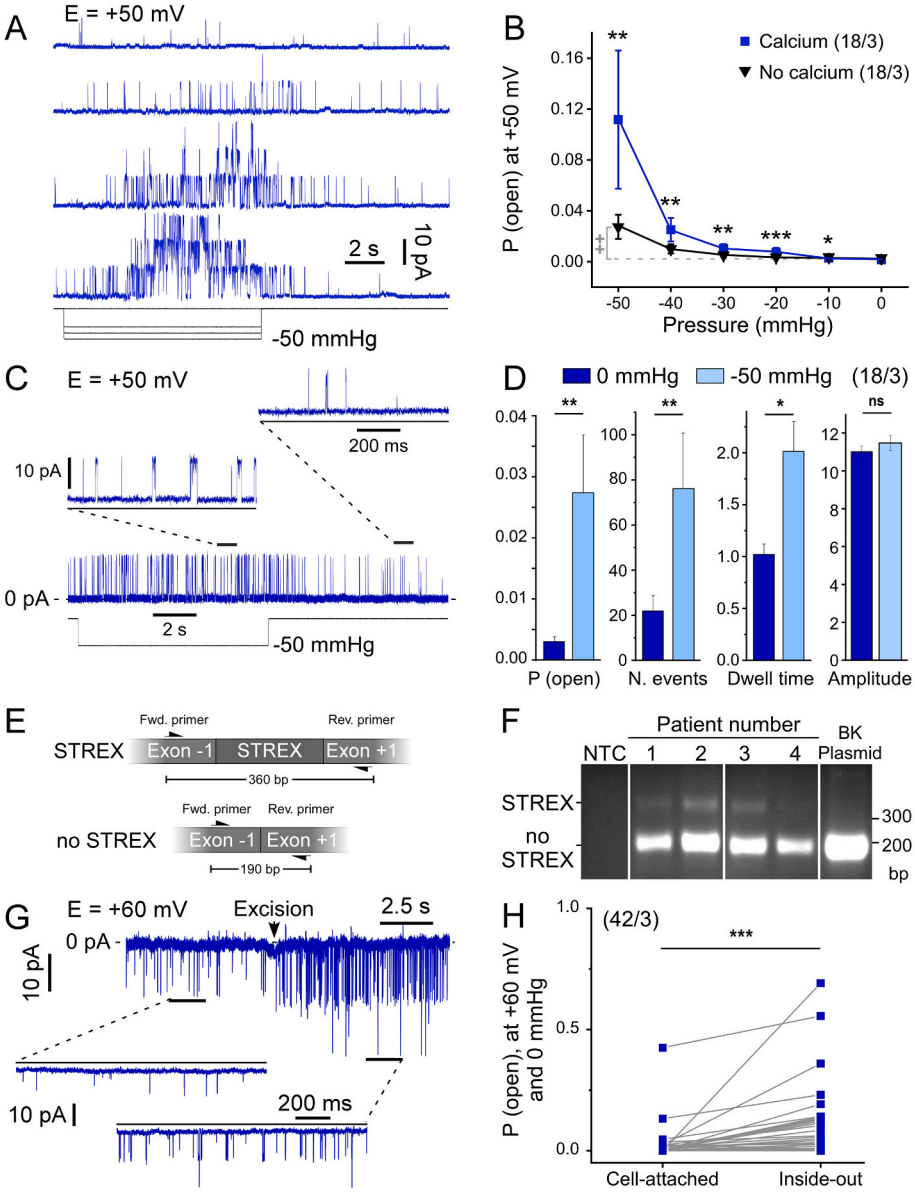

Fig. 4. BK_{Ca} stretch-response in human atrial fibroblasts from patients in SR.
A: Representative current traces at +50 mV in a cell-attached patch from a fibroblast subjected to negative pressure pulses. B: BK_{Ca} open probability in response to stretch with (2 mmol/L) and without Ca^{2+} in the pipette solution. Asterisks indicate statistical significance *versus* control (with Ca^{2+}), '+' indicate statistical significance *versus* no pressure. C: Representative recording showing single channel events with (−50 mmHg) and without pressure in a nominally Ca^{2+}-free environment pipette solution at +50 mV. D: Quantification of the channel open probability, number of single channel events (N. events), dwell time (ms) and single channel amplitude (pA) under conditions described in C. E: Schematic representing the position of the two PCR primers used to detect presence or absence of STREX in whole cell mRNA from freshly isolated non-myocytes. bp: base pairs. F: PCR results showing presence of BK_{Ca} mRNA with and without STREX in 4 patients. NTC: no template control. A purified BK_{Ca} plasmid without STREX was used as a positive control. G: Representative recording illustrating the effect of patch excision (from cell-attached to the inside-out configuration) on single channel activity at +60 mV and without pressure; standard Ca^{2+} conditions: nominally Ca^{2+}-free bath solution and 2 mmol/L Ca^{2+} in the pipette solution. H: Quantification of the channel open probability in the conditions described in G. Functional data obtained from cells at passages 0 to 4.

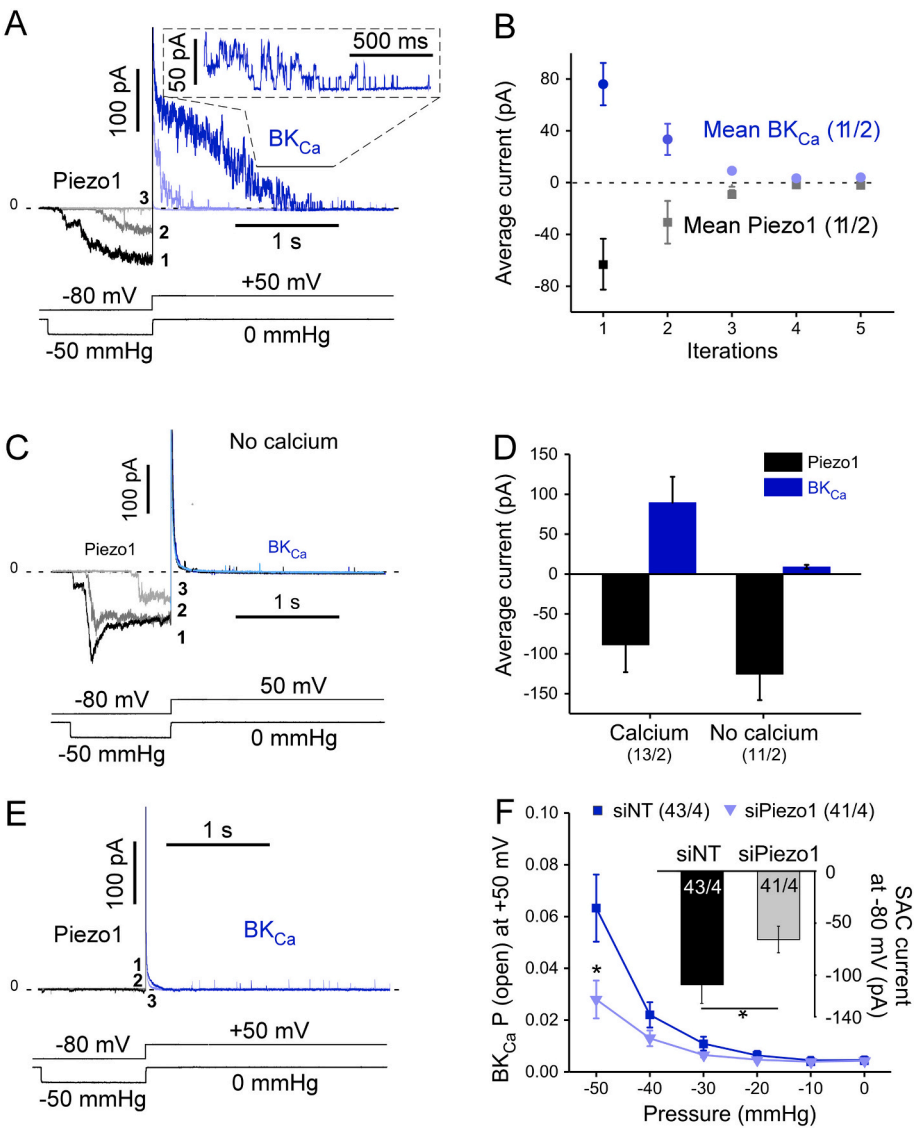

Fig. 5. Functional coupling between BK_{Ca} channels and Piezo1 in cells from SR patients.
A: Piezo1 and BK_{Ca} currents, activated during 3 consecutive sweeps (at 1-min intervals) with the indicated voltage clamp/pressure pulse protocol. The initial suction-induced inward currents are carried by Piezo (shades of grey), while the subsequent outward currents mainly represent BK_{Ca} (shades of blue). B: Mean values of average Piezo1 and BK_{Ca} currents during 5 consecutive runs of the voltage clamp/pressure pulse protocol. C: Absence of Ca^{2+} in the pipette solution drastically reduces activation of BK_{Ca} currents during the same voltage clamp/pressure pulse protocol as in A). D: Average Piezo1 and BK_{Ca} currents in the presence of 2 mmol/L Ca^{2+} (left) and in a nominally Ca^{2+}-free pipette solution (first sweep of the protocol shown in C is quantified). E: Lack of BK_{Ca} activation in the rare patches without Piezo1 activity. F: Open probability of BK_{Ca} channels (same protocol as in A) in fibroblasts transfected with siRNA targeted against Piezo1 or non-targeting contol (siNT; cells from same patients in SR). Inset: amplitude of average SAC currents, induced by −80 mmHg in the same batch of cells (holding potential −80 mV). Cells from passages 1 to 4. (For interpretation of the references to colour in this figure legend, the reader is referred to the web version of this article.)

and D). In some rare patches in which no SAC current was observed at −50 mmHg, the protocol also failed to yield BK_{Ca} activity (Fig. 5E, BK_{Ca} channel presence was confirmed by activating them, using membrane depolarisation [not shown]). Following the same line of thought, after down-regulation of Piezo1 by siRNA, stretch-dependent BK_{Ca} channel open probability was reduced (Fig. 5F).

Overall, these results suggest that in human right atrial fibroblasts the apparent mechano-sensitivity of BK_{Ca} channels is mainly secondary to cation non-selective SAC activity, involving Piezo1.

Functional coupling between BK_{Ca} and Piezo1 was also observed in fibroblasts obtained from AF patients (Fig. 6). A large outward current compatible with BK_{Ca} activity was detected subsequent to Piezo1 activation. This activity decayed as Piezo1 ran down (Fig. 6A and B) and no activation was detected when Piezo1 activity could not be observed (Fig. 6C and D), even though BK_{Ca} channels were present (single channels, visible in Fig. 6C; BK_{Ca} activation was verified by prior membrane depolarisation, not shown). As these cells were from passage 1 and higher, Piezo1 current was not significantly different in cells from AF *versus* SR patients (*cf.* Fig. 3F and S6), while BK_{Ca} current was significantly smaller in cells from AF compared to SR patients. Functional coupling between Piezo1 and BK_{Ca} is present also at passage 0 (see Fig. S7).

3.6. Assessment of Piezo1 - BK_{Ca} structural coupling

To investigate whether the functional interactions of Piezo1 and BK_{Ca} require a physical link of the two channel proteins, co-immunoprecipitation experiments were performed.

Using either Piezo1 to immunoprecipitate BK_{Ca}, or BK_{Ca} to immunoprecipitate Piezo1, no interactions were detected in fibroblast primary cultures (Fig. 7A). Because the quantity of material is limited when working with primary cultures and to improve Piezo1 signal (presence of smear, possibly due to post-translational modifications) additional experiments were performed in a human atrial fibroblast cell line obtained from a patient in SR [36]. In these cells, no interactions between the two channels were observed either (Fig. 7B) while the Na^+/K^+-ATPase, a known binding-partner of BK_{Ca} [55], co-immunoprecipitated with BK_{Ca} (Fig. 7C).

In agreement with these findings, immunocytochemistry experiments, performed on primary cultures of right atrial fibroblasts from a SR patient, revealed distinct localisation profiles of Piezo1 and BK_{Ca} with limited overlap (Fig. 7D). The Pearson's correlation coefficient of the two signals is 0.46 ± 0.03 (n = 22, N = 1), which indicates no significant degree of correlation.

These results suggest that, although Piezo1 and BK_{Ca} are frequently present in the same membrane patches in electrophysiological

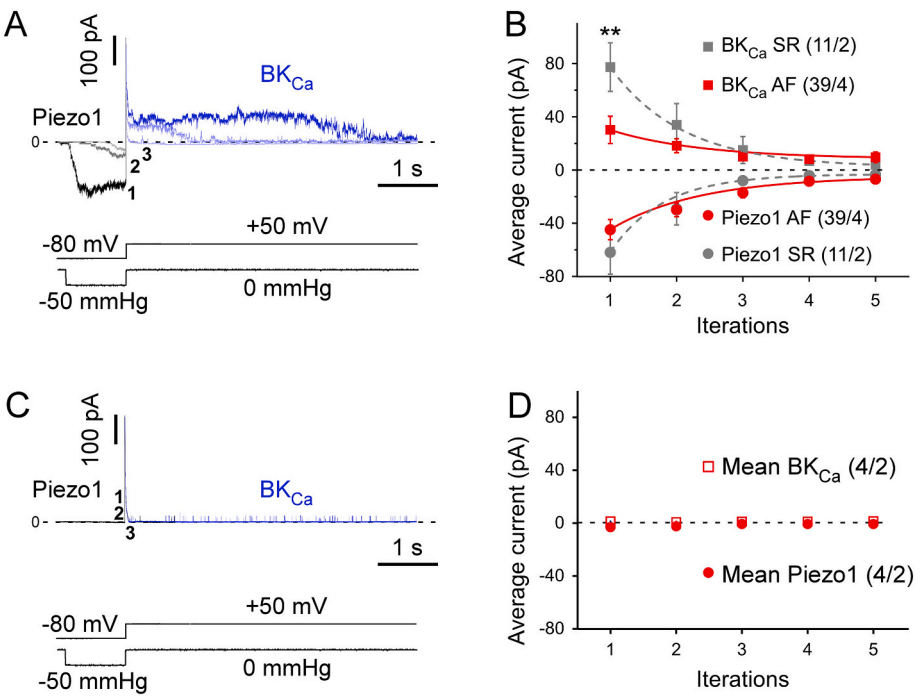

Fig. 6. Functional coupling between BK_{Ca} channels and Piezo1 in cells from AF patients.
A: Piezo1 (shades of grey) and BK_{Ca} (shades of blue) currents, activated in response to the indicated voltage clamp/pressure pulse protocol (same as in Fig. 5). B: Mean values of average Piezo1 and BK_{Ca} currents during 5 consecutive runs of the voltage clamp/pressure pulse protocol. Currents obtained from cells isolated from AF (red) and SR (grey) patients (SR data same as in Fig. 5B). C and D: Lack of BK_{Ca} activation in patches without Piezo1 activity. Cells from passages 1 to 5. (For interpretation of the references to colour in this figure legend, the reader is referred to the web version of this article.)

experiments, they are not physically linked.

4. Discussion

We confirm the presence, in human right atrial fibroblasts from patients in SR and AF, of at least two different types of ion currents that are activated during stretch: the cation-nonselective Piezo1 and the potassium-selective BK_{Ca}. Our main findings are: (i) activity and expression of Piezo1 are larger in non-passaged right atrial fibroblasts from AF patients than in cells from SR patients; (ii) activity, but not expression, of BK_{Ca} channels is lower in AF than in SR cells; (iii) mechano-sensitivity of BK_{Ca} channels in human atrial fibroblasts is largely secondary to stretch-induced activation of other SAC, including Piezo1, and (iv) upon passaging of fibroblasts, the difference in Piezo1 activity between AF and SR cells disappears (as SR cells become 'more AF-like'), whereas the lower activity of BK_{Ca} in AF cells compared to SR is maintained.

4.1. Cell identities

As reported in the literature, various cells migrate from small chunks of atrial tissue when placed into appropriate culture medium [35]. In our hands, this 'outgrowth technique' yields 98% vimentin positive cells. In previous work with the same model, we used human fibroblast surface protein as an additional marker to confirm that the vimentin-positive cells are largely fibroblasts [35]. The endothelial cell marker CD31 was detected in only 1% of our cells, indicating that the majority of the population is of non-endothelial origin. Upon activation, fibroblasts differentiate into myofibroblasts that express αSMA [56]. The percentage of cells that stained positively for αSMA varied between individuals, with an average of 18% in passage 0 (values ranged from 4% to 38%). In live cell experiments, *i.e.* in the absence of antibody staining, fibroblasts and myofibroblasts could not be differentiated with certainty, based on morphological criteria including size, capacitance and shape. Functional results will therefore reflect a mix of cells, of which ≥80% are taken to be fibroblasts.

4.2. SAC in human atrial fibroblasts involve Piezo1 channels

In human atrial fibroblasts, voltage-dependent ion channels have been reported [31,32,35], though relatively little is known about SAC. Negative pressure pulses, applied to the patch pipette at a holding potential of −80 mV, activate inward currents with variable inactivation kinetics. These currents deactivate completely upon pressure release. Using GsMTx4 and a knockdown approach targeting Piezo1, we demonstrate that these SAC in human right atrial fibroblasts are carried largely by Piezo1 (Fig. 1). This result is in line with a recent report by Blythe *et al.*, also on human atrial fibroblasts [21].

4.3. BK_{Ca} channels in human atrial fibroblasts

Robust BK_{Ca} channel activity has been reported previously in 88% of human ventricular fibroblasts [57]. In our study, BK_{Ca} channel activity was present in 40% of right atrial fibroblasts of AF and 66% of SR samples, showing the typical large single channel conductance (125.1 ± 4.9 pS). BK_{Ca} activity was observed in cells from all patients studied. Currents were blocked by paxilline, iberiotoxin and increased in the presence of NS11021. Their open probability was raised both by elevated internal Ca^{2+} concentrations (as previously reported for BK_{Ca} [58]) and by patch excision suggesting sensitivity to cytoskeletal integrity, another known feature of BK_{Ca} channels [53]. These properties confirm that the observed current is carried by BK_{Ca} channels (Fig. 2).

This study is focussed on right atrial appendage tissue, which is available in the context of open-heart surgery involving extra-corporal circulation, as left atrial tissue is removed more rarely. However, both Piezo1- and BK_{Ca}-like activities were confirmed in right and left atrial free wall tissue (Fig. S8). In these cells, single channel amplitudes for Piezo1- and BK_{Ca}-like currents were not different from the activity of right auricular fibroblasts included in this paper (not shown), suggesting that the observations reported here are not restricted to right atrial appendage.

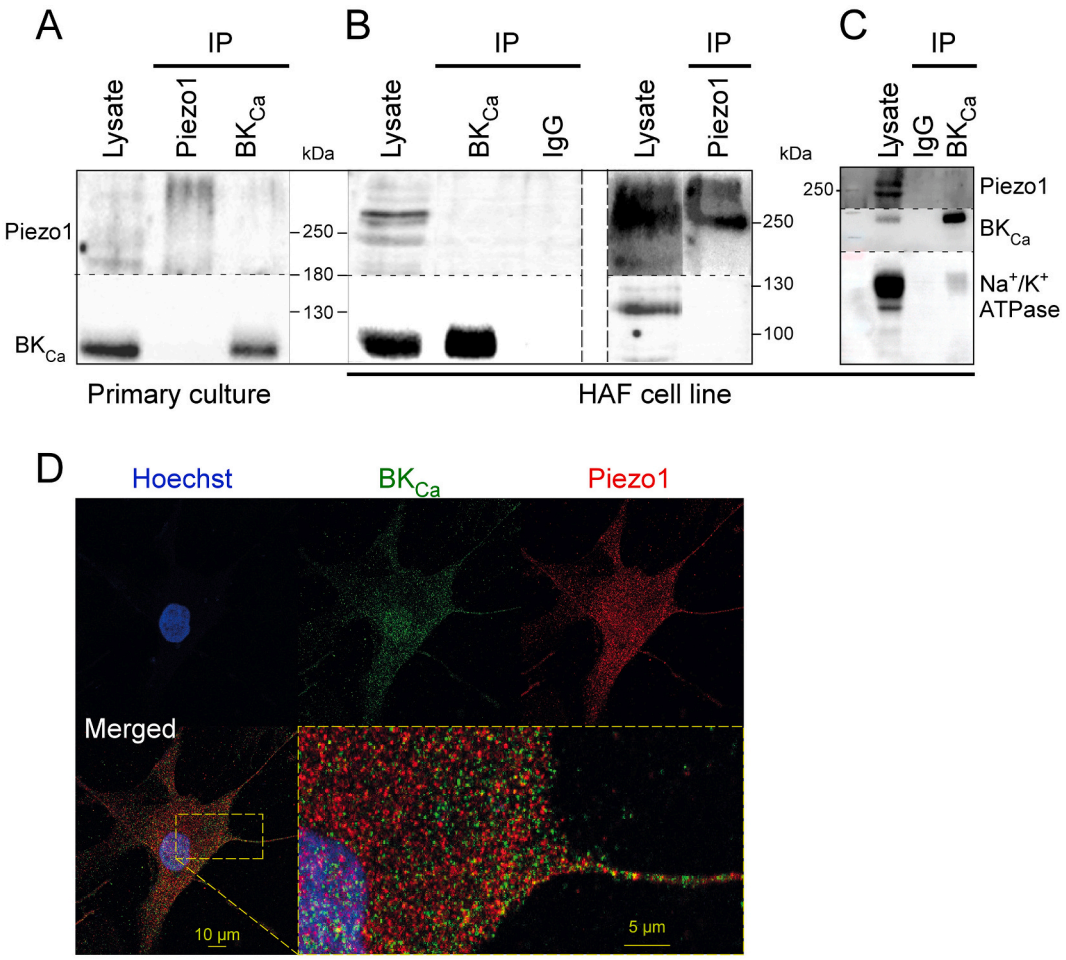

Fig. 7. Piezo1 and BK_{Ca} channels do not co-immunoprecipitate and have distinct localisation profiles.
A: Representative Western blots, showing co-immunoprecipitations with anti-Piezo1 or anti-BK of human atrial fibroblast lysates. B: Same experiment performed using a human atrial fibroblast cell line. A column with mouse nonspecific IgG was used as negative control. C: Co-immunoprecipitation of Na^+/K^+-ATPase and BK_{Ca} in the human atrial fibroblast cell line (positive control). D: Immuno-staining showing Piezo1 and BK_{Ca} in a primary human right atrial fibroblast.

4.4. Piezo1 and BK_{Ca} currents in human atrial fibroblasts are differentially remodelled during AF

Cells in fibrillating atria are exposed to mechanical loads that may activate SAC. Perhaps surprisingly, cells from SR and AF patients kept their respective phenotype during the first 20–28 days of primary culture. The two channel types investigated here were altered in opposite directions (Fig. 3): whilst presence and stretch-induced activity of Piezo1 were significantly larger in non-passaged cells from AF compared to SR patients, consistent with an up-regulation of *PIEZO1* expression, the open probability of BK_{Ca} channels was lower in AF compared to SR, while no differences in expression levels was detected. This difference in BK_{Ca} activity in spite of unchanged mRNA levels may be caused by modifications in trafficking, leading to diminished presence of BK_{Ca} channels in the plasma membrane, or an alteration in the regulation of BK_{Ca} gating. The reduced BK_{Ca} activity was sustained over multiple passages (up to 5; Fig. 6B). In contrast, Piezo1 activity was found to increase in cells from SR patients after passaging, rising towards levels that were indistinguishable from AF cells, whilst the activity in cells from AF patients remained unchanged (Figs. 3F and S6).

To avoid effects of prolonged culturing on ion channel activity, we focussed analyses of channel cross-talk on passage-0 cells. We also attempted to record from freshly isolated fibroblasts. In most cases, repeated negative pressure pulses of significant amplitude (above −20 mmHg) were necessary to obtain seals, in contrast to cultured fibroblasts where seals were generally achieved by a single approach with mild suction (<10 mmHg). As Piezo1 desensitises with repeat pressure application [54], freshly isolated cells were not well-suited for obtaining reproducible measurements of SAC activity.

4.5. Piezo1 and BK_{Ca} channels are linked functionally, but not structurally

BK_{Ca} channels in human right atrial fibroblasts increased their open probability during mechanical stimulation, applied by stretching the membrane patch in the pipette. Several lines of our experimental evidence suggest that this is, in large part, caused by functional crosstalk between stretch-induced activation of Piezo1 and BK_{Ca} activity.

Firstly, we induced transient stretch-activation of Piezo1, followed immediately by recording BK_{Ca} channel activity in the absence of stretch. These experiments identified BK_{Ca} activation (in the absence of stretch) as related to the amplitude of the immediately preceding mechanically-triggered Piezo1 activity (Fig. 5). Desensitisation of Piezo1 during successive activation steps [54] reduced subsequent BK_{Ca} activity. Similarly, when no Piezo1 activity was detected in a patch (rare cases), no BK_{Ca} activation was observed either.

Secondly, the functional crosstalk of Piezo1 and BK_{Ca} depends on the presence of Ca^{2+} in the pipette solution: in the absence of extracellular Ca^{2+}, Piezo1 currents were still detectable (non-selective cation channel), but BK_{Ca} activation was strongly reduced (Fig. 5C and D). This suggests that a stretch-induced trans-membrane Ca^{2+} flux *via* Piezo1 may increase intracellular Ca^{2+} concentration near BK_{Ca} channels and

activate them.

Thirdly, knockdown of Piezo1 (see Fig. 5F) reduced the stretch-dependent activation of BK_{Ca}. This suppression was incomplete (to about 25% of control at the highest suction levels). This may be due to partial knockdown of Piezo1 (as shown in the inset of Fig. 5F), to a contribution from other cation non-selective SAC, or indeed to a residual level of BK_{Ca} mechano-sensitivity. A number of other SAC, including Piezo2 (Fig. S2), and canonical transient receptor potential (TRP) channels, including TRPC3 and 6 [59,60], are expressed in cardiac fibroblasts, which could influence BK_{Ca} activity. Interestingly, Piezo1 and Piezo2 have similar expression levels (Fig. S2), although the contribution from Piezo2 to the electrical activity recorded after Piezo1 knockdown (Fig. 1F), if any, seems limited.

Taken together, our data suggests that the two channels are functionally coupled in cells from SR (Fig. 5) and AF (Fig. 6) patients. Application of negative pressure to a patch, held at +50 mV, will allow Ca^{2+} entry *via* Piezo1 (the calculated Ca^{2+} reversal potential, with 2 mmol/L Ca^{2+} in the pipette and assuming an intracellular free Ca^{2+} concentration of 100 nmol/L is +125 mV). Similar connections between Ca^{2+}-dependent K^+ channels and Ca^{2+}-permeable channels, such as L-type Ca^{2+}-channels or SAC, have been described previously [52,61,62], but so far not in human heart cells. In addition, Piezo1-mediated Ca^{2+} influx in human atrial fibroblasts has been reported [33], which supports our observations. Interestingly, the functional coupling of Piezo1 and BK_{Ca} does not seem to require protein-protein interactions (Fig. 7). It may not depend on the specific pair of proteins studied here, *i.e.* Piezo1 (and, possibly, other cation non-selective SAC) could influence the activity of other Ca^{2+}-dependent channels, potentially making them indirectly mechano-sensitive.

Since Piezo1 is non-selective for cations [22], Na^+ will also enter the cell during stretch- activation of Piezo1. Elevated intracellular Na^+ can increase intracellular Ca^{2+} levels *via* secondary effects, such as mediated by the Na^+/Ca^{2+} exchanger [52]. We therefore used Ca^{2+}-free conditions, both in the pipette and the bath solution, which would have reduced any contribution by such secondary effects.

While downregulation of Piezo1 and use of Ca^{2+}-free conditions strongly reduced BK_{Ca} channel activity, these interventions did not completely abolish it. We interpret the remaining (roughly 25%) BK_{Ca} channel activity as evidence for a possible direct stretch-mediated activation of BK_{Ca} channels. This is supported by the detection of STREX (Fig. 4F) in keeping with previous work [26,28]. The lower expression of the STREX-containing variant compared to BK_{Ca} without STREX corresponds to the electrophysiological observations: the direct stretch-mediated activation represents a fraction only of the total BK_{Ca} stretch-induced response (Fig. 4B and F).

4.6. Possible functional relevance

The role of, both, the coupling between Piezo1 and BK channels, and the differential remodelling of their activity in the context of AF, for (patho-)physiology of atrial cell and tissue remains to be elucidated. The resting membrane potentials of fibroblasts, isolated from AF and SR patients and cultured on a static substrate, did not differ [35], so functional contributions may need to be explored in the context of cell stretching.

If Piezo1 or/and BK_{Ca} were to alter fibroblast membrane potential during stretch, this could have implications for fibroblasts biology and, possibly, have consequences for electrical excitability, refractoriness, and conduction in myocytes, as fibroblasts and cardiomyocytes can be electrotonically coupled, as demonstrated in murine heart lesions [63,64].

We anticipate possible contributions of Piezo1 and BK_{Ca} channels to tissue remodelling, as suggested in non AF-related settings [21,31]. Piezo1 expression and activity have further been proposed to contribute to the control of pro-fibrotic interleukin-6 (IL-6) expression and secretion [21]. The increased Piezo1 expression and activity reported here in fibroblasts from AF patients, may correspond to an increase in IL-6 signalling. Interestingly, elevated levels of IL-6 correlate with increased left atrial size (as a potential mechanical input [65]), and AF [66,67].

4.7. Study limitations and future work

Cells recorded in this study form a mixed population of fibroblasts and myofibroblasts. We did not separately quantify the percentage of myofibroblasts *versus* fibroblasts in cells from AF patients and from passaged cells. The ratio of myofibroblasts in AF tissue or at later stages of culturing may be higher, compared to control. Further studies will investigate whether fibroblast-myofibroblast phenoconversion influences Piezo1 and BK_{Ca} channels and their cross-talk.

Additional research will be required to characterise the mechanisms by which Piezo1 and BK_{Ca} are differentially regulated in fibroblasts from AF patients compared to cells from SR patients. Also, other essential elements of the BK_{Ca} channel signalling complex will need to be analysed, as either or both of the beta and gamma subunits may be changed in the context of AF. This, together with a detailed analysis of BK_{Ca} localisation, would help in revealing why less BK_{Ca} activity is detected in AF fibroblasts compared to SR, while Piezo1 activity is higher.

BK_{Ca} is obviously not the only Ca^{2+}-activated conductance in fibroblasts. Analysing the effects of Piezo1 opening, for example on the Ca^{2+}-activated chloride channel anoctamin-1, could be quite relevant in the context of AF, as up-regulation of that channel has been reported to prevent fibrosis after myocardial infarction [68].

In conclusion, we describe two ion channel populations in human right atrial fibroblasts whose activity is increased during stretch, either directly (Piezo1 and, probably, a subset of BK_{Ca} channels) or indirectly (most BK_{Ca} channels, whose activation depends on functional cross-talk with Piezo1). The two channels are differentially regulated in AF, with an increase in Piezo1 activity and expression, and a down-regulation of BK_{Ca} activity. The patho-physiological relevance of these changes remains to be explored.

Author contributions

DJ, AK, SNH, PK, UR and RP contributed to conception, design and interpretation of the study. DJ, AK and ED performed and analysed electrophysiological experiments. DA, EARZ, SP and CS performed and analysed quantitative RT-PCR experiments. DJ and TG performed and analysed immunocytochemical experiments. DA and ASC isolated cells. BA and HG performed and analysed the co-immunoprecipitation and localisation experiments. RE performed the PCR to assess the presence of STREX. SRK provided HAF cells. FB, CS, MK and FAK provided access to surgical tissue samples. DJ, AK, UR and RP drafted the manuscript. All authors contributed to manuscript revision, read and approved the submitted version.

Funding

This work was supported by the ERC Advanced Grant *CardioNECT* (project ID: #323099, PK), a research grant from the Ministry of Science, Research and Arts Baden-Württemberg (MWK-BW Sonderlinie Medizin, #3091311631, PK), and a DFG Emmy Noether Fellowship (to EARZ, 285 #396913060). This research was funded by the German Research Foundation (DFG) under the Excellence Strategy (CIBSS-EXC-2189-Project ID 390939984). ED, PK, UR and RP acknowledge support by Amgen Inc. ED, RE, ASC, EARZ, FB, FAK, CS, PK, UR and RP are members of the Collaborative Research Centre SFB1425 of the German Research Foundation (#422681845).

Declaration of Competing Interest

None.

Acknowledgments

The authors thank all colleagues at the Department for Cardiovascular Surgery of the University Heart Centre Freiburg - Bad Krozingen, and at the CardioVascular BioBank Freiburg, for providing access to human atrial tissue. Special thanks for technical support go to Cinthia Walz, Anne Hetkamp, Kristina Kollmar and Gabriele Lechner. We would like to also thank Dr. Simone Nübling and Dr. Hannah Fürniss for their help concerning patient demographics. We thank Dr. Bo Bentzen (University of Copenhagen) for providing us with the compound NS11021. We acknowledge support from SCI-MED for image acquisition and analysis.

Appendix A. Supplementary data

Supplementary data to this article can be found online at https://doi.org/10.1016/j.yjmcc.2021.05.002.

References

[1] C.X. Wong, A.G. Brooks, D.P. Leong, K.C. Roberts-Thomson, P. Sanders, The increasing burden of atrial fibrillation compared with heart failure and myocardial infarction: a 15-year study of all hospitalizations in Australia, Arch. Intern. Med. 172 (2012) 739–741.
[2] H. Zulkifly, G.Y.H. Lip, D.A. Lane, Epidemiology of atrial fibrillation, Int. J. Clin. Pract. 72 (2018), e13070.
[3] L. Staerk, J.A. Sherer, D. Ko, E.J. Benjamin, R.H. Helm, Atrial fibrillation: epidemiology, pathophysiology, and clinical outcomes, Circ. Res. 120 (2017) 1501–1517.
[4] M.C. Wijffels, C.J. Kirchhof, R. Dorland, M.A. Allessie, Atrial fibrillation begets atrial fibrillation. A study in awake chronically instrumented goats, Circulation 92 (1995) 1954–1968.
[5] D. Dobrev, U. Ravens, Remodeling of cardiomyocyte ion channels in human atrial fibrillation, Basic Res. Cardiol. 98 (2003) 137–148.
[6] K. Kumagai, S. Akimitsu, K. Kawahira, F. Kawanami, Y. Yamanouchi, T. Hiroki, K. Arakawa, Electrophysiological properties in chronic lone atrial fibrillation, Circulation 84 (1991) 1662–1668.
[7] B.M. Psaty, T.A. Manolio, L.H. Kuller, R.A. Kronmal, M. Cushman, L.P. Fried, R. White, C.D. Furberg, P.M. Rautaharju, Incidence of and risk factors for atrial fibrillation in older adults, Circulation 96 (1997) 2455–2461.
[8] F. Bode, F. Sachs, M.R. Franz, Tarantula peptide inhibits atrial fibrillation, Nature 409 (2001) 35–36.
[9] A. Kamkin, I. Kiseleva, K.D. Wagner, K.P. Leiterer, H. Theres, H. Scholz, J. Gunther, M.J. Lab, Mechano-electric feedback in right atrium after left ventricular infarction in rats, J. Mol. Cell. Cardiol. 32 (2000) 465–477.
[10] F. Ravelli, Mechano-electric feedback and atrial fibrillation, Prog. Biophys. Mol. Biol. 82 (2003) 137–149.
[11] F. Ravelli, M. Allessie, Effects of atrial dilatation on refractory period and vulnerability to atrial fibrillation in the isolated Langendorff-perfused rabbit heart, Circulation 96 (1997) 1686–1695.
[12] F. Ravelli, M. Mase, M. del Greco, M. Marini, M. Disertori, Acute atrial dilatation slows conduction and increases AF vulnerability in the human atrium, J. Cardiovas. Electrophysiol. 22 (2011) 394–401.
[13] S. Thanigaimani, E. McLennan, D. Linz, R. Mahajan, T.A. Agbaedeng, G. Lee, J. M. Kalman, P. Sanders, D.H. Lau, Progression and reversibility of stretch induced atrial remodeling: characterization and clinical implications, Prog. Biophys. Mol. Biol. 130 (2017) 376–386.
[14] P. Tavi, C. Han, M. Weckstrom, Mechanisms of stretch-induced changes in $[Ca^{2+}]_i$ in rat atrial myocytes: role of increased troponin C affinity and stretch-activated ion channels, Circ. Res. 83 (1998) 1165–1177.
[15] S.A. Nazir, M.J. Lab, Mechanoelectric feedback and atrial arrhythmias, Cardiovasc. Res. 32 (1996) 52–61.
[16] R. Kaufmann, U. Theophile, Autonomously promoted extension effect in Purkinje fibers, papillary muscles and trabeculae carneae of rhesus monkeys, Pflugers Archiv fur die gesamte Physiologie des Menschen und der Tiere. 297 (1967) 174–189.
[17] M.J. Lab, Depolarization produced by mechanical changes in normal and abnormal myocardium [proceedings], J. Physiol. 284 (1978) 143p–144p.
[18] R. Peyronnet, J.M. Nerbonne, P. Kohl, Cardiac mechano-gated ion channels and arrhythmias, Circ. Res. 118 (2016) 311–329.
[19] T.A. Quinn, P. Kohl, Cardiac mechano-electric coupling: acute effects of mechanical stimulation on heart rate and rhythm, Physiol. Rev. 101 (2021) 37–92.
[20] A. Kamkin, I. Kiseleva, K.D. Wagner, A. Lammerich, J. Bohm, P.B. Persson, J. Gunther, Mechanically induced potentials in fibroblasts from human right atrium, Exp. Physiol. 84 (1999) 347–356.
[21] N.M. Blythe, K. Muraki, M.J. Ludlow, V. Stylianidis, H.T.J. Gilbert, E.L. Evans, K. Cuthbertson, R. Foster, J. Swift, J. Li, M.J. Drinkhill, F.A. van Nieuwenhoven, K. E. Porter, D.J. Beech, N.A. Turner, Mechanically activated Piezo1 channels of cardiac fibroblasts stimulate p38 mitogen-activated protein kinase activity and interleukin-6 secretion, J. Biol. Chem. 294 (2019) 17395–17408.
[22] B. Coste, J. Mathur, M. Schmidt, T.J. Earley, S. Ranade, M.J. Petrus, A.E. Dubin, A. Patapoutian, Piezo1 and Piezo2 are essential components of distinct mechanically activated cation channels, Science 330 (2010) 55–60.
[23] B. Coste, B.L. Xiao, J.S. Santos, R. Syeda, J. Grandl, K.S. Spencer, S.E. Kim, M. Schmidt, J. Mathur, A.E. Dubin, M. Montal, A. Patapoutian, Piezo proteins are pore-forming subunits of mechanically activated channels, Nature 483 (2012) 176–U72.
[24] D.J. Beech, A.C. Kalli, Force sensing by piezo channels in cardiovascular health and disease, Arterioscler. Thromb. Vasc. Biol. 39 (2019) 2228–2239.
[25] Z. Petho, K. Najder, E. Bulk, A. Schwab, Mechanosensitive ion channels push cancer progression, Cell Calcium 80 (2019) 79–90.
[26] H. Zhao, M. Sokabe, Tuning the mechanosensitivity of a BK channel by changing the linker length, Cell Res. 18 (2008) 871–878.
[27] G. Iribe, H. Jin, K. Naruse, Role of sarcolemmal BKCa channels in stretch-induced extrasystoles in isolated chick hearts, Circ. J. 75 (2011) 2552–2558.
[28] K. Naruse, Q.-Y. Tang, M. Sokabe, Stress-Axis regulated exon (STREX) in the C terminus of BKCa channels is responsible for the stretch sensitivity, Biochem. Biophys. Res. Commun. 385 (2009) 634–639.
[29] L. Ge, N.T. Hoa, Z. Wilson, G. Arismendi-Morillo, X.T. Kong, R.B. Tajhya, C. Beeton, M.R. Jadus, Big potassium (BK) ion channels in biology, disease and possible targets for cancer immunotherapy, Int. Immunopharmacol. 22 (2014) 427–443.
[30] Zhao H-C, H. Agula, W. Zhang, F. Wang, M. Sokabe, L.-M. Li, Membrane stretch and cytoplasmic Ca^{2+} independently modulate stretch-activated BK channel activity, J. Biomech. 43 (2010) 3015–3019.
[31] J. Sheng, W. Shim, H. Wei, S.Y. Lim, R. Liew, T.S. Lim, B.H. Ong, Y.L. Chua, P. Wong, Hydrogen sulphide suppresses human atrial fibroblast proliferation and transformation to myofibroblasts, J. Cell. Mol. Med. 17 (2013) 1345–1354.
[32] A. Klesen, D. Jakob, R. Emig, P. Kohl, U. Ravens, R. Peyronnet, Cardiac fibroblasts: active players in (atrial) electrophysiology? Herzschrittmacherther. Elektrophysiol. 29 (2018) 62–69.
[33] N.M. Blythe, K. Muraki, M.J. Ludlow, V. Stylianidis, H.T. Gilbert, E.L. Evans, K. Cuthbertson, R. Foster, J. Swift, J. Li, Mechanically activated Piezo1 channels of cardiac fibroblasts stimulate p38 mitogen-activated protein kinase activity and interleukin-6 secretion, J. Biol. Chem. 294 (2019) 17395–17408.
[34] P. Kirchhof, S. Benussi, D. Kotecha, A. Ahlsson, D. Atar, B. Casadei, M. Castella, H. C. Diener, H. Heidbuchel, J. Hendriks, G. Hindricks, A.S. Manolis, J. Oldgren, B. A. Popescu, U. Schotten, B. Van Putte, P. Vardas, S. Agewall, J. Camm, G. Baron Esquivias, W. Budts, S. Carerj, F. Casselman, A. Coca, R. De Caterina, S. Deftereos, D. Dobrev, J.M. Ferro, G. Filippatos, D. Fitzsimons, B. Gorenek, M. Guenoun, S. H. Hohnloser, P. Kolh, G.Y. Lip, A. Manolis, J. McMurray, P. Ponikowski, R. Rosenhek, F. Ruschitzka, I. Savelieva, S. Sharma, P. Suwalski, J.L. Tamargo, C. J. Taylor, I.C. Van Gelder, A.A. Voors, S. Windecker, J.L. Zamorano, K. Zeppenfeld, 2016 ESC guidelines for the management of atrial fibrillation developed in collaboration with EACTS, Europace 18 (2016) 1609–1678.
[35] C. Poulet, S. Kunzel, E. Buttner, D. Lindner, D. Westermann, U. Ravens, Altered physiological functions and ion currents in atrial fibroblasts from patients with chronic atrial fibrillation, Phys. Rep. 4 (2016).
[36] S.R. Künzel, J.S. Rausch, C. Schäffer, M. Hoffmann, K. Künzel, E. Klapproth, T. Kant, N. Herzog, J.H. Küpper, K. Lorenz, Modeling atrial fibrosis in vitro—generation and characterization of a novel human atrial fibroblast cell line, FEBS Open Bio. 10 (2020) 1210–1218.
[37] G. Isenberg, U. Klockner, Calcium tolerant ventricular myocytes prepared by preincubation in a "KB medium", Pflugers Arch. - Eur. J. Physiol. 395 (1982) 6–18.
[38] N. Phansalkar, S. More, A. Sabale, M.S. Joshi, Adaptive local thresholding for detection of nuclei in diversity stained cytology images, in: 2011 International Conference on Communications and Signal Processing, IEEE, 2011, pp. 218–220.
[39] R. Peyronnet, J.R. Martins, F. Duprat, S. Demolombe, M. Arhatte, M. Jodar, M. Tauc, C. Duranton, M. Paulais, J. Teulon, E. Honore, A. Patel, Piezo1-dependent stretch-activated channels are inhibited by Polycystin-2 in renal tubular epithelial cells, EMBO Rep. 14 (2013) 1143–1148.
[40] O.P. Hamill, D.W. McBride Jr., The pharmacology of mechanogated membrane ion channels, Pharmacol. Rev. 48 (1996) 231–252.
[41] C. Bae, F. Sachs, P.A. Gottlieb, The mechanosensitive ion channel Piezo1 is inhibited by the peptide GsMTx4, Biochemistry 50 (2011) 6295–6300.
[42] H. Li, J. Xu, Z.-S. Shen, G.-M. Wang, M. Tang, X.-R. Du, Y.-T. Lv, J.-J. Wang, F.-F. Zhang, Z. Qi, The neuropeptide GsMTx4 inhibits a mechanosensitive BK channel through the voltage-dependent modification specific to mechano-gating, J. Biol. Chem. 294 (2019) 11892–11909.
[43] C. Schmidt, F. Wiedmann, X.B. Zhou, J. Heijman, N. Voigt, A. Ratte, S. Lang, S. M. Kallenberger, C. Campana, A. Weymann, R. De Simone, G. Szabo, A. Ruhparwar, K. Kallenbach, M. Karck, J.R. Ehrlich, I. Baczko, M. Borggrefe, U. Ravens, D. Dobrev, H.A. Katus, D. Thomas, Inverse remodelling of K2P3.1 K^+ channel expression and action potential duration in left ventricular dysfunction and atrial fibrillation: implications for patient-specific antiarrhythmic drug therapy, Eur. Heart J. 38 (2017) 1764–1774.
[44] M. Sanchez, O. McManus, Paxilline inhibition of the alpha-subunit of the high-conductance calcium-activated potassium channel, Neuropharmacology. 35 (1996) 963–968.
[45] Y. Zhou, C.J. Lingle, Paxilline inhibits BK channels by an almost exclusively closed-channel block mechanism, J. Gen. Physiol. 144 (2014) 415–440.
[46] S. Candia, M.L. Garcia, R. Latorre, Mode of action of iberiotoxin, a potent blocker of the large conductance Ca $^{2+}$-activated K^+ channel, Biophys. J. 63 (1992) 583–590.

[47] B.H. Bentzen, A. Nardi, K. Calloe, L.S. Madsen, S.P. Olesen, M. Grunnet, The small molecule NS11021 is a potent and specific activator of Ca^{2+}-activated big-conductance K^+ channels, Mol. Pharmacol. 72 (2007) 1033–1044.
[48] P.A. Gottlieb, F. Sachs, Piezo1: properties of a cation selective mechanical channel, Channels (Austin, Tex) 6 (2012) 214–219.
[49] F. Maqoud, M. Cetrone, A. Mele, D. Tricarico, Molecular structure and function of big calcium-activated potassium channels in skeletal muscle: pharmacological perspectives, Physiol. Genomics 49 (2017) 306–317.
[50] K. Takahashi, K. Naruse, Stretch-activated BK channel and heart function, Prog. Biophys. Mol. Biol. 110 (2012) 239–244.
[51] J. Taniguchi, W.B. Guggino, Membrane stretch: a physiological stimulator of Ca^{2+}-activated K^+ channels in thick ascending limb, Am. J. Phys. 257 (1989) F347–F352.
[52] G. Iribe, H. Jin, K. Kaihara, K. Naruse, Effects of axial stretch on sarcolemmal BKCa channels in post-hatch chick ventricular myocytes, Exp. Physiol. 95 (2010) 699–711.
[53] A.G. Ehrhardt, N. Frankish, G. Isenberg, A large-conductance K^+ channel that is inhibited by the cytoskeleton in the smooth muscle cell line DDT1 MF-2, J. Physiol. 496 (1996) 663–676.
[54] A.H. Lewis, A.F. Cui, M.F. McDonald, J. Grandl, Transduction of repetitive mechanical stimuli by Piezo1 and Piezo2 ion channels, Cell Rep. 19 (2017) 2572–2585.
[55] S. Jha, S.E. Dryer, The β1 subunit of Na^+/K^+-ATPase interacts with BK_{Ca} channels and affects their steady-state expression on the cell surface, FEBS Lett. 583 (2009) 3109–3114.
[56] J. Baum, H.S. Duffy, Fibroblasts and myofibroblasts: what are we talking about? J. Cardiovasc. Pharmacol. 57 (2011) 376–379.
[57] G.R. Li, H.Y. Sun, J.B. Chen, Y. Zhou, H.F. Tse, C.P. Lau, Characterization of multiple ion channels in cultured human cardiac fibroblasts, PLoS One 4 (2009), e7307.
[58] J. Cui, H. Yang, U.S. Lee, Molecular mechanisms of BK channel activation, Cell. Mol. Life Sci. 66 (2009) 852–875.
[59] L. Han, J. Li, Canonical transient receptor potential 3 channels in atrial fibrillation, Eur. J. Pharmacol. 837 (2018) 1–7.
[60] J. Davis, A.R. Burr, G.F. Davis, L. Birnbaumer, J.D. Molkentin, A TRPC6-dependent pathway for myofibroblast transdifferentiation and wound healing in vivo, Dev. Cell 23 (2012) 705–715.
[61] S.M. Cahalan, V. Lukacs, S.S. Ranade, S. Chien, M. Bandell, A. Patapoutian, Piezo1 links mechanical forces to red blood cell volume, eLife 4 (2015).
[62] A. Marcantoni, D.H. Vandael, S. Mahapatra, V. Carabelli, M.J. Sinnegger-Brauns, J. Striessnig, E. Carbone, Loss of Cav1.3 channels reveals the critical role of L-type and BK channel coupling in pacemaking mouse adrenal chromaffin cells, J. Neurosci. 30 (2010) 491–504.
[63] T.A. Quinn, P. Camelliti, E.A. Rog-Zielinska, U. Siedlecka, T. Poggioli, E. T. O'Toole, T. Knöpfel, P. Kohl, Electrotonic coupling of excitable and nonexcitable cells in the heart revealed by optogenetics, Proc. Natl. Acad. Sci. 113 (2016) 14852–14857.
[64] M. Rubart, W. Tao, X.-L. Lu, S.J. Conway, S.P. Reuter, S.-F. Lin, M.H. Soonpaa, Electrical coupling between ventricular myocytes and myofibroblasts in the infarcted mouse heart, Cardiovasc. Res. 114 (2018) 389–400.
[65] S.N. Psychari, T.S. Apostolou, L. Sinos, E. Hamodraka, G. Liakos, D.T. Kremastinos, Relation of elevated C-reactive protein and interleukin-6 levels to left atrial size and duration of episodes in patients with atrial fibrillation, Am. J. Cardiol. 95 (2005) 764–767.
[66] G.M. Marcus, M.A. Whooley, D.V. Glidden, L. Pawlikowska, J.G. Zaroff, J.E. Olgin, Interleukin-6 and atrial fibrillation in patients with coronary artery disease: data from the heart and soul study, Am. Heart J. 155 (2008) 303–309.
[67] M. Grymonprez, V. Vakaet, M. Kavousi, B.H. Stricker, M.A. Ikram, J.J. Heeringa, O. H. Franco, G.G. Brusselle, L. Lahousse, The Role of Interleukin 6 on Incident Atrial Fibrillation in COPD Patients, 2018.
[68] Y. Gao, Y.M. Zhang, L.J. Qian, M. Chu, J. Hong, D. Xu, ANO1 inhibits cardiac fibrosis after myocardial infraction via TGF-β/smad3 pathway, Sci. Rep. 7 (2017) 1–9.

SK2 channels set a signalling hub bolstering CAF-triggered tumourigenic processes in pancreatic cancer.

Rapetti-Mauss, R., Nigri, J., Berenguier, C., Finetti, P., Tubiana, S. S., Labrum, B., ... & Soriani, O. (2023). *Gut*, *72*(4), 722-735.

Contexte :

C’est article réalisé en collaboration avec les autres membres de l’équipe. Nous mettons évidence le rôle de SK2 dans l’activation de voie de signalisations pro-tumorales dans le cancer du pancréas.

Original research

SK2 channels set a signalling hub bolstering CAF-triggered tumourigenic processes in pancreatic cancer

Raphael Rapetti-Mauss ,[1] Jérémy Nigri ,[2] Camille Berenguier,[1] Pascal Finetti,[2] Sarah Simha Tubiana,[2] Bonnie Labrum,[1] Benoit Allegrini,[1] Bernard Pellissier,[1] Georgios Efthymiou,[2] Zainab Hussain ,[2] Corinne Bousquet ,[3] Nelson Dusetti ,[2] François Bertucci,[2] Hélène Guizouarn,[1] Patricia Melnyk,[4] Franck Borgese,[1] Richard Tomasini ,[2] Olivier Soriani [1]

► Additional supplemental material is published online only. To view, please visit the journal online (http://dx.doi.org/10.1136/gutjnl-2021-326610).

[1]Université Côte d'azur, CNRS, Inserm, iBV, Nice, France
[2]INSERM, U1068, Cancer Research Center of Marseille, Institut Paoli-Calmettes, CNRS UMR7258, Université Aix-Marseille, Marseille, France
[3]Centre de Recherche en Cancérologie de Toulouse (CRCT), INSERM Unité Mixte de Recherche UMR-1037, CNRS Equipe de Recherche Labellisée ERL5294, Equipe de Recherche Labellisée "Ligue Contre le Cancer" & "LabEx Toucan", Université de Toulouse, Toulouse, France
[4]Lille Neuroscience and Cognition Research Center UMR-S 1172, University of Lille, INSERM, CHU Lille, Lille, France

Correspondence to
Pr Olivier Soriani and Dr Raphael Rapetti-Mauss, iBV, Université Côte d'Azur, CNRS, Inserm, Nice, France;
soriani@unice.fr,
Raphael.Rapetti-Mauss@univ-cotedazur.fr

JN and CB contributed equally.
RT and OS contributed equally.

Received 19 November 2021
Accepted 12 August 2022
Published Online First
1 September 2022

To cite: Rapetti-Mauss R, Nigri J, Berenguier C, *et al*. *Gut* 2023;**72**:722–735.

ABSTRACT

Objective Intercellular communication within pancreatic ductal adenocarcinoma (PDAC) dramatically contributes to metastatic processes. The underlying mechanisms are poorly understood, resulting in a lack of targeted therapy to counteract stromal-induced cancer cell aggressiveness. Here, we investigated whether ion channels, which remain understudied in cancer biology, contribute to intercellular communication in PDAC.

Design We evaluated the effects of conditioned media from patient-derived cancer-associated fibroblasts (CAFs) on electrical features of pancreatic cancer cells (PCC). The molecular mechanisms were deciphered using a combination of electrophysiology, bioinformatics, molecular and biochemistry techniques in cell lines and human samples. An orthotropic mouse model where CAF and PCC were co-injected was used to evaluate tumour growth and metastasis dissemination. Pharmacological studies were carried out in the Pdx1-Cre, Ink4a$^{fl/fl}$ LSL-Kras^{G12D} (KIC^{pdx1}) mouse model.

Results We report that the K^+ channel SK2 expressed in PCC is stimulated by CAF-secreted cues (8.84 vs 2.49 pA/pF) promoting the phosphorylation of the channel through an integrin–epidermal growth factor receptor (EGFR)–AKT (Protein kinase B) axis. SK2 stimulation sets a positive feedback on the signalling pathway, increasing invasiveness in vitro (threefold) and metastasis formation in vivo. The CAF-dependent formation of the signalling hub associating SK2 and AKT requires the sigma-1 receptor chaperone. The pharmacological targeting of Sig-1R abolished CAF-induced activation of SK2, reduced tumour progression and extended the overall survival in mice (11.7 weeks vs 9.5 weeks).

Conclusion We establish a new paradigm in which an ion channel shifts the activation level of a signalling pathway in response to stromal cues, opening a new therapeutic window targeting the formation of ion channel-dependent signalling hubs.

WHAT IS ALREADY KNOWN ON THIS TOPIC

⇒ Pancreatic ductal adenocarcinoma (PDAC) remains a therapeutic dead-end partially due to the lack of targeted therapy.
⇒ Intercellular communication between cancer-associated fibroblast (CAF) and pancreatic cancer cells largely contributes to PDAC aggressiveness.
⇒ Sig-1R is an ion channel chaperone involved in the remodelling of electrical signature in various diseases.

WHAT THIS STUDY ADDS

⇒ SK2 channel, chaperoned by Sig-1R, is a mediator of the intercellular communication.
⇒ SK2 activity is increased by direct AKT phosphorylation and stimulates a CAF secretome-activated β1-integrin–EGFR–AKT signalling hub.
⇒ The inhibition of this signalling hub leads to a decrease in metastasis spreading and an increase in survival in PDAC mouse models.

HOW THIS STUDY MIGHT AFFECT RESEARCH, PRACTICE OR POLICY

⇒ Our findings highlight the SK2 channel as an original target to counteract stromal-induced cancer cell aggressiveness in PDAC that can be targeted through Sig-1R, a druggable chaperone.

INTRODUCTION

Pancreatic ductal adenocarcinoma (PDAC) still represents a therapeutic dead end. Despite a slight improvement of the overall survival, the global 5-year survival rate hardly progresses. As a hallmark of PDAC, the predominant intratumoral microenvironment—stroma—surrounding pancreatic cancer cells (PCC) is one of the main causes of treatment failure, emerging as a source of knowledge improvement and a niche for new therapeutic targets.[1] The stroma is composed of immune cells, blood and lymphatic vasculature, nerve fibres and cancer-associated fibroblasts (CAFs), all embedded in an abundant network of extracellular matrix (ECM) proteins. CAFs participate in the dense fibrotic reaction in PDAC by sustaining ECM deposition, therefore, largely contributing to PDAC aggressiveness. By interacting physically with PCC and through the secretion of soluble factors[2] or extracellular vesicles,[3] CAFs promote PCC invasive potency leading to metastasis formation[4] and exacerbate drug resistance.[1] CAFs were widely described as tumour promoters. However, primary attempts to

target the communication between the stroma and PCC revealed that non-specific targeting may enhance tumour development, suggesting a complex interplay between both compartments.[1 5 6] A finer strategy consists in focusing on the specific molecular mechanisms controlling the communication between CAF and PCC,[7 8] but the landscape remains incomplete. This situation illustrates the urgent need to understand the crosstalk between CAF and PCC, its impact on PCC abilities and PDAC evolution and investigate original drug targets.

SigmaR1 (Sig-1R) is a stress-activated and ligand-operated ion channel chaperone, controlling the electrical remodelling occurring in heart and brain diseases.[9–12] We showed in previous studies that Sig-1R induced electrical remodelling in cancers, promoting cell invasiveness.[13 14] In the context of PDAC, we reasoned that (1) Sig-1R may participate in intercellular communication by promoting the remodelling of PCC's ion channels activity under the influence of CAF and (2) Sig-1R regulated channels could be specifically targeted in PDAC using Sig-1R ligands.

A deep remodelling of the cells' electrical signature accompanies the development of numerous illnesses, including cardiopathies, neurodegenerative diseases, inflammation and cancers.[15 16] The role of ion channels has been appreciated in cancers, and growing evidence show their implication in cancer cell hallmarks by regulating Ca^{2+} homeostasis,[15 17] cell shape[18] and, nascently, signalling transduction pathways through the control of membrane potential (ie, Wnt[19] and KRAS).[20] However, the contribution of ion channels to intercellular communication within cancer tissues remains unknown.

Therefore, we aimed to understand the significance of CAF secretome-induced ion channel regulation on PDAC progression. We show that CAF secretome triggers the activation of the calcium-dependent K^+ channel SK2 through its direct phosphorylation by AKT (Protein Kinase B). SK2 is thenceforth included in a β1-integrin–epidermal growth factor receptor (EGFR)–AKT signalling hub and sets a positive feedback loop amplifying tumourigenic processes. The activation and spatial dynamics of SK2 on CAF secretome exposure is dependent on Sig-1R. The pharmacological inhibition of Sig-1R abrogated CAF-induced metastatic spreading and improved overall survival. Altogether, these results demonstrate the unforeseen function for SK2 channel in tuning the intercellular communication between CAF and PCC and pave the way for potent therapeutic options in PDAC.

MATERIALS AND METHODS

Cell culture and CAF conditioned media production

HEK293T, PANC-1 and MiaPaCa-2 cell lines obtained from ATCC were maintained in Dulbecco's modified Eagle's medium (DMEM) with 10% fetal bovine serum (FBS), 100 U/mL penicilline/streptomycin under 5% CO_2 and 37°C in a humidified atmosphere. Cells were tested routinely for *Mycoplasma* contamination. CAFs were obtained as previously described.[3] Briefly, CAF features were verified by immunofluorescence by a positive alpha smooth muscle actin (α-SMA) staining and a negative pan cytokeratin staining. We also further used a CD45, CD326 (Epcam), pan cetokeratin (CK) and CD31 flow cytometry sorting to confirm that CAFs cultured are not immune, vascular or tumorous cells. CAFs were cultured in Dulbecco′s Modified Eagle′s Medium/Nutrient Mixture F-12 Ham (DMEM/F12), 10% FBS, 2 mmol/L l-glutamine, 1% antibiotic-antimycotic and 0.5 mM sodium pyruvate and used between passages 4 and 10. When the monolayer reached 70%–80% confluence, they were incubated in DMEM/F12 with 1% FBS (used as a control medium in experiments), and this conditioned media was collected every 2 days and stored at −20°C. Normal human fibroblasts (NHF) were isolated from healthy neonatal foreskins and cultured in DMEM, 10% FBS, 2 mmol/L l-glutamine and 1% antibiotic–antimycotic. Conditioned media was collected as described for CAFs.

Animal studies

For GEMM studies, Pdx1-Cre, $Ink4a^{fl/fl}$ LSL-$Kras^{G12D}$ (KIC^{pdx1}) male mice were obtained by crossing the following strains: Pdx1-Cre, $Ink4a^{fl/fl}$ and LSL-$Kras^{G12D}$ mice provided by D Melton (Harvard Stem Cell Institute, Cambridge, Massachusetts, USA), R Depinho (Dana-Farber Cancer Institute, Boston, Massachusetts, USA) and T Jacks (David H. Koch Institute for Integrative Cancer Research, Cambridge, Massachusetts, USA), respectively. PDAC-bearing 5-week-old and 8-week-old mice were treated once a week with vehicle or 1(S) (0.1 mg/injection/mouse) for survival follow-up until experimental endpoint: mice reaching sacrificing time or mice reaching physiological endpoints (cachexia criteria, limited movement, drinking or feeding of the mice). No exclusion has to be reported in all experiments as no mice reached a criteria of exclusion such as a fight-related wound or the development of ear inflammation. To study final tumour volume, mice were euthanised at 9 weeks and tumours were weighed and fixed in 4% (wt/vol) formaldehyde for immunochemistry. For survival analyses, male mice were euthanised when they reached ethical clinical end points defined by our institutional guidelines and European animal protection law. For orthotopic tumour studies: the mice were anaesthetised by isoflurane (Vetflurane; Virbac) inhalation in 30% air and 70% O_2. NMRI nude mice (Janvier Labs) under anaesthesia were injected subcutaneous with 0.2 mg/kg buprenorphine (Vetergesic; Sogeval) and were administered lidocaine (Xylovet; Ceva) at 3.5 mg/kg by infiltration in the abdominal cavity. A first incision was made at the top left of the abdomen and a second at the peritoneum to reach the pancreas. PANC ShRD/PANC ShSig-1R/PANC ShSK2 cells alone (500 000 cells) or plus CAF (1 500 000 cells) contained in 40 µL of PBS were injected into the pancreas. The abdominal musculature was then closed with 4–0 sutures and the external skin with inverted stitches. The mice were euthanised 8 weeks later. The pancreas was removed and weighed and the liver removed and analysed for macroscopic metastases. These organs were fixed in 4% formaldehyde for immunochemistry. Liver metastases were confirmed and counted per mouse using H&E staining.

For all experiments, sample size was predicted following a Mann-Whitney statistical approach involving power calculation of 0.8 with an false discovery rate (FDR) of 0.05. A minimum number of 7 mice per group was predicted as able to reach significance. Bonferroni post-hoc test was used for multiples test comparison (two variance with time and/or treatment). Experimental technicians were proceeding with injections, while personnel related to mice follow-up worked in a blinded approach.

Gene expression analysis of human PDAC samples

We gathered clinicopathological and gene expression data of clinical pancreatic samples from 16 publicly available data sets (online supplemental table S2). Data were collected from ArrayExpress, EGA, National Center for Biotechnology Information/Genbank GEO and TCGA databases and had been generated using DNA microarrays (Affymetrix, Agilent and Illumina) and RNA-seq (Illumina). The pooled data set contained 1017 samples, including 925 primary PC samples, and 92 metastases.

Statistical analysis

Each experiment was repeated independently at least three times. Results are presented as median with IQR unless stated otherwise. For comparison between two quantitative variables, we used the Mann-Whitney test. When more than two variables were compared, Kruskal-Wallis tests were used followed by a Dunn's post-test, unless stated otherwise. For comparison between fold change, a one sample t-test was applied. Log-rank (Mantel-Cox) test was used to evaluate mice survival. Analyses were performed using either GraphPad Prism V.8.0.1 or R software. A p value of <0.05 was considered statistically significant.

Additional materials and methods are provided in the online supplemental material.

RESULTS

Secreted cues from CAF stimulate SK2 in pancreatic cancer cells

To determine whether Sig-1R participates in electrical remodelling in PDAC, we recorded ion channel activity in PCC (ie, PANC-1 and MiaPaCa-2), where Sig-1R expression was silenced by short hairpin (sh) RNA. Abrogation of Sig-1R expression led to the inhibition of a K^+ conductance exhibiting an inward rectification typical of small conductance calcium-dependent K^+ channels. Further pharmacological and molecular analysis revealed that the current was suppressed by the SK channels inhibitor apamin, the SK2-specific inhibitor leiurotoxin-1 Dab-7 (figure 1A,B), and by molecular silencing of SK2 channel (online supplemental figure S1A, S1B). Interestingly, immunostaining of human PDAC specimens confirmed that Sig-1R and SK2 are effectively expressed in PDAC (figure 1C). To investigate the influence of secreted factors from CAF on SK2 channel in PCC, we have generated a conditioned media using human primary CAF (CAF-CM) obtained from patients with PDAC (CAF-CM; figure 2A). CAF subtyping was investigated by flux cytometry using a panel of markers, including iCAF, myCAF and apCAF markers as well as more transverse markers recently identified such as CD105. As shown in online supplemental figure 2, the CAF cultured for this study were mainly Podoplanin^{high}, CD105^{high}, PDGFRβ^{high}, FAP^{high} and α-SMA^{low}. We observed that PANC-1 incubation with CAF-CM (overnight) increased the Dab-7-sensitive current (ISK2; figure 2B), an effect abolished by the molecular silencing of SK2 using shRNA or Crispr/Cas9 technology (figure 2B,C). Importantly, CM harvested from NHF cells failed to stimulate the current, indicating that the effect is specific to CAF-secretome (figure 2D). Furthermore, boiled CAF-CM had no impact on the current, ruling out any involvement of secreted metabolites (online supplemental figure S3). The CAF-CM-mediated activation of ISK2 was dependent on

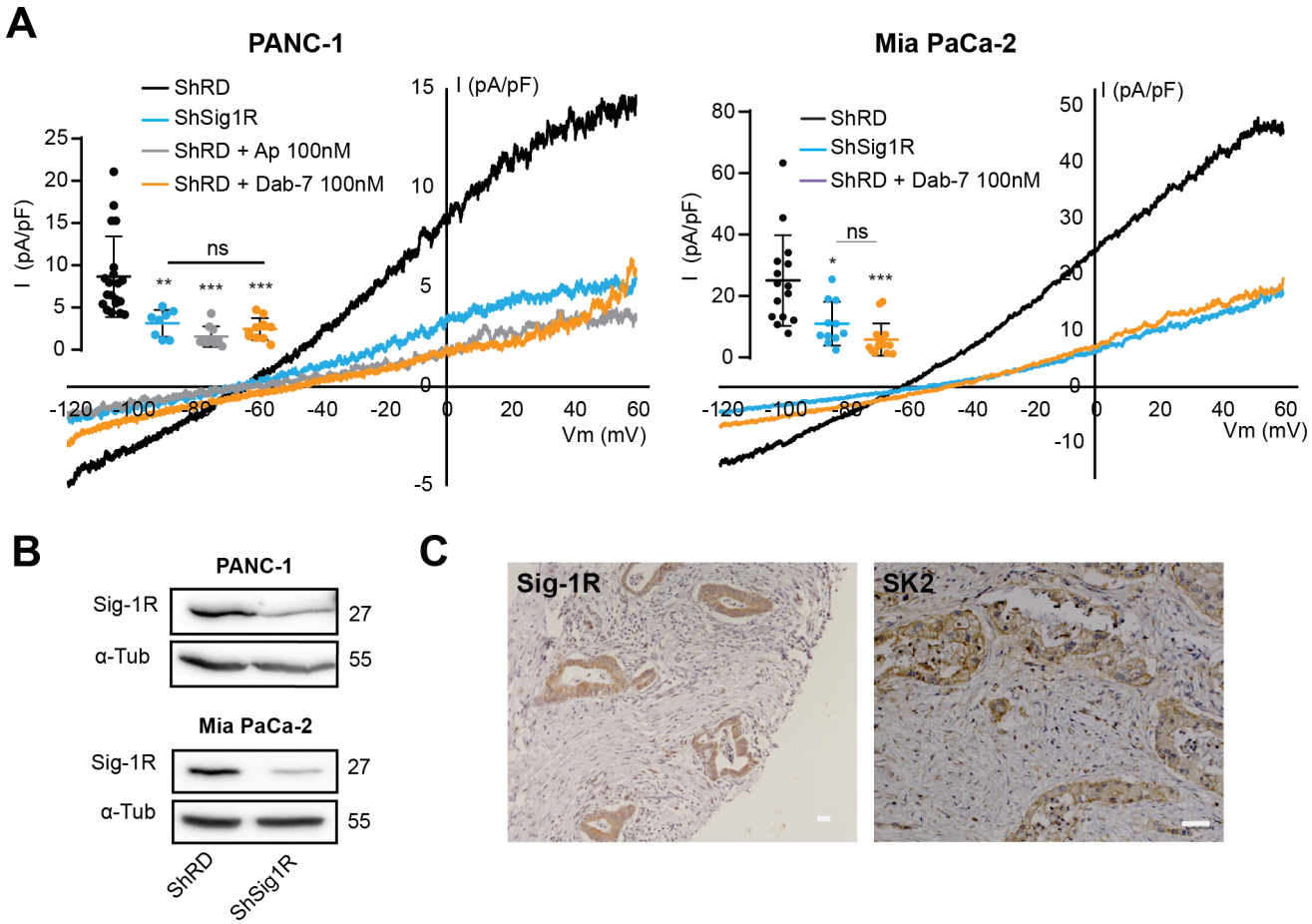

Figure 1 Sig-1R regulates a potassium current in Pancreatic cancer cells. (A) Patch clamp recordings of current elicited in control (ShRD PANC-1, n=20; MiaPaCa-2, n=15) or Sig-1R-silenced (ShSig-1R PANC-1, n=8; MiaPaCa-2, n=11) PCC, in the absence or presence of SK2 channel inhibitors apamin (apamin:100 nM; PANC-1, n=10) or leiurotoxin-1 Dab-7 (Dab-7: 100 nM; PANC-1, n=10; MiaPaCa-2, n=15). (B) Western blot analysis of shRNA-mediated Sig-1R silencing efficiency in PANC-1 and MiaPaCa-2 cells. (C) Representative immunohistochemistry staining for Sig-1R and SK2 expression in patient with PDAC samples. Scale bar: 50 µm. *p<0.05; **p<0.01; ***p<0.001. ns: not significant; PCC, pancreatic cancer cells; PDAC, pancreatic ductal adenocarcinoma; shRNA, short hairpin RNA.

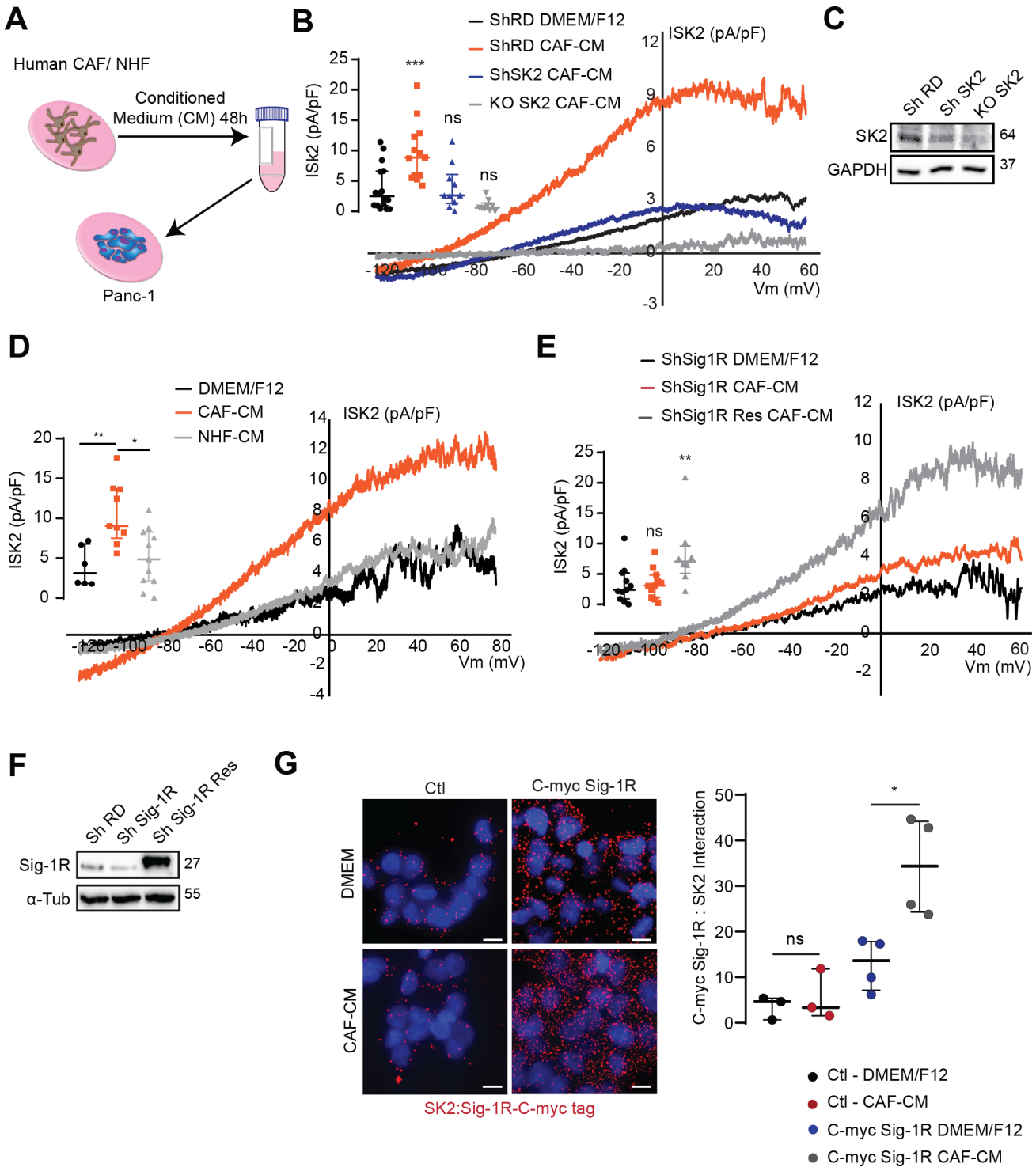

Figure 2 Secreted cues from CAF derived from patients with PDAC stimulate SK2 channel. (A) Schematic representation of conditioned medium production from patients-derived CAF (CAF-CM) and NHF-CM. (B) Patch clamp recordings of Dab-7-sensitive current (ISK2) from the following conditions: ShRD PANC-1 cells exposed to 1% FBS DMEM/F12 (negative control: DMEM/F12, n=16) or ShRD PANC-1 cells (n=13), ShSK2 PANC-1 cells (n=10), and KO-SK2 PANC-1 cells (n=9) exposed to CAF-CM overnight. (C) Western blot analysis of shRNA (ShSK2) and Crispr/Cas9-mediated (KO-SK2) SK2 silencing efficiency in PANC-1 cells. (D) Patch clamp recordings of Dab-7-sensitive current (ISK2) from the following conditions: ShRD PANC-1 cells exposed to 1% FBS DMEM/F12 (negative control: DMEM/F12, n=6) or ShRD PANC-1 cells exposed to either CAF-CM (n=9) or NHF-CM (n=11) overnight. (E) Patch clamp recordings of Dab-7-sensitive current (ISK2) from the following conditions: ShSig-1R PANC-1 cells exposed to 1% FBS DMEM/F12 (negative control: DMEM/F12, n=11), or ShSig-1R PANC-1 cells (n=11) and ShSig-1R PANC-1 cells, where Sig-1R has been rescued using a C-myc Sig-1R construct (ShSig-1R Res n=8), exposed to CAF-CM overnight. (F) Western blot analysis of Sig-1R protein expression, showing the rescue of Sig-1R in ShSig1R-Res PANC-1 cells. (G) PLA analysis of the interaction between SK2 and C-myc-Sig-1R in Ctl or C-myc Sig-1R PANC-1 cells treated with DMEM/F12 or CAF-CM, n=3–4. Scale bar: 10 µm. *p<0.05; **p<0.01; ***p<0.001. CAF, cancer-associated fibroblasts; Ctl, control; NHF, normal human fibroblast; ns: not significant; PDAC, pancreatic ductal adenocarcinoma; PLA, proximity ligation assay; shRNA, short hairpin RNA.

Sig-1R since this effect was abolished by the molecular silencing of Sig-1R and rescued by the expression of C-myc Sig-1R in the shSig-1R cell line (figure 2E,F). Since Sig-1R modulates ion channel function through protein–protein associations,[21 22] we asked whether Sig-1R and SK2 could form complexes on CAF-CM exposure using proximity ligation assay (PLA). In PANC-1 challenged with CAF-CM, the interaction between SK2 and Sig-1R was significantly increased (figure 2G). Altogether, these results show that CAF-CM triggers SK2 in a Sig-1R-dependent manner in PCC.

CAF secretome activates SK2 through an integrin–EGFR–AKT pathway

To understand how CAF-CM stimulates SK2 current (ISK2), we examined the activation state of a subset of signalling kinases in PANC-1 using a phosphokinase array. We observed that the most robustly CAF-CM-activated kinases were associated to two main signalling clusters: one associated to the EGFR–AKT axis (EGFR, Src, AKT, Wnk1, AMPKa1, mTor and CREB) and the other to integrin signalling (Focal Adhesion Kinase (FAK) -Src) (figure 3A). We thus evaluated the effects of treatments altering each of these pathways on SK2 activity. EGF treatment induced a significant increase in ISK2, which was dependent on Sig-1R (figure 3B). Accordingly, the EGFR inhibitor erlotinib and the AKT inhibitor DEBC (10-(4′-(N-diethylamino)butyl)-2-chlorophenoxazine . HCl) both suppressed the CAF-CM-induced ISK2 (figure 3C,D). These data indicate that CAF-CM-induced SK2 stimulation depends on EGFR-associated signalling. Given that CAF-CM treatment triggered FAK in the phosphokinase array, we tested the effect of fibronectin (FN), an element of the stroma that activates FAK via the α5β1-integrin in PCC.[23] FN mimicked the effects of CAF-CM on ISK2 (figure 3E). Incubation of cells with a functional anti-β1-integrin antibody abolished the CAF-CM-induced increase in ISK2 (figure 3E), further demonstrating that CAF-CM-dependent SK2 activation requires integrin/FAK transduction. To confirm the functional links between the different partners at the molecular level, we performed PLA experiments and observed that SK2 associates with EGFR, the β1-integrin subunit and AKT. These associations were promoted by CAF-CM treatment and required Sig-1R, as shown by experiments using ShSig-1R PANC-1 cells (figure 3F). These results reveal that SK2 activity is modulated by a CAF-CM stimulated signalling hub, stabilised by Sig-1R. We, therefore, looked for the presence of EGF and FN in CAF-CM. Surprisingly, we were able to detect EGF neither in a proteomic analysis of the CAF-CM nor using a sensible EGF ELISA test (online supplemental figure S4A). Note that EGF could not be detected in the culture media of PANC-1 cells cultivated with control medium or CAF-CM (online supplemental figure S4B). In support of this, neither EGF nor other EGFR ligands (ie, tumour growth factor alpha (TGFα), heparin binding EGF like growth factor (HBEGF), betacellulin (BTC), amphiregulin (AREG), epiregulin (EREG) and epithelial mitogen (EPGN)) could be detected in the proteomic analysis. By contrast, the analysis revealed that FN is one of the most abundant components of CAF secretome (online supplemental table S1), a result confirmed by an immune-dot blot assay (figure 3G). Interestingly, the treatment of PANC-1 with FN induced the association between AKT and SK2, mimicking the effects of CAF-CM (figure 3H). Since β1-integrin can form complex with other α-subunit integrins, we next ask whether other components of the CAF-CM could participate in the stimulation of the current. Proteomic analysis of CAF-CM revealed the presence of collagen I, a ligand of the α2β1-integrin, which is expressed in PDAC cells and participates in PDAC cell phenotype.[24 25] Interestingly, the specific α2-integrin blocking antibody Gi9 significantly reduced CAF-CM-induced stimulation of SK2 current (online supplemental figure S5), while collagen I stimulated AKT/SK2 association (figure 3H). Finally, these results are globally reinforced by the colocalisation between Sig-1R/SK2 and p-AKT observed by immunohistochemistry from PDAC patient samples (figure 3I). Altogether, these data indicate that components secreted by CAF-CM that stimulate β1-dependent integrins such as FN or collagen I potentially activate SK2 via the same signalling hub.

SK2 is a pivotal regulator of the AKT signalling pathway

Since the activation of ISK2 by the CAF-CM depends on AKT, we hypothesised that SK2 could be a target protein of AKT. Using sequence alignment, we identified three residues (S562, S568 and S569) corresponding to the AKT consensus phosphorylation motif in the SK2 sequence (RxRxxST). Strikingly, this motif was conserved in SK2 orthologs from different species (figure 4A) but was absent in SK1, SK3 and SK4 sequences, suggesting a specificity of AKT for SK2 among the SK family. Co-expression of SK2 and a constitutively active form of AKT (Myr-AKT) in HEK293 cells resulted in a significant increase in SK2 current compared with the control condition. Co-expression of Myr-AKT with SK2 carrying a triple phosphoresistant mutation (S562A, S568A and S569A) failed to increase channel activity, suggesting that AKT stimulates ISK2 by phosphorylating the channel on at least one of the three phosphorylation sites (figure 4B). To further demonstrate that SK2 is a target of AKT, we used a phospho-specific antibody that recognises the AKT phosphorylation consensus motif. Co-immunoprecipitation experiments show that Myr-AKT indeed phosphorylated the WT SK2 channel but failed to phosphorylate the triple phosphoresistant mutant of SK2 (figure 4C). Patch clamp recording in HEK293 transfected with SK2 revealed that S568 and S569 residues were phosphorylated by AKT activation on CAF-CM exposure (figure 4D), demonstrating that SK2 is a specific target of AKT. To further understand how AKT phosphorylation impacts the regulation of the channel, we used the phosphomimetic mutation S568D, which abolished the calcium sensitivity of SK2 (figure 4E). Moreover, on CAF-CM treatment, the activity of SK2 in PANC-1 cells did not change after decreasing the intracellular calcium concentration from 1 µM to 0.1 µM (online supplemental figure S6), indicating that the AKT-dependent phosphorylation of SK2 following CAF-CM exposure renders the channel independent on intracellular calcium concentration. However, at this stage, the functional consequences of AKT-dependent SK2 activation on cancer cell behaviour remained an open question. Therefore, we looked for the signalling pathways regulated by CAF-CM-mediated activation of SK2. We measured the phosphorylation levels of the individual kinases monitored with a phosphokinase array in control and SK2-silenced PANC-1 cells challenged with CAF-CM. We observed that the silencing of SK2 blocked CAF-CM-induced phosphorylation of 8 kinases among the 12 that were CAF-CM sensitive (figure 4F). Only kinases showing a significant reduction in their phosphorylation level in both SK2-silenced cell lines (ie, ShSK2 and Crispr-Cas9 KO-SK2 PANC-1 cell lines) were considered and we found that AKT (S473), Yes (Y426), Src (Y419), FAK (Y397), EGFR (Y1086), WnK1 (T60), AMPKa1 (T183) and GSK3β (S21/S9) were activated in an SK2-dependent manner (figure 4G). Since these kinases belong to the EGFR-AKT-β1-integrin-associated signalosomes targeting the channel, these results suggest that

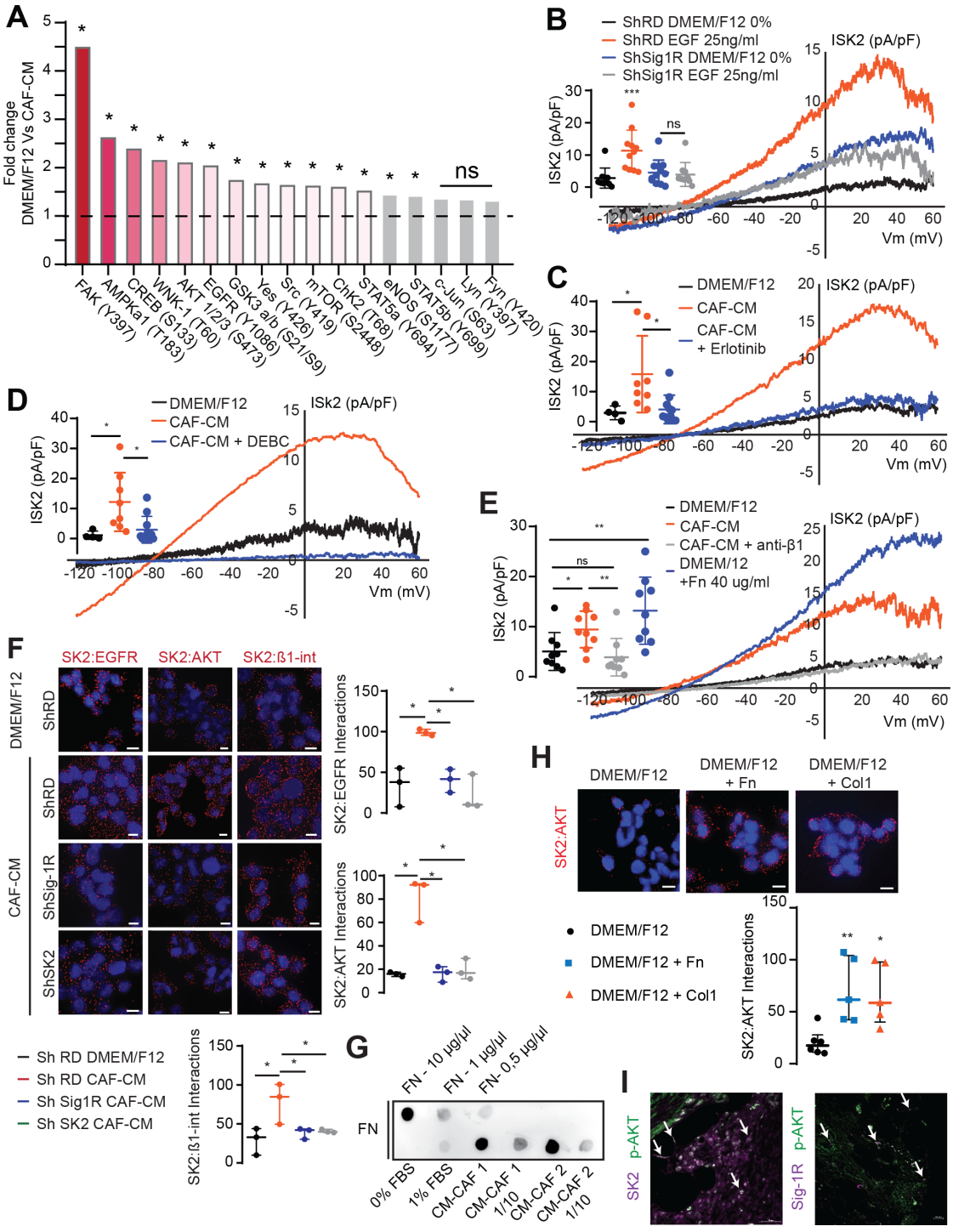

Figure 3 FN from CAF secretome activates SK2 through an integrin/EGFR–PI3K–AKT pathway. (A) Bar graph showing fold change in phosphorylation levels of a set of signalling proteins on overnight exposure of PANC-1 cells to CAF-CM relative to control (DMEM/F12). Experiments were performed in experimental duplicates (n=3; *p<0,05). (B) ISK2 was recorded in ShRD and ShSig-1R PANC-1 cells, treated overnight with 0% FBS DMEM/F12 (ShRD, n=10; ShSig-1R, n=12) or 0% FBS DMEM/F12 supplemented with 25 ng/mL EGF (ShRD, n=11; ShSig-1R, n=10). (C)–(E) Patch clamp recording of ISK2 in PANC-1 cells exposed overnight to (C) control medium (n=4) or CAF-CM (n=8) pretreated or not treated 1 hour with 10 µM erlotinib before adding CAF-CM (n=12), (D) control medium (n=4) or CAF-CM (n=8) treated or not treated 10 min before recording with 10 µM DEBC (n=11) and (E) control medium (n=9), CAF-CM (n=9), 40 µg/mL FN (n=9) or CAF-CM treated on ice with a functional antibody against the β1-integrin 30 min before recording (10 µg/µl; n=9). (F) PLA analysis of the interaction between SK2/EGFR, SK2/AKT and SK2/β1-integrin in ShRD, ShSig-1R or ShSK2 PANC-1 cells treated overnight with control medium or CAF-CM (n=3). Scale bar: 10 µm. (G) Dot blot assay showing the presence of FN in different conditions: DMEM/F12 0% FBS or 1% FBS, and in 2 different batches of CAF-CM. (H) PLA analysis of the interaction between SK2 and AKT in PANC-1 cells, treated overnight with control medium (n=6), 40 µg/mL FN (n=5) or 10 µg/mL collagen I (n=5). Scale bar: 10 µm. (I) Representative images of SK2/Sig-1R and p-AKT-S473 staining in patient with PDAC samples. Arrows highlight cells where SK2/Sig-1R colocalise with p-AKT. Scale bar: 50 µm. *p<0.05; **p<0.01; ***p<0.001. CAF, cancer-associated fibroblasts; FN, fibronectin; ns: not significant; PDAC, pancreatic ductal adenocarcinoma; PLA, proximity ligation assay.

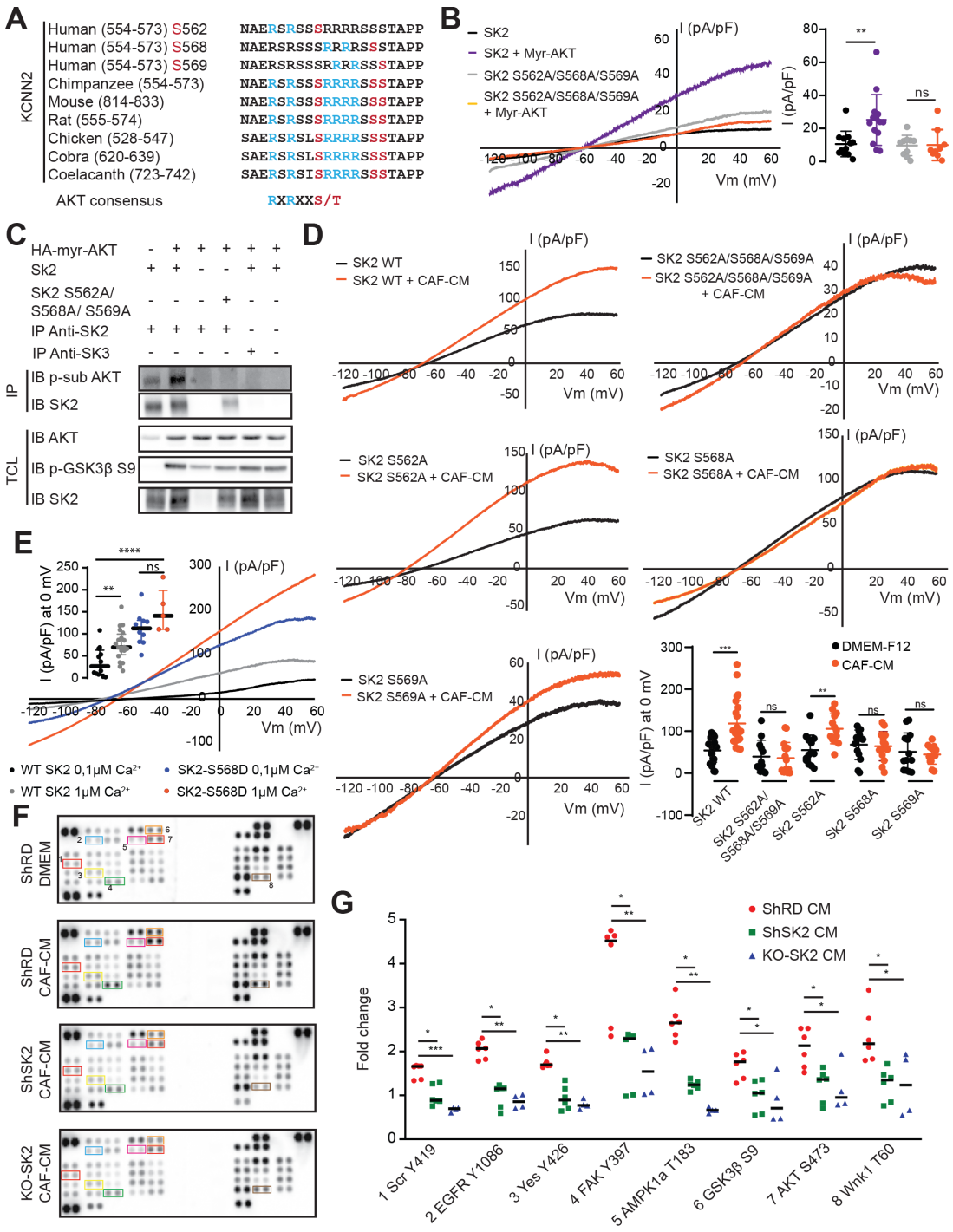

Figure 4 SK2 is a pivotal regulator of AKT signalling. (A) Sequence alignment of the AKT phosphorylation consensus site within SK2 orthologs from different species. (B) Patch clamp recording of ISK2 in HEK293 expressing either wild type SK2 alone (n=12), wild-type SK2 with a HA-Myr-AKT construct (n=14), SK2 carrying a triple mutation (S562A, S568A and S569A) alone (n=10) or SK2 carrying the triple mutation with a HA-Myr-AKT construct (n=9). (C) IB of total cell lysate and IP from HEK293 cells transfected with SK2 WT or SK2 carrying the triple mutation and HA-Myr-Akt construct as indicated. The protein precipitation has been done with SK2 antibody (or SK3 antibody: negative control) and revealed with a p-AKT substrate (RXRXXpS/pT) antibody, n=3. (D) Patch clamp recording of SK2 currents recorded in HEK293 cells transfected with WT SK2 (Ctl, n=24; CAF-CM, n=24), SK2 carrying the triple mutations (Ctl, n=12; CAF-CM, n=16) or SK2 carrying each single mutation S562A (Ctl, n=13; CAF-CM, n=13), S568A, (Ctl, n=14; CAF-CM, n=14) and S569A (Ctl, n=13; CAF-CM, n=13) treated overnight with control medium (black) or CAF-CM (red). (E) Patch clamp recording of SK2 currents in HEK293 cells transfected with WT SK2 or SK2 carrying the mutation S568D and exposed to two different concentrations of extracellular Ca^{2+}, 1 µM and 100 nM (WT SK2 100 nM, n=12; WT SK2 1 µM, n=20; S568D 100 nM, n=10; S568D 1 µM, n=5). (F) Representative images showing the phospho-kinase array for ShRD PANC-1 cells exposed to control medium (DMEM/F12) or CAF-CM, and from ShSK2 or KO-SK2 PANC-1 cells exposed to CAF-CM. Each kinase is spotted in duplicate and the location of EGFR, AKT (S473), Yes, Src, FAK, GSK3, AMPK and Wnk1 is indicated using coloured boxes. (G) Quantitative analysis of the spots from (F) was performed by densitometry and presented as fold change versus control cells. Experiments were performed in experimental duplicates (n=3). *p<0.05; **p<0.01; ***p<0.001; ****p<0.0001. CAF, cancer-associated fibroblasts; Ctl, control; IB, immunoblot; IP, immunoprecipitants; ns, not significant.

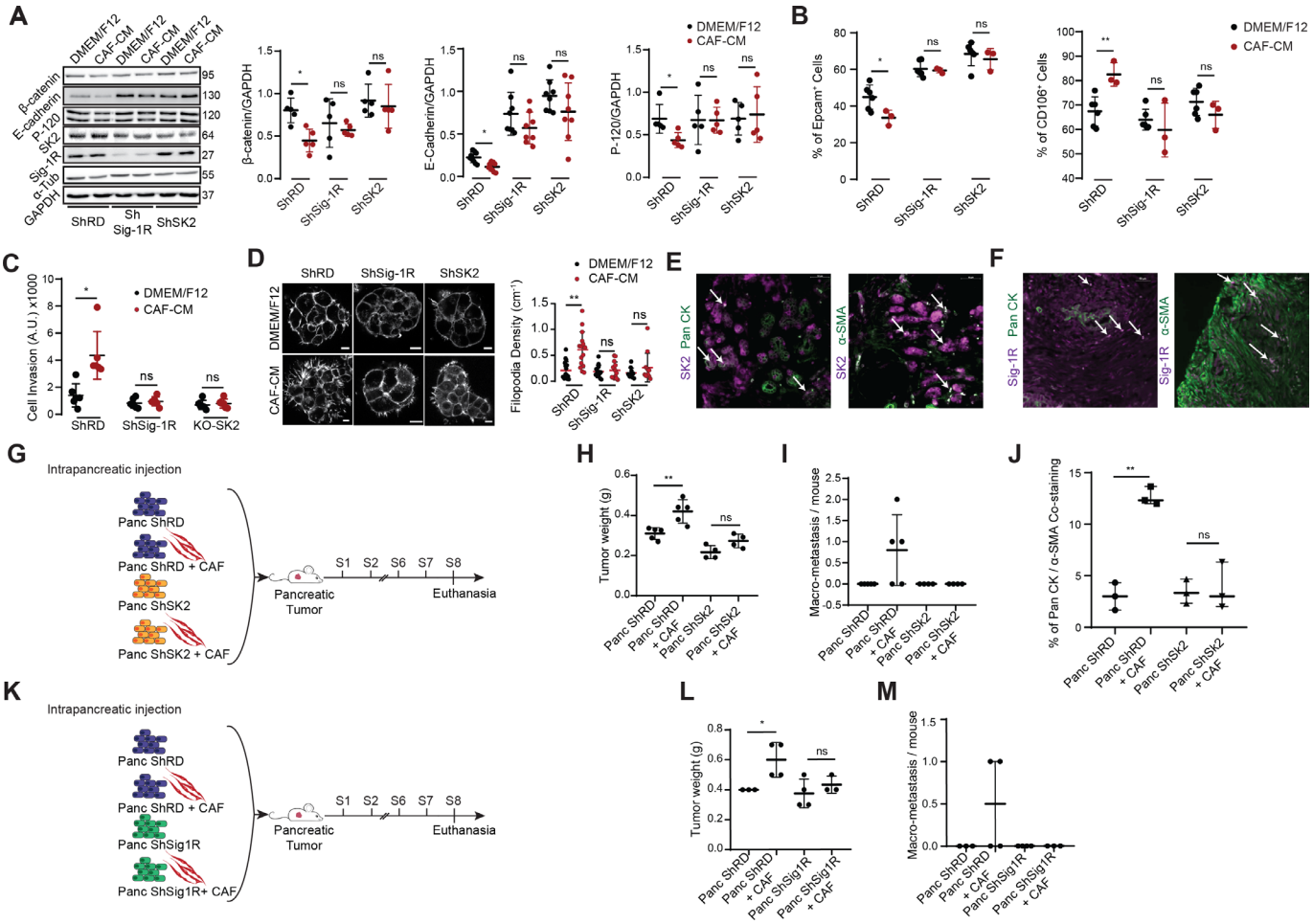

Figure 5 SK2 drives PCC aggressiveness in response to CAF secretome. (A) Western blot analysis showing the protein expression of adherens junction markers in ShRD, ShSig-1R or ShSK2 PANC-1 cells, exposed overnight to control medium (DMEM/F12) or CAF-CM. Densitometric quantifications are shown as scatter plots (E-cadherin, n=9; β-catenin, n=5; p-120 catenin, n=5; Sig-1R, n=4; SK2, n=8). (B) Graphs showing the percentage of cells positive for Epcam (left panel) or CD106 (right panel) markers in Sh-RD, ShSig-1R and ShSK2 challenged with control (DMEM/F12) or CAF-CM (CAF-CM). Labelling was quantified by flow cytometry (n=3, *p<0,05). (C) ShRD, ShSig-1R and ShSk2 PANC-1 cells were treated with control medium or CAF-CM and subjected to cell invasion assay (n=5; *p<0,05). (D) Confocal immunofluorescence images from ShRD, ShSig-1R and ShSK2 PANC-1 cells, grown in Matrigel (3D cell culture) showing F-actin staining. The scatter plot represents data dispersion and median values of Filopodia density (ShRD DMEM/F12, n=18; ShRD CAF-CM, n=15; ShSig-1R DMEM/F12, n=13; ShSig-1R CAF-CM, n=13; ShSK2, n=11; ShSK2 CAF-CM, n=12). Scale bar: 10 µm. (E) Representative immunofluorescence images of SK2 (magenta), pan CK (green, left panel) or α-SMA (green, right panel) in patient with PDAC samples. Scale bar: 50 µm. (F) Representative immunofluorescence images of Sig-1R (magenta), pan CK (green, left panel) or α-SMA (green, right panel) in patient with PDAC samples. Scale bar: 50 µm. (G) Graphical scheme explaining the experimental workflow for (H)–(J). (H) Graph showing pancreatic tumour weight of PANC ShRD (n=5), PANC ShRD+CAF (n=5), PANC ShSK2 (n=4) and PANC ShSK2+CAF (n=4), 8 weeks after orthotopic injection. Corresponding counted liver macro metastasis per mouse are presented in (I). (J) Corresponding graphs showing the percentage of pan CK labelled cells positive for α-SMA staining (n=3, each). (K) Graphical scheme explaining the experimental workflow for (L) and (M). (L) Graph showing pancreatic tumour weight of PANC-1 ShRD (n=3), PANC-1 ShRD+CAF (n=4), PANC-1 ShSig-1R (n=4) and PANC-1 ShSig-1R+CAF (n=3), 8 weeks after orthotopic injection. Corresponding counted liver macro metastasis per mouse are presented in (M). ANOVA was used for statistical analysis. *p<0.05; **p<0.01. ANOVA, analysis of variance; CAF, cancer-associated fibroblasts; Ctl, control; ns, not significant;.PCC, pancreatic cancer cells; PDAC, pancreatic ductal adenocarcinoma.

activating SK2 sets a positive feedback loop on this signalling axis, which is largely involved in cancer physiopathology.[26]

SK2 drives PCC aggressiveness in response to CAF secretome in vitro and in vivo

To test whether SK2 stimulation could favour PCC aggressiveness, we first evaluated the expression of adherens junctions (AJ) markers since loss of AJ coincides with loss of epithelial features and increases invasive phenotypes.[27] Using PCC ShRD as controls, we confirmed that CAF-CM provoked a decrease in E-cadherin, β-catenin and P-120 catenin levels—three AJ markers (figure 5A). The molecular silencing of SK2 (or Sig-1R) abolished the effect of CAF-CM on AJ markers (figure 5A; online supplemental figure S7A, B). To further explore this idea, we performed flow cytometry analyses using an epithelial marker (Epcam/CD326) and a mesenchymal marker, classically activated following epithelial-to-mesenchymal transition (EMT) (CD106).[28] The addition of CAF-CM on control PCC (ShRD) enhances their EMT phenotype, whereas EMT reprogramming is lost in PCC depleted for Sig-1R or SK2 (figure 5B). As a main functional consequence of epithelial markers loss and EMT reprogramming, we then explored invasive potency of PANC-1.

As expected, CAF-CM exposure significantly enhanced PCC invasive abilities (figure 5C). Consistent with epithelial and EMT markers data, the enhanced invasive properties driven by CAF-CM were lost in SK2-deficient or Sig-1R-deficient PCC (figure 5C). Moreover, when grown in 3D condition, CAF-CM increased the formation of protrusions in ShRD control cells, as shown by F-Actin immunofluoresence (figure 5D, left panel) and Filopodia density measurement (figure 5D, right panel), but not in SK2- or Sig-1R-deficient PCC (figure 5D). Interestingly, Sig1R or SK2 silencing altered neither cell growth, nor cell survival, but strongly decreased cell migration (online supplemental figure S8A, B, and C). Moreover, using a public PDAC patient database ((Dataset) oncoR2 platform; http://r2.amc.nl; n=130),[29] we revealed that the expression of both SK2 and Sig-1R are negatively correlated to AJ markers expression (online supplemental figure S9). Reinforcing this result, co-staining between SK2 or Sig-1R and an epithelial marker (pan CK) or a mesenchymal marker (α-SMA) in patient with PDAC samples showed that Sig-1R and SK2 expression patterns are strictly limited to pan cytokeratin-expressing cells and co-localise with α-SMA (figure 5E,F). These results suggest that Sig-1R and SK2 are expressed in epithelial cancer cells that have undergone EMT, a process favoured under CAF crosstalk condition, and reported to impact metastatic burden.[30] To further challenge this hypothesis, we orthotopically transplanted either ShRD, ShSK2 or ShSig-1R PANC-1 cells in the presence, or not, of CAF into the pancreas of NMRI-nude mice (figure 5G–M). As expected, co-injection of ShRD PCC and CAF revealed an increase in tumour weight (figure 5H,L), development of liver metastasis (figure 5I,M) and EMT reprogramming of epithelial cells (figure 5J). Interestingly, silencing of SK2 or Sig-1R in PCC abrogated CAF-induced increase in tumour weight (figure 5H,L), metastasis formation (figure 5I,M) and EMT (pan CK/α-SMA co-labelling; figure 5J) corroborating our hypothesis. Of interest, we controlled the presence of CAFs by the time of euthanasia in co-injected mice by identifying cells only labelled by α-SMA staining as a CAF marker, and could validate their presence, consistently with previous publications using CAF/tumour cell orthotopic co-injections[3] (online supplemental figure S10). Altogether, these results support the idea that SK2 constitutes an essential signal transducer for the intercellular communication between CAF and PCC, bolstering PCC aggressiveness, tumourigenesis and metastasis development.

A Sig-1R ligand inhibits SK2 activity and improves survival in vivo

Considering that the coupling between SK2 and AKT relies on Sig-1R, we sought to test whether targeting SK2 via Sig-1R in PDAC would be a valuable therapeutic strategy. Sig-1R ligands are synthetic small molecules that modify the coupling of Sig-1R with its partners, including ion channels.[10 13] Compound 1(S) is a Sig-1R ligand exhibiting nanomolar affinity for Sig-1R (IC_{50}=3.9 nM), high Sig-2R/Sig-1R selectivity (greater than 120) and very low cytotoxicity (selectivity index; ratio: CC_{50}/IC_{50}, greater than 50 000).[31] We first validated in vitro that 1(S) abolished the CAF-CM-mediated activation of SK2 and prevented the association of SK2 and AKT by patch clamp experiments (figure 6A) and PLA experiments (figure 6B). Proliferation and viability assays, on control Panc-1 cells or cells silenced for Sig1R or SK2, demonstrated that 1(S) treatment does not exhibit any effect on these parameters (online supplemental figure S8A, B). We next evaluated the effect of 1(S) in an endogenous PDAC mice model (KIC^{pdx1}).[32] By using a first protocol treating the KIC^{pdx1} mice at 5 weeks old, before the onset of PDAC (figure 6C), we observed that 1(S) treatment significantly delayed tumour progression and extended the overall survival. The median survival time of KIC^{pdx1} non-treated animals was 9.5 weeks, whereas median survival of KIC^{pdx1}-1(S)-treated mice was 11.7 weeks (figure 6D). This data were confirmed on a similar treatment protocol combined to an end-point study at 9 weeks of age (figure 6E), representing the median survival of KIC^{pdx1} non-treated mice, validating that 1(S) treatment delayed tumour progression. Indeed, as shown in figure 6F, in 1(S)-treated KIC^{pdx1} mice, the pancreatic tumour/body mass ratio showed a drastic reduction of 69% compared with non-treated ones, decreasing from 0.065 for KIC^{pdx1} non-treated mice to 0.021 for 1(S)-treated KIC^{pdx1} mice. Histological examination of pancreas from 1(S)-treated KIC^{pdx1} mice revealed an almost lack of malignant lesions contrasting with pancreas of non-treated KIC^{pdx1} mice exhibiting typical PDAC development (figure 6G). In addition, 1(S)-treated mice exhibited a lower number of EMT-reprogramming epithelial cells (pan CK/α-SMA co-staining, figure 6H) and a lower ECM density reflecting a decreased desmoplasia in treated animals (trichrome labelling; figure 6I–K). Furthermore, we have tested the efficiency of 1(S) treatment on PDAC evolution using an alternative protocol starting the treatment of KIC^{pdx1} mice at 8 weeks of age (figure 6L), when PDAC has already developed. Using this experimental design, we confirmed that 1(S) treatment significantly extended the overall survival. Indeed, the median survival time of KIC^{pdx1} non-treated animals was 8.8 weeks, whereas median survival of KIC^{pdx1}-1(S)-treated mice was 11 weeks (figure 6M). Together, these results illustrate that SK2 inhibition via Sig-1R ligand delays PDAC development and significantly extends survival, supporting 1(S) as a valuable therapeutic option to treat PDAC.

SK2 and Sig-1R expression in PDAC correlates with metastatic phenotype

To characterise the expression of Sig-1R in human PDAC, we interrogated publicly available gene expression datasets from 1017 patients with pancreatic carcinoma ((Dataset) online supplemental table S2). First, we found that SIGMAR1 (encoding Sig-1R: figure 7A) and KCNN2 genes (encoding SK2: figure 7B) were more expressed in metastases than in primary tumours, and preferentially in liver metastases. Second, in an analysis limited to the 925 primary cancers, SIGMAR1 expression, assessed as binary value (cut-off equal to median expression level), was not associated with patients' age and gender, pathological tumour type and grade, and American Joint Committee on Cancer stage (online supplemental table S3). Regarding the molecular subtypes (online supplemental table S4), no correlation existed between SIGMAR1 expression (figure 7C) and the (Dataset) Bailey *et al*'s classification[33] (pancreatic progenitor, immunogenic and squamous), the (Dataset) Collisson *et al*'s classification[34] (quasi-mesenchymal, classical) and the (Dataset) Moffitt *et al*'s classification[35] (basal, classical). By contrast, KCNN2 expression was higher in the squamous Bailey's subtype, the quasi-mesenchymal Collisson's subtype, and the basal Moffitt's tumour subtype (figure 7D). These results revealed higher gene expression of SK2 and Sig-1R in metastases versus primary cancers, and higher expression of SK2 in aggressive molecular subtypes.

DISCUSSION

The stromal compartment participates in PDAC onset, development and aggressiveness. However, recent studies refined the variety of stromal cellular components such as CAF, and

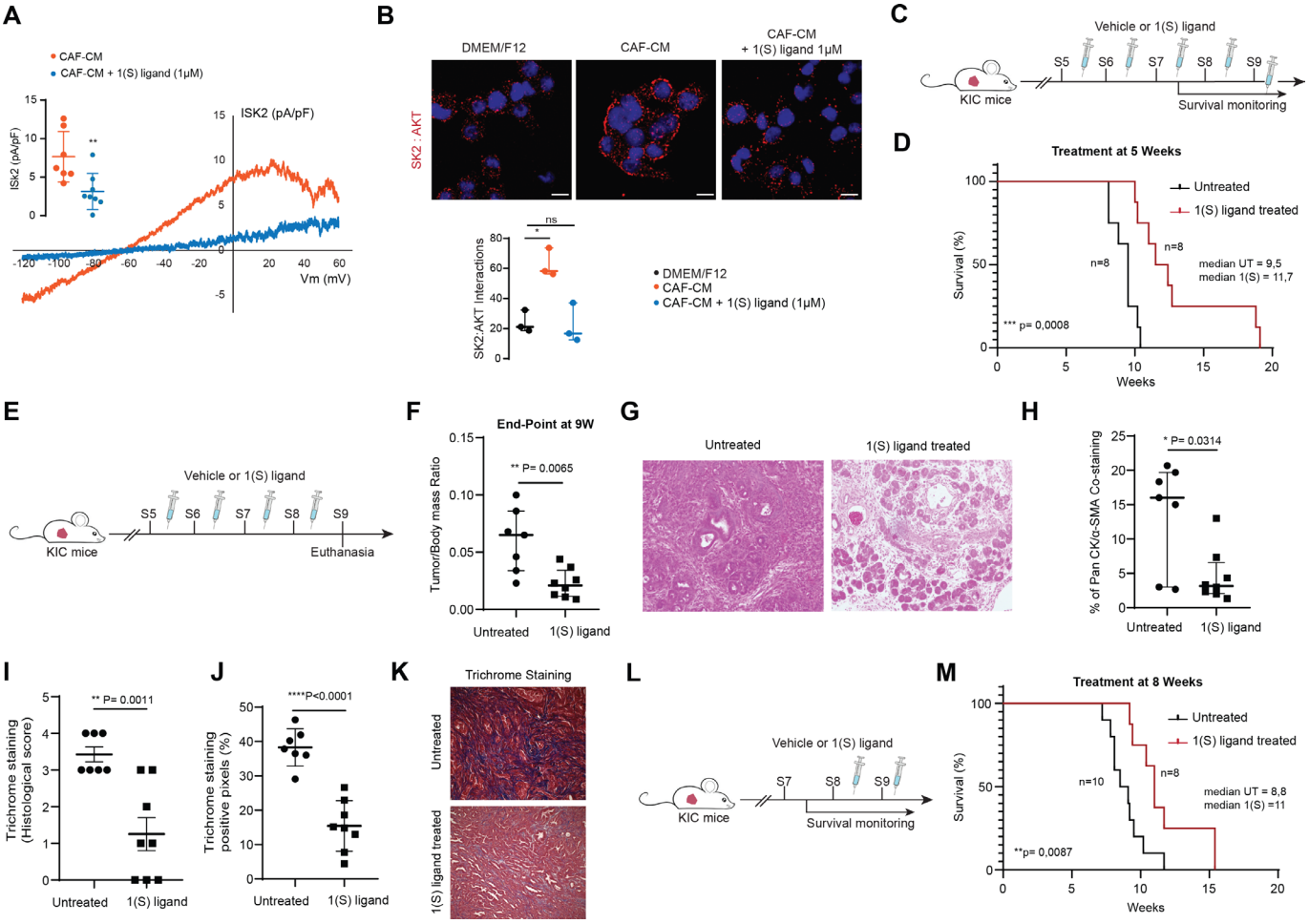

Figure 6 Sig-1R ligand 1(S) inhibits SK2 activity and reduces CAF secretome-induced aggressiveness. (A) Patch clamp recording of ISK2 in PANC-1 cells exposed to CAF-CM (n=7) or CAF-CM+1(S) ligand (1 µM; n=8) overnight. (B) PLA analysis of SK2/AKT interaction in ShRD PANC-1 cells, treated with control medium, CAF-CM or CAF-CM+1(S) ligand (1 µM; n=3) overnight. Scale bar: 10 µm. (C) Graphical scheme describing the KIC mice treatment workflow. KIC mice were injected at 5 weeks with vehicle or 1(S) ligand treatments, once a week until each animal reached clinical endpoint. (D) Kaplan-Meier survival of KIC mice treated with vehicle (n=8) or 1(S) ligand (n=8) from 5 weeks old. (E) Graphical scheme describing the KIC mice treatment workflow. KIC mice were injected at 5 weeks with vehicle or 1(S) ligand treatment, once a week until the animals were euthanised at 9 weeks old. (F) Graphs showing pancreatic tumour mass over body mass ratio at end point of 9 weeks for KIC mice treated with vehicle (n=7) or 1(S) ligand (n=8). (G) Representative pictures of H&E staining of KIC mice pancreatic tumours treated with vehicle or 1(S) ligand. (H) Graphs showing the percentage of pan CK labelled cells positive for α-SMA staining in control (untreated, n=7) and 1(S) ligand-treated mice (1(S) ligand, n=8). (I) Graphs showing the histological score of trichrome labelling in control (untreated, n=7) and 1(S) ligand-treated mice (1(S) ligand, n=8). (J) Graphs showing the percentage of trichrome staining positive pixels in control (untreated, n=7) and 1(S) ligand-treated mice (1(S) ligand, n=8). (K) Corresponding micrographs showing representative trichrome labelling in control (untreated) and treated animals (1(S) ligand treated). (L) Graphical scheme describing the KIC mice treatment workflow. KIC mice were injected at 8 weeks with vehicle or 1(S) ligand treatment, once a week until each animal reached clinical endpoint. (M) Kaplan-Meier survival of KIC mice treated with vehicle (n=10) or 1(S) ligand (n=8) from 8 weeks old. *p<0.05; **p<0.01; ***p<0.001. CAF, cancer-associated fibroblasts; ns, not significant; PLA, proximity ligation assay.

their abilities to potentially support or restrain PDAC progression.[1 5 6 36 37] This knowledge highlighted the necessity to precisely identify and target stromal cues and mechanisms that underlie the protumorous intercellular communication between CAF and PCC. Herein, the potassium channel SK2 was found to mediate intercellular communication between PCC and CAF by amplifying an EGFR–AKT axis on CAF secretome stimulation, promoting metastatic spreading and poor survival in pancreatic cancer. The association between SK2 and its partners is controlled by the ligand-modulated ion channel chaperone Sig-1R, which can be pharmacologically targeted to reduce CAF-induced tumourigenic processes particularly metastasis.

Interestingly, we have shown that exposure to CAF-CM induces an increase in SK2 current in PCC, suggesting that this channel participates in the CAF secretome mediated intercellular communication in PDAC. Several secreted factors from CAF, within PDAC stroma, like growth factors,[38] cytokines[7] and lipids,[8] were shown to mediate paracrine communication that stimulate PCC aggressive features. Our data show that the CAF-CM-mediated activation of SK2 was dependent on EGFR activity. Indeed, this effect was mimicked by EGF treatment and completely abolished using erlotinib. Surprisingly, we have been unable to detect EGF (or other EGFR ligands) in the CAF secretome. Looking deeper, we found that FN and collagen I, two major components of CAF-CM, activate a β1-integrin/EGFR/AKT signalling axis that increases SK2 activity in PCC. The abundant presence of FN and collagen I has been revealed in patients with stromal PDAC and mouse models samples[37 39] as well as

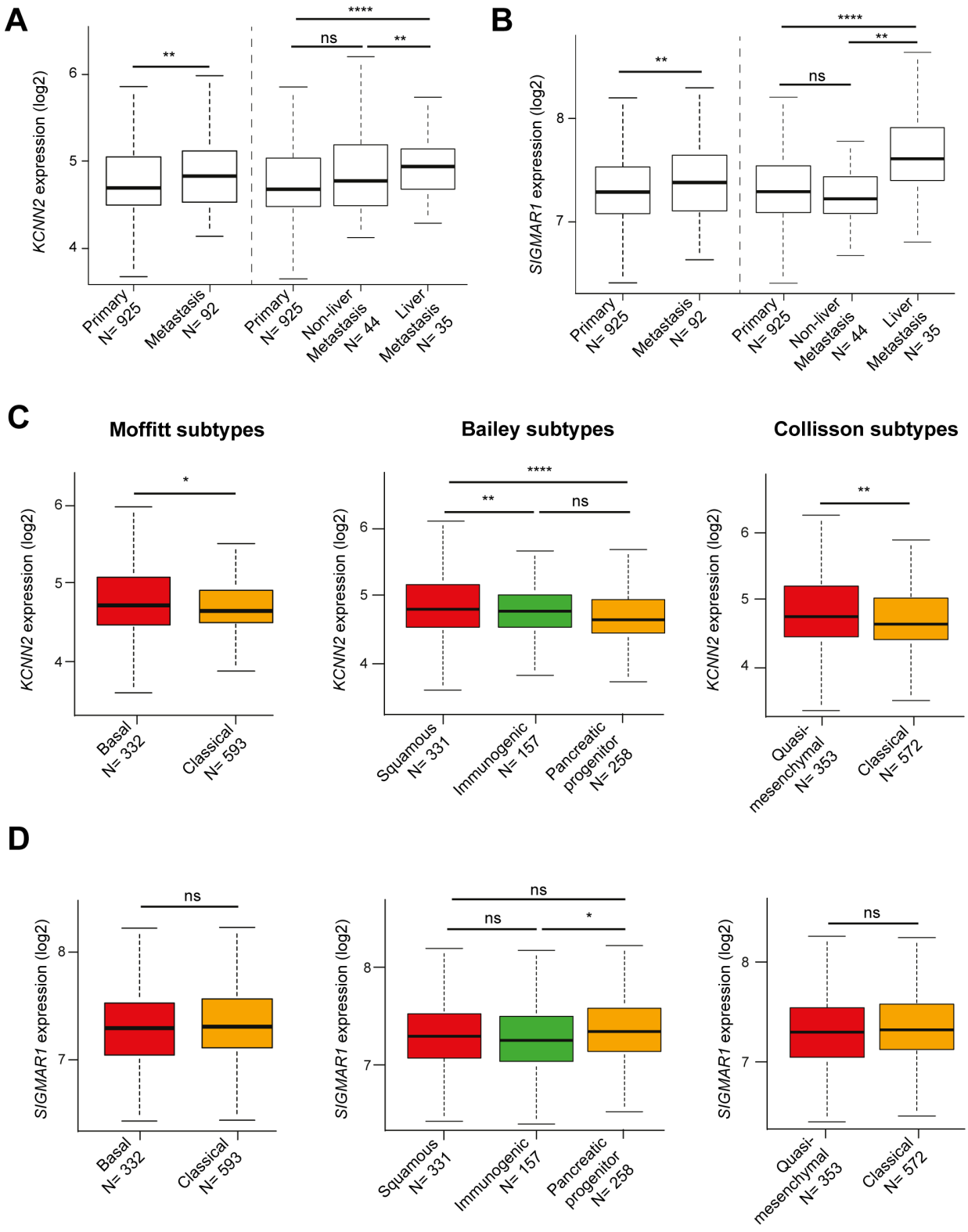

Figure 7 Gene expression of KCNN2 and SIGMAR1 in clinical PDAC samples. (A) Box plots of and *KCNN2* and (B) *SIGMAR1* expression (log2) in primary cancers versus metastases, and in liver metastases versus non-liver metastases. (C) Box plots of *KCNN2* and (D) *SIGMAR1* expression (log2) in primary cancers according to the molecular PDAC subtypes identified by Moffit *et al*[35] (left), Bailey *et al* (middle) and Collisson *et al* (right). For each box plot, median and ranges are indicated. Student t-test: *p<0.05; **p<0.01; ***p<0.001; ****p<0.0001. As shown in online supplemental table S4, these results remained similar and significant after adjustment for the estimated tumour cellularity (ESTIMATE algorithm, R-library, V.1.0.13), for both SIGMAR1 and KCNN2. ns: not significant; PDAC, pancreatic ductal adenocarcinoma.

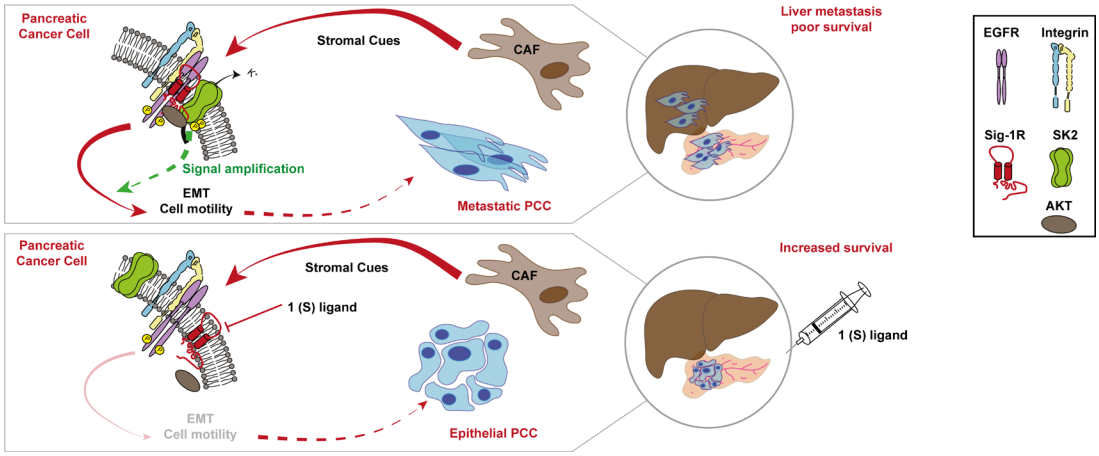

Figure 8 Schematic diagram showing the mechanism by which CAF secretome activates an SK2-dependent β1-integrin–EGFR–AKT signalling hub that promotes PCC aggressiveness. This mechanism can be pharmacologically targeted through Sig1-R to counteract the intercellular communication between CAF and PCC in PDAC. CAF, cancer-associated fibroblasts; EMT, epithelial-to-mesenchymal transition; PCC, pancreatic cancer cells; PDAC, pancreatic ductal adenocarcinoma.

in the secretome obtained from human primary CAF.[40] Several studies have demonstrated that FN and collagen I contribute to PCC aggressiveness, survival and chemoresistance.[24 41] These results strongly suggest a transactivation mechanism of EGFR, that has been previously reported as integrin-related and FAK-related in PDAC.[26 42] Our data support the idea that secretion of ECM components within PDAC microenvironment would be a key mediator in the CAF-stimulated formation of a signalling hub, including SK2, the β1-integrin, EGFR and AKT, that finely tunes the activity level of the downstream intracellular signalling pathway supporting PDAC development and metastasis formation.

SK2 seems to have a pivotal role in this signalling hub. Indeed, we reveal that the channel is a direct target of AKT, since we identified an AKT-specific motif within the channel sequence containing two serine residues that are phosphorylated on CAF-CM treatment (S568 and S569), both being necessary to mediate CAF-CM induced SK2 activity. We also found that the AKT-specific phosphorylation site in SK2 is highly conserved among species but lacks in the other members of the SK channel family (ie, SK1, SK3 and SK4), reinforcing the idea of a functional and specific coupling between SK2 and AKT-dependent pathways. Interestingly, we found that the channel phosphorylation by AKT stimulated the current by increasing its activity at subthreshold intracellular Ca^{2+} concentrations. These findings highlight an unexpected direct upregulation of SK2 activity by AKT.

EGFR activation is associated to AKT phosphorylation in PDAC[42 43] and the EGFR–PI3K–AKT signalling axis is one of the main signalling pathways involved in PDAC progression.[44] Therefore, we reasoned that the AKT-dependent activation of SK2 could be crucial in the integrin–EGFR–AKT axis. Our results, showing that SK2 silencing reduced CAF-dependent signalisation, suggest that without a functional channel, PCC remain in a subthreshold state that prevents the metastatic process despite stimulation by CAF. Accordingly, SK2 inhibition reversed the capacity of CAF to induce aggressiveness, and stabilised cells in an epithelial state. Thus, these data provide arguments to propose that SK2 sets an activation threshold that switches PCC from an epithelial state when SK2 activity is low, to a pro-invasive state when channel activity is high, underlined by EMT reprogramming. To support this model, SK2 silencing decreased CAF-induced cell invasiveness, tumour growth and metastasis formation in vivo. These results correlate with our investigation of human PDAC expression datasets revealing that SK2 expression is increased in liver metastasis compared with primary tumours, and that SK2 expression is significantly higher in the more aggressive subtype of PDAC cancer cells. Thus, these results highlighted SK2 as an ion channel playing a pivotal role in transducing extracellular signals from the tumour microenvironment onto intracellular activation of oncogenic signalling pathways in PCC.

Currently, the therapeutic armamentarium to treat PDAC is restricted and poorly efficient. A better understanding of the molecular components that participate in intercellular communication suggests novel strategies for treating PDAC. Here, we have shown that the ligand-modulated chaperone Sig-1R was required for the activation of SK2 current and the assembly of the SK2–AKT–β1-integrin–EGFR signalling hub on PCC stimulation by CAF. This observation is in line with previous studies showing that Sig-1R contributes to electrical remodelling by promoting channel/channel or channel/receptor associations.[13 14 45] Interestingly, Sig-1R silencing recapitulates the effects of SK2 silencing in vitro and in vivo.

On another hand, we have demonstrated that PCC treatment with the selective Sig-1R ligand 1(S) abolished CAF-CM-driven association between SK2 and AKT, underlying current inhibition. More importantly, pharmacological inhibition of Sig-1R was efficient in vivo as mouse models of PDAC treated with 1(S) dramatically delayed tumour development, reduced metastasis onset and extended survival. Although stromal ablation for PDAC treatment remains controversial, our results suggest a potential therapeutic opportunity by targeting an ion channel-dependent signalling hub through its regulator, Sig-1R, a druggable ion channel chaperone,[9 46] to reduce stromal-induced PDAC aggressiveness (figure 8). Because Sig-1R activity is stimulated by stress in diseased tissues,[47] the use of Sig-1R ligands should specifically target SK2 in tumours but not in brain or heart. In support of this, a recent study revealed that Sig-1R ligands modulate ion channels in cardiomyocytes from long QT syndrome patients but not in cardiomyocytes from isogenic controls.[12]

Prospective studies combining Sig-1R targeting with other therapeutic approaches, as chemotherapeutics agents, are necessary to evaluate their potential as long-term durable anti-PDAC

response. Further evaluation of the Sig-1R/SK2/CAF crosstalk in other solid tumours would open new avenues to consider channel and chaperone proteins targeting as anticancer therapeutic options.

Twitter Jérémy Nigri @jeremynigri, Richard Tomasini tomasini richard@TomasiniRichard and Olivier Soriani soriani olivier @OlivierSoriani

Acknowledgements We thank the Cancer Research Center of Marseille shared resources: Karim Sari and Regis Vitestelle for the PSEA (Platform for Stabling and Animal Experimentation) animal facility, Michel Baccini, Bernard Chetrit and Eric Orlandi for informatical support and Bruno Olivier and Tahagan Titus for technical assistance. We also thank the Prism imagery facility of the iBV (institut de Biologie Valrose): Baptiste Monterroso and Sameh Ben Aicha. We are grateful to Véronique Rigot and Frédéric André for the kind gift of Gi9 antibody.

Contributors RR-M, CBérenguier, BA, BL and OS performed patch clamp experiments and statistical analysis. RR-M, CBérenguier, BA, SST, BP and HG performed in vitro experiments, WB and related statistical analysis. SST, GE and ZH performed flow cytometry experiments and data analysis. SST, JN and RT performed in vivo experiments and related IHC and statistical analysis. FB established pancreatic ductal adenocarcinoma cell lines silences for SK2 or sigma-1 receptor and performed all proximity ligation assay experiments. PF, FB and ND performed in silico analysis. PM synthesised and provided 1(S) ligand. CBousquet provided the proteomic analysis of cancer-associated fibroblasts' secretum. RR-M, RT and OS conceived, designed, supervised, analysed and interpreted the study and provided critical review. OS is responsible for the overall content as guarantor.

Funding The work described in this paper was supported by grants from the Fondation de France (RT: 00087538; OS: 00038330 and 00059283), the French National Institute of Cancer (RT: INCA, PLBio13-134), La Ligue contre le Cancer (RR-M: GB/MA/IQ-10607 and GB/MA/CD/IQ-12187), Foundation ARC (RT: PJA20191209372; OS: PJA 2016 120 4740 and PJA 2019 120 9546; RR-M: PJA 2018 207701) and the Agence Nationale pour la Recherche (HG: ANR19-14-0049-01). JN was supported by Ministère de la Recherche and by Ligue contre le Cancer. CB was supported by the Fondation pour la Recherche Medicale. ST was supported by the French National Institute of Cancer (INCA, Pancreas 2017). BA was supported by the Ministère de la Recherche, de l'Enseignement Supérieur et de l'Innovation.

Competing interests None declared.

Patient and public involvement Patients and/or the public were not involved in the design, or conduct, or reporting, or dissemination plans of this research.

Patient consent for publication Not applicable.

Ethics approval The study was approved by our institutional board. All animal care and experimental procedures were performed in agreement with the Animal Ethics Committee of Marseille and the French ministry of research and innovation (reference number: Apafis#16 998–2018100814458519).

Provenance and peer review Not commissioned; externally peer reviewed.

Data availability statement Data are available in a public, open access repository.

ORCID iDs
Raphael Rapetti-Mauss http://orcid.org/0000-0002-3518-4845
Jérémy Nigri http://orcid.org/0000-0003-1358-1863
Zainab Hussain http://orcid.org/0000-0002-5641-5569
Corinne Bousquet http://orcid.org/0000-0002-2501-0593
Nelson Dusetti http://orcid.org/0000-0002-6161-8483
Richard Tomasini http://orcid.org/0000-0003-0869-0811
Olivier Soriani http://orcid.org/0000-0001-9485-3992

REFERENCES

1 Neesse A, Bauer CA, Öhlund D, *et al*. Stromal biology and therapy in pancreatic cancer: ready for clinical translation? *Gut* 2019;68:159–71.
2 Schnittert J, Bansal R, Prakash J. Targeting pancreatic stellate cells in cancer. *Trends Cancer* 2019;5:128–42.
3 Leca J, Martinez S, Lac S, *et al*. Cancer-associated fibroblast-derived annexin A6+ extracellular vesicles support pancreatic cancer aggressiveness. *J Clin Invest* 2016;126:4140–56.
4 Hwang RF, Moore T, Arumugam T, *et al*. Cancer-associated stromal fibroblasts promote pancreatic tumor progression. *Cancer Res* 2008;68:918–26.
5 Özdemir BC, Pentcheva-Hoang T, Carstens JL, *et al*. Depletion of carcinoma-associated fibroblasts and fibrosis induces immunosuppression and accelerates pancreas cancer with reduced survival. *Cancer Cell* 2014;25:719–34.
6 Rhim AD, Oberstein PE, Thomas DH, *et al*. Stromal elements act to restrain, rather than support, pancreatic ductal adenocarcinoma. *Cancer Cell* 2014;25:735–47.
7 Shi Y, Gao W, Lytle NK, *et al*. Targeting LIF-mediated paracrine interaction for pancreatic cancer therapy and monitoring. *Nature* 2019;569:131–5.
8 Auciello FR, Bulusu V, Oon C, *et al*. A stromal Lysolipid-Autotaxin signaling axis promotes pancreatic tumor progression. *Cancer Discov* 2019;9:617–27.
9 Kourrich S, Su T-P, Fujimoto M, *et al*. The sigma-1 receptor: roles in neuronal plasticity and disease. *Trends Neurosci* 2012;35:762–71.
10 Kourrich S, Hayashi T, Chuang J-Y, *et al*. Dynamic interaction between sigma-1 receptor and Kv1.2 shapes neuronal and behavioral responses to cocaine. *Cell* 2013;152:236–47.
11 Tsai S-Y, Hayashi T, Mori T, *et al*. Sigma-1 receptor chaperones and diseases. *Cent Nerv Syst Agents Med Chem* 2009;9:184–9.
12 Song L, Bekdash R, Morikawa K, *et al*. Sigma non-opioid receptor 1 is a potential therapeutic target for long QT syndrome. *Nat Cardiovasc Res* 2022;1:142–56.
13 Gueguinou M, Crottès D, Chantôme A, *et al*. The SigmaR1 chaperone drives breast and colorectal cancer cell migration by tuning SK3-dependent Ca^{2+} homeostasis. *Oncogene* 2017;36:3640–7.
14 Crottès D, Rapetti-Mauss R, Alcaraz-Perez F, *et al*. Sigmar1 regulates membrane electrical activity in response to extracellular matrix stimulation to drive cancer cell invasiveness. *Cancer Res* 2016;76:607–18.
15 Prevarskaya N, Skryma R, Shuba Y. Ion channels in cancer: are cancer hallmarks Oncochannelopathies? *Physiol Rev* 2018;98:559–621.
16 Pardo LA, Stühmer W. The roles of K(+) channels in cancer. *Nat Rev Cancer* 2014;14:39–48.
17 Crottès D, Lin Y-HT, Peters CJ, *et al*. TMEM16A controls EGF-induced calcium signaling implicated in pancreatic cancer prognosis. *Proc Natl Acad Sci U S A* 2019;116:13026–35.
18 Renaudo A, L'Hoste S, Guizouarn H, *et al*. Cancer cell cycle modulated by a functional coupling between sigma-1 receptors and Cl- channels. *J Biol Chem* 2007;282:2259–67.
19 Rapetti-Mauss R, Bustos V, Thomas W, *et al*. Bidirectional KCNQ1:β-catenin interaction drives colorectal cancer cell differentiation. *Proc Natl Acad Sci U S A* 2017;114:4159–64.
20 Zhou Y, Wong C-O, Cho K-jin, *et al*. Signal transduction. Membrane potential modulates plasma membrane phospholipid dynamics and K-Ras signaling. *Science* 2015;349:873–6.
21 Crottès D, Martial S, Rapetti-Mauss R, *et al*. Sig1R protein regulates hERG channel expression through a post-translational mechanism in leukemic cells. *J Biol Chem* 2011;286:27947–58.
22 Balasuriya D, Stewart AP, Crottès D, *et al*. The sigma-1 receptor binds to the Nav1.5 voltage-gated Na+ channel with 4-fold symmetry. *J Biol Chem* 2012;287:37021–9.
23 Jiang H, Hegde S, Knolhoff BL, *et al*. Targeting focal adhesion kinase renders pancreatic cancers responsive to checkpoint immunotherapy. *Nat Med* 2016;22:851–60.
24 Grzesiak JJ, Bouvet M. The alpha2beta1 integrin mediates the malignant phenotype on type I collagen in pancreatic cancer cell lines. *Br J Cancer* 2006;94:1311–9.
25 Zaghdoudi S, Decaup E, Belhabib I, *et al*. FAK activity in cancer-associated fibroblasts is a prognostic marker and a druggable key metastatic player in pancreatic cancer. *EMBO Mol Med* 2020;12:e12010.
26 Ricono JM, Huang M, Barnes LA, *et al*. Specific cross-talk between epidermal growth factor receptor and integrin alphavbeta5 promotes carcinoma cell invasion and metastasis. *Cancer Res* 2009;69:1383–91.
27 Rhim AD, Mirek ET, Aiello NM, *et al*. EMT and dissemination precede pancreatic tumor formation. *Cell* 2012;148:349–61.
28 Pastushenko I, Brisebarre A, Sifrim A, *et al*. Identification of the tumour transition states occurring during EMT. *Nature* 2018;556:463–8.
29 Stratford JK, Bentrem DJ, Anderson JM, *et al*. A six-gene signature predicts survival of patients with localized pancreatic ductal adenocarcinoma. *PLoS Med* 2010;7:e1000307.
30 Fiori ME, Di Franco S, Villanova L, *et al*. Cancer-associated fibroblasts as abettors of tumor progression at the crossroads of EMT and therapy resistance. *Mol Cancer* 2019;18:70.
31 Oxombre B, Lee-Chang C, Duhamel A, *et al*. High-affinity σ1 protein agonist reduces clinical and pathological signs of experimental autoimmune encephalomyelitis. *Br J Pharmacol* 2015;172:1769–82.
32 Collignon A, Silvy F, Robert S, *et al*. Dendritic cell-based vaccination: powerful resources of immature dendritic cells against pancreatic adenocarcinoma. *Oncoimmunology* 2018;7:e1504727.

33 Bailey P, Chang DK, Nones K, *et al*. Genomic analyses identify molecular subtypes of pancreatic cancer. *Nature* 2016;531:47–52.
34 Collisson EA, Sadanandam A, Olson P, *et al*. Subtypes of pancreatic ductal adenocarcinoma and their differing responses to therapy. *Nat Med* 2011;17:500–3.
35 Moffitt RA, Marayati R, Flate EL, *et al*. Virtual microdissection identifies distinct tumor- and stroma-specific subtypes of pancreatic ductal adenocarcinoma. *Nat Genet* 2015;47:1168–78.
36 Provenzano PP, Cuevas C, Chang AE, *et al*. Enzymatic targeting of the stroma ablates physical barriers to treatment of pancreatic ductal adenocarcinoma. *Cancer Cell* 2012;21:418–29.
37 Chen Y, Kim J, Yang S, *et al*. Type I collagen deletion in αSMA^{+} myofibroblasts augments immune suppression and accelerates progression of pancreatic cancer. *Cancer Cell* 2021;39:548–65.
38 Ligorio M, Sil S, Malagon-Lopez J, *et al*. Stromal microenvironment shapes the intratumoral architecture of pancreatic cancer. *Cell* 2019;178:160–75.
39 Jiang SH, Zhu LL, Zhang M. GABRP regulates chemokine signalling, macrophage recruitment and tumour progression in pancreatic cancer through tuning KCNN4-mediated Ca. *Gut* 2019.
40 Samain R, Brunel A, Douché T, *et al*. Pharmacologic normalization of pancreatic cancer-associated fibroblast secretome impairs prometastatic cross-talk with macrophages. *Cell Mol Gastroenterol Hepatol* 2021;11:1405–36.
41 Jagadeeshan S, Krishnamoorthy YR, Singhal M, *et al*. Transcriptional regulation of fibronectin by p21-activated kinase-1 modulates pancreatic tumorigenesis. *Oncogene* 2015;34:455–64.
42 Kim Y-J, Jung K, Baek D-S, *et al*. Co-targeting of EGF receptor and neuropilin-1 overcomes cetuximab resistance in pancreatic ductal adenocarcinoma with integrin β1-driven Src-Akt bypass signaling. *Oncogene* 2017;36:2543–52.
43 Navas C, Hernández-Porras I, Schuhmacher AJ, *et al*. EGF receptor signaling is essential for K-ras oncogene-driven pancreatic ductal adenocarcinoma. *Cancer Cell* 2012;22:318–30.
44 Ardito CM, Grüner BM, Takeuchi KK, *et al*. EGF receptor is required for KRAS-induced pancreatic tumorigenesis. *Cancer Cell* 2012;22:304–17.
45 Rodríguez-Muñoz M, Cortés-Montero E, Pozo-Rodrigálvarez A, *et al*. The ON:OFF switch, σ1R-HINT1 protein, controls GPCR-NMDA receptor cross-regulation: implications in neurological disorders. *Oncotarget* 2015;6:35458–77.
46 Abatematteo FS, Niso M, Contino M, *et al*. Multi-Target Directed Ligands (MTDLs) Binding the σ_1 Receptor as Promising Therapeutics: State of the Art and Perspectives. *Int J Mol Sci* 2021;22. doi:10.3390/ijms22126359. [Epub ahead of print: 14 Jun 2021].
47 Chu UB, Ruoho AE. Biochemical pharmacology of the sigma-1 receptor. *Mol Pharmacol* 2016;89:142–53.

Remerciements

Je voudrais remercier Hélène Guizouarn, ma directrice de thèse, avec qui j'ai eu la chance de travailler pendant ces quatre années. Merci infiniment pour ton soutien. Tu as su être à l'écoute et m'aider pour l'avancée de mes travaux. Merci de m'avoir formé, de m'avoir encadré, de m'avoir fait confiance et de m'avoir accompagné jusqu'au bout. Merci !

Merci à tous les membres de l'équipe Canaux Ioniques et Cancers :

Olivier Soriani, notre directeur d'équipe. Merci pour ton expertise ton l'aide lorsque les aspects fondamentaux de l'électrophysiologie pouvaient m'échapper.

Morgane Mignotet, notre ingénieur. Merci de ton aide pour la réalisation de ces travaux. Heureusement que tu étais là pour la bio mol !

Raphaël Rapetti-Mauss, mon ancien directeur de stage. Merci de m'avoir formé à cette merveilleuse technique qu'est le patch-clamp. Merci pour les gâteaux qui étaient bien trop souvent ratés... hmhm, Non ils étaient délicieux. Et le rhum (steak bien sûr). Et sans oublier… c'est la misère !

Franck Borgese. Merci pour ton aide quotidienne.

Bernard Pelissier. Ce fut un plaisir de travailler avec toi ! Ta bonne humeur et tes jeux de mots manquent à tout le monde.

Et bien sûr, merci Camille Berenguier, ma co-thésarde. On a rejoint cette équipe ensemble et on s'est soutenu jusqu'au bout. Merci de ton aide, aussi bien dans la vie professionnelle que privée (merci d'avoir pris soin de nos plantes :p). Nos discussions à la pause-café vont beaucoup me manquer... et les blagues qu'on a pu faire à ce pauvre Arnaud... Tu remercieras Nico l'expert en microscopie pour son aide ;).

Merci à tous ! et merci pour les binouzes, qui se sont faites rares sur la fin malheureusement.

Merci aux collègues du 4ème :

L'équipe de Guillaume Sandoz et notamment Brigitte pour son aide concernant la biologie moléculaire.

Arnaud, camarade de patch. C'était un plaisir de te côtoyer même si tu n'étais pas dans la bonne équipe... Désolé de pas avoir dit oui plus souvent pour les pauses-café du matin, nous on fait pas semblant de travailler chez les Soriani ! Désolé pour les pranks, la plupart du temps c'était Cam tu le sais très bien…

Merci à Serena, qui m'a fait découvrir le milieu de la recherche pour mon premier stage.

Je voudrais remercier tout particulièrement Wassim el Nemer et Stéphane Egée pour avoir accepté d'être mes rapporteurs. Merci également aux autres membres du jury : Sébastien Roger, Véronique Picard et Isabelle Mouro-Chanteloup.

…

Merci, à ma famille, ma mère, mon frère, dont la distance qui nous sépare n'a en rien entaché l'attachement que je vous porte.

Merci à Melba, mon chat. Tu ne liras probablement jamais cette thèse mais sache que malgré la haine immense que tu me voue, je t'apprécie quand même.
(Cette chatte me déteste pour une raison que j'ignore…)

Maël :
Merci à toi mon fils, si tu as le courage de lire cette thèse un jour… Tu es ma plus grande fierté.

Emilie :
Merci à toi mon amour, de m'avoir supporté pendant toutes ces années et de me supporter encore, ce travail est aussi le tien. Tu as été là pour moi dans les meilleurs et les mauvais moments, je t'ai suivi à une période de ma vie où mon chemin était encore incertain et… nous voilà. Merci <3.

On peut être fières de notre petit monstre :D

MERCI !

Rôle de l’interaction entre PIEZO1 et KCNN4 dans la physiopathologie érythrocytaire

Le globule rouge (GR) est la cellule la plus abondante du corps humain et assure le transport d’O_2 et de CO_2 tout en étant dépourvue de noyau et d'organelles. Durant ses 120 jours de vie le GR effectue plus de 200 000 passages dans la circulation, lors desquels il est soumis à d'intenses stress physiques, osmotiques et oxydatifs. La moindre défaillance face à ces stress peut le fragiliser et raccourcir son espérance de vie comme c’est le cas dans la Xérocytose Héréditaire (XH). La XH est une anémie hémolytique autosomique dominante qui touche 1/50 000 personnes. Elle est due à une altération de la perméabilité ionique et hydrique du GR, entraînant une hémolyse précoce par déshydratation. Cette maladie est causée génétiquement par des mutations gain de fonction sur deux canaux ioniques : PIEZO1 ou KCNN4, qui sont couplés fonctionnellement. PIEZO1 est un canal mécanosensible cationique non sélectif dont la découverte en 2010 est à l’origine du prix Nobel de médecine et physiologie en 2021. KCNN4 est un canal potassique sensible au calcium, responsable de l’effet « Gardos » découvert dans les années 1950. Fonctionnellement, l’activation de PIEZO1 induit une entrée de calcium dans le GR qui stimule KCNN4 dont l’ouverture permet au K^+ de sortir. Cette sortie de K^+ est accompagnée de Cl^- et d’eau osmotiquement liée. Il est donc proposé que la XH résulte d’une suractivation de PIEZO1 ou KCNN4 due aux mutations gain de fonction qui provoque une perte de KCl et d’eau ne pouvant pas être compensées car le GR humain est dépourvu de mécanisme de régulation de volume. Néanmoins, nous avons observé que la plupart des mutations gain de fonction sur KCNN4, qui est l’effecteur final de la déshydratation, ne sont pas associées à une déshydratation des GR contrairement aux mutations sur PIEZO1. C’est un paradoxe qui traduit la forte hétérogénéité phénotypique de la XH rendant le diagnostic long et difficile. Ce dernier repose bien souvent sur la nécessité de caractériser les mutations en laboratoire permettant de confirmer ou d’infirmer la pathogénicité d’une mutation. Mes travaux de thèse s’inscrivent dans ce contexte et visent à corréler le changement de fonctionnement des canaux PIEZO1 et KCNN4 induit par les mutations et le phénotype érythrocytaire des patients atteints d’anémie hémolytique héréditaire. En collaboration avec des cliniciens nous avons caractérisé de nombreuses nouvelles mutations portées par PIEZO1 ou KCNN4 dans des suspicions de XH. Nos résultats confirment la grande disparité de phénotype observée entre les mutations sur PIEZO1 ou KCNN4. Les méthodes d’analyse mises au point se sont avérées indispensables pour caractériser le phénotype des mutations à des fins diagnostic. Dans un contexte plus fondamental mes travaux ont permis de mieux comprendre les mécanismes qui sous-tendent le couplage fonctionnel entre PIEZO1 et KCNN4. Nous avons mis en évidence un nouveau mécanisme de régulation du canal KCNN4 par la pompe calcium ATP dépendante, PMCA. Ce mécanisme permet un découplage entre l’influx de Ca^{2+} dans le GR et l’activation du canal KCNN4 et donc la déshydratation. C’est une découverte majeure dans le contrôle de l’homéostasie hydrique des GR et une piste pour le traitement de la XH.

Mots clés : PIEZO1, KCNN4, Erythrocyte, Anémie, Electrophysiologie.